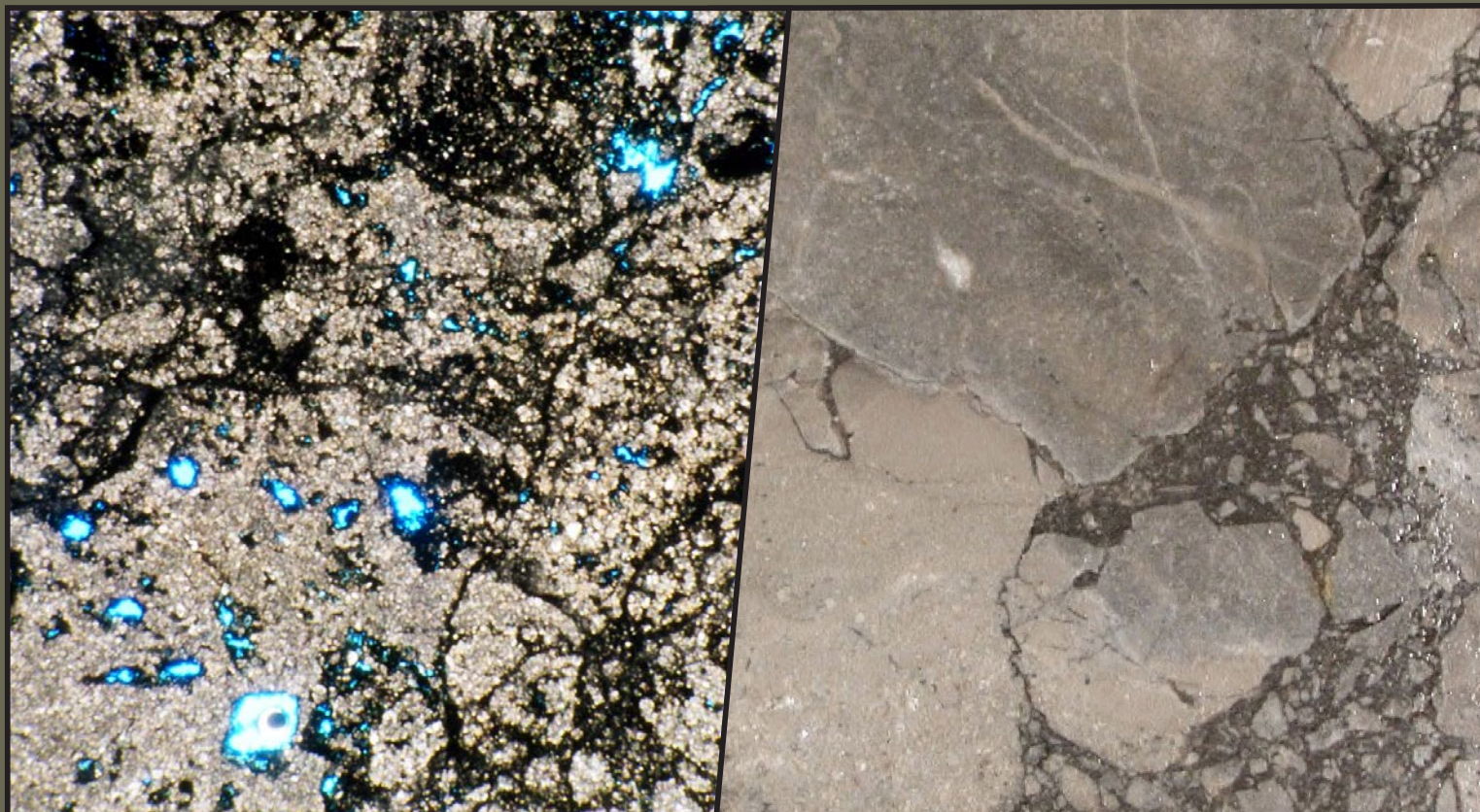


THE MISSISSIPPIAN LEADVILLE LIMESTONE OIL AND GAS PLAY, PARADOX BASIN, SOUTHEASTERN UTAH AND SOUTHWESTERN COLORADO—LISBON FIELD, REGIONAL, AND ANALOG STUDIES

Thomas C. Chidsey, Jr., Compiler and Editor



BULLETIN 139
UTAH GEOLOGICAL SURVEY
UTAH DEPARTMENT OF NATURAL RESOURCES
2020

Blank pages are intentional for printing purposes.

THE MISSISSIPPIAN LEADVILLE LIMESTONE OIL AND GAS PLAY, PARADOX BASIN, SOUTHEASTERN UTAH AND SOUTHWESTERN COLORADO—LISBON FIELD, REGIONAL, AND ANALOG STUDIES

Thomas C. Chidsey, Jr., Compiler and Editor

Cover photos: *Photomicrograph (left) under plane light, showing intensely brecciated dolomite within a bitumen-lined fracture zone. Mississippian Leadville Limestone, Lisbon field, San Juan County, Utah. Conventional core slab (right) showing a dolomite “autobreccia” in which the clasts have moved very little. The black material surrounding the in-place clasts is composed of porous late dolomite coated with pyrobitumen.*

Suggested citation:

Chidsey, T.C., Jr., compiler and editor, 2020, The Mississippian Leadville Limestone oil and gas play, Paradox Basin, southeastern Utah and southwestern Colorado—Lisbon field, regional, and analog studies: Utah Geological Survey Bulletin 139, 246 p., 9 appendices, <https://doi.org/10.34191/B-139>.



BULLETIN 139
UTAH GEOLOGICAL SURVEY
UTAH DEPARTMENT OF NATURAL RESOURCES
2020

STATE OF UTAH

Gary R. Herbert, Governor

DEPARTMENT OF NATURAL RESOURCES

Brian C. Steed, Executive Director

UTAH GEOLOGICAL SURVEY

R. William Keach II, Director

PUBLICATIONS

contact

Natural Resources Map & Bookstore

1594 W. North Temple

Salt Lake City, UT 84116

telephone: 801-537-3320

toll-free: 1-888-UTAH MAP

website: utahmapstore.com

email: geostore@utah.gov

UTAH GEOLOGICAL SURVEY

contact

1594 W. North Temple, Suite 3110

Salt Lake City, UT 84116

telephone: 801-537-3300

website: geology.utah.gov

Although this product represents the work of professional scientists, the Utah Department of Natural Resources, Utah Geological Survey, makes no warranty, expressed or implied, regarding its suitability for a particular use. The Utah Department of Natural Resources, Utah Geological Survey, shall not be liable under any circumstances for any direct, indirect, special, incidental, or consequential damages with respect to claims by users of this product.

The Utah Geological Survey does not endorse any products or manufacturers. Reference to any specific commercial product, process, service, or company by trade name, trademark, or otherwise, does not constitute endorsement or recommendation by the Utah Geological Survey.

CONTENTS

PREFACE	xv
ABSTRACT.....	xvi
CHAPTER 1: INTRODUCTION.....	1
OVERVIEW.....	3
BENEFITS AND POTENTIAL APPLICATION	3
GENERAL GEOLOGY OF THE PARADOX BASIN	4
CHAPTER 2: LISBON FIELD CASE STUDY, SAN JUAN COUNTY, UTAH—GENERAL FIELD CHARACTERISTICS AND RESERVOIR MAPPING	9
INTRODUCTION AND FIELD SYNOPSIS.....	11
LOG-BASED CORRELATION SCHEME.....	15
RESERVOIR MAPPING.....	15
CHAPTER 3: LITHOFACIES IN THE LEADVILLE LIMESTONE, LISBON FIELD CASE STUDY	29
REGIONAL SETTING OF THE LEADVILLE LIMESTONE	31
CORE DESCRIPTIONS.....	31
LISBON FIELD LITHOFACIES	31
Open Marine	31
Ooid and Peloid Shoals.....	35
Middle Shelf	37
CHAPTER 4: DIAGENETIC ANALYSIS OF THE LEADVILLE LIMESTONE, LISBON FIELD CASE STUDY	41
INTRODUCTION	43
BASIC THIN SECTION PETROGRAPHIC AND CORE PLUG PETROPHYSICAL ANALYSIS	43
Thin Section Description and Interpretation.....	43
Syntaxial Cement	43
Dolomitization and Porosity Development	43
Post-Burial Brecciation	48
Karst-Related Processes	48
Anhydrite and Sulfides	53
Late Macrocalcite.....	53
Porosity and Permeability Cross Plots.....	53
SCANNING ELECTRON MICROSCOPY.....	58
Porosity Types.....	58
Lithology, Diagenesis, and Cements	61
EPIFLUORESCENCE.....	61
Previous Work.....	61
Methodology.....	63
Epifluorescence Petrography of Leadville Limestone Thin Sections	66
Lisbon No. D-816 Well	66
Lisbon No. D-616 Well	66
Lisbon No. B-610 Well	66
Lisbon No. B-816 Well	66
Lisbon NW USA No. B-63 Well	66
CATHODOLUMINESCENCE.....	72
Methodology.....	72
Cathodoluminescence Petrography of Leadville Limestone Thin Sections	72
Lisbon No. D-816 Well	72
Lisbon No. B-816 Well	76
Lisbon No. D-616 Well	76
FLUID-INCLUSION SYSTEMATICS OF LISBON FIELD SAMPLES	76
Fluid-Inclusion Measurements	76
Caveats and Practical Aspects of Fluid-Inclusion Studies.....	80
Lisbon Fluid Inclusions	80
Fluid Inclusions in Early Calcite.....	80
Fluid Inclusions in Dolomite.....	83

Fluid Inclusions in Quartz	83
Fluid Inclusions in Late Calcite.....	88
Late Oil Inclusions	92
ISOTOPIC ANALYSIS	92
Stable Carbon and Oxygen	92
Methodology	92
Stable Carbon and Oxygen Isotopes for Leadville Limestone Samples at Lisbon Field	94
Strontium	94
Applications and Background	94
Strontium Isotope Age Curve for Marine Carbonate Rocks	98
Strontium Isotopes as Tracers for Diagenetic Fluids.....	99
Strontium Isotopic Ratios for Leadville Limestone Samples at Lisbon Field	99
Discussion	100
LEADVILLE LIMESTONE BURIAL HISTORY AND POSSIBLE HEAT SOURCES	101
CHAPTER 5: LEADVILLE LIMESTONE HYDROCARBON PLAY— GENERAL REGIONAL CHARACTERISTICS	105
INTRODUCTION	107
STRATIGRAPHY AND THICKNESS	107
PALEODEPOSITION AND LITHOLOGY	107
General Characteristics.....	107
Facies of the Paradox Fold and Fault Belt.....	117
HYDROCARBON TRAPS	118
Structural Setting	118
Trapping Mechanisms.....	118
Hydrocarbon Source and Seals.....	119
Hydrocarbon Potential	119
CHAPTER 6: POTENTIAL OIL-PRONE AREAS IN THE PARADOX FOLD AND FAULT BELT, UTAH, BASED ON SHOWS IN DRILL CUTTINGS USING EPIFLUORESCENCE MICROSCOPY TECHNIQUES	121
INTRODUCTION	123
SAMPLING COMPILATION, EXAMINATION, AND EVALUATION.....	123
DISCUSSION	123
CHAPTER 7: DEVONIAN/MISSISSIPPIAN AND PENNSYLVANIAN BRINE CHEMISTRY AND TRENDS WITHIN THE PARADOX BASIN, UTAH	131
INTRODUCTION	133
BRINE CHEMISTRY	133
Devonian/Mississippian Brines	133
Pennsylvanian Brines.....	133
DIRECTION OF BRINE MOVEMENT.....	135
SUMMARY	137
CHAPTER 8: REGIONAL MIDDLE PALEOZOIC HYDRODYNAMIC PRESSURE REGIME OF THE PARADOX BASIN, UTAH AND COLORADO	151
INTRODUCTION	153
Previous Work.....	153
Depth to the Mississippian and General Structure.....	153
DATA SOURCE AND METHODOLOGY	154
PRESSURE TRENDS BY QUADRANGLE	155
Glen Canyon Quadrangle	156
West Green River Quadrangle	156
Aneth Quadrangle	157
Lisbon Quadrangle.....	158
Dolores Quadrangle.....	165
Cortez Quadrangle.....	165
COMPOSITE MISSISSIPPIAN PRESSURE TREND.....	165
INTERPRETATION	165

CHAPTER 9: MODERN RESERVOIR ANALOGS FOR THE LEADVILLE LIMESTONE—SOUTHERN FLORIDA AND THE BAHAMAS	169
INTRODUCTION	171
BASIC PRINCIPLES OF CARBONATE DEPOSITION	171
Carbonate Factories and Platforms	171
Taphonomic Processes	172
Warm-Water Biologic Communities	173
Cyanobacteria	173
Protozoans	173
Plants	173
Invertebrates	173
SOUTHERN FLORIDA – FLORIDA BAY TO THE OUTER REEF	183
Florida Bay	183
Shallow Bay Basins (“Lakes”)	185
Mud Mounds (Mud Banks)	187
Reef Tract	187
Mud Mounds	188
Patch Reefs	188
Carbonate Sand Shoals	190
GREAT BAHAMA BANK – ANDROS ISLAND AREA	191
Basic Depositional Setting	191
Platform Facies	191
Ooid Shoals	191
Shallow-Shelf Lagoon	198
Carbonate Tidal Flats	198
CHAPTER 10: OUTCROP RESERVOIR ANALOGS FOR THE LEADVILLE LIMESTONE— SOUTHERN FLANK OF THE UINTA MOUNTAINS, UTAH	201
INTRODUCTION	203
SOUTHERN FLANK OF THE UINTA MOUNTAINS, UTAH	203
General Characteristics	203
Study Sites	208
Study Site 1 – South Fork Provo River	208
Study Site 2 – Dry Fork Canyon	211
Study Site 3 – Crouse Reservoir/Diamond Mountain Plateau	218
Discussion	218
CHAPTER 11: SUMMARY AND CONCLUSIONS	229
LISBON FIELD, SAN JUAN COUNTY, UTAH—A CASE STUDY OF LEADVILLE LIMESTONE LITHOFACIES AND DIAGENETIC HISTORY	231
Lithofacies	231
Diagenetic History	231
Scanning Electron Microscopy	231
Epifluorescence	232
Cathodoluminescence	232
Fluid Inclusions	233
Isotopic Analysis	233
Burial History and Possible Heat Sources	234
REGIONAL STUDIES OF THE MISSISSIPPIAN LEADVILLE LIMESTONE HYDROCARBON PLAY	234
General Regional Leadville Play Characteristics	234
Potential Oil-Prone Areas in the Paradox Fold and Fault Belt Based on Shows in Drill Cuttings Using Epifluorescence	
Microscopy Techniques	235
Devonian/Mississippian and Pennsylvanian Brine Chemistry and Trends within the Paradox Basin, Utah	235
Regional Middle Paleozoic Hydrodynamic Pressure Regime of the Paradox Basin, Utah and Colorado	235
MODERN AND OUTCROP ANALOGS FOR LEADVILLE LIMESTONE RESERVOIRS	236
Modern Reservoir Analogs—Southern Florida and the Bahamas	236
Outcrop Reservoir Analogs—Southern Flank of the Uinta Mountains, Utah	236

ACKNOWLEDGMENTS	237
REFERENCES	237
APPENDIX A: FIELD MAPS AND CROSS SECTIONS, LISBON FIELD, SAN JUAN COUNTY, UTAH.....	247
APPENDIX B: CORE DESCRIPTIONS, CORE PHOTOGRAPHS, AND CORE ANALYSIS, LISBON FIELD, SAN JUAN COUNTY, UTAH.....	248
APPENDIX C: GEOPHYSICAL WELL LOGS TIED TO CORE DESCRIPTIONS, LISBON FIELD, SAN JUAN COUNTY, UTAH.....	249
APPENDIX D: CATALOG OF LEADVILLE POROSITY TYPES AND DIAGENESIS, LISBON FIELD, SAN JUAN COUNTY, UTAH.....	250
APPENDIX E: SCANNING ELECTRON MICROSCOPY, EPIFLUORESCENCE, CATHODOLUMINESCENCE, AND FLUID INCLUSIONS, LISBON FIELD, SAN JUAN COUNTY, UTAH.....	251
APPENDIX F: EPIFLUORESCENCE ANALYSES AND DESCRIPTIONS OF WELLCUTTINGS FROM THE PARADOX FOLD AND FAULT BELT AREA, UTAH.....	252
APPENDIX G: REGIONAL STRATIGRAPHIC CROSS SECTIONS, PARADOX BASIN, UTAH	253
APPENDIX H: REGIONAL LEADVILLE FACIES AND CORE DESCRIPTIONS FROM WELLS IN THE PARADOX AND FAULT BELT AREA, UTAH.....	254
APPENDIX I: MEASURED STRATIGRAPHIC SECTIONS, MISSISSIPPIAN MADISON LIMESTONE, SOUTHERN FLANK OF THE UINTA MOUNTAINS	255

FIGURES

Figure 1.1. Regional setting of the Paradox Basin and oil and gas fields.....	4
Figure 1.2. Stratigraphic section for the central Paradox Basin	5
Figure 1.3. Fields producing from the Mississippian Leadville Limestone, and thickness of the Leadville, Utah and Colorado.....	6
Figure 1.4. Schematic block diagram of basement-involved structural traps for the Leadville Limestone fields.....	7
Figure 2.1. General surface geology of the Lisbon field area.....	12
Figure 2.2. Cross section through the Lisbon and Lightning Draw Southeast fields.....	13
Figure 2.3. Map of top of structure, Leadville Limestone, Lisbon field.....	14
Figure 2.4. Schematic east-west structural cross section through Lisbon field	14
Figure 2.5. Typical gamma ray-sonic log, Leadville Limestone, Lisbon field discovery well.....	16
Figure 2.6. Isochore of zone 1, Leadville Limestone, Lisbon field	17
Figure 2.7. Isochore of zone 2, Leadville Limestone, Lisbon field	18
Figure 2.8. Isochore of zone 3, Leadville Limestone, Lisbon field	19
Figure 2.9. Isochore of zone 4, Leadville Limestone, Lisbon field	20
Figure 2.10. Zone 1 porosity, Leadville Limestone, Lisbon field.....	21
Figure 2.11. Zone 2 porosity, Leadville Limestone, Lisbon field.....	22
Figure 2.12. Zone 3 porosity, Leadville Limestone, Lisbon field.....	23
Figure 2.13. Zone 4 porosity, Leadville Limestone, Lisbon field.....	24
Figure 2.14. Bottom-hole temperature, Leadville Limestone, Lisbon field.....	25
Figure 2.15. Initial flowing potential, Leadville Limestone, Lisbon field	26
Figure 2.16. Cumulative oil production, Leadville Limestone, Lisbon field.....	27
Figure 3.1. Paleogeography of Utah during the Mississippian.....	32
Figure 3.2. Block diagram displaying major depositional facies for the Leadville Limestone, Lisbon field.....	33
Figure 3.3. Block diagram displaying post-Leadville karst and fracture overprint.....	33
Figure 3.4. Typical Leadville vertical sequence from Lisbon field, including geophysical well logs, porosity/permeability plots, and core description.....	34
Figure 3.5. Core photographs showing high-energy, open-marine crinoidal shoal facies.....	36
Figure 3.6. Core photographs showing moderate-to low-energy, open-marine, Waulsortian-type buildup facies.....	37
Figure 3.7. Core photograph showing moderate-energy, open-marine, shoal-flank facies	38
Figure 3.8. Core photograph showing moderate-energy, restricted-marine, “hard” peloid shoal facies	38
Figure 3.9. Core photograph showing low-energy, middle-shelf facies	39
Figure 4.1. Ideal diagenetic sequence through time, Leadville Limestone, Lisbon field	44
Figure 4.2. Classification of pores and pore systems in carbonate rocks.....	45
Figure 4.3. Lisbon No. D-816 well – conventional core slab showing partially dolomitized crinoidal grainstone/packstone, and photomicrograph showing early syntaxial overgrowths on crinoid ossicles	46

Figure 4.4. Lisbon No. D-816 well – conventional core slab of early and late dolomite, photomicrograph of finely crystalline dolomite with isolated grain molds, and photomicrograph of coarse replacement dolomite	47
Figure 4.5. Photomicrograph showing saddle dolomite cement filling large pore, Lisbon No. D-816 well	48
Figure 4.6. Lisbon NW USA No. B-63 well – conventional core slab showing a dolomite autobreccia, thin section of low-porosity dolomite clasts surrounded by solution-enlarged fractures, and thin section of black, porous, dolomite clasts surrounded by coarse, low-porosity saddle dolomites	49
Figure 4.7. Lisbon No. D-816 well – conventional core slab of a dolomitized, packstone/wackestone with swarms of fractures marked by black, coarse dolomite, and photomicrograph showing highly deformed and brecciated dolomite within a bitumen-lined fracture zone.....	50
Figure 4.8. Lisbon No. D-816 well – photomicrograph showing intensely brecciated dolomite within a bitumen-lined fracture zone, and photomicrograph showing large autoclasts and bitumen in an intensely brecciated dolomite	51
Figure 4.9. Karst-related processes from the Lisbon No. D-616 well – conventional core slab of a limey grainstone with a dolomitized sediment-filled cavity, low magnification photomicrographs showing the contact between limestone matrix and dolomitized and siliciclastic karst-cavity filling, and higher magnification photomicrograph of detrital quartz grains and small carbonate clasts within dolomitized mud-filled karst cavity	52
Figure 4.10. Lisbon No. D-816 well photomicrograph showing lathes of late anhydrite cement filling a dissolution pore.....	53
Figure 4.11. Possible sulfide mineralization from the Lisbon No. D-816 well – photomicrograph showing moldic pore lined black pyrobitumen and possible sulfide minerals, and photomicrograph showing black pyrobitumen and sulfide minerals on and between rhombic dolomite crystals	54
Figure 4.12. Late calcite from the Northwest Lisbon No. B-63 well – photomicrograph showing saddle dolomite crystals and a single late macrocalcite crystal filling part of a large dissolution pore, photomicrograph showing saddle replacement dolomite, pyrobitumen, and late macrocalcite, and dissolution pores filled completely with bitumen and late macrocalcite that resemble saddle dolomite molds	55
Figure 4.13. Lisbon Unit No. B-610 well permeability versus porosity cross plot by diagenesis	56
Figure 4.14. Lisbon Unit No. B-816 well permeability versus porosity cross plot by diagenesis	56
Figure 4.15. Lisbon Unit No. D-816 well permeability versus porosity cross plot by diagenesis	57
Figure 4.16. Lisbon Unit No. D-616 well permeability versus porosity cross plot by diagenesis	57
Figure 4.17. Lisbon Unit No. B-63 well permeability versus porosity cross plot by diagenesis	58
Figure 4.18. Scanning electron microscope photomicrograph showing typical Leadville dolomite crystals at Lisbon field	59
Figure 4.19. Scanning electron microscope photomicrograph showing probable pyrobitumen coating the rhombic dolomite	60
Figure 4.20. Scanning electron microscope photomicrograph showing enlargement of a fracture partially filled with secondary dolomite	60
Figure 4.21. Scanning electron microscope photomicrograph showing the composition of typical replacement rhombic dolomite, and showing poorly crystalline, an early dolomite core and dense overgrowth that forms the dolomite into coarser rhombs	62
Figure 4.22. Scanning electron microscope photomicrograph showing anhydrite cement lathes partially filling a small dissolution vug	63
Figure 4.23. Scanning electron microscope photomicrographs showing euhedral quartz void fillings within late dissolution pores.....	64
Figure 4.24. Scanning electron microscope photomicrograph showing possible sulfide minerals on large dolomite rhombs	65
Figure 4.25. Generalized microscope optical configuration for observing fluorescence under incident light	65
Figure 4.26. Photomicrographs showing fluorescence zonation within coarse dolomite crystals, and same field of view under plane light showing bitumen masking crystal boundaries of dolomite.....	67
Figure 4.27. Photomicrographs fine- to medium-sized crystals of replacement dolomite using epifluorescence, and same field of view under plane light.....	68
Figure 4.28. Photomicrographs showing yellow-fluorescing dolomite rhombs “floating” in a non-fluorescing dolomite matrix, and same field of view under plane light	69
Figure 4.29. Photomicrographs showing zoned, rhombic replacement dolomite with dead cores and highly fluorescent rims, and same field of view under plane light	70
Figure 4.30. Photomicrographs showing dolomitized detrital fill within a karst cavity under epifluorescence, and same field of view under plane light.....	71
Figure 4.31. Generalized microscope optical configuration for observing cathodoluminescence	73
Figure 4.32. Cathodoluminescence setup used for the Leadville samples from Lisbon field	74
Figure 4.33. Photomicrographs of outlines between the dolomite crystals and adjoining pore spaces using cathodoluminescence and plane light	75
Figure 4.34. Photomicrographs showing zonation in dolomite crystals under cathodoluminescence, and replacement dolomite and saddle dolomite under plane light	77

Figure 4.35. Photomicrographs showing early replacement dolomite that displays intense red luminescence, and large dolomite crystals under play light displaying sweeping extinction and curved crystal faces that are probable saddle dolomites	78
Figure 4.36. Photomicrograph showing sharp contact between bright red luminescing dolomite and orangish luminescing limestone	79
Figure 4.37. Schematic diagram of basic fluid inclusion types	79
Figure 4.38. Early mottled-appearing calcite due to abundant fluid inclusions.....	81
Figure 4.39. Fluid inclusions in early calcite with different liquid to vapor ratios resulting from necking after trapping.....	81
Figure 4.40. Brown primary oil inclusion and clear aqueous inclusions in calcite	82
Figure 4.41. Primary oil inclusion in calcite.....	82
Figure 4.42. Ice-melting temperatures of fluid inclusions in early calcite.....	83
Figure 4.43. Cloudy-appearing dolomite crystals due to abundant fluid inclusions.....	84
Figure 4.44. Ice-melting temperatures of dolomite-hosted fluid inclusions	84
Figure 4.45. Oil inclusions in saddle dolomite	85
Figure 4.46. Saddle dolomite showing truncated dark growth zones	85
Figure 4.47. Homogenization temperatures of oil inclusions trapped in saddle dolomite	86
Figure 4.48. Quartz crystals partially filling a cavity in dolomite	86
Figure 4.49. Quartz encapsulating dolomite.....	87
Figure 4.50. Encapsulated anhydrite in coarse-grained quartz crystal	87
Figure 4.51. Two-phase, liquid-rich inclusions defining a growth zone in the interior of a quartz crystal	88
Figure 4.52. Primary liquid-rich inclusions and anhydrite inclusions in quartz.....	89
Figure 4.53. Coexisting primary liquid- and gas-rich inclusions in quartz	89
Figure 4.54. Homogenization and ice-melting temperatures of quartz-hosted aqueous inclusions	90
Figure 4.55. Corroded and dissolved dolomite encapsulated in calcite.....	90
Figure 4.56. Image showing coarse-grained calcite postdating quartz and dolomite.....	91
Figure 4.57. Ice-melting temperatures of late, calcite-hosted fluid inclusions	91
Figure 4.58. Comparison of ice-melting temperatures of fluid inclusions in calcite and quartz	92
Figure 4.59. Secondary oil inclusions in late calcite	93
Figure 4.60. Secondary oil inclusions in calcite	93
Figure 4.61. Comparison of homogenization temperatures of primary and secondary oil inclusions in calcite.....	94
Figure 4.62. Comparison of homogenization temperatures of oil inclusions in calcite and saddle dolomite	94
Figure 4.63. Carbon versus oxygen isotope compositions	95
Figure 4.64. The Colorado School of Mines stable isotope ratio mass spectrometer.....	96
Figure 4.65. MultiPrep for high-precision dual-inlet analysis of carbon and oxygen isotopes.....	96
Figure 4.66. Stable carbon versus oxygen isotopic compositions for Leadville dolomite and calcite for Lisbon field	97
Figure 4.67. Cross plot of the $\delta^{13}\text{C}/\delta^{18}\text{O}$ Leadville Limestone data, Lisbon field.....	97
Figure 4.68. Stable oxygen isotope for dolomites versus temperature, Lisbon field.....	98
Figure 4.69. Strontium isotope seawater composition curve.....	99
Figure 4.70. Strontium isotope compositions of saddle dolomites from the Canadian Rockies and Michigan Basin.....	100
Figure 4.71. Strontium isotope composition for Leadville Limestone samples at Lisbon field along with the Phanerozoic marine carbonate curve for Sr ratios	101
Figure 4.72. Possible heat sources and convection cells for late dolomitization of the Leadville Limestone in Lisbon field.....	102
Figure 4.73. Strontium isotope values for limestone and dolomite of the Ordovician Trenton Formation and anhydrite and brine from the Silurian Salina Formation.....	102
Figure 4.74. Burial history and temperature profile for Lisbon field	103
Figure 4.75. Burial history and temperature profiles with inferred diagenetic windows at Lisbon field.....	103
Figure 4.76. Top of structure of the Leadville Limestone, Lisbon field, showing possible thermal convection cells	104
Figure 5.1. Devonian through Middle Pennsylvanian stratigraphic column, Paradox Basin	108
Figure 5.2. Thickness of the Leadville Limestone and location of cores from regional exploration wells and Leadville fields used in the study	109
Figure 5.3. North-south stratigraphic cross section through the Utah part of the Paradox Basin showing regional Paleozoic correlations	110
Figure 5.4. East-west stratigraphic cross section through the Utah part of the Paradox Basin showing regional Paleozoic correlations	111
Figure 5.5. Paleogeographic map of Utah showing approximate present thicknesses of deposits of the late Kinderhookian to early Meramecian time.....	112

Figure 5.6. Paleogeographic map of the southwest United States during the Early Mississippian.....	113
Figure 5.7. Diorama of a Mississippian crinoid meadow	113
Figure 5.8. Cores displaying Leadville open marine facies.....	114
Figure 5.9. Paleogeographic map of Utah showing approximate present thicknesses of deposits of the late Meramecian to late Chesterian time.....	115
Figure 5.10. Paleogeographic map of the western United States during the Late Mississippian to Early Pennsylvanian	116
Figure 5.11. Map showing depositional facies profiles determined from regional cores used in the study	117
Figure 5.12. Very generalized facies map of the Leadville Limestone, northern Paradox Basin, based on inferred average depositional profiles	118
Figure 5.13. Top of structure of Leadville Limestone, Big Flat field, Grand County, Utah	119
Figure 6.1. Examples of cuttings selected from various Leadville zones as observed with a binocular microscope	124
Figure 6.2. Selected cuttings from various Leadville zones placed on Petrologs™ for epifluorescence examination	125
Figure 6.3. Petrographic characteristics of cuttings selected from various Leadville zones as observed with a binocular microscope	127
Figure 6.4. Photomicrographs showing examples of visually rated epifluorescence	128
Figure 6.5. Map of the highest maximum epifluorescence based on visual rating of well cuttings, Paradox fold and fault belt, Utah.....	129
Figure 6.6. Map of the highest average epifluorescence based on visual rating of well cuttings, Paradox fold and fault belt, Utah	130
Figure 7.1. Well used for Devonian/Mississippian brine analyses and oil and gas fields in the Paradox Basin, Utah.....	134
Figure 7.2. Elevation of the top of the sampled interval for the Devonian/Mississippian brine samples	135
Figure 7.3. Piper diagrams for Devonian and Mississippian brines in the Paradox Basin and vicinity, Utah	136
Figure 7.4. Stiff diagrams for Devonian and Mississippian brines in the Paradox Basin and vicinity, Utah.....	137
Figure 7.5. Scatter plots showing sample interval elevation top, and sodium, magnesium, and calcium contents versus geographic location for Devonian/Mississippian samples.....	138
Figure 7.6. Scatter plots of chloride, sulfate, bicarbonate, and total dissolved solids versus geographic location for Devonian/Mississippian samples	140
Figure 7.7. Wells used for Pennsylvanian brine analyses and oil and gas fields in the Paradox Basin, Utah	142
Figure 7.8. Elevation of the sampled interval top of for Pennsylvanian brine samples	143
Figure 7.9. Piper diagram for Pennsylvanian brines in the Paradox Basin by county.....	143
Figure 7.10. Stiff diagrams for Pennsylvanian brines in the Paradox Basin and vicinity, Utah.....	144
Figure 7.11. Scatter plots showing sample interval elevation top, and sodium, magnesium, and calcium contents versus geographic location for Pennsylvanian samples	145
Figure 7.12. Scatter plots of chloride, sulfate, bicarbonate, and total dissolved solids versus geographic location for Pennsylvanian samples.....	147
Figure 8.1. Potentiometric map for the Mississippian stratigraphic section derived from oil and gas DST pressure data through 1961	154
Figure 8.2. Stratigraphic section for the central Paradox Basin near Monticello, Utah	155
Figure 8.3. Depth to top of the Mississippian Leadville Limestone derived from oil and gas exploration wells	156
Figure 8.4. Structural contours on the top of the Leadville Limestone derived from oil and gas exploration wells.....	157
Figure 8.5. Subdivision of the Paradox Basin into six, 1° by 1° quadrangles, for which DST pressure data are consolidated.....	158
Figure 8.6. Location of wells with DST measurements from the Mississippian (and older) strata within the Glen Canyon quadrangle, and pressure trend graph.....	159
Figure 8.7. Location of wells with DST measurements from the Mississippian (and older) strata within the West Green River quadrangle, and pressure trend graph.....	160
Figure 8.8. Location of wells with DST measurements from the Mississippian (and older) strata within the Aneth quadrangle, and pressure trend graph.....	161
Figure 8.9. Location of wells with DST measurements from the Mississippian (and older) strata within the Lisbon quadrangle, and pressure trend graph.....	162
Figure 8.10. Location of wells with DST measurements from the Mississippian (and older) strata within the Dolores quadrangle, and pressure trend graph.....	163
Figure 8.11. Location of wells with DST measurements from the Mississippian (and older) strata within the Cortez quadrangle, and pressure trend	164
Figure 8.12. Compilation of DST pressure measurements from all six quadrangles for the Mississippian and older formations	166
Figure 8.13. Distribution of pressure differences between the actual DST pressure measurement and the pressure inferred from the composite line for that elevation.....	166

Figure 8.14. Summary of the region of anomalous pressures for Mississippian and older rocks of the Paradox Basin	167
Figure 9.1. Satellite image of southern Florida and the Bahama Islands	172
Figure 9.2. Microbial mats in a supratidal environment on Cotton Key, Florida Bay	174
Figure 9.3. Foraminifera attached to sea grass, Florida Bay	175
Figure 9.4. Green algae <i>Halimeda</i> and <i>Penicillus</i> growing on the sandy bottom of Florida Bay	175
Figure 9.5. <i>Halimeda</i> and the sand grains it makes	176
Figure 9.6. Mud-making green algae <i>Penicillus</i> , <i>Udotea</i> , and <i>Rhiphocephalus</i>	176
Figure 9.7. Branching red algae <i>Neogoniolithon</i> near Rodriguez Bank, Florida	177
Figure 9.8. Turtle grass (<i>Thalassia</i>) illustrating its ability to act as a sediment trap, Florida Bay	177
Figure 9.9. Red mangrove (<i>Rhizophora mangle</i>), Florida Bay area	178
Figure 9.10. Black mangrove (<i>Avecinnia</i>), Florida Bay area	179
Figure 9.11. Branching fire coral <i>Millepora</i>	180
Figure 9.12. Alcyonarian sea fans and sea whips	180
Figure 9.13. Scleractinian moosehorn, elkhorn, finger, star, brain, golfball, and rose corals	181
Figure 9.14. Gastropods on carbonate tidal-flat muds, northwestern side of Andros Island, Bahamas	182
Figure 9.15. Numerous mounds made by the burrowing shrimp <i>Callinassa</i> , Bahamas	182
Figure 9.16. Typical grain-making sand dollar echinoid	183
Figure 9.17. Features of the southern Florida carbonate platform	184
Figure 9.18. Generalized northwest-southeast cross section through the southern Florida carbonate platform	185
Figure 9.19. Oblique aerial view of Florida Bay shallow bay basins, mud mounds, and islands	186
Figure 9.20. Florida Bay from sea level of a shallow bay basin and islands	186
Figure 9.21. Coarse, shelly sediment from the shallow bay basin near Sign Bank, Florida Bay	187
Figure 9.22. Generalized cross section through a typical Florida Bay mud mound	188
Figure 9.23. Generalized map of sediments and environments of Rodriguez Key	189
Figure 9.24. Clean, rippled, calcareous sands of the White Bank sand shoal	190
Figure 9.25. Coarse, clean skeletal (primarily coral) sand grains, White Bank sand shoal	190
Figure 9.26. Satellite image of the Great Bahama Bank and its physiographic features	192
Figure 9.27. Generalized facies map of the Great Bahama Bank	193
Figure 9.28. Biological communities on the Great Bahama Bank	194
Figure 9.29. Satellite image of the Joulter's Cay ooid shoal complex and northern end of Andros Island	195
Figure 9.30. Features of Joulter's Cay ooid shoal complex	196
Figure 9.31. Great Bahama Bank shelf lagoon, Red Bay and pellet shoals, and pellet-bearing muds undergoing early marine dolomitization	199
Figure 9.32. Features of carbonate tidal flats, Three Creeks area, northwestern side of Andros Island	200
Figure 10.1. Mississippian outcrop and geologic map showing reservoir analogs in Utah and Uinta Mountain study sites	204
Figure 10.2. Lithologic column of a part of the Paleozoic section along the western end of the southern flank of the Uinta Mountains	206
Figure 10.3. Lithologic column of a part of the Paleozoic section along the eastern end of the southern flank of the Uinta Mountains	206
Figure 10.4. Mississippian Deseret Limestone, North Fork of the Duchesne River, Utah	207
Figure 10.5. Characteristics of the Mississippian Madison Limestone along the southern flank of the Uinta Mountains, Whiterocks Canyon, Utah	208
Figure 10.6. Location of study site 1, South Fork Provo River	209
Figure 10.7. Large breccia pipe penetrating the Deseret Limestone at study site 1	210
Figure 10.8. Typical characteristics of the Deseret Limestone at study site 1	211
Figure 10.9. Characteristics of the breccia pipe at study site 1	212
Figure 10.10. Possible paleokarst characteristics at study site 1	213
Figure 10.11. Location of the study site 2, Dry Fork	214
Figure 10.12. Madison Limestone stratigraphic column and outcrop section at study site 2	215
Figure 10.13. Examples of Madison Limestone lithofacies from study site 2	216
Figure 10.14. Megabreccia in study site 2	219
Figure 10.15. High-amplitude stylolites in bioturbated mudstone	220
Figure 10.16. Location of study site 3, Crouse Reservoir/Diamond Mountain Plateau	221
Figure 10.17. Madison Limestone stratigraphic column and outcrop section at study site 3	222
Figure 10.18. Examples of Madison Limestone lithofacies from study site 3	223
Figure 10.19. Topographic depressions (sags) at the sites of major breccia zones in Madison Limestone at study site 3	224
Figure 10.20. Slabbed specimen of highly brecciated rock from study site 3	224

Figure 10.21. Coarse calcite vein in a highly brecciated dolomitic matrix	225
Figure 10.22. Photomicrographs from breccia samples at study site 3	226
Figure 10.23. Basal Cambrian Lodore Formation	227

TABLES

Table 2.1. General characteristics of the oil and gas produced from the Leadville Limestone at Lisbon field.....	15
Table 3.1. Conventionally slabbed well core examined and described from the Leadville Limestone, Lisbon field.....	33
Table 4.1. Summary of characteristics observed with scanning electron microscopy in samples from Lisbon field.....	59
Table 4.2. Stable carbon and oxygen isotope data from the Mississippian Leadville Limestone, Lisbon field core samples.....	95
Table 4.3. Strontium isotopic data from the Lisbon NW USA No. B-63 well core samples.....	100
Table 6.1. Wells in the Paradox fold and fault belt, Utah, containing Leadville Limestone cuttings evaluated using epifluorescence techniques	126
Table 6.2. Key to the epifluorescence qualitative visual “rating” scale.....	127
Table 7.1. Averaged ground elevation, top and bottom elevation of the sampled interval, TDS, and ions for individual counties, and for township intervals within San Juan County, Utah.....	149
Table 7.2. Total dissolved solids and ions on a dry-weight-percent basis for brines from the Paradox Basin, Utah	149

PREFACE

The Mississippian Leadville Limestone is a major producer of oil and gas in the Paradox Basin of southeastern Utah and southwestern Colorado. The Leadville was deposited in a warm, shallow-shelf marine environment and contains a wide variety of carbonate facies, which have undergone extensive dolomitization, brecciation, and other types of diagenesis. Traps are formed by both folds (anticlines) and faults; however, there is the untested potential for both stratigraphic and diagenetic traps particularly in the Paradox fold and fault belt in the vastly underexplored northern part of the basin.

This Bulletin is based on the final report of a project titled, “The Mississippian Leadville Limestone Exploration Play, Utah and Colorado—Exploration Techniques and Studies for Independents,” which was funded, in part, by the U.S. Department of Energy and conducted by the Utah Geological Survey between 2003 and 2008. The goals of the project were to (1) increase production from Leadville fields in the Paradox Basin through detailed reservoir characterization, (2) target new areas for exploration, (3) reduce exploration costs and risk, and (4) add new hydrocarbon discoveries and increase reserves. The project final report was updated, shortened, revised, and peer reviewed to produce this Bulletin.

This Bulletin consists of three components: (1) description of lithofacies and diagenetic history of the Leadville Limestone at Lisbon field, San Juan County, Utah (Chapters 2 through 4); (2) regional studies of the Leadville play (identification of oil-prone areas using epifluorescence in well cuttings, and estimation of potential oil migration directions from evaluating the middle Paleozoic hydrodynamic pressure regime and water chemistry) (Chapters 5 through 8); and (3) description of modern and outcrop depositional analogs (Chapters 9 and 10). The research, data, conclusions, and recommendations contained in this Bulletin are anticipated to be a valuable resource for hydrocarbon exploration and production in the Paradox Basin and similar shallow-shelf marine regions worldwide, as well as for students and researchers studying carbonate rocks for years to come.

Thomas C. Chidsey, Jr.
Utah Geological Survey

ABSTRACT

The Mississippian Leadville Limestone is a classic shallow, open-marine, carbonate-shelf deposit. The Leadville has produced over 53 million barrels of oil/condensate and 830 billion cubic feet of gas from seven fields in the Paradox fold and fault belt of the Paradox Basin, Utah and Colorado. This environmentally sensitive, 7500-square-mile (19,400 km²) area that makes up the fold and fault belt is relatively unexplored. The overall goals of this study were to (1) increase production from Leadville fields through detailed reservoir characterization, (2) target new areas for exploration, (3) reduce exploration costs and risk, and (4) add new discoveries and reserves. This Bulletin consists of three components: (1) description of lithofacies and diagenetic history of the Leadville at Lisbon field, San Juan County, Utah; (2) regional studies of the Leadville play (identification of oil-prone areas using epifluorescence in well cuttings, and estimation of potential oil migration directions from evaluating the middle Paleozoic hydrodynamic pressure regime and water chemistry); and (3) description of modern and outcrop depositional analogs.

Leadville lithofacies at Lisbon field include open marine (crinoidal banks and Waulsortian-type buildups), ooid and peloid shoals, and middle shelf. Rock units with open-marine and restricted-marine lithofacies constitute significant reservoir potential, having both effective porosity and permeability when dissolution of skeletal grains, followed by dolomitization, has occurred. Two major types of diagenetic dolomite are observed in the Leadville Limestone at Lisbon field: (1) low-permeability, “early” dolomite consisting of very fine grained, interlocking crystals that preserve depositional fabrics and (2) porous, coarser, rhombic and saddle crystals that discordantly replace limestone and earlier dolomite. Most reservoir rocks within Lisbon field appear to be associated with the second, late type of dolomitization and associated leaching events. Brecciation (autobrecciation) caused by natural hydrofracturing is widespread within Lisbon field. Sediment-filled cavities, related to karstification of the exposed Leadville, are present in the upper one-third of the formation. Fluid analysis indicates late dolomitization may have developed from hydrothermal events which can greatly improve reservoir quality. The result can be the formation of large, diagenetic-type hydrocarbon traps regionally or represent untapped, but difficult to identify, resources in other currently producing Leadville fields.

Stable carbon and oxygen isotope data indicate that all Lisbon field Leadville dolomites were likely associated with brines whose composition was enriched in ¹⁸O compared with Late Mississippian seawater. Late burial diagenetic phases of the Leadville have high strontium isotope ratios indicating water enriched in ⁸⁷Sr, derived from either Precambrian granitic rocks or the Devonian McCracken Sandstone, likely entered the formation along basement-involved high-angle normal faults. Brines from evaporites in the Pennsylvanian Paradox Formation may also have entered the Leadville along the large fault bounding the northeastern flank of Lisbon field. We propose that thermal convection cells bounded by basement-rooted faults transferred heat and fluids from possible granitic basement, Pennsylvanian evaporites, and Oligocene igneous intrusive complexes.

Epifluorescence (EF) petrography identified hydrocarbon shows in Leadville cuttings from regional exploration wells selected for study. The highest maximum and highest average EF readings from each well, based on a qualitative visual rating scale, were plotted and mapped. A regional southeast-northwest trend of relatively high EF parallels the southwestern part of the Paradox fold and fault belt. The northeastern part of the fold and fault belt shows a regional trend of low EF. Exploration efforts should be concentrated in suggested oil-prone areas along the southwestern part of the fold and fault belt.

A systematic change in the chemistry of Middle Paleozoic brine systems through the Paradox Basin suggests that groundwater movement is generally southwestward. The regional hydrodynamic trends, based on drill-stem test pressure data from wells, indicate that Mississippian strata have high permeability.

Depositional environments of the Leadville Limestone have modern analogs in the southern Florida–Bahamas region, a warm-water carbonate factory where one can observe carbonate deposition and the conditions (physical, biological, and chemical), which create various carbonate sediments as well as the processes by which the deposits change. Shallow bay basins, mud mounds, patch reefs, and sand shoals from Florida Bay to offshore of the Keys are modern Leadville Limestone analogs. Ooid shoals and shelf lagoonal sedimentation of the Great Bahama Bank are also modern Leadville analogs. Recognizing the modern characteristics of carbonate tidal flats of the Bahamas in the Leadville cores, a facies which is produced in other carbonate reservoirs, may lead to additional target areas for drilling.

Representative outcrop analogs (depositional or diagenetic) for the Leadville Limestone are present in the Mississippian section along the southern flank of the Uinta Mountains. They have similar lithofacies observed in Leadville cores from Lisbon field. These outcrops also contain local zones of breccia due to either collapse related to paleokarstification or natural hydrofracturing similar to that identified in Lisbon cores. Breccia pipes may be related to past hydrothermal activity but are only found where there are underlying sandstones that served as aquifers supplying hot water from below. This relationship suggests that targeting Leadville areas for potential hydrothermal dolomite and enhanced reservoir quality due to hydrofracturing may require an aquifer below as a necessary ingredient.

CHAPTER 1: INTRODUCTION

by

Thomas C. Chidsey, Jr., Utah Geological Survey

CHAPTER 1: INTRODUCTION

OVERVIEW

The Mississippian (late Kinderhookian to early Meramecian) Leadville Limestone has produced over 53 million barrels (bbls) of oil/condensate and 830 billion cubic feet of gas (BCFG) as of July 1, 2020, from seven fields in the northern Paradox Basin region (Colorado Oil and Gas Conservation Commission, 2020; Utah Division of Oil, Gas and Mining, 2020), referred to as the Paradox fold and fault belt, of Utah and Colorado (figure 1.1). No significant new oil discoveries have been made since the early 1960s, and only independent producers continue to explore for Leadville oil and gas targets in the region, 85% of which is under the stewardship of the federal government. This environmentally sensitive, 7500-square-mile (19,400 km²) area is relatively unexplored with only about 100 exploratory wells that penetrated the Leadville (less than one well per township), and thus the potential for new discoveries remains significant.

The overall goals of this study are to (1) increase production from old and potential new Leadville fields through detailed reservoir characterization, (2) target areas for exploration, (3) reduce exploration costs and risk especially in environmentally sensitive areas, and (4) add new oil discoveries and reserves. To achieve these goals, we conducted:

- a case study of lithofacies and the diagenetic history of the Leadville reservoir at Lisbon field (the largest Leadville oil producer in the Paradox Basin), San Juan County, Utah, for regional application;
- regional studies of
 - general characteristics of the Leadville play,
 - oil-prone areas using epifluorescence in well cuttings from regional wells,
 - an estimation of potential oil migration directions by evaluating the hydrodynamic pressure regime, and
 - water chemistry of the middle Paleozoic strata of the Paradox Basin; and
- a comparison of modern and outcrop depositional analogs.

This Utah Geological Survey (UGS) Bulletin covers the research and results of the five-year Leadville Limestone exploration play project. Appendices provide the complete data compilations, maps, photographs, core descriptions, measured sections, etc., either collected or generated from the study. As part of the UGS project we also conducted a surface geochemical survey over the Lisbon and Lightning Draw Southeast fields (figure 1.1), and areas in between, to evaluate the effectiveness of this low-cost, non-invasive method, which success-

fully confirmed the presence, or lack, of underlying Leadville hydrocarbon reservoirs. The details and complete results of the surface geochemical survey were published as separate papers in the Rocky Mountain Association of Geologists Special Publication, *The Paradox Basin Revisited—New Developments in Petroleum Systems and Basin Analysis* and the UGS Miscellaneous Publication *New Techniques for New Hydrocarbon Discoveries—Surface Geochemical Surveys in the Lisbon and Lightning Draw Southeast Field Areas, San Juan County, Utah* (see Seneshen and others, 2009 and 2010, respectively).

BENEFITS AND POTENTIAL APPLICATION

Exploring the Leadville Limestone is high risk, with less than a 10% chance of success based on the drilling history of the region. Prospect definition often requires expensive, three-dimensional (3D) seismic acquisition in environmentally sensitive areas. These facts make exploring difficult, especially for independents who are the primary explorers and operators in the Paradox Basin. We believe that one or more of the project results will reduce the risk taken by an independent producer in looking for Leadville oil and gas.

Another problem in exploring for oil and gas in the Leadville Limestone is the lack of published or publicly available geologic and reservoir information, such as regional lithofacies maps, complete reservoir characterization studies, surface geochemical surveys, regional hydrodynamic pressure regime maps, and hydrocarbon show data and migration interpretations. This UGS Bulletin provides this information to save independents and other operators monetary and staff resources which they simply do not possess or normally have available only for drilling. The technology, maps, and interpretive results generated from this project will help to identify or eliminate areas and exploration targets prior to spending significant financial resources on seismic data acquisition and potential environmental litigation, and therefore increase the chance of successfully finding new economic accumulations of Leadville oil and gas.

These benefits may also apply to other high-risk, sparsely drilled basins or regions that have potential shallow-marine carbonate reservoirs equivalent to the Mississippian Leadville Limestone. These areas include the Utah-Wyoming-Montana thrust belt (Madison Limestone), the Kaiparowits Basin in southern Utah (Redwall Limestone), the Basin and Range Province of Nevada and western Utah (various Mississippian and other Paleozoic units), and the Eagle Basin of Colorado (various Mississippian and other Paleozoic units).

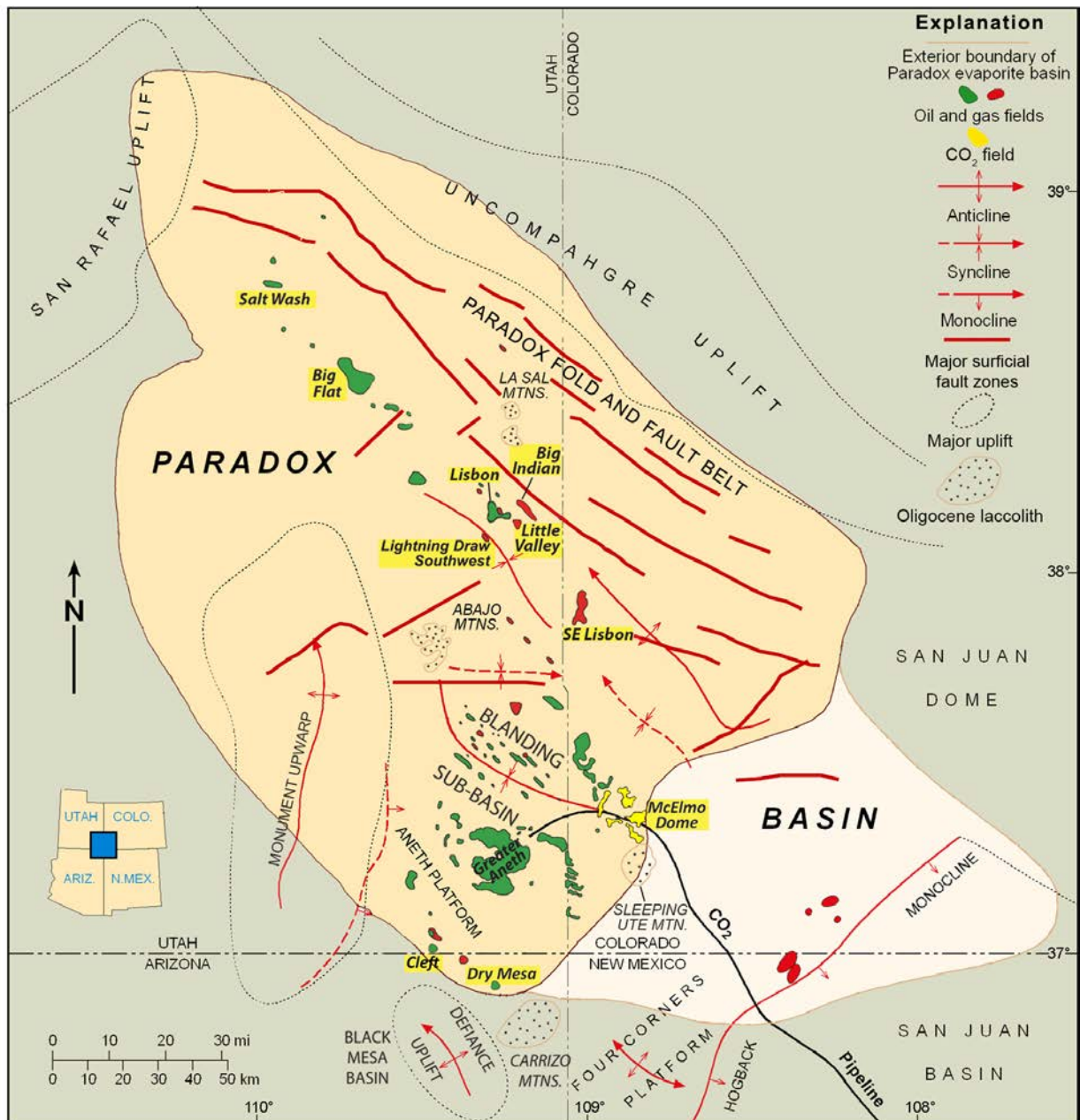


Figure 1.1. Regional setting and oil and gas fields in the Paradox Basin of Utah, Colorado, Arizona, and New Mexico. Leadville fields are highlighted in yellow. Modified from Kitcho (1981) and Harr (1996).

Many mature basins have productive carbonate reservoirs of shallow-marine shelf origin. These mature basins include the Eastern Shelf of the Midland Basin, West Texas (Pennsylvanian-age reservoirs in the Strawn, Canyon, and Cisco Formations); the Permian Basin, West Texas and southeastern New Mexico (Permian-age Abo and other formations along the northwestern shelf of the Permian Basin); and the Illinois Basin (various Silurian units). The techniques we used in the Paradox Basin could be applied to these other basins. In general, the average field size in these other mature basins is larger than fields in the Paradox Basin. Even though there are differences in depositional lithofacies and structural styles between the Paradox Basin and other basins, the fundamental use of this project's studies is a critical commonality.

GENERAL GEOLOGY OF THE PARADOX BASIN

The Paradox Basin is located mainly in southeastern Utah and southwestern Colorado, with small parts in northeastern Arizona and the northwestern corner of New Mexico (figure 1.1). The Paradox Basin is an elongate, northwest-southeast-trending, evaporitic basin that predominately developed during the Pennsylvanian, about 330 to 310 million years ago (Ma). The basin can generally be divided into three areas: the Paradox fold and fault belt in the north, the Blanding sub-basin in the south-southwest, and the Aneth platform in southeasternmost Utah (figure 1.1). The Mississippian Leadville Limestone is one of two major oil and gas reservoirs in the Paradox Basin,

the other being the Pennsylvanian Paradox Formation (figure 1.2); minor amounts of oil are produced from the McCracken Sandstone Member of the Devonian Elbert Formation at Lisbon field. Most Leadville production is from the Paradox fold and fault belt (figure 1.3).

The most obvious structural features in the basin are the spectacular anticlines that extend for miles in the northwesterly trending fold and fault belt. The events that caused these and many other structural features to form began in the Proterozoic, when movement initiated on high-angle basement faults around 1700 to 1600 Ma (Stevenson and Baars, 1986, 1987). During Cambrian through Mississippian time, this region, as well as most of eastern Utah, was the site of typical thin, shallow-shelf marine carbonate deposition on the western part of the North American craton while thick deposits accumulated in the miogeocline to the west (Hintze and Kowallis, 2009). However, major changes began in the Pennsylvanian when a pattern of basins and fault-bounded uplifts developed from Utah to Oklahoma as a consequence of the collision of South America, Africa, and southeastern North America (Kluth and Coney, 1981; Kluth, 1986), or from a smaller-scale collision of a microcontinent with south-central North America (Harry and Mickus, 1998). One result of this tectonic event was the uplift of the Ancestral Rockies in the western United States. The Uncompahgre Highlands (uplift) in eastern Utah and western Colorado initially formed as the westernmost range of the Ancestral Rockies during this ancient mountain-building period.

The Uncompahgre Highlands are bounded along their southwestern flank by a large, basement-involved, high-angle reverse fault identified from seismic surveys and exploration drilling (Frahme and Vaughn, 1983). As the highlands rose,

an accompanying depression, or foreland basin, formed to the southwest—the Paradox Basin. The shape and formation of the Paradox Basin was strongly influenced by rejuvenation of pre-existing (late Precambrian) northwesterly trending structures (Baars and Stevenson, 1981). Rapid basin subsidence, particularly during the Pennsylvanian and continuing into the Permian, accommodated large volumes of evaporitic and marine sediments that intertongue with non-marine arkosic material shed from the highland area to the northeast (Hintze and Kowallis, 2009).

The present Paradox Basin includes or is surrounded by other uplifts that formed during the Late Cretaceous–early Tertiary Laramide orogeny, such as the Monument upwarp in the west-southwest, and the Uncompahgre uplift, corresponding to the earlier Uncompahgre highlands, forming the northeastern boundary (figure 1.1). Oligocene laccolithic intrusions form the La Sal and Abajo Mountains in the north and central parts of the basin in Utah, whereas the Carrizo Mountains in Arizona, and the Ute, La Plata, and San Miguel Mountains in Colorado were intruded along the southeastern boundary of the basin (figure 1.1).

The area now occupied by the Paradox fold and fault belt was also the site of greatest Pennsylvanian/Permian subsidence and salt deposition. Folding in the Paradox fold and fault belt began as early as the Late Pennsylvanian as sediments were laid down thinly over, and thickly in areas between, rising salt (Doelling, 2010). The Paradox fold and fault belt was created during the Late Cretaceous through Quaternary by a combination of (1) reactivation of basement normal faults, (2) additional salt flowage followed by dissolution and collapse, and (3) regional uplift (Doelling, 2010). Trudgill and Paz (2009)

Age	Stratigraphic Unit		Thickness (ft)	Lithology	Products
PENN	Hermosa Group	Paradox Fm	0–14,000'		potash & salt
		Pinkerton Trail Fm	0–150'		
	Molas Formation		0–100'		unconformity
M	Leadville Limestone		300–600'		
DEV	Ouray Limestone		0–150'		
	Elbert Formation		100–200'		
	McCracken Ss M		25–100'		
Є	"Lynch" Dolomite		800–1000'		

Oil and gas production Condensate and oil production

Figure 1.2. Paleozoic stratigraphic section for the central Paradox Basin, Utah. After Hintze and Kowallis (2009).

suggest that salt movement initiated during the Late Pennsylvanian/Early Permian due to sediment loading. The relatively undeformed Blanding sub-basin and Aneth platform developed on a subsiding shallow-marine shelf.

Most oil and gas produced from the Leadville Limestone is found in discrete, seismically defined basement-involved,

northwest-trending structural traps that have closure on both anticlines and faults (figure 1.4). Lisbon, Big Indian, Little Valley, Lightning Draw Southeast, and Lisbon Southeast fields (figure 1.3) are sharply folded anticlines that close against the Lisbon fault zone. Salt Wash and Big Flat fields (figure 1.3), northwest of the Lisbon area, are east-west- and north-south-trending anticlines, respectively.

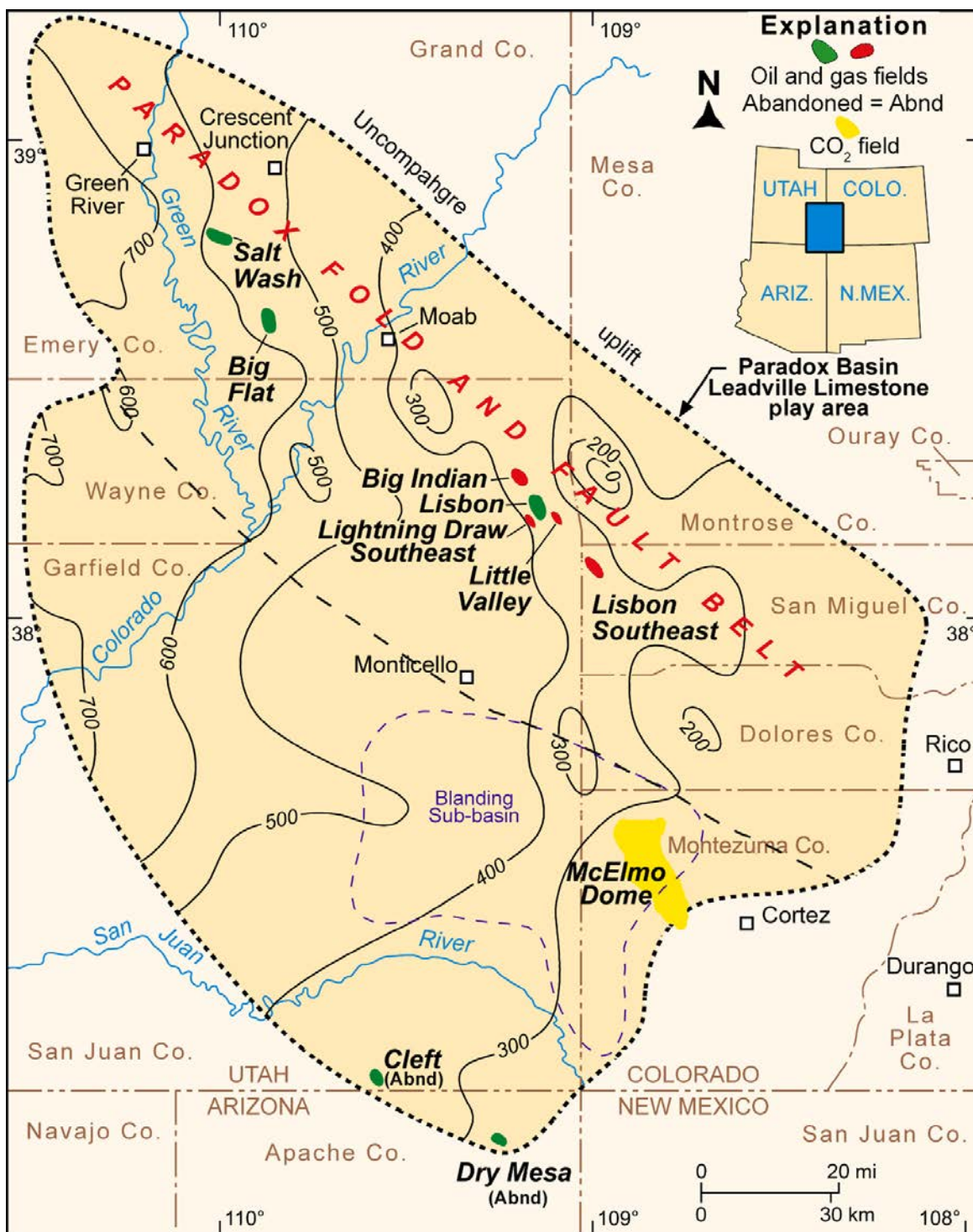


Figure 1.3. Regional setting of the Paradox Basin, showing fields that produce oil and gas from the Mississippian Leadville Limestone, and thickness of the Leadville (contour interval is 100 feet [30 m]). Modified from Parker and Roberts (1963).

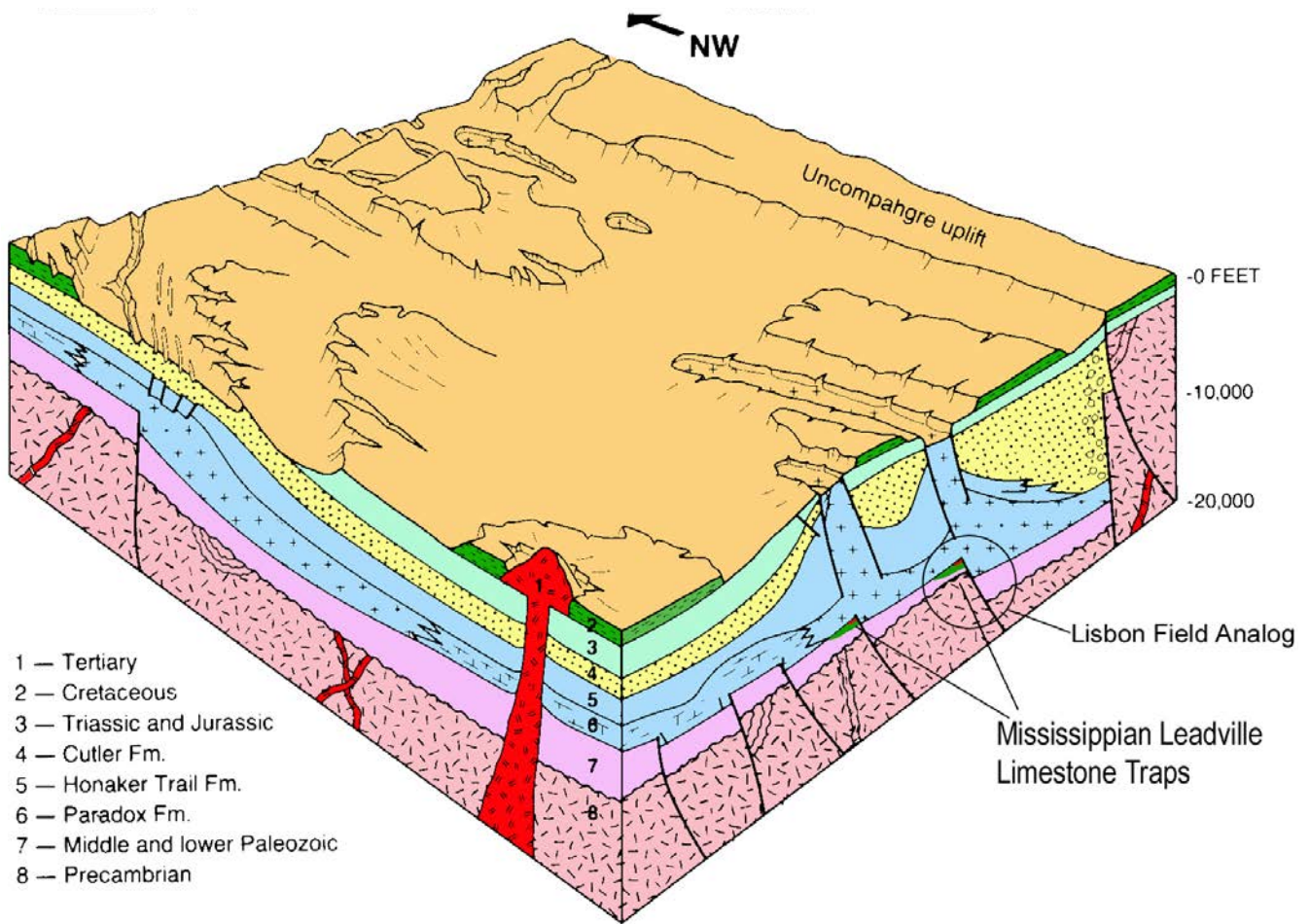


Figure 1.4. Schematic block diagram of the Paradox Basin displaying basement-involved structural trapping mechanisms for the Leadville Limestone fields. Modified from *Petroleum Information* (1984; original drawing by J.A. Fallin).

CHAPTER 2: LISBON FIELD CASE STUDY, SAN JUAN COUNTY, UTAH—GENERAL FIELD CHARACTERISTICS AND RESERVOIR MAPPING

by

Thomas C. Chidsey, Jr., and Craig D. Morgan (retired), Utah Geological Survey
and
David E. Eby, Eby Petrography & Consulting, Inc.

CHAPTER 2:

LISBON FIELD CASE STUDY, SAN JUAN COUNTY, UTAH— GENERAL FIELD CHARACTERISTICS AND RESERVOIR MAPPING

INTRODUCTION AND FIELD SYNOPSIS

Lisbon field, San Juan County, Utah (figure 2.1), accounts for most of the Leadville oil and gas production in the Paradox Basin. A wealth of Lisbon core, petrographic, and other data is available at the UGS's Utah Core Research Center (UCRC) in Salt Lake City. Reservoir characteristics, particularly diagenetic overprinting and history, and Leadville lithofacies can be applied regionally to other fields and exploration trends in the Paradox Basin. Therefore, we selected Lisbon field as the major case study for the Leadville Limestone project. This evaluation included data collection and construction of various maps (top of structure, thickness, porosity, etc.) and cross sections as summarized in this Bulletin.

The regional surface geology is dominated by the major northwest-southeast-trending Lisbon Valley anticline (tens of miles in length) (figure 2.1), a classic example of the structures in the northwesterly trending Paradox fold and fault belt created due to salt movement in the Pennsylvanian Paradox Formation. However, here the Lisbon fault, which parallels the crest of the anticline, has displaced the Pennsylvanian Honaker Trail Formation against Cretaceous strata (figures 2.1 and 2.2). The Lisbon fault dies out in Paradox salt. Permian through Jurassic strata dip gently to the southwest along the southwestern flank of the Lisbon Valley anticline (figures 2.1 and 2.2).

The trap for Lisbon field is not the Lisbon Valley anticline but a separate structure beneath the Paradox Formation. The Lisbon trap is an elongate, asymmetric, northwest-trending anticline that has nearly 2000 feet (600 m) of structural closure, bounded on the northeast flank by a major, basement-involved normal fault that has over 2500 feet (760 m) of displacement (Smith and Prather, 1981) (figures 2.3 and 2.4). Several minor, northeast-trending normal faults divide the Lisbon Leadville reservoir into compartments. Four miles (6.4 km) to the southwest of Lisbon field, Lightning Draw Southeast field (figures 2.1 and 2.2) is similar to Lisbon in terms of Leadville reservoir structure, lithology, and gas composition.

Producing units in Lisbon field contain crinoidal/skeletal dolograins, dolopackstone, and dolowackestone fabrics. Diagenesis includes fracturing, autobrecciation, karst development, hydrothermal dolomite, and bitumen plugging (described in detail in Chapter 4). The net reservoir thickness is 225 feet (69 m) over a 5120-acre (2100 ha) area (Clark, 1978; Smouse, 1993). Reservoir quality is improved by natural fracturing associated with the Paradox fold and fault belt. Porosity averages 6% in fracture-enhanced intercrystalline and moldic networks; permeability averages 22 millidarcies

(mD). Reservoir drive is via an expanding gas cap and gravity drainage; original water saturation was 39% (Clark, 1978; Smouse, 1993). The bottom-hole temperature ranges from 133° to 189°F (56°–87°C). The oil and gas characteristics are summarized in table 2.1.

Oil and gas in the Leadville Limestone (and the McCracken Sandstone Member of the underlying Devonian Elbert Formation) were likely generated from the source rocks in the overlying Pennsylvanian Paradox Formation (figure 1.2) (Chidsey, 2018). Organic-rich informal units, such as the Cane Creek, Chimney Rock, and Gothic shales, are well-established source rocks (Hite and others, 1984; Nuccio and Condon, 1996). These rocks are composed of black, sapropelic shale and shaly dolomite (Morgan, 1993). The average total organic carbon (TOC) content of the black shale in the Cane Creek is 15% and some samples contain up to 28% (Grummon, 1993; Morgan and others, 2014). The Chimney Rock shale has from 1% to 3% TOC and a mean vitrinite reflectance (R_o mean) of 1.3% to 2.5% (Hite and others, 1984; Peterson, 1992). The Gothic shale has from 1.5% to near 4% TOC and an R_o mean of 0.8% to 1.2% (Hite and others, 1984; Peterson, 1992). Other, deeper shale facies in the Paradox Formation contain as much as 13% TOC (Hite and others, 1984). Hydrocarbons were expelled and subsequently migrated along faults in the Lisbon field structure where the Leadville and McCracken are juxtaposed directly against these Pennsylvanian source rocks.

Lisbon field was discovered in 1960 with the completion of the Pure Oil Company No. 1 NW Lisbon USA well, NE1/4NW1/4 section 10, T. 30 S., R. 24 E., Salt Lake Base Line and Meridian (SLBL&M) (figure 2.3), that had an initial flowing potential (IFP) of 179 bbls of oil per day (BOPD) and 4376 thousand cubic feet of gas per day (MCFGPD). The original reservoir field pressure was 2982 pounds per square inch (psi [20,560 kPa]) (Clark, 1978). Currently, 13 producing (or shut in) Leadville wells, 13 abandoned producers, 5 injection wells (4 gas injection wells and one water/gas injection well), and 4 dry holes are in the field. Cumulative Leadville production as of July 1, 2020, was 50,679,482 bbls of oil, 761.5 BCFG (cycled gas), and 50,511,202 bbls of water (Utah Division of Oil, Gas and Mining, 2020). Hydrocarbon gas, re-injected into the crest of the structure to control pressure decline, is now being produced; acid gas is still re-injected.

Three factors create reservoir heterogeneity within productive zones: (1) variations in carbonate fabrics and facies, (2) diagenesis (including karstification), and (3) fracturing. The extent of these factors and how they are combined affect the degree to which they create barriers to fluid flow.

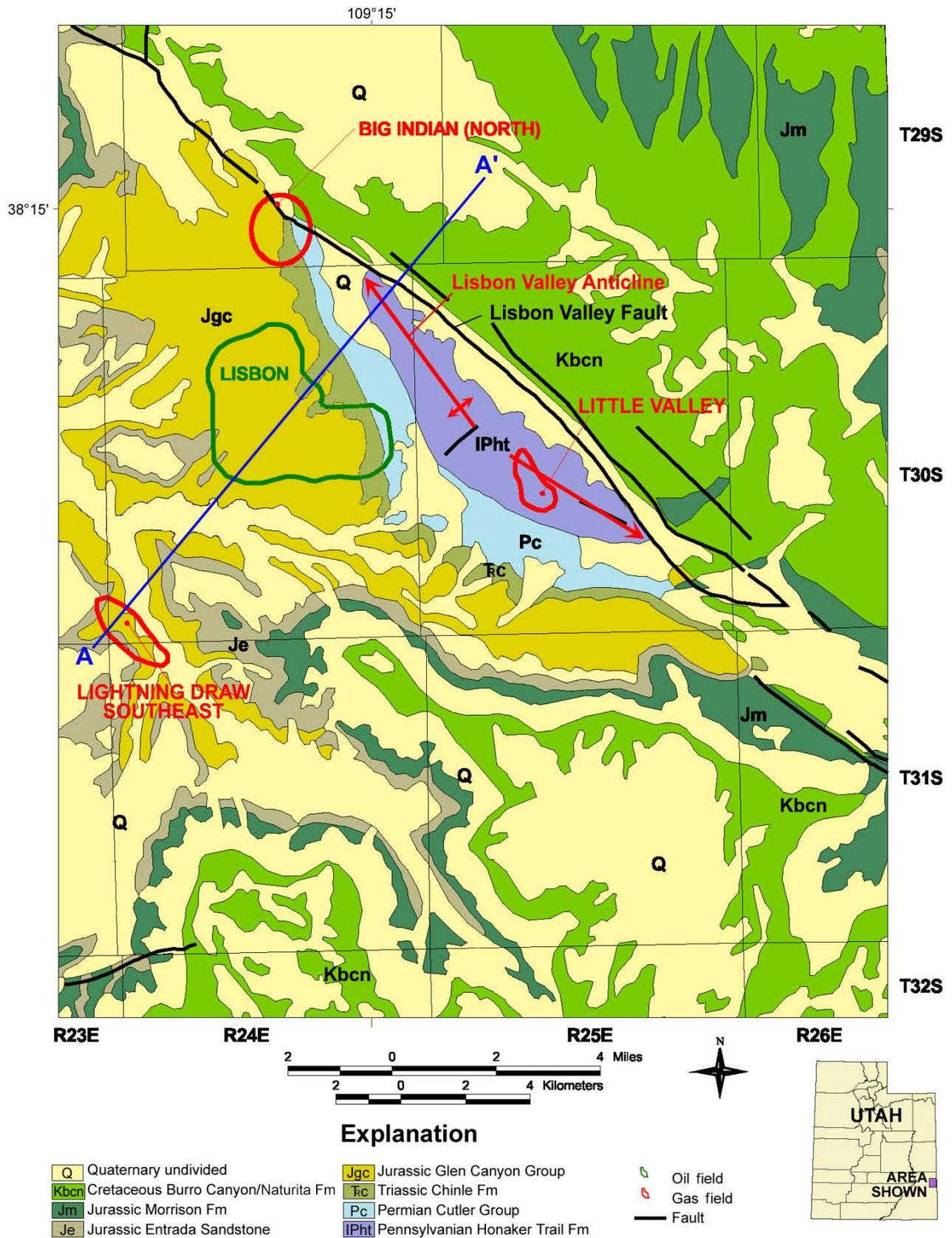


Figure 2.1. General surface geology of the Lisbon field area, San Juan County, Utah. Modified from Hintze and others (2000). Cross section A-A' shown on figure 2.2.

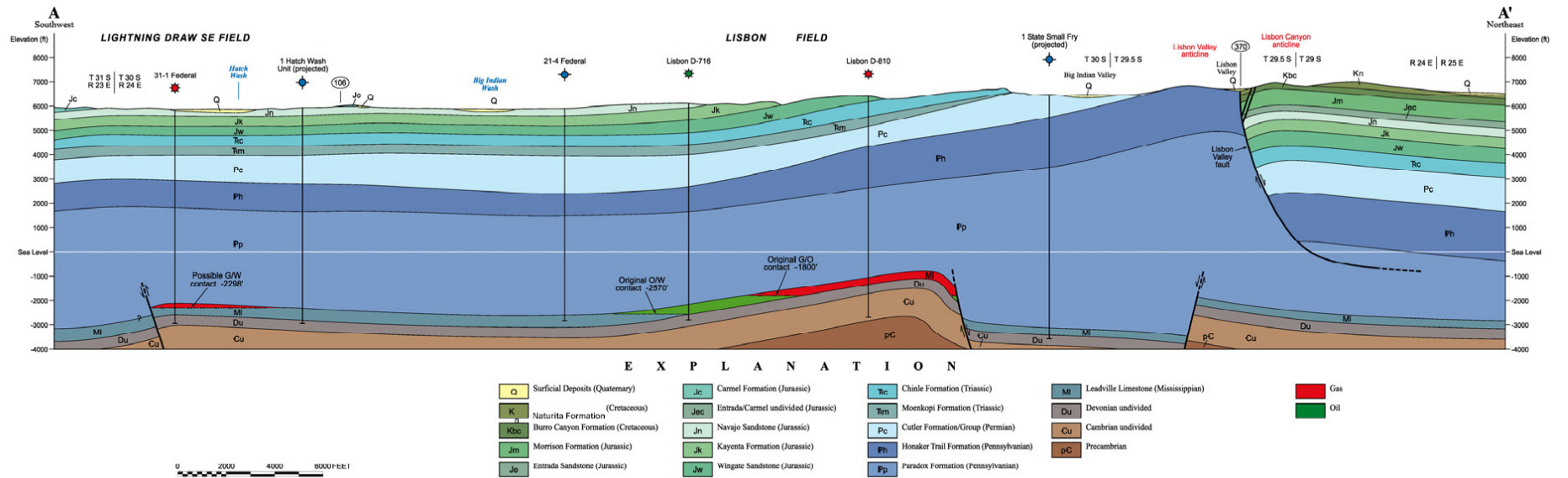


Figure 2.2. Detailed cross section through the Lisbon and Lightning Draw Southeast fields showing the fault-bounded Leadville Limestone hydrocarbon reservoirs. Line of section shown on figure 2.1. G/O contact = gas-oil contact, O/W contact = oil-water contact, G/W contact = gas-water contact.

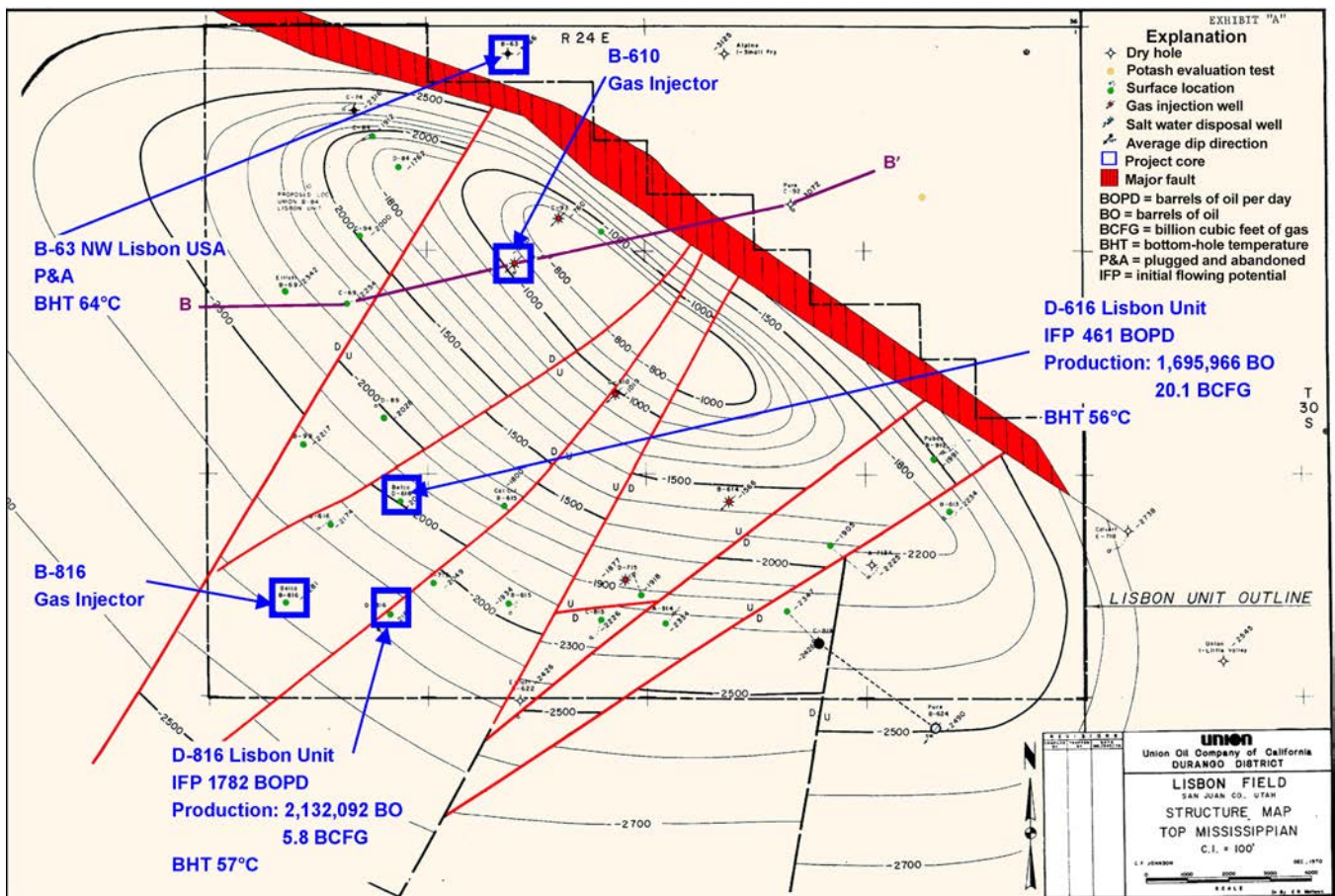


Figure 2.3. Top of structure of the Leadville Limestone, Lisbon field. Modified from C.F. Johnson, Union Oil Company of California files (1970) courtesy of Tom Brown, Inc. Cross section B–B' shown on figure 2.4. Also displayed are wells from which cores were described in this study.

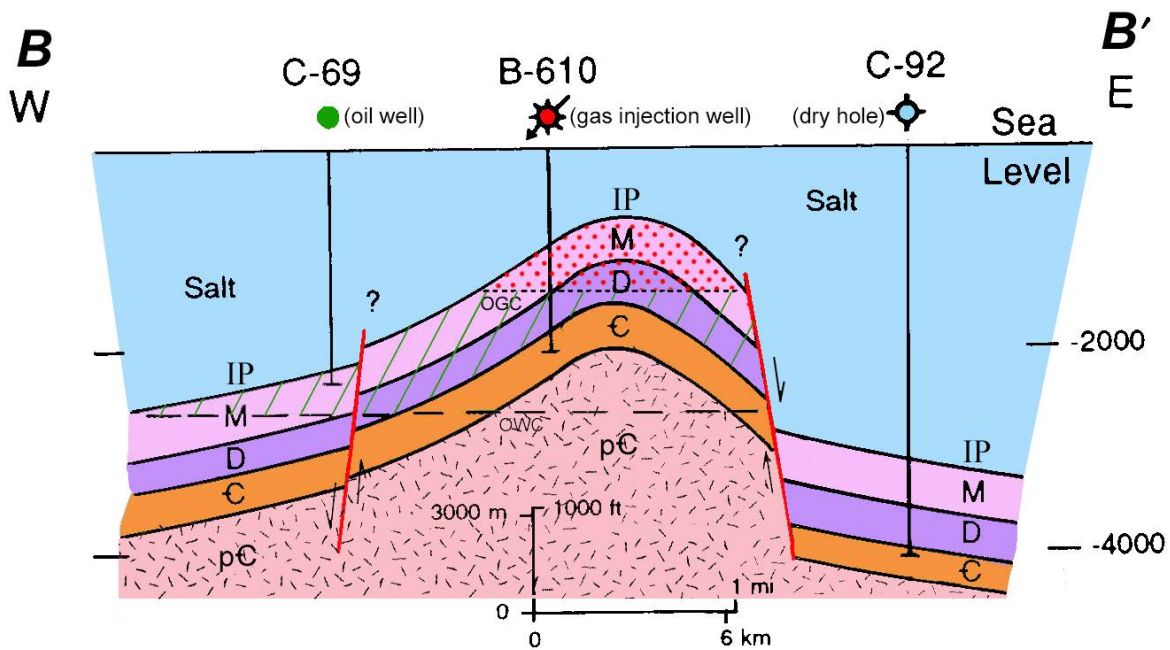


Figure 2.4. Schematic east-west structural cross section, Lisbon field. Line of section shown on figure 2.3. Note the juxtaposition of the Mississippian (M) section against the Pennsylvanian (IP) section which includes evaporites (salt) and organic-rich shale. OGC = oil-gas contact, OWC = oil-water contact. Modified from Clark (1978).

Table 2.1. General characteristics of the oil and gas produced from the Leadville Limestone at Lisbon field, San Juan County, Utah (Stowe, 1972; Morgan, 1993; Chidsey, 2018).

Oil		Gas	
Gravity	54–62.6° API	Methane	48%
Specific Gravity	0.765	Higher Fractions	13%
Color	Yellow to Red	Nitrogen	24%
Pour Point	-35°F	Carbon Dioxide	14%
Viscosity (cst)*	1.03 @ 104°F	Hydrogen Sulfide	1.2%
Viscosity (sus)†	29.2 @ 104°F	Helium	trace–1.1%
Sulfur	0.2%	Specific Gravity	0.89
Nitrogen	0.002%	Heating Value	685 BTU/ft ³

* centistokes

† Saybolt Universal Seconds

LOG-BASED CORRELATION SCHEME

The Leadville Limestone is divided into two informal members in Lisbon field, identified by a characteristic geophysical log response (figure 2.5) (Fouret, 1982, 1996). Mitchell (1961) noted that the contact between the upper and lower members at Lisbon field is unconformable and characterized by an abundance of chert clasts.

The typical vertical sequence or cycle of depositional lithofacies from Lisbon field, as determined from conventional core, was tied to the corresponding gamma-ray and neutron-density curves from geophysical well logs (figure 2.5). The correlation scheme enabled us to identify the major zone contacts, seals or barriers, baffles, producing or potential reservoirs, and depositional lithofacies. These contacts were used to produce field cross sections (figure 2.2 and plates 1 and 2 in appendix A) and a variety of structure and isochore maps (figures 2.3 and 2.6 through 2.13).

Seals or barriers include thick shales of the Molas Formation, which overlies the Leadville Limestone. Baffles are those rock units that restrict fluid flow in some parts of the field but may develop enough porosity and permeability in other parts, through diagenetic processes or lithofacies changes, to provide a conduit for fluid flow or even oil and gas storage. Baffles are found throughout the Leadville stratigraphic section. The four reservoir zones defined in this study (1 through 4, from top to bottom) are those units containing 8% or more porosity based on the average of the neutron and density porosity values (figure 2.5).

Depositionally, rock units are divided into crinoid banks/shoals, Waulsortian-type carbonate buildups (mounds) (bafflestone, bindstone, grainstone, and packstone), and inter-bank/shoal and inter-mound seals or barriers (mudstone and shale). Associated with Waulsortian carbonate-buildup rock units are flank/off buildups (floatstone, rudstone, wackestone, and mudstone). Porosity units, and reservoir or potential reservoir layers, are identified within

the crinoid banks/shoals and carbonate-buildup and flank/off-buildup intervals. These units contain all productive reservoir lithofacies.

The correlation scheme was used for (1) predicting changes in reservoir and non-reservoir rocks across the field, (2) comparing field to non-field areas, (3) estimating the reservoir properties and identifying lithofacies in wells which were not cored, and (4) determining potential units suitable for horizontal drilling. The scheme can be applied to other fields in the Paradox Basin, both those with cores and without.

RESERVOIR MAPPING

Isochore maps were constructed of reservoir zones 1 through 4 in the Leadville Limestone for Lisbon field (figures 2.6 through 2.9). These field maps incorporate zone tops and thickness from all geophysical well logs in the area; the maps also include faulting. We generated the net feet of porosity isochore maps for reservoir zones 1 through 4 (figures 2.10 through 2.13) of the Leadville for those parts of the reservoir units containing 10% or more porosity based on the average of the neutron and density porosity values. Whereas 8% or more porosity defines the reservoir zones, we used 10% or more porosity for greater definition of the zones mapped. The maps display well names, Leadville completions, and interval thickness for each well.

The bottom-hole temperature was plotted for most wells in Lisbon field (figure 2.14). Contoured temperatures identify possible patterns in temperature data. All wells with available core show evidence of hydrothermal dolomitization. The presence of hydrothermal dolomite and its relationship to reservoir temperature and faulting are critical in identifying diagenetic trends.

Production analysis was conducted for Lisbon field by compiling data through two principal tasks: (1) review of existing well-completion data, and (2) determination of production

history from monthly production reports available through the Utah Division of Oil, Gas and Mining. This information was merged with geological characterization data and incorporated into the interpretation of reservoir diagenesis (described in Chapter 4).

Well-test data can provide key insights into the nature of reservoir heterogeneities, and also provide “large-scale” quantitative data on actual reservoir properties and lithofacies from

the Lisbon case-study reservoir. Although several well tests have been conducted in all of the target reservoirs, only the IFP well tests provide quantitative reservoir property information. Thus, IFP well tests for each well were plotted (figure 2.15). Oil production from Lisbon field has steadily declined since peaking in the 1970s. Cumulative production for each well was also plotted (figure 2.16). These plots were used to determine possible production “sweet spots” and their relationship to faulting and reservoir diagenesis.

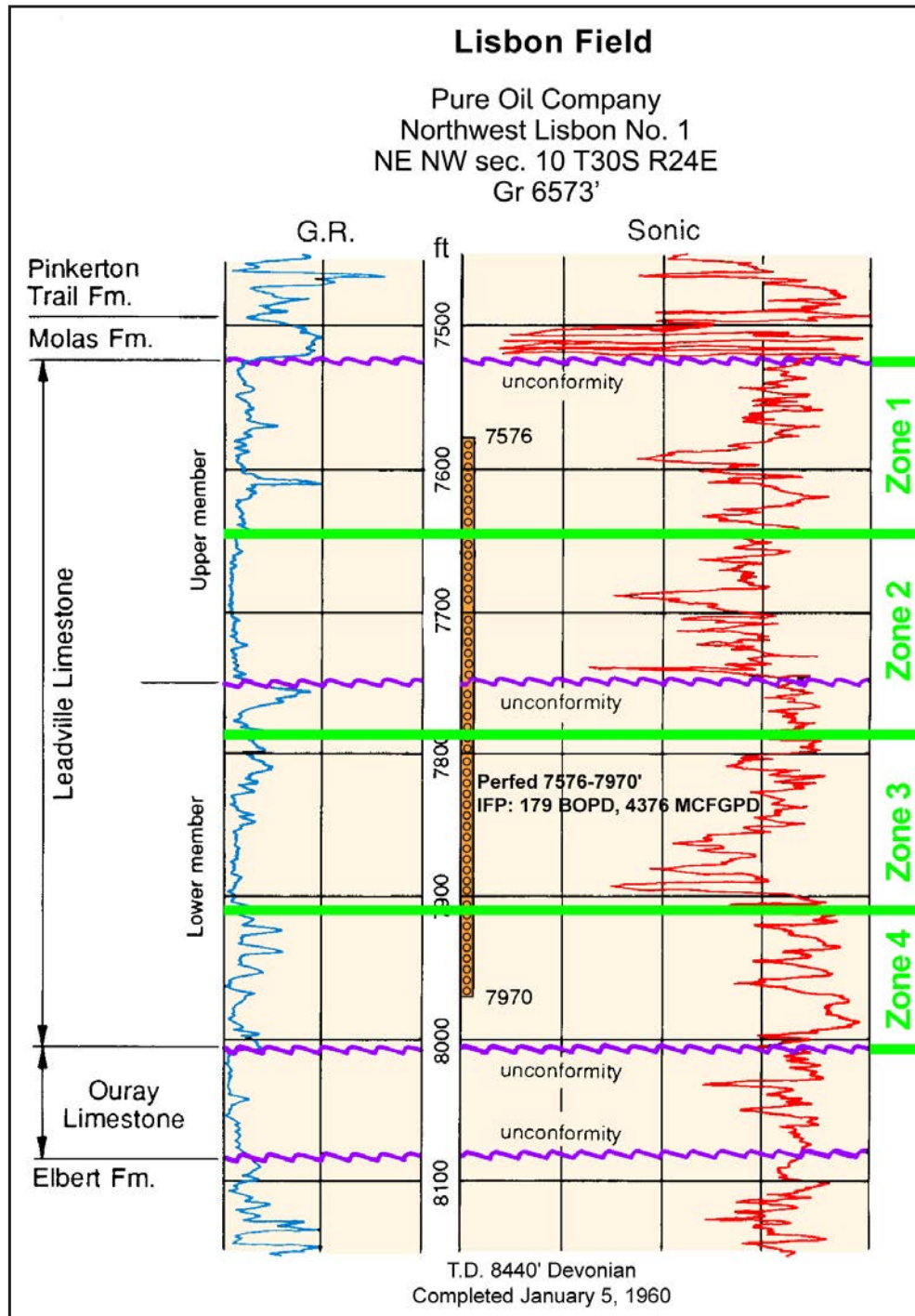
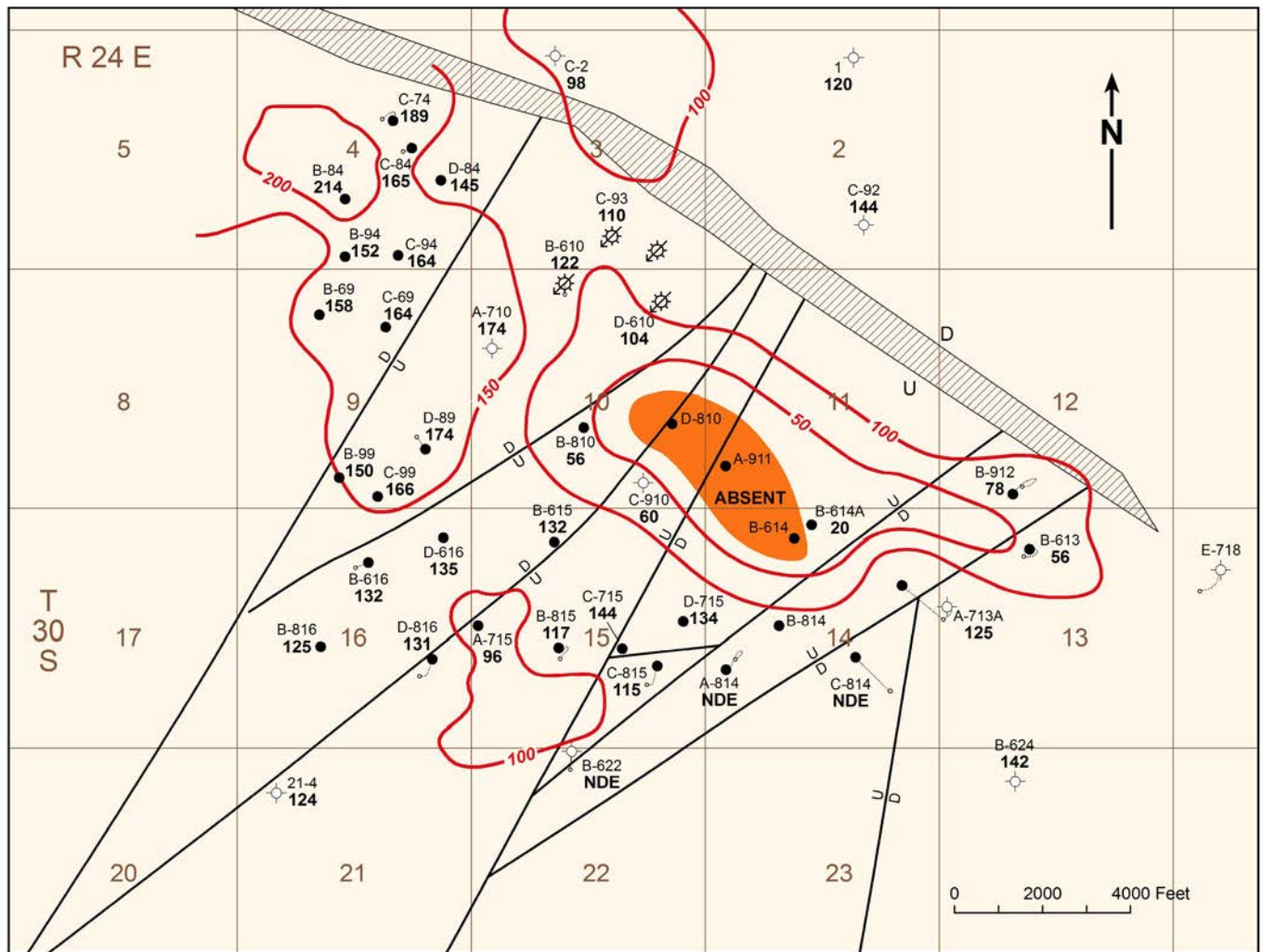


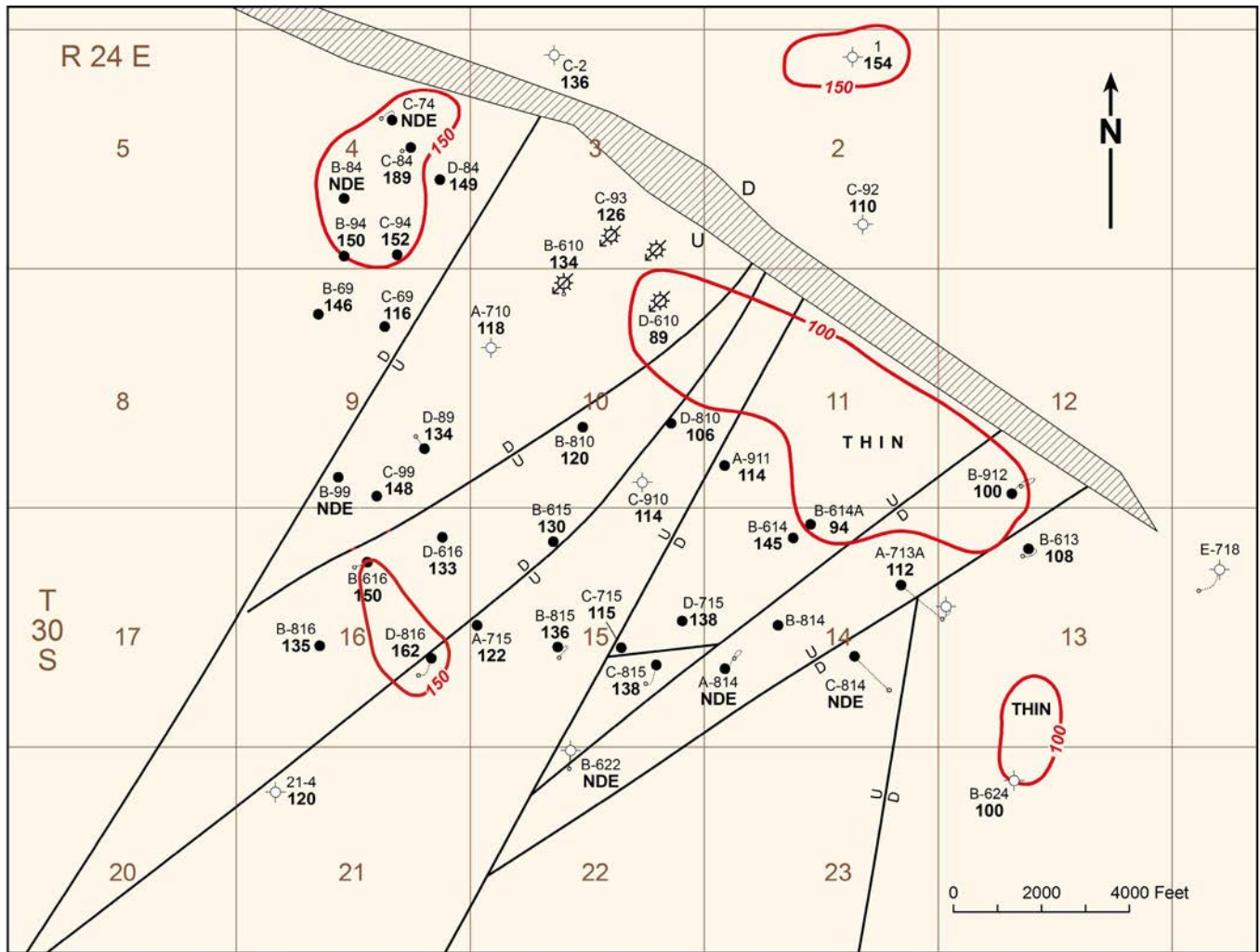
Figure 2.5. Typical gamma ray-sonic log of the Leadville Limestone showing the two informal members (Fourret, 1982, 1996) and four reservoir zones defined in this study; Lisbon field discovery well, San Juan County, Utah. See figure 2.3 for well location.



EXPLANATION

- Oil well
 - Dry hole
 - ★ Gas injection well
 - $\frac{D}{U}$ Minor fault
 - $\frac{H}{H}$ Major fault
 - Well name
 - C-815 115 Interval thickness (ft)
 - Surface location
 - Bottom-hole location
 - NDE = Not deep enough
- Contour interval 50 feet

Figure 2.6. Isochore of zone 1, Leadville Limestone, Lisbon field.



EXPLANATION

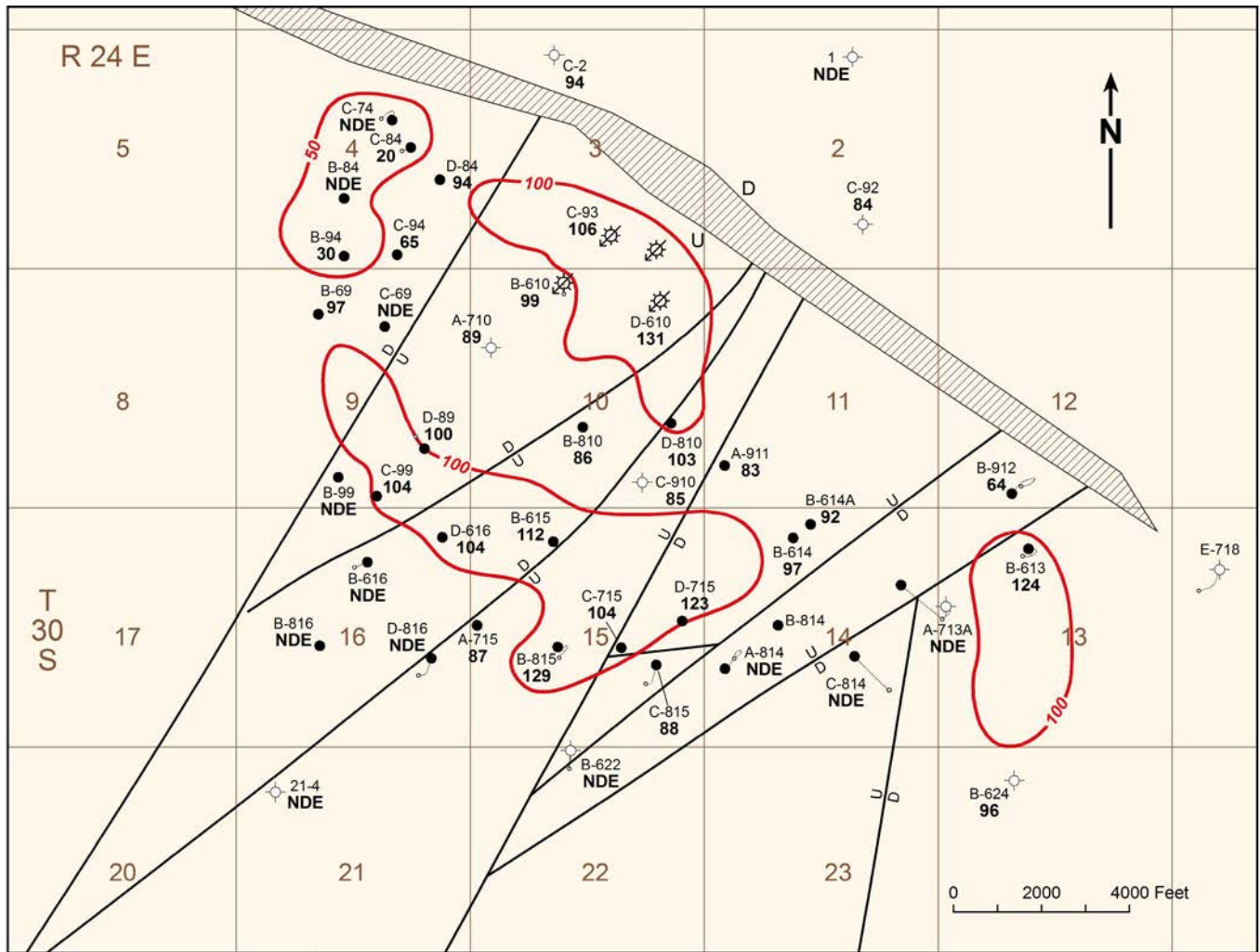
- Oil well
- ⊕ Dry hole
- ⊗ Gas injection well
- D/U Minor fault
- ▨ Major fault
- Well name
- Interval thickness (ft)
- Surface location
- Bottom-hole location
- NDE = Not deep enough

Contour interval 50 feet

Figure 2.7. Isochore of zone 2, Leadville Limestone, Lisbon field.



Figure 2.8. Isochore of zone 3, Leadville Limestone, Lisbon field.



EXPLANATION

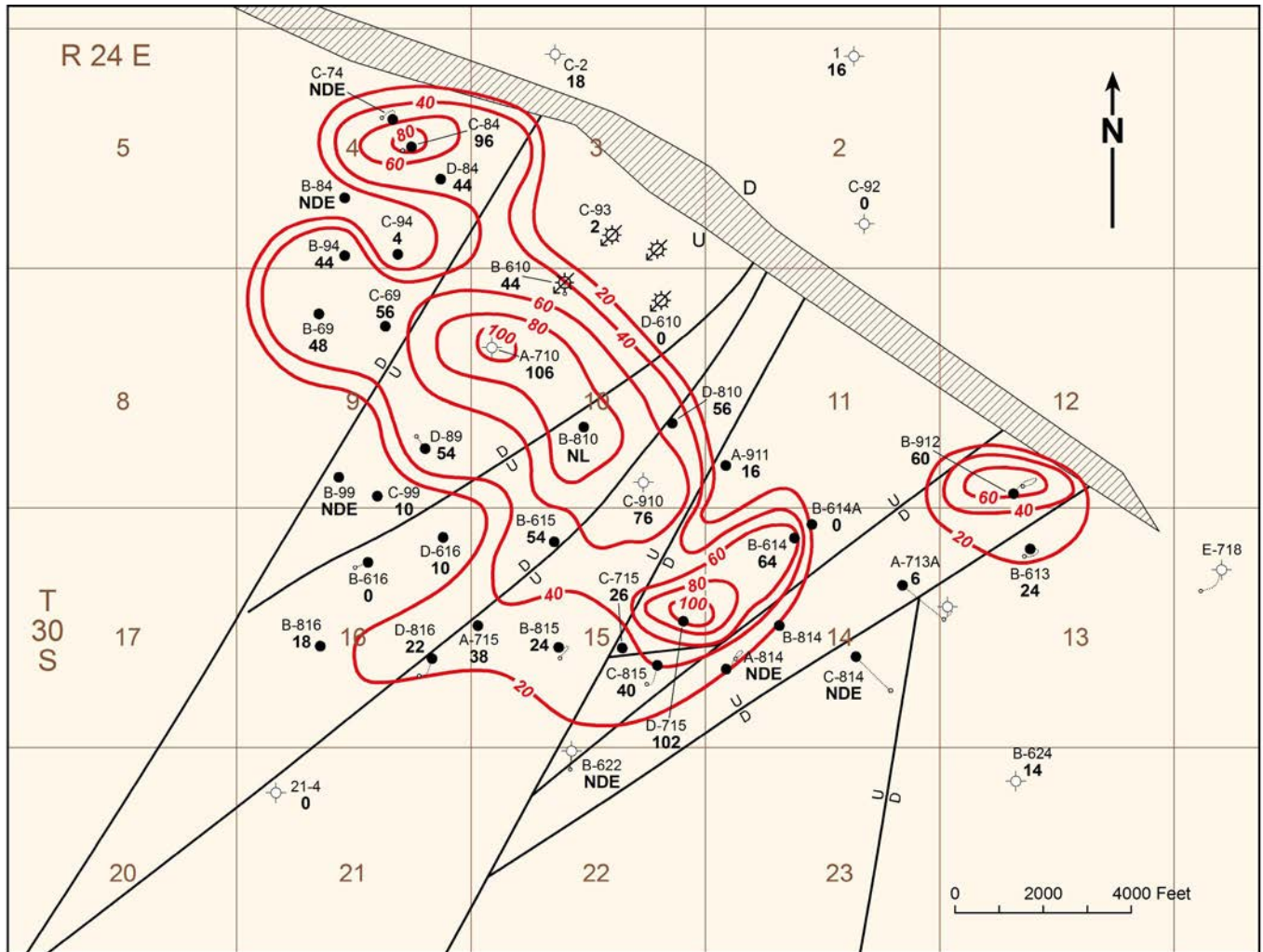
- Oil well
- Dry hole
- ⊗ Gas injection well
- D— Minor fault
- ▨ Major fault
- Well name
- Interval thickness (ft)
- Surface location
- Bottom-hole location
- NDE = Not deep enough

Contour interval 50 feet

Figure 2.9. Isochore of zone 4, Leadville Limestone, Lisbon field.



Figure 2.10. Net feet of porosity isochore for reservoir zone 1, Leadville Limestone, Lisbon field.



EXPLANATION

- Oil well
- ⊕ Dry hole
- ⊗ Gas injection well
- Minor fault
- ▨ Major fault
- Well name
- Interval thickness (ft)
- Surface location
- Bottom-hole location
- NDE = Not deep enough

Contour interval 20 feet

Figure 2.11. Net feet of porosity isochore for reservoir zone 2, Leadville Limestone, Lisbon field.



Figure 2.12. Net feet of porosity isochore for reservoir zone 3, Leadville Limestone, Lisbon field.

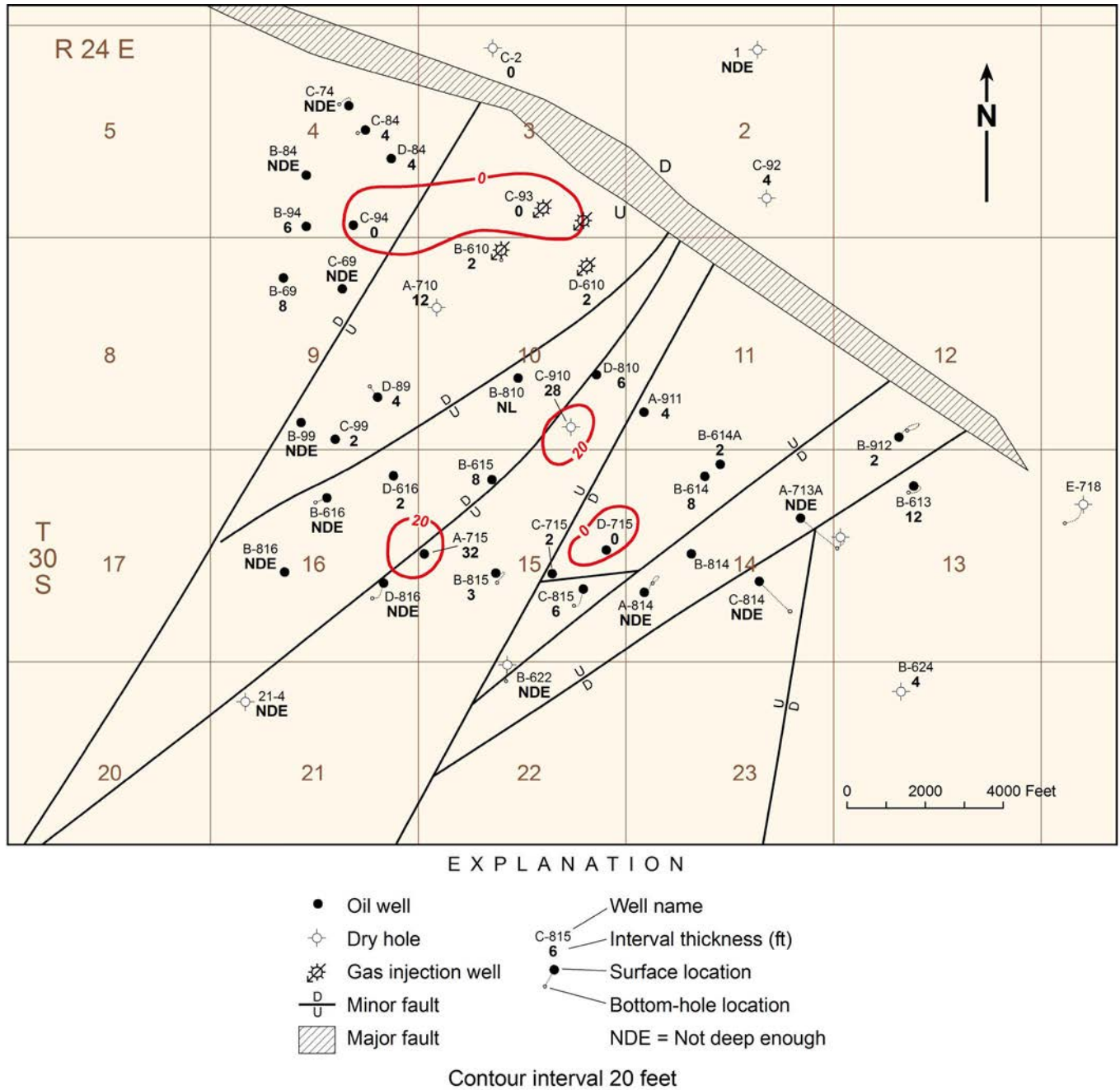
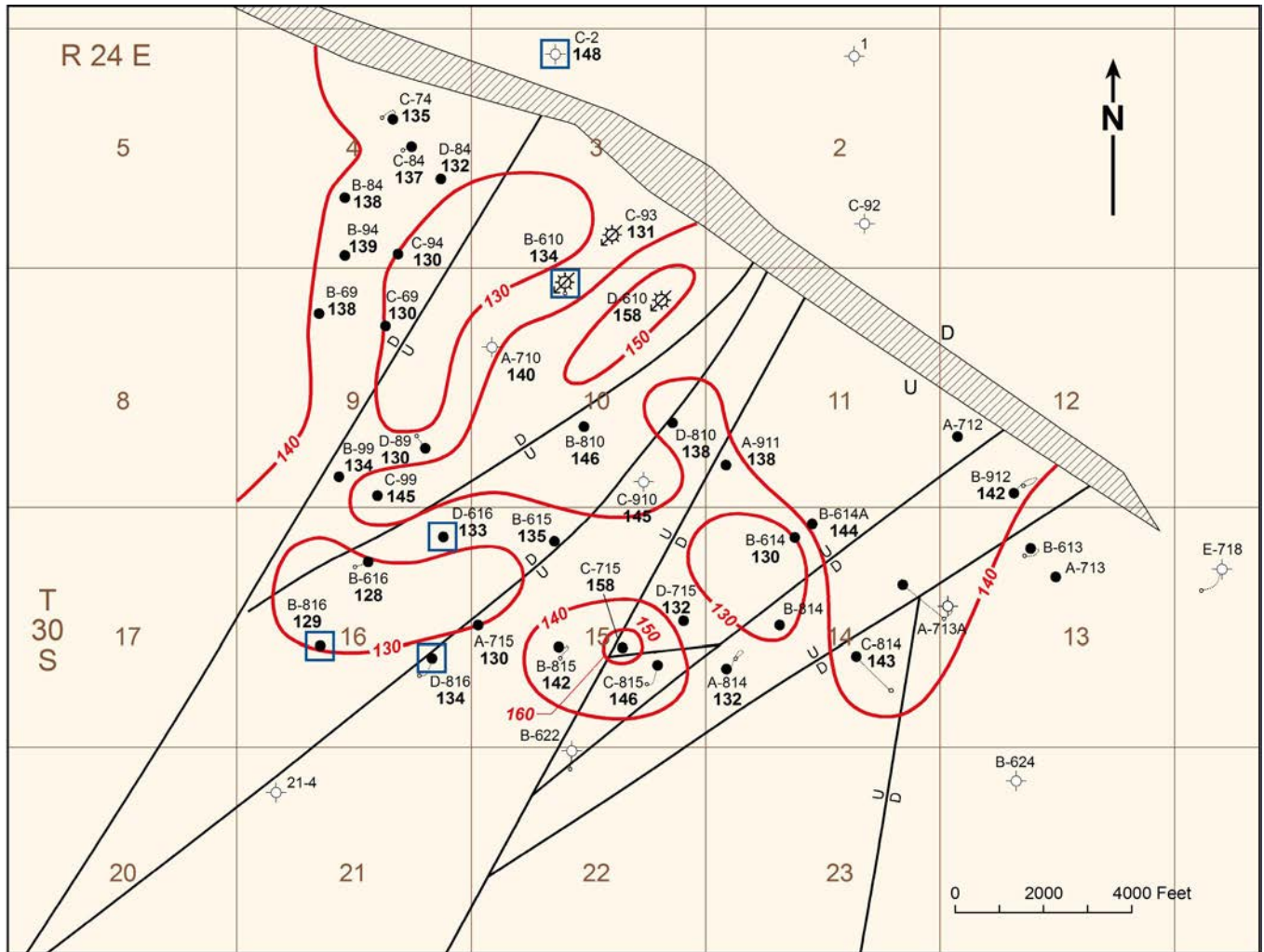


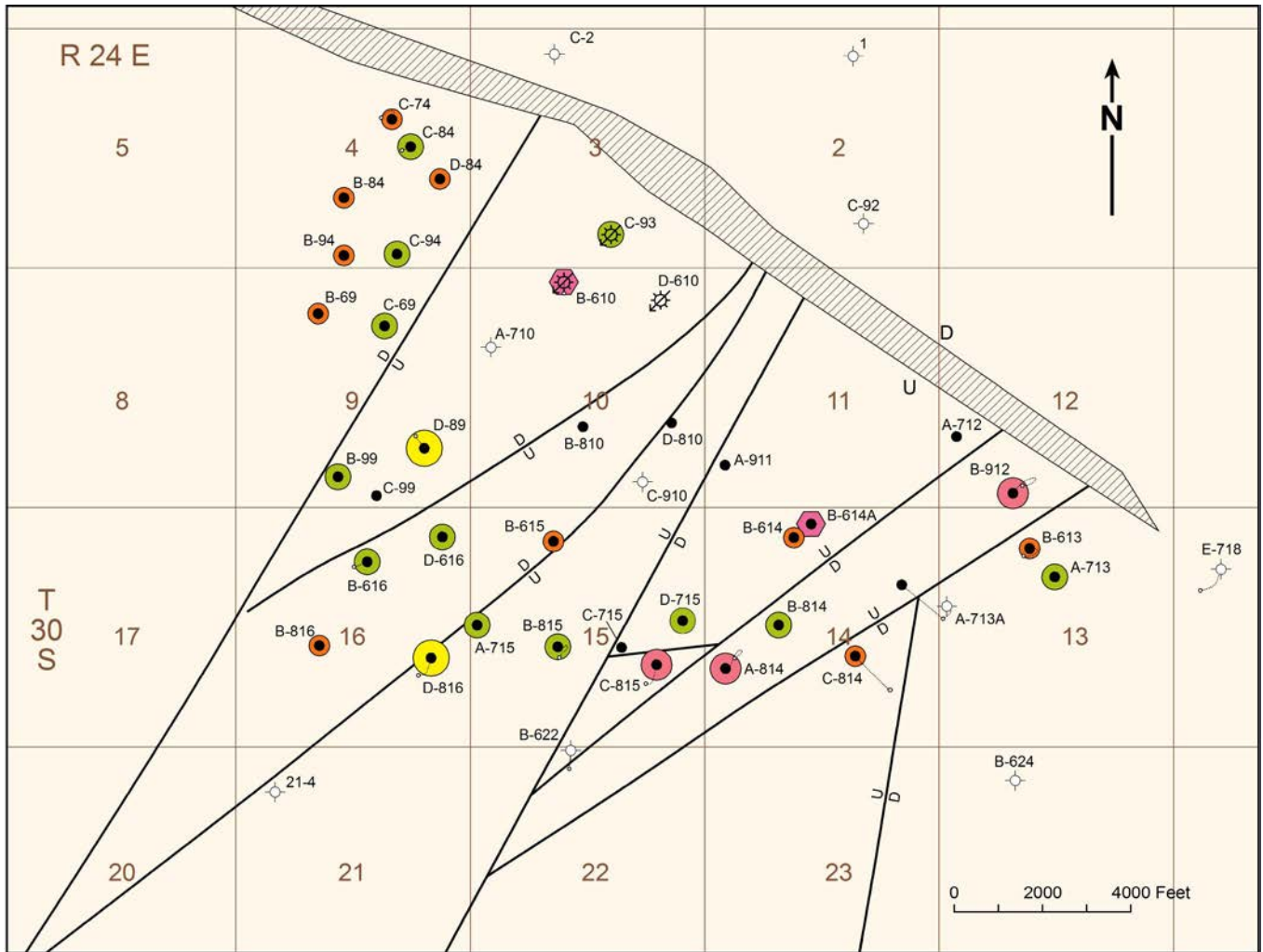
Figure 2.13. Net feet of porosity isochore for reservoir zone 4, Leadville Limestone, Lisbon field.



EXPLANATION

- Oil well
 - ⊕ Dry hole
 - ⊗ Gas injection well
 - |— Minor fault
 - ▨ Major fault
 - Project core
 - Well name
 - C-815 146 Interval thickness (ft)
 - Surface location
 - Bottom-hole location
 - NDE = Not deep enough
- Contour interval 10 degrees Fahrenheit

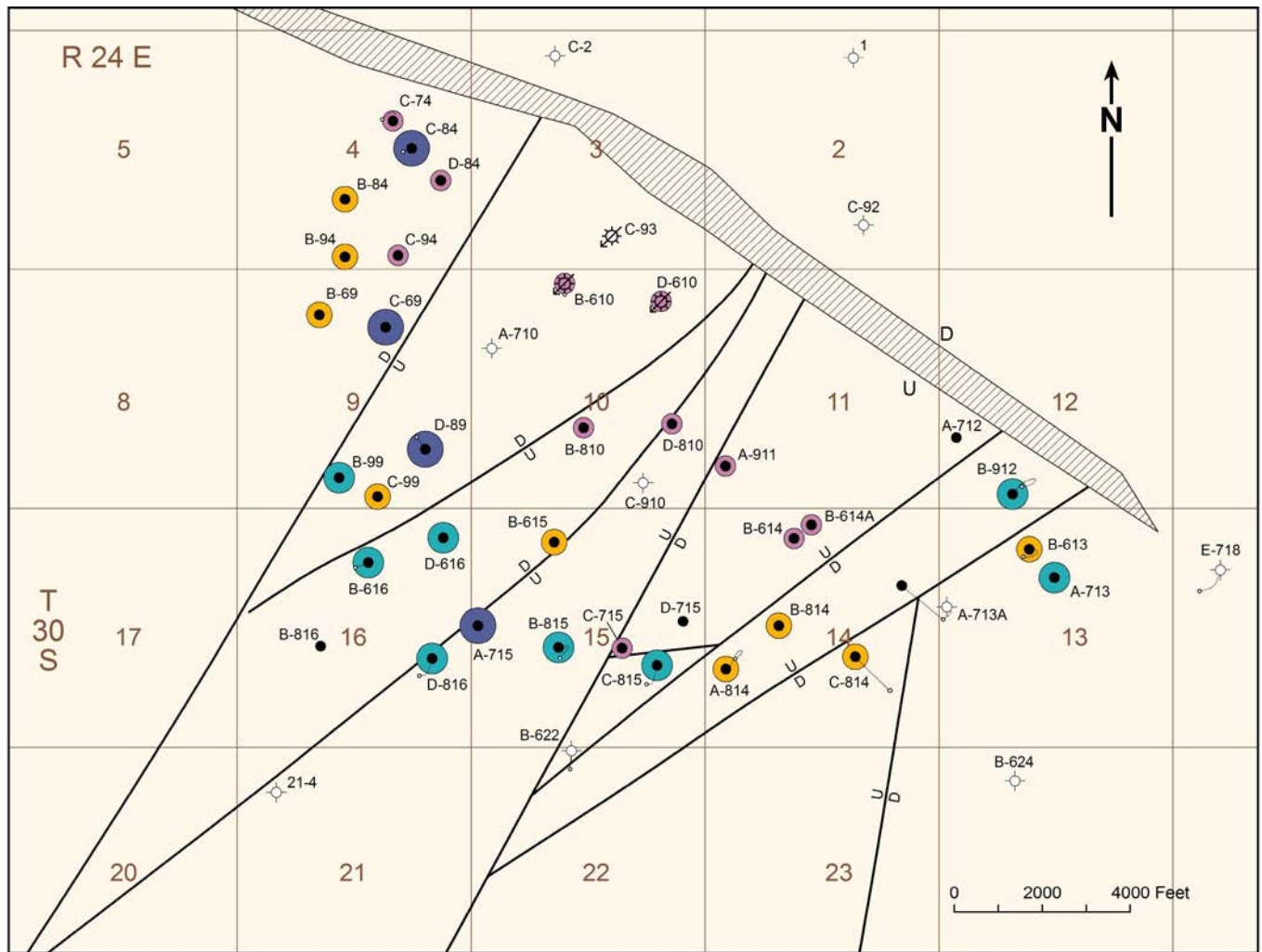
Figure 2.14. Bottom-hole temperature map, Leadville Limestone, Lisbon field.



EXPLANATION

- | | | |
|----------------------|------------------------|---------------------|
| ● Oil well | Well name | ○ 100 to 500 BOPD |
| ⊕ Dry hole | ● Surface location | ● 500 to 1000 BOPD |
| ⊕ Gas injection well | ○ Bottom-hole location | ● 1000 to 1500 BOPD |
| D Minor fault | NDE = Not deep enough | ● >1500 BOPD |
| ▨ Major fault | | ● 2 to 4.4 MMCFGPD |

Figure 2.15. Initial flowing potential, Leadville Limestone, Lisbon field.



EXPLANATION

- | | | |
|----------------------|------------------------|--------------------|
| ● Oil well | Well name | ● <100 MBO |
| ⊕ Dry hole | ● Surface location | ● 100 to 1000 MBO |
| ⊗ Gas injection well | ○ Bottom-hole location | ● 1000 to 5000 MBO |
| — — Minor fault | NDE = Not deep enough | ● >5000 MBO |
| ▨ Major fault | | |

Figure 2.16. Cumulative oil production, Leadville Limestone, Lisbon field.

CHAPTER 3:

LITHOFACIES IN THE LEADVILLE LIMESTONE, LISBON FIELD CASE STUDY

by

Thomas C. Chidsey, Jr., Utah Geological Survey

and

David E. Eby, Eby Petrography & Consulting, Inc.

CHAPTER 3:

LITHOFACIES IN THE LEADVILLE LIMESTONE, LISBON FIELD CASE STUDY

REGIONAL SETTING OF THE LEADVILLE LIMESTONE

The Mississippian (late Kinderhookian to early Meramecian time) Leadville Limestone is a shallow, open-marine, carbonate-shelf deposit (figures 3.1A and 3.2). The western part of the Paradox fold and fault belt includes a regional, reflux-dolomitized, interior bank lithofacies containing Waulsortian mounds (Welsh and Bissell, 1979). During Late Mississippian (Chesterian) time, the entire carbonate platform in southeastern Utah and southwestern Colorado was subjected to subaerial erosion resulting in formation of a lateritic regolith (figure 3.1B) (Welsh and Bissell, 1979). This regolith and associated carbonate dissolution are important factors in Leadville reservoir potential (figure 3.3). Solution breccia and karstified surfaces are common, including possible local development of cavernous zones (Fouret, 1982, 1996).

The Leadville Limestone thins from more than 700 feet (>230 m) in the northwestern corner of the Paradox Basin to less than 200 feet (<70 m) in the southeastern corner (Morgan, 1993) (figure 1.3). Thinning is a result of both depositional onlap onto the western North American cratonic shelf and subaerial erosion. The Leadville is overlain by the Pennsylvanian Molas Formation and underlain by the Devonian Ouray Limestone (figure 1.2).

Periodic movement along northwest-trending faults affected deposition of the Leadville Limestone. Crinoid banks or mounds, the primary reservoir lithofacies (figure 3.2), accumulated in shallow-water environments on upthrown fault blocks or other paleotopographic highs. In areas of greatest paleorelief, the Leadville is completely missing as a result of non-deposition or subsequent erosion (Baars, 1966).

The Leadville Limestone is divided into two members (see figure 2.3) separated by an intraformational disconformity. The dolomitic lower member is composed of mudstone, wackestone, packstone, and grainstone deposited in shallow-marine, subtidal, supratidal, and intertidal environments (Fouret, 1982, 1996). Fossils include crinoids, fenestrate bryozoans, and brachiopods. Locally, mud-supported boundstone creates buildups or mud mounds (Waulsortian facies), involving the growth of "algae" (Wilson, 1975; Fouret, 1982, 1996; Ahr, 1989). The upper member is composed of mudstone, packstone, grainstones (limestone and dolomite), and terrigenous clastics also deposited in subtidal, supratidal, and intertidal environments (Fouret, 1982, 1996). Fossils include crinoids and rugose coral. Reservoir rocks are crinoid-bearing packstone (Baars, 1966).

CORE DESCRIPTIONS

All available conventional cores from Lisbon field (figure 2.1, table 3.1) were photographed and described (see appendices B and C). Special emphasis was placed on identifying flow unit bounding surfaces and depositional environments. The core descriptions follow the guidelines of Bebout and Loucks (1984), which include (1) basic porosity types, (2) mineral composition in percentage, (3) nature of contacts, (4) carbonate structures, (5) carbonate textures in percentage, (6) carbonate fabrics, (7) grain size (dolomite), (8) fractures, (9) color, (10) fossils, (11) cement, and (12) depositional environment. Carbonate fabrics were determined according to Dunham's (1962) and Embry and Klovan's (1971) classification schemes.

Geological characterization on a local scale focused on reservoir heterogeneity, quality, and lateral continuity, as well as possible compartmentalization within Lisbon field. This utilized representative core and modern geophysical well logs to characterize and initially grade various untested intervals in the field for possible additional completion attempts.

The typical vertical sequence or cycle of lithofacies from Lisbon field, as determined from conventional core, was tied to its corresponding log response (figure 3.4). These sequences graphically include (1) carbonate fabric, pore type, physical structures, texture, framework grain, and facies described from core; (2) plotted porosity and permeability analysis from core plugs; and (3) gamma-ray and neutron-density curves from geophysical well logs. The graphs can be used for identifying reservoir and non-reservoir rock, determining potential untested units suitable for completion or possible horizontal drilling projects, and comparing field to non-field areas.

LISBON FIELD LITHOFACIES

Three depositional lithofacies were identified from Leadville Limestone cores described from the Lisbon field case study (figure 3.2). Recognizing and mapping of these lithofacies regionally helped delineate prospective reservoir trends containing porous and productive buildups or zones. Leadville lithofacies include (1) open marine, (2) ooid and peloid shoals, and (3) middle shelf.

Open Marine

Open-marine lithofacies are represented by crinoidal banks or shoals and Waulsortian-type buildups (figure 3.2). Crinoidal

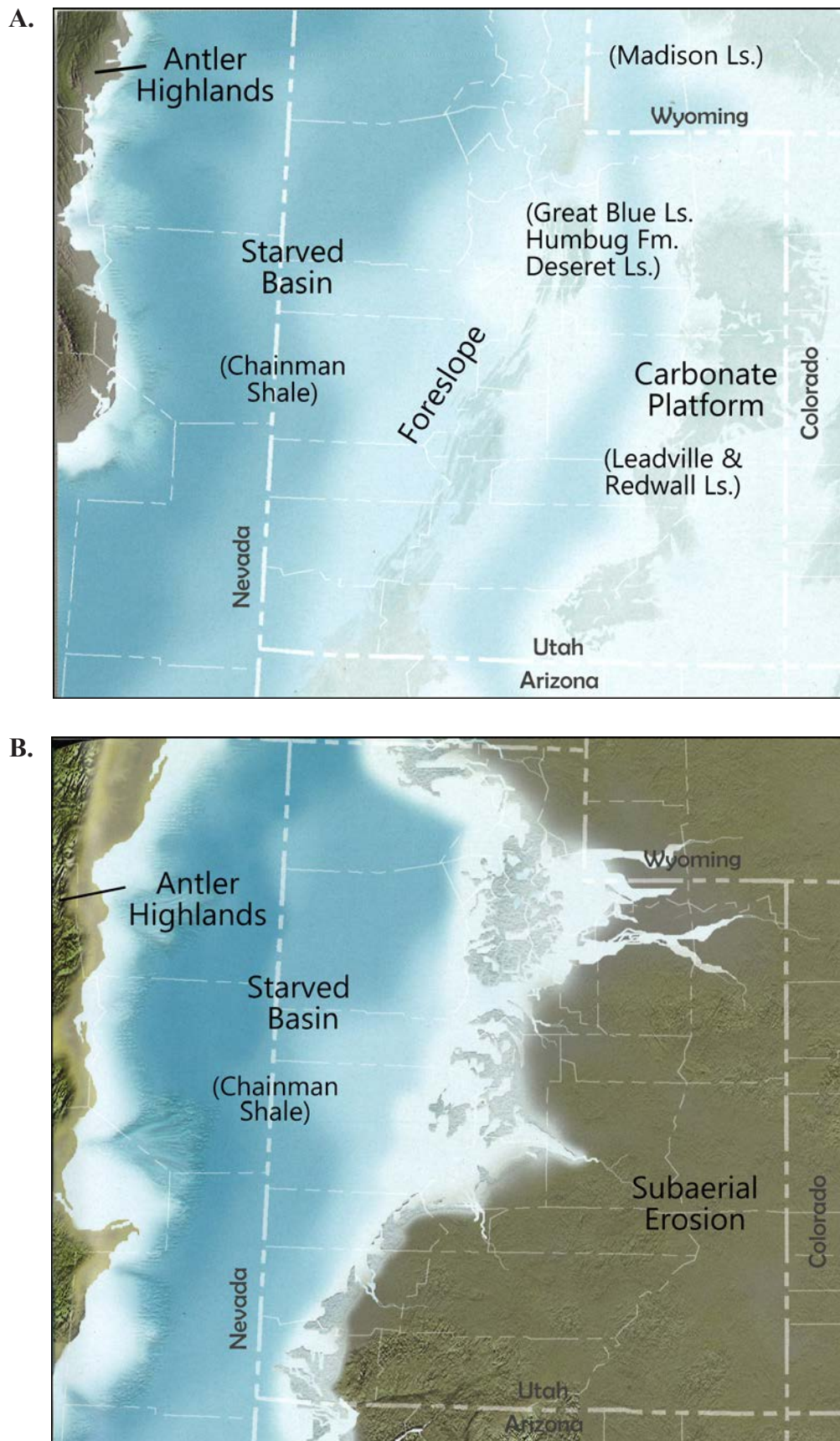


Figure 3.1. Paleogeography of Utah during Mississippian time. **(A)** A warm shallow sea covered much of Utah during the early Meramecian. **(B)** During Late Mississippian (Chesterian) time, the entire carbonate platform in southeastern Utah and southwestern Colorado was subjected to subaerial erosion. Modified from Blakey and Ranney (2008).

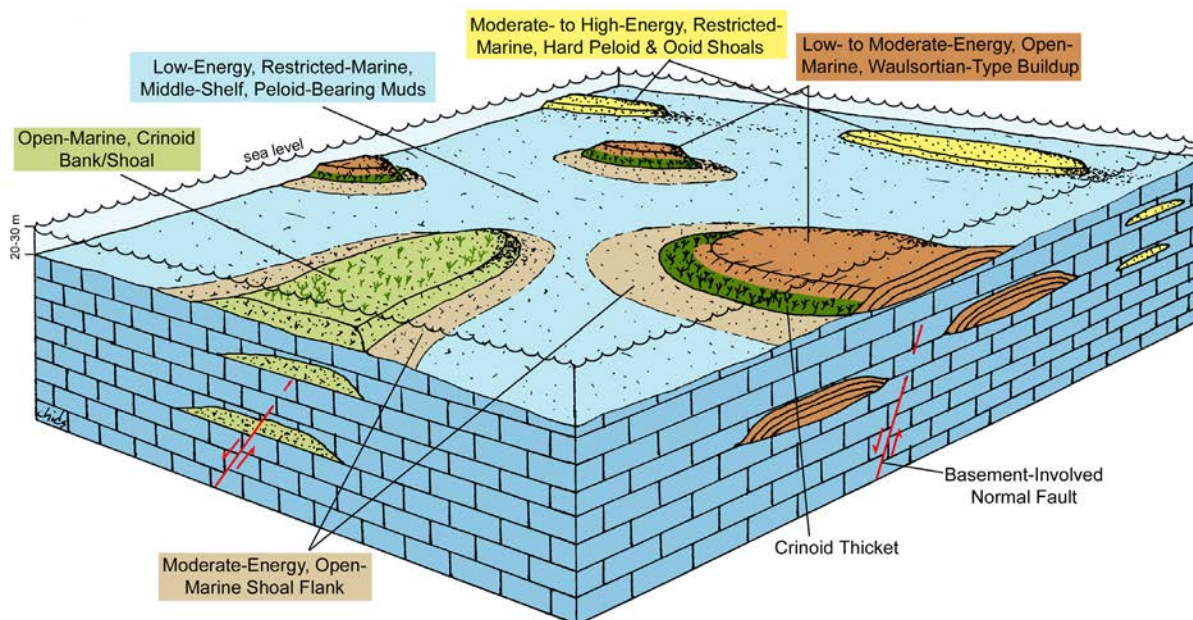


Figure 3.2. Block diagram displaying major depositional facies, as determined from core, for the Leadville Limestone, Lisbon field, San Juan County, Utah.

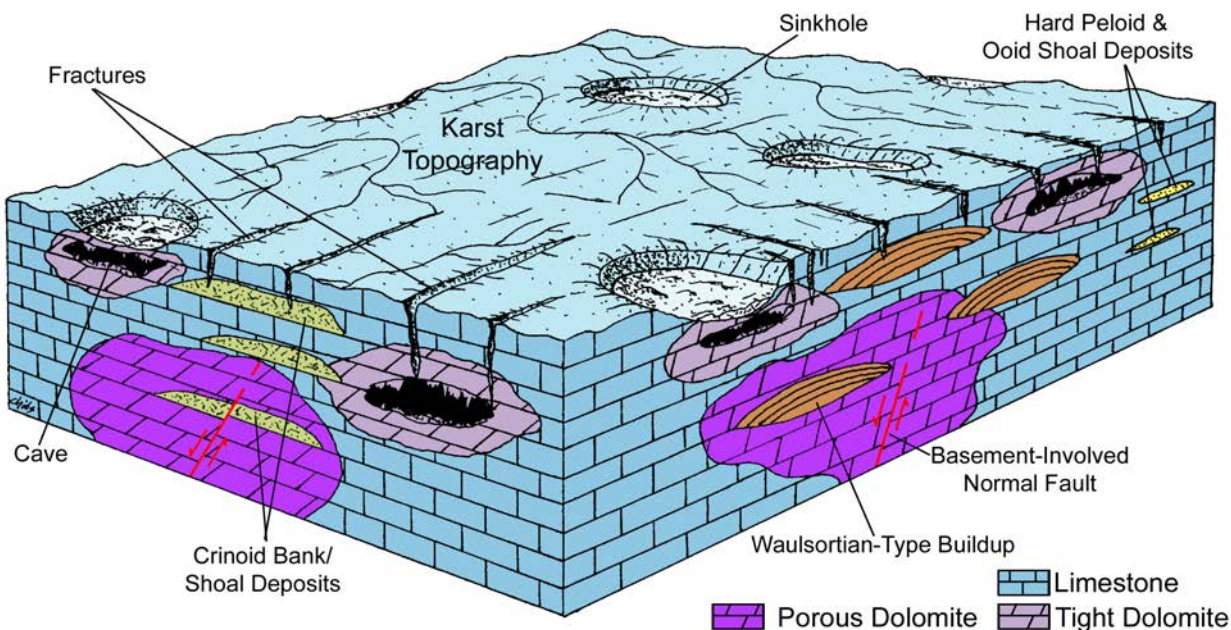
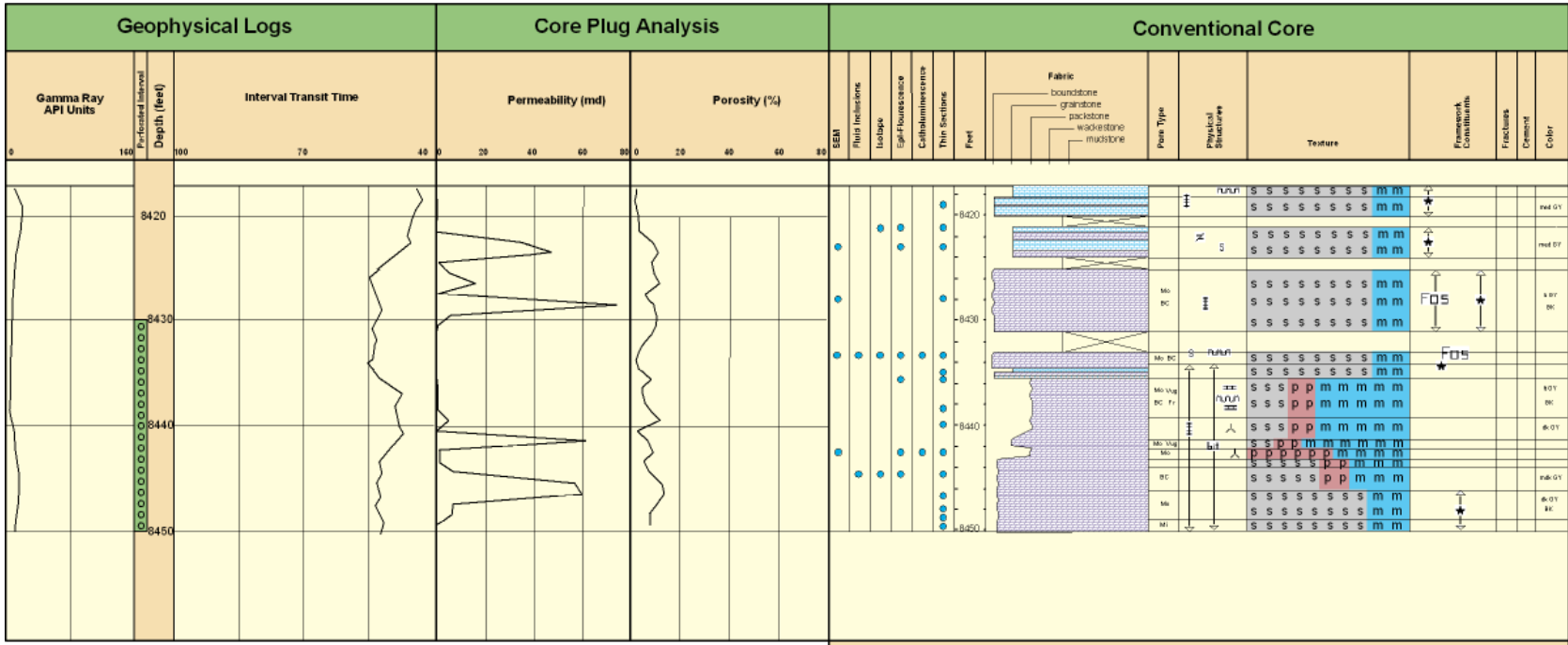


Figure 3.3. Block diagram displaying post-Leadville karst and fracture overprint.

Table 3.1. Conventionally slabbed well core examined and described from the Leadville Limestone, Lisbon field, San Juan County, Utah. See figure 2.3 for well locations.

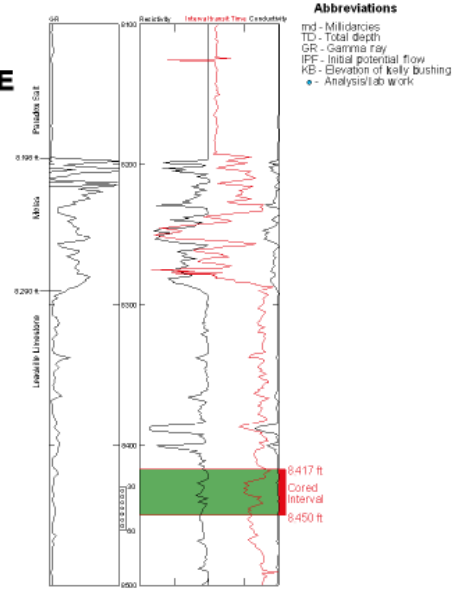
Well	Location	API No.	Core Interval (feet)	Thin Sections
Lisbon D-816	NE SE 16, T. 30 S., R. 24 E.	43-037-16253	8417–8450	15
Lisbon D-616	C NE NE 16, T. 30 S., R. 24 E.	43-037-15049	8300–9110	13
NW Lisbon B-63	NE NW 3, T. 30 S., R. 24 E.	43-037-11339	9934–10,005	14
Lisbon B-816	NE SW 16, T. 30 S., R. 24 E.	43-037-16244	8463–8697	22
Lisbon B-610	NE NW 10, T. 30 S., R. 24 E.	43-037-16469	7590–8001.5	18

Repository: Utah Core Research Center.



Lisbon D-816
NESE Section 16, T30S, R24E
KB 6108 feet

TD 8666 feet
 IPF: 1782 BPD, no gas, no water
 Completed: 11-1-1962



Abbreviations
 md - Millidarcies
 TD - Total depth
 GR - Gamma ray
 IPF - Initial potential flow
 KB - Elevation of Kelly bushing
 • - Analysis/ID work

Lithologic Composition		Explanation	
Texture		Pore Types	Physical Structures
	Limestone	Mo Moldic	n/n/n - Stylolites
	Dolomite	BC Intercrystal	≡ - Fractures
	Skeletal grains	Vug Vug	s - Sulfide minerals
	Micrite	Mi Microporosity	z - Slickensides
	Peloid	Fr Fracture	人 - Anhydrite, mosaic
Framework Constituents		Abundance	bit - Bitumen
★ - Crinoids		↑ Pervasive	
Fos - Unidentified fossils		↑ Abundant	
		↑ Rare	

Figure 3.4. Typical Leadville vertical sequence from Lisbon field, including geophysical well logs, porosity/permeability plots, and core description, of the Lisbon No. D-816 well (figure 2.3), San Juan County, Utah.

banks and shoals are common throughout Leadville deposition, often located on paleotopographic highs developed along the upthrown side of older basement-involved fault blocks. This lithofacies represents high-energy environments with well-circulated, normal-marine salinity water in a subtidal setting, although they can also be present in restricted marine, middle shelf settings. Wave action was strong (leaving broken crinoid columns and winnowing out mud) to moderate (leaving articulated crinoid columnals and some muddy matrix). Low- to medium-scale cross-bedding is common. Crinoid columnals were not transported far from the thickets where they grew. Rugose corals were also abundant in this environment. According to Wilson (1975), crinoid columnals or segments were covered with organic matter, which allowed them to float until accumulating on nearby shoals and banks. We estimate that water depths ranged from 5 to 45 feet (1.5–14 m). The depositional fabrics of crinoidal banks and shoals include grainstone and packstone (figure 3.5). Rocks representing crinoidal banks and shoals typically contain the following diagnostic constituents: dominantly crinoids and rugose corals, and lesser amounts of broken fenestrate bryozoans, brachiopods, ostracods, and endothyroid forams as skeletal debris. Rock units with this lithofacies constitute a significant reservoir potential, having both effective porosity and permeability when dissolution of skeletal grains, followed by dolomitization, has occurred.

Waulsortian buildups or mud mounds developed exclusively during the Mississippian in many parts of the world (Wilson, 1975), and Waulsortian-type buildups were first described in Lisbon field by Fouret (1982) and are steep-sloped tabular, knoll, or sheet forms composed of several generations of mud deposited in a subtidal setting (Fouret, 1982, 1996; Lees and Miller, 1995) (figure 3.2). Lime mud was precipitated by bacteria and fungal/cyanobacterial filaments (Lees and Miller, 1995). Cyanobacteria (microbialites) were a likely precursor to the green algae *Ivanovia* responsible for Pennsylvanian buildups in the Paradox Basin (Fouret, 1982, 1996). Crinoids and sheet-like fenestrate bryozoans, in the form of thickets, are associated with the deeper parts of the mud mounds and are indicative of well-circulated, normal-marine salinity. We estimate that water depths ranged from 60 to 90 feet (20–30 m). The thickets surrounded and helped to stabilize the mound. Burrowing organisms added a pelletal component to the mud and burrowing often destroyed laminations or made them discontinuous. Individual mounds range from a few feet to tens of feet thick, and cover hundreds of feet in areas with distinctive flank deposits. They form thick, extensive aggregates often located on paleotopographic highs associated with basement-involved faults (figure 3.2). This lithofacies represents a low- to moderate-energy environment. The depositional fabrics of the Waulsortian-type buildups include mud-supported boundstone, packstone, and wackestone (figure 3.6). Rocks representing Waulsortian-type buildups typically contain the following diagnostic constituents: peloids, crinoids, bryozoans, and associated skeletal debris, and *stromatactis*. Rock

units having this lithofacies constitute a significant reservoir potential, having both effective porosity and permeability, especially after dolomitization. Waulsortian-type buildups are recognized in several additional cores described by Fouret (1982, 1996).

Shoal-flank lithofacies are associated with both crinoid bank/shoal and Waulsortian-type buildup facies (figure 3.2). This lithofacies represents a moderate-energy environment, again with well-circulated, normal-marine salinity water in a subtidal setting. We estimate that water depths ranged from 60 to 90 feet (20–30 m). In the shallower areas, wave action was strong to moderate, eroding the flanks of the shoals and mud mounds into a breccia. Bedding is generally absent in cores. The depositional fabrics of the shoal-flank lithofacies include peloidal/skeletal packstone and wackestone (figure 3.7). Rocks representing this lithofacies typically contain the following diagnostic constituents: peloids, crinoids, bryozoans, brachiopods, and associated skeletal debris, and talus, depositional breccia, and conglomerate (Fouret, 1982, 1996). Rock units having shoal-flank lithofacies constitute a limited reservoir potential, having little effective porosity and permeability.

Ooid and Peloid Shoals

Ooid and “hard” peloid shoals developed as a result of agitated, shallow-marine processes on the open-marine or bordering restricted-marine middle shelf (figure 3.2). Like crinoidal banks and Waulsortian-type buildups, hard peloid and ooid shoals were common throughout Leadville deposition, especially on paleotopographic highs. This lithofacies represents a moderate- to high-energy environment, with moderately well-circulated water in a shoal setting. The water probably had slightly elevated salinity compared to the other lithofacies. Sediment deposition and modification probably occurred in water depths that we estimate ranged from near sea level to 20 feet (6 m) below sea level. Wave action winnowed out mud leaving various well-sorted grains. Characteristic features of this lithofacies include medium-scale cross-bedding and bar-type carbonate sand-body morphologies that formed not only shoals, but beaches and tidal bars (Fouret, 1982). Well-developed ooids were produced from movement of particles over algal or cyanobacterial (microbial) mats by intertidal currents and continuous wave action (Mitchell, 1961; Fouret, 1982).

The depositional fabrics of the ooid and peloid shoal lithofacies include grainstone and packstone (figure 3.8). Rocks representing this lithofacies typically contain the following diagnostic constituents: ooids, coated grains, and hard peloids. Fossils are relatively rare.

Rock units having ooid and peloid shoal lithofacies constitute good reservoir potential. Remnants of visible interparticle and moldic porosity may be present in this lithofacies. Dolomitization significantly increases the reservoir quality of this lithofacies.

A.

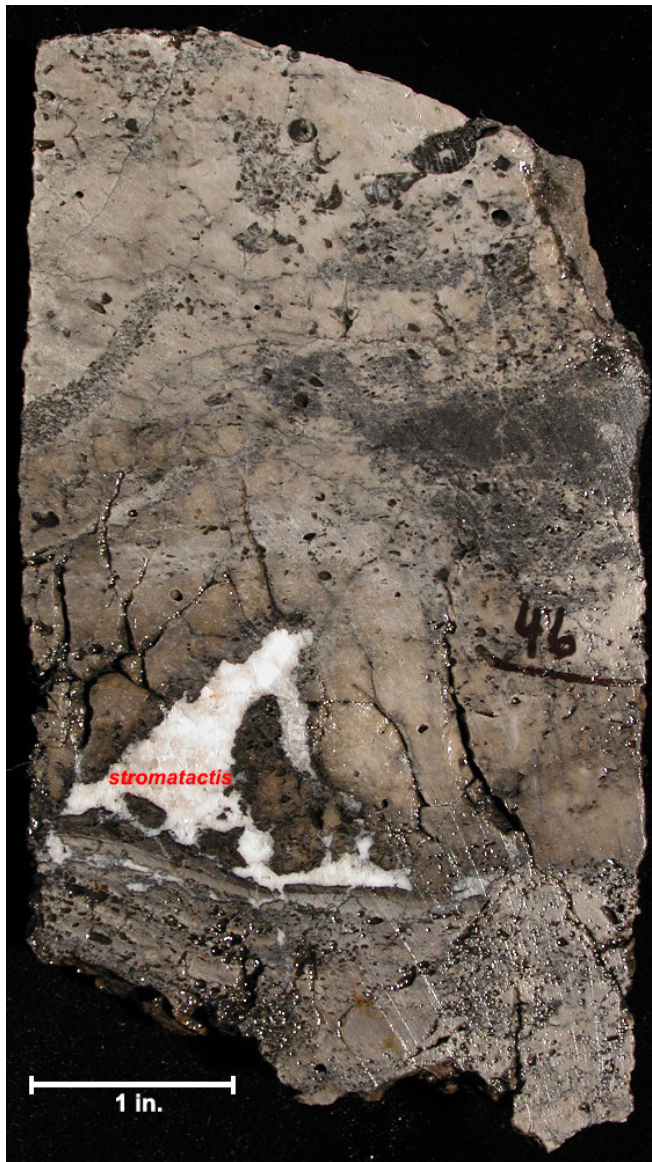


B.



Figure 3.5. Typical crinoidal/skeletal grainstone/packstones representing high-energy, open-marine shoal lithofacies, Lisbon No. B-816 (NE1/4SW1/4 section 16, T. 30 S., R. 24 E., SLBL&M [figure 2.3]). (A) Slabbed core from 8506.5 feet (2592.8 m). Note the large rugose coral. (B) Slabbed core from 8547 feet (2605 m).

A.



B.



Figure 3.6. Typical peloidal/skeletal packstone/wackestones representing moderate- to low-energy, open-marine (and occasionally middle shelf), Waulsortian-type buildup lithofacies. (A) Lisbon No. B-816 (NE1/4SW1/4 section 16, T. 30 S., R. 24 E., SLBL&M [figure 2.3]); slabbed core from 8646 feet (2635 m). (B) Lisbon No. D-616 (NE1/4NE1/4 section 16, T. 30 S., R. 24 E., SLBL&M); slabbed core from 8514 feet (2595 m).

Middle Shelf

Middle-shelf lithofacies covered extensive areas across the shallow platform and represent a low-energy, often restricted-marine environment (figure 3.2). Mud and some sand were deposited in a subtidal (burrowed), inter-buildup/shoal setting. We estimate that water depths ranged from 60 to 90 feet (20–30 m).

The depositional fabrics of the middle-shelf lithofacies include wackestone and mudstone (figure 3.9). The most common is bioturbated lime to dolomitic mudstone having sub-horizontal feeding burrows. Rocks representing this lithofacies typically contain the following diagnostic constituents:

soft pellet muds, “soft” peloids, grain aggregates, crinoids and associated skeletal debris, and fusulinids.

Rock units having middle-shelf lithofacies act as barriers and baffles to fluid flow, having very little effective porosity and permeability. This lithofacies has few megafossils and little visible matrix porosity, with the exception of an occasional moldic pore. However, recognizing this lithofacies is important because low-energy carbonates of the middle shelf form the substrate for the development of the higher energy crinoid banks, ooid/hard peloid shoals, and Waulsortian-type buildups (figure 3.2). The middle-shelf lithofacies can contain reservoir-quality rocks if dolomitized.



Figure 3.7. Typical peloidal/skeletal packstone/wackestone representing moderate-energy, open-marine, shoal-flank lithofacies. Lisbon No. B-816 (NE1/4SW1/4 section 16, T. 30 S., R. 24 E., SLBL&M [figure 2.3]); slabbed core from 8521 feet (2597 m).

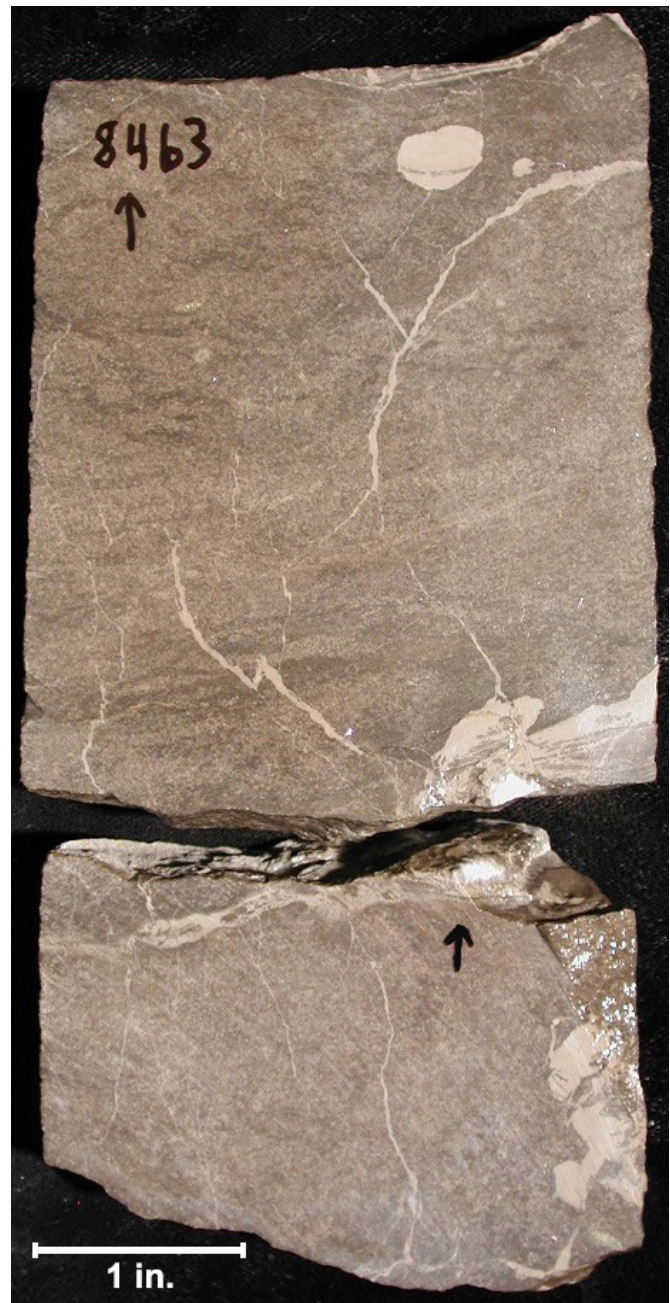


Figure 3.8. Typical peloidal grainstone/packstone representing moderate-energy, "hard" peloid shoal lithofacies. Lisbon No. B-816 (NE1/4SW1/4 section 16, T. 30 S., R. 24 E., SLBL&M [figure 2.3]); slabbed core from 8463 feet (2580 m).



Figure 3.9. Typical skeletal/“soft” peloidal wackestone/mudstone representing low-energy, restricted-marine, middle-shelf lithofacies. Lisbon No. B-816 (NE1/4SW1/4 section 16, T. 30 S., R. 24 E., SLBL&M [figure 2.3]); slabbed core from 8649 feet (2636 m).

CHAPTER 4:

DIAGENETIC ANALYSIS OF THE LEADVILLE LIMESTONE, LISBON FIELD CASE STUDY

by

David E. Eby, Eby Petrography & Consulting, Inc.

Thomas C. Chidsey, Jr., Utah Geological Survey

Joseph N. Moore, Energy & Geoscience Institute

Louis H. Taylor, Standard Geological Services, Inc.
(now at the Denver Museum of Nature & Science)

and

John D. Humphrey, Colorado School of Mines
(now at King Fahd University of Petroleum and Minerals)

CHAPTER 4:

DIAGENETIC ANALYSIS OF THE LEADVILLE LIMESTONE, LISBON FIELD CASE STUDY

INTRODUCTION

The diagenetic fabrics and porosity types found in the various hydrocarbon-bearing rocks of Lisbon field can be indicators of reservoir flow capacity, storage capacity, and untested potential. Diagenetic characterization is focused on reservoir heterogeneity, quality, and compartmentalization within the field. All depositional, diagenetic, and porosity information can be combined with the production history to analyze the potential for the Leadville Limestone regionally.

The petrographic techniques employed consisted of (1) basic thin section petrographic descriptions, (2) porosity and permeability cross-plot evaluation, (3) scanning electron microscope (SEM) analysis of various dolomites to determine reservoir quality of the dolomites as a function of diagenetic history, and (4) epifluorescence (EF) and cathodoluminescence (CL) petrography for the sequence of diagenesis. Geochemical analysis included (1) fluid inclusion (FI) evaluation to determine the temperatures of secondary dolomite formation and the salinity of the original brines, (2) stable carbon and oxygen isotope analysis of diagenetic components such as cementing minerals and different generations of dolomites, and (3) strontium isotope analysis for tracing the origin of fluids responsible for different diagenetic events.

An ideal diagenetic sequence based on our analysis of Leadville Limestone thin sections from Lisbon field is presented in figure 4.1. Leadville reservoir quality at Lisbon is greatly enhanced by dolomitization and dissolution of limestone. There are two basic types of dolomite: very fine, early dolomite and coarse, late dolomite. The early dolomitization and leaching of skeletal grains resulted in low-porosity and/or low-permeability rocks. Most reservoir rocks within Lisbon field appear to be associated with the second, late type of dolomitization and associated leaching events. Other diagenetic products include pyrobitumen, syntaxial cement, sulfide minerals, anhydrite cement and replacement, and late macrocalcite. Fracturing and brecciation caused by hydrofracturing are widespread within Lisbon field. Sediment-filled cavities, related to karstification of the exposed Leadville, are present in the upper third of the formation. Late dolomitization, sulfides, and brecciation may have developed from hydrothermal events that can greatly improve reservoir quality.

BASIC THIN SECTION PETROGRAPHIC AND CORE PLUG PETROPHYSICAL ANALYSIS

To determine the diagenetic histories of the various Leadville Limestone rock fabrics, including both reservoir and non-reservoir, 64 thin sections of representative samples were selected from the conventional cores (figure 2.1 and table 3.1) for petrographic description and geochemical analysis. Carbonate fabrics were determined according to Dunham's (1962) and Embry and Klovan's (1971) classification schemes. Pores and pore systems were described using Choquette and Pray's (1970) classification (figure 4.2). Each thin section was photographed with additional close-up photos of (1) typical preserved primary and secondary pore types, (2) cements, (3) sedimentary structures, (4) fractures, and (5) where present, pore-plugging anhydrite, halite, and bitumen.

Thin Section Description and Interpretation

The early diagenetic history of the Leadville Limestone sediments, including some early dolomitization and leaching of skeletal grains, resulted in low-porosity and/or low-permeability rocks. Most of the porosity and permeability associated with hydrocarbon production was developed during deeper subsurface dolomitization and dissolution. Some of these important subsurface processes are shown with the purple bars in figure 4.1 and are discussed below generally in the order in which they occur. For the complete descriptions and photomicrographs of Lisbon thin sections refer to appendix D.

Syntaxial Cement

Syntaxial cementation is an early diagenetic event (figure 4.1). This type of cementation is found exclusively as overgrowths on echinoderms (figure 4.3), in this case dominantly crinoids deposited in banks or shoals of the open-marine facies. Crinoid ossicles often appear to be "floating" in cement with little evidence of compaction. If extensive syntaxial cementation has occurred, the result will be a significant reduction of porosity. However, the thin sections evaluated show this diagenetic process has been relatively minor.

Dolomitization and Porosity Development

Two basic types of dolomite have been identified in the cores (figure 4.4A). The first type consists of "stratigraphic" dolo-

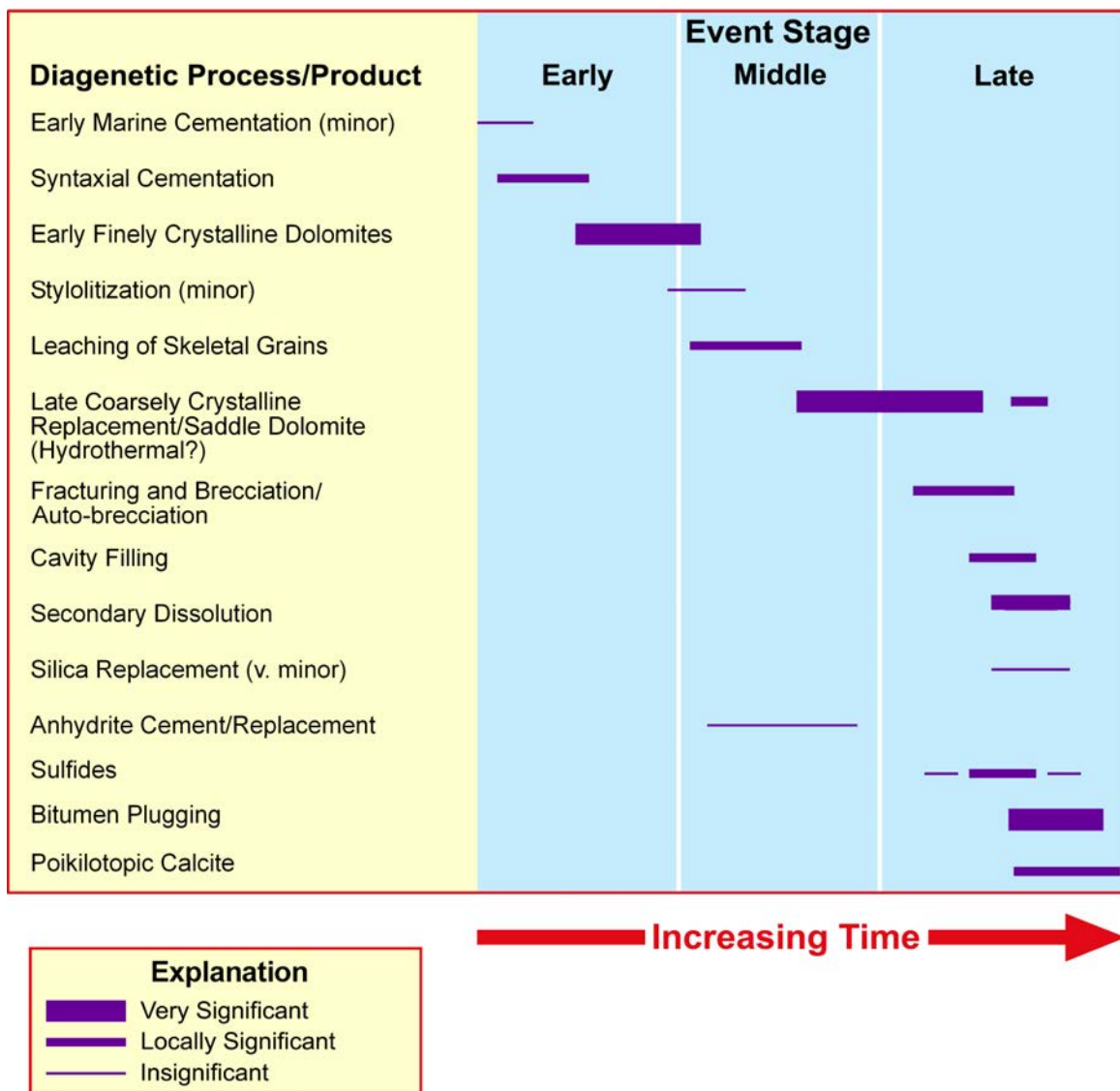


Figure 4.1. Ideal diagenetic sequence through time based on thin section analysis, Leadville Limestone, Lisbon field.

mite that preserves original depositional grains and textures. Very fine (<5 μm), interlocking dolomite crystals with no intercrystalline pore spaces are the norm (figure 4.4B). Commonly, this type of dolomite can be correlated across the field in several relatively thin intervals. The second type of dolomite is a much coarser (>10–20 μm), later replacement of all types of limestone and earlier “stratigraphic” dolomites (figure 4.4C). Crosscutting relationships with carbonate bedding and variable dolomite thickness across the field are common. Petrographically, the coarse, second dolomite type consists of crystals with thick, cloudy, inclusion-rich cores and thin, clear overgrowths that have planar crystal terminations. Often, these coarser dolomites show saddle dolomite characteristics of curved crystal shape (figure 4.5) and sweeping extinction under cross-polarized lighting. Pervasive leaching and dissolution episodes, which predate or concomitant with saddle dolomite formation, crosscut the carbonate host rocks and result in late vugs, as well as extensive microporosity. Pyrobitumen

appears to coat most intercrystalline dolomite, as well as dissolution pores associated with the second type of dolomite. Most reservoir rocks within Lisbon field appear to be associated with the second, late type of dolomitization and associated leaching events.

Later dolomitization, saddle dolomite, and dolomite cement precipitation may have occurred at progressively higher temperatures, that is, hydrothermal dolomite. Hydrothermal events can improve reservoir quality by increasing porosity through dolomitization, leaching, development of microporosity, and natural fracturing (forming breccia) kept open with various minerals (Smith, 2004, 2006; Davies and Smith, 2006; Smith and Davies, 2006). Hydrothermal dolomite precipitates under temperature and pressure conditions greater than the ambient temperature and pressure of the host limestone (Davies, 2004; Davies and Smith, 2006; Smith, 2006; Smith and Davies, 2006). The result can be the formation of large, diagenetic-type hydrocarbon traps.

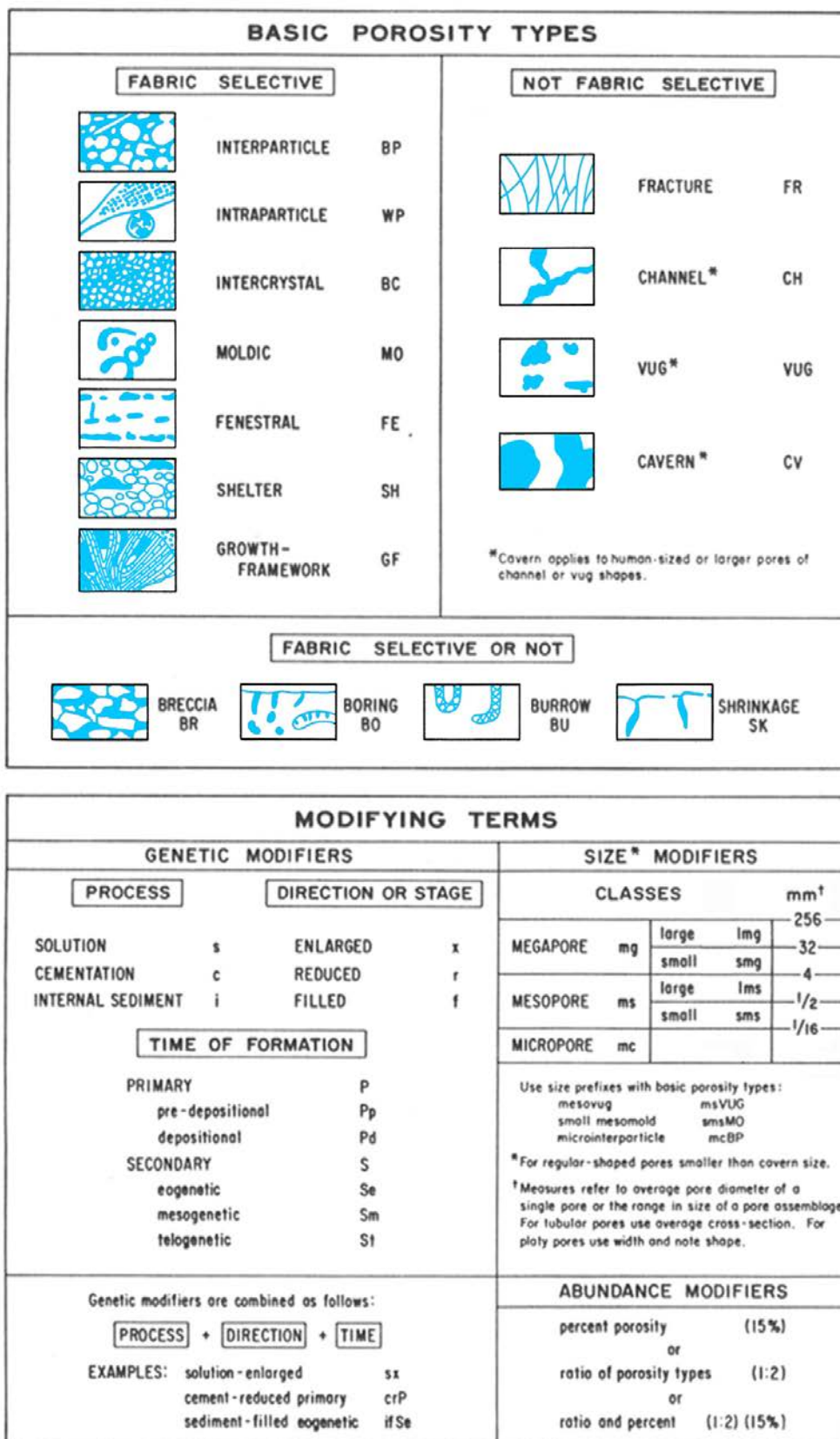


Figure 4.2. Classification of pores and pore systems in carbonate rocks. From Choquette and Pray (1970).

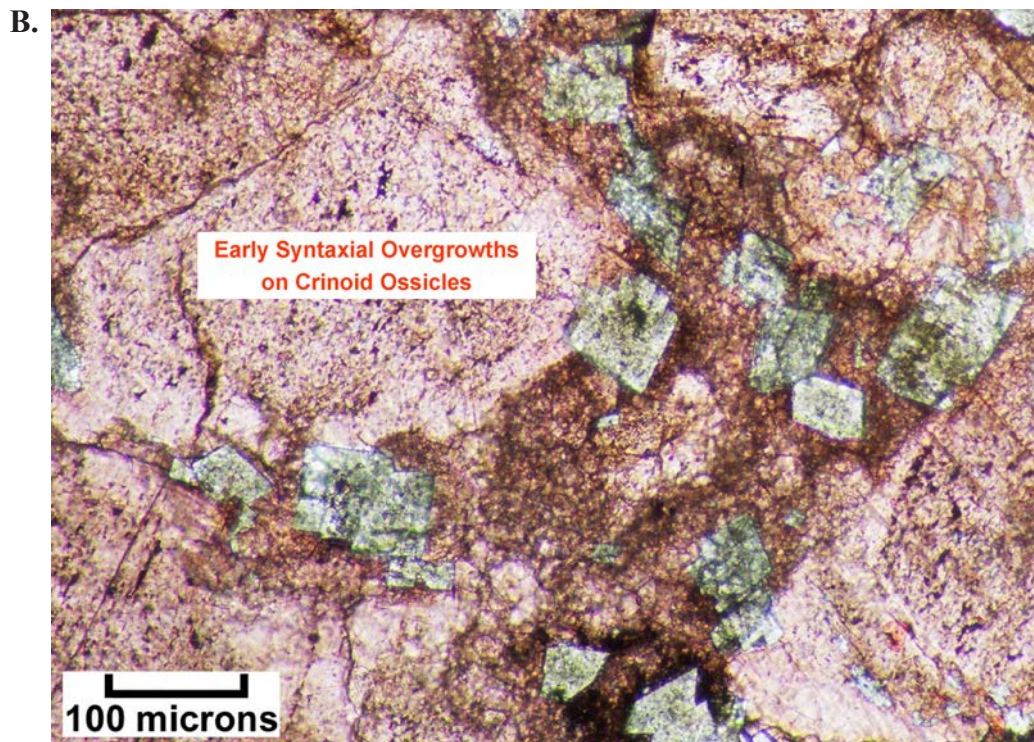
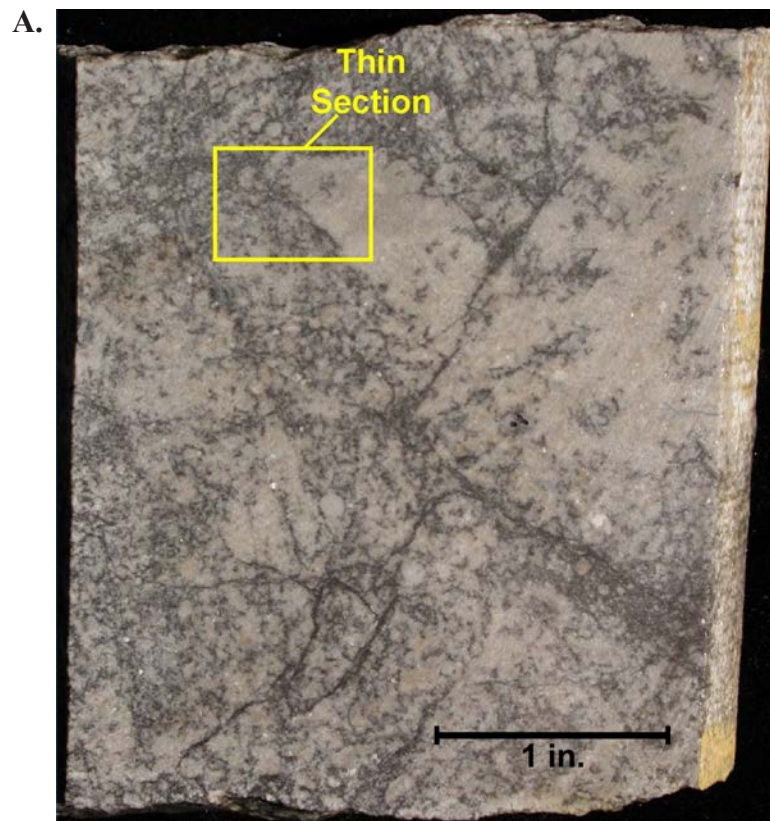


Figure 4.3. (A) Conventional core slab showing partially dolomitized crinoidal/grainstone packstone. (B) Representative photomicrograph (plane light) from the core in A, showing early syntaxial overgrowths on crinoid ossicles. Crinoids appear cloudy due to inclusions of organic matter. Lisbon No. D-816 well (figure 2.3), 8435 feet (2571 m), porosity = 7.5%, permeability = 0.03 mD.

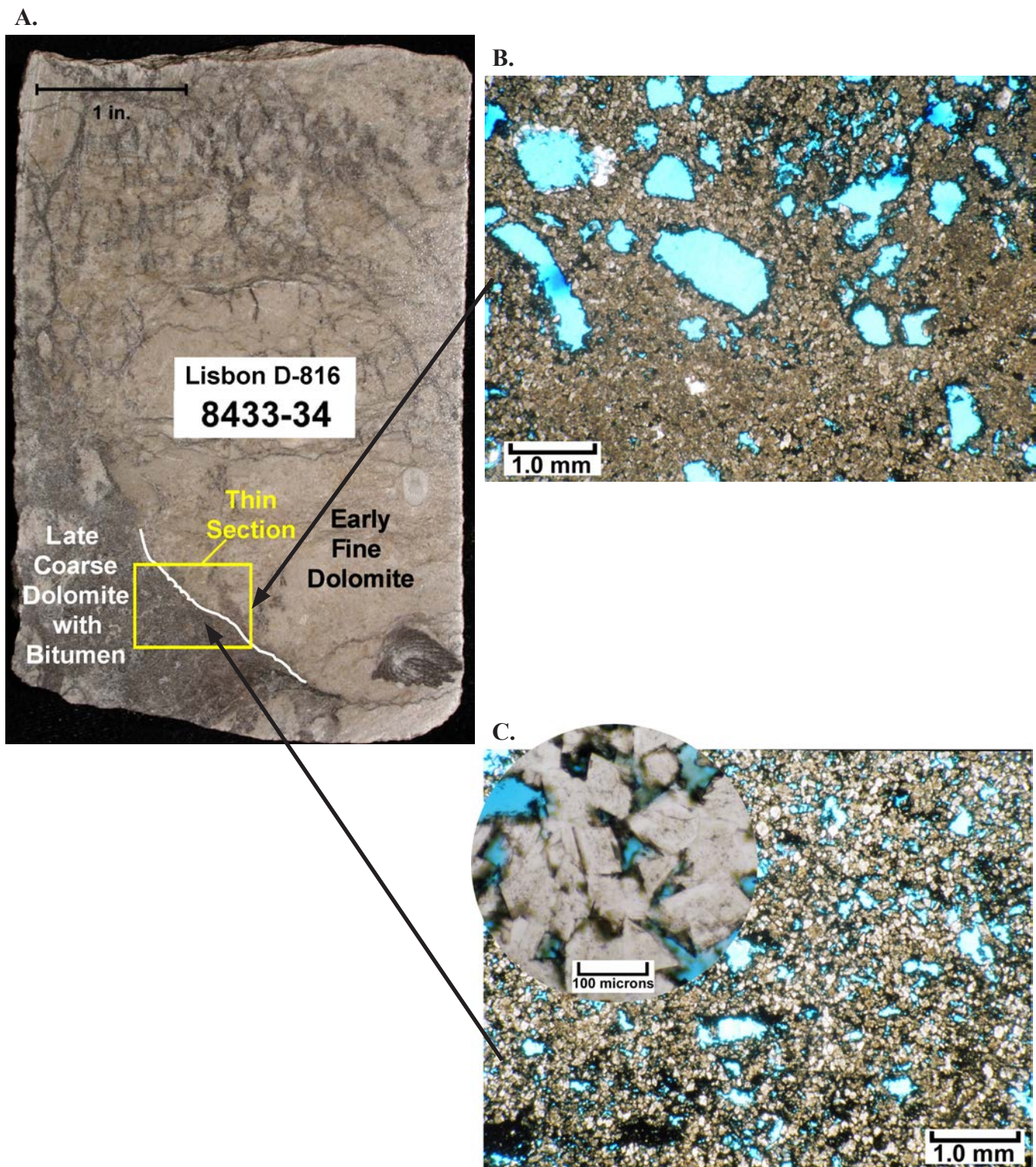


Figure 4.4. (A) Conventional core slab showing low-permeability, fabric-selective, very fine early dolomite as well as porous, coarser late dolomite. Most of the late dolomite crystal faces are coated with films of pyrobitumen. Hence, most of the areas of crosscutting coarser dolomites are black in this view. Note the position of the thin section, which captures the contact between low-permeability early dolomite (upper right part of the thin section) and high-permeability late, “black dolomite” (lower left). (B) Representative photomicrograph (plane light) of the low-permeability, finely crystalline dolomite with isolated grain molds. Most of this fabric-selective dolomite formed early in the diagenetic history of the skeletal/peloid sediment. (C) Representative photomicrograph (plane light) of the coarser replacement dolomite (both euhedral rhombs and occasional “saddle” overgrowths [close-up view in inset]). The black (opaque) areas are the result of pyrobitumen films and minor sulfide precipitation. Lisbon No. D-816 well (figure 2.3), 8433 feet (2570 m), porosity = 2%, permeability <0.1 mD.

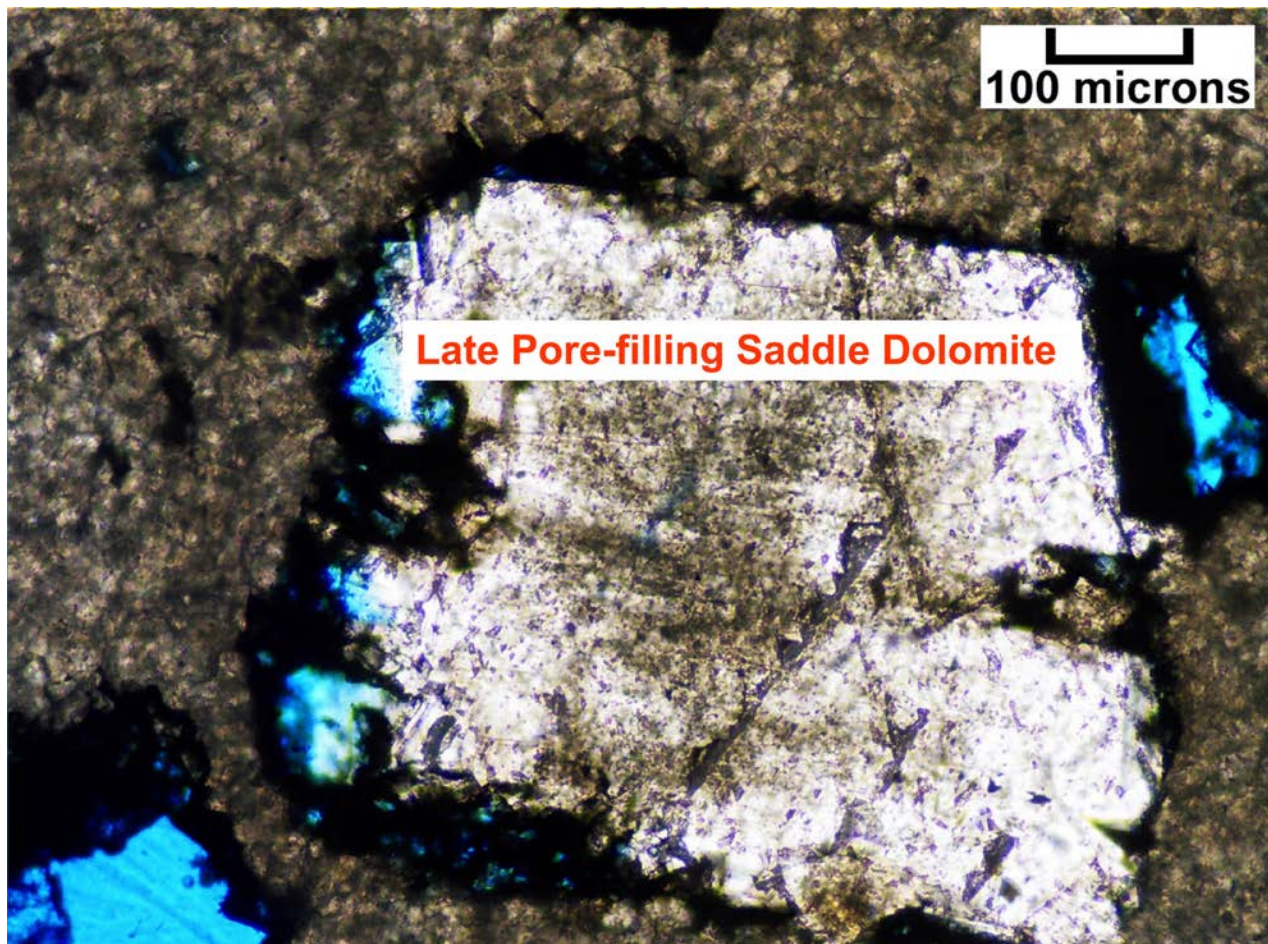


Figure 4.5. Thin section photomicrograph (plane light) showing a saddle dolomite cement that is filling a large pore (either a grain mold or small vug). The dolomite cement has been surrounded by a coating of pyrobitumen (in black). This late dolomite cement has been partially dissolved or corroded around its margins after the bitumen coating. Lisbon No. D-816 well (figure 2.3), 8421 feet (2567 m), porosity = 8.3%, permeability = 34 mD.

Post-Burial Brecciation

Fracturing and brecciation are quite common within Leadville Limestone reservoirs at Lisbon field (figures 4.6 through 4.8) (Chidsey and others, 2020). However, brecciation is most commonly caused by natural hydrofracturing, creating an explosive-looking, pulverized rock, an “autobreccia” as opposed to a collapse breccia. Clasts within autobreccias remained in place and moved very little. Dolomite clasts are commonly surrounded by solution-enlarged fractures partially filled with coarse rhombic and saddle dolomites that are coated with pyrobitumen. Areas between clasts exhibit good intercrystalline porosity or microporosity, or are filled by dolomite cements. Intense bitumen plugging is concurrent or takes place shortly after brecciation. Rimmed microstructures or stair-step fractures are occasionally present, reflecting shear and explosive fluid expulsion from buildup of pore pressure.

Karst-Related Processes

Sediment-filled cavities are common throughout the upper one-third of the Leadville Limestone in Lisbon field (figure

4.9). These cavities or cracks were related to karstification of the subaerially exposed Leadville (figures 3.1B and 3.3). Infilling of the cavities by detrital carbonate and siliciclastic sediments occurred before the deposition of the Pennsylvanian Molas Formation; however, Evans and Reed (2006, 2007) described redeposition of debrites and loess from the Molas in southwestern Colorado as cave sediments in paleokarst features of the Leadville. The contact between the transported material and country rock can be sharp, irregular, and corroded with small associated mud-filled fractures. Transported material consists of poorly sorted detrital quartz grains (silt size), chert fragments, carbonate clasts, clay, and occasional clasts of mud balls (desiccated and cracked). Carbonate mud infiltration of karst cavities are dolomitized (a later diagenetic process). Dolomitized infilling is non-porous and consists of very fine crystals. Infilling sometimes displays a crude lamination.

Other karst features observed in Leadville thin sections include the presence of “root hair,” which is thin, sinuous cracks filled with dolomitized mud. Clasts also may have a coating of clay. Both of these features are evidence of a soil zone.

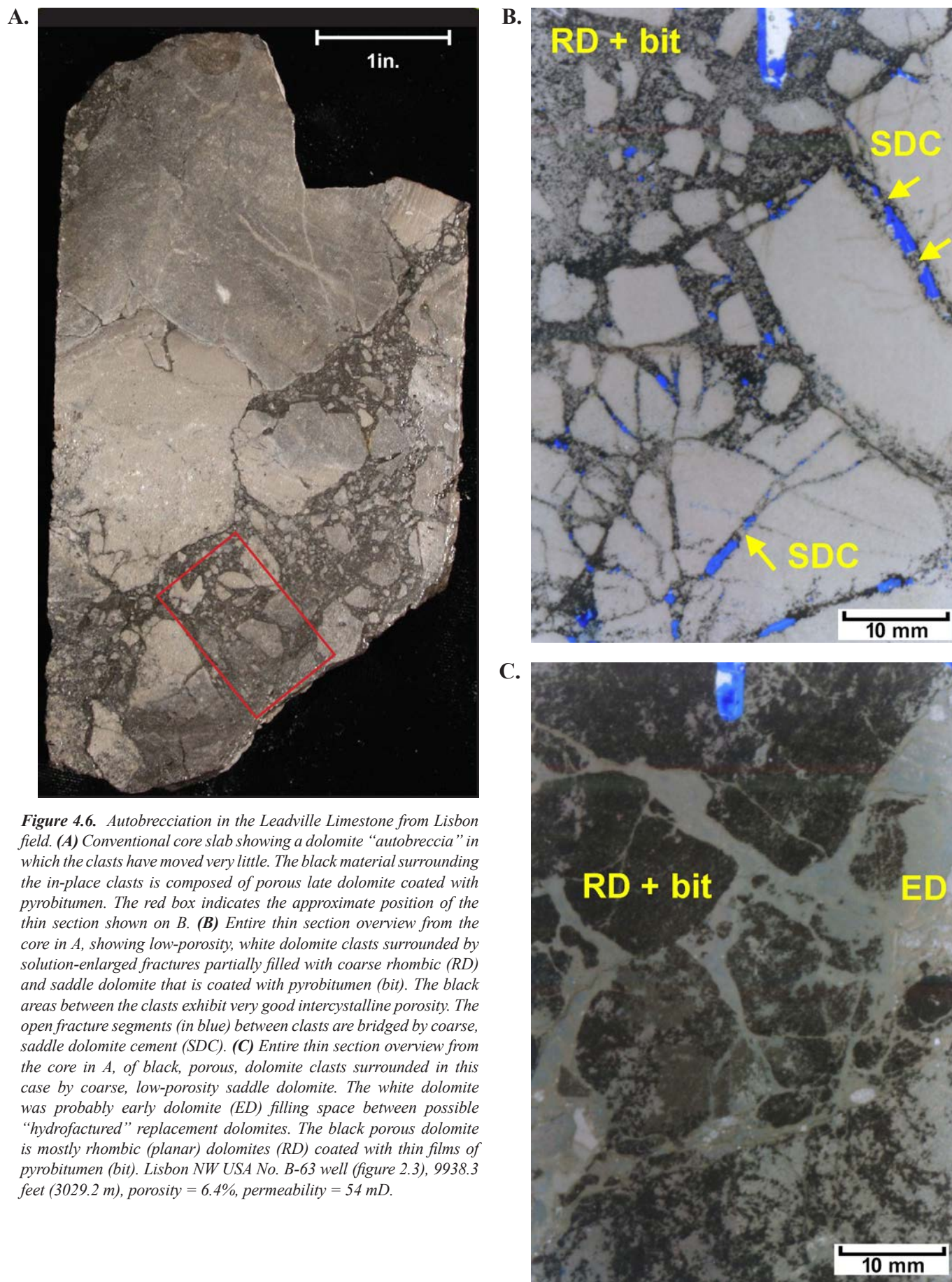


Figure 4.6. Autobrecciation in the Leadville Limestone from Lisbon field. **(A)** Conventional core slab showing a dolomite “autobreccia” in which the clasts have moved very little. The black material surrounding the in-place clasts is composed of porous late dolomite coated with pyrobitumen. The red box indicates the approximate position of the thin section shown on B. **(B)** Entire thin section overview from the core in A, showing low-porosity, white dolomite clasts surrounded by solution-enlarged fractures partially filled with coarse rhombic (RD) and saddle dolomite that is coated with pyrobitumen (bit). The black areas between the clasts exhibit very good intercrystalline porosity. The open fracture segments (in blue) between clasts are bridged by coarse, saddle dolomite cement (SDC). **(C)** Entire thin section overview from the core in A, of black, porous, dolomite clasts surrounded in this case by coarse, low-porosity saddle dolomite. The white dolomite was probably early dolomite (ED) filling space between possible “hydrofractured” replacement dolomites. The black porous dolomite is mostly rhombic (planar) dolomites (RD) coated with thin films of pyrobitumen (bit). Lisbon NW USA No. B-63 well (figure 2.3), 9938.3 feet (3029.2 m), porosity = 6.4%, permeability = 54 mD.

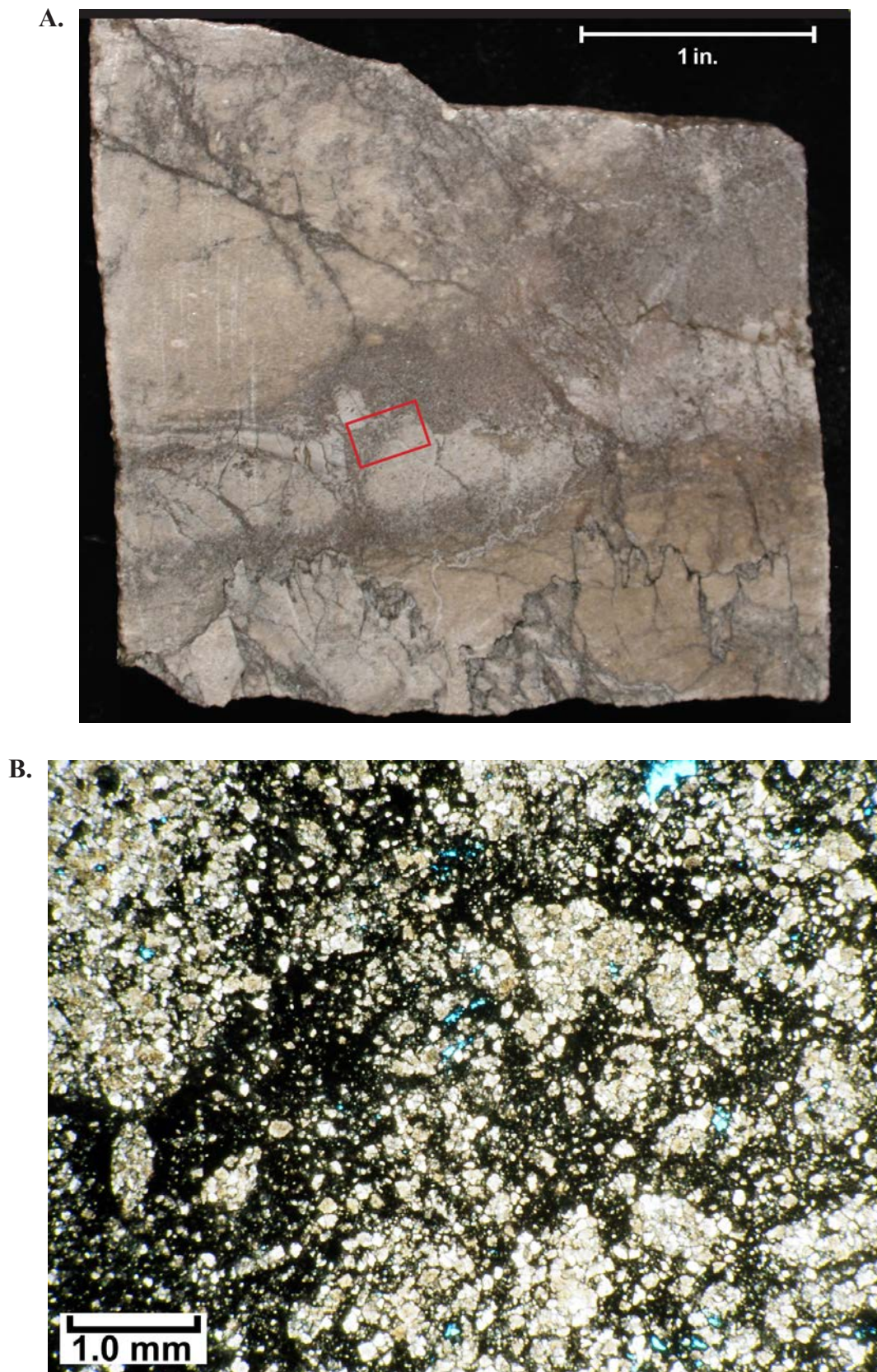


Figure 4.7. Brecciation in dolomite from the Leadville Limestone from Lisbon field. **(A)** Conventional core slab of a dolomitized, peloidal/crinoidal packstone/wackestone with swarms of fractures marked by black, coarse dolomite. The red box indicates the approximate position of the tin section photomicrograph shown on B. **(B)** Representative photomicrograph (plane light) from the core in A, showing highly deformed and brecciated dolomite within a bitumen-lined fracture zone. Lisbon No. D-816 well (figure 2.3), 8438.5 feet (2572.1 m), porosity = 11%, permeability = 5 mD.

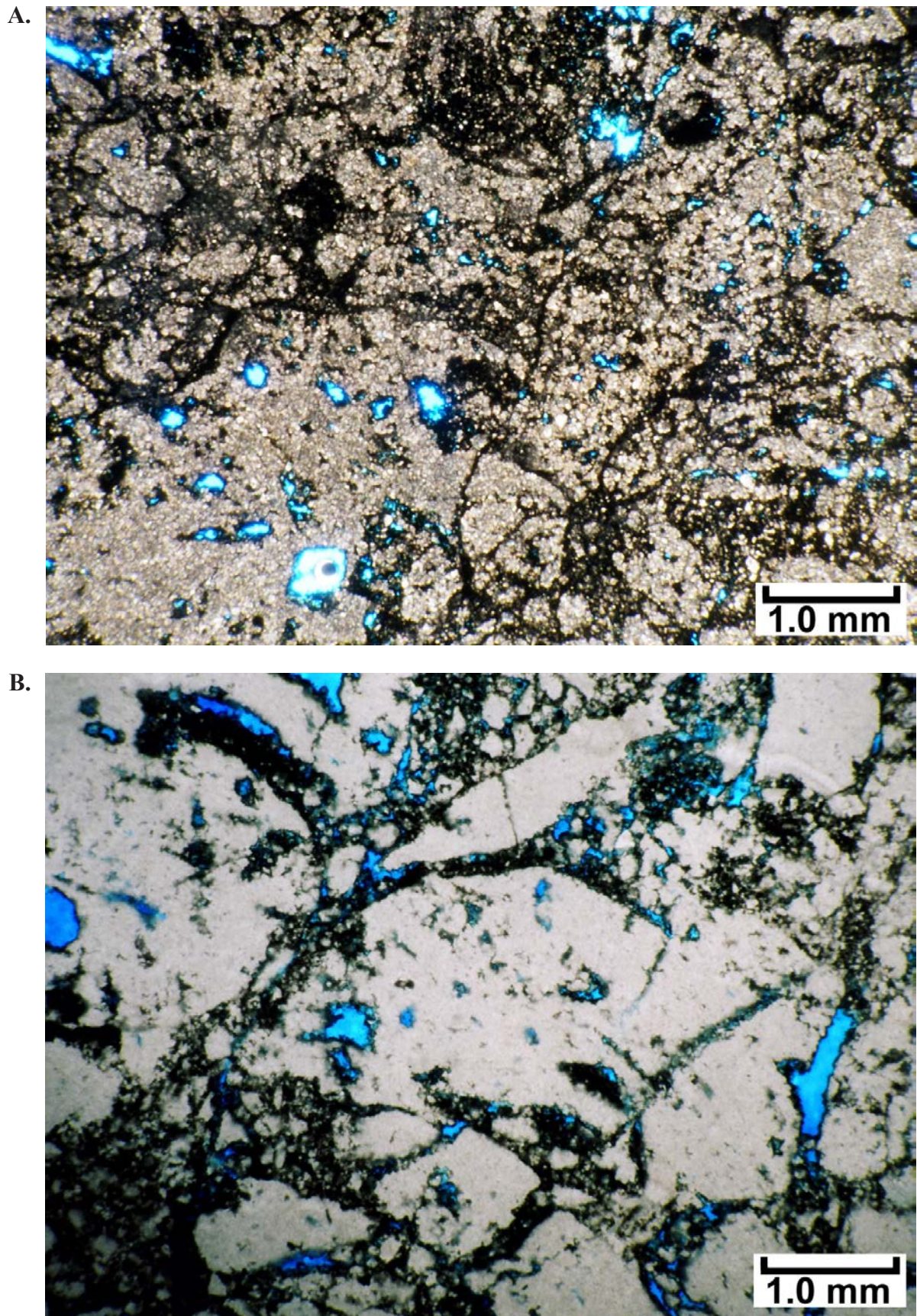
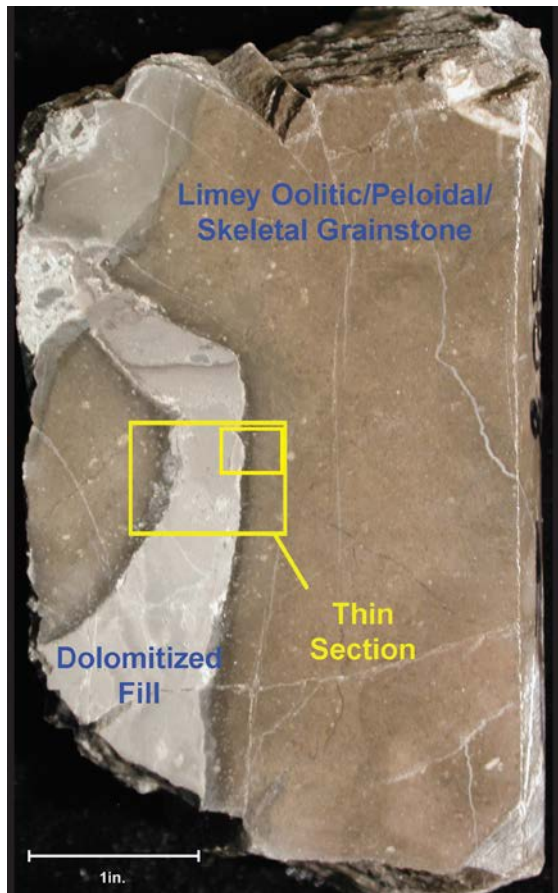
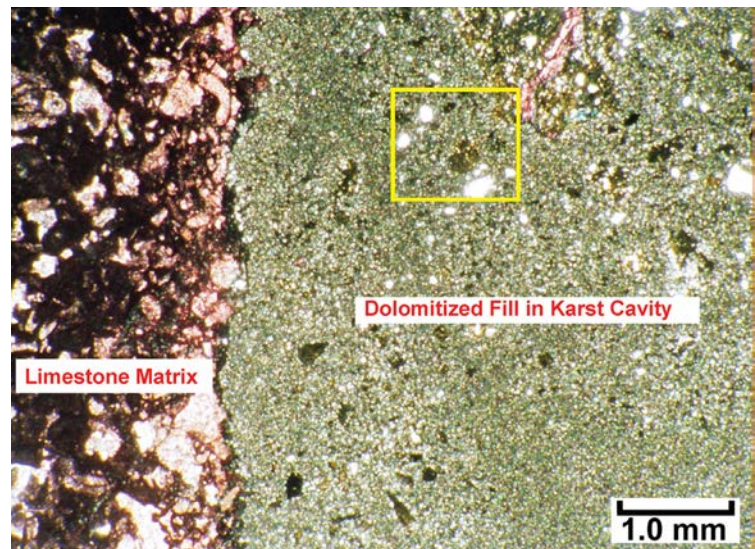


Figure 4.8. Representative photomicrographs (plane light) of brecciation and bitumen in the Leadville Limestone from Lisbon field. (A) Another example of intensely brecciated dolomite within a bitumen-lined fracture zone. (B) Large autoclasts and bitumen in an intensely brecciated dolomite. Lisbon No. D-816 well (figure 2.3), 8423 feet (2567 m), porosity = 10.5%, permeability = 47 mD.

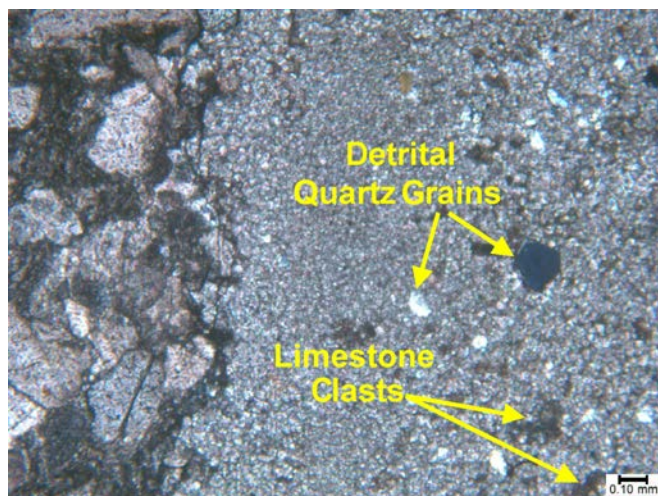
A.



B.



C.



D.

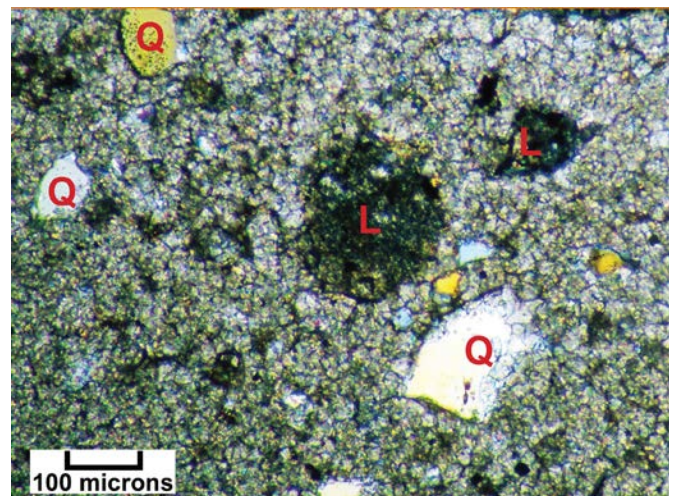


Figure 4.9. Karst-related processes. (A) Conventional core slab of a limey, oolitic, peloidal/skeletal grainstone with a dolomitized sediment-filled cavity. The yellow box indicates the approximate position of the thin section photomicrograph shown on B. (B) Low-magnification photomicrograph (plane light) showing the contact between the non-porous limestone matrix and the non-porous dolomitized and siliciclastic karst cavity filling. The yellow box indicates the approximate position of the close-up photomicrograph shown on D. (C) Photomicrograph (cross-polarized light) showing the contact between limestone matrix and the dolomitized karst cavity filling; note that the dolomitized filling is composed of very fine crystals. The siliciclastic grains within the microcrystalline dolomite field display plane extinction positions with colors ranging from white to yellow to dark gray. The polygonal grain in the right center contains overgrowths that form a prismatic quartz form in cross section. In the limestone field to the left, many of the fossils are surrounded by straight extinction syntaxial cements. (D) Higher magnification photomicrograph (cross-polarized light) of white detrital quartz grains (Q) and small dark gray carbonate clasts (L) within the non-porous, dolomitized mud filling the karst cavity. Lisbon No. D-616 well (figure 2.3), 8308 to 8309 feet (2532–2533 m), porosity = 1.2%, permeability = 11.1 mD.

Anhydrite and Sulfides

Dissolution pores (molds) and pore throats are sometimes plugged or bridged by lathes of late anhydrite cement (figure 4.10). In the photomicrographs studied, complete plugging of porosity was rare, and the overall presence of anhydrite cement and replacement was relatively insignificant for the Leadville Limestone in the Lisbon reservoir rocks.

Possible sulfide minerals are observed in several Leadville thin sections (figure 4.11). They appear as small, angular, brassy crystals and tend to line moldic pores or form on, and between, rhombic dolomite crystals. These minerals may be associated with hydrothermal fluids responsible for the coarse saddle dolomite. They may also be related to copper mineralization found a few miles to the east at the Lisbon Valley copper mine. The copper deposit includes fracture filling and disseminated copper sulfides (chalcocite, bornite, and covellite) replacing dead oil and pyrite (Hahn and Thorson, 2006).

Late Macrocalcite

Macrocalcite, also referred to as poikilotopic calcite, is viewed as late, large, slow-growing crystals (figure 4.12), and although not extensive in the Leadville Limestone at Lis-

bon field, its presence provides some significant insight into the diagenetic history of these rocks. The examples in figure 4.12 show an autobreccia that retains small amounts of early, finely crystalline (low permeability) dolomite replaced by “mini-saddles” and medium crystalline (euhedral) dolomite. Early during this sample’s history, it once had intercrystalline porosity that was enhanced by dissolution to form additional pores. Subsequently, the pores were partially filled with coarsely crystalline saddle dolomite and bitumen. Finally, the remaining solution-enlarged pores were occluded by poikilotopic calcite. Poikilotopic calcite may have formed as oil-field water rose following the gas/condensate cap.

Porosity and Permeability Cross Plots

Porosity and permeability data from 380 core plugs were obtained from the five well cores described (figure 2.1 and table 3.1). Cross plots (figures 4.13 through 4.17) of these data are used to (1) determine the most effective pore systems for oil storage versus drainage, (2) identify reservoir heterogeneity, (3) predict potential untested compartments, (4) infer porosity and permeability trends where core-plug data are not available, and (5) match diagenetic processes, pore types, mineralogy, and other attributes to porosity and permeability distribution. Porosity and permeability cross plots were constructed using the available data (appendix B).

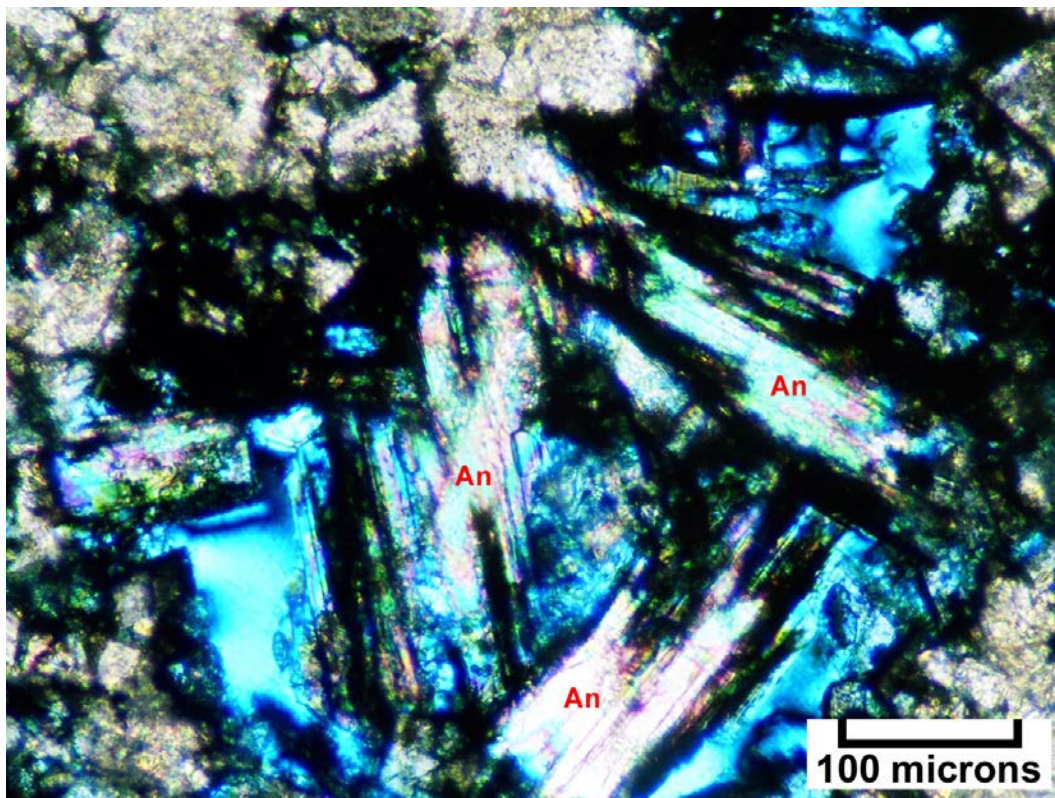


Figure 4.10. Representative photomicrograph (cross-polarized light) showing lathes of late anhydrite cement (An, in the pastel colors) filling a dissolution pore. The unfilled parts of the pore are seen in the blue areas. Lisbon No. D-816 well (figure 2.3), 8426 to 8431 feet (2568–2570 m), porosity = 11.1%, permeability = 15 mD.

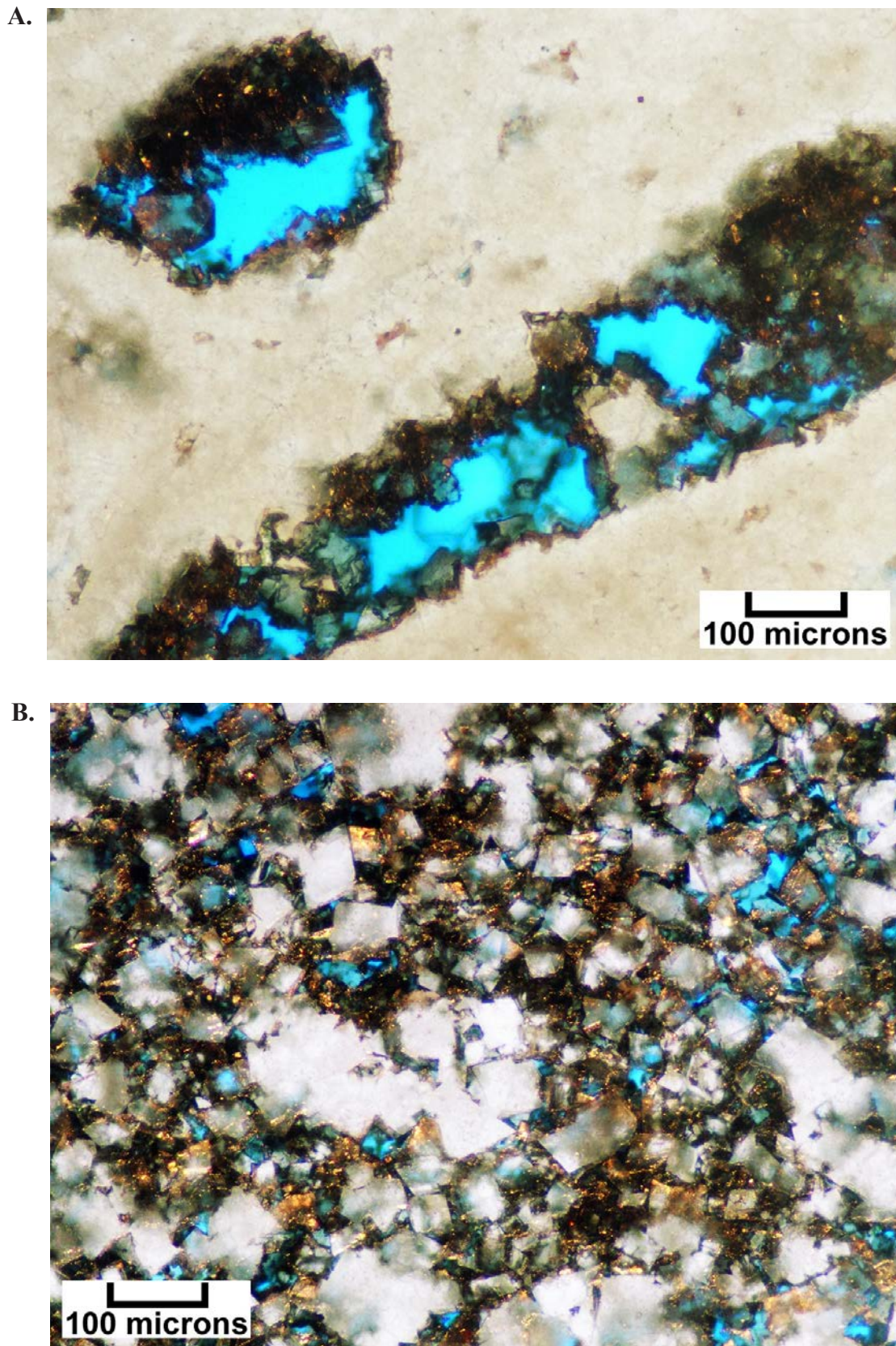


Figure 4.11. Possible sulfide mineralization within the Leadville Limestone at Lisbon field. **(A)** Photomicrograph (“white card” and reflected light) showing moldic pore lined with black pyrobitumen and possible sulfide minerals (small brassy crystals). Lisbon No. D-816 well (figure 2.3), 8444 to 8445 feet (2573–2574 m), porosity = 6.6%, permeability = 7 mD. **(B)** Photomicrograph (“white card” and reflected light) showing black pyrobitumen and sulfide minerals on and between rhombic dolomite crystals (in white and light gray). Lisbon No. D-816 well (figure 2.3), 8446 to 8447 feet (2574–2575 m), porosity = 13%, permeability = 59 mD.

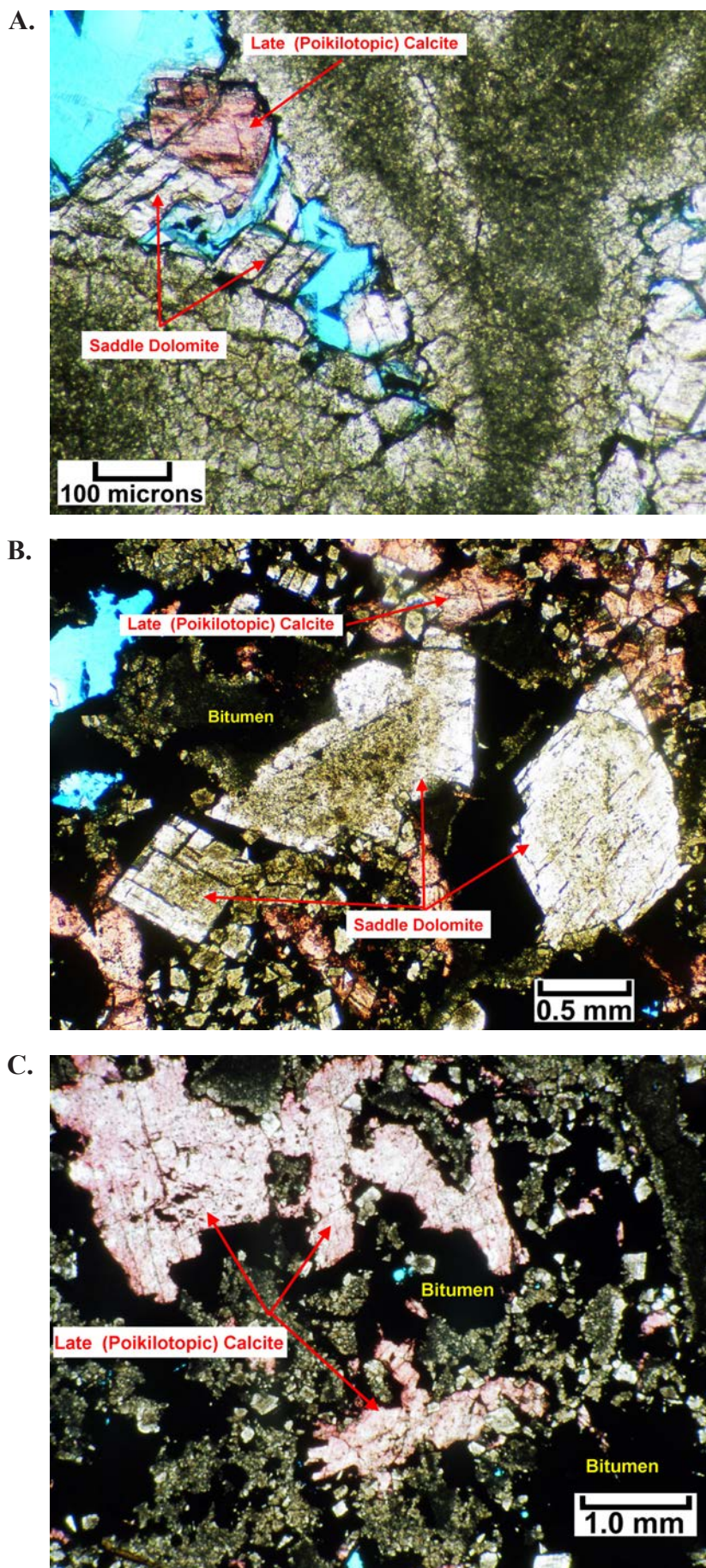


Figure 4.12. (A) Photomicrograph (plane light) showing coarse, white saddle dolomite crystals and a single, coarse, clear late macrocalcite cement crystal (stained red) filling part of a large dissolution pore (blue) in a finely crystalline, sucrosic replacement dolomite matrix. Northwest Lisbon No. B-63 well (figure 2.3), 9991.8 feet (3045.5 m), porosity = 6.2%, permeability = 0.3 mD. (B) Photomicrograph (plane light) showing coarse rhombic and saddle replacement dolomite that displays cloudy cores and clear rims. Dissolution pores are filled with pyrobitumen (black) and late macrocalcite (stained red). An additional episode of dissolution is seen as the open (blue) pores that appear to post-date most of the pyrobitumen emplacement. (C) Dissolution pores filled completely with bitumen (black) and late macrocalcite (stained red) that resemble saddle dolomite molds. B and C from Northwest Lisbon No. B-63 well, 10,004 to 10,005 feet (3049–3050 m), porosity = 14.4%, permeability = 1.9 mD.

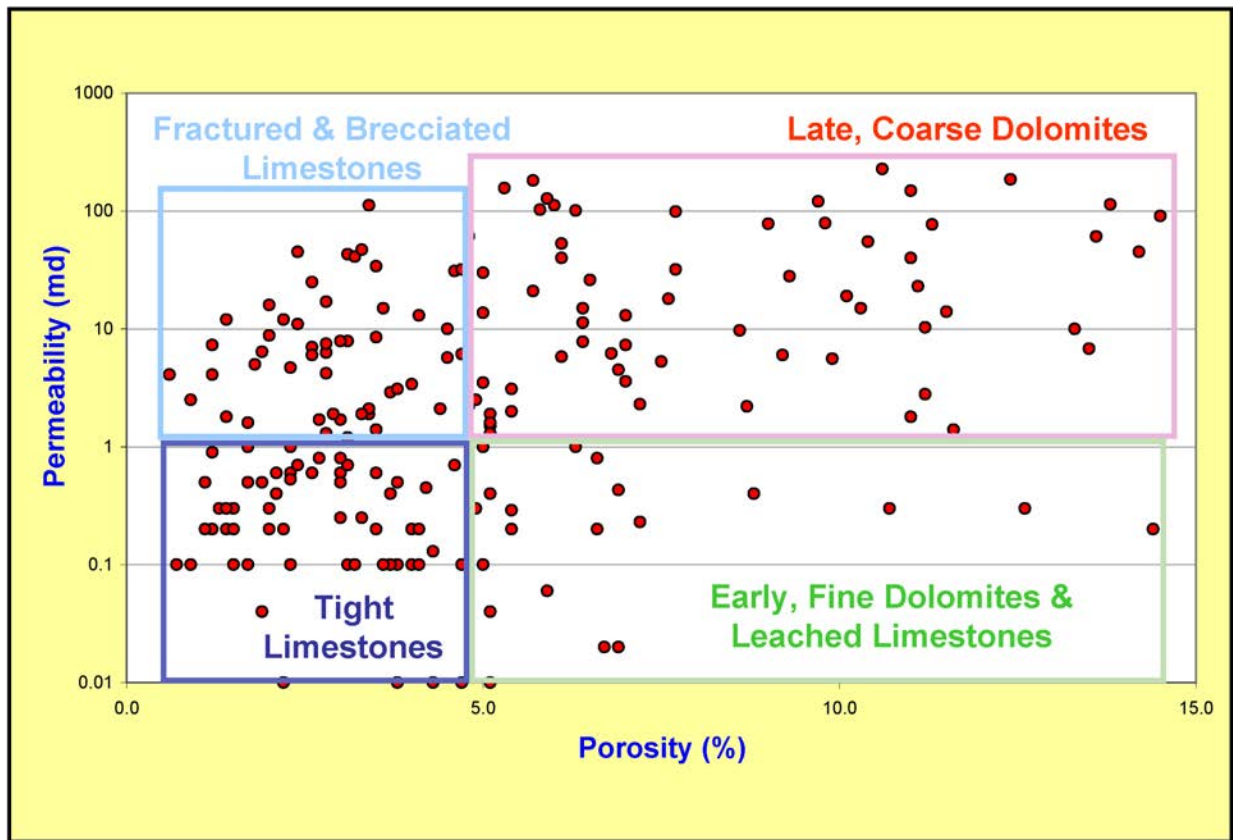


Figure 4.13. Lisbon Unit No. B-610 well permeability versus porosity cross plot by diagenesis.

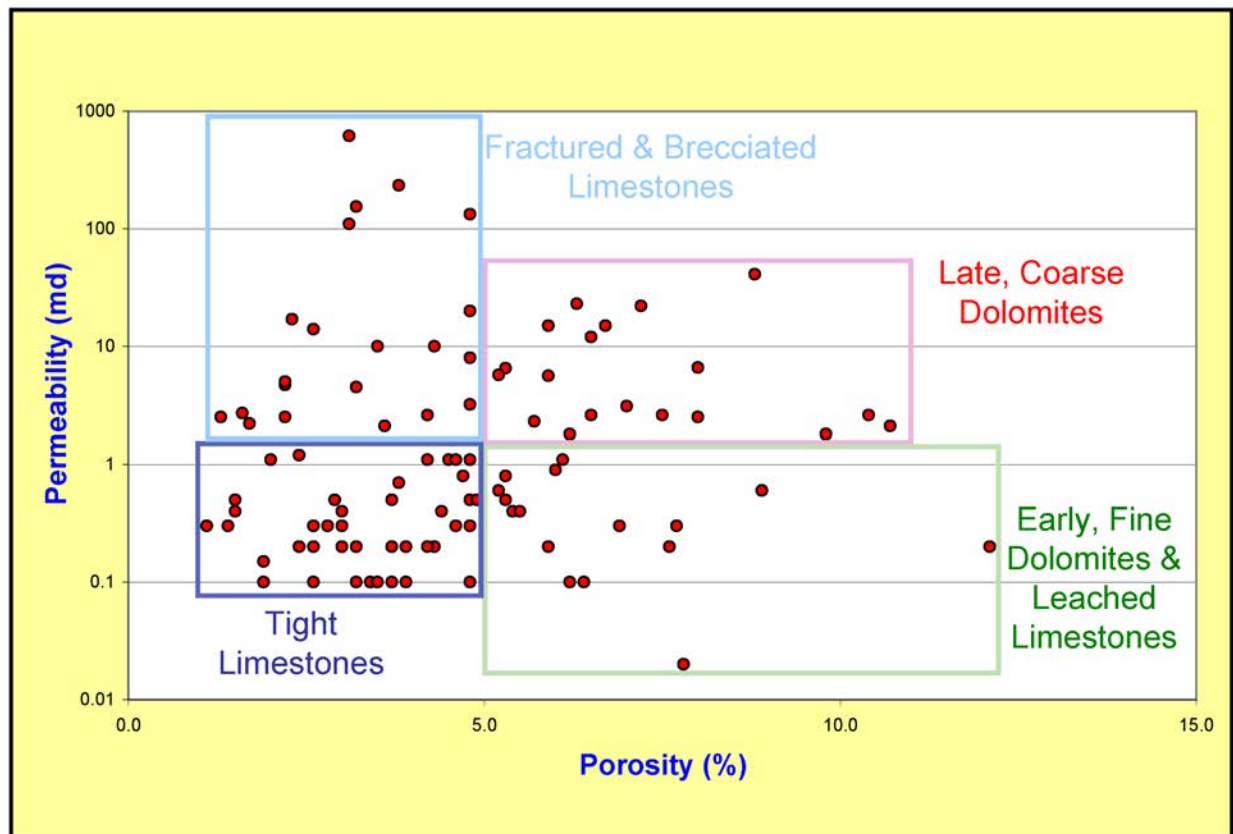


Figure 4.14. Lisbon Unit No. B-816 well permeability versus porosity cross plot by diagenesis.

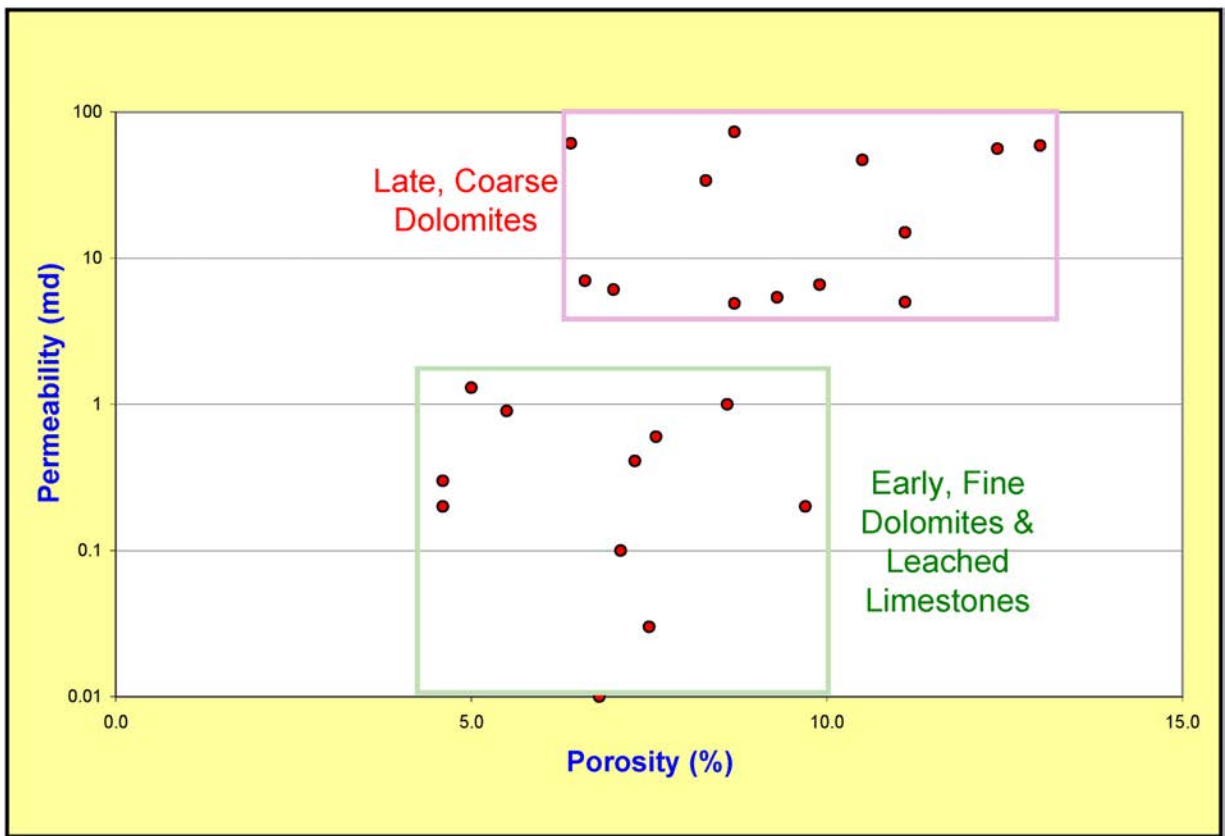


Figure 4.15. Lisbon Unit No. D-816 well permeability versus porosity cross plot by diagenesis.

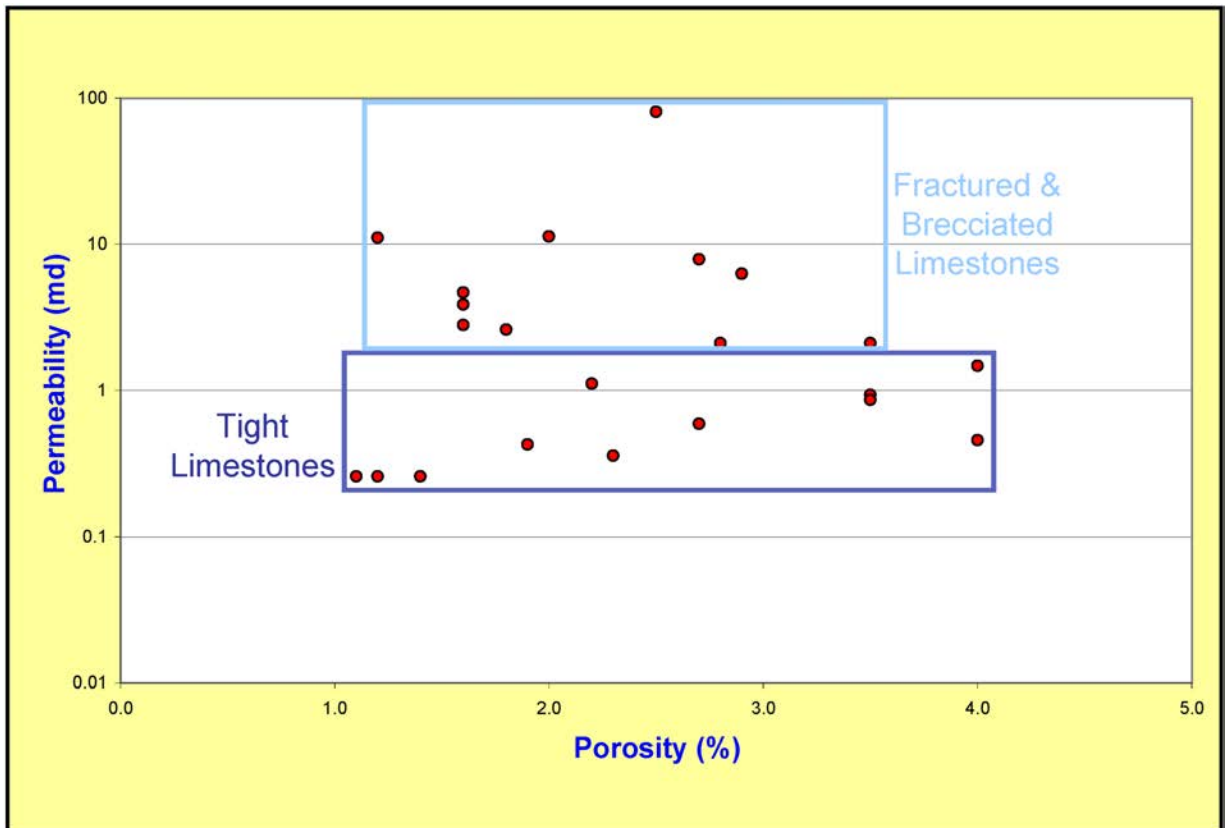


Figure 4.16. Lisbon Unit No. D-616 well permeability versus porosity cross plot by diagenesis.

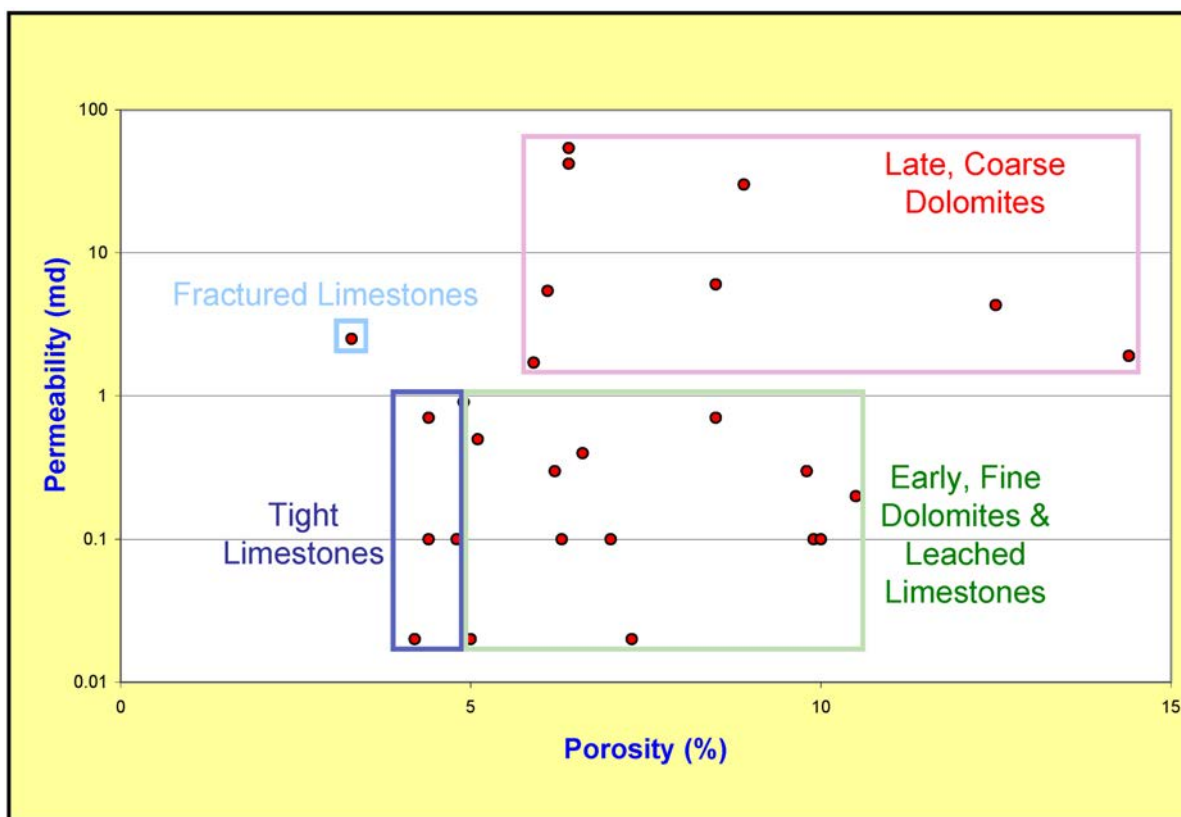


Figure 4.17. Lisbon Unit No. B-63 well permeability versus porosity cross plot by diagenesis.

A representative set of core analyses from the Leadville Limestone in Lisbon field shows the dominant pore types are intercrystalline, moldic, fracture, and channel in dolomite and limestone and are reflected in plots of permeability versus porosity (appendix D). Plots of permeability versus porosity also show two distinct populations of dolomites with respect to diagenesis (figures 4.13 through 4.15, and 4.17). The early, finely crystalline dolomites (with or without isolated molds) display low permeability. The coarser, late dolomites (with or without late dissolution) display high permeability. In addition, analysis of the plots shows that zones that have been dolomitized have better reservoir potential than those that remain limestone, even where the limestone has been fractured and brecciated (figure 4.16).

SCANNING ELECTRON MICROSCOPY

To further determine the diagenetic history of the Leadville reservoir at Lisbon field, representative samples were selected for scanning electron microscopy (SEM) analysis from the conventional cores which were used for thin sections. The SEM was used to photograph (1) typical preserved primary and secondary pore types and pore throats, (2) cements, (3) sedimentary structures, (4) fractures, and (5) pore plugging anhydrite, halite, and bitumen. Of special interest is the identification of possible hydrothermal dolomite and the determination of the most effective pore systems for oil drainage versus storage.

Scanning electron microscope analyses were conducted on 12 thin section blanks from the core samples that displayed characteristics of interest (table 4.1). Complete descriptions and SEM images from the Leadville reservoir at Lisbon field are in appendix E.

Porosity Types

All samples exhibit microporosity in the form of intercrystalline porosity (figure 4.18). Dissolution has contributed to porosity in most samples as well. Dissolution has created moldic, vuggy, and channel porosity. Dissolution pores are most often in the mesopore size range (62.5 microns to 4.0 mm.).

Permeability is related to the size and number of pore throats, and, particularly, to the continuity of pore throats. In general, permeability is good in the samples studied, but is limited slightly by mineral cements and pyrobitumen (figure 4.19).

Fractures enhance the permeability in several intervals (figure 4.20). SEM examination identified fractures in the 8423- and 8442-foot (2567 and 2573 m) intervals of the Lisbon No. D-816 well, and the 8356- and 8682-foot (2547 and 2646 m) intervals of the Lisbon No. D-616 well. In addition to the fractures reported here, petrographic analysis revealed fractures in the 8308- and 8619-foot (2532 and 2627 m) intervals of the Lisbon No. D-616 well, and the 7886-foot (2404 m) interval of the Lisbon No. B-610 well.

Table 4.1. Summary of characteristics observed with scanning electron microscopy in samples from the Lisbon No. D-816, Lisbon No. D-616, and Lisbon No. B-610 wells, Lisbon field.

Well	Lisbon D-816					Lisbon D-616					Lisbon B-610	
	8423'	8426'	8433'	8442'	8486'	8308'	8356'	8559'	8619'	8682'	7886'	7897'
POROSITY												
Intergranular (Micro) (BC)	X	X	X	X	X	X	X	X	X	X	X	X
Dissolution (MO)	X	X	X	X	X		X		X		X	X
Dissolution (VUG)		X	X	X	X				X		X	X
Dissolution (CH)											X	
Fractures	X			X		X	X		X	X	X	
CEMENTS												
Anhydrite		X	X							X		
Calcite					X	X	X				X	
Quartz					X	X	X		X			
Dolomite	X	X	X	X	X	X	X	X	X	X	X	X
Illitic Clay	X					?				X		X
Pyrobitumen	X	X	X	X	X				X			
Sulfides	X		X	X	X				X		X	X
DIAGENESIS												
Dolomitization	X	X	X	X	X	X	X		X	X	X	X
Dissolution	X	X	X	X	X	X	X		X	X	X	X
Calcite Cementation					X	X	X					
Quartz Cementation					X	X	X		X			
Illitic Clay Deposition	X					X			X	X	X	X
Anhydrite Cementation		X	X							X		
Pyrobitumen Emplacement	X	X	X	X	X				X			
Fracturing	X			X		X	X		X	X	X	

Data from SEM, EDS, and optical microscopy by Standard Geological Services, Inc., and petrography by Eby Petrography & Consulting, Inc.

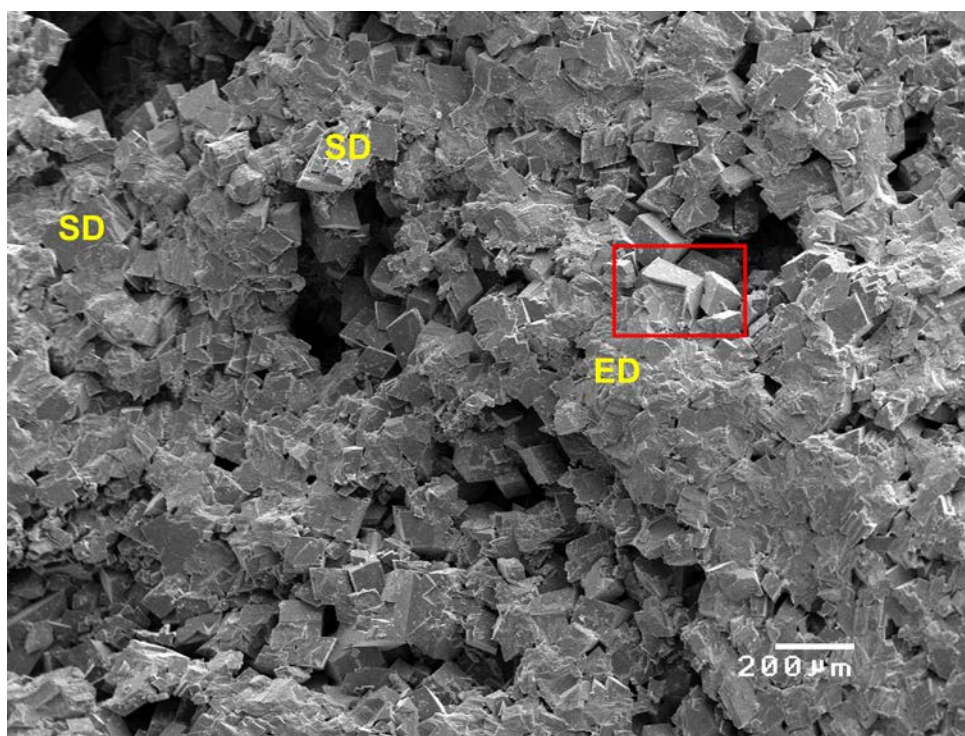


Figure 4.18. Scanning electron microscope photomicrograph of a core plug from 8433 feet (2570 m), Lisbon No. D-816 well, showing typical Leadville dolomite crystals at Lisbon field (red box shows area of figure 4.21A). Note the very fine, low-permeability, early dolomite crystals (ED) that have been replaced with late, rhombic and saddle (SD) dolomite crystals. A significant porosity increase is associated with the late dolomite replacement. Scale bar represents 200 microns (0.2 mm). Porosity = 2%; permeability <0.1 mD based on core-plug analysis.

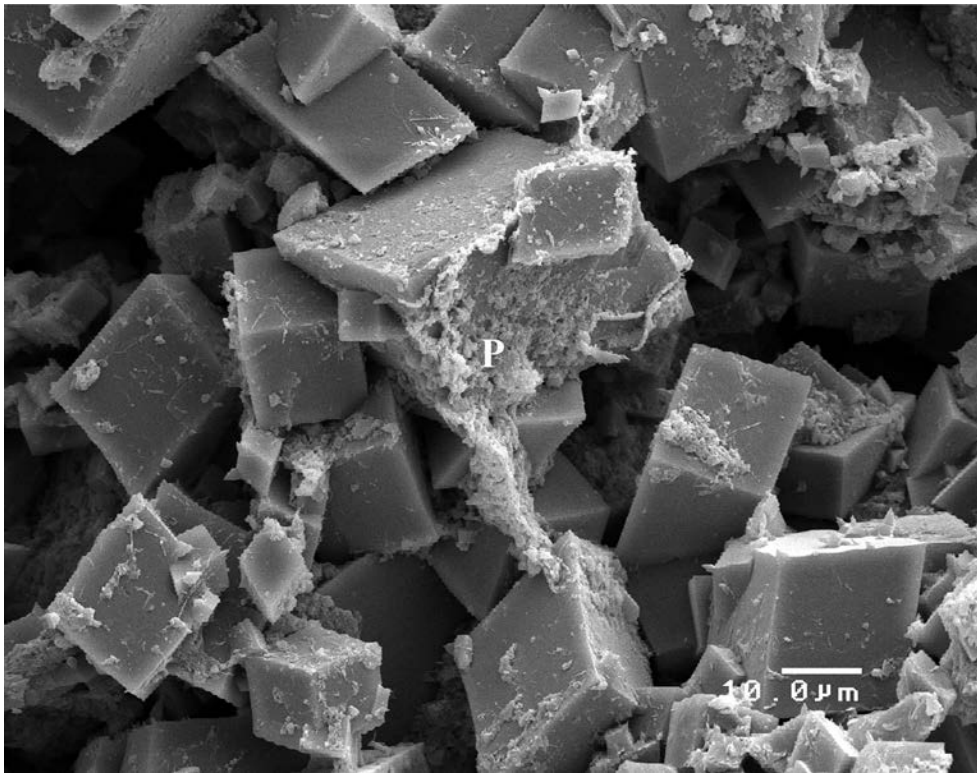


Figure 4.19. Scanning electron microscope photomicrograph of a core plug from 7886 feet (2404 m), Lisbon No. B-610 well, showing probable pyrobitumen (P) coating the rhombic dolomite crystal in the center. Pyrobitumen coats many other dolomite crystals as well. Scale bar represents 10 microns (0.01 mm). Porosity = 13.8%; permeability = 114 mD based on core-plug analysis.

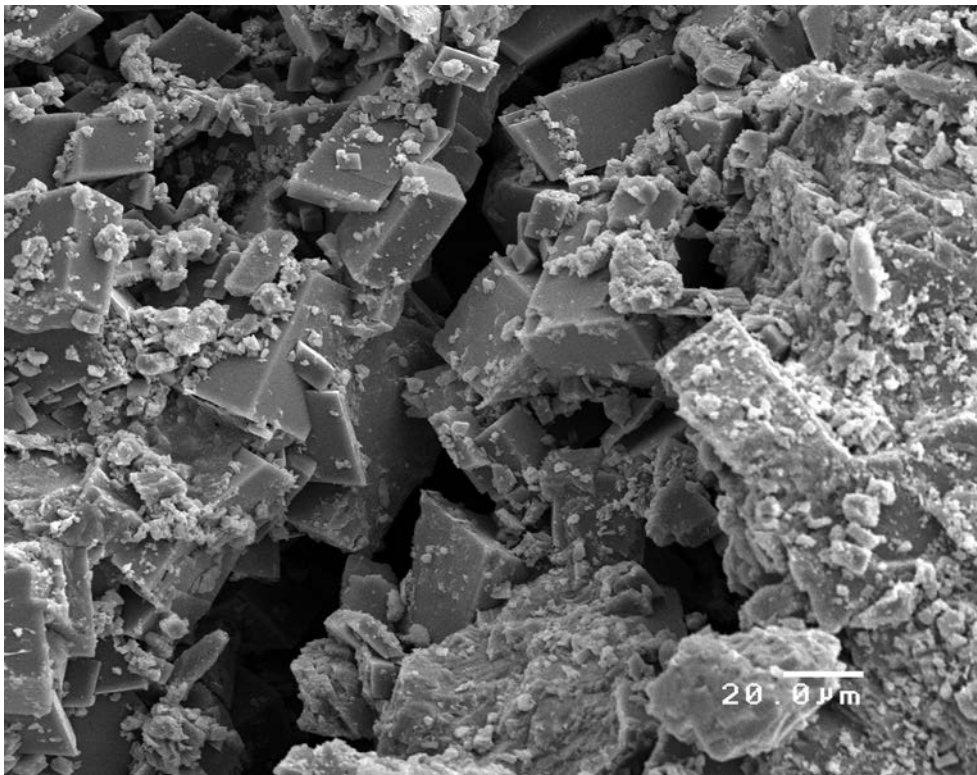


Figure 4.20. Scanning electron microscope photomicrograph of a core plug from 8423 feet (2567 m), Lisbon No. D-816 well, showing enlargement of a fracture partially filled with secondary dolomite. Scale bar represents 20 microns (0.02 mm). Porosity = 10.5%; permeability = 47 mD based on core-plug analysis.

Undoubtedly, fractures enhance the permeability in the 8423- and 7886-foot (2567 and 2404 m) samples given their respective measured values of 46 mD and 114 mD. The 83 mD measured permeability of the 7897-foot (2407 m) interval and the 15 mD of the 8426-foot (2568 m) interval suggest that fractures are present in these intervals as well. They were not observed during analysis, however.

Lithology, Diagenesis, and Cements

All samples are dolomite except for the limestone matrix present in the 8308-foot (2532 m) sample of the Lisbon No. D-616 well. That sample, however, contains dolomite as fill material. Secondary materials present include dolomite, calcite, clays, and pyrobitumen. Their presence is discussed below and included in table 4.1.

Dolomite is the dominant cement (figure 4.18) in all samples except the 8426-foot (2568 m) sample from the Lisbon No. D-816 well, where anhydrite is the abundant cement. The two basic types of dolomite are well displayed by SEM (figure 4.18): the low-porosity and/or low-permeability, very fine, early dolomite and higher porosity and/or high permeability, coarse, late dolomite (figure 4.21).

Pores in the 8426-foot (2568 m) sample from the Lisbon No. D-816 well are partially filled with anhydrite (figure 4.22). Anhydrite is also reported from petrographic analysis of the 8433-foot (2570 m) interval of this well and the 8682-foot (2646 m) sample of the Lisbon No. D-616 well. Scanning electron microscopic analysis indicates that anhydrite is abundant in the 8426-foot (2568 m) sample; it is most likely much less abundant in the other intervals.

Minor euhedral quartz is present in several samples (figure 4.23). Rare illitic clays, possibly illite/smectite mixed-layer clays, are also present. Sulfide mineral(s) containing an unknown cation are present in moderate abundance (figure 4.24). Calcite cement, although rare, was observed in a few samples. The minor constituents of quartz, clays, calcite, and sulfides contribute little to the overall lithology and are relatively insignificant with respect to reservoir quality. The quartz, clay, and calcite cements are rare, and the more abundant sulfide mineral(s) consist of extremely small crystals about 2 microns or smaller.

An approximate diagenetic sequence based on SEM is listed below (not all diagenetic events were identified in every sample). The various diagenetic events are included in table 4.1.

1. Dolomitization
2. Dissolution
3. Dolomite cementation
4. Fracturing
5. Quartz cementation

6. Calcite cementation
7. Clay precipitation
8. Anhydrite cementation
9. Pyrobitumen emplacement
10. Sulfide precipitation

EPIFLUORESCENCE

Epifluorescence microscopy (EF) provides additional information on diagenesis, pores, and organic matter (including “live” hydrocarbons) within sedimentary rocks. The technique is a rapid, non-destructive procedure that can be done using a high-quality petrographic (polarizing) microscope equipped with reflected light capabilities. The basic principles and equipment for EF were largely developed in the 1960s and 1970s for applications in coal petrology and palynology (see reviews by van Gijzel, 1967, and Teichmuller and Wolf, 1977). All applications depend upon the emission of light (by a material capable of producing fluorescence) that continues only during absorption of the excitation-generating light beam (Rost, 1992; Scholle and Ulmer-Scholle, 2003).

Epifluorescence techniques have been used within industry and research for three objectives. Firstly, EF microscopy has been used extensively for enhancing petrographic observations, including the recognition of depositional and diagenetic fabrics within recrystallized limestone and massive dolomite (see, for instance, Dravis and Yurewicz, 1985; Cercone and Pedone, 1987; Dravis, 1991; LaFlamme, 1992). Secondly, the study of pore structures, microfractures, and microporosity within both carbonates and sandstones has been greatly facilitated by impregnating these voids with epoxy spiked with fluorescing dyes (Yanguas and Dravis, 1985; Gies, 1987; Cather and others, 1989a, 1989b; Soeder, 1990; Dravis, 1991). Thirdly, the evaluation of “oil shows” (Eby and Hager, 1986; Kirkby and Tinker, 1992; Chidsey and Eby, 2017) and determination of the gravity or type cements and minerals has been facilitated by EF microscopy (Burruss, 1981, 1991; Burruss and others, 1986; Guihaumou and others, 1990; LaVoie and others, 2001). Only the first two objectives were pursued in this chapter, the third is covered in Chapter 6.

Previous Work

There is no known published use of EF microscopy on the Leadville Limestone of the Paradox Basin. However, the published work cited above applies to carbonate reservoirs listed in Eby and Hager (1986) for a study done within a Permian Basin carbonate field, and case studies documented by Dravis (1988, 1992) provided incentives to apply EF petrography to Leadville reservoir rocks within the Lisbon field case study.

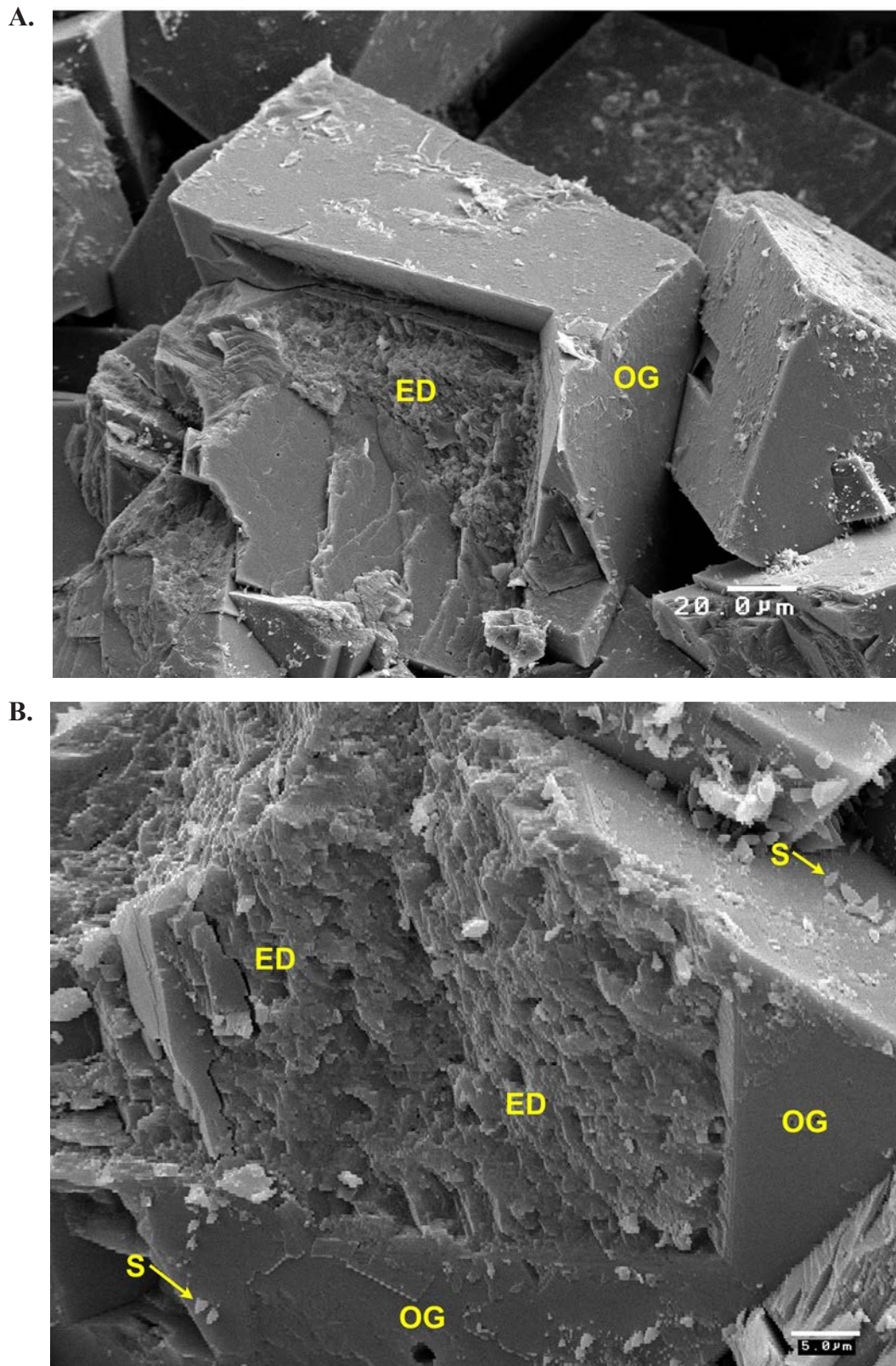


Figure 4.21. Scanning electron microscope photomicrograph of a core plug from 8433 feet (2570 m), Lisbon No. D-816 well. (A) Close-up (see red box on figure 4.18) shows the composition of typical replacement rhombic dolomite. The core of each rhombic crystal is composed of a dense remnant of fine, early dolomite (ED), which is surrounded by a euhedral dolomite overgrowth (OG). The rhombic dolomite faces are often covered with a thin film of pyrobitumen. Scale bar represents 20 microns (0.02 mm). (B) High magnification across a section of poorly crystalline, early dolomite core (ED) and dense overgrowth (OG) that forms the dolomite into coarser rhombs. The very small, angular decorations on the crystal surfaces may very well be small sulfide precipitates (S). Scale bar represents 5 microns (0.005 mm). Porosity = 2%; permeability < 0.1 mD based on core-plug analysis.

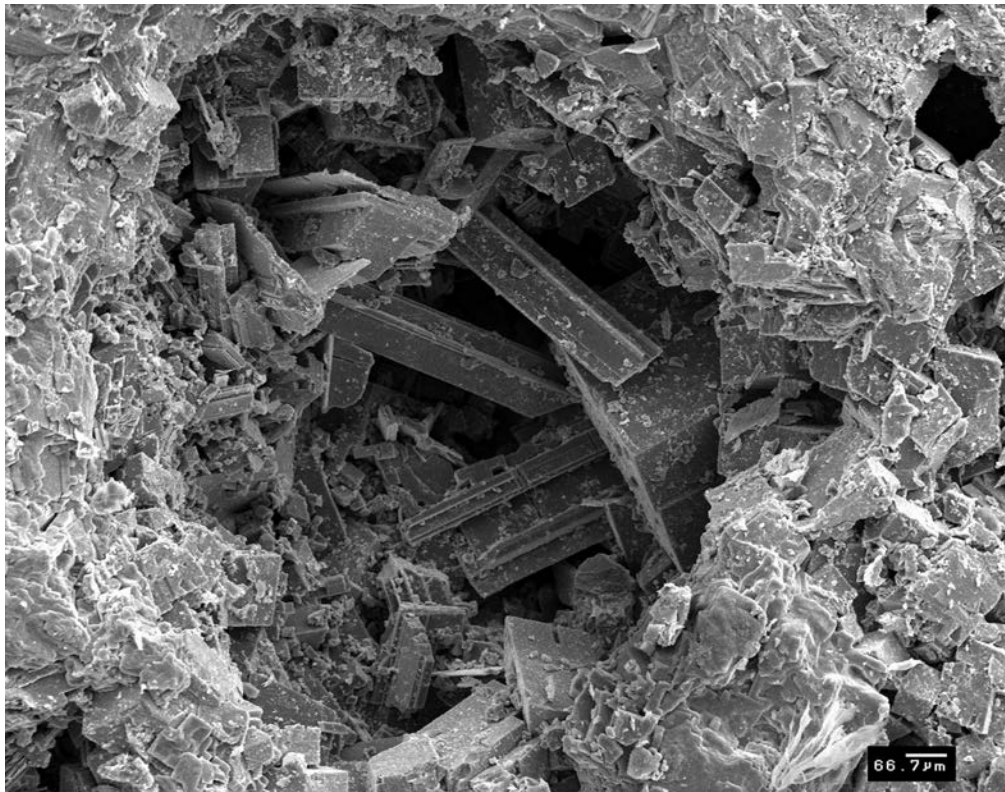


Figure 4.22. Scanning electron microscope photomicrograph of a core plug from 8426 feet (2568 m), Lisbon No. D-816 well, showing anhydrite cement lathes partially filling a small dissolution vug. Scale bar represents 66.7 microns (0.067 mm). Porosity = 11.1%; permeability = 15 mD based on core-plug analysis.

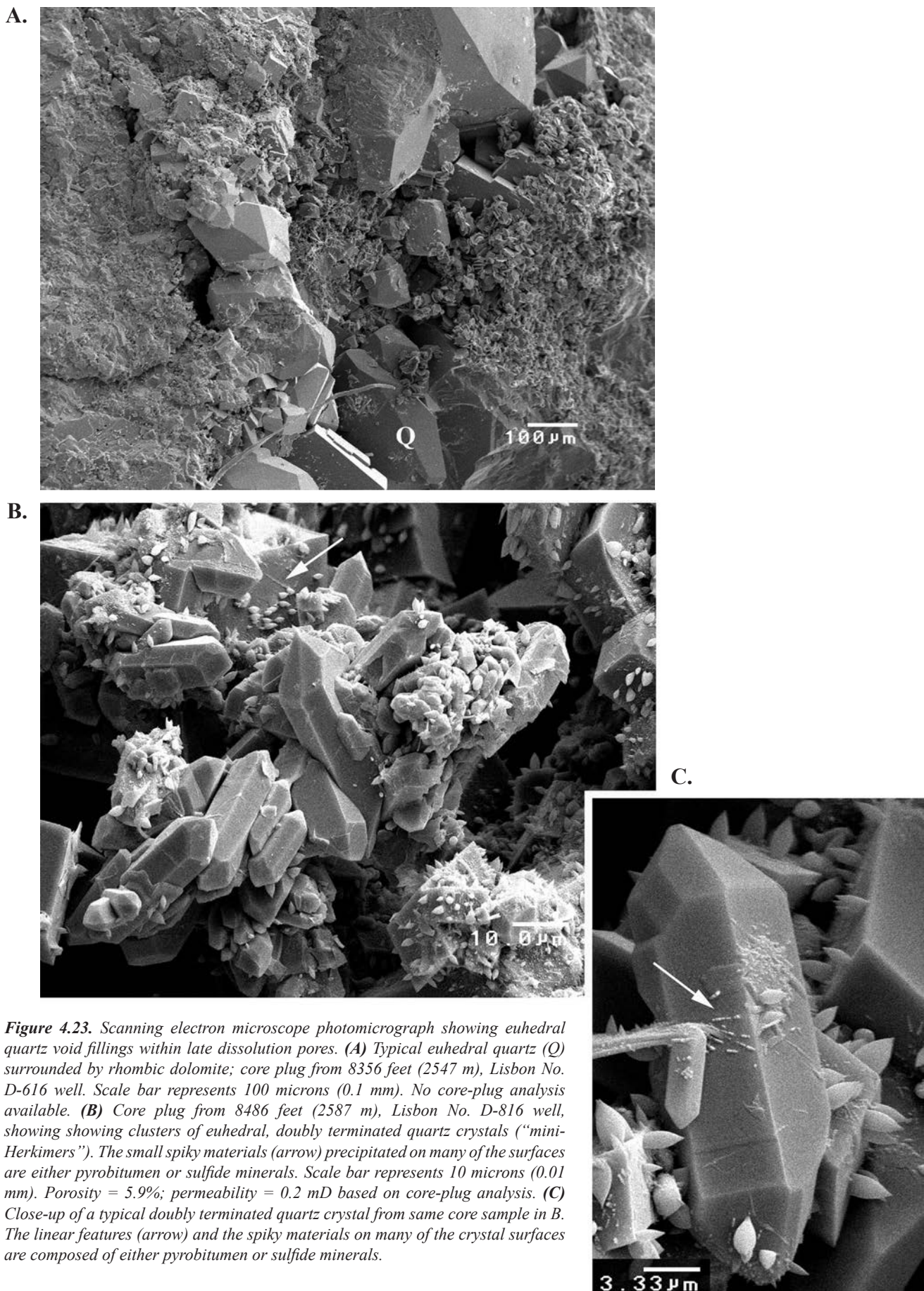
Methodology

For the EF petrography in this study, we used incident (reflected) blue-light fluorescence microscopy employing the general procedures outlined by Dravis and Yurewicz (1985), including the use of the modified “white card” technique outlined by Folk (1987) and Dravis (1991). Ultraviolet (UV) fluorescence did not effectively add any textural or pore structure information that could not otherwise be seen under blue-light excitation, even though some workers utilize UV fluorescence for evaluating fluid inclusions and compositional zoning within dolomite crystals (see Scholle and Ulmer-Scholle, 2003). Fluorescence data and observations collected for this study utilized a Jena (now part of Carl Zeiss) research-grade combination polarizing-reflected light microscope equipped with a high-pressure mercury vapor lamp for EF excitation, a Zeiss IIRS epifluorescence nosepiece, and a 35-mm camera system. Magnification ranges for examination and photo-documentation were between about 130x and 320x. The EF optical configuration used is similar to that shown in figure 4.25.

The light pathways and mechanics of the EF used in this study have been generally described by Soeder (1990). As described by Burruss (1991), “these excitation wavelengths are reflected to the microscope objective and sample by a dichroic beamsplitter which has a dielectric coating that reflects a specific short wavelength range. Fluorescence emission and reflected

short wavelength excitation light is collected by the objective. The dichroic beamsplitter transmits the long wavelength fluorescence emission but reflects the short wavelengths back toward the light source. The fluorescence emission passes through a barrier filter which removes any remaining short wavelength excitation light.” Blue light (~420 to 490 nm exciter filter/520 nm barrier filter) was used to excite the cuttings and core-chip samples. We have found broad-band, blue-light EF to be the most helpful in observational work on dolomite. Finally, the greater depth of investigation into a sample by the reflected fluorescence technique than by transmitted polarized light or other forms of reflected light makes it possible to resolve grain boundary and compositional features that are normally not appreciated in cutting or thin-section petrography.

Sample preparation is inexpensive and rapid, involving standard thin section preparation techniques. Thin sections were prepared from representative Leadville fabrics. These thin sections were vacuum- and pressure-impregnated with blue-dyed epoxy (see Gardner, 1980) that was spiked with a fluorescing compound. Microscopy used only uncovered polished surfaces. Examination for each thin section area of interest included photo-documentation under EF and plane-polarized light at the same magnification. Photomicrography of the compositional, textural, and pore structure attributes was done using high-speed film (ISO 800 and 1600) with some bracketing of exposures as camera metering systems do not always



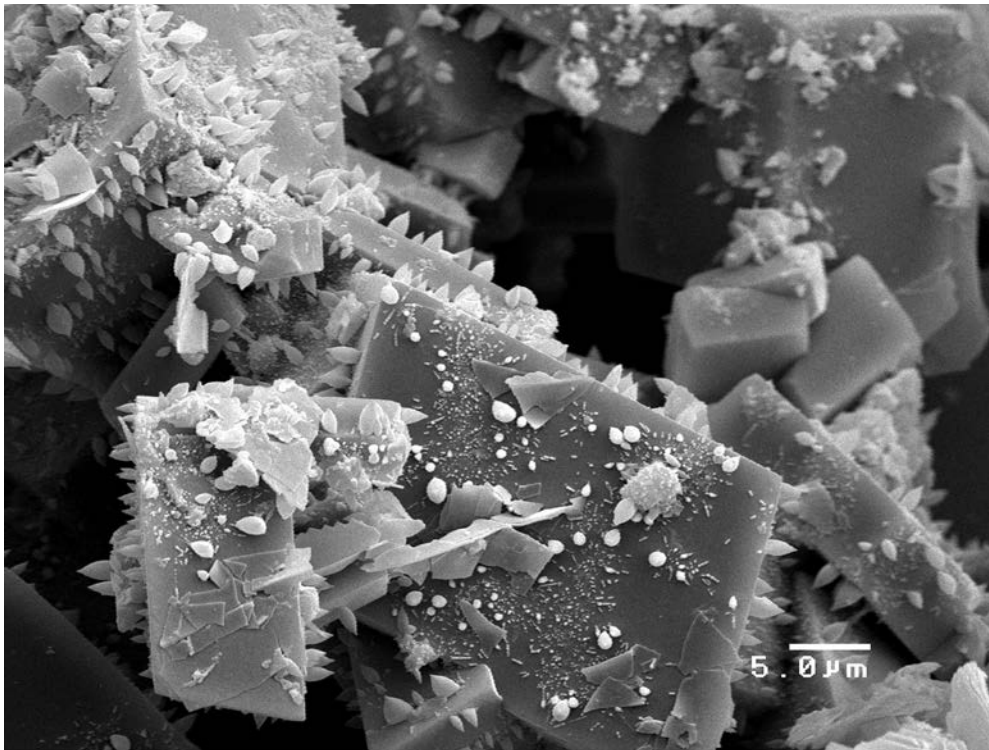


Figure 4.24. Scanning electron microscope photomicrograph of a core plug from 8442 feet (2573 m), Lisbon No. D-816 well, showing possible sulfide minerals on large dolomite rhombs. Scale bar represents 5 microns (0.005 mm). Porosity = 8.6%; permeability = 1.0 mD based on core-plug analysis.

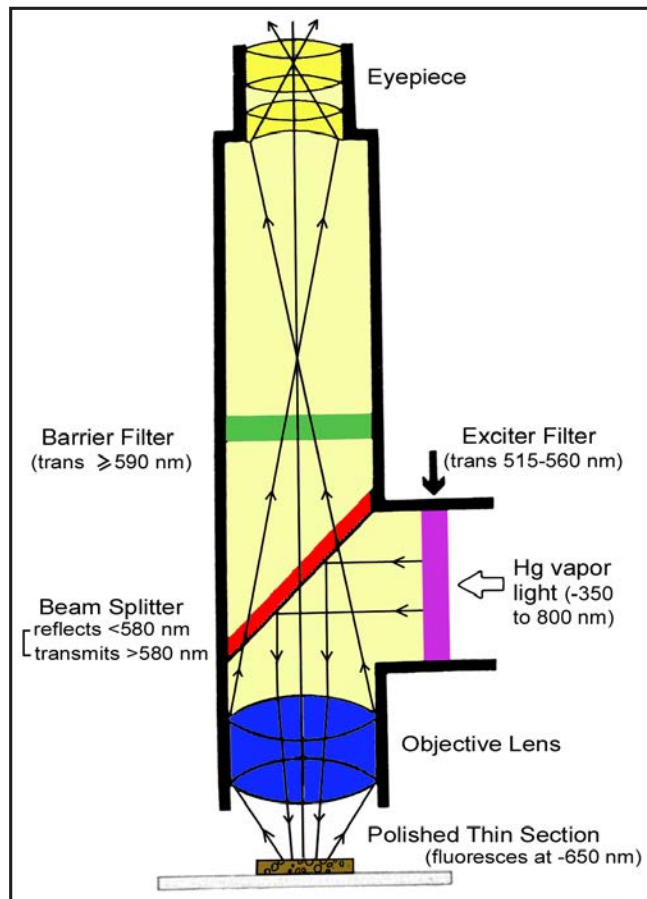


Figure 4.25. Generalized microscope optical configuration for observing fluorescence under incident light. Modified from Soeder (1990).

reliably read these high-contrast images in the yellow and green light spectrum. Since the image brightness is directly proportional to magnification, the best images are obtained at relatively high magnifications (such as greater than 100x). Low-power fluorescence is often too dim to effectively record on film. These techniques are applicable to thin sections from both core and cuttings samples.

Epifluorescence Petrography of Leadville Limestone Thin Sections

Blue-light, EF microscopy was completed on 15 core samples to identify a variety of rock textures and diagenetic phases of Leadville limestone and dolomite within Lisbon field. These samples were selected because they are representative of the compositional, diagenetic, and pore types encountered within the five cored wells (see figure 2.3 for core locations). A detailed description and interpretation of the fluorescence petrography of each sample follows along with photomicrographs (as figures 4.26 through 4.30) to show representative views under both blue-light EF and plane-polarized light. Short descriptive captions for these photomicrographs are included with each photograph pair. For the complete descriptions and EF images from the Leadville reservoir at Lisbon field refer to appendix E.

Lisbon No. D-816 Well

Blue-light, EF microscopy nicely shows pore spaces and structures that are not readily seen under transmitted, plane-polarized lighting and shows the range of crystal sizes or shapes within bitumen-rich areas (figure 4.26). Samples from this well consist of fairly massive dolomite, which is generally non-fluorescent but has a slight hint of fluorescence showing vague relict grains.

Some samples display complex zoning, alternating from dull to bright fluorescence within rhombs. Blue-light EF also shows the clear difference between dull replacement dolomite and much lighter replacement dolomite cement. Rare saddle dolomite cements in molds appear to show crystal zonation.

Microfractures cutting through low-permeability dolomite matrix are visible only with blue-light EF. Some pores (isolated molds) are lined with bright, yellow oil film fluorescence possibly from oil staining whereas others show no oil staining.

Lisbon No. D-616 Well

Blue-light, EF microscopy shows replacement dolomite that is fine- to medium-crystalline with planar to curved crystal faces, and weakly yellow fluorescence with possible fluid inclusions (figure 4.27); limestone does not fluoresce. Saddle dolomite cements growing into some of the moldic pores display moderately dull blue fluorescence. Blue-light EF dis-

plays replacement rhombic dolomite outlines with high inter-crystalline porosity despite the appearance of significant bitumen plugging.

Blue-light, EF microscopy also shows syngenetic dolomite, laminated microbial (cryptoalgal [?]) mudstone with soft pellets and abundant wispy seam, low-amplitude stylolites; moderate yellow fluorescence is observed throughout the samples. Ghosts of original skeletal/pelletal grains show moderate yellow fluorescence transitioning into coarse replacement dolomite displaying modest intercrystalline porosity. The replacement rhombs have generally dead cores and moderate yellow fluorescent overgrowths.

Lisbon No. B-610 Well

Ultraviolet-light, EF microscopy shows two regions within the sample. Region 1 consists of white, syngenetic dolomite with no visible porosity and blue-purple moderate fluorescence. The UV fluorescence nicely shows a variety of corrosion and dissolution fabrics, which sometimes mimic original grain boundaries. Region 2 consists of black, non-fluorescent, finely crystalline dolomite, as well as "floating" large dolomite rhombs that appear to have precipitated out of the finely crystalline groundmass (figure 4.28).

Blue-light EF also displays syngenetic dolomite, both unaltered and corroded, with moderate yellow fluorescence. Within the black dolomite region, the larger floating dolomite rhombs have a dull green fluorescence.

Lisbon No. B-816 Well

Blue-light, EF microscopy shows replacement dolomite with highly yellow fluorescent rims (figure 4.29). Saddle dolomite cement has moderate yellow-green fluorescence. Late calcite cements are generally non-fluorescent.

Lisbon NW USA No. B-63 Well

Blue-light, EF microscopy shows massive, very finely crystalline, non-porous syngenetic dolomite displaying a mottled dull to medium yellow fluorescence with occasional ghosts of original grain types (grain outlines are visible with fluorescence). Dolomitized grains include detrital carbonate (pellets) and siliciclastic (quartz silts and clays) components of the karst cavity infilling (figure 4.30); clay minerals between grains display a pale reddish fluorescence. Outside of the cavity, the host rock is almost pure limestone composed of fossils and coated grains, all of which are calcitic with little visible fluorescence.

Late calcite (poikilotopic) also displays no fluorescence. This late calcite occurs as cement within former isolated molds, fracture fillings, and some replacement of syngenetic dolomitic matrix.

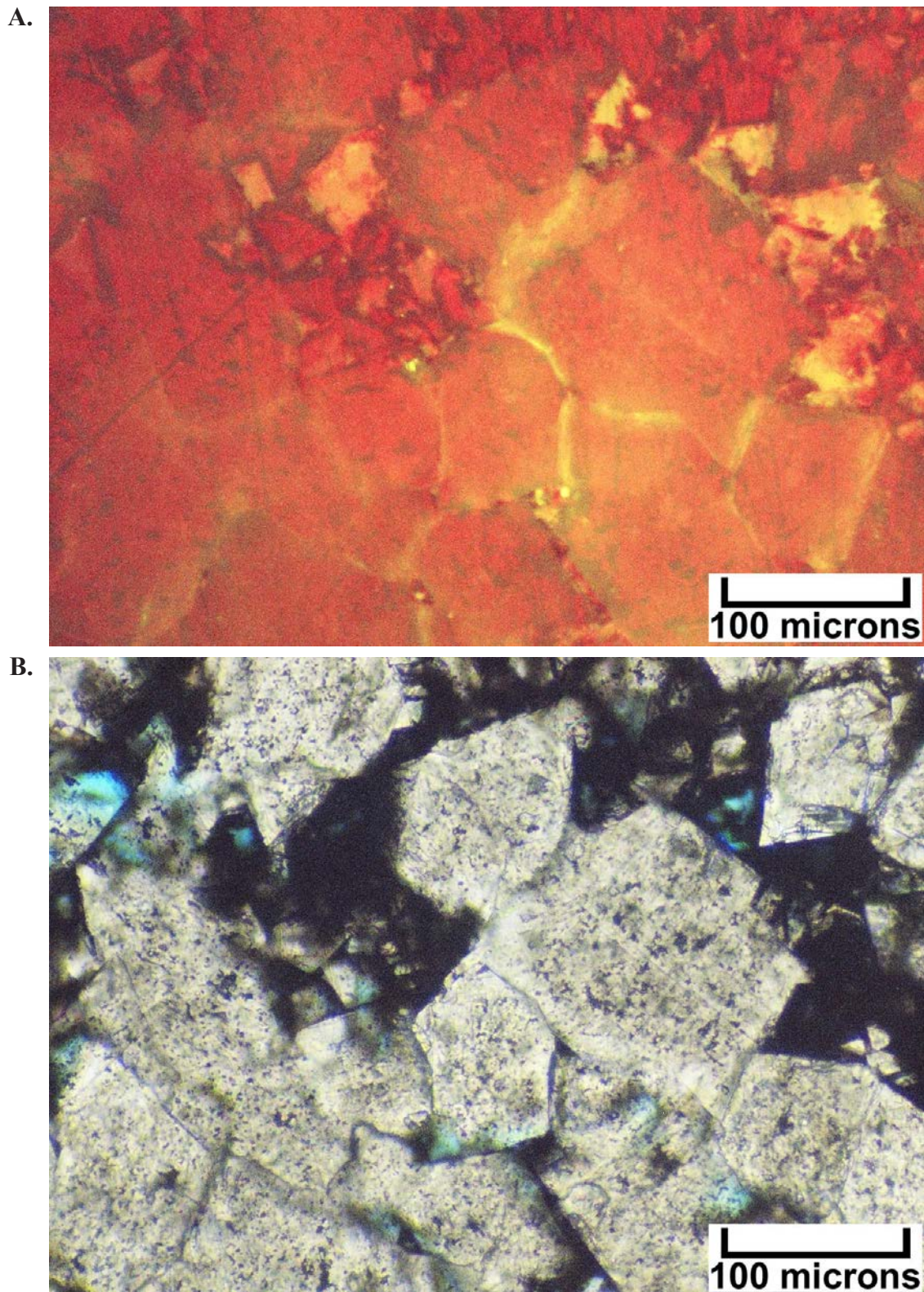
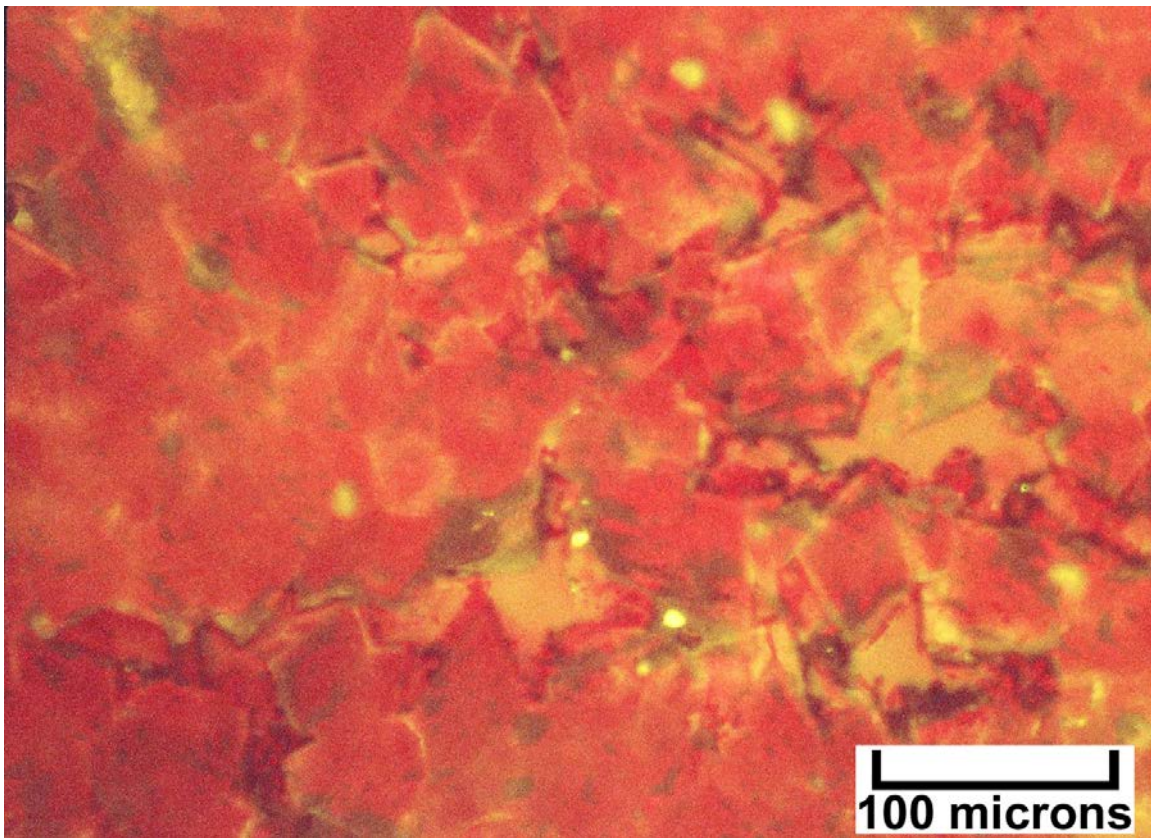


Figure 4.26. Photomicrographs from Lisbon No. D-816 well at 8435.8 feet (2571.2 m). **(A)** Epifluorescence under moderate magnification showing a representative area of fluorescence zonation within coarse dolomite crystals. The reddish areas are pores that have abundant bitumen linings and plugging (see figure 4.26B). Fluorescence petrography makes it possible to clearly see the dolomite crystals versus the pore space. In places, very small rhombic outlines of dolomite crystals can be resolved. Many of these pores appear to be surrounded by an interlocking network of dolomite crystals. **(B)** The same field of view as above is shown under plane light at the same magnification. Note that the black (and opaque) areas composed of bitumen mask the crystal boundaries of the dolomite as well as individual pore outlines. The white and gray areas are remnants of the dolomite matrix that are not masked by the bitumen. Only a small amount of pore space (blue-dyed areas) can be seen in this view compared to the fluorescence photomicrograph above.

A.



B.

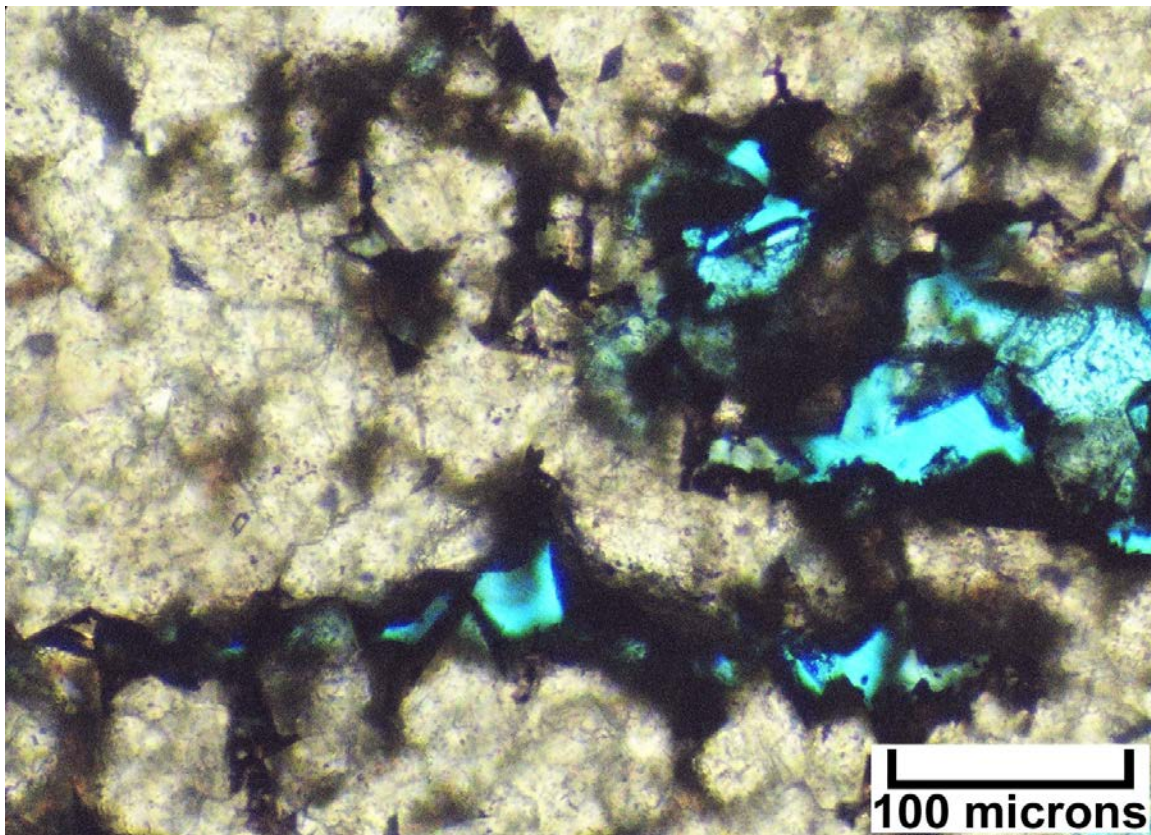
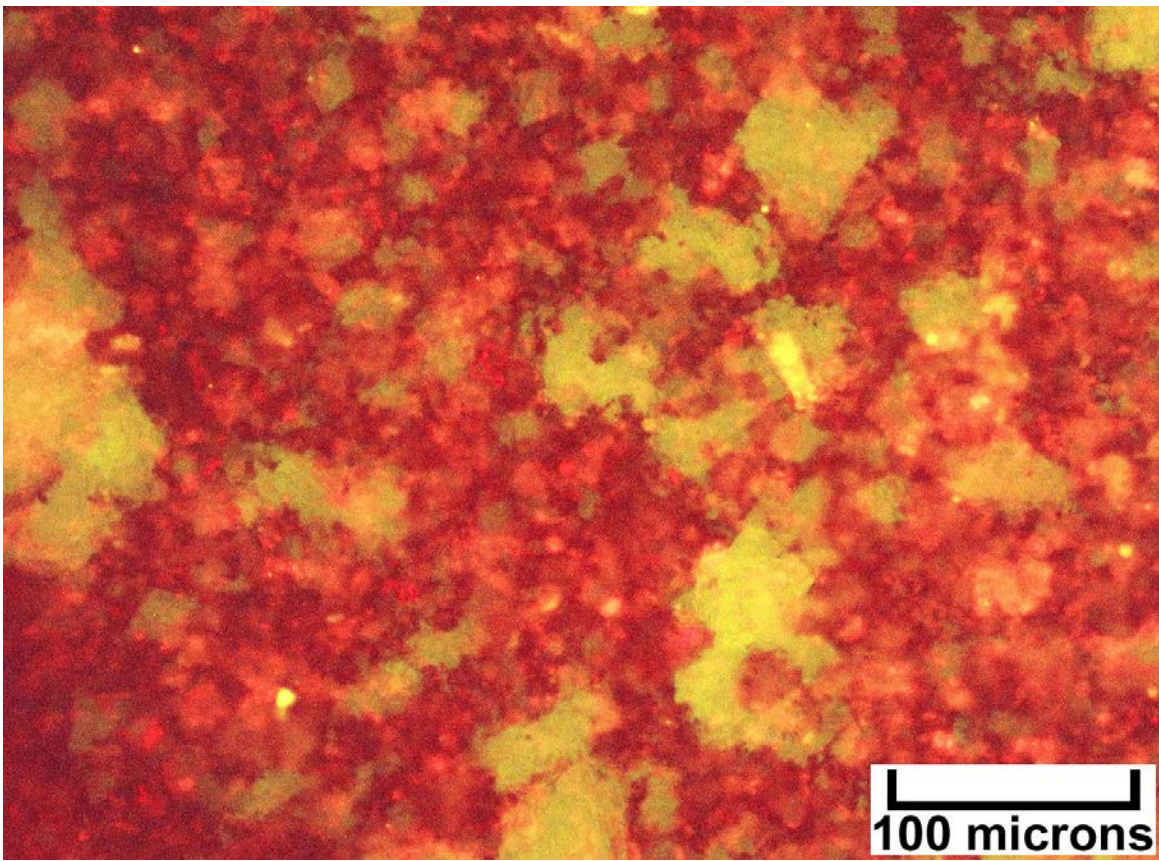


Figure 4.27. Photomicrographs from Lisbon No. D-616 well at 8435.8 feet (2571.2 m). (A) Epifluorescence under moderate magnification showing fine- to medium-sized crystals of replacement dolomite. The rhombs display dead cores and fluorescent rims. (B) The same field of view as above is shown under plane light at the same magnification. Note that the black (and opaque) areas composed of bitumen mask the crystal boundaries of the dolomite as well as individual pore outlines.

A.



B.

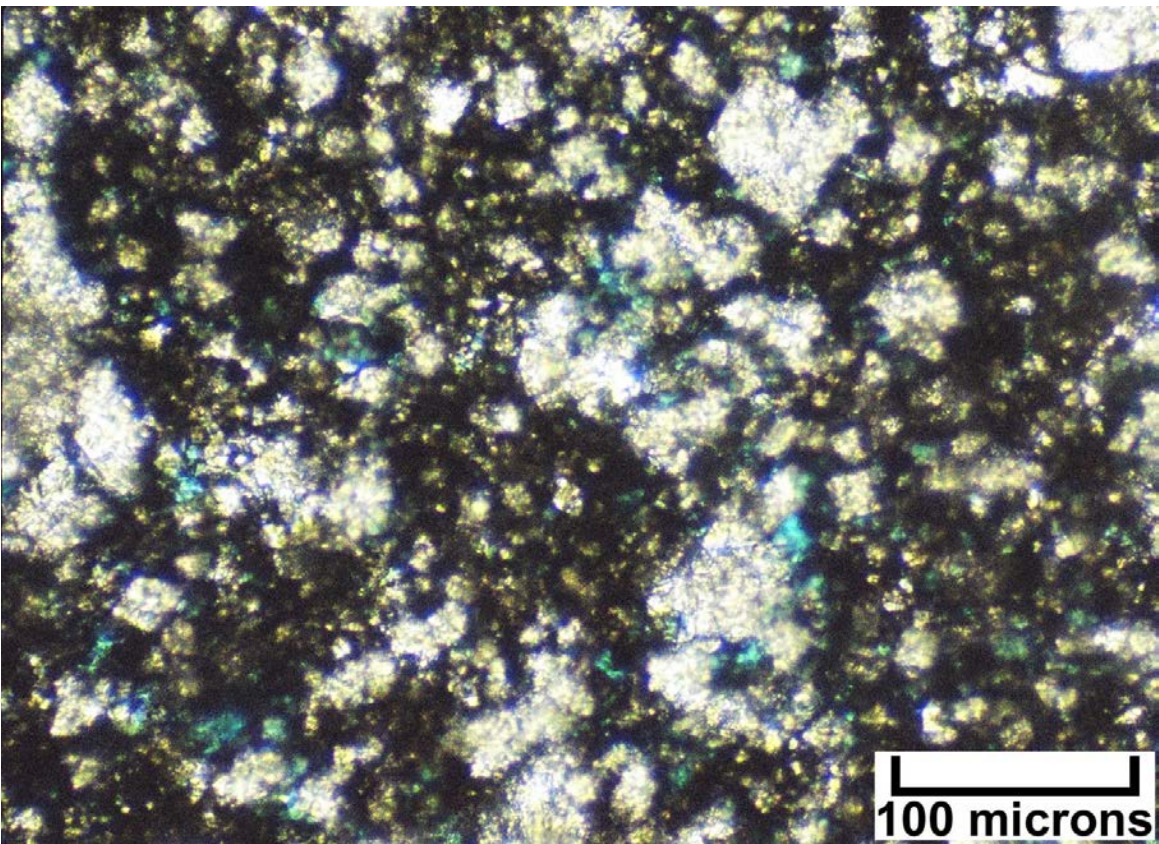
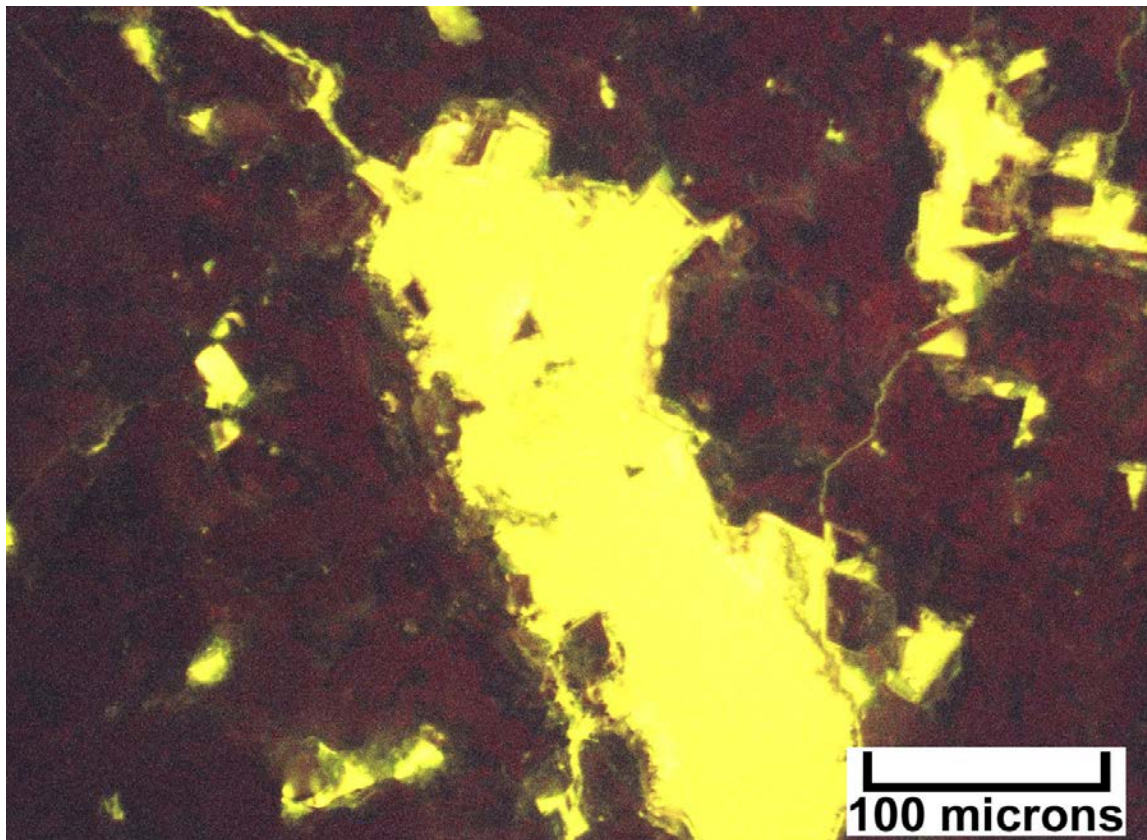


Figure 4.28. Photomicrographs from Lisbon No. B-610 well at 7897 feet (2407 m). (A) Epifluorescence under moderate magnification showing individual, yellow-fluorescing dolomite rhombs “floating” in a non-fluorescing dolomite matrix. (B) The same field of view as above is shown under plane light at the same magnification.

A.



B.

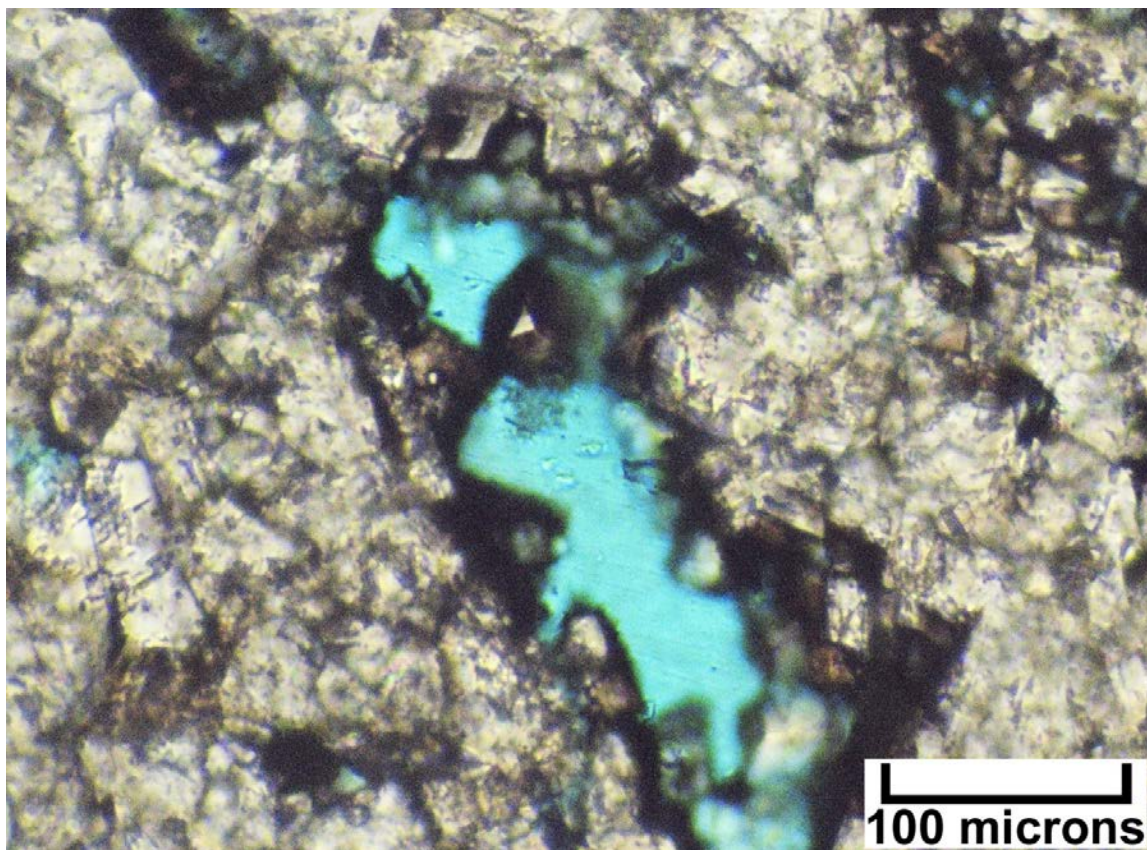
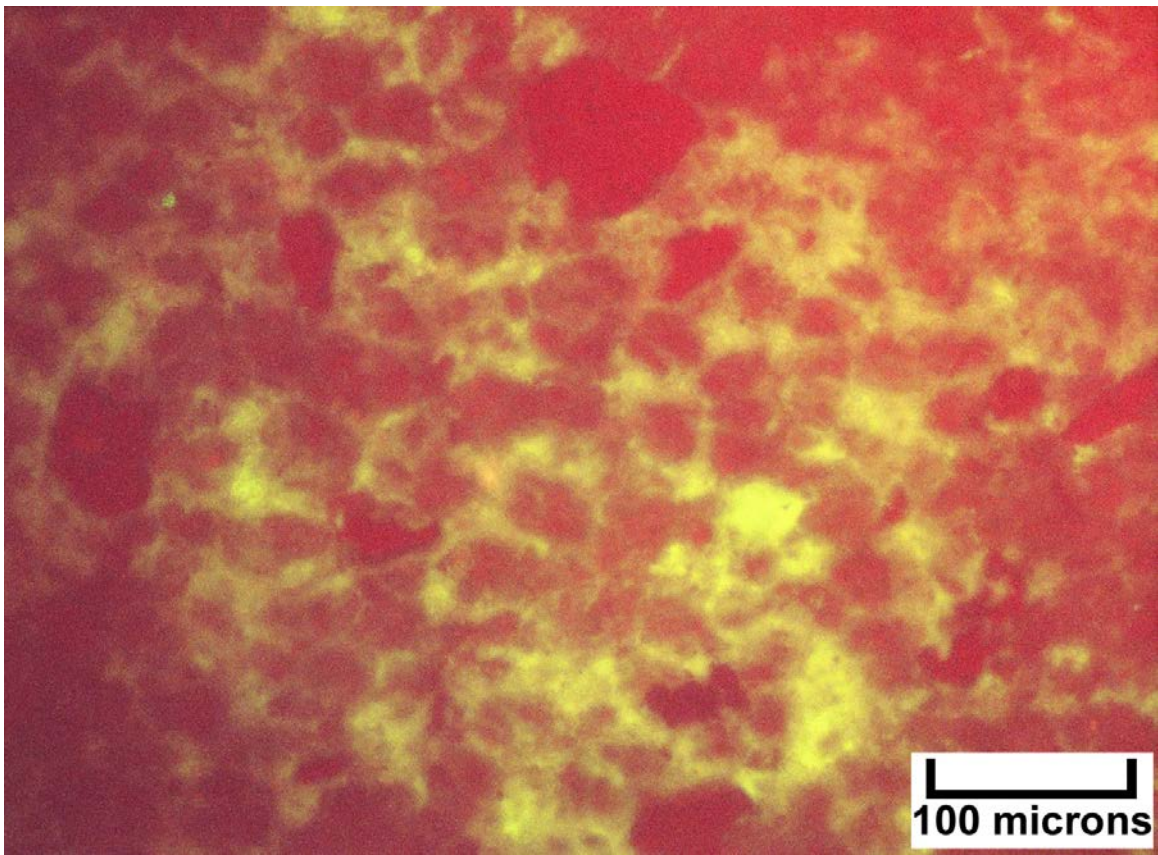


Figure 4.29. Photomicrographs from Lisbon No. B-816 well at 8486 feet (2587 m). (A) Epifluorescence under moderate magnification showing zoned, rhombic replacement dolomite with dead cores and highly fluorescent rims. (B) The same field of view as above is shown under plane light at the same magnification. Note the large solution pore (blue area).

A.



B.

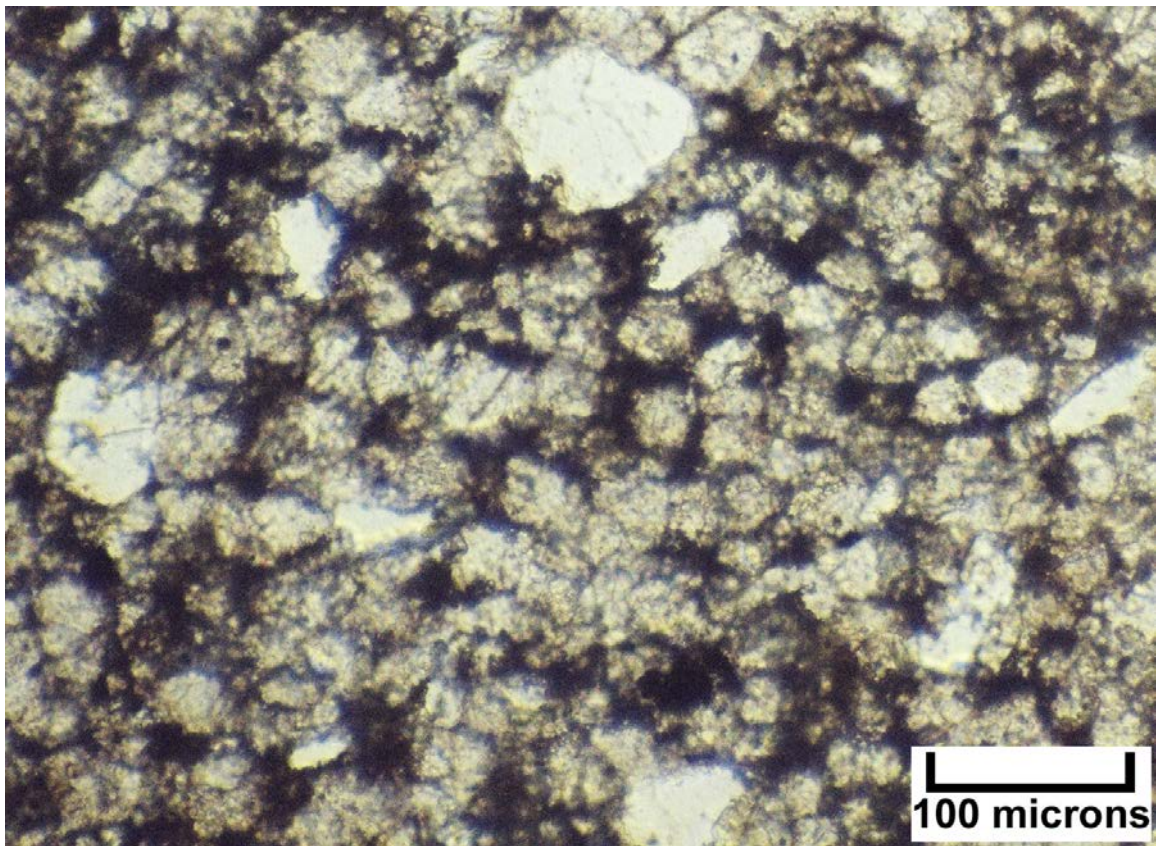


Figure 4.30. Photomicrographs from Lisbon NW USA No. B-63 well at 9935.6 feet (3028.4 m). (A) Epifluorescence under moderate magnification showing dolomitized detrital fill within a karst cavity. (B) The same field of view as above is shown under plane light at the same magnification. Note the large quartz grains, and angular limestone and dolomite clasts. These clasts do not fluoresce.

CATHODOLUMINESCENCE

Cathodoluminescence (CL) is the emission of light resulting from the bombardment of materials using a cathode ray (Allan and Wiggins, 1993). This petrographic technique can be an invaluable tool in petrographic studies of carbonate rocks. This technique can provide important information about the complex modification of rock fabrics and porosity within the Leadville Limestone of the Paradox Basin. Diagenesis played a major role in the development of reservoir heterogeneity in Lisbon field as well as throughout other Leadville fields. Diagenetic processes started during deposition and continued throughout burial history (figure 4.1).

Cathodoluminescence provides insights into the chemical differences between preserved remnants of depositional components resulting from various diagenetic events in carbonate rocks as recognized from core examination and thin section petrography. In particular, CL provides visual information on the spatial distribution of certain trace elements, especially manganese (Mn^{+2}) and iron (Fe^{+2}) in calcite and dolomite (Machel and Burton, 1991; Scholle and Ulmer-Scholle, 2003). The visible CL responses are red to orange in color, and their intensity is usually described as non-luminescent, dull luminescent, and brightly luminescent. As a general rule, incorporation of Mn^{+2} into the calcite lattice stimulates luminescence and the incorporation of Fe^{+2} quenches or reduces luminescence (Fairchild, 1983; Allan and Wiggins, 1993; Scholle and Ulmer-Scholle, 2003). Qualitative interpretation of CL usually assigns nonluminescent responses to oxidizing settings in which the reduced forms of both Mn and Fe are unavailable for incorporation into the lattices of carbonate mineral precipitates. Oxidized forms of Mn and Fe are not incorporated into calcite or dolomite crystals. Therefore, there is nothing in these crystals to excite luminescence. Bright luminescence is related to carbonate precipitates with high Mn/Fe trace element ratios, typically as a result of reducing environments during early (near-surface) to intermediate stages of burial diagenesis. Dull luminescence seems to happen where the Mn/Fe trace element ratios are present in carbonate precipitates. Thus, dull luminescence is thought to be the result of intermediate to late stages of burial diagenesis. Elements other than Mn and Fe do not have any appreciable effect in enhancing or reducing luminescence (Budd and others, 2000).

Particularly useful references on the uses and limitations of CL interpretations in studies of ancient carbonate include Sipple and Glover (1965), Frank and others (1982, 1996), Marshall (1988), Hemming and others (1989), Barker and Kopp (1991), Gregg and Karakus (1991), Machel (2000), Lavoie and others (2001), Coniglio and others (2003), and Lavoie and Morin (2004).

Methodology

The analysis done in this study was completed using uncovered, polished thin sections, although rock chips and unpol-

ished thin sections could be used. The equipment needed for CL can be installed on almost any polarizing microscope (see Marshall, 1988; Miller, 1988). A Cambridge Image Technology Ltd. luminoscope (model CLmk3A/4) mounted on an Olympus petrographic microscope (figure 4.31; see also Marshall, 1988) belonging to the Colorado School of Mines Department of Geological Engineering was used for this analysis (figure 4.32). Operating conditions were generally at 10–16kV accelerating potential, 0.5–0.7 mA of beam current and a beam focused at about 2 cm. All the work involved visual observations and some photographic documentation. Photomicrographs were recorded on a digital camera. No attempt was made to measure intensities or spectral information on the CL responses (e.g., Marshall, 1991; Filippelli and Delaney, 1992) to the Leadville carbonate samples. Image analysis and regional mapping of cement zones (i.e., “cement stratigraphy”) have been done by some workers on carbonate cements (e.g., Meyers, 1974, 1978, 1991; Dorobek and others, 1987; Cander and others, 1988; Dansereau and Bourque, 2001), but these applications are beyond the scope of diagenesis documentation attempted in this project.

Cathodoluminescence Petrography of Leadville Limestone Thin Sections

Cathodoluminescence examination was completed on thin-section samples from the Leadville limestone and dolomite within Lisbon field. These thin-section samples were selected because they are representative of the mineralogical (e.g., dolomite, calcite, anhydrite, and quartz), compositional, diagenetic, and pore types encountered in the five core wells from the field (see figure 2.3 for core locations). For the complete descriptions and CL images from the Leadville reservoir at Lisbon field refer to appendix E. The following remarks summarize our findings.

Lisbon No. D-816 Well

Cathodoluminescence shows a wide range of crystal size and growth habits within the dull red luminescing, matrix-replacing dolomite as displayed from 8442 to 8443 feet (2573.1–2573.4 m) (figure 4.33). Most of the dolomite within areas of fabric-selective dolomitization is a deep or intense red color. A lighter red luminescence occurs between many of the grains where early cements have been dolomitized. Some of the coarser dolomite crystals appear to have an overgrowth of brighter red luminescent material. The range in dolomite rhomb sizes may reflect rapid precipitation. The amount of open porosity under CL is considerably greater than that visible under plane-light microscopy. Cathodoluminescence also displays original depositional textures and the outlines of original carbonate grains. Between other grains, some interparticle pores are still open. In a few areas, these early pores have been solution-enlarged and lined with a later generation of coarse rhombic dolomite.

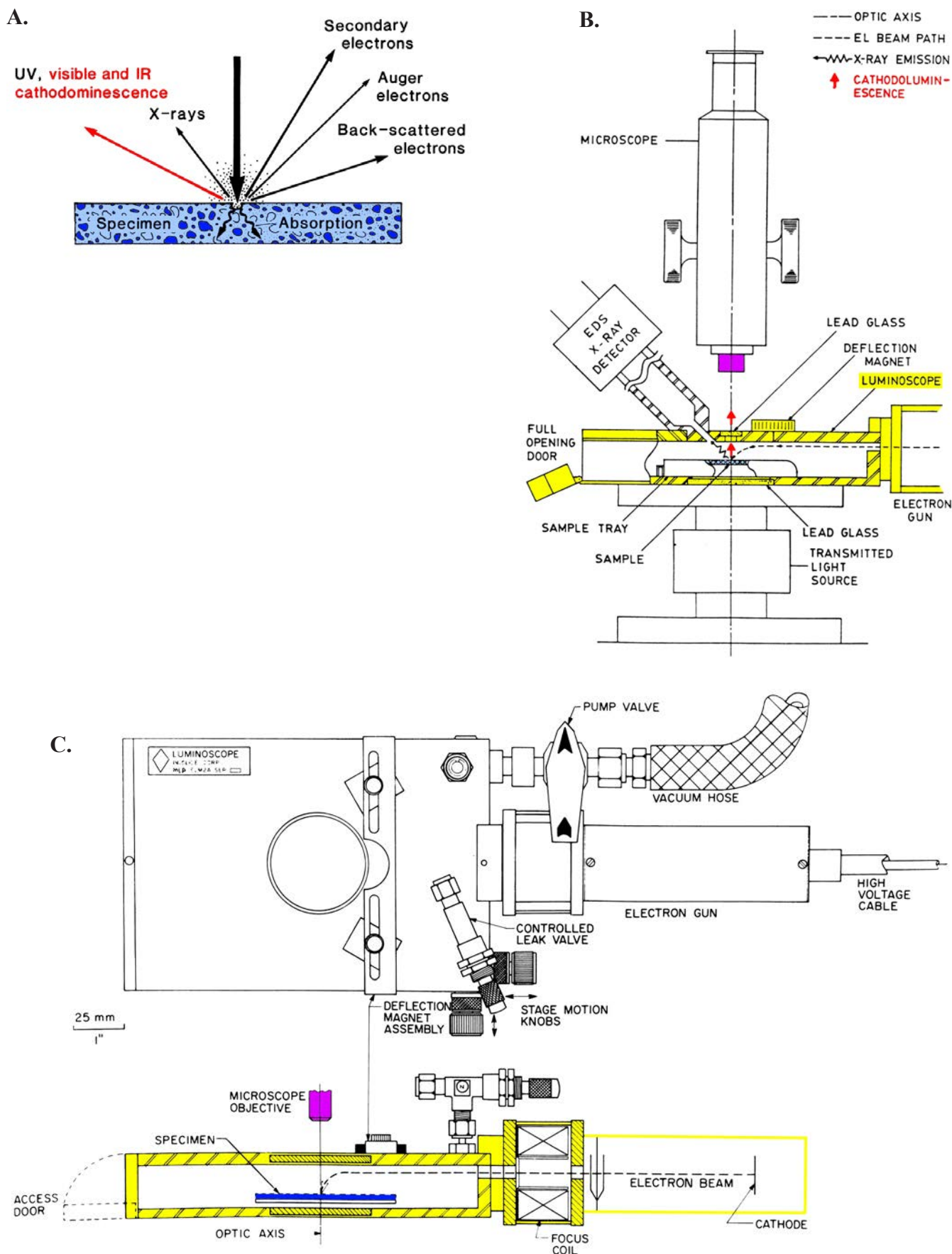


Figure 4.31. Generalized microscope optical configuration for observing cathodoluminescence: (A) modified from Walker and Burley (1991); (B) modified from Marshall (1991); and (C) modified from Marshall (1988).

A.



B.

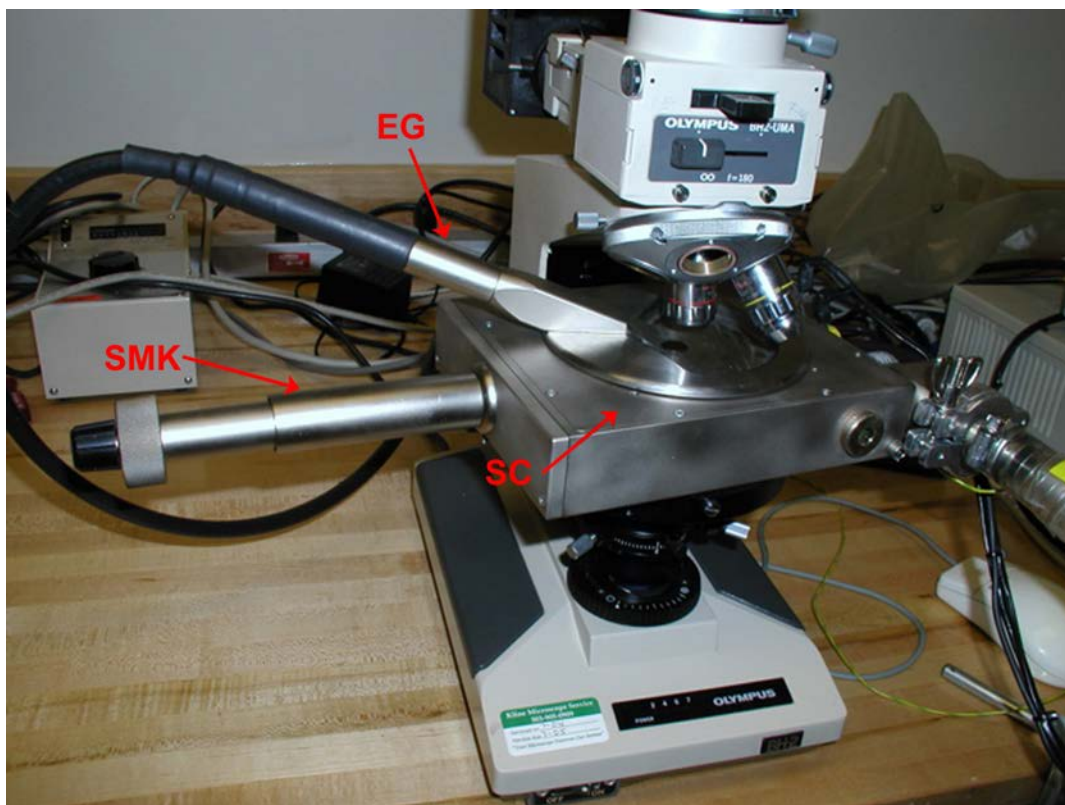


Figure 4.32. Colorado School of Mines cathodoluminescence setup used for the Leadville samples from Lisbon field. **(A)** Cambridge Image Technology Ltd. CLmk3A/4 cathodoluminescence instrument is mounted on an Olympus BH2 petrographic microscope. The electron gun (EG) is in the inclined position to the left of the sample chamber. The stage motion knob (SMK) is the silver cylinder to the left of the sample chamber. The hose to the vacuum pump is to the right of the chamber. The front panel controls (beneath the video monitor) include (from left to right) the diagnostic selector; vacuum and diagnostic metering, gun current metering, Gun kV metering, and main power switch. The video monitor and CPU were used for handling and displaying the CL images captured by a digital camera. **(B)** Close-up of the cathodoluminescence instrument sample chamber (SC), electron gun (EG) and stage motion knob (SMK) mounted on an Olympus BH2 petrographic microscope.

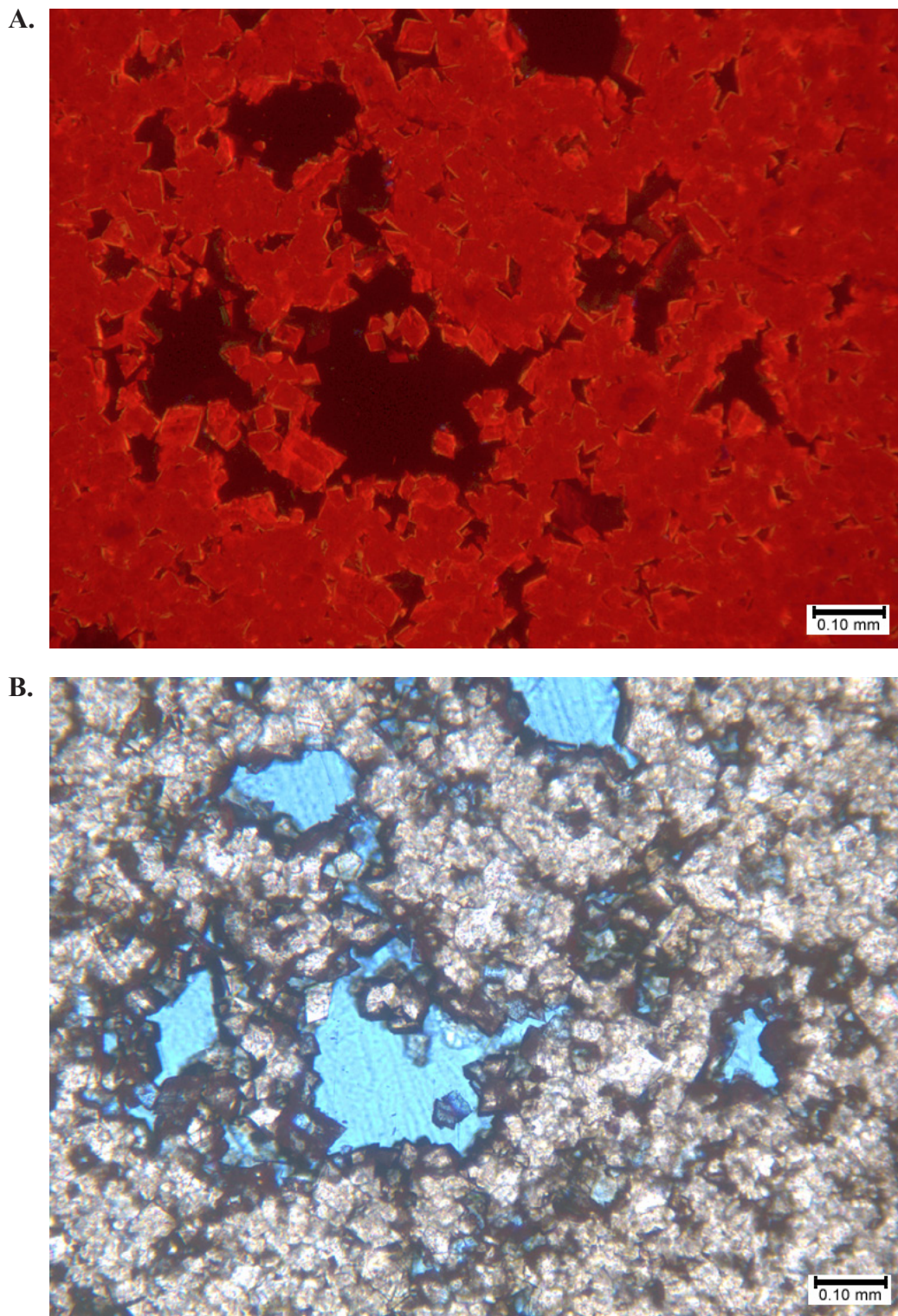


Figure 4.33. Photomicrographs from Lisbon No. D-816 well at 8442 to 8443 feet (2573–2573 m). **(A)** Cathodoluminescence shows sharp outlines between the dolomite crystals and adjoining pore spaces. Note that the porosity (in black) in this sample seems to be a combination of intercrystalline space and solution-enlarged molds. Most of the dolomite seen here consists of bright red luminescing dolomite with only occasional thin rinds of dull luminescing overgrowth. Also, rare non-luminescing dolomite cement crystals are within some of the smaller pore spaces (see, for instance, the cement occluding a small pore in the lower center of this image). Finally, note that “ghosts” of former grains such as “hard” peloids can be seen in the luminescing pattern of the dolomites in the upper right corner of this view. **(B)** The same field of view under plane light. The outlines of the dolomite crystals are not nearly as distinct and crisp here as in the previous CL view. In fact, it is difficult to pick out the crystal outlines or faces in this type of lighting. Black pyrobitumen makes it difficult to see the smaller, but important, intercrystalline pores. The larger solution-enlarged molds in blue are easy to see, but their interconnection through the smaller intercrystalline space is better seen under CL imaging.

Cathodoluminescence imaging was very useful in identifying various generations of dolomite. Two types of CL response are visible within moderately coarse dolomite crystals as observed at 8433 feet (2570.4 m). Bright red luminescence can be seen within the interiors of most of the replacement dolomite (figure 4.34). However, many of the crystals exhibit non-luminescent overgrowths of variable thickness. In addition, some crystals exhibit mostly non-luminescent material. These crystals may be largely dolomite cements. Finally, some dolomite crystals exhibit a thin rind of red-luminescing dolomite overlying the non-luminescent overgrowth stage. The red-luminescing dolomite is possibly the product of the replacement of a previous limestone or earlier dolomite matrix while the non-luminescing crystal additions may be overgrowth cements growing into open pores. Dissolution and corrosion of some crystals is evident between the second (non-luminescent) and the final luminescent rim.

Lisbon No. B-816 Well

Cathodoluminescence imaging was very useful in identifying the presence of saddle dolomites (Radke and Mathis, 1980) within microporous dolomites (figure 4.35). Large dolomite crystals (1.0 to 2.0 mm in diameter) with distinctly curved crystal faces occur as both replacements of finer, earlier dolomites, and as pore-filling cements. These saddle dolomites display dull, red luminescence in their core areas and slightly bright, orange-red luminescence toward their rim areas. In addition, CL makes it possible to see the growth bands in these coarse dolomite crystals due to slight luminescence differences between each growth zone.

In general, the presence of saddle dolomites within a carbonate sample is indicative of the growth of strained, slightly iron-rich, dolomite replacements and cements under elevated temperatures during burial conditions (Radke and Mathis, 1980). Thus, saddle dolomite, as well as the other coarse dolomite crystals with reddish luminescence, are probably late burial or hydrothermal dolomites. Additional published descriptive work on saddle dolomites using CL may be found in LaVoie and Morin (2004).

Lisbon No. D-616 Well

Sediment-filled cavities are relatively common throughout the upper one-third of the Leadville Limestone in Lisbon field. These cavities or cracks were formed by karstification of the exposed Leadville. Infilling of the cavities by detrital carbonate and siliciclastic sediments occurred before the deposition of the Pennsylvanian Molas Formation. Cathodoluminescence imaging shows that the contact between the transported material and the limestone country rock can be sharp, irregular, and corroded with small associated mud-filled fractures (figure 4.36). The transported material consists of poorly sorted detrital quartz grains (silt size), chert fragments, carbonate clasts, clay, and occasional clasts of mud balls (desiccated and cracked). The carbonate muds infilling the karst cavities

are largely dolomitized (a later diagenetic process), very finely crystalline, and non-porous.

FLUID-INCLUSION SYSTEMATICS OF LISBON FIELD SAMPLES

During crystal growth, imperfections may trap fluids present in the environment at that time. Later mineral precipitation and deformation, such as the development of fractures, can create additional crystal imperfections that may also trap fluids (figure 4.37). These fluid inclusions are defined as fluid-filled vacuoles, typically 5 to 20 microns in size. They provide pressure, volume, and temperature information about the conditions when the crystal precipitated (Bodnar, 2017). The fluids in the inclusion may be connate water, oil, or a sample of the mineralizing fluid. The following properties are assumed not to have changed since an inclusion formed: (1) the composition of the trapped fluid, (2) the density of the trapped fluid, and (3) the volume of the inclusion (Bodnar, 2017). The study of fluid inclusions can help determine (1) the temperature of mineral precipitation, (2) the composition and origin of mineralizing fluids, (3) later history of temperature, pressure, and fluid composition, (4) petroleum migration history, (5) relative timing of porosity occlusion, and (6) deformation event conditions (Bodnar, 2017).

Fluid inclusions trapped in calcite, quartz, and dolomite were studied from three wells: Lisbon NW USA No. B-63, Lisbon No. D-616, and Lisbon No. D-816 (figure 2.3). The inclusions were categorized based on origin, number of phases present, and composition. All inclusions were classified as either primary or secondary. Primary inclusions are trapped at the time of mineral growth; secondary inclusions are trapped along healed fractures. Primary inclusions typically define growth zones, although in quartz, large isolated inclusions are typical. All inclusions observed contained either one or two fluid phases at room temperature. Inclusions containing brine and vapor are the most common, but single-phase aqueous inclusions, gas-rich inclusions, and inclusions consisting of oil and vapor are present. Single-phase aqueous inclusions are indicative of trapping at temperatures less than 50°C (122°F) (Goldstein and Reynolds, 1994).

Fluid-Inclusion Measurements

Heating and freezing measurements were made on doubly polished thick sections and hand-picked crystals using a Linkham THSMG 600 freezing and heating stage calibrated with synthetic fluid inclusions (the data are tabulated in part 3 of appendix E). The precision of the measurements is estimated to be $\pm 0.1^\circ\text{C}$ at 0.0°C (32°F) and $\pm 3^\circ\text{C}$ at 374°C ($\pm 43^\circ\text{F}$ at 705°F).

Homogenization and ice-melting temperatures were measured. Homogenization temperatures are minimum trapping

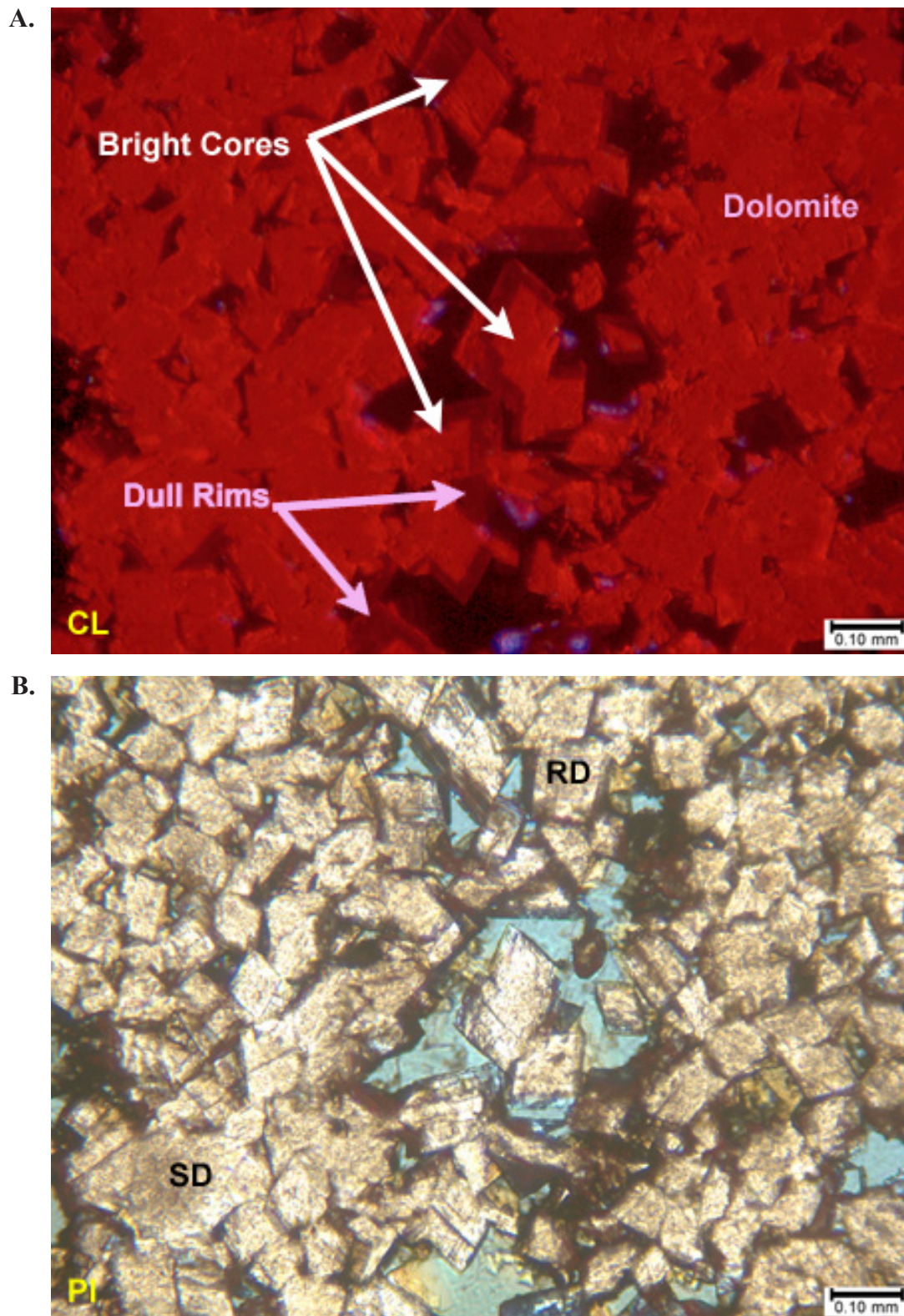


Figure 4.34. Photomicrographs from Lisbon No. D-816 well at 8433 feet (2570 m). **(A)** This CL image shows beautiful luminescence zonation of many of the dolomite crystals, especially in a band from the top center to the bottom center of the image. Note the bright red luminescing dolomite cores surrounded by rim zones of non-fluorescent overgrowth. The black areas on this image are currently open pore spaces. **(B)** The same field of view under plane light showing replacement dolomite (RD) and saddle dolomite (SD). The dolomite crystals shown here are well formed with planar crystal faces and generally rhombic outlines. Note that some crystal terminations may display curved (or saddle) outlines. Plane light does not make it possible to distinguish the crystal composition zonation imaged in the CL photomicrograph. The black areas within this field of view are due to pyrobitumen coatings on many of the dolomite crystal surfaces. The blue areas between many of the replacement dolomite crystals are open pores.

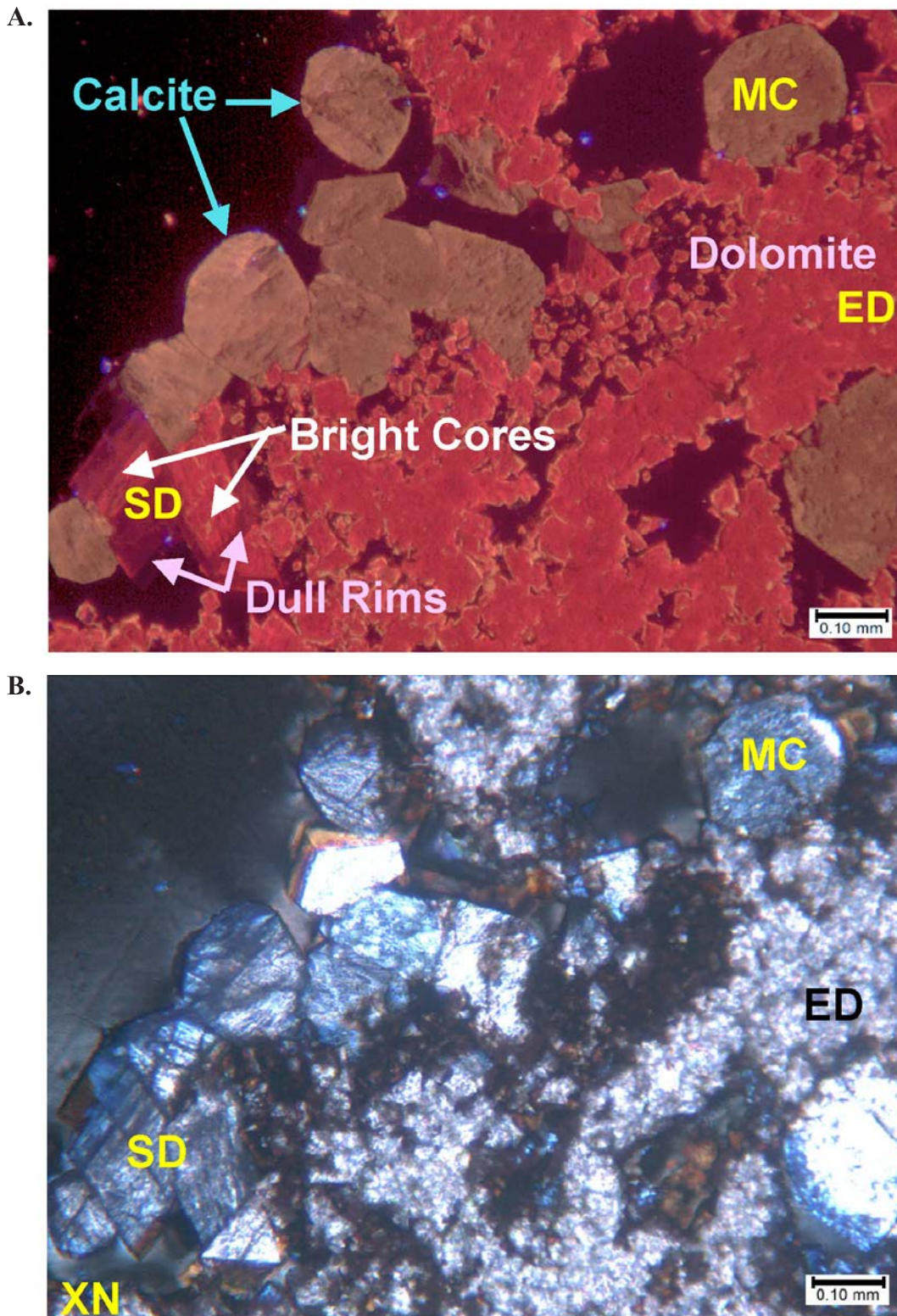


Figure 4.35. Photomicrographs from Lisbon No. B-816 well at 8486 feet (2587 m). **(A)** This area of high matrix porosity (in black) shows early replacement dolomite (ED) that displays intense red luminescence. Some of these replacement crystals display very thin orange overgrowths. However, some of the largest dolomite rhombs (saddle dolomite [SD]) in this field of view display a coarser crystal zonation in which the bright red luminescent core is overgrown with thick, dull luminescent rims (the lower left corner of this photomicrograph). Finally, note the large, late calcite spar crystals (macrocalcite [MC]) that have orange luminescence within the large pores from lower left to upper right as well as in the lower right. **(B)** The same field of view under crossed nicols. Note that some of the large dolomite crystals in the lower left of this image display sweeping extinction and possibly curved crystal faces that are consistent with probable saddle dolomite. The replacement dolomite throughout most of this field of view are too small or too inclusion-rich to distinguish extinction patterns. The late calcite spar cements generally display straight extinction.



Figure 4.36. Photomicrograph from Lisbon No. D-616 well at 8308 feet (2532 m). This low-magnification image nicely shows a sharp contact that runs from top to bottom toward the left side of the photomicrograph. The bright red field is composed mostly of dolomite, whereas the field with the orangish cast (to the left) is almost entirely limestone. The dolomite area is composed of carbonate grains and sediments that have filled a karst-related crack or cavity. The poorly sorted, angular grains that are “floating” within the dolomite field are a combination of detrital siliciclastic (mostly quartz) grains and lithified limestone clasts. The limestone field along the left side of the photomicrograph is composed of non-luminescent skeletal (crinoid-rich) sediments with orangish cements. Neither the dolomite with siliclastic sediments nor the limestone display any visible matrix porosity. The contact between the dolomite and limestone fields is irregular but sharp. Finally, few scattered replacement dolomite rhombs (also with red luminescence) are within the well-cemented limestone. Figure 4.9C is the same field of view under crossed nicols.

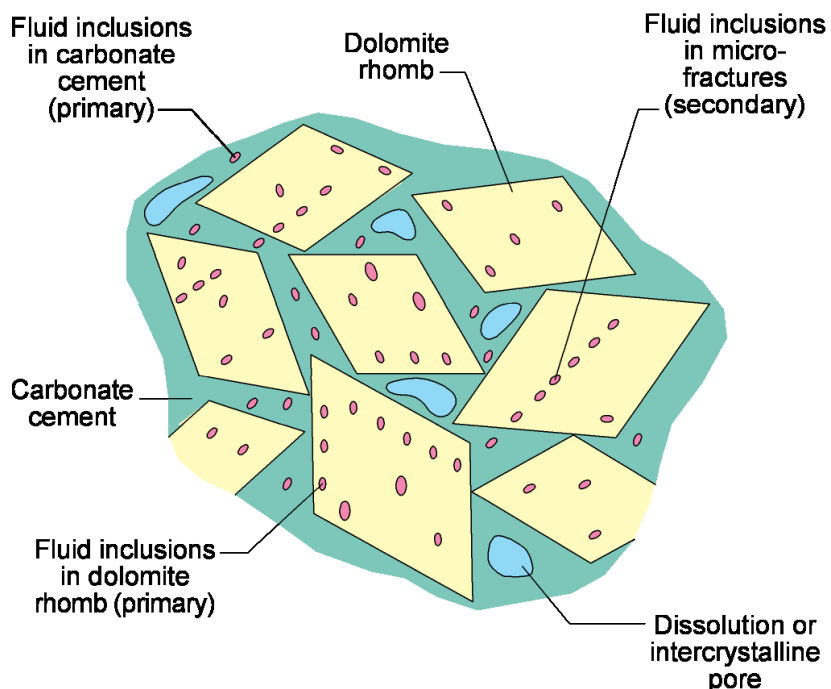


Figure 4.37. Schematic diagram of basic fluid inclusion types.

temperatures. Ice-melting temperatures provide a measure of the fluid salinity. The salinities of the two-phase aqueous inclusions that have ice-melting temperatures between 0° and -21.2°C (32° and -6.2°F) were converted to weight percent (wt.%) NaCl equivalent using the equation of Bodnar (1993). Salinities of inclusions that have lower ice-melting temperatures displayed eutectic (first melting) temperatures of less than -45°C (-49°F), indicating the presence of divalent ions (most likely Ca and Mg). These inclusions had ice-melting temperatures as low as about -27°C (-17°F). The equation of Bodnar (1993) cannot be used to calculate the salinities of these fluids. As a first approximation, assuming that only Ca, Na, and water are present in the inclusions, the salinities would be in the range of 25 wt.% to 30 wt.% NaCl-CaCl₂ equivalent (Yanatieva, 1946). Such high-salinity brines imply interactions with evaporite deposits.

Caveats and Practical Aspects of Fluid-Inclusion Studies

Several factors can affect the utility and validity of fluid-inclusion measurements and these factors can play a significant role in sedimentary environments. Two general tenets of fluid-inclusion research are that (1) the volume of the cavity has not changed since generation of the vapor bubble, and (2) the bulk composition of the inclusion has remained constant. However, both the volume and compositions of the inclusions can be modified by necking, stretching, refilling, and leakage. Typically, a population of fluid inclusions that formed contemporaneously (termed a fluid inclusion assemblage by Goldstein and Reynolds, 1994) will yield homogenization temperatures within 15° to 20°C (59°–68°F).

All fluid inclusions neck or anneal after trapping as the temperature decreases. This process typically leads to the splitting of a large inclusion into several smaller inclusions. Necking occurring after generation of the vapor bubble is recognized by the petrographic association of inclusions having variable liquid to vapor ratios. Many of the inclusions in calcite and dolomite have variable liquid to vapor ratios. Qualitatively, the presence of all inclusions with vapor bubbles, but variable ratios, suggests necking occurred at elevated temperatures greater than at least 50°C (122°F). Although the homogenization temperatures of necked inclusions are not meaningful, because they can be both greater and lower than the true homogenization temperature, the minimum homogenization temperatures can provide a qualitative measure of the minimum temperatures that have affected the rocks. The salinities of necked inclusions, however, are not greatly affected by necking and can be measured and used. Oil inclusions are less prone to necking than aqueous inclusions, although some secondary inclusions in the latest calcite clearly displayed evidence of necking.

Stretching is the inelastic expansion of the fluid inclusion resulting in an increase in its volume. This can lead to the generation or growth of a vapor bubble, which in turn yields an

anomalously high temperature of homogenization. The degree of stretching is highly variable even within a single crystal and its effect is dependent on original fluid inclusion size, shape, and location in a crystal; degree of overheating; pressure; and fluid composition. Often a significant percentage of the inclusions will retain their original characteristics. For example, single-phase inclusions, if originally present, will persist after stretching. Stretched inclusions do not yield meaningful homogenization temperatures. The salinities of stretched inclusions, however, can be utilized.

Refilling of fluids may be common but is difficult to recognize. Both the homogenization temperatures and compositions can be utilized. Refilling of fluids can be recognized by comparison of fluid inclusion characteristics of minerals whose relative ages are known.

Leakage of fluids, particularly the liquid phase, from fluid inclusions is also common. Inclusions that leak are typically vapor-rich. Leakage can often be recognized because it will affect only a small percentage of the total fluid inclusion population.

Lisbon Fluid Inclusions

Fluid Inclusions in Early Calcite

Early calcite represents original fossil material (figure 4.38) and is characteristically coarsely crystalline and decorated with abundant aqueous liquid-rich inclusions that have variable liquid to vapor ratios (figure 4.39). Less commonly, oil inclusions are present (figures 4.40 and 4.41). The vast majority of both the aqueous and oil inclusions are randomly distributed throughout the calcite crystals and appear to be primary in origin. Secondary inclusions defining healed fractures are uncommon.

The characteristically variable liquid to vapor ratios of the aqueous inclusions are interpreted as resulting from necking. Reconnaissance homogenization temperature measurements on spatially associated inclusions have temperatures greater than 20°C (68°F) and are consistent with this interpretation. These homogenization temperatures are not considered meaningful and are not reported here. However, the occurrence of all two-phase inclusions, in contrast to the presence of numerous single-phase, liquid inclusions in dolomite suggests the inclusions in calcite were trapped at elevated temperatures.

Ice-melting temperatures were measured on the aqueous inclusions in two samples from the Lisbon No. D-616 well (figure 4.42). These temperatures ranged from -19.5° to -25.5°C (-3.1°–13.9°F) indicating that the fluids were highly saline.

Early calcite containing primary oil inclusions was found in the Lisbon No. D-616 well at a depth of 8356 feet (2547 m) (figures 4.40 and 4.41). The color of the oil under fluorescent light suggests it has an API gravity of 35° to 45° (Goldstein

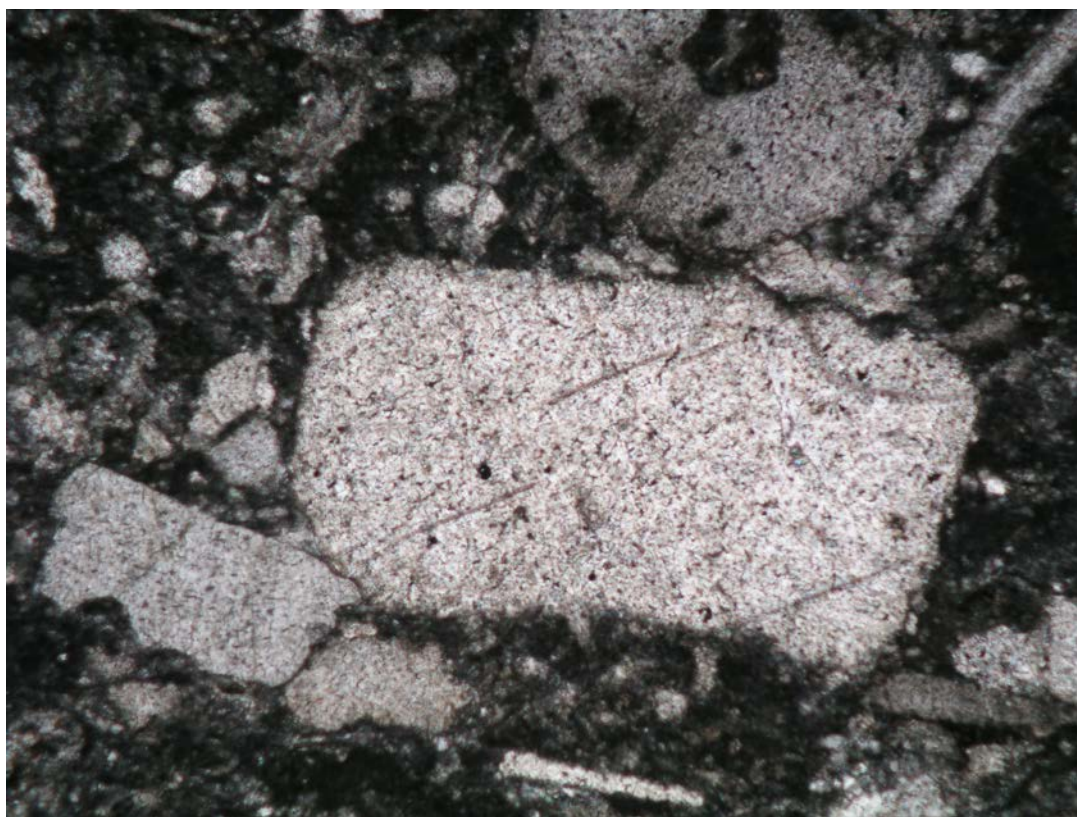


Figure 4.38. Early calcite from the Lisbon No. D-616 well at 8356 feet (2550 m). The mottled appearance of the calcite is due to abundant fluid inclusions. Width of image is 3.3 mm.

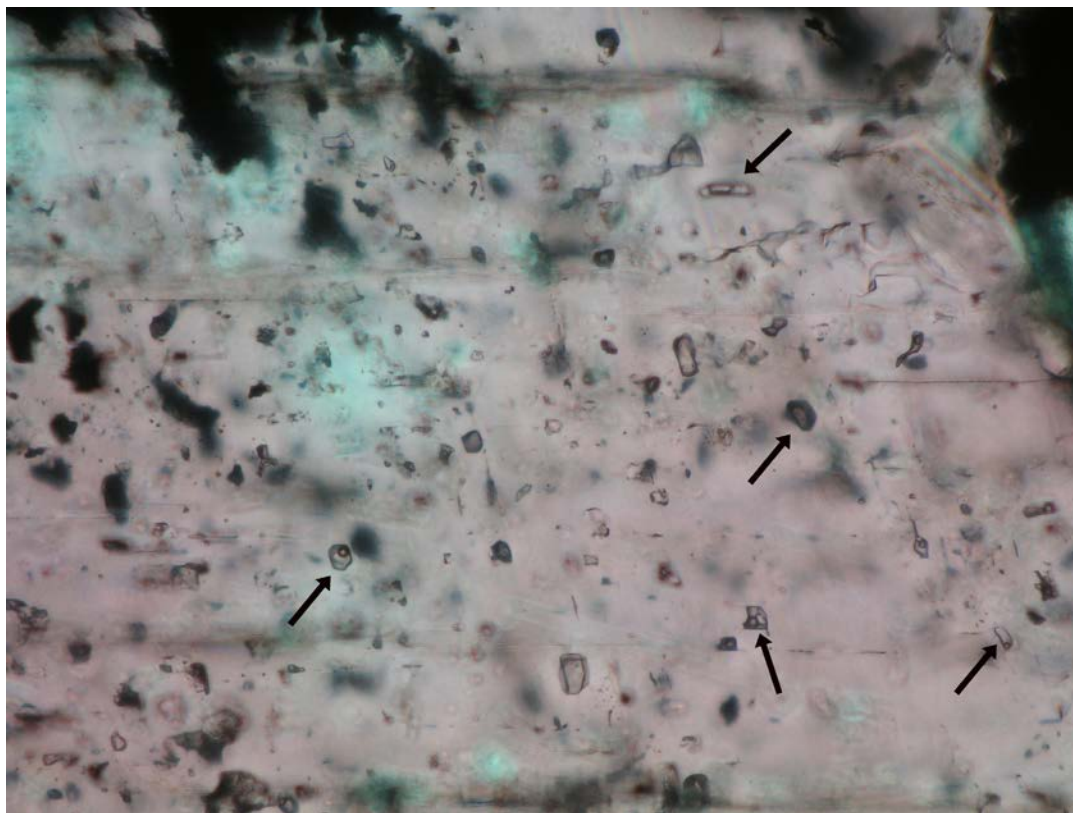


Figure 4.39. Fluid inclusions in early calcite from the Lisbon No. D-616 well at 8356 feet (2550 m). Arrows point to inclusions that have different liquid to vapor ratios, resulting from necking after trapping. Width of image is 0.7 mm.

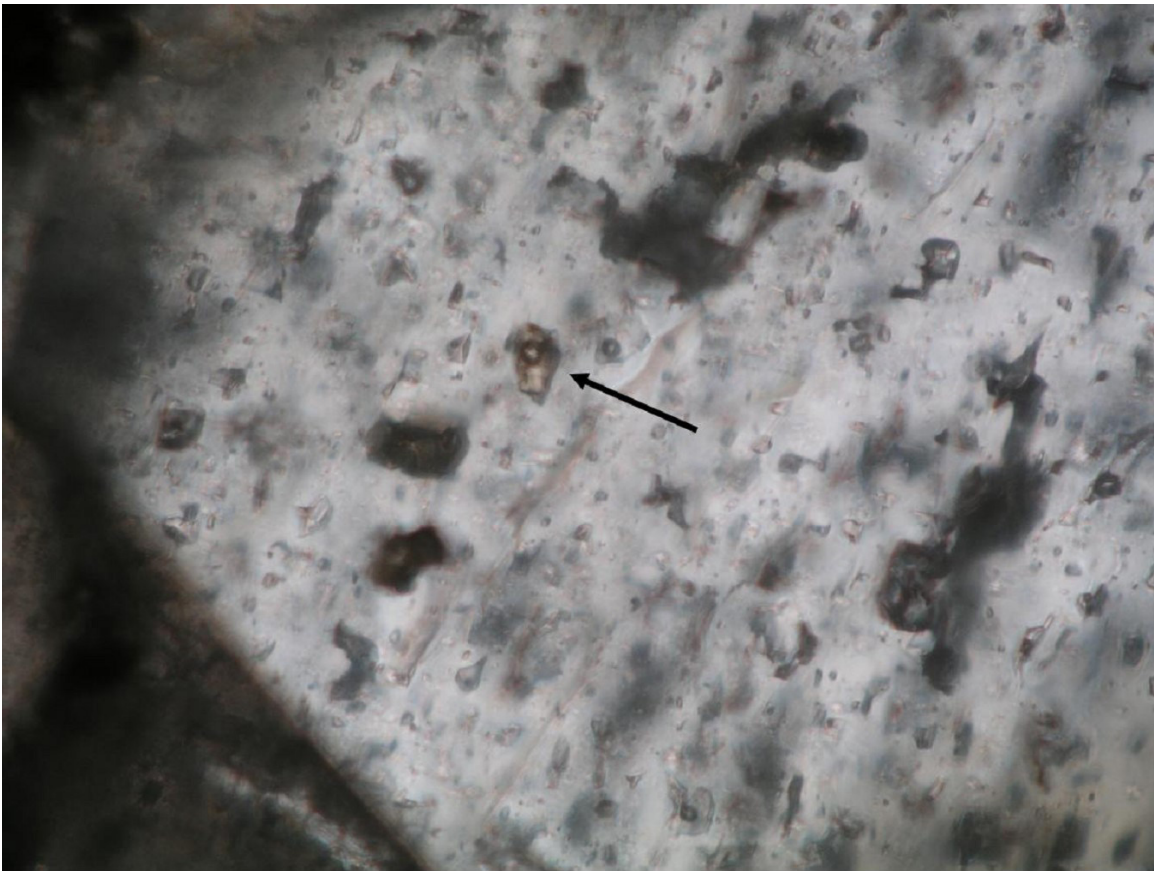


Figure 4.40. Brown primary oil inclusion (arrow) in calcite from the Lisbon No. D-616 well at 8356 feet (2550 m). Clear inclusions are aqueous. Width of image is 0.3 mm.

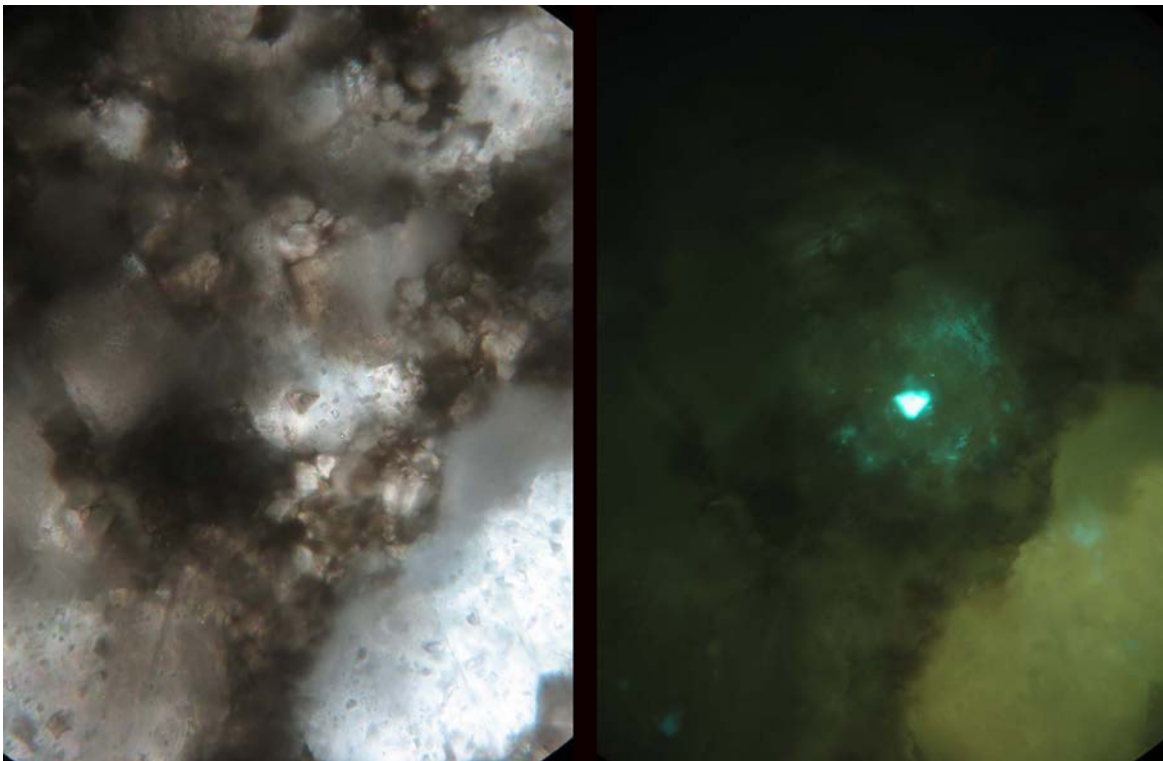


Figure 4.41. Primary oil inclusion in calcite from the Lisbon No. D-616 well at 8356 feet (2550 m). Right-hand image taken under fluorescent light shows that the oil is live. Height of image is 0.3 mm.

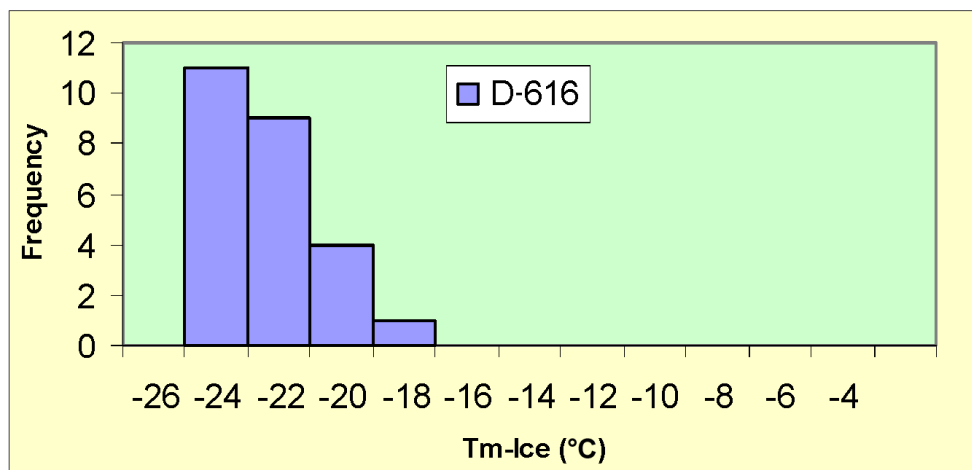


Figure 4.42. Ice-melting temperatures (T_m) of fluid inclusions in early calcite from the Lisbon No. D-616 well at 8356 feet (2550 m) and 8372 feet (2552 m).

and Reynolds, 1994). Twelve primary oil inclusions were measured in a single calcite crystal. All but two yielded homogenization temperatures ranging from 48° to 68°C (118°–154°F). The oil is interpreted as having formed in place from trapped organic material. The homogenization temperatures are minimum trapping temperatures.

Although the aqueous and oil inclusions appear primary in origin, they clearly could not have been present at the time the fossils were deposited. Furthermore, the phase relationships indicate the aqueous inclusions cannot be regarded as original inclusions that have stretched. The most likely explanation for the distribution and character of these calcite-hosted inclusions is that the original calcite has recrystallized and that the fluids were trapped during recrystallization. Oil inclusions in saddle dolomite suggest a similar history.

Fluid Inclusions in Dolomite

Dolomite fills voids and replaces early calcite. Early dolomite is typically fine grained; later saddle dolomite is coarser grained. Small fluid inclusions, most of which are less than a few micrometers in length, are common in dolomite (figure 4.43). These inclusions define growth zones, and consequently are interpreted as being primary in origin. Coarse-grained saddle dolomite frequently contains cloudy cores and clear rims.

Only aqueous inclusions were observed in the early fine-grained dolomite. Later saddle dolomite contains both aqueous and oil inclusions. Although many of the aqueous inclusions appear to contain only a single liquid phase, aqueous inclusions with variable liquid to vapor ratios are not uncommon. Reconnaissance measurements indicate that the two-phase (liquid plus vapor) inclusions commonly have homogenization temperatures ranging from 70° to 135°C (158°–275°F), although inclusions having homogenization temperatures several tens of degrees higher are locally abundant. Fluid inclusions trapped during mineral growth at temperatures greater than 70°C (158°F) will typically con-

tain a vapor bubble. The common absence of a vapor bubble in many of the primary inclusions is inconsistent with dolomite formation at elevated temperatures and suggests that (1) the dolomite formed at temperatures of less than about 50°C (122°F), (2) the fluid inclusions have re-equilibrated (necked, stretched, or refilled), and (3) the homogenization temperatures of the two-phase inclusions are meaningless. Ice-melting temperatures of inclusions trapped in fine-grained dolomite from depths of 8372 feet (2552 m) in the Lisbon No. D-616 well and 8444 feet (2574 m) in the Lisbon No. D-816 well and from the clear rims of saddle dolomite from a depth of 9939 feet (3029 m) in the Lisbon NW USA No. B-63 well are shown in figure 4.44.

Oil inclusions occur in saddle dolomite from a depth of 9939 feet (3029 m) in the Lisbon NW USA No. B-63 well (figure 4.45). The inclusions appear primary, occurring in light-colored parts of the crystal. The early, dark-colored growth zones are truncated by the lighter-colored dolomite, suggesting that the dolomite recrystallized during burial (figure 4.46). These relationships indicate that the oil was trapped during recrystallization. Homogenization temperatures of the oil inclusions, which range from 60° to 70°C (140°–158°F) (figure 4.47), provide a minimum temperature for this recrystallization.

Fluid Inclusions in Quartz

Quartz occurs as fine- to medium-grained crystals that post-date dolomite. Figure 4.48 shows small quartz crystals filling cavities in dolomite. Larger euhedral quartz crystals encapsulate dolomite and anhydrite (figures 4.49 and 4.50). The anhydrite inclusions are frequently oriented and rounded, indicating they are remnants of large, partially dissolved crystals. Anhydrite has retrograde solubility (deposits as water is heated) whereas quartz has prograde solubility (deposits as fluids cool). These relationships suggest that the anhydrite formed from refluxing brines, while the later laterally migrating or ascending cooling fluids that deposited quartz were undersaturated in anhydrite, leading to its dissolution.

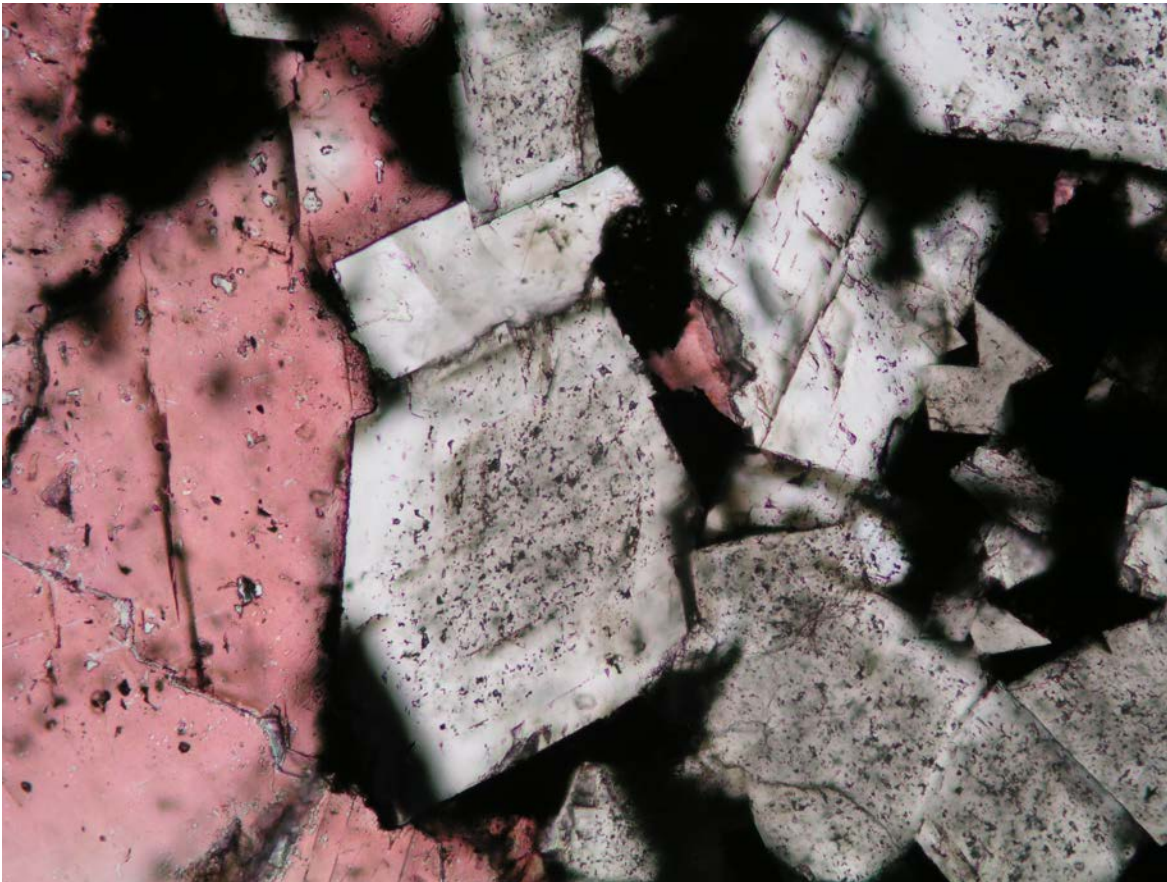


Figure 4.43. Dolomite (colorless) and calcite (red) from the Lisbon NW USA No. B-63 well at 10,004 feet (3049 m). The cloudy appearance of the dolomite is due to abundant fluid inclusions. Saddle dolomite crystals (center of photomicrograph) typically have cloudy cores and clear rims. Width of image is 0.7 mm.

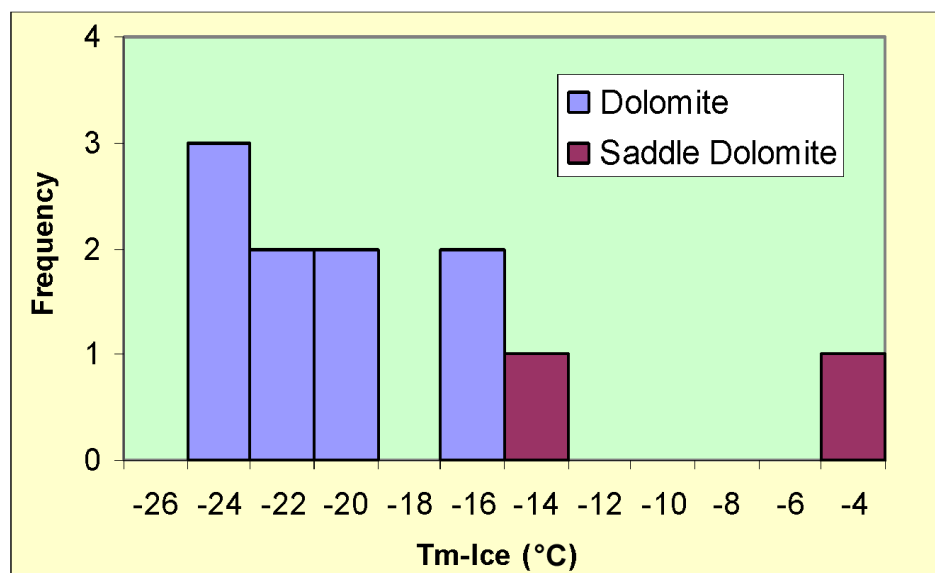


Figure 4.44. Ice-melting temperatures (T_m) of dolomite-hosted fluid inclusions. Samples from depths of 8372 feet (2552 m) in the Lisbon No. D-616 well, 8444 feet (2574 m) in the Lisbon No. D-816 well, and from the clear rims of saddle dolomite from a depth of 9939 feet (3029 m) in the Lisbon NW USA No. B-63 well.

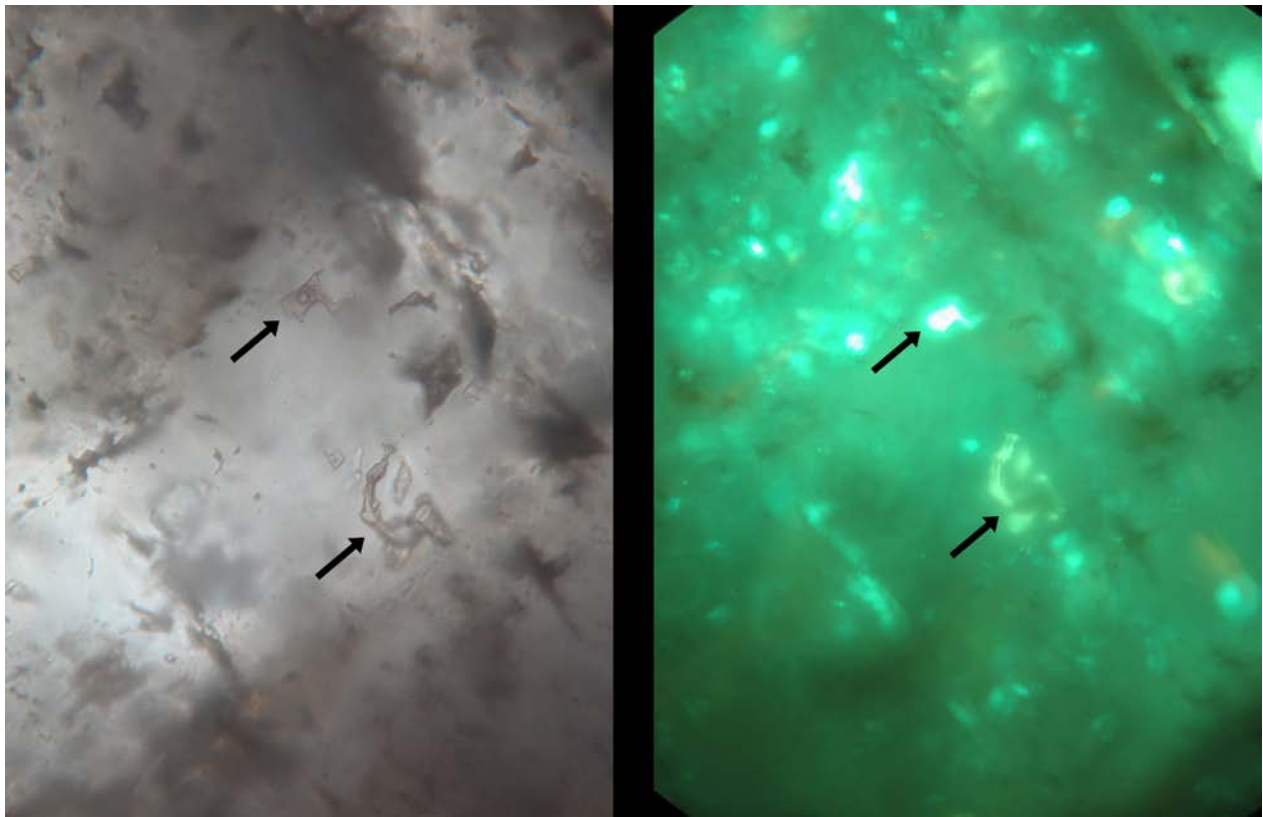


Figure 4.45. Oil inclusions in saddle dolomite from the Lisbon NW USA No. B-63 well at 9939 feet (3029 m). Arrows point to two of the inclusions; others are apparent in the right-hand image taken under fluorescent light. Height of images is 0.3 mm.

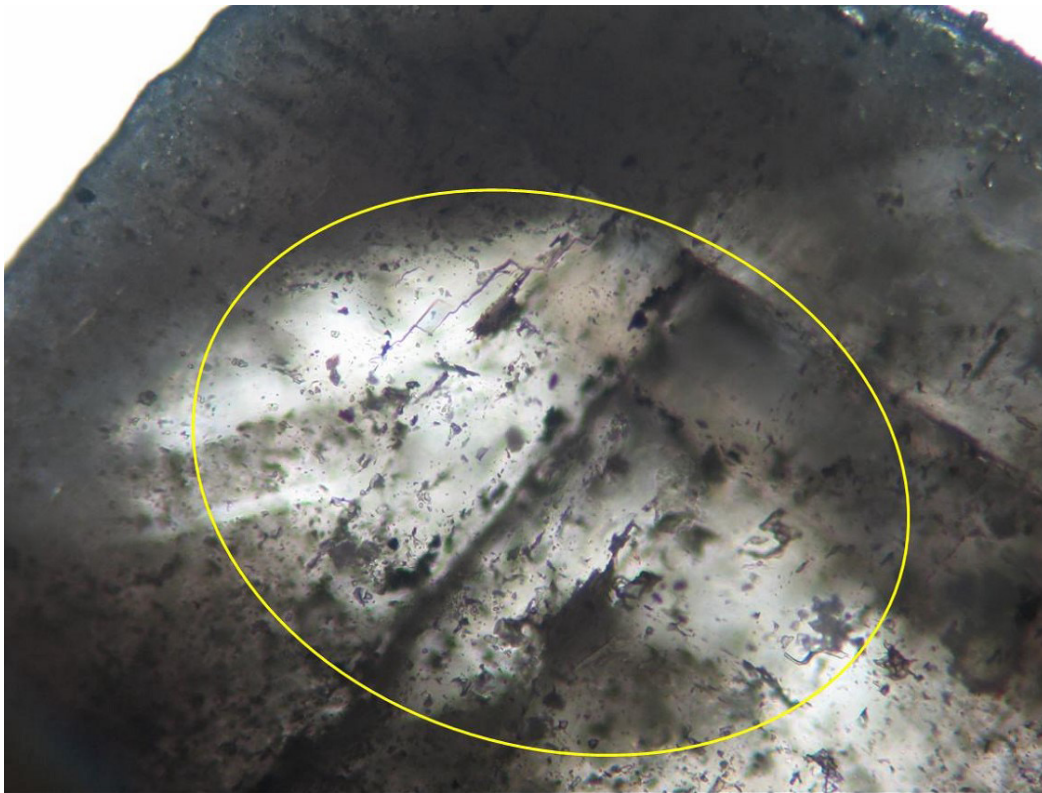


Figure 4.46. Low-magnification image of saddle dolomite shown in figure 4.45. Dark growth zones are truncated near the left side of the oval. Oil inclusions in figure 4.45 occur in the light-colored dolomite on right side of oval. Width of image is 0.7 mm.

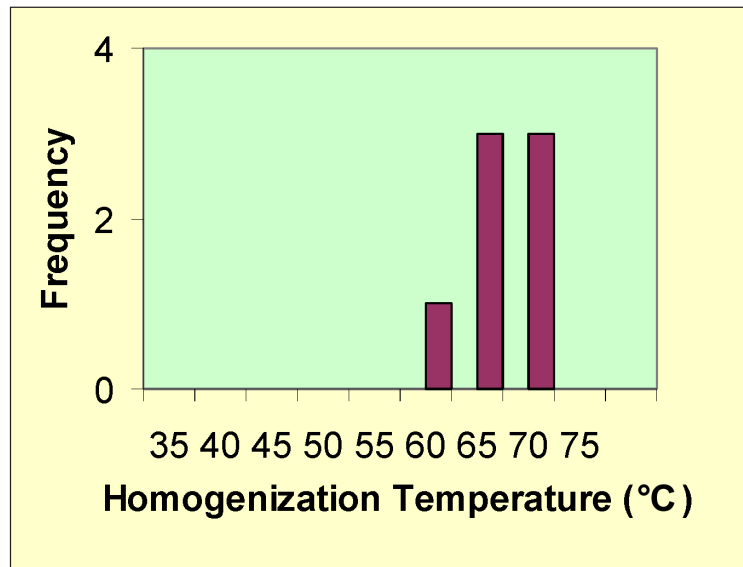


Figure 4.47. Homogenization temperatures of oil inclusions trapped in saddle dolomite from the Lisbon NW USA No. B-63 well at 9939 feet (3029 m).

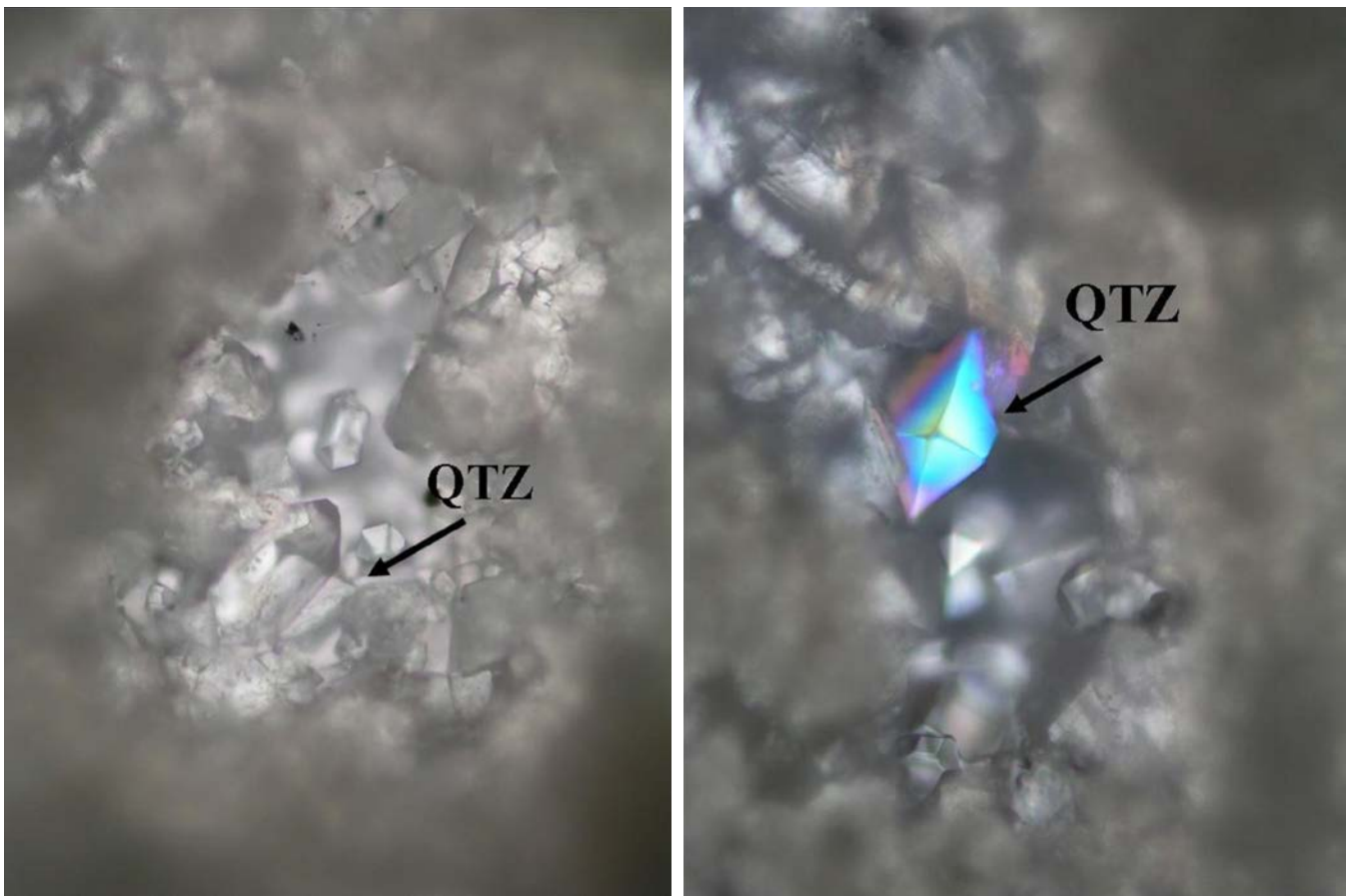


Figure 4.48. Quartz crystals partially filling a cavity in dolomite from the Lisbon NW USA No. B-63 well at 9981 feet (3042 m). The right-hand image was taken under partially crossed nicols. Height of images 0.7 mm.

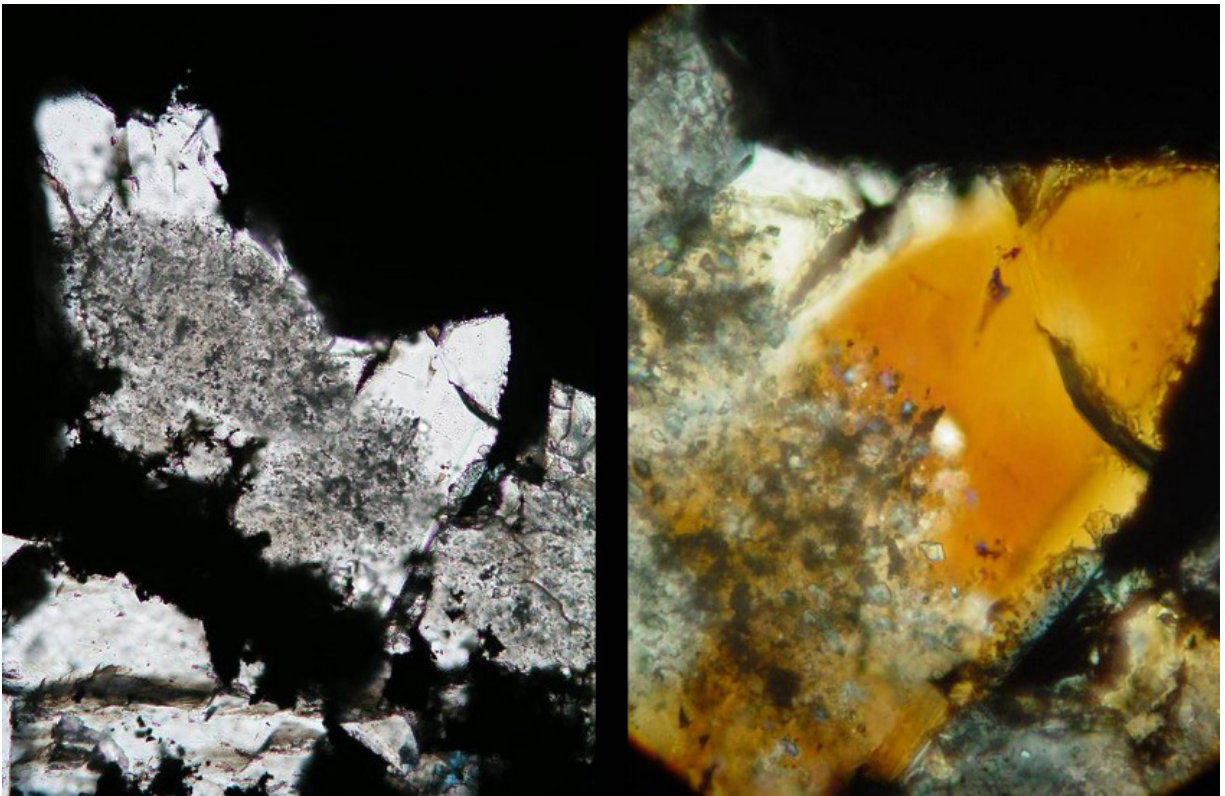


Figure 4.49. Quartz encapsulating dolomite from the Lisbon NW USA No. B-63 well at 10,004 feet (3049 m). Height of images is 1.3 mm (left) and 0.7 mm (right). Right-hand image taken under crossed nicols.

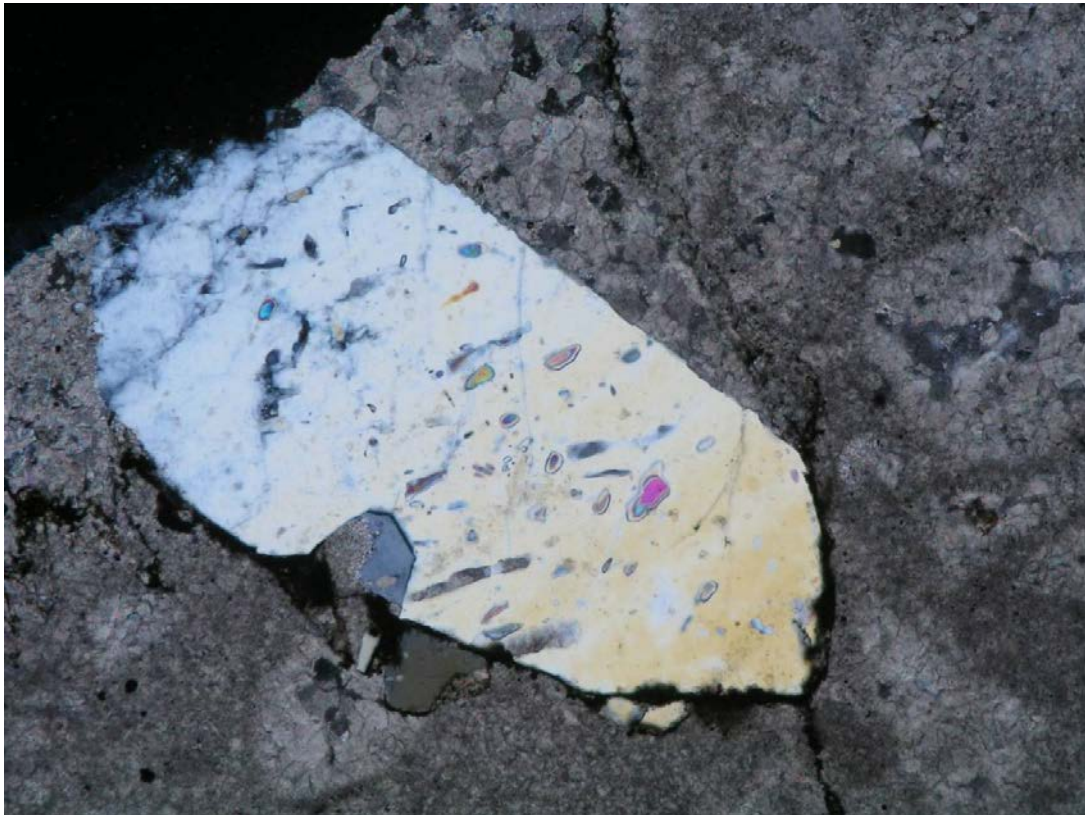


Figure 4.50. Coarse-grained quartz crystal from the Lisbon No. D-616 well at 8356 feet (2547 m). Small oriented grains of anhydrite are encapsulated in the quartz. Width of image is 1.3 mm.

The quartz crystals from a depth of 8356 feet (2547 m) in the Lisbon No. D-616 well commonly contain numerous two-phase aqueous inclusions; rarely, gas-rich and single-phase, liquid-rich inclusions are present. Figures 4.51 and 4.52 show quartz crystals containing primary liquid-rich inclusions. In figure 4.51, primary inclusions define a growth zone within the interior of the crystal. Large isolated primary inclusions, up to 50 micrometers across occur in the quartz crystals shown in figure 4.52. Coexisting liquid- and vapor-rich inclusions were observed in the crystal shown in figure 4.53. Because of the small size of the gas-rich inclusions, it was not possible to estimate their compositions from phase changes during freezing and heating. However, in this environment, the gas is probably methane-rich. No primary oil inclusions were observed in the quartz crystals.

Secondary aqueous inclusions that define healed fractures are common in some of the quartz crystals. The majority of these inclusions contain liquid and vapor at room temperature; rarely single-phase aqueous inclusions are present. As noted above, these single-phase inclusions could represent the local incursion of low-temperature (less than about 50°C [122°F]) waters.

Homogenization and ice-melting temperatures of quartz-hosted inclusions were measured (figure 4.54). Primary in-

clusions yielded homogenization temperatures ranging from 118° to 133°C (244°–271°F) and ice-melting temperatures of -20.5° to -22.8°C (-4.9°–9°F). Secondary inclusions yielded lower homogenization temperatures but a much broader range of ice-melting temperatures that overlapped those of the primary inclusions.

The presence of coexisting gas- and liquid-rich inclusions is particularly significant because this suggests that the homogenization temperatures closely approximate the true trapping temperatures (see discussion in Goldstein and Reynolds, 1994). The quartz-hosted inclusions provide the best measure of the maximum burial temperature and depth of any of the minerals studied.

Fluid Inclusions in Late Calcite

Late calcite from depths of 9936 feet, 9991 feet, and 10,005 feet (3028 m, 3045 m, and 3049 m) in the Lisbon NW USA No. B-63 well was studied. The calcite encapsulates dolomite (figure 4.55) and fills vugs. The textural relationships between dolomite, quartz, and calcite imply that the calcite also post-dates quartz (figure 4.56), and dissolution of dolomite occurred prior to calcite deposition (figure 4.55).

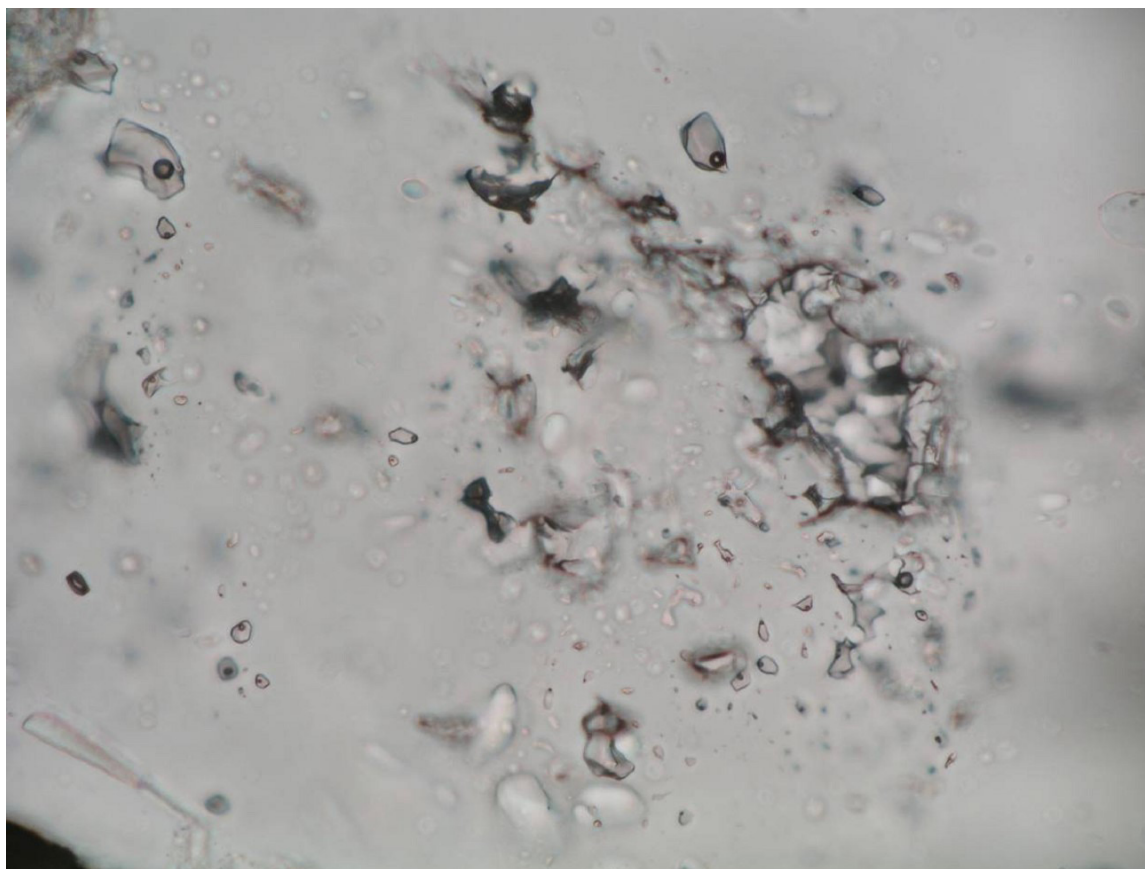


Figure 4.51. Two-phase, liquid-rich inclusions defining a growth zone in the interior of a quartz crystal from the Lisbon No. D-616 well at 8356 feet (2547 m). The large, irregular cavity on the right may have been initially filled with anhydrite. Width of image is 0.3 mm.

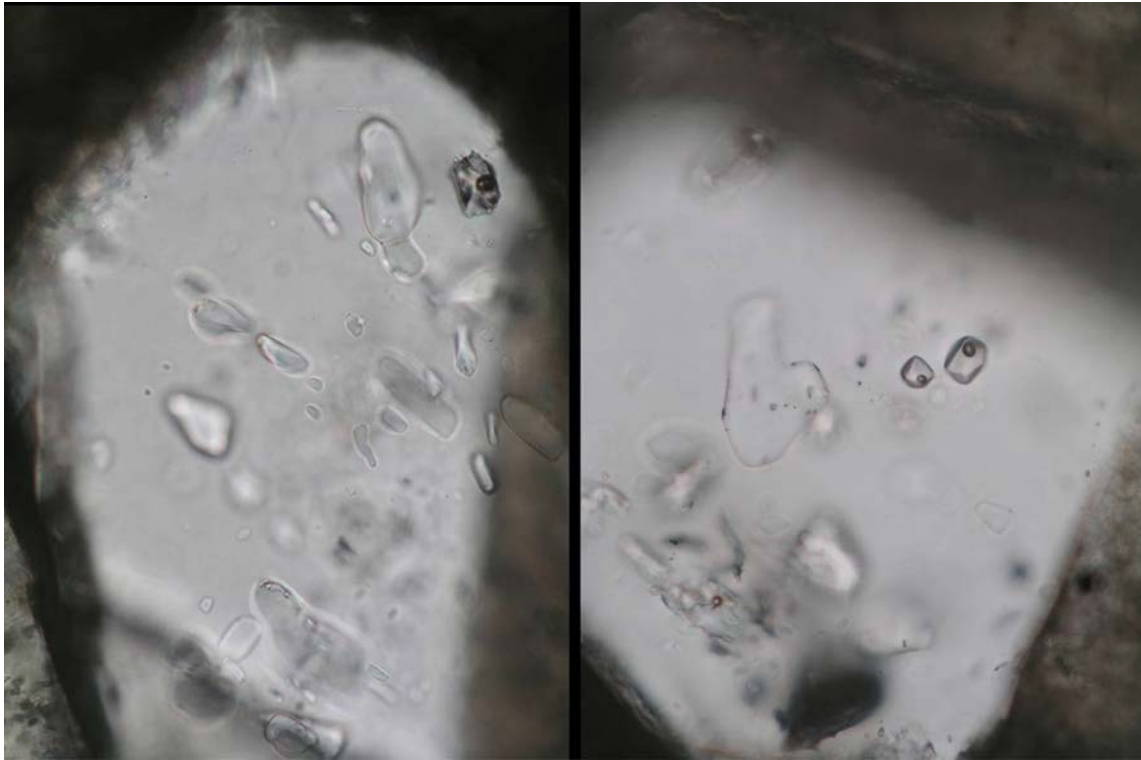


Figure 4.52. Primary liquid-rich inclusions in quartz from the Lisbon No. D-616 well at 8356 feet (2547 m). Height of image is 0.3 mm. Irregular shaped inclusions are anhydrite.

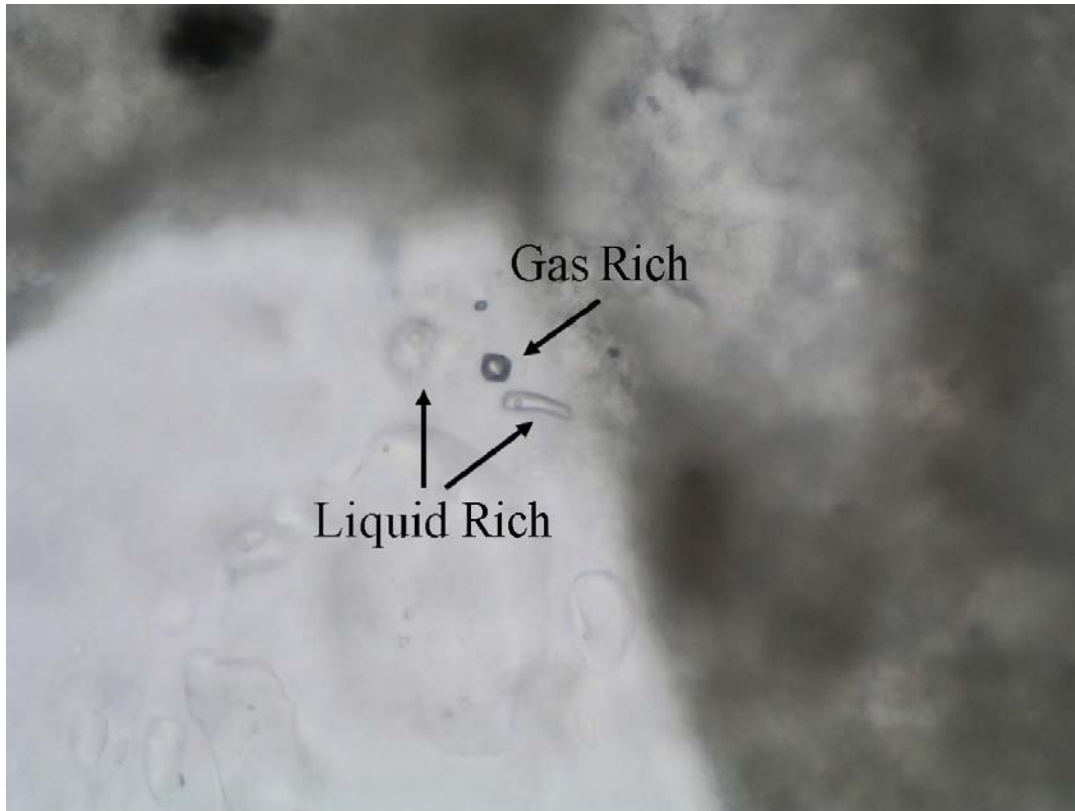


Figure 4.53. Coexisting primary liquid- and gas-rich inclusions in quartz from the Lisbon No. D-616 well at 8356 feet (2547 m). Width of image is 0.3 mm.

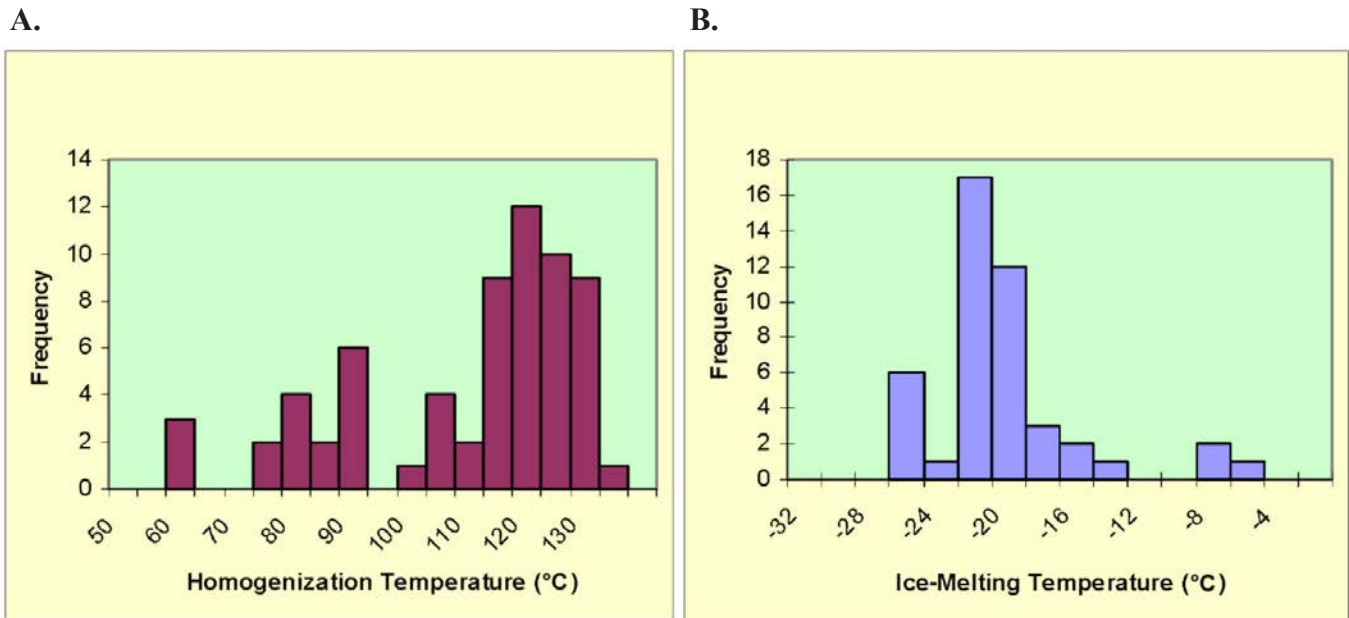


Figure 4.54. Homogenization (A) and ice-melting (B) temperatures of quartz-hosted aqueous inclusions from the Lisbon No. D-616 well at 8356 feet (2547 m).

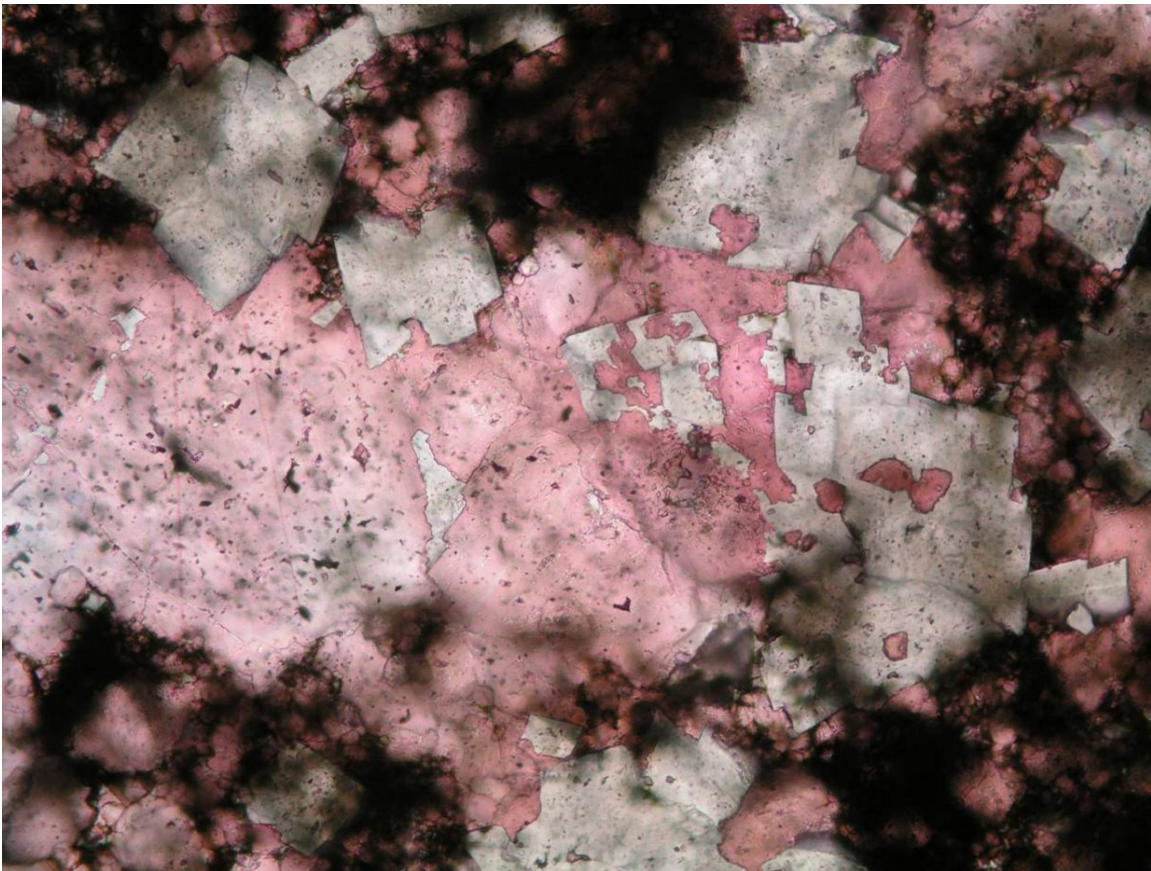


Figure 4.55. Corroded and dissolved dolomite (white) encapsulated in calcite (pink) from the Lisbon NW USA No. B-63 at 9936 feet (3028 m). Width of image is 1.3 mm.

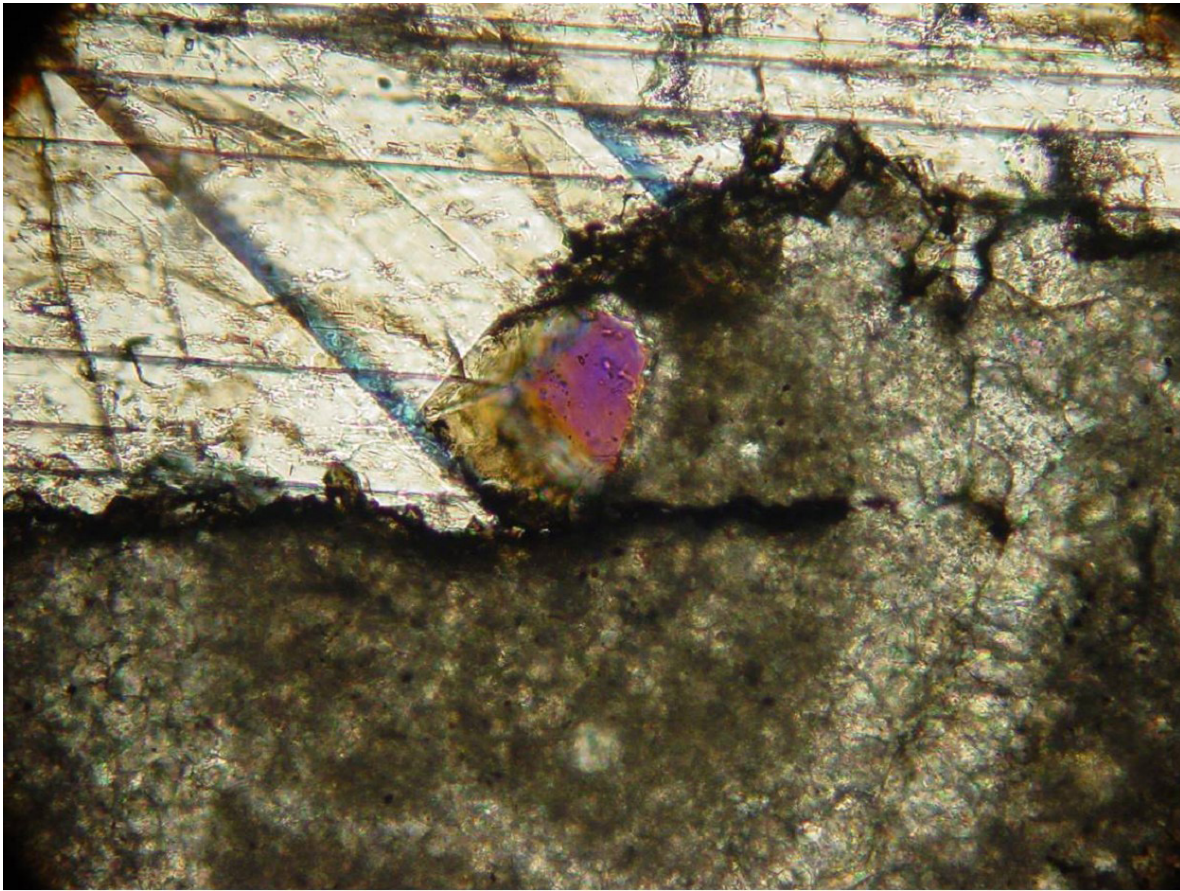


Figure 4.56. Coarse-grained calcite (upper half of image) that appears to postdate quartz (purple crystal in center) and dolomite (lower half of image). Lisbon NW USA No. B-63 well at 10,004 feet (3049 m). Width of image is 0.7 mm.

Secondary aqueous and oil inclusions occur in the late calcite. All aqueous inclusions display variable liquid to vapor ratios indicative of necking. Ice-melting temperatures of calcite-hosted inclusions were measured (figures 4.57 and 4.58A). The ice-melting temperatures of the aqueous inclusions in calcite vary from well to well and the frequencies are highest at the opposite ends of the ranges in the Lisbon No. D-616 and Lisbon NW USA No. B-63 wells (figure 4.58A). The range of ice-melting temperatures of the fluid inclusions in calcite versus quartz are similar; however, the frequencies for quartz are highest around -20°C (-4°F) versus two widely separated frequency peaks for calcite in the Lisbon No. D-616 and Lisbon NW USA No. B-63 wells at -25°C (-13°F) and -5°C (23°F), respectively (figure 4.58).

The majority of the inclusions in calcite from depths of 9939 feet and 10,005 feet (3029 m and 3049 m) yielded comparatively high ice-melting temperatures ranging from -5.5° to about -12°C (22.1° to about 10°F), corresponding to salinities of 8.6 to 16 wt.% NaCl equivalent. Inclusions from a depth of 9991.8 feet (3045 m) had higher salinities, up to 18 wt.% NaCl equivalent. These relationships suggest that at least two distinct groups of fluids interacted with the rocks from the Lisbon NW USA No. B-63 well.

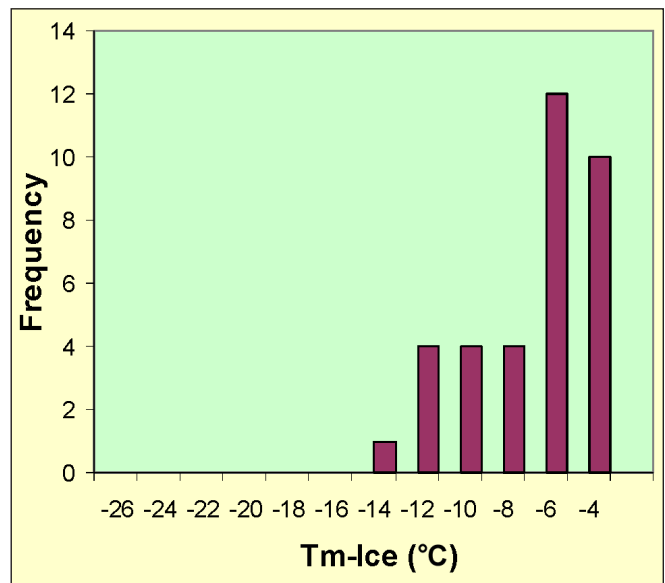


Figure 4.57. Ice-melting temperatures (T_m) of late, calcite-hosted fluid inclusions from the Lisbon NW USA No. B-63 well.

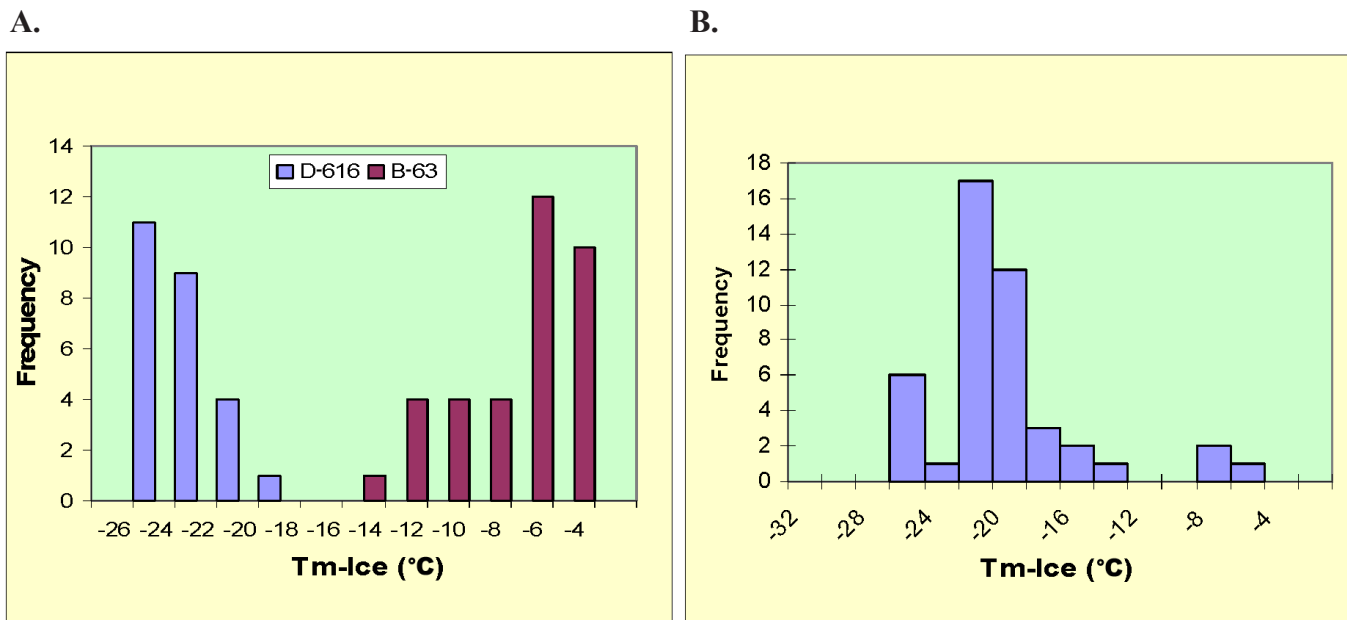


Figure 4.58. Comparison of ice-melting temperatures (T_m) of fluid inclusions in calcite (A) and quartz (B) from the Lisbon No. D-616 well.

Late Oil Inclusions

The youngest significant diagenetic event recorded in the rocks is represented by the presence of the bitumen observed in numerous thin sections. Secondary inclusions trapped in late calcite from a depth of 9936 feet (3028 m) in the Lisbon NW USA No. B-63 well provide unequivocal evidence for a mobile oil phase that postdates calcite deposition. The oil inclusions shown in figure 4.59 display variable liquid to vapor ratios caused by necking. The oil is fluorescent with an estimated API gravity of 35° to 45°, based on its color, which contrasts with the produced oil API gravity that ranges from 54° to 63°. Similar appearing secondary oil inclusions were observed in calcite from a depth of 8372 feet (2552 m) in the Lisbon No. D-616 well (figure 4.60), although it is not possible to uniquely assign an age to these inclusions. These inclusions yielded consistent homogenization temperatures ranging from 39° to 43°C (102°–109°F) (figure 4.61). The homogenization temperatures of primary oil inclusions have both a wider and higher temperature range than secondary oil inclusions (figure 4.61). Finally, the homogenization temperatures of oil inclusions in calcite have both a wider and lower temperature range than oil inclusions in saddle dolomite (figure 4.62).

ISOTOPIC ANALYSIS

Stable Carbon and Oxygen

Modification of rock fabrics and porosity within the Leadville Limestone in Lisbon field is quite complex. Stable isotope geochemistry has been used to provide insights into the chemical differences between preserved remnants of depositional

components and the various diagenetic events in carbonate rocks, as recognized from core examination and thin section petrography. A graph of carbon versus oxygen isotope compositions for a range of carbonate rock types (figure 4.63), from various published sources compiled by Roylance (1990), serves as a guide for comparisons with data obtain in our study. Broad fields of carbon and oxygen isotope compositions for various carbonate rock settings are indicated, including modern marine (“subsea”) cements, various marine skeletons and sediments, deep-water (“pelagic”) limestone, Pleistocene carbonates, and meteoric carbonates (“speleothems and veins”).

Methodology

Isotopic composition analyses for stable carbon and oxygen, as well as strontium, were completed on a variety of diagenetic phases from Lisbon field core samples (table 4.2). Individual samples were collected as powdered rock using a Dremel drill equipped with precision bits.

All analyses were completed at the Colorado School of Mines (CSM) Stable Isotope Laboratory, Golden, Colorado. The CSM lab possesses the capabilities of analyzing the stable isotopes of hydrogen, carbon, nitrogen, oxygen, and sulfur (H, C, N, O, and S) from a wide array of sample matrices. The GV Instruments IsoPrime mass spectrometer (figure 4.64) is the keystone around which several on-line preparation devices operate. Traditional dual-inlet applications (waters, carbonates, off-line prepared gases) are prepared with a MultiPrep auto sampler capable of performing carbon dioxide (CO₂) and H₂ equilibration on water samples, and acid digestion of carbonate samples (figure 4.65). A 50-port manifold can also be fitted for dual-inlet analysis of off-line gases. The IsoPrime mass spectrometer is also interfaced with continuous-flow preparation devices, including two elemental analyzers and a

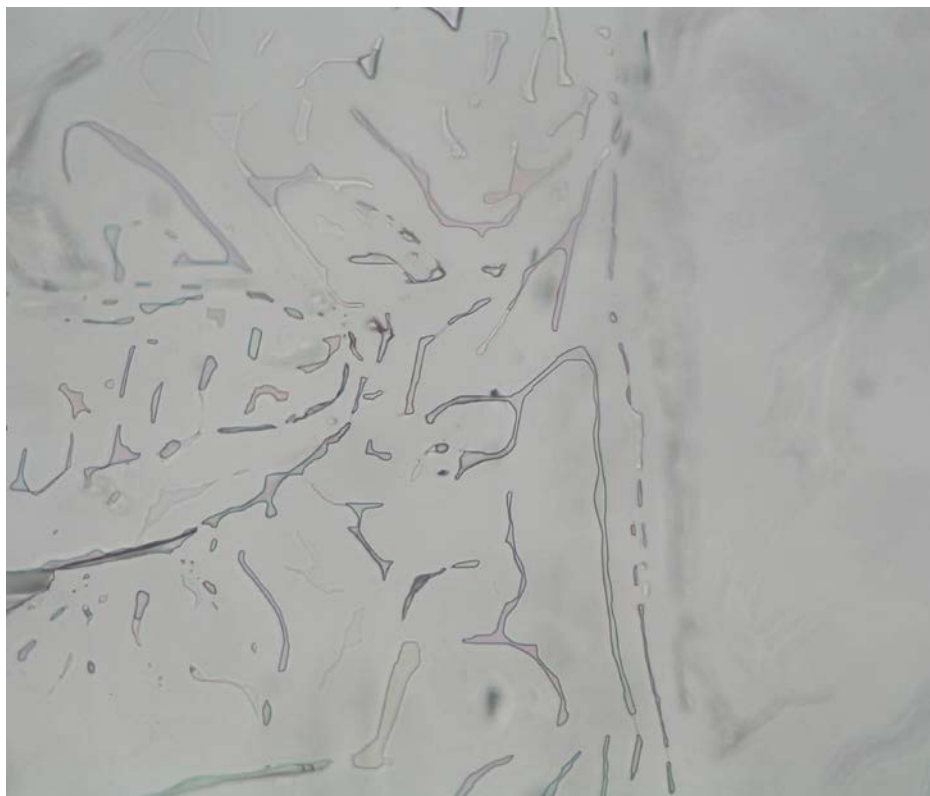


Figure 4.59. Secondary oil inclusions in late calcite from the Lisbon NW USA No. B-63 well at 9936 feet (3029 m). The inclusions are necked. The large brown inclusion at bottom center contains only liquid; others contain variable ratios of liquid and gas. Width of image is 0.7 mm.



Figure 4.60. Secondary oil inclusions in calcite from the Lisbon No. D-616 well at 8372 feet (2552 m). The height of each image is 0.3 mm. Right-hand image was taken under fluorescent light.

trace-gas preconcentrator. The elemental analyzers generate gases by combustion or pyrolysis, which are then carried in an inert stream of helium to the mass spectrometer for analysis of H, C, N, O, and S. Common applications include analysis of phosphates, nitrates, waters, organics, soils, plant and animal matter, sulfides, sulfates, and oils. The trace-gas preconcentrator cryogenically focuses trace quantities of gases for isotopic analysis. Common applications include analysis of methane, carbon dioxide, and nitrous oxide from atmospheric and soil-gas samples.

The internal standard used in the CSM lab is the University of California at Los Angeles (UCLA) Carrara marble. The accepted values for this internal standard were matched consistently during the analysis of the Leadville core samples selected for this study. All isotopic compositions are reported relative to Vienna Pee Dee Belemnite (VPDB) (see Land, 1980, figure 6 for definition relative to Standard Mean Ocean Water [SMOW]).

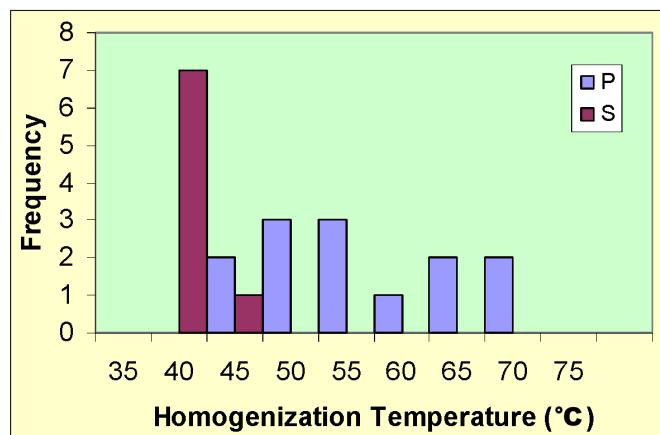


Figure 4.61. Comparison of homogenization temperatures of primary (P) and secondary (S) oil inclusions in calcite.

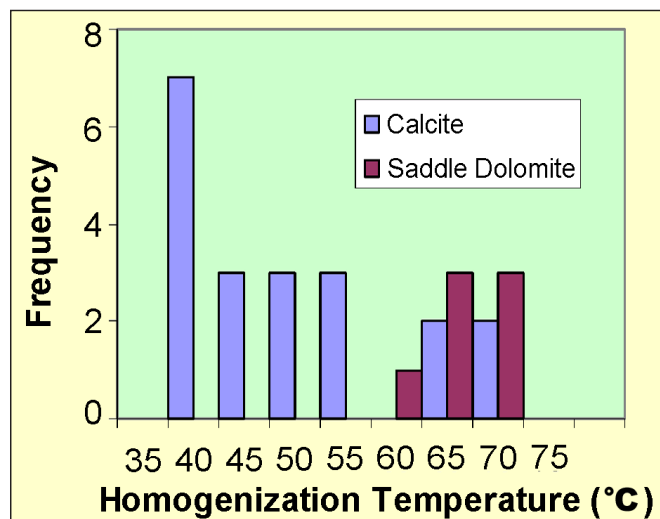


Figure 4.62. Comparison of homogenization temperatures of oil inclusions in calcite and saddle dolomite. All inclusions are primary except 35° to 40°C inclusions in calcite.

Stable Carbon and Oxygen Isotopes for Leadville Limestone Samples at Lisbon Field

Carbon isotopic compositions for the 25 Leadville Limestone (limestone and dolomite) samples from Lisbon field (table 4.2 and figure 4.66) cluster in a very narrow range around the mean value of -2.95‰ VPDB; the range is -1.92‰ to -6.09‰ VPDB (one notable exception of +4.4‰ was excluded). Oxygen isotopic compositions for these samples, however, are more widespread (table 4.2 and figure 4.66). The range is -0.96‰ to -12.26‰ VPDB; the mean value is -4.61‰ VPDB.

Stable carbon and oxygen isotope data indicate that all Lisbon Leadville dolomites were likely associated with brines whose composition was enriched in $\delta^{18}\text{O}$ compared with Late Mississippian seawater. Stable oxygen isotope analyses of dolomites show a linear trend with a fairly narrow range of carbon isotope values (figure 4.66). Figure 4.67 shows a cross plot of the same $\delta^{13}\text{C}/\delta^{18}\text{O}$ Leadville Limestone data from Lisbon field with the regions of dolomite temperatures of formation suggested by Allan and Wiggins (1993), based upon their interpretation of many ancient dolomites. Note that most of the Leadville data points plot in the region that Allan and Wiggins have called the “overlap of low and high temperature dolomites.”

Stable oxygen isotopes for Mississippian seawater were in the range of -2‰ to -1‰ (Veizer and others, 1999). Dolomitizing fluid compositions enriched with respect to $\delta^{18}\text{O}$ are thought to be heavier than normal Mississippian seawater (bracketed by the yellow arrows on figure 4.68). Leadville Limestone reflux dolomitization likely resulted from evaporated brines, several per mil heavier than normal seawater (e.g., modern Arabian Gulf water in the range of 2.5‰ to 4‰ [Wood and others, 2002]). Assuming similar oxygen enrichment of Mississippian seawater values, a dolomitizing fluid would be in the range of 0.5‰ to 3‰. This factor, coupled with Leadville dolomite isotope values, constrain Leadville replacement dolomitization temperatures to between 140° and 194°F (60°–90°C) (figure 4.68). Saddle dolomite cements were precipitated at temperatures greater than 194°F (90°C).

Strontium

Strontium (Sr) isotope analysis was used to assist with the diagenetic interpretation of different subsurface mineral phases within Leadville Limestone samples from Lisbon field. The interpretation of these analyses is discussed after the following comments about the nature of the Sr isotope analysis, as well as a description of the analytical technique and laboratory used.

Applications and Background

Strontium isotope analysis is used most frequently as an age-dating tool in marine carbonates. The Sr composition of an-

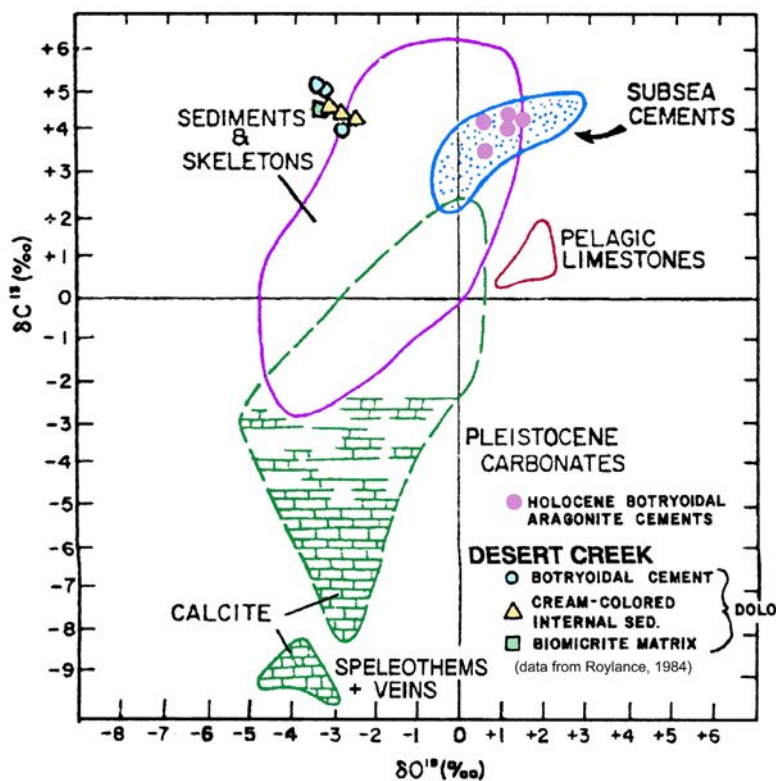


Figure 4.63. Carbon versus oxygen isotope compositions. Other compositional facies compiled from various published work (modified from James and Ginsburg, 1979, by Roylance, 1990).

Table 4.2. Stable carbon and oxygen isotope data from the Leadville Limestone, Lisbon field core samples.

Sample No.	Well	Depth (ft)	del ¹³ C	del ¹⁸ O	Comments
1	B-63	9960.6	-2.441	-6.830	Late calcite
2	B-63	9960.6	-1.918	-1.435	Syngenetic dolomite
3	B-63	10,004-05	-6.092	-11.297	Late calcite
4	D-816	8444-45	-2.696	-3.069	Dolomite cement
5	D-816	8444-45	-2.648	-2.441	Replacement dolomite
6	D-816	8444-45	-3.008	-2.287	Matrix dolomite
7	D-816	8421	-2.584	-3.699	Dolomite cement
8	D-816	8421	-2.978	-4.265	Replacement dolomite
9	D-616	8356-57	-3.709	-4.613	Saddle dolomite in fractures
10	D-616	8356-57	-2.793	-4.422	Limestone matrix/crinoids
11	D-816	8433	-2.815	-3.375	Late replacement matrix dolomite
12	B-610	7897	-2.951	-0.963	White, low permeability early dolomite
13	B-610	7897	-3.348	-2.808	Black, porous late dolomite
14	B-610	7886	-3.294	-2.601	White, low permeability early dolomite
15	B-610	7886	-3.126	-2.890	Black, porous late dolomite
16	D-616	8559	-2.851	-3.313	Black, porous late replacement dolomite
17	D-616	8682	4.407	-2.086	Syngenetic dolomite
18	B-63	9935.6	-2.795	-4.012	Dolomite (possible cross-cutting karst sediment fill)
19	B-63	9935.6	-2.785	-5.564	Limestone, peloidal/skeletal grainstone; sampled only black non-skeletal grains which appear microporous
20	D-616	8308-09	-4.418	-3.038	Dolomitized sediment within karst cavity
21	D-616	8308-09	-2.783	-4.147	Limestone country rock
22	B-63	9991.8	-3.510	-7.668	Late calcite, poiklotopic
23	B-63	9939	-3.499	-7.644	Saddle dolomite
24	B-63	9909	-4.794	-12.255	Late calcite
25	D-616	8308	-4.224	-2.694	Karst-fill dolomite



Figure 4.64. The Colorado School of Mines Stable Isotope Laboratory's GV Instruments IsoPrime stable isotope ratio mass spectrometer. Several peripheral devices are interfaced with the IsoPrime for both dual-inlet and continuous flow applications.

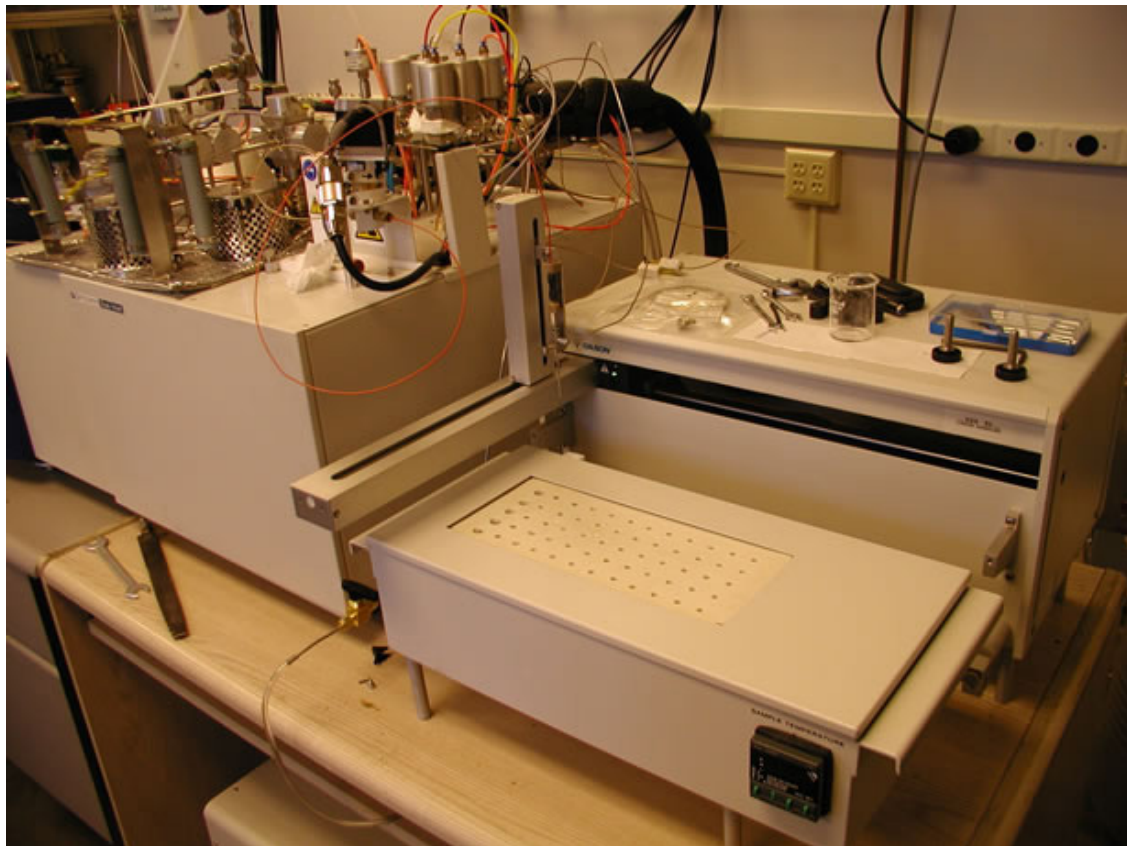


Figure 4.65. MultiPrep intended for high-precision dual-inlet analysis of carbon and oxygen isotopes of carbonate samples, and oxygen isotopes for waters by traditional equilibration techniques. Sample sizes for carbonates ranges from 10 to 100 μg ; water samples are 200 μL .

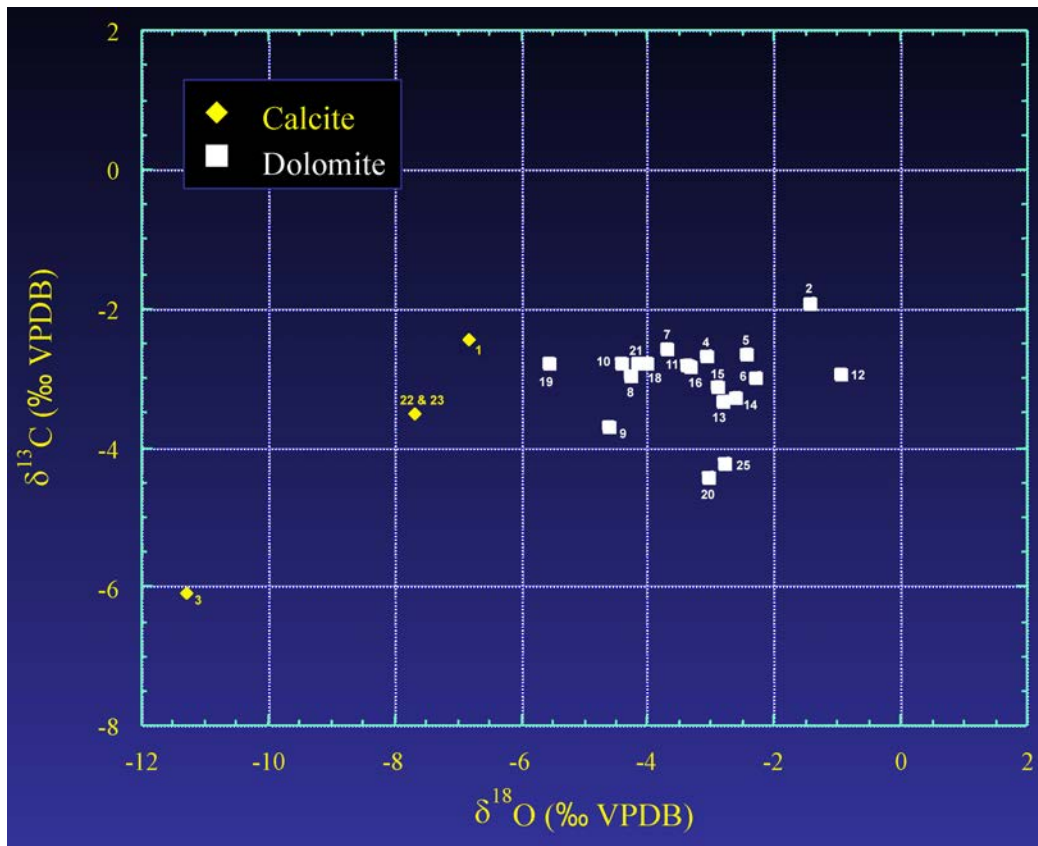


Figure 4.66. Stable carbon versus oxygen isotopic compositions for Leadville dolomite and calcite from Lisbon field. Sample numbers 17 and 24 not shown. Refer to table 4.2 for isotopic data.

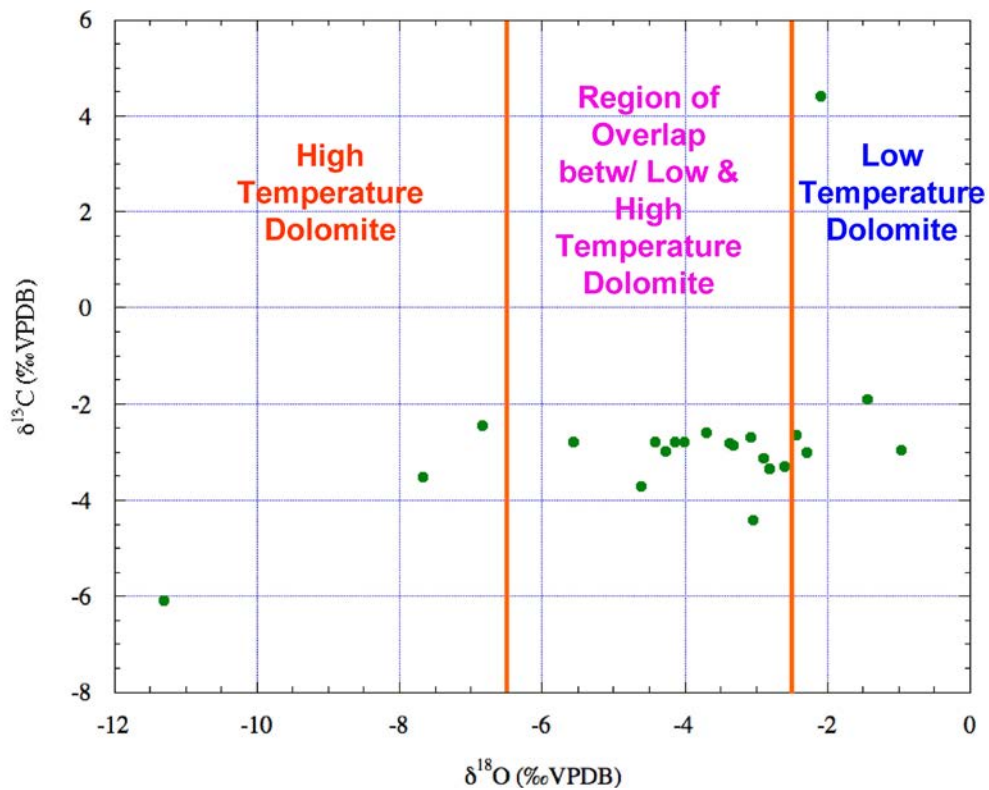


Figure 4.67. Cross plot of the $\delta^{13}\text{C}/\delta^{18}\text{O}$ Leadville Limestone data from Lisbon field with the regions of dolomite temperatures of formation suggested by Allan and Wiggins (1993).

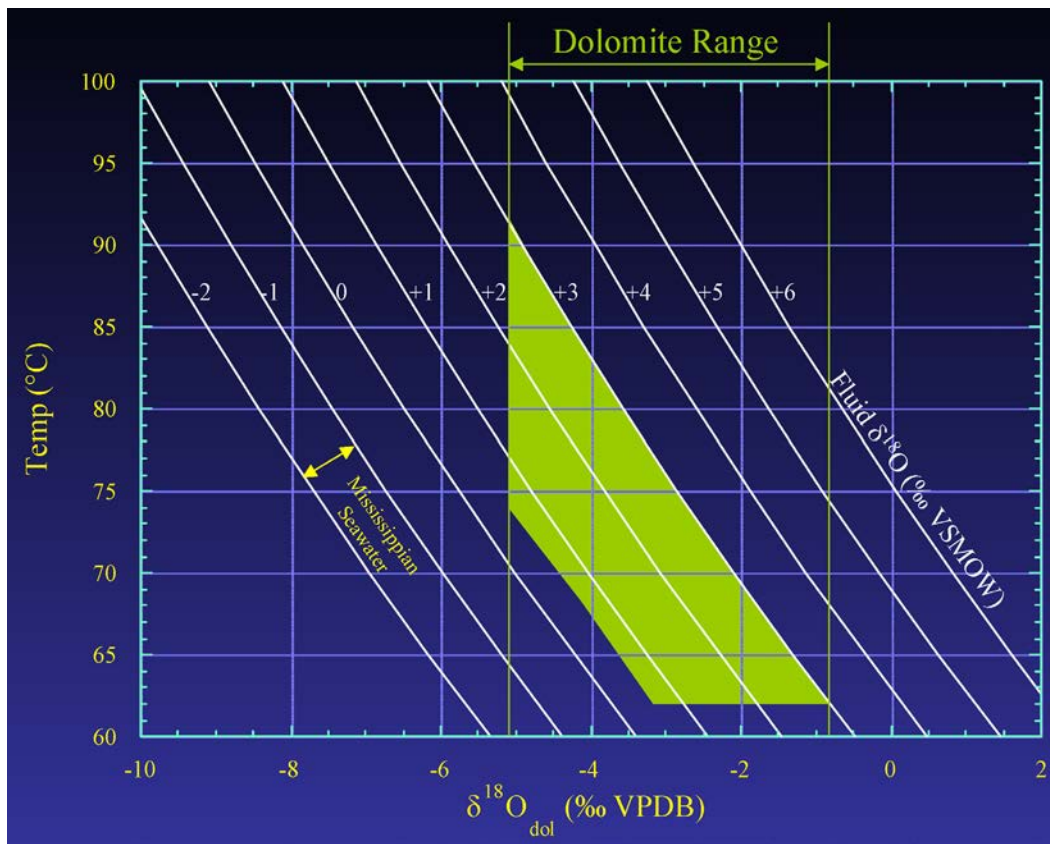


Figure 4.68. Dolomite stable oxygen isotope values versus temperature data. The green field shows our estimate of $\delta^{18}\text{O}$ of dolomitizing fluids at between 0.5‰ and 3.0‰. Precipitation temperatures were up to about 90°C (194°F).

cient seawater and its variation through geologic time have been determined from common marine carbonate minerals, especially calcite, aragonite, and dolomite (Brass, 1976; Burke and others, 1982; Allan and Wiggins, 1993).

Among the four known isotopes of Sr, the ratio of $^{87}\text{Sr}/^{86}\text{Sr}$ is the most useful for tracking the secular changes of seawater Sr. These two isotopes come from separate sources in the Earth. Strontium-87 is radiogenic (from the radioactive decay of rubidium-87 with a half-life of about 50 billion years), whereas strontium-86 is non-radiogenic (Faure and Powell, 1972; Faure, 1977). These secular changes in the Sr ratio of seawater are the result of the interplay of tectonism and erosion versus seafloor spreading (Allan and Wiggins, 1993). In general, erosion resulting from increased tectonism increases the ratio of $^{87}\text{Sr}/^{86}\text{Sr}$; during times of high seafloor spreading the ratio is decreased. The assumed reason for these changes is that continental (sialic) crustal rocks (e.g., granites, gneisses, and their derivatives such as arkoses) contribute radiogenic Sr ratios (i.e., relatively high Sr isotopic numbers). On the other hand, mantle (simatic) rocks (e.g., basalts, other volcanic, undifferentiated basic rock types, and their derivatives such as lithic sandstones) are much less radiogenic (i.e., relatively low Sr isotopic ratios). The high contribution of Sr into the oceans from highly radiogenic continental materials and less radiogenic mantle minerals, combined with the rapid mixing rate of the oceans and the long oceanic residence time of Sr, have allowed the Sr isotope ratio of seawater

to be the same globally at any given time. For useful discussions and explanations of these factors, see Veizer (1989) and Allan and Wiggins (1993, p. 49–52).

Most workers believe that the Sr isotopic composition of seawater throughout the world has changed through geologic time as a function of the relative fluxes in contributions from mantle and continental Sr. The mantle contributions are highest during times of rapid seafloor spreading. The continental contributions are highest during times of orogenesis or during climatic periods of increased erosion of the continents (see, for instance, Veizer, 1989).

Strontium Isotope Age Curve for Marine Carbonate Rocks

The $^{87}\text{Sr}/^{86}\text{Sr}$ ratio of a carbonate mineral can be measured with great precision (i.e., to five significant figures). Workers at the Mobil (Oil) Field Research Lab successfully constructed a reference curve that traced the secular change in the Sr isotopic composition of seawater through all of Phanerozoic time (Burke and others, 1982; Elderfield, 1986; McArthur and Howard, 2004; see figure 4.69). Index fossil samples were used to construct and constrain the original curve. Initially, the curve served as a reference for Sr isotope dating of marine carbonates without diagnostic index fossils. Cenozoic marine limestone and chert can be dated with very small margins of er-

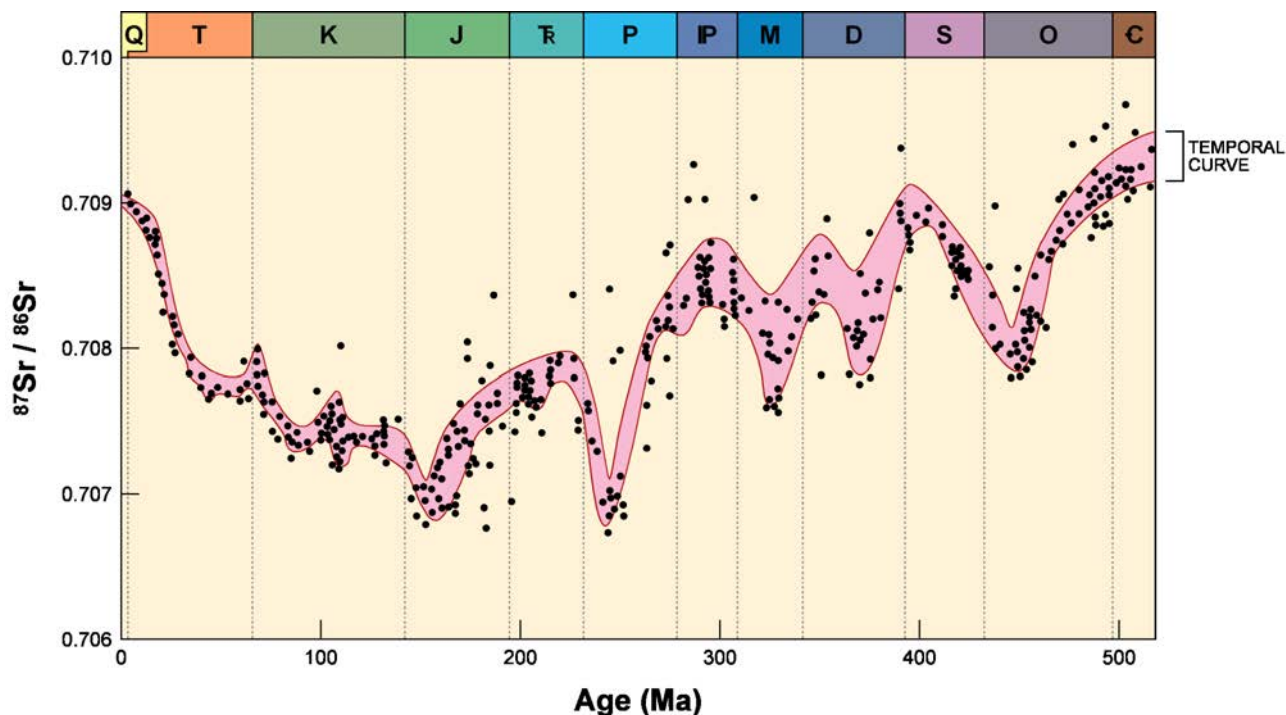


Figure 4.69. Strontium isotope seawater composition curve. From Burke and others (1982), Elderfield (1986), and Allan and Wiggins (1993).

ror (e.g., DePaolo and Ingram, 1985; DePaolo, 1986; DePaolo and Finger, 1991) because of the availability of Cenozoic index fossils in good condition and the very steep, monotonic nature of the curve during this time period (figure 4.69). For older marine carbonates, dating is less accurate due to poor preservation of fossils as well as the oscillating trends of the Sr isotope age curve (figure 4.69). The amplitudes and high frequency of these oscillations over geologic time are probably the result of climatic, tectonic-erosional, and seafloor-spreading cycles (Allan and Wiggins, 1993). The Sr isotope curve is most useful for dating during geologic time intervals when the curve is unidirectional and steep (for instance, during the Permian).

Strontium Isotopes as Tracers for Diagenetic Fluids

Strontium isotopes can have significant value in tracing subsurface fluid movement (Burtner, 1987; Allan and Wiggins, 1993). Marine waters throughout geologic time apparently displayed a relatively narrow range of $^{87}\text{Sr}/^{86}\text{Sr}$ ratios from about 0.7068 to 0.7095 (figure 4.69). Any ratios from carbonates that are significantly above or below this range of Phanerozoic seawater $^{87}\text{Sr}/^{86}\text{Sr}$ ratios indicate contribution by diagenetic waters in carbonate minerals that are of non-marine origin. Higher Sr isotope values indicate addition of radiogenic (high $^{87}\text{Sr}/^{86}\text{Sr}$ ratio) contaminants from crystalline (granitic or sialic) basement rocks or potassic feldspar-rich siliciclastic sediments (see, for instance Burtner, 1987). Lower Sr isotope values indicate contributions from mafics, ultramafics, and lithic sandstones with calcic plagioclase feldspar (see, for instance, Schultz and others, 1989).

Strontium is a doubly charged cation, which easily substitutes into the carbonate crystal lattice (Allan and Wiggins, 1993). When Sr is released by diagenetic processes, it is partitioned into dolomites and carbonate cements in various subsurface settings (figure 4.70). Therefore, Sr analysis is an excellent tool for identifying hydrothermal dolomite.

Strontium Isotopic Ratios for Leadville Limestone Samples at Lisbon Field

Three Leadville samples of different diagenetic mineral phases were selected from Lisbon field for Sr isotopic analysis. Mineral separates were carefully drilled or plucked out of a conventional core segment from the Lisbon NW USA No. B-63 well, Lisbon field (figure 2.3), at a depth of 9939 feet (3030 m). One sample each of (1) replacement, brownish “sucrosic” (rhombic euhedral) dolomite, (2) coarse, white saddle dolomite, and (3) coarse, clear to white calcite spar cement (figure 4.12 is a thin section photomicrograph showing the same mineral phases from 9991.8 feet [3045.4 m]) were analyzed by Geochron Laboratories (a Division of Krueger Enterprises, Inc., Cambridge, Massachusetts) for $^{87}\text{Sr}/^{86}\text{Sr}$ isotopic ratios (table 4.3). The precision of these analyses was reported to six significant figures (i.e., 0.00000X).

All three samples exhibit highly radiogenic Sr isotopic values, each in excess of 0.711. These values are far higher than the secular range of $^{87}\text{Sr}/^{86}\text{Sr}$ ratios for marine carbonate fossils and rocks during the Mississippian or for any time during the Phanerozoic (Burke and others, 1982; Allan and Wiggins, 1993; Denison and others, 1994; Bruckschen and others,

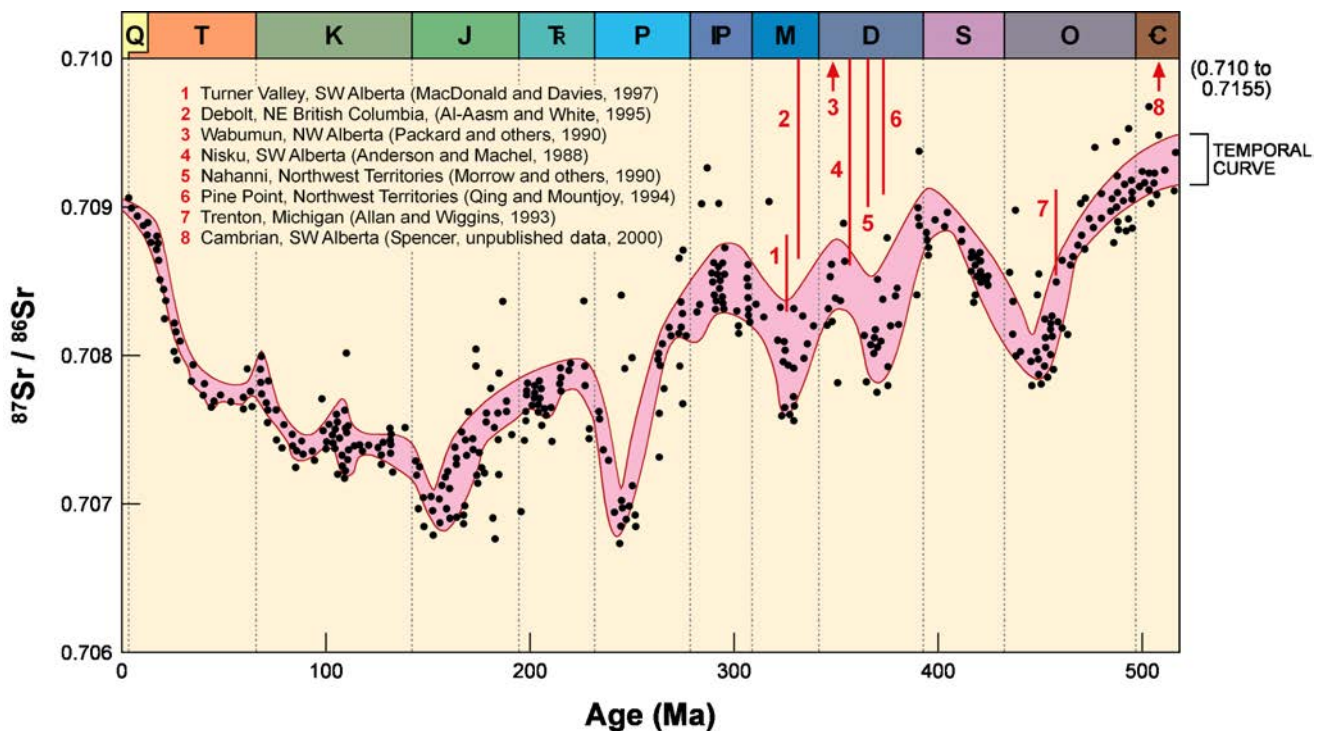


Figure 4.70. Strontium isotope compositions of saddle dolomites from the Canadian Rockies and Michigan Basin. From Burke and others (1982), Elderfield (1986), Allan and Wiggins (1993), and McArthur and Howard (2004).

Table 4.3. Strontium isotopic data from the Lisbon NW USA No. B-63 well core samples.

Sample No.	Well	Depth (ft)	$^{87}\text{Sr}/^{86}\text{Sr}$	Comments
1	B-63	9939	0.712068	Late calcite
2	B-63	9939	0.711961	Saddle dolomite
3	B-63	9939	0.711464	Matrix sucrosic dolomite

1999; McArthur and Howard, 2004). A plot of the Sr isotope composition for the three Leadville samples from Lisbon field, along with the Phanerozoic marine carbonate curve for Sr ratios, is shown in figure 4.71.

Discussion

For the Leadville samples, the high Sr isotopic ratios for the three late (burial) diagenetic mineral phases indicate contributions from diagenetic waters enriched in ^{87}Sr that were derived from granitic or arkosic sandstone terrains. The most logical terrain for ^{87}Sr enrichment is either Precambrian basement rocks or the Devonian McCracken Sandstone. Both sources are at depths considerably below the Leadville reservoir rocks sampled for this study. However, early Tertiary reactivation of basement-involved, high-angle normal faults associated with Precambrian tectonics may have allowed hot, deep-seated fluids from the granitic basement or the McCracken (figure 4.72) to communicate upwards with the Leadville Limestone carbonate section. Brines from evaporites in the Pennsylvanian Paradox Formation may also have entered the Leadville along the large fault bounding the northeastern flank of Lisbon field (figures 2.2

through 2.4, and 4.72). Interestingly, these radiogenic fluids were involved in precipitation of replacement “sucrosic” dolomite, saddle dolomite, and late calcite spar cement.

Strontium isotope composition from many (but not all) burial replacement dolomites are radiogenic (Allan and Wiggins, 1993, p. 95). The high $^{87}\text{Sr}/^{86}\text{Sr}$ ratio is indicative of allochthonous dolomitizing brines that interacted with potassic feldspars from basement rocks or from arkosic siliciclastic sediments prior to dolomitization. For instance, matrix replacement and white saddle dolomites in Upper Devonian (Frasnian) pinnacle reefs, Alberta Basin, Canada, surrounded by deeper-water facies, contain radiogenic Sr well above the Sr isotope seawater curve (Anderson, 1985; Allan and Wiggins, 1993, figure 95). Burial replacement dolomites in the Ordovician Trenton Formation of southern Michigan also have Sr isotope similarities to the Leadville Limestone at Lisbon field. Reactivation of a basement-involved, Precambrian, left-lateral wrench system allowed brines to migrate from the Silurian Salina Formation along faults and fractures into the Trenton (Allan and Wiggins, 1993). Strontium in the Trenton limestone has Ordovician seawater values whereas dolomite has Silurian seawater values (figure 4.73).

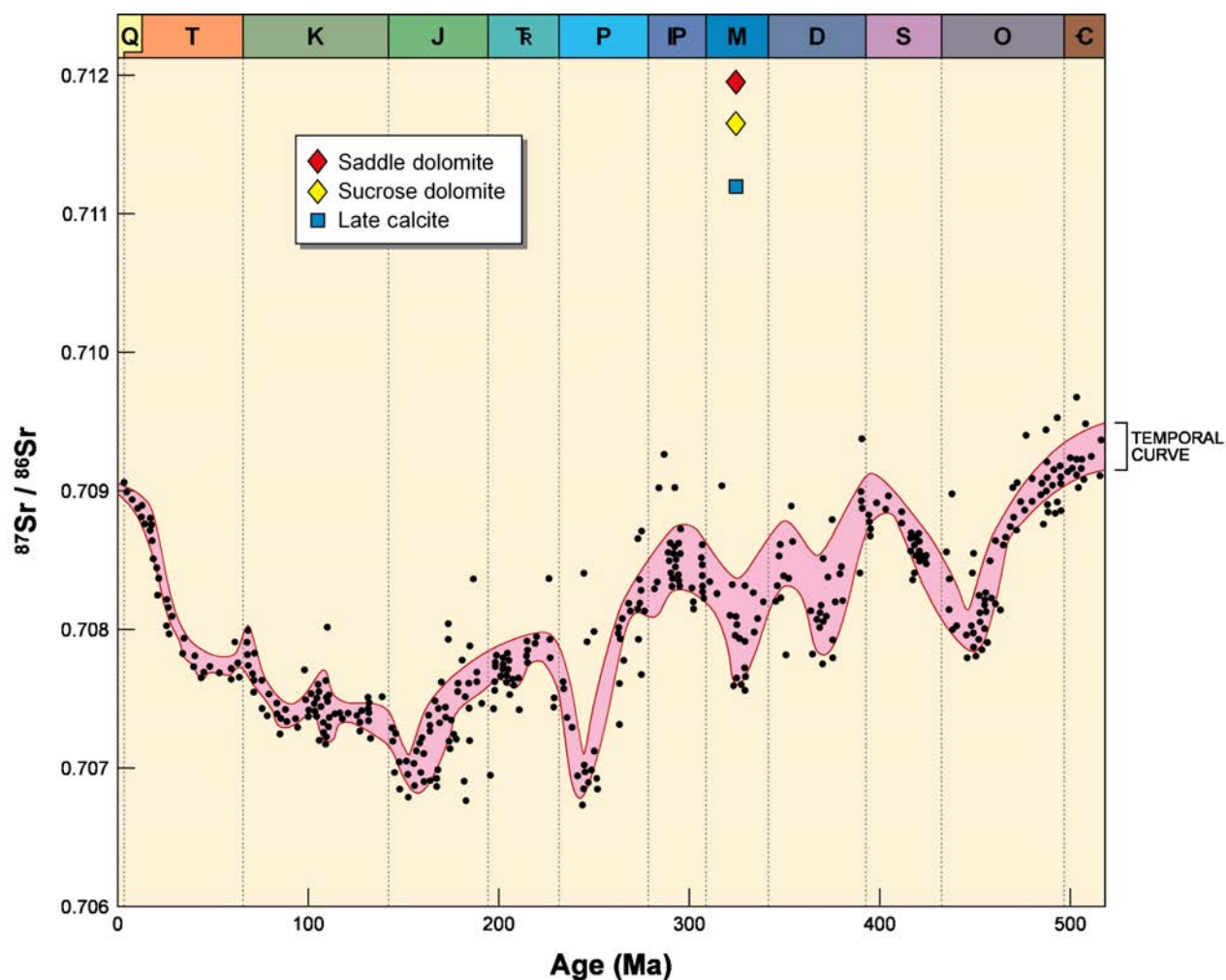


Figure 4.71. Strontium isotope seawater composition for the three Leadville Limestone samples from Lisbon field along with the Phanerozoic marine carbonate curve for Sr ratios. Modified from Burke and others (1982), Elderfield (1986), and Allan and Wiggins (1993).

LEADVILLE LIMESTONE BURIAL HISTORY AND POSSIBLE HEAT SOURCES

Burial history and temperature profiles for the Leadville Limestone at Lisbon field provide some guidance as to when important tectonic, diagenetic, and porosity-forming events occurred. These profiles (figure 4.74) were estimated using formation tops derived from well logs, a calculated geothermal gradient from bottom-hole temperatures of Lisbon wells (figure 2.14), regional measured stratigraphic sections, geologic maps, and various publications summarizing the geologic history of the area. The burial history profile shows rapid burial during the Pennsylvanian corresponding to the development of the Paradox Basin. This period is followed by a relatively gradual increase in burial depth, with minor spikes representing times of erosion or non-deposition, until the rapid and maximum depth of burial (16,500 feet [5500 m]) occurred during the Late Cretaceous. The maximum temperature at that time was about 244°F (118°C). In addition to the calculated temperature profile, we have inferred anomalous temperature spikes for (1) late Laramide reactivation

along normal faults that extend to basement, and (2) Oligocene igneous events such as the emplacement of the nearby La Sal and Abajo laccolith complexes, 10 miles (16 km) north and 23 miles (37 km) southwest, respectively, of Lisbon field (figure 1.1).

Porous replacement dolomite probably formed during the early and middle parts of the burial history at Lisbon field. Figure 4.75 displays suggested windows for important diagenetic phases in the reservoir history of the Leadville Limestone at Lisbon field: (1) the formation of rhombic dolomites and major intercrystalline (“sucrosic”) porosity; (2) saddle dolomite clear rims and cements; (3) euhedral quartz, dissolution of limestone and dolomite matrix, and pyrobitumen development; and (4) late calcite cements (with live oil inclusions). The inferred elevated temperature spikes during maximum burial, late Laramide fault reactivation/uplift, and Oligocene igneous activity may account for the high temperatures responsible for quartz precipitation, sulfide mineralization, pyrobitumen formation, late dissolution of carbonates, and late saddle dolomite cements.

Lisbon field

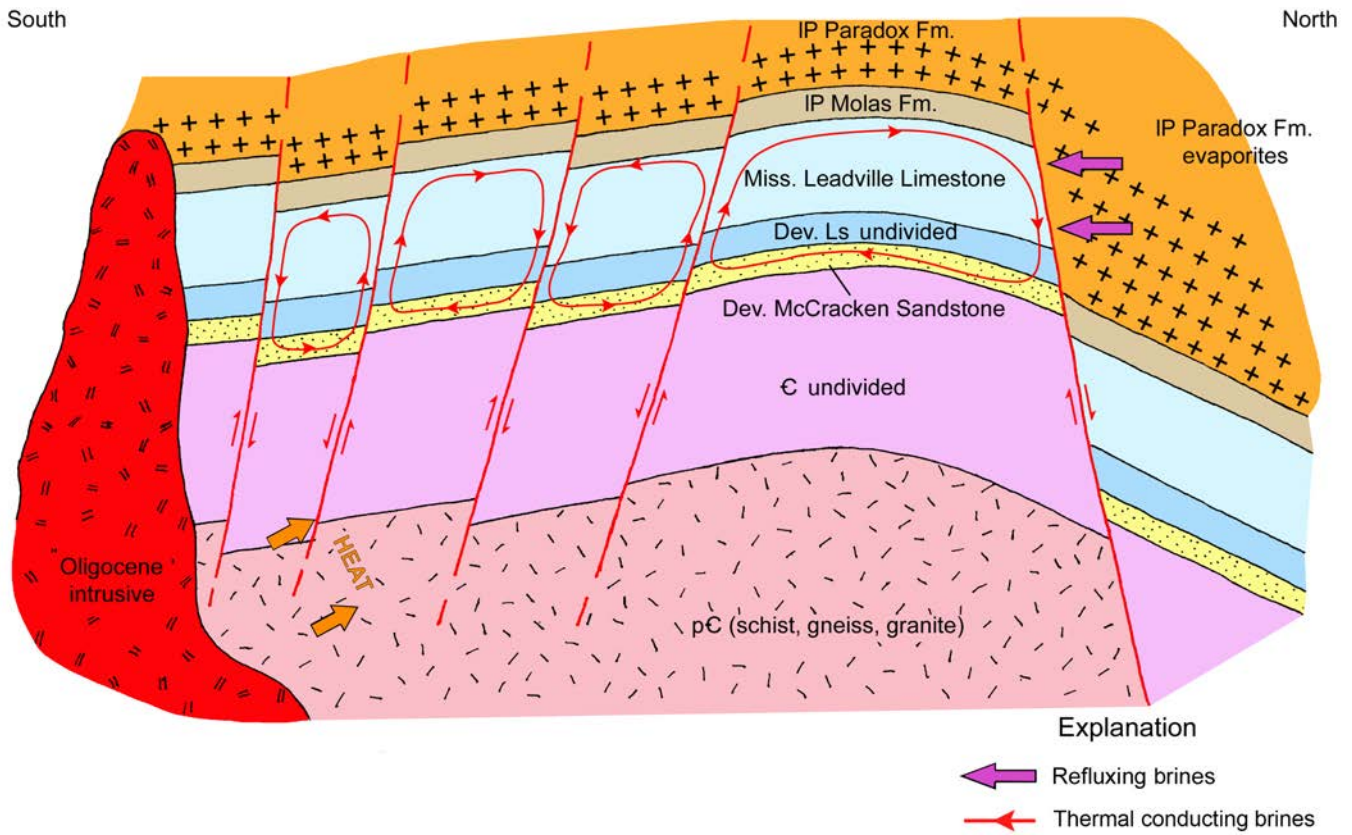


Figure 4.72. Possible heat sources and convection cells for late dolomitization of the Leadville Limestone in Lisbon field.

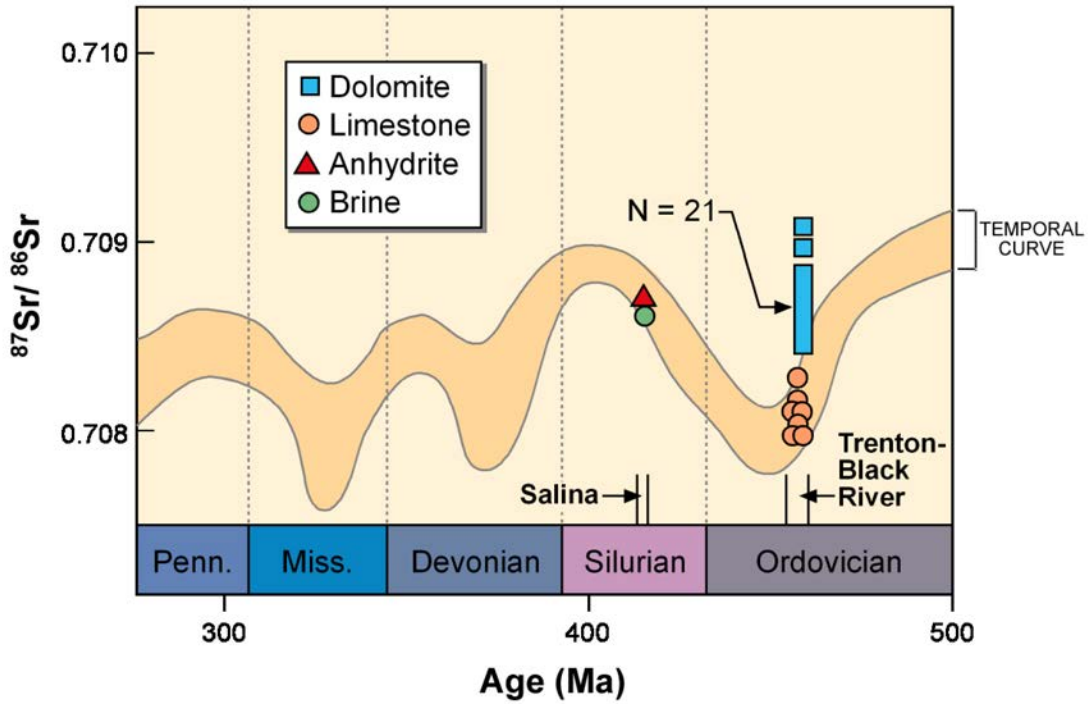


Figure 4.73 Strontium isotope values for limestone and dolomite of the Ordovician Trenton Formation and anhydrite and brine from the Silurian Salina Formation. From Allan and Wiggins (1993).

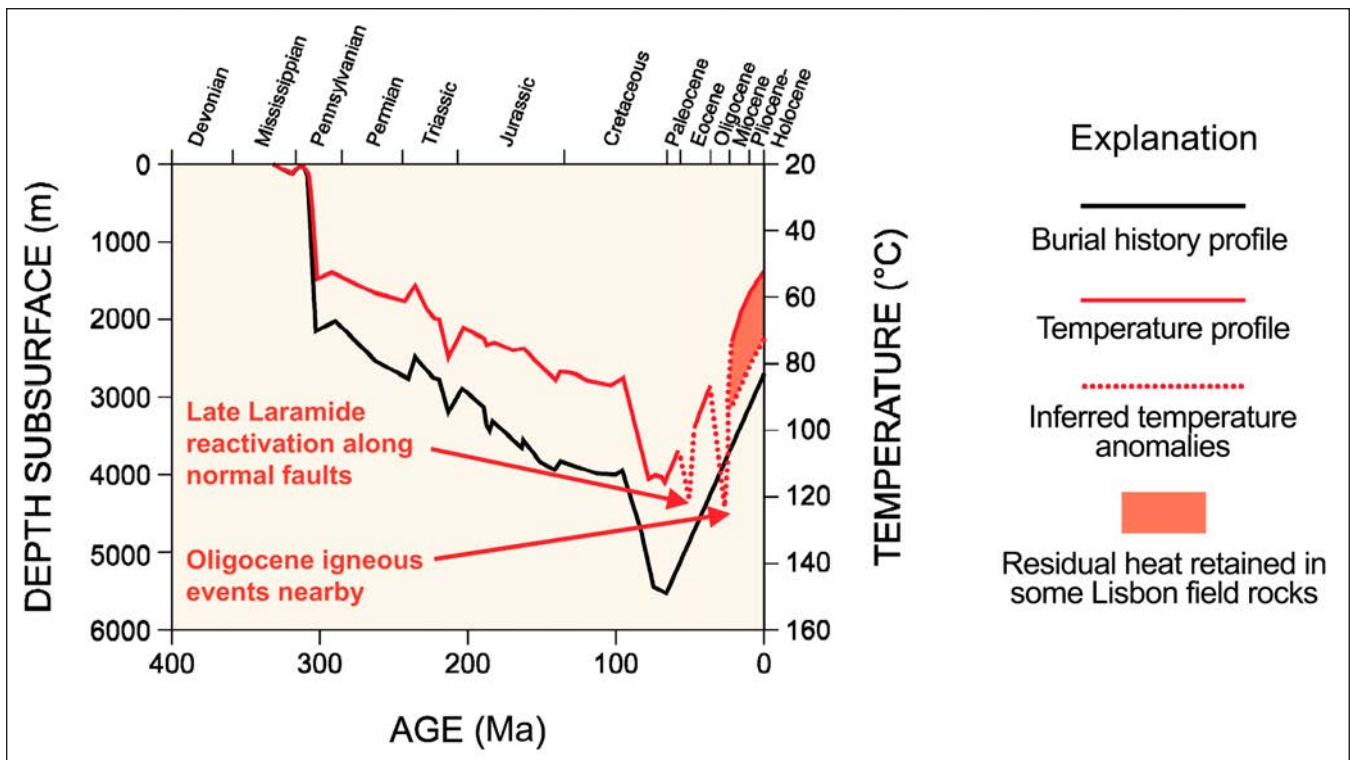


Figure 4.74. Burial history and temperature profile for Lisbon field.

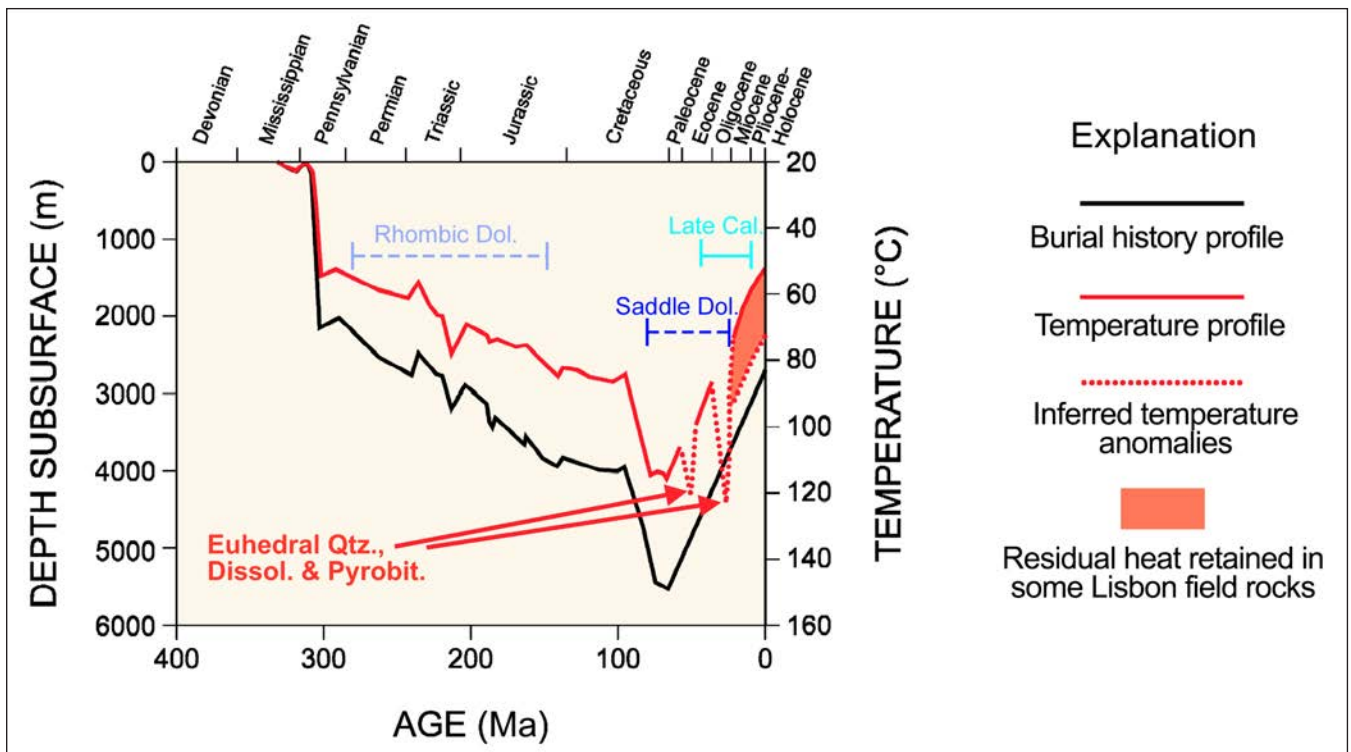


Figure 4.75. Burial history and temperature profiles with inferred diagenetic windows at Lisbon field.

We propose a model with convection cells bounded by basement-rooted faults to transfer heat and fluids possibly from the crystalline basement, Pennsylvanian evaporites, and Oligocene igneous complexes. Large volumes of water are required to produce the brecciation and amount, type, and generations of dolomite present at Lisbon field. There is probably not enough water moving through the regional hydrodynamic system to account for the Leadville dolomite. Therefore, convection or circulation cells would be much larger from surface feeder systems into the subsurface, most likely sweeping through igneous intrusives and basement to acquire heat, and form circulation systems. Fault movement at various scales provided the power to pressure up and move fluids throughout the subsurface. Recycling hot, brine-bearing water in convection cells may have driven dolomitization.

A diagrammatic south-to-north cross section of the greater Lisbon field area (figure 4.72) shows the possible convection cells of the circulation model for ascending warm fluids responsible for late dolomite (also see block diagram on figure 3.3), high-temperature quartz, pyrobitumen, aggressive dissolution of limestone and dolomite, and sulfide mineralization. The basal aquifer for these inferred fault-controlled cells could be the Devonian McCracken Sandstone. This sandstone is locally porous enough to produce oil at Lisbon field. Sources of heat may have been from Precambrian basement rocks and/or from Oligocene igneous intrusives. Mapped faults cutting Lisbon field may have been involved with thermal convection cells circulating fluids during late burial diagenesis (figure 4.76). Wells near faults appear to have better reservoir quality, produce greater volumes of oil, and have higher residual bottom-hole temperatures than wells away from these faults.

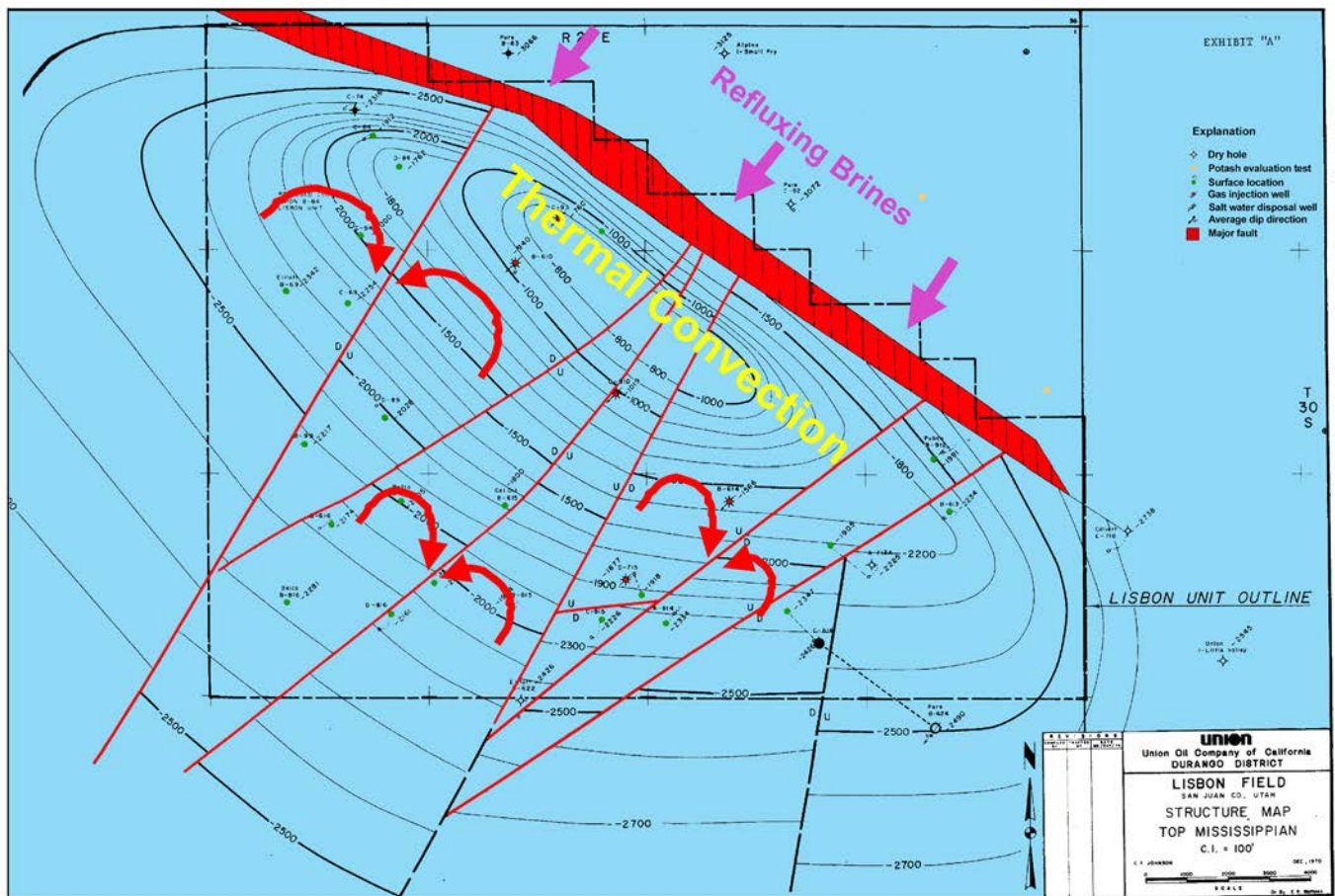


Figure 4.76. Top of structure of the Leadville Limestone, Lisbon field, showing possible thermal convection cells between small, northeast-southwest-trending normal faults. Modified from C.F. Johnson, Union Oil Company of California files (1970) courtesy of Tom Brown, Inc.

CHAPTER 5: LEADVILLE LIMESTONE HYDROCARBON PLAY— GENERAL REGIONAL CHARACTERISTICS

by

Thomas C. Chidsey, Jr., Utah Geological Survey

David E. Eby, Eby Petrography & Consulting, Inc.

and

Craig D. Morgan (retired), Utah Geological Survey

CHAPTER 5: LEADVILLE LIMESTONE HYDROCARBON PLAY— GENERAL REGIONAL CHARACTERISTICS

INTRODUCTION

The Mississippian Leadville Limestone (figure 5.1) is one of two major oil and gas plays in the Paradox Basin (figures 2.2 and 5.2); the other is the Pennsylvanian Paradox Formation (Chidsey and Eby, 2016; Chidsey and others, 2016). The Paradox Basin is within the west-central part of the Colorado Plateau physiographic province. The basin area is often referred to as the Four Corners area because it is where the boundary of four states, Utah, Arizona, New Mexico, and Colorado, all join. The play outline for the Leadville Limestone represents the maximum extent of petroleum potential in the Paradox Basin as defined by producing lithofacies, basement-involved fault trends, hydrocarbon shows and possible migration paths, the likelihood of hydrothermal dolomitization, and untested hypotheses (figure 5.2).

The Leadville in the Paradox Basin is a shallow, open-marine carbonate shelf deposit having a variety of facies. The traps for hydrocarbons in the Leadville Limestone are faults and fault-related anticlines (figure 1.4), as is the case for Lisbon field described in Chapter 2 (also see Morgan, 1993; Chidsey and Eby, 2016). As a result, hydrocarbon production and most drilling oil shows are found along the northwest-trending Paradox fold and fault belt (figure 1.1).

STRATIGRAPHY AND THICKNESS

The Mississippian (late Kinderhookian to early Meramecian) Leadville Limestone is a shallow, open-marine, carbonate-shelf deposit (figures 3.1A and 3.2). The same deposits are referred to as the Redwall Limestone (Grand Canyon nomenclature) in parts of the study area, but for convenience we use Leadville Limestone in this report. Unconformities separate the Leadville from the Devonian Ouray Limestone below and the Pennsylvanian Molas Formation (where present) or Hermosa Group above (figures 1.2, 2.5, and 5.1). The average depth to the Leadville in Paradox Basin fields is 8760 feet (2920 m).

The Leadville Limestone is typically 300 to 600 feet (100–200 m) thick in the Paradox Basin (Hintze and Kowallis, 2009). The Leadville thins from more than 700 feet (200 m) in the northwestern corner of the basin to less than 200 feet (60 m) in the southeastern corner (figures 5.2 through 5.4; appendix G) due to depositional onlap onto the shelf and erosion during periods when the shelf was subaerially exposed (figure 5.1). In addition, Parker and Roberts (1963)

demonstrated that there is both erosional wedging out and depositional thinning of individual limestone members of the Leadville in a southeasterly direction. On figure 5.2, Leadville thicknesses are generalized and thus, many areas of local fault-related thinning are not displayed.

Like at Lisbon field, the Leadville Limestone is divided into two informal members: a dolomitic lower member and a limestone and dolomite upper member, separated by a regional disconformity within the formation (figure 2.5). According to Baars (1966) this disconformity can be correlated throughout the Paradox Basin. Each member has a subtle but distinctly characteristic geophysical log response (figure 2.5) (Fouret, 1982, 1996).

PALEODEPOSITION AND LITHOLOGY

General Characteristics

During the Mississippian, the Colorado Plateau was covered by a shallow-shelf marine bank or platform with the shelf break into the deeper starved basin west of the Four Corners area (figures 3.1A, 5.5, and 5.6). The platform was an area of extensive carbonate deposition of nearly pure limestone implying arid conditions in the shallow sea lying south of the paleoequator (Blakey and Ranney, 2008). Little sand or mud was transported into the shallow, clear sea, providing favorable sites for the growth of lime-secreting marine organisms such as brachiopods, bryozoans, corals, and crinoids and other echinoderms (figure 5.7), and microbialites (Blakey and Ranney, 2008; Eby and others, 2014).

Leadville facies include open marine (crinoidal banks or ooid shoals and Waulsortian-type buildups, figure 5.8), middle shelf, and restricted marine (peloidal muds) (figure 3.2) based on evaluation of cores (stored at the UGS's UCRC) from regional exploration wells and Leadville fields in Utah (figure 5.2). In the interior of the Leadville carbonate bank, conditions were right for early marine reflux dolomitization from magnesium-bearing brines (figure 5.5). During the Late Mississippian, the entire carbonate platform in southeastern Utah and southwestern Colorado was subjected to subaerial erosion resulting in formation of a lateritic regolith (Welsh and Bissell, 1979) (figures 3.1B, 3.3, 5.9, and 5.10). Brecciation and sediment-filled cavities, related to karstification of the exposed Leadville, are relatively common throughout the upper third of the formation (see Chapter 4; Evans and Reed, 2006, 2007).

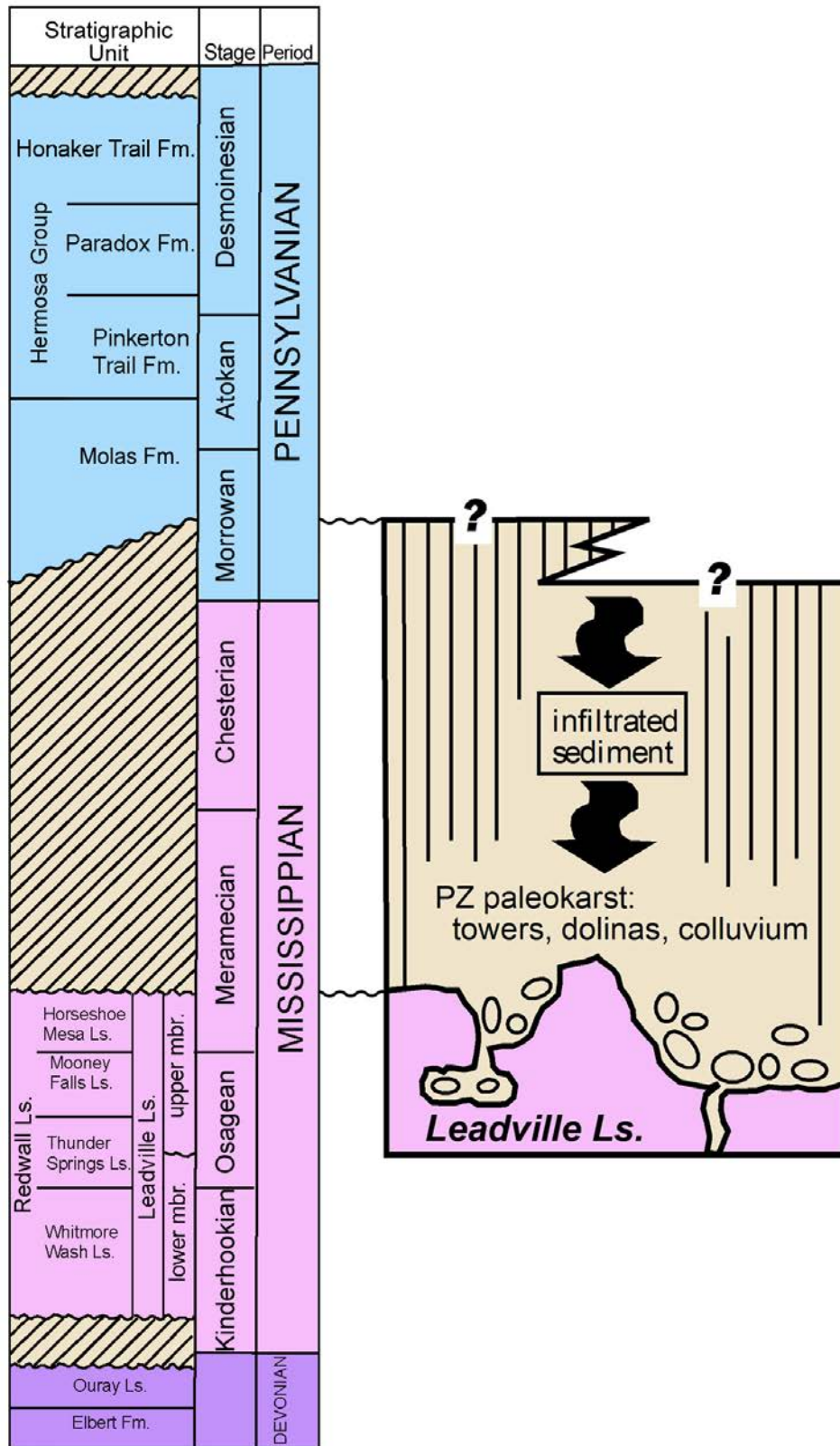


Figure 5.1. Devonian through Middle Pennsylvanian stratigraphic column for the Paradox Basin showing the major unconformity (defined by paleokarst features) between the Mississippian Leadville Limestone and the overlying Pennsylvanian Molas Formation. Note that the Leadville is divided into two informal members separated by an unconformity. Modified from Welsh and Bissell (1979) and Evans and Reed (2007).

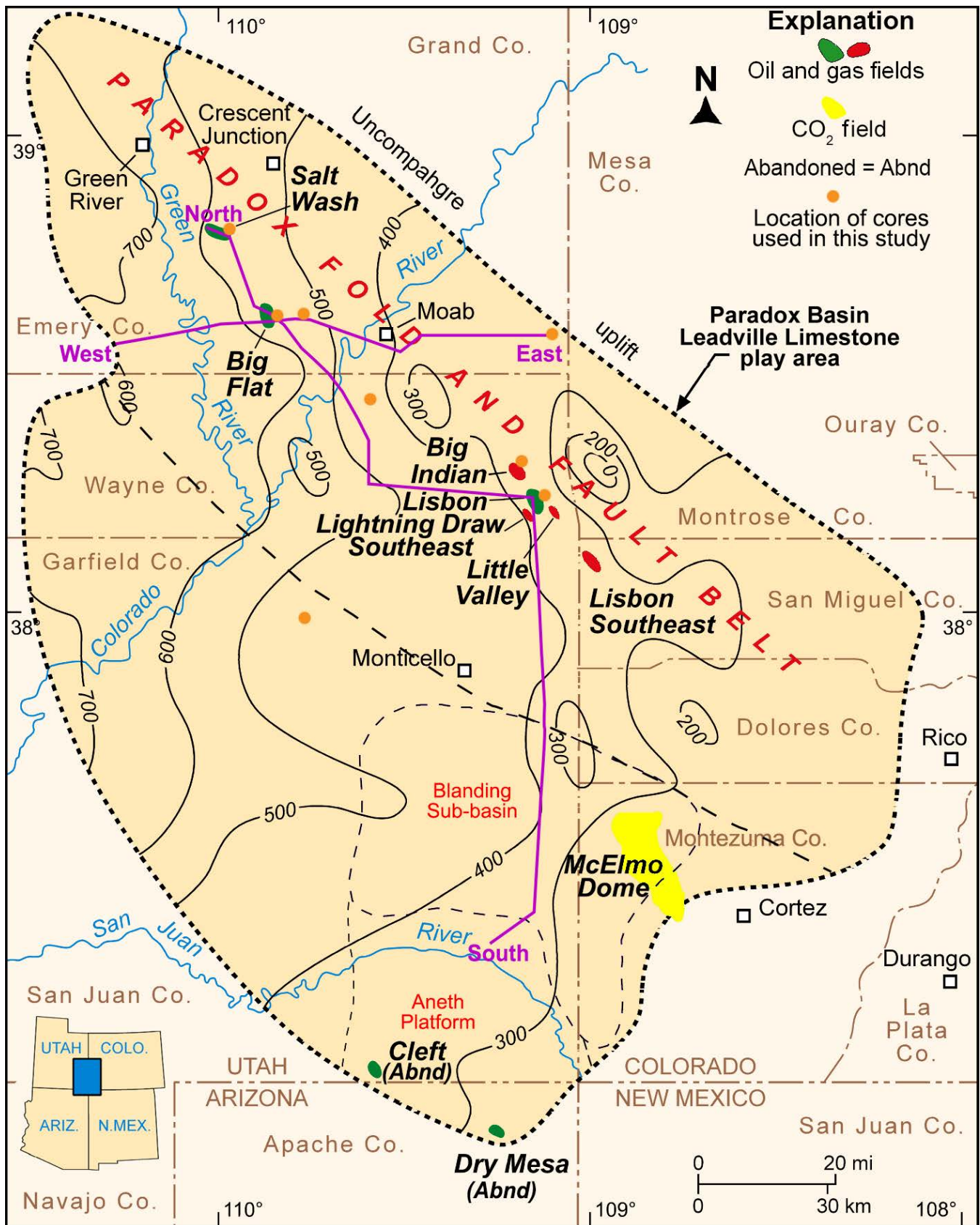


Figure 5.2. Thickness of the Mississippian Leadville Limestone, Utah and Colorado; contour interval is 100 feet (30 m) (modified from Parker and Roberts, 1963). Thicknesses are generalized, and many areas of local fault-related thinning are not displayed. Also shown are oil (green) and gas (red) fields that produce from the Leadville and location of cores from regional exploration wells and Leadville fields used in the study. Locations of north-to-south cross section (figure 5.3) and east-to-west cross section (figure 5.4) in purple.

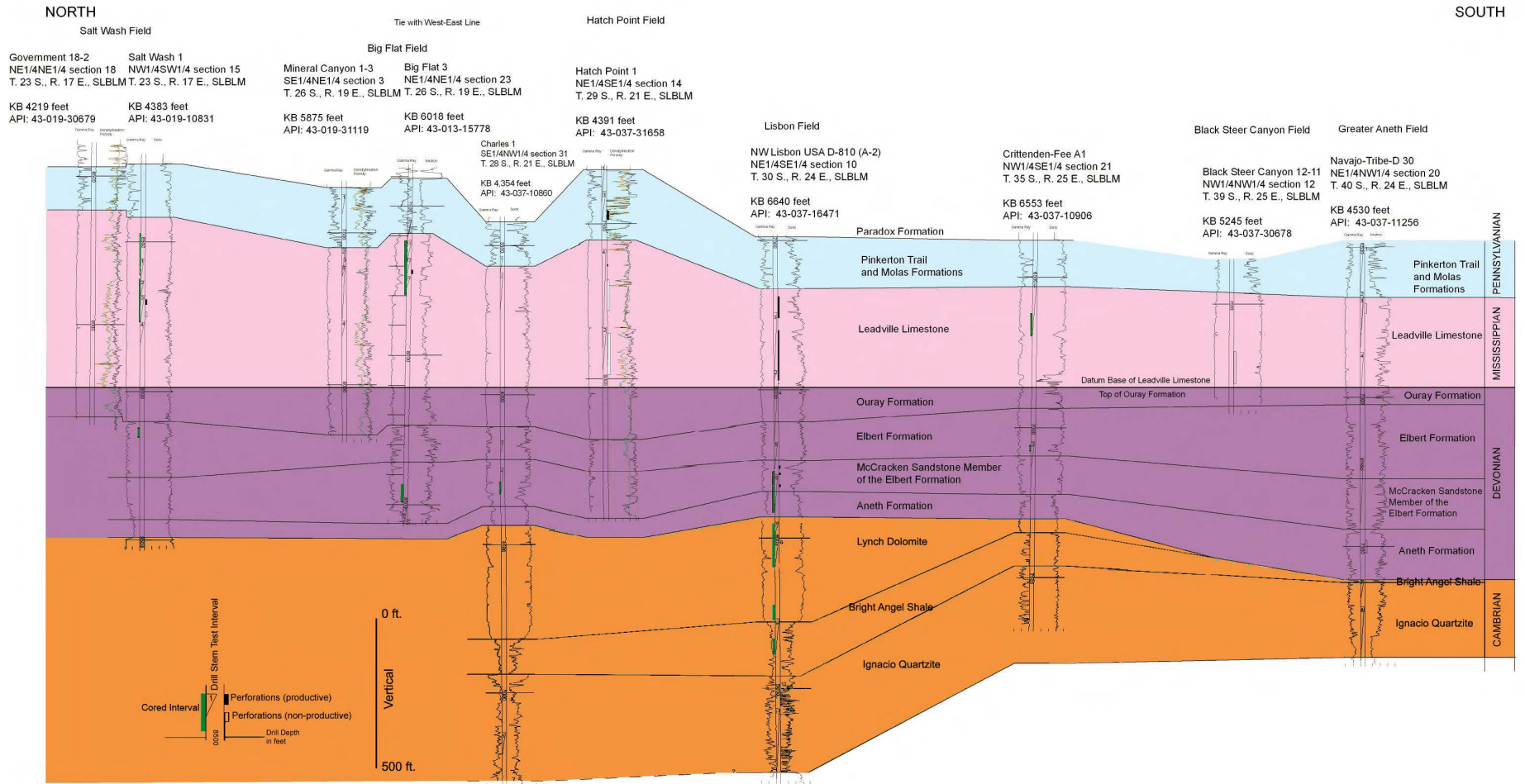


Figure 5.3. North-south stratigraphic cross section through the Utah part of the Paradox Basin showing regional Paleozoic correlations. No horizontal scale. See figure 5.2 for location of cross section.

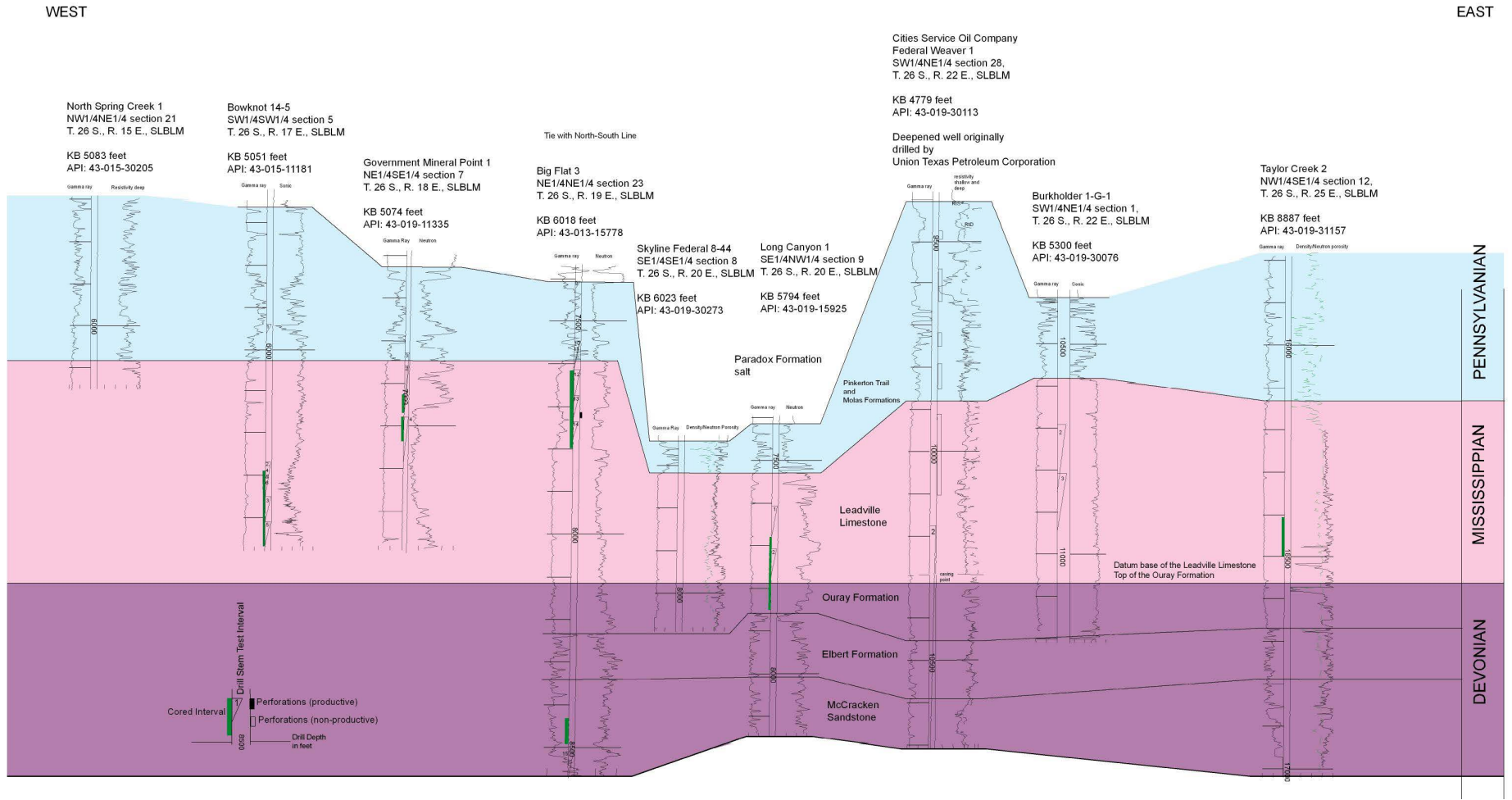


Figure 5.4. East-west stratigraphic cross section through the Utah part of the Paradox Basin showing regional Paleozoic correlations. No horizontal scale. See figure 5.2 for location of cross section.

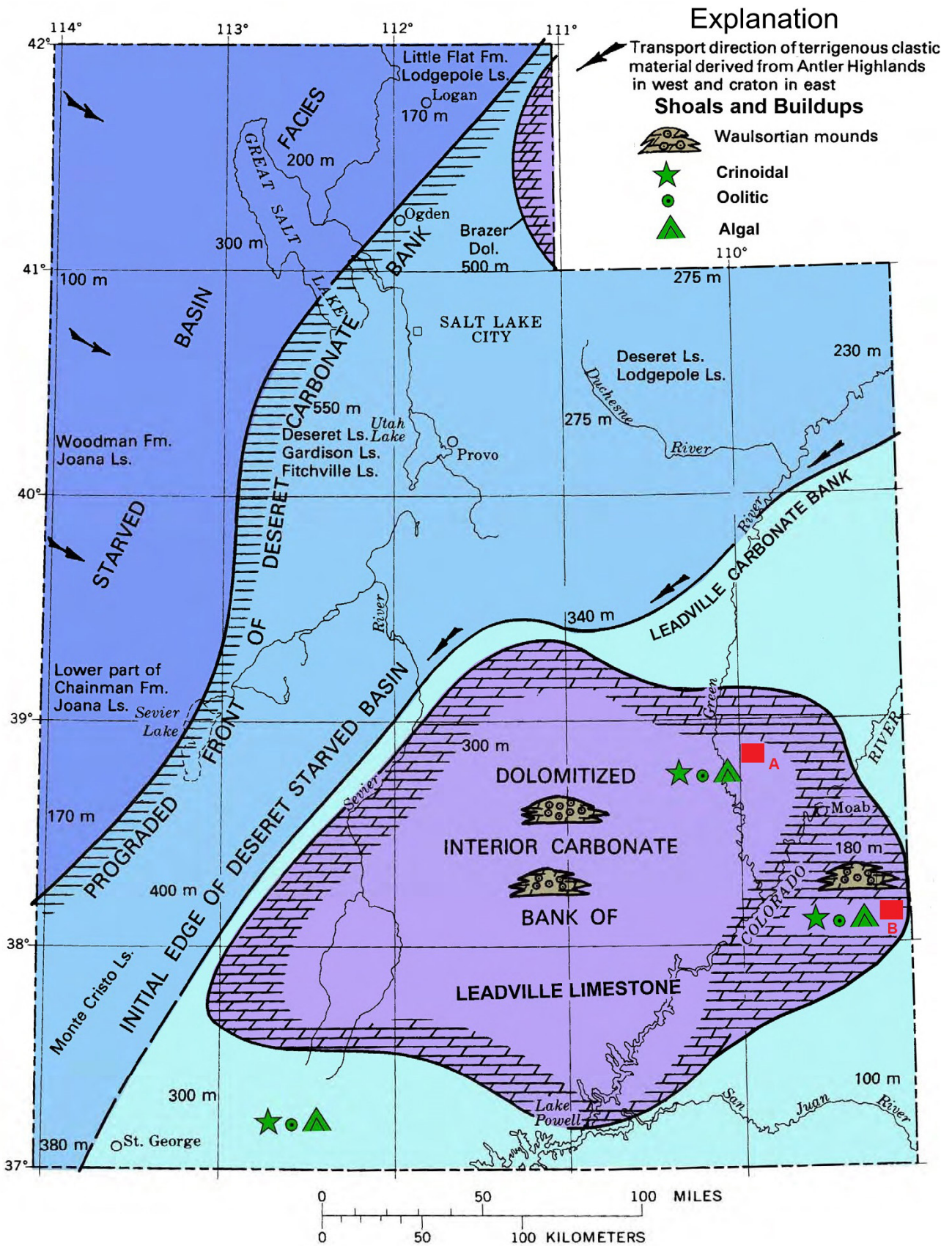


Figure 5.5. Paleogeographic map of Utah showing approximate present thicknesses in meters of deposits of late Kinderhookian to early Meramecian time. Modified from Welsh and Bissell (1979).

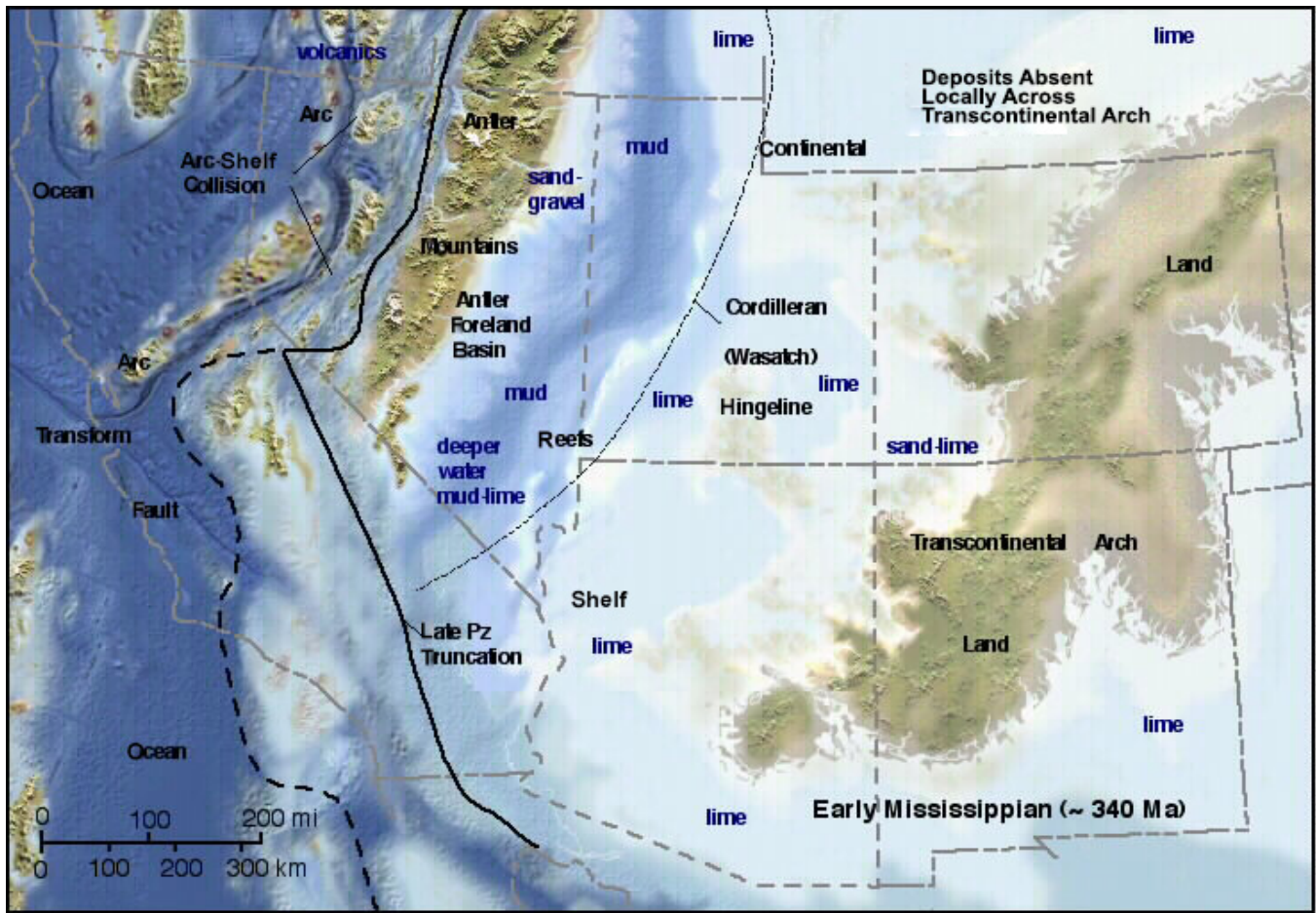


Figure 5.6. Paleogeographic map of the southwest United States during the Early Mississippian. From Blakey, <http://jan.ucc.nau.edu/~rcb7/>, accessed December 2008.



Figure 5.7. Diorama of a Mississippian crinoid meadow. Illinois State Museum, http://www.museum.state.il.us/exhibits/changes/htmls/tropical/underwater_mississippian.html.

A.



B.



Figure 5.8. Cores displaying Leadville open marine facies. **(A)** Crinoidal/skeletal packstone to grainstone representing a shallow crinoidal shoal; Salt Wash No. 1 Floy well, 9469 feet (2886 m), Salt Wash field (figure 5.2). **(B)** Porous algal (microbial) boundstone to mudstone representing a possible Waulsortian mound; No. 1 Big Indian well, 10,081 feet (3073 m), Big Indian field (figure 5.2).

The Leadville carbonate bank is composed of oolitic, pelletal, birdseye, micritic, stromatolitic, and fossiliferous carbonates (figure 3.2). Some of the Leadville Limestone is dolomitized (both early and late observed in Lisbon field [Chapters 3 and 4]), crosscutting lithologies within the interior of the bank (Welsh and Bissell, 1979). The oil reservoir at Big Flat field (figures 1.3 and 5.2) is an example of a dolomitized Waulsortian mound on the shallow-shelf bank (Welsh and Bissell, 1979). The more dolomitic lower member is composed of mudstone, wackestone, packstone, and grainstone deposited

in shallow-marine, subtidal, supratidal, and intertidal environments (Fouret, 1996). The upper member is composed of mudstone, packstone, grainstone, and terrigenous clastics also deposited in subtidal, supratidal, and intertidal environments (Fouret, 1996). Reservoir rocks in the upper member are dolomitized crinoidal carbonate-mud deposits (Baars, 1966). For the complete descriptions of Leadville depositional environments and lithology, refer to Chapter 3. Although these descriptions are primarily based on cores from Lisbon field, they can be applied to the Leadville on the regional scale.

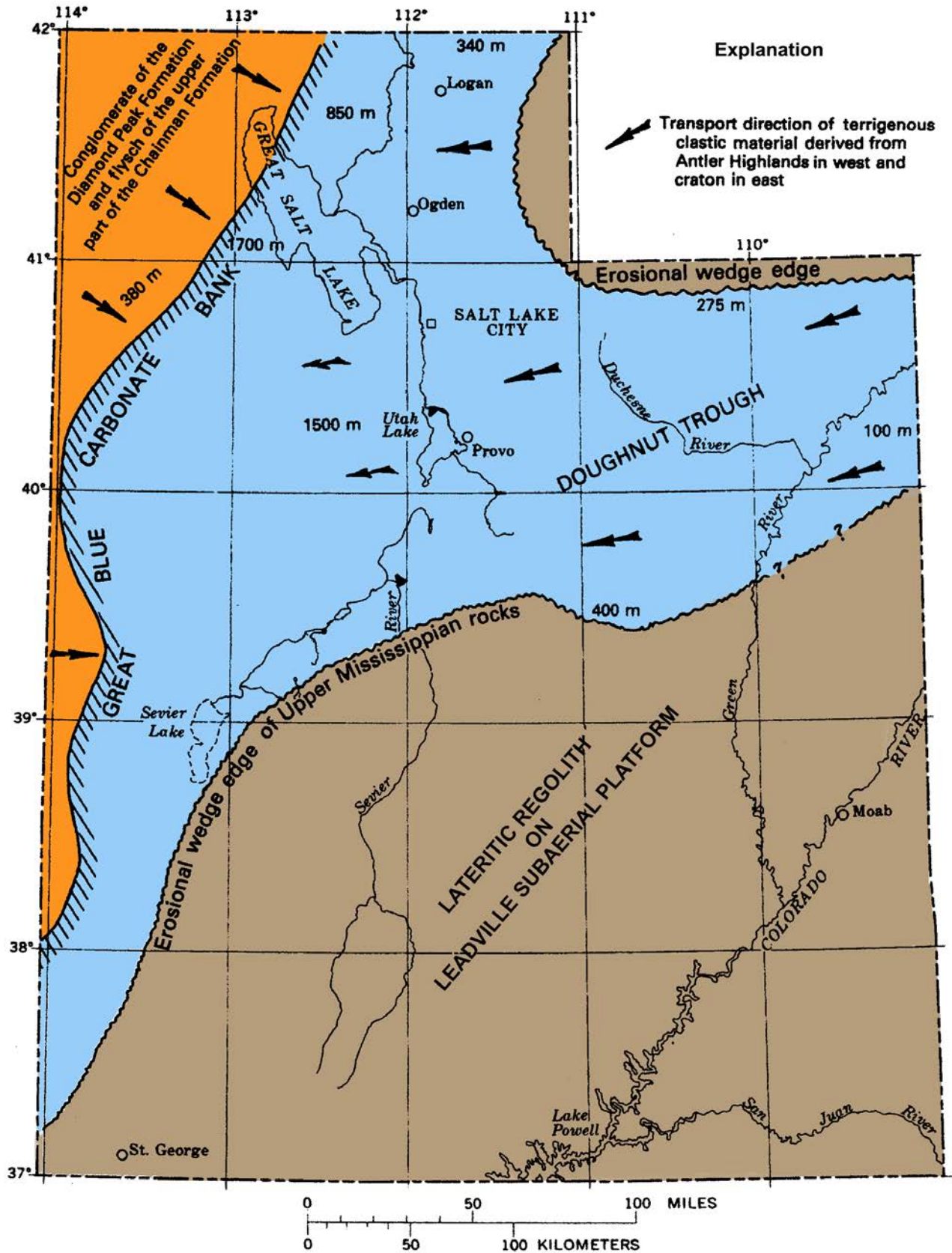


Figure 5.9. Paleogeographic map of Utah showing approximate present thicknesses in meters of upper Meramecian to upper Chesterian deposits. After Welsh and Bissell (1979).

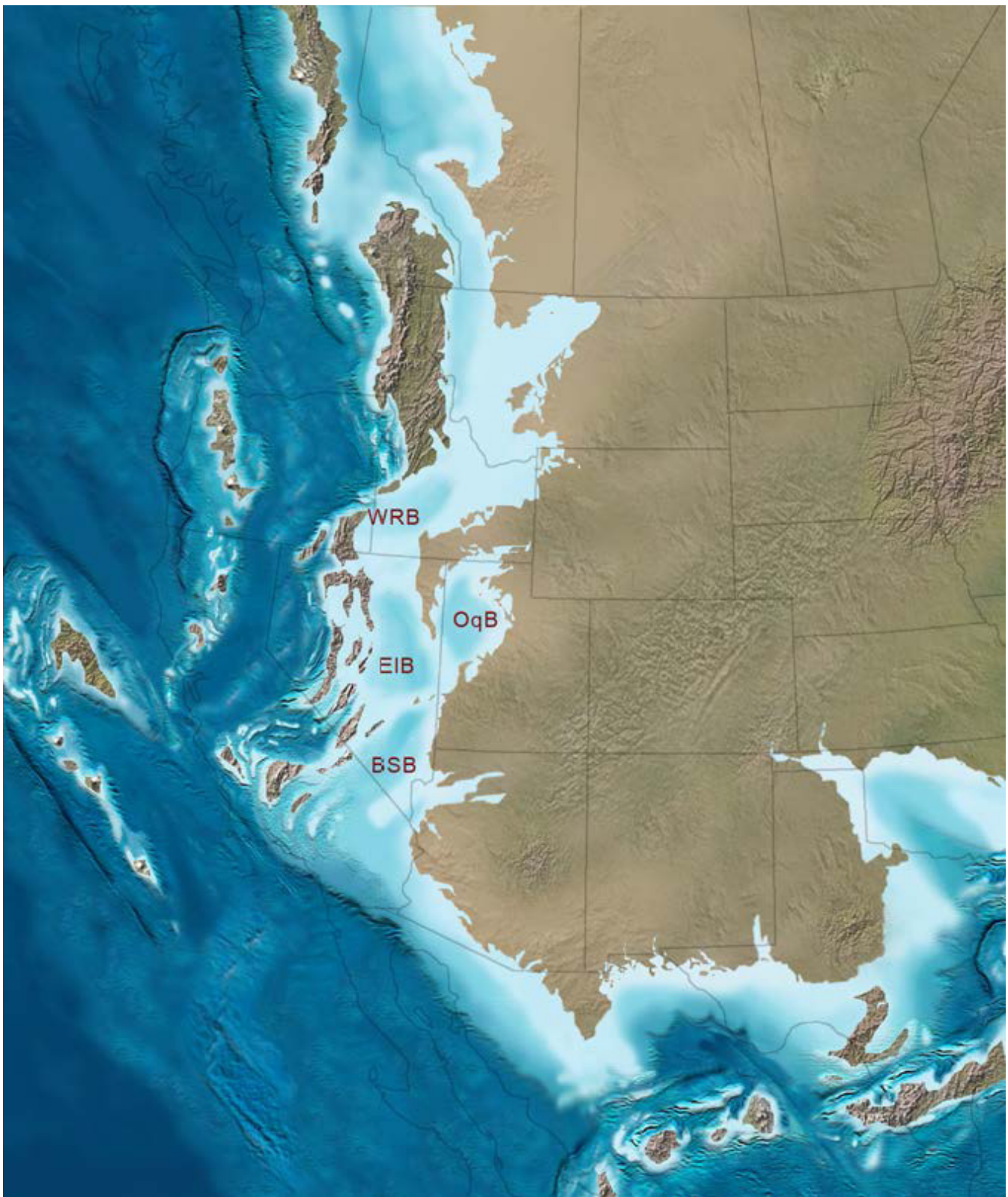


Figure 5.10. Paleogeographic map of the western United States during the Late Mississippian to Early Pennsylvanian when the Mississippian Leadville Limestone carbonate platform was subaerially exposed resulting in erosion and formation of a lateritic regolith in the Four Corners area. WRB = Wood River Basin, OqB = Oquirrh Basin, BSB = Bird Springs Basin, and EIB = Ely Basin. From Blakey, <http://jan.ucc.nau.edu/~rcb7/>, accessed December 2008.

Facies of the Paradox Fold and Fault Belt

Specifically, for the Paradox fold and fault belt, we examined cores from 11 wells to determine the general facies of the Leadville Limestone in the northern Paradox Basin. Four regional facies were recognized in these cores (figure 5.11):

1. open-marine, moderate- to high-energy shoals or banks represented by crinoidal grainstones (figure 5.8);
2. restricted marine, high-energy shoals represented by cross-stratified grainstones consisting of ooids, coated grains, and “hard” peloids;
3. low-energy, below wave base (rarely at sea level), open-marine platform represented by peloidal and skeletal packstones and wackestone; and
4. low-energy, nearshore, often restricted marine (with some tidal-flat features and cryptotalgal laminae) represented by “soft” peloidal mudstone which was frequently converted by early dolomitization.

Each core was described including carbonate fabrics, lithology, bedding, constituent grains/texture, porosity, carbonate structures, diagenesis, and most importantly, facies (see appendix H). One of the four facies described above was as-

signed to each unit and plotted on the well logs for each well. A depositional facies profile was created for each well from the core descriptions with minor or thin facies eliminated (figure 5.11). We created a very generalized facies map of the Leadville Limestone in the Paradox fold and fault belt based on the inferred average depositional facies profiles identified in the cores of the study wells (figure 5.12).

The dominant Leadville facies is open-marine, moderate- to high-energy crinoidal banks particularly in the southwestern half of the region. We infer two areas of ooid-peloid shoals in the northeastern part of the regions separated by open-marine crinoid bank facies. These areas of ooid-peloid shoals represent excellent targets for exploration whereas the extensive areas dominated by open-marine, moderate to high-energy crinoidal bank facies require diagenetic overprints (late dolomitization, hydrofracturing, etc.), similar to those at Lisbon and likely most other Leadville fields on trend, to have hydrocarbon potential.

The northwestern and southeastern areas are inferred to be low-energy, open-marine platform facies. The low-energy, nearshore, often restricted-marine facies does not dominate, although it is present in some cores. Like the open-marine, moderate to high-energy crinoidal banks, these facies also require dolomitization to create good reservoir rock.

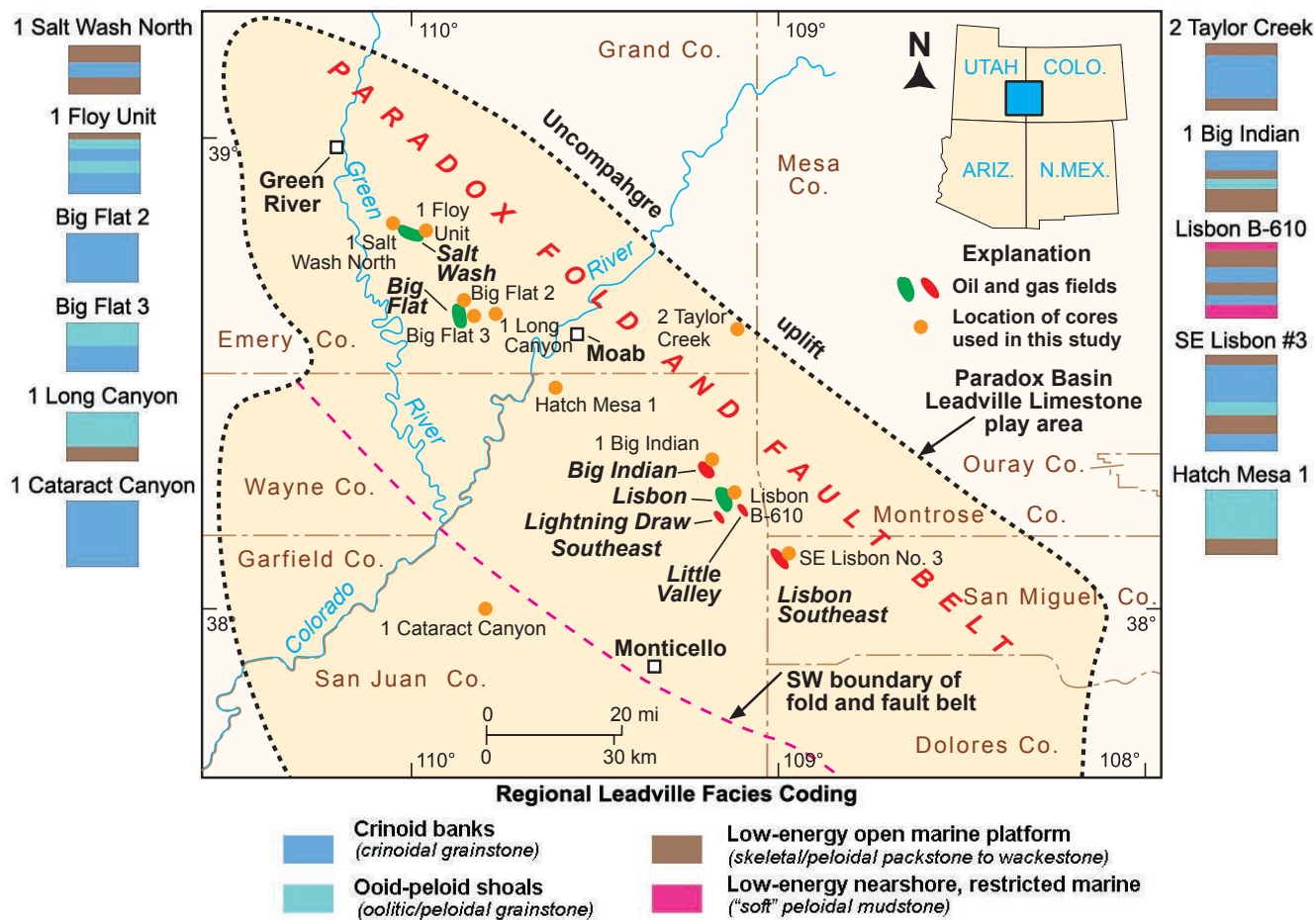


Figure 5.11. Map showing depositional facies profiles determined from regional cores used in the study.

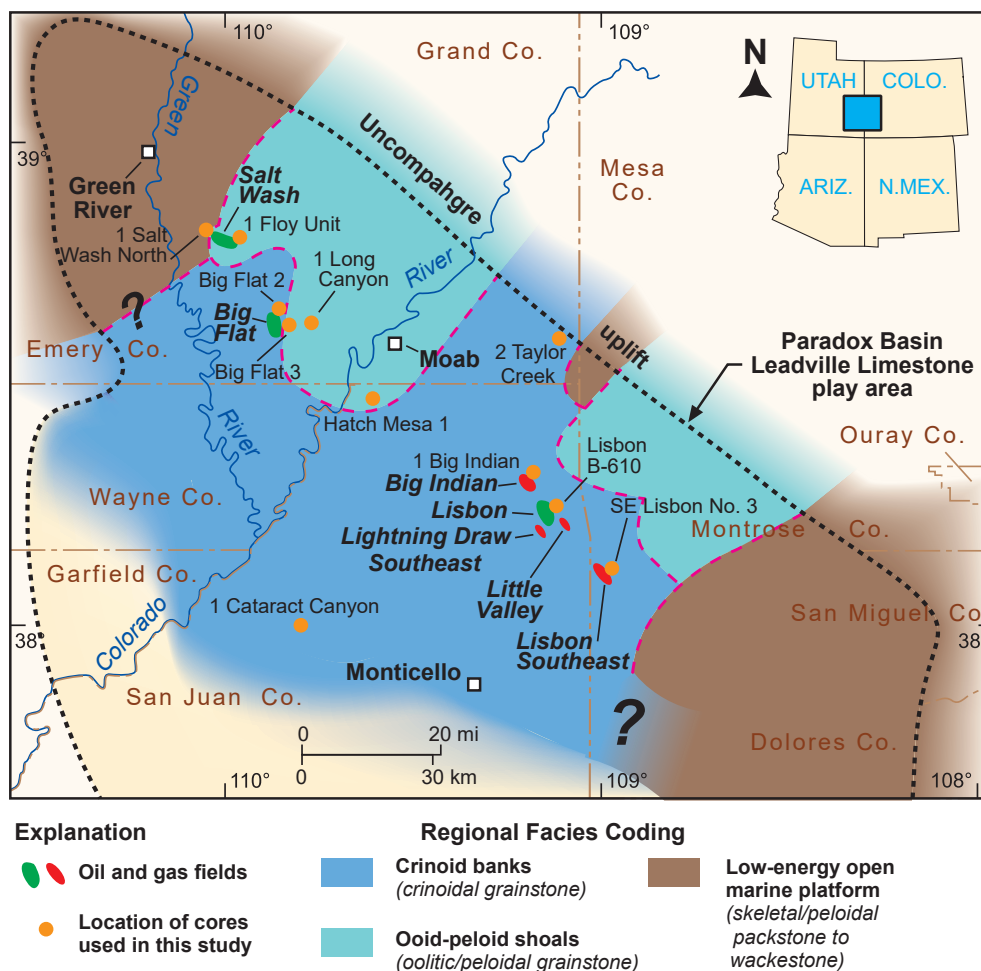


Figure 5.12. Very generalized facies map of the Leadville Limestone, northern Paradox Basin, based on inferred average depositional profiles shown on figure 5.11.

HYDROCARBON TRAPS

Structural Setting

High-angle, basement-involved faults and other structural features in the Paradox Basin initially formed in the Proterozoic, around 1700 to 1600 Ma (Stevenson and Baars, 1986, 1987). Minor fault movement and related topography may have begun in the Mississippian with the reactivation of these ancient faults. Additional faulting within the basin began in the Middle Pennsylvanian and was associated with the development of the Uncompahgre Highlands and Ancestral Rocky Mountains, although in areas of greatest paleorelief the Leadville is completely missing as a result of nondeposition or subsequent erosion (Baars, 1966).

Periodic movement along “blind,” northwest-trending, basement-involved faults affected deposition of the Leadville Limestone. Ahr (1989) and Wilson (1975) presented evidence that structure may have influenced deposition of the Waulsortian mound facies in the Leadville (figure 3.2). Crinoid banks accumulated in shallow-water environments on upthrown fault blocks or other paleotopographic highs.

Trapping Mechanisms

Most oil and gas produced from the Leadville Limestone is in basement-involved, northwest-trending structural traps with closure on both anticlines and faults (figure 1.4). Lisbon (described in detail in Chapters 2 through 4), Big Indian, Little Valley, and Lisbon Southeast fields (figure 5.2) are on sharply folded anticlines that close against the Lisbon fault zone. Salt Wash and Big Flat fields (figure 5.2), northwest of the Lisbon area, are on unfaulted, east-west- and north-south-trending anticlines, respectively. The unfaulted structures probably developed from movement on deep, basement-involved faults that do not extend upward to the level of the Leadville. These and other faults affecting the Leadville probably reflect the reactivation of pre-existing, Precambrian-age faults during the Laramide orogeny or later.

Big Flat field, Grand County, Utah (figure 5.2), was the first Mississippian Leadville discovery (1957) in the Paradox Basin. The trap is a doubly plunging anticline with 276 feet (84 m) of structural closure (figure 5.13) that produced 83,469 bbls of oil and 5.2 million cubic feet of gas from Leadville limestone and dolomite (Stowe, 1972; Smith, 1978). The

net reservoir thickness is 30 feet (10 m), which extends over a 480-acre (190 ha) area. The field now produces oil from horizontal wells in the Cane Creek shale zone of the Paradox Formation on a separate structure north of the original, abandoned Leadville feature.

Stratigraphic oil accumulations may exist to the west and southwest of the fold and fault belt. Traps may be formed by porous Waulsortian mounds or other carbonate buildups where porosity is further enhanced by early dolomitization. Traps may also be developed in the regolith deposits in both the upper and lower members of the Leadville. Diagenetic traps formed from late, possibly hydrothermal dolomite may be present especially along major fault trends (figure 1.1).

Hydrocarbon Source and Seals

As described in detail in Chapter 2, hydrocarbons in Leadville Limestone reservoirs were likely generated from source rocks in the Pennsylvanian Paradox Formation (figures 1.2 and 5.1). Organic-rich units are the source for oil and gas produced from the Paradox Formation itself (Hite and others, 1984; Nuccio and Condon, 1996). Hydrocarbon generation in the Paradox Formation occurred during maximum burial in the Late Cretaceous and early Tertiary. Hydrocarbons subsequently migrated, primarily along fault planes, into carrier beds or Leadville structures. Fracture systems developed along fault systems may have provided secondary migration routes. Oil generated from non-Pennsylvanian source rocks requires long-distance migration.

The seals for the Leadville producing zones are the overlying clastic beds of the Pennsylvanian Molas Formation (figures 1.2 and 5.1). Hydrocarbons in the Leadville are further sealed by evaporite (salt and anhydrite) beds within the overlying Pennsylvanian Paradox Formation.

Hydrocarbon Potential

The Leadville Limestone has produced over 53 million bbls of oil/condensate and 830 BCFG from the seven fields in the northern Paradox Basin of Utah and Colorado (Utah Division of Oil, Gas and Mining, 2020; Colorado Oil and Gas Conservation Commission records, 2020). However, much of the gas included in the production figures is cycled gas used in the past for pressure maintenance at Lisbon field, Utah. The 7500-mi² (19,400 km²) play area is relatively unexplored (Morgan, 1993; Chidsey and Eby, 2016); only about 100 wells penetrate the Leadville (less than one well per township), thus the potential for new discoveries remains great.

The production and most of the drilling oil shows have been from wells in the northwest-trending Paradox fold and fault belt. Buried fault blocks have been the most common target for exploration of hydrocarbons in the Leadville because they have a proven history of success and fault blocks can be identified on gravity, aeromagnetic, and seismic geophysical data.

Subtle stratigraphic and diagenetic traps are difficult to identify in the Paradox Basin and, therefore, have not been significant exploration targets. Surface geochemical surveys and high-resolution 3D seismic may improve the ability of explorationists to identify these traps.

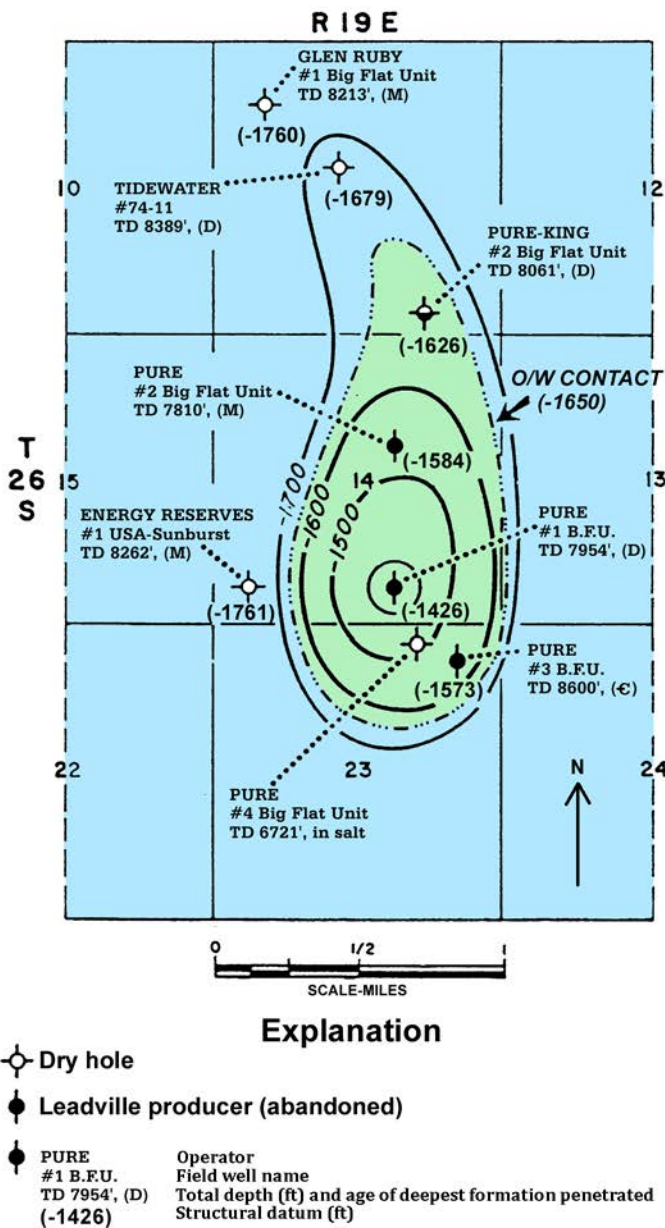


Figure 5.13. Top of structure of the Leadville Limestone, Big Flat field, Grand County, Utah. Contour interval = 100 feet (30 m), datum = mean sea level. Modified from Smith (1978).

CHAPTER 6:

POTENTIAL OIL-PRONE AREAS IN THE PARADOX FOLD AND FAULT BELT, UTAH, BASED ON SHOWS IN DRILL CUTTINGS USING EPIFLUORESCENCE MICROSCOPY TECHNIQUES

by

David E. Eby, Eby Petrography & Consulting, Inc.

and

Thomas C. Chidsey, Jr., and Craig D. Morgan (retired), Utah Geological Survey

CHAPTER 6:

POTENTIAL OIL-PRONE AREAS IN THE PARADOX FOLD AND FAULT BELT, UTAH, BASED ON SHOWS IN DRILL CUTTINGS USING EPIFLUORESCENCE MICROSCOPY TECHNIQUES

INTRODUCTION

Potential oil-prone areas for the Mississippian Leadville Limestone were identified in the northern Paradox Basin (Paradox fold and fault belt), Utah, based on hydrocarbon shows using low-cost epifluorescence (EF) techniques. The trapping mechanisms for Leadville producing fields in this region are usually anticlines bounded by large, basement-involved normal faults. Epifluorescence microscopy is a technique used to provide information on diagenesis, pore types, and organic matter (including “live” hydrocarbons) within sedimentary rocks (Chidsey and Eby, 2017). EF is a rapid, non-destructive procedure that uses a petrographic microscope equipped with reflected-light capabilities, a Hg-vapor light, and appropriate filtering. For an overview of EF principles, previous work, and methodology, refer to Chapter 4.

SAMPLING COMPILATION, EXAMINATION, AND EVALUATION

Wells penetrating the Leadville Limestone in the Utah part of the Paradox fold and fault belt were plotted and all Leadville well cuttings available from the collection at the UCRC were compiled. Cuttings were examined under a binocular microscope and porous samples of dolomite and some limestone were selected from various zones within the Leadville section (figure 6.1): generally, four to ten samples per depth interval from each well. The cuttings were placed on Petrologs™, a small plastic, self-adhesive compartmentalized cutting storage unit, for EF examination (figure 6.2). (All Petrologs™ containing Leadville cuttings from the project are stored at the UCRC and are available to the public.) Thus, sample preparation is inexpensive and rapid.

Approximately 900 cutting samples were selected from 32 wells penetrating the Leadville Limestone (6 producing gas, condensate, and oil wells, as well as 26 non-productive wells) throughout the region (table 6.1; see appendix F for detailed descriptions, binocular microscope images of selected cuttings, and thin section photomicrographs). These cuttings display mainly intercrystalline porosity, occasional small vugs or molds, and other pore types (figure 6.3). Oil staining, bitumen, and stylolites are also observed (figure 6.3).

Examination of cuttings included photo-documentation under EF and plane-polarized light at the same magnification. Photomicrography of the compositional, textural, and pore structure attributes was done using high-speed film (ISO 800 and 1600) with some bracketing of exposures as camera metering systems do not always reliably read these high-contrast images in the yellow and green light spectrum. Since the image brightness is directly proportional to magnification, the best images are obtained at relatively high magnifications (such as greater than 100X). Low-power fluorescence is often too dim to effectively record on film.

Epifluorescence petrography makes it possible to clearly identify hydrocarbon shows in Leadville cuttings selected for study. A qualitative visual rating scale (a range and average) based on EF evaluation was applied to the group of cuttings from each depth in each well (table 6.2 and figure 6.4). Using the qualitative visual rating scale, the highest maximum and highest average EF reading from each well were plotted and mapped (figures 6.5 and 6.6).

DISCUSSION

Epifluorescence allows one to observe the presence of any soluble hydrocarbons. Samples displaying fluorescence represent areas where hydrocarbons may have migrated or accumulated. The best fluorescence in this study, when present, was gold and occurred in high-porosity (figure 6.4A), low-permeability dolomites (thus the major reason the collection effort concentrated on porous dolomites). Pale-yellow fluorescence indicated possible high-gravity oil (figure 6.4B). If no fluorescence was observed in porous dolomites, the samples were also good representatives of areas where hydrocarbons had not migrated or accumulated. Bitumen (pyrobitumen), which has no activity within the hydrocarbon molecules and therefore does not fluoresce (figure 6.4D), was common in many samples.

As expected, productive Leadville wells (in fields such as Lisbon and Salt Wash) have cuttings distinguished by generally higher EF readings (figures 6.5 and 6.6). However, a regional southeast-northwest trend of relatively high EF from Leadville cuttings parallels the southwestern part of the Paradox fold and fault belt from Lisbon field to west of the town of Green River. A visual reading of 2.0 to 3.0 for the highest maximum

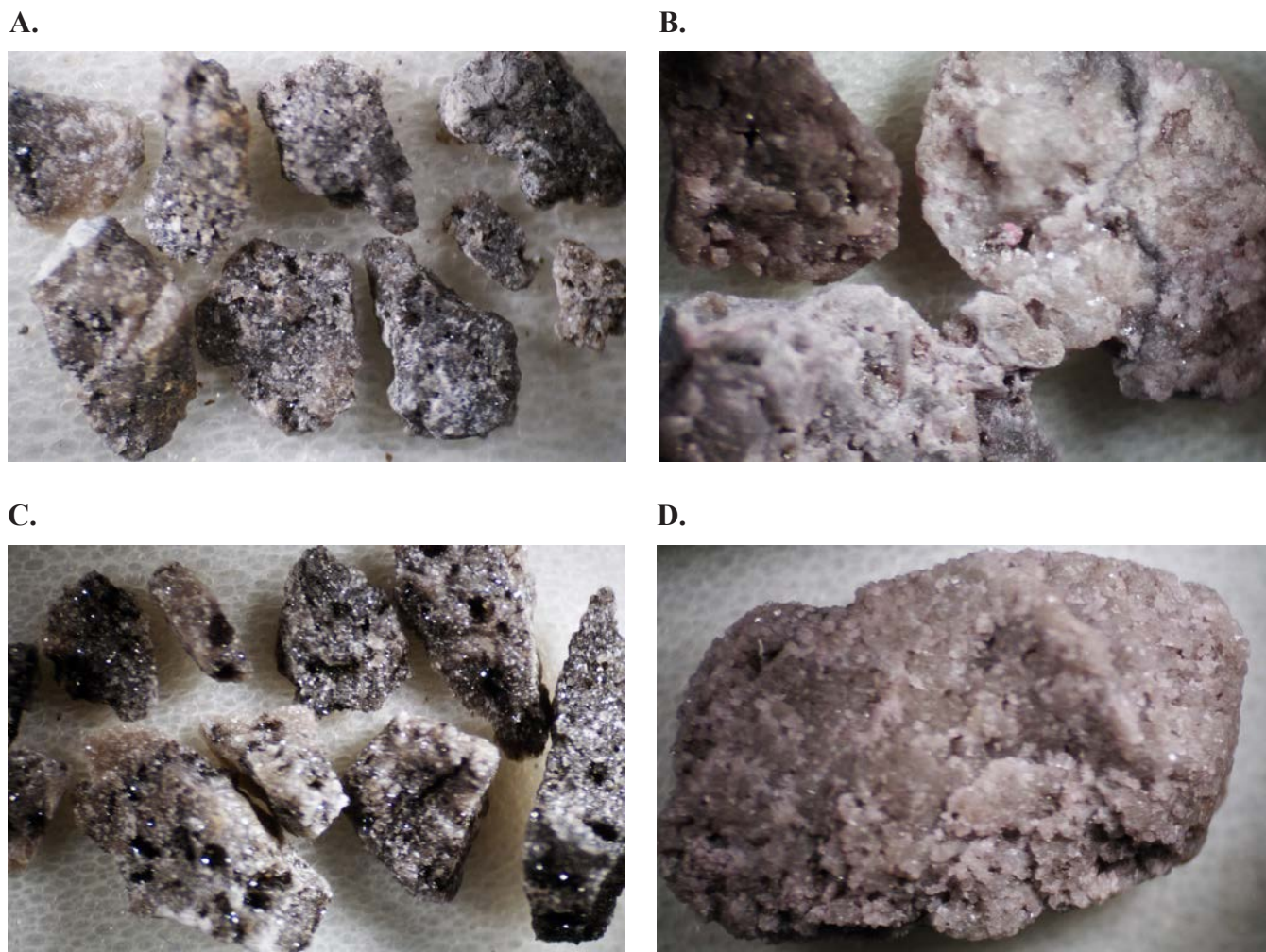


Figure 6.1. Examples of cuttings selected from various Leadville zones as observed with a binocular microscope. **(A)** Overview of dolomite cuttings (16X) from 9410 to 9420 feet (2868–2871 m) containing porosity and bitumen in the Spiller Canyon State No. 1 well (SW1/4SW1/4 section 16, T. 30 S., R. 25 E., SLBL&M, San Juan County). **(B)** Overview of dolomite cuttings (13X) from 7800 to 7810 feet (2377–2380 m) containing porosity and stylolites in the Hatch Mesa No. 1 well (SE1/4SW1/4 section 22, T. 28 S., R. 21 E., SLBL&M, San Juan County). **(C)** Overview of dolomite cuttings (12X) from 10,020 to 10,023 feet (3054–3055 m) containing porosity and bitumen in the USA Big Indian No. 1 well (SE1/4SE1/4 section 33, T. 29 S., R. 24 E., SLBL&M, San Juan County). **(D)** Single white dolomite cutting (14X) with good intercrystalline porosity from 7790 to 7800 feet (2374–2871 m) containing porosity and stylolites in the Hatch Mesa No. 1 well.

EF (figure 6.5) and 2.0 to 2.5 for the highest average EF occur in this trend, even though these values come from dry holes in this large but sparsely drilled region (figure 6.6). The northeastern part of the fold and fault belt shows a regional trend of low EF including a large area of essentially no EF (a visual reading of less than 0.4 for the maximum highest average EF) centered around the town of Moab (figure 6.6).

These EF maps imply hydrocarbon migration and dolomitization was associated with regional northwest-trending faults and fracture zones, which created potential oil-prone areas along the southwest trend as shown by high visual EF readings in the scattered dry holes (figures 6.5 and 6.6). Hydrocarbons may have migrated from organic-rich shales in the Pennsylvanian Paradox Formation where they are in contact with the Leadville Limestone along faults. Hydrothermal al-

teration associated with these faults and related fracture zones may have generated late, porous dolomite and thus produced diagenetic traps indicated by EF.

Alternative interpretations for the lack of significant EF in the northeast trend is the possibility that (1) most hydrocarbons may have been flushed out to the southwest by hydrodynamic processes, and (2) the northeastern part of the Paradox fold and fault belt has passed the oil window and gone into the dry gas/post-oil window stage maturation. A final explanation is that these EF trends could be related to facies or karst development in the Leadville Limestone. At any rate, the mapping of hydrocarbon shows based on EF indicates exploration efforts should be concentrated in suggested oil-prone areas along the southwestern part of the Paradox fold and fault belt.

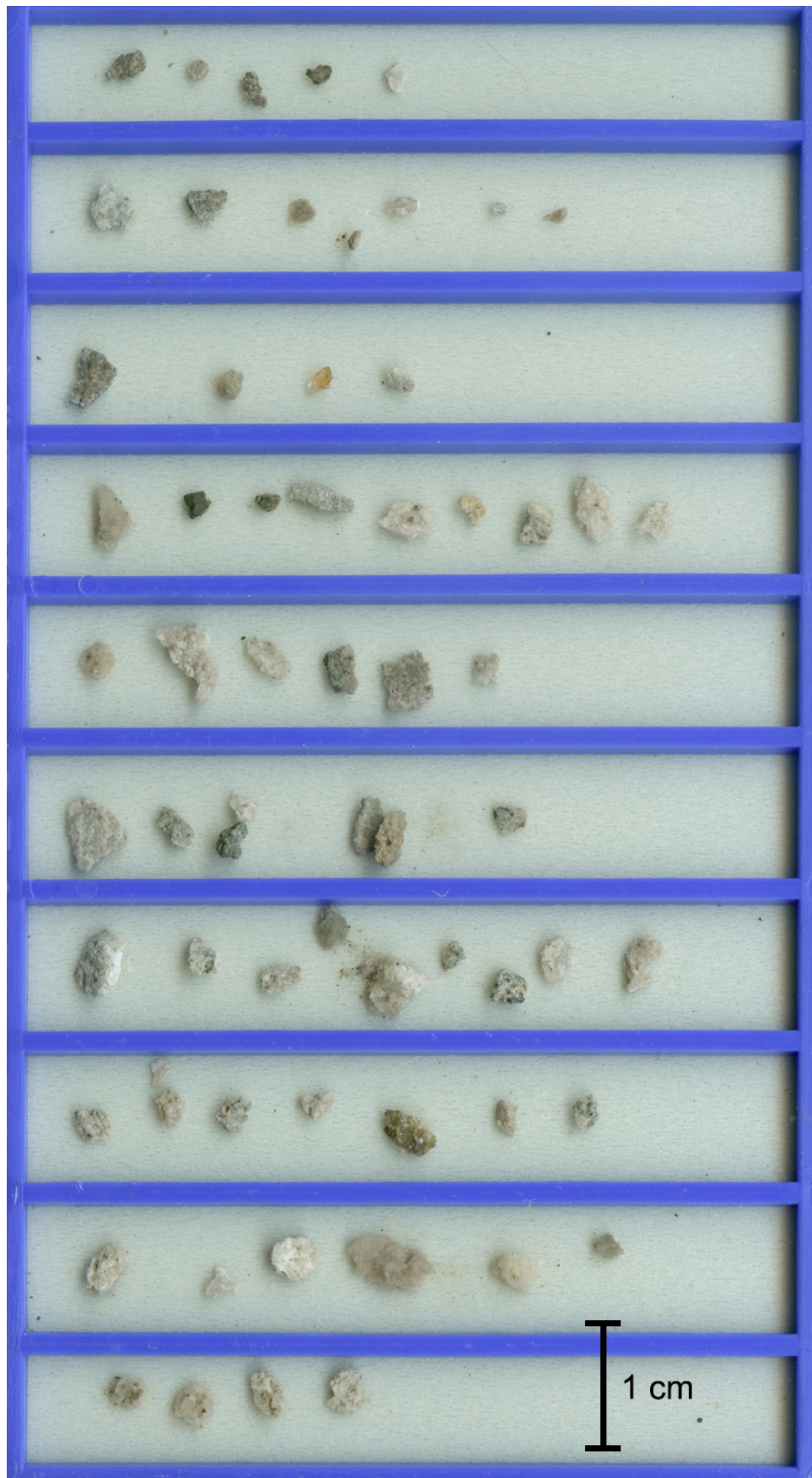


Figure 6.2. Example of cuttings selected from various Leadville zones between 6875 to 7075 feet (2096–2156 m), Mineral Point No. 1 well (section 7, T. 26 S., R. 18 E., SLBL&M, Grand County), placed on Petrologs™ for epifluorescence examination.

Table 6.1. Wells in the Paradox fold and fault belt, Utah, containing Leadville Limestone cuttings evaluated using epifluorescence techniques. *N* = number of samples.

Map #	Well Name	Location	County	Interval (ft)	N	Visual EF Rating	
						Highest Maximum	Highest Average
1	Woodside 1	SESE 12 19S 13E	Emery	6580–6750	23	1.5	1.2
2	Hatch Sphinx Unit 1-A	SWNW 35 19S 14E	Emery	8670–8715	45	1.0	0.8
3	Denison Mines 5-1	5 21S 14E	Emery	5830–5870	23	2.5	1.5
4	Salt Wash 22-34	34 22S 17E	Grand	10,070–10,085	16	0.3	0.1
5	Government Smoot 1	CSENE 17 23S 17E	Grand	8732–8737	16	2.5	2.0
6	Chaffin 1	NENW 21 23S 15E	Emery	7460–7540	26	1.5	1.2
7	Federal Hatt 1	SESE 19 23S 14 E	Emery	5905–6020	33	3.0	2.3
8	Gov 45-5	5 24S 15E	Emery	6899–6935	5	0.5	0.2
9	State 12-11	SWNW 11 24S 20E	Grand	11,810–11,850	50	1.0	0.7
10	Federal 31	NWSE 31 24S 23E	Grand	10,450–10,760	27	1.5	0.3
11	Gruvers Mesa 2	10 25S 16E	Emery	6750–6910	32	2.2	1.8
12	McRae Fed 1	SWSW 10 25S 18E	Grand	8485–8550	8	2.5	0.8
13	Bow Knot Unit 1	NESE 20 25S 17.5E	Grand	6075–6400	31	2.5	2.0
14	Big Flat/Bartlett Flat 1	NENE 26 25S 19 E	Grand	8560–8650	17	2.0	1.5
15	Lookout Point 1	SWSW 29 25S 16E	Emery	6380–6520	22	3.0	2.5
16	Fed Bowknoll 1	NESE 30 25S 18 E	Grand	7375–7390	12	2.5	1.8
17	Long Canyon 1	NENW 9 26S 20E	Grand	7560–7630	44	1.5	0.4
18	Mineral Point 1	7 26S 18E	Grand	6875–7075	65	2.5	2.0
19	Big Flat 3	NENE 23 26S 19E	Grand	7714–7725	51	1.0	0.8
20	Federal Ornsby 1	NWNE 3 27S 19E	Wayne	7740–7810	25	2.0	1.5
21	Gold Basin 1	NWNW 15 27S 24E	San Juan	14,300–14,410	37	2.0	0.8
22	Putnam 1	SENE 15 27S 22 E	San Juan	7410–7490	30	0.8	0.3
23	Unit 1 Bridger Sack Mesa	SESE 17 27S 22 E	San Juan	7030–7070	53	1.0	0.8
24	Muleshoe 1	2 28S 23E	San Juan	10,240–10,280	9	2.0	0.2
25	Lockhard Fed 1	SW 22 28S 20E	San Juan	5130–5050	37	2.5	2.0
26	Hatch Mesa 1	SESW 22 28S 21E	San Juan	7780–7820	23	2.5	1.0
27	USA Big Indian 1	NWSESE 33 29S 24E	San Juan	9960–10,090	55	1.5	1.0
28	State 1	32 29.5S 24E	San Juan	9835–9852	16	3.0	2.5
29	NW Lisbon St. A	2 30S 24E	San Juan	9710–9725	12	2.0	1.0
30	Lisbon Valley C-1	NENW 9 30S 24E	San Juan	8765–8770	20	1.5	1.0
31	Lisbon 814-A	CNWSW 14 30S 24E	San Juan	8870–8930	80	3.0	2.0
32	Spiller Canyon State 1	SWSW 16 30S 25E	San Juan	9080–9420	75	1.5	0.7

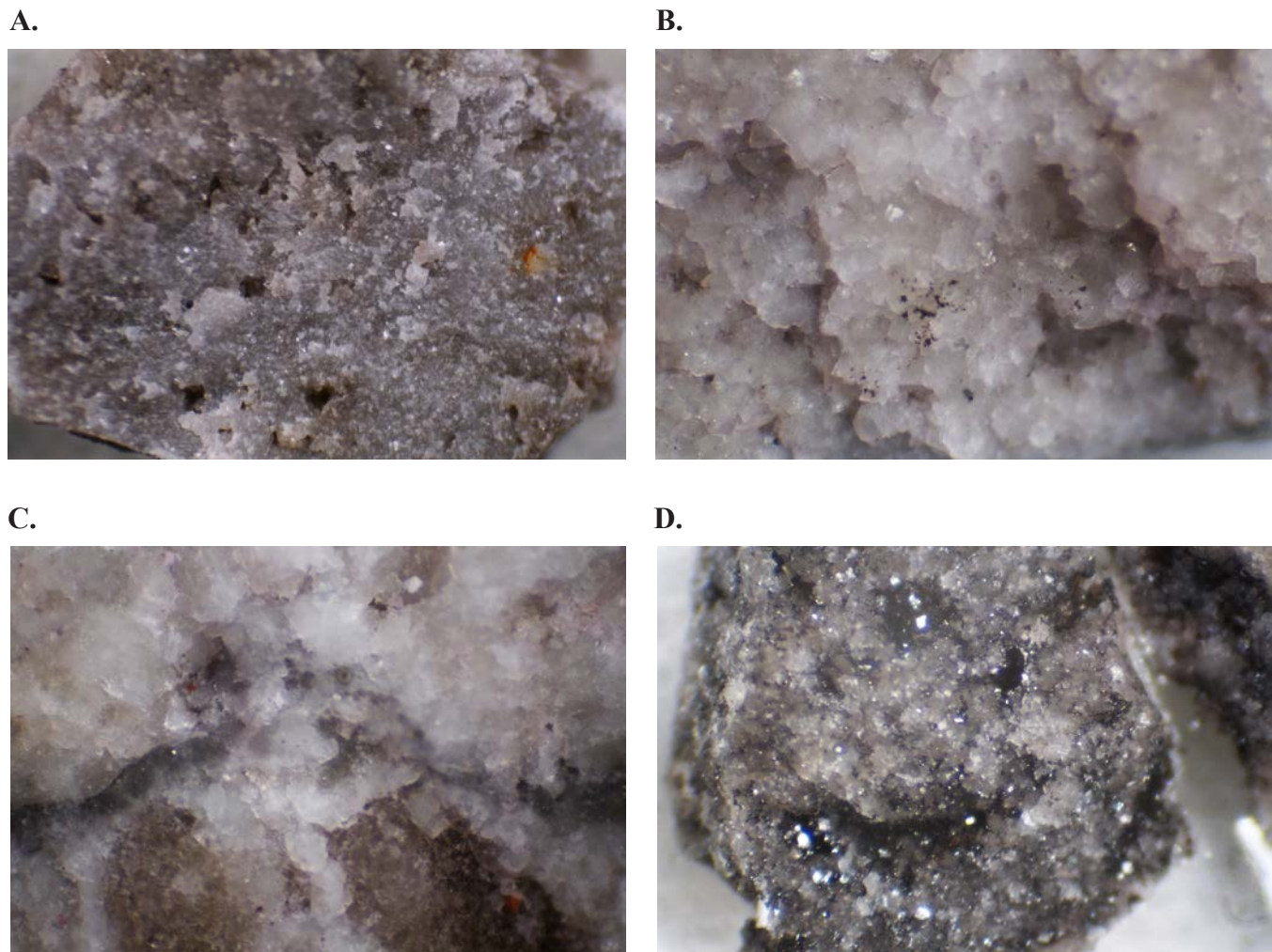


Figure 6.3. Close-up views of petrographic characteristics of Leadville cuttings as observed with a binocular microscope. **(A)** Large, single sample of low-permeability, dolomite (24X) having widely spaced small vugs from 7780 to 7790 feet (2371–2374 m) in the Hatch Mesa No. 1 well (SE1/4SW1/4 section 22, T. 28 S., R. 21 E., SLBL&M, San Juan County). **(B)** Sample of white dolomite (45X) that has good intercrystalline porosity from 7790 to 7800 feet (2371–2871 m) contain porosity and bitumen in the Hatch Mesa No. 1 well; note possible sulfide replacement (opaque). **(C)** Sample (45X) showing stylolite overprinted with dolomite replacement from 7800 to 7810 feet (2371–2380 m) in the Hatch Mesa No. 1 well; note possible sulfide replacement. **(D)** Sample showing dolomite (45X) containing small vugs and intercrystalline porosity lined with bitumen from 10,020 to 10,023 feet (3054–3055 m) in the USA Big Indian No. 1 well (SE1/4SE1/4 section 33, T. 29 S., R. 24 E., SLBL&M, San Juan County).

Table 6.2. Key to the epifluorescence qualitative visual “rating” scale.

Rating	Generalized Interpretation
0–0.5	No Fluorescence: Not capable of oil production. May be wet, if not a gas-bearing zone.
1.0–1.5	Weak Fluorescence: An “oil” show. Indicative of oil in the system, but not necessarily capable of production. Some dull or weak fluorescence may exist in a wet zone (especially if there is “speckled” fluorescence) or in a mixed oil/water zone.
2.0–2.5	Moderate Fluorescence: A good indication of oil within this zone. Probably capable of some oil production if there is adequate porosity and permeability.
3.0–3.5	Bright Fluorescence: A very good to excellent indication of oil within this zone. Should be capable of some oil production if there is adequate porosity and permeability.
3.5–4.0	Very Bright, Intense Fluorescence: Also a very good to excellent indication of oil within this zone. However, some very bright fluorescence may indicate very low permeability, oil-bearing rocks or mature, oil-generating source rocks.

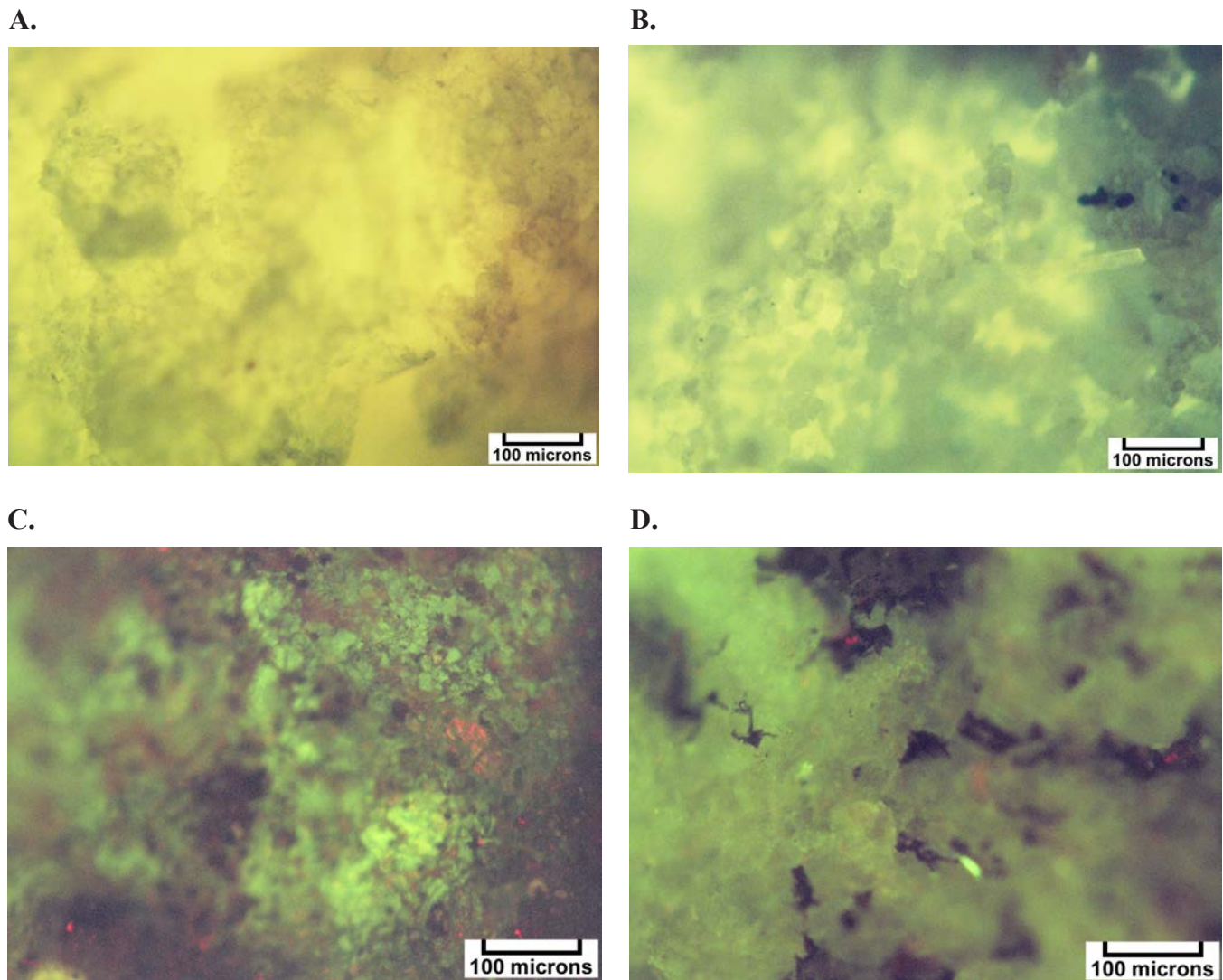


Figure 6.4. Photomicrographs under moderate magnification showing examples of visually rated epifluorescence. **(A)** Bright fluorescence, rated 3.0, in medium crystalline dolomite with fair to good intercrystalline porosity from 5935 to 5945 feet (1809–1812 m) in the Federal Hatt No. 1 well (SE1/4SE1/4 section 19, T. 23 S., R. 14 E., SLBL&M, Emery County). **(B)** Moderate fluorescence, rated 2.0, fine- to medium-crystalline dolomite from 10,240 to 10,250 feet (3121–3124 m) in the Muleshoe No. 1 well (section 2, T. 28 S., R. 23 E., SLBL&M, San Juan County). **(C)** Weak fluorescence, rated 1.0, medium- to coarse-crystalline dolomite with fairly good bitumen-lined, intercrystalline porosity from 9150 to 9160 feet (2789–2792 m) in the Spiller Canyon No. 1 well (SW1/4SW1/4 section 16, T. 30 S., R. 25 E., SLBL&M, San Juan County); note abundant iron distribution (red), bitumen is black. **(D)** No to very weak fluorescence, rated 0.2, medium- to coarse-crystalline dolomite containing bitumen and iron from 10,020 to 10,023 feet (3054–3055 m) in the USA Big Indian No. 1 well (SE1/4SE1/4 section 33, T. 29 S., R. 24 E., SLBL&M, San Juan County).

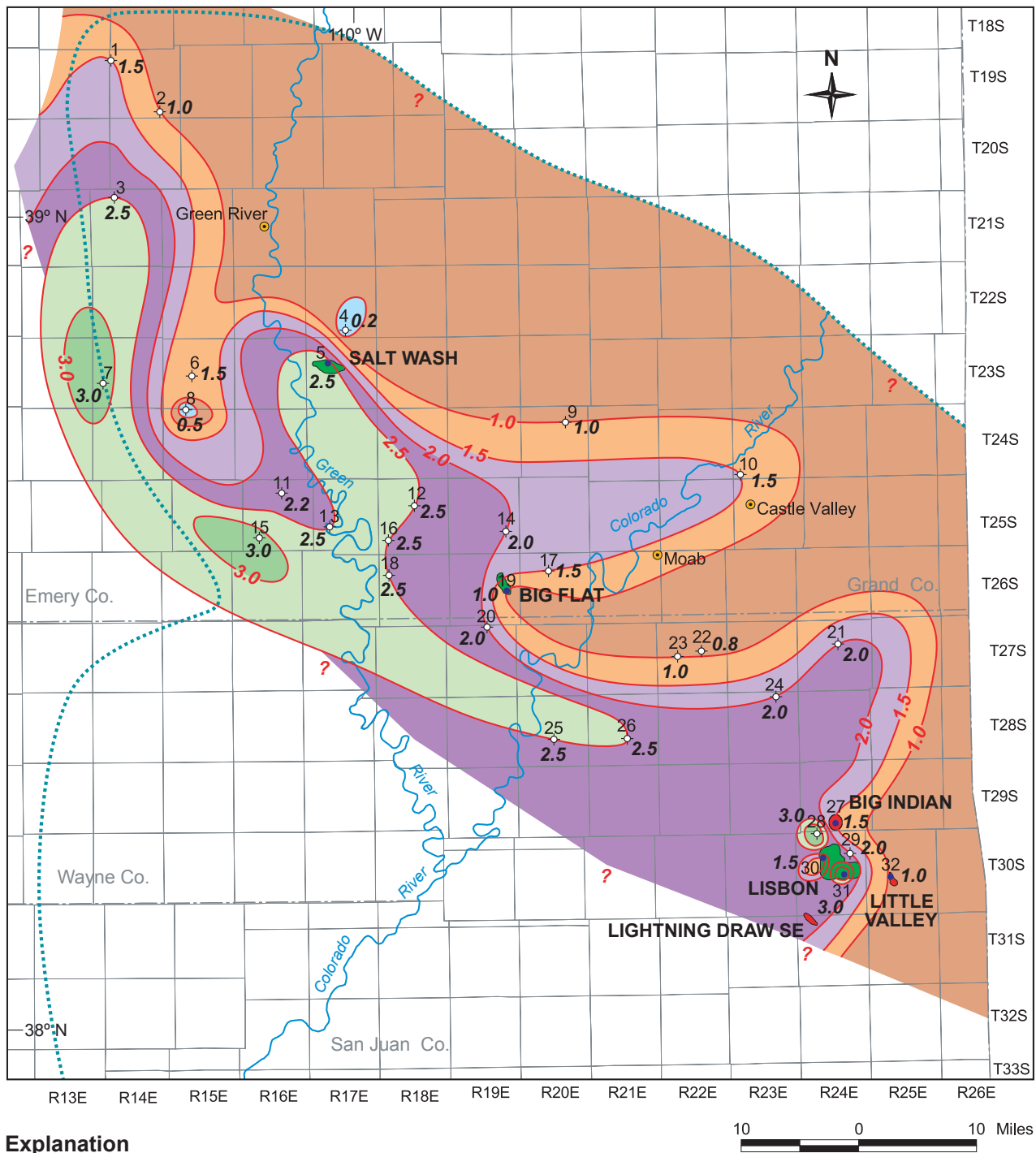
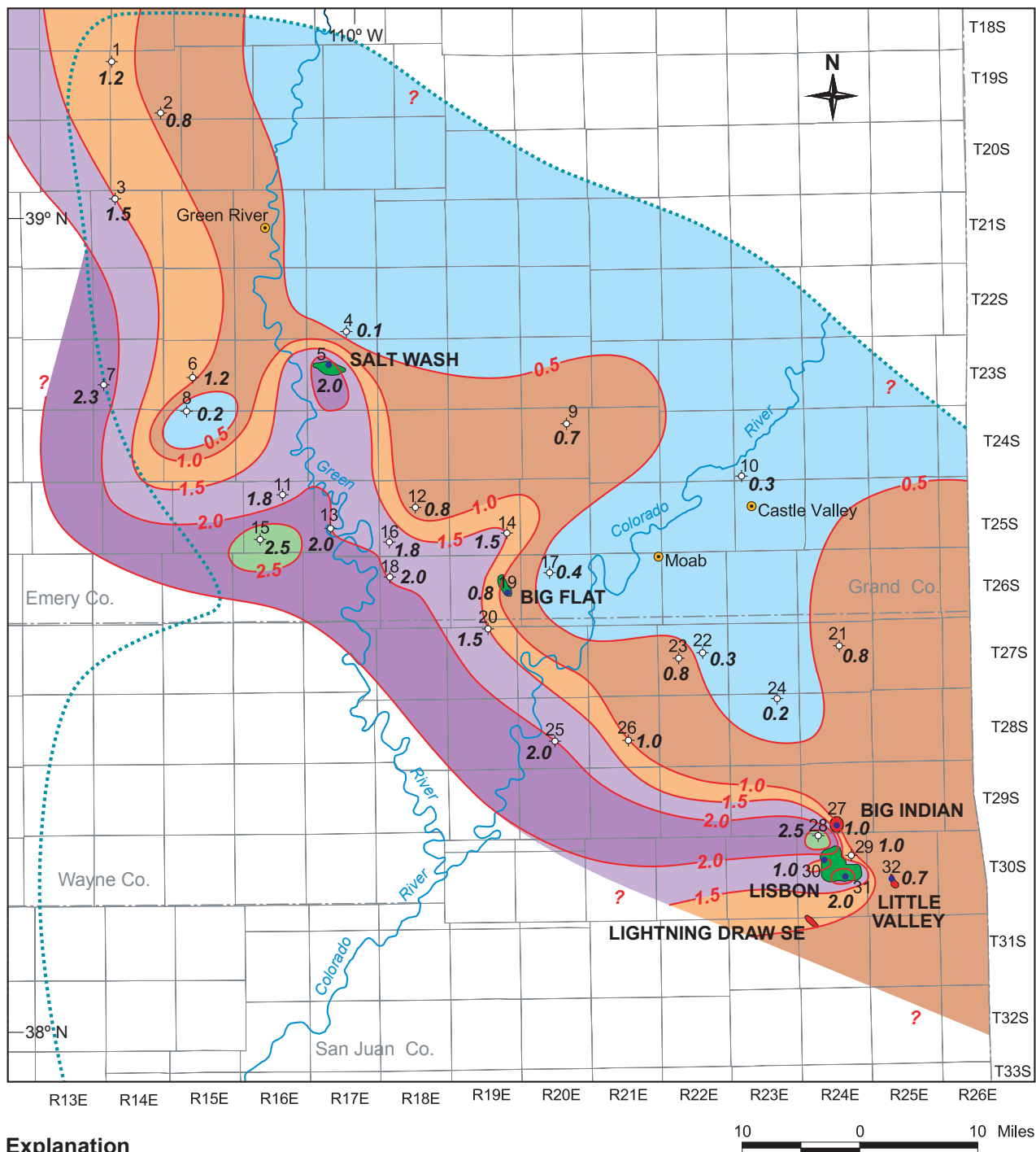


Figure 6.5. Map of the highest maximum epifluorescence based on visual rating of well cuttings, Paradox fold and fault belt, Utah.



Explanation

Color code	Epifluorescence/visual rating	Generalized interpretation	Symbol	Description
Light Blue	0-0.5	No fluorescence	◇	Dry oil and gas exploratory well
Orange	0.5-1.5	Weak fluorescence	●	Oil well
Purple	1.5-2.5	Moderate fluorescence (potential target)	●	Gas field
Green	2.5-3.5	Bright fluorescence (good target)	●	Oil field
			●	Town site
			Paradox Basin boundary

Figure 6.6. Map of the highest average epifluorescence based on visual rating of well cuttings, Paradox fold and fault belt, Utah.

CHAPTER 7: DEVONIAN/MISSISSIPPIAN AND PENNSYLVANIAN BRINE CHEMISTRY AND TRENDS WITHIN THE PARADOX BASIN, UTAH

by

J. Wallace Gwynn (retired), Utah Geological Survey

CHAPTER 7:

DEVONIAN/MISSISSIPPIAN AND PENNSYLVANIAN BRINE CHEMISTRY AND TRENDS WITHIN THE PARADOX BASIN, UTAH

INTRODUCTION

The focus of this chapter is the chemistry and changes in chemistry of the brines found in the Devonian/Mississippian and Pennsylvanian formations in the Paradox Basin. From analyses of this information inferences can be made as to the migration history, including possible pathways and direction, of hydrocarbons in the Leadville Limestone.

Chemical data for Devonian/Mississippian and Pennsylvanian oil-well brines from the Paradox Basin were obtained from published literature; Utah Division of Oil, Gas and Mining files; oil companies; and various other sources (Breit, no date; Gwynn, 1995). These data include analyses from production, drill-stem, swab, and other types of well tests. Considerable effort was expended to ensure that the analyses from Gwynn (1995) were within a mole imbalance of less than 5%. The mole imbalances of the samples from Breit (no date) were not determined. Data are displayed as (1) histograms to show the elevation intervals of the samples, (2) Piper and Stiff diagrams to show the distribution of the major cations and anions, and (3) scatter plots overlain by best-fit lines to show the north-to-south variations of these ions within the Paradox Basin.

Previous studies on the brine chemistry of the Paradox Basin include those of Hanshaw and Hill (1969), Huntoon (1979), Howells (1990), and Spangler and others (1996). Howells (1990) provides detailed information on the stratigraphy within San Juan County, including the maximum reported strata thickness, lithology, and hydrologic characteristics and significance of the various formations. Spangler and others (1996) provide information on the hydrology, chemical quality, and salinity in the Jurassic Navajo Sandstone aquifer in the Greater Aneth field area in the southern Paradox Basin (figure 1.1), which is the largest oil field in Utah having produced over 496 million bbls of oil from the Pennsylvanian Paradox Formation (Utah Division of Oil, Gas and Mining, 2020).

BRINE CHEMISTRY

Devonian/Mississippian Brines

Most of the Devonian/Mississippian samples were taken from the northern part of the Paradox Basin within Grand, Emery, Wayne, and San Juan Counties (figure 7.1). A few samples are

from the southern part of the Paradox Basin (the southeastern corner of San Juan County) in the Greater Aneth field area. The elevation of the “top of the sampled interval” for most of the samples lies within the -4000 (subsea) to 2000-foot (-1200–600 m) elevation interval (figure 7.2). This elevation range is much broader than for the Pennsylvanian samples, but the sampled intervals for the northern and southern areas are probably much different.

The distribution of the chemical composition of the Devonian/Mississippian brine samples is shown in the Piper and Stiff diagrams for the Devonian, Mississippian, and combined Devonian and Mississippian samples (figures 7.3 and 7.4). The cation components of the brines are predominantly sodium (Na) with minor amounts of calcium (Ca) and magnesium (Mg). The anion components in the brine are dominantly chloride (Cl) and a small number of brine samples have relatively high concentrations of sulfate (SO₄). Bicarbonate (HCO₃) is uniformly very low in these brines. Brines departing from the general trends occur mainly in San Juan and Wayne Counties.

Scatter plots (figures 7.5 and 7.6) show the elevation of the top of the sample interval, the chemistry of the samples (as individual ions), and total dissolved solids (TDS) versus their UTM northing positions (from 4,325,000 on the north to 4,075,000 on the south). Fifth-degree polynomial best-fit lines indicate data trends from north (left) to south (right) through the length of the Paradox Basin. However, the plotted data shows considerable spread away from the best-fit lines, especially for (1) Na from north to south through the basin (figure 7.5B), (2) Mg and Cl in northern San Juan County (figures 7.5C and 7.6A, respectively), and (3) Ca in southern San Juan County (figure 7.5D).

Pennsylvanian Brines

Most of the Pennsylvanian brine samples were collected from the southern part of the Paradox Basin (the southeastern corner of San Juan County), in and around the Greater Aneth and Bug fields (figure 7.7). A few scattered samples are also from within or near the central and northern parts of the basin. The top of the sampled interval for most of the samples lies at about zero to 1000 feet (0–300 m) above mean sea level (figure 7.8).

The distribution of the chemical composition of the Pennsylvanian brine samples is shown on Piper and Stiff diagrams

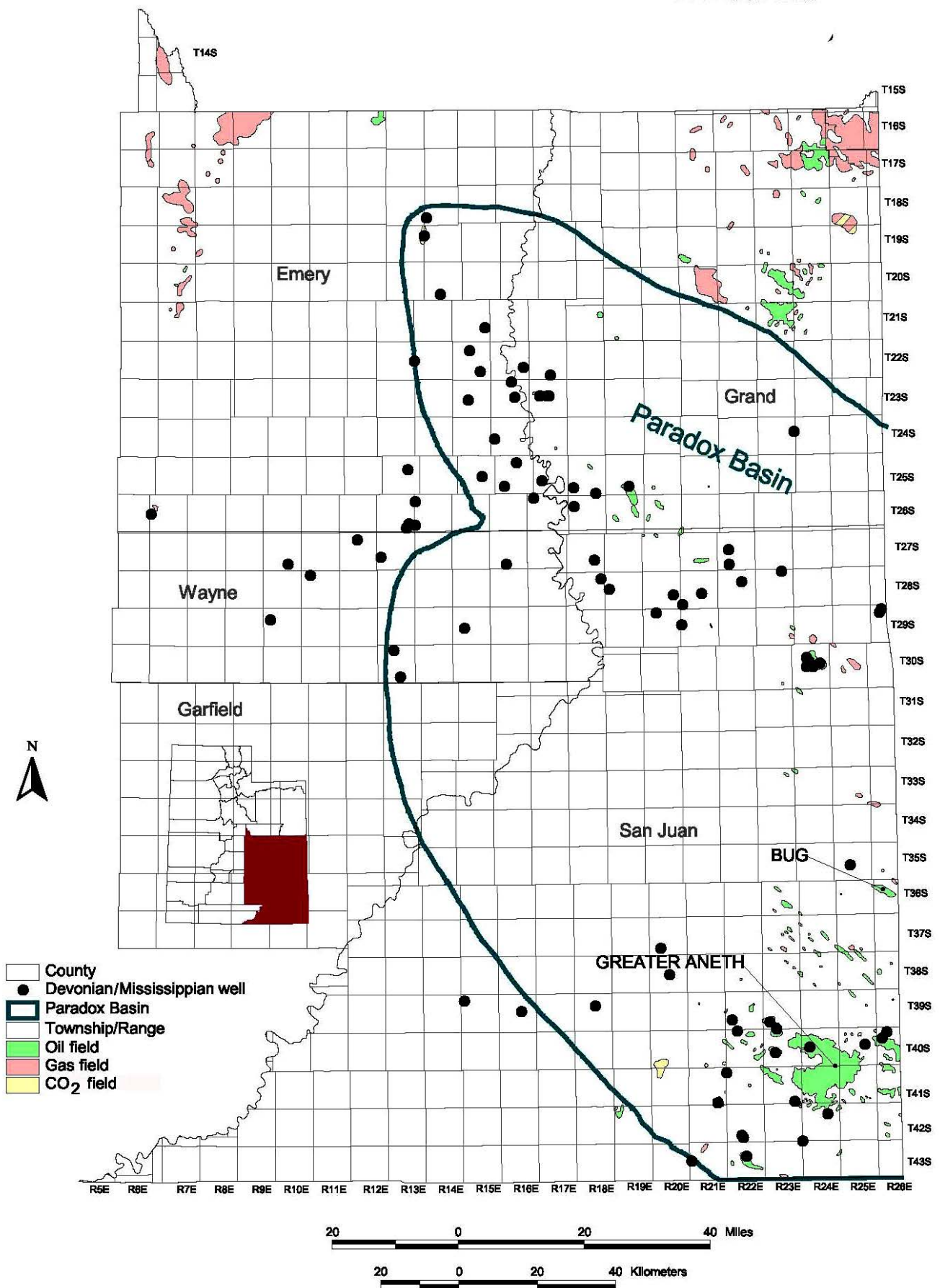


Figure 7.1. Wells used for Devonian/Mississippian brine analyses and oil and gas fields in the Paradox Basin and vicinity, Utah.

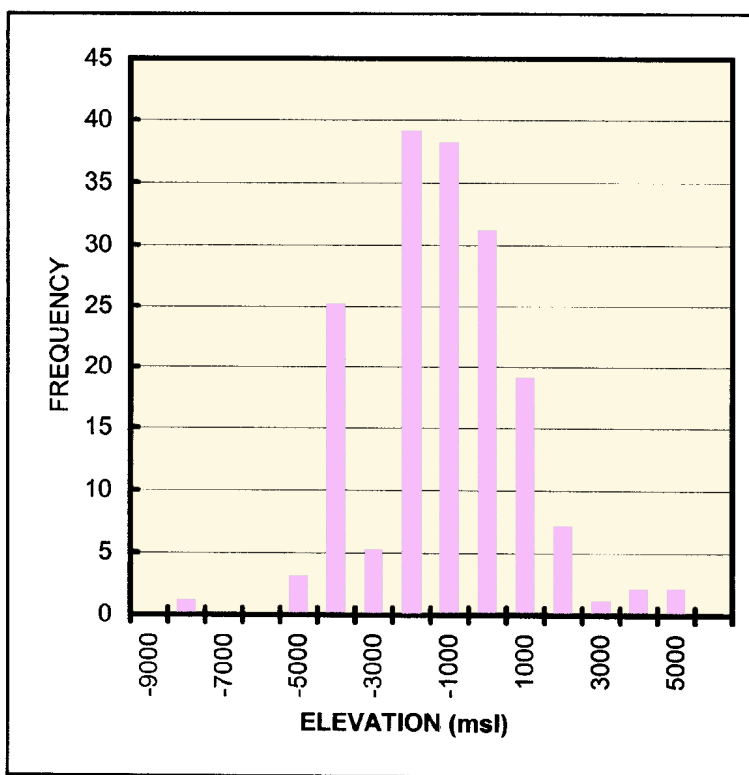


Figure 7.2. Elevation (feet) of the top of the sampled interval for the Devonian/Mississippian brine samples. msl = mean sea level.

(figures 7.9 and 7.10). The cations in most brine samples are Na-rich with a few samples containing greater percentages of Ca and to a lesser extent Mg. The anion components in the brine are Cl dominated and a smaller number of samples contain relatively high concentrations of SO_4 . Bicarbonate is very low in these brines. Brines departing from the general trends are found mainly in San Juan and Wayne Counties. The high salinity of Pennsylvanian brines is probably due to their association with the bedded salts in the Paradox Formation (figures 1.2 and 5.1).

Based on scatter plots (figures 7.11 and 7.12), the few Pennsylvanian samples present in the northern part of the Paradox Basin suggest lower concentrations of Na, Mg, Ca, Cl, TDS, and higher SO_4 as compared to brine samples from the Bug and Greater Aneth field areas. The elevation of the top of the sampled interval in the northern part of the basin is somewhat lower than it is in the vicinity of Bug field, but higher than in the Greater Aneth field area. However, like that of the Devonian/Mississippian brines shown on figures 7.5 and 7.6, the plotted Pennsylvanian brine data shows considerable spread away from the best-fit lines.

Sodium, Mg, Ca, Cl, and TDS concentrations approach a maximum value in the area of Bug field, and then show decreasing concentration southward through the Greater Aneth field area. Bicarbonate and SO_4 concentrations both reach minimum values between Bug field and the Greater Aneth field area, but then rise southward toward T. 43 S., SLBL&M.

DIRECTION OF BRINE MOVEMENT

Hanshaw and Hill (1969) provided a detailed discussion of the geochemistry and hydrodynamics of the Paradox Basin region and included potentiometric maps of the Mississippian Leadville Limestone; the Pennsylvanian Pinkerton Trail, Paradox, and Honaker Trail Formations of the Hermosa Group; and the Permian formations. In their discussion, they summarized the areas of recharge and movement of groundwater as follows:

The principal areas of recharge to aquifers in the Paradox Basin are the west flank of the San Juan Mountains and the west flank of the Uncompahgre uplift. The direction of groundwater movement in each unit studied [Mississippian rocks, Pinkerton Trail Limestone, Paradox Member of the Hermosa Formation, Honaker Trail Formation, and the Permian formations] is principally southwestward toward the topographically low outcrop areas along the Colorado River in Arizona. However, at any point in the basin, flow may be in some other direction owing to the influence of intrabasin recharge areas or local obstructions to flow, such as faults or dikes. Many structurally and topographically high areas within the basin are above the regional potentiometric surface; recharge in these areas will drain rapidly off the highs and adjust to the regional water level.

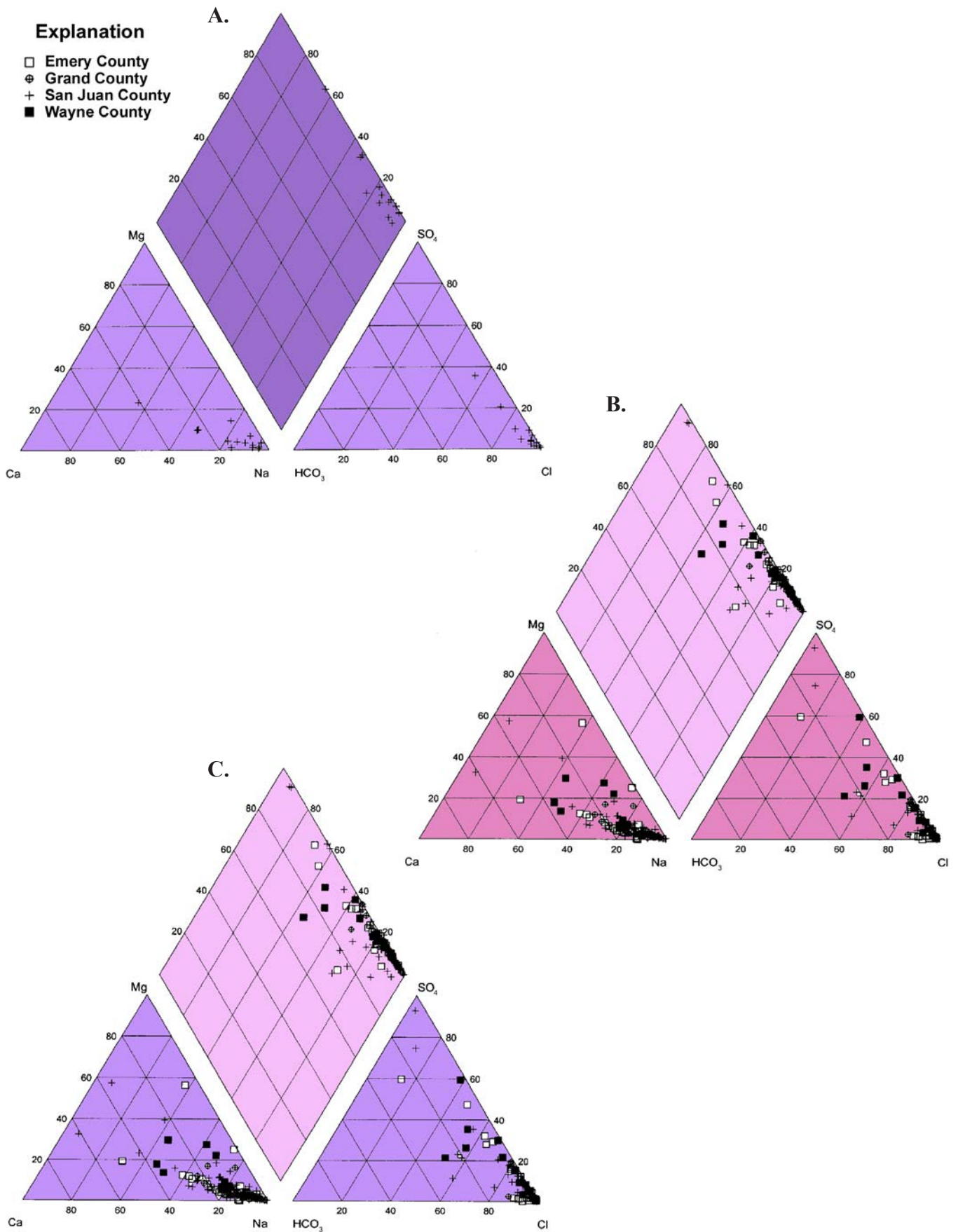


Figure 7.3. Piper diagrams showing the composition of (A) Devonian brines, (B) Mississippian brines, and (C) Devonian and Mississippian brines combined, in the Paradox Basin and vicinity, Utah.

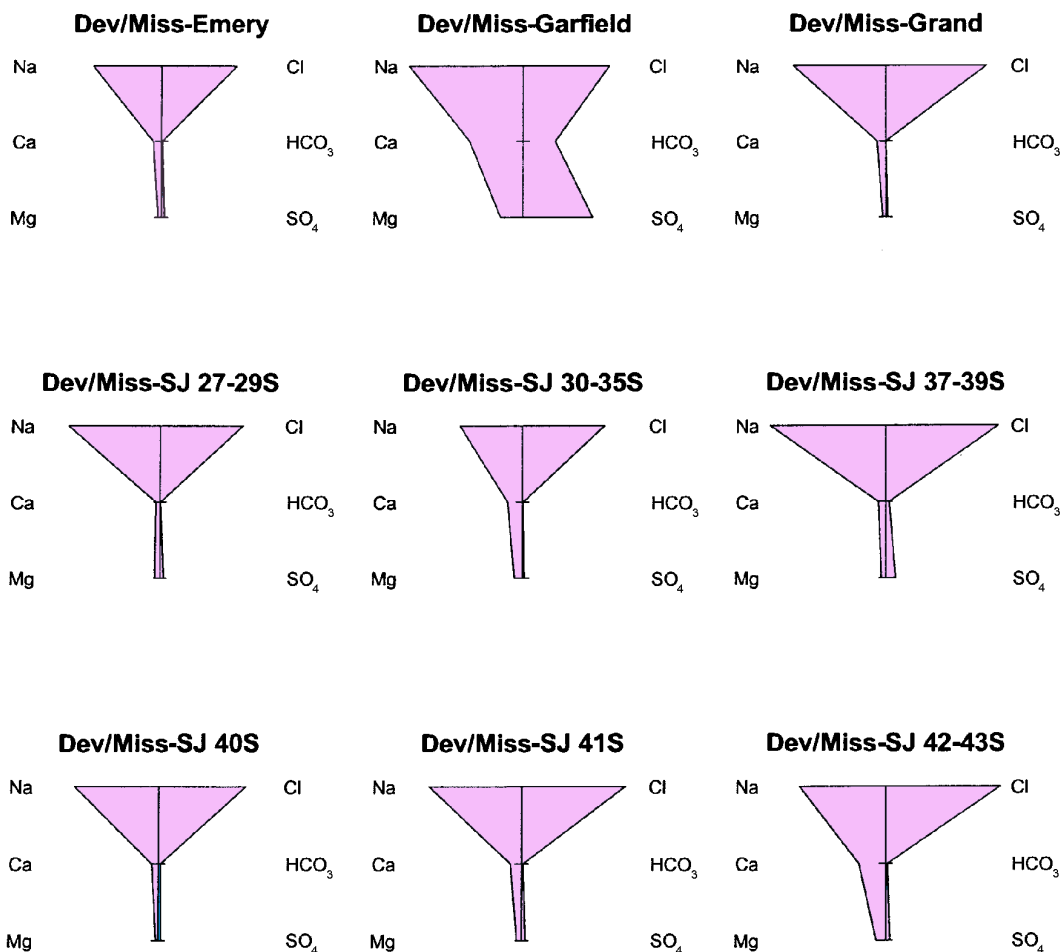


Figure 7.4. Stiff diagrams for Devonian and Mississippian (Dev/Miss) brines combined by county (SJ = San Juan County) and township interval within the range indicated above the diagram.

SUMMARY

Table 7.1 gives averaged values for ground elevation, top and bottom elevation of the sampled interval, TDS, and ions for individual counties, and for township intervals within San Juan County. Based on the data in table 7.1, the following can be said:

1. For Devonian/Mississippian brines, the samples from Grand County have the highest average TDS values, followed by San Juan, Emery, and Garfield. For Pennsylvanian brines, the samples from Grand County also have the highest average TDS of all the counties in the study area, followed by San Juan, Emery, and Wayne.
2. The Na, Mg, Ca, and Cl contents of the Pennsylvanian brines are consistently higher, in a given county or township interval (for instance T. 40 S., SLBL&M, in San Juan County), than the Devonian/Mississippian brines in the same interval, whereas the average values for SO₄ and HCO₃ are lower.
3. Piper and Stiff diagrams (figures 7.3A, 7.3B, 7.4, 7.9, and 7.10) show that the brines in both the Devonian/Mississippian and Pennsylvanian systems are mainly NaCl in nature, with end-member samples whose cations contain

about 70% Ca and 30% Mg, and whose anion makeup approaches a high-SO₄ brine. Scatter plots (figures 7.5, 7.6, 7.11, and 7.12) show that these end-member brines are found south of the Greater Aneth field area.

A comparison of the various average chemistries in table 7.1 is difficult to visualize because of the varied salt concentrations of the samples. Table 7.2 gives these data on a dry-weight basis. Based on these data, the following conclusions can be drawn regarding the Devonian/Mississippian and Pennsylvanian brine chemistries in the various counties:

1. The Devonian/Mississippian brines from Grand, Emery, and San Juan Counties are very similar, even though the TDS concentration of the Grand County brines is considerably higher than either Emery or San Juan County. Garfield County brines, like the Wayne County brines, are totally dissimilar.
2. The Pennsylvanian brines from Grand and San Juan Counties are very similar, even though the TDS concentration of the Grand County brines is considerably higher. The brines from Emery and Wayne Counties are not similar to the brines of the other two counties, and the brines from Wayne County are totally dissimilar.

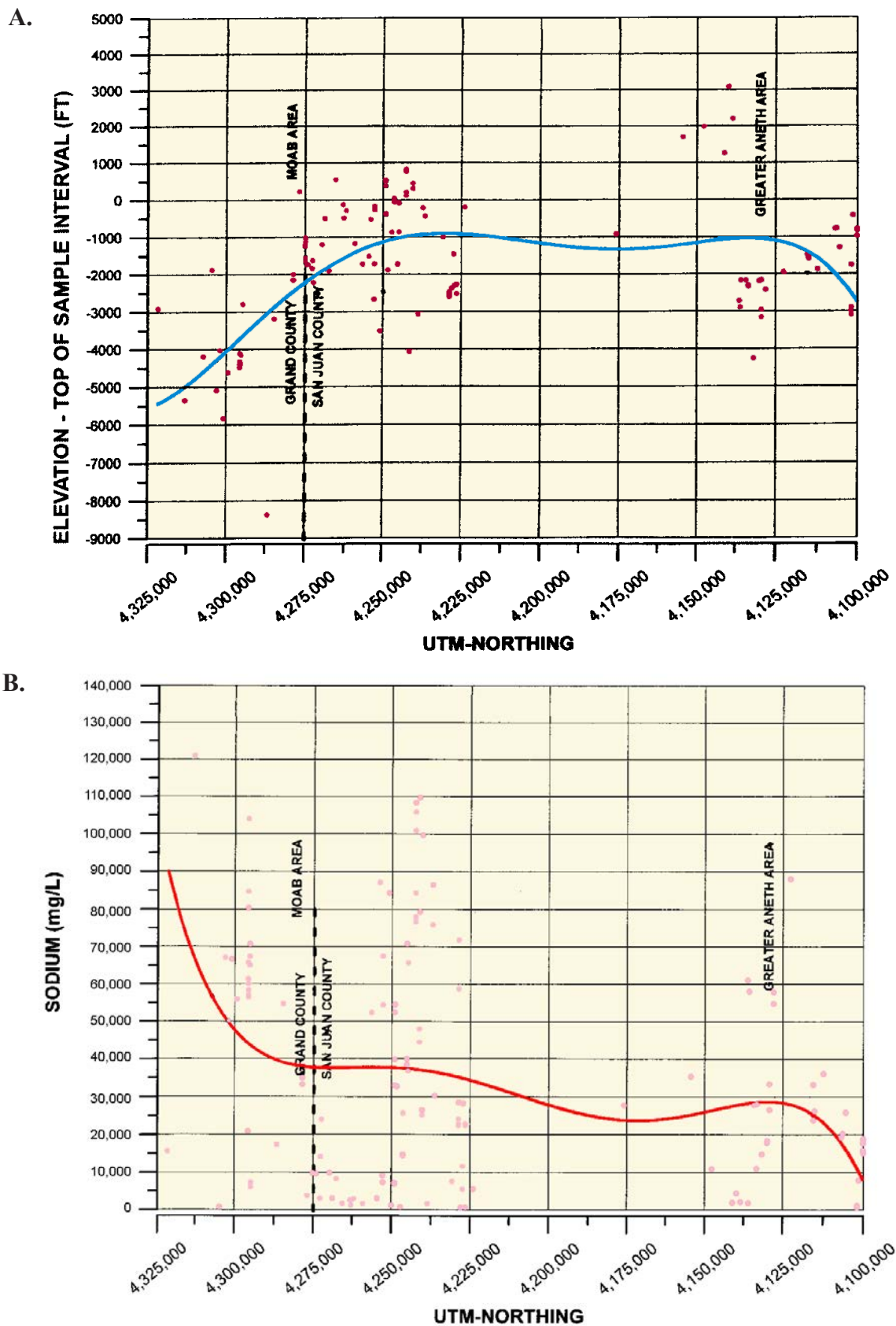


Figure 7.5. Scatter plots showing the elevation of the top of the sample interval (A), and sodium (B), magnesium (C), and calcium (D) concentrations versus geographic location (UTM-northing) for the Devonian/Mississippian samples. Fifth-degree polynomial best-fit lines indicate data trends from north (left) to south (right) through the length of the Paradox Basin. The general Greater Aneth and Moab areas are shown, as well as the Grand-San Juan County line.

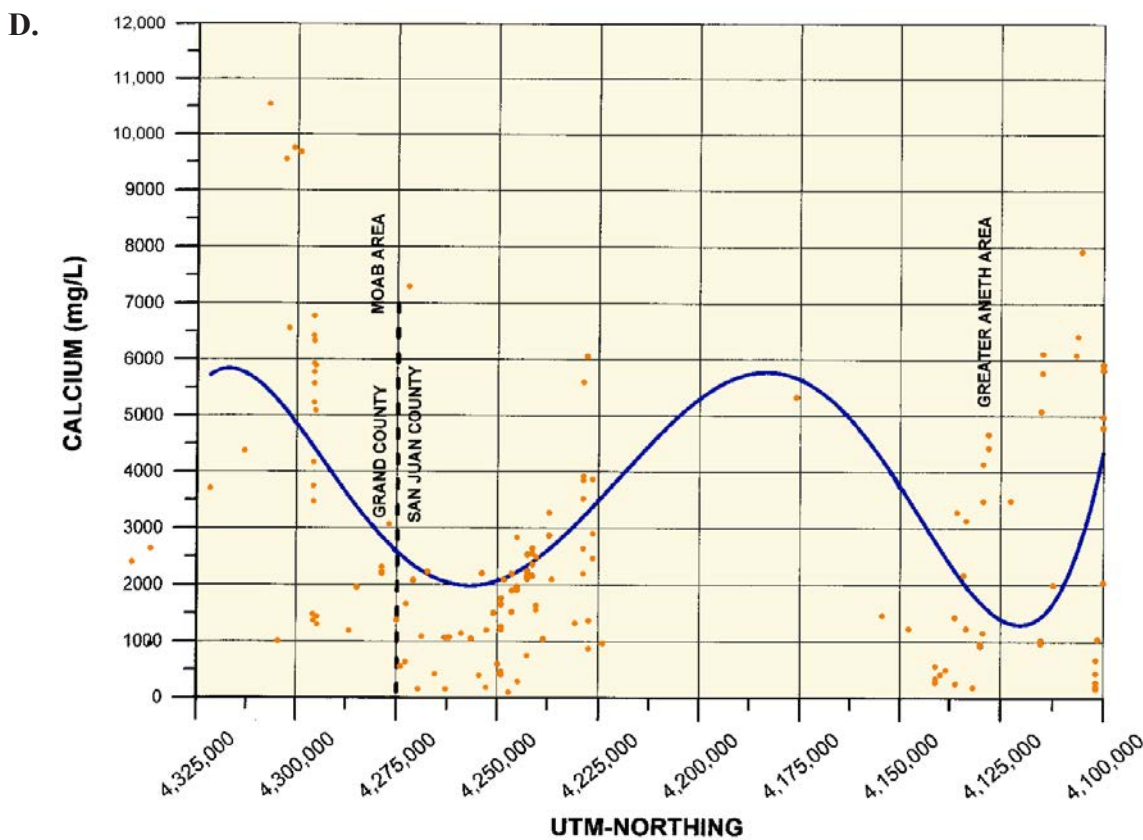
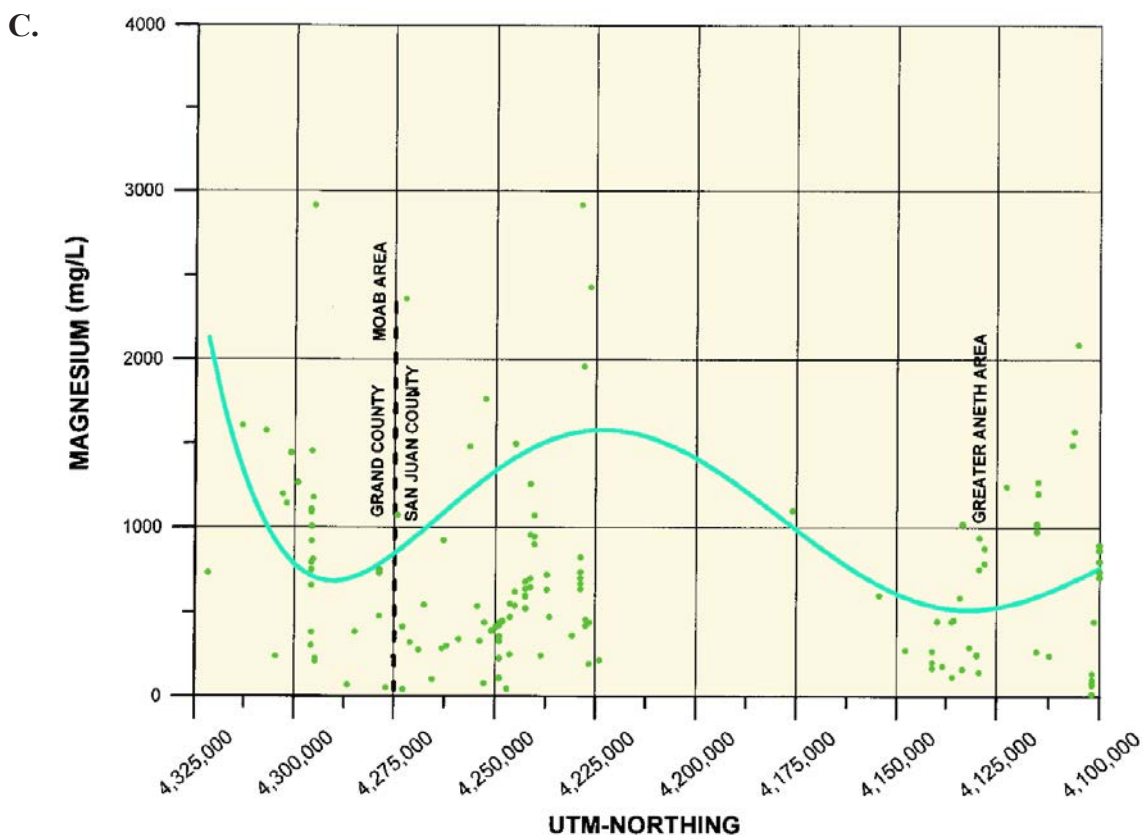


Figure 7.5 continued. Scatter plots showing the elevation of the top of the sample interval (A), and sodium (B), magnesium (C), and calcium (D) concentrations versus geographic location (UTM-northing) for the Devonian/Mississippian samples. Fifth-degree polynomial best-fit lines indicate data trends from north (left) to south (right) through the length of the Paradox Basin. The general Greater Aneth and Moab areas are shown, as well as the Grand-San Juan County line.

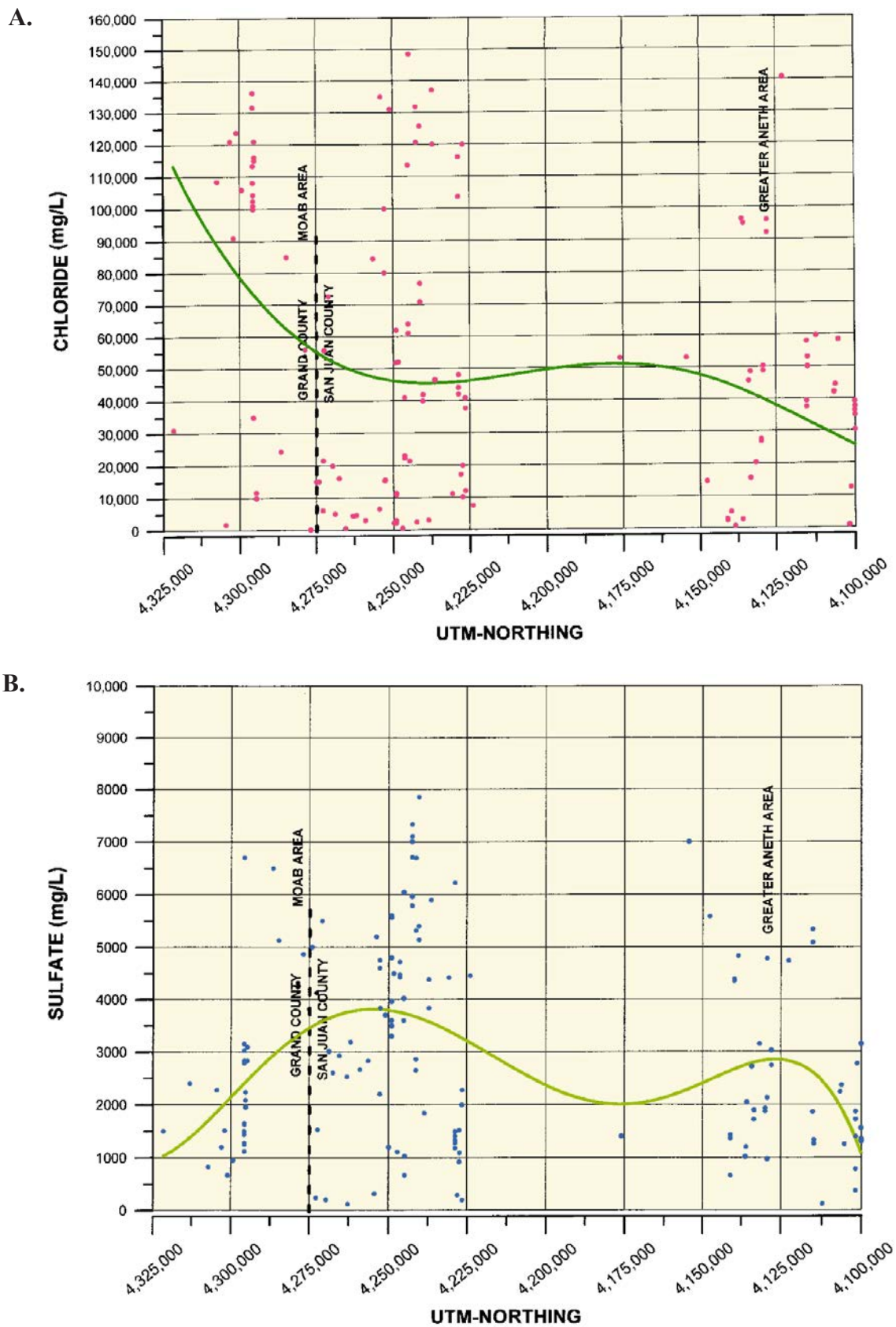


Figure 7.6. Scatter plots of chloride (A), sulfate (B), bicarbonate (C), and total dissolved solids (D) concentrations versus geographic location (UTM-northing) for the Devonian/Mississippian samples. Fifth-degree polynomial best-fit lines indicate data trends from north (left) to south (right) through the length of the Paradox Basin. The general Greater Aneth and Moab areas are shown, as well as the Grand-San Juan County line.

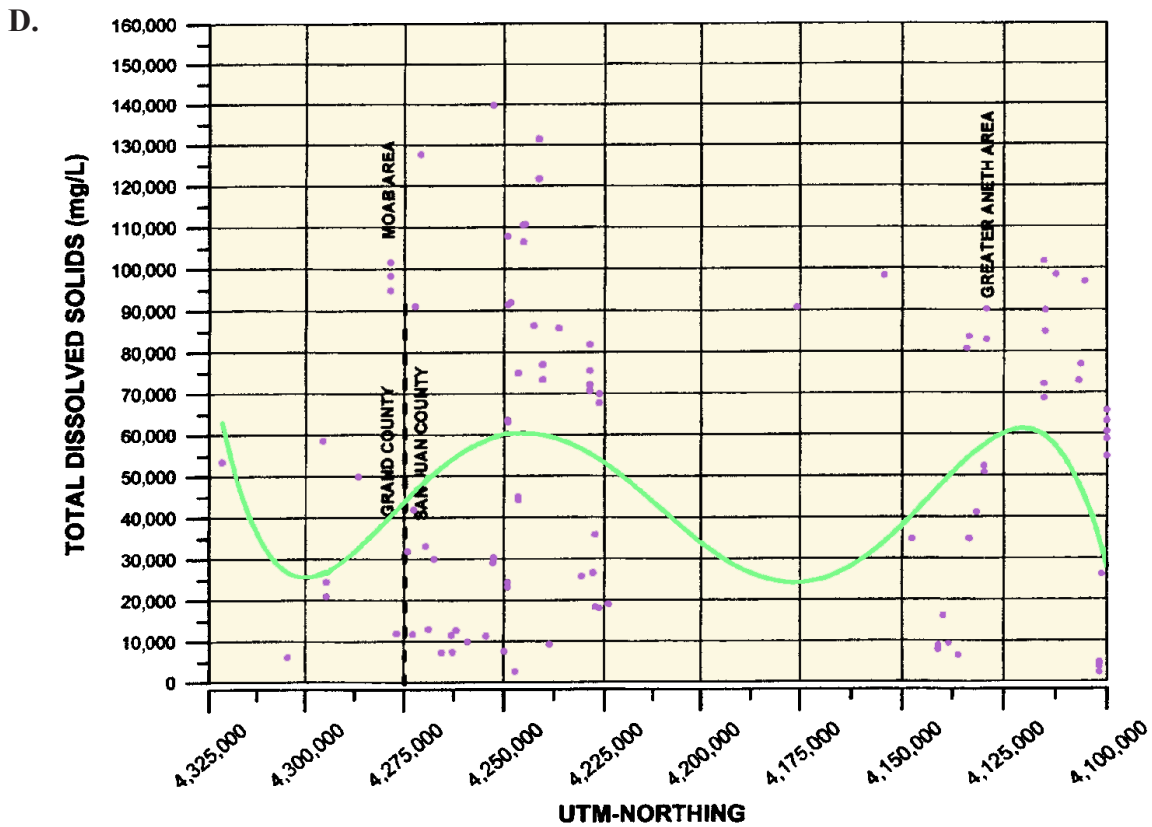
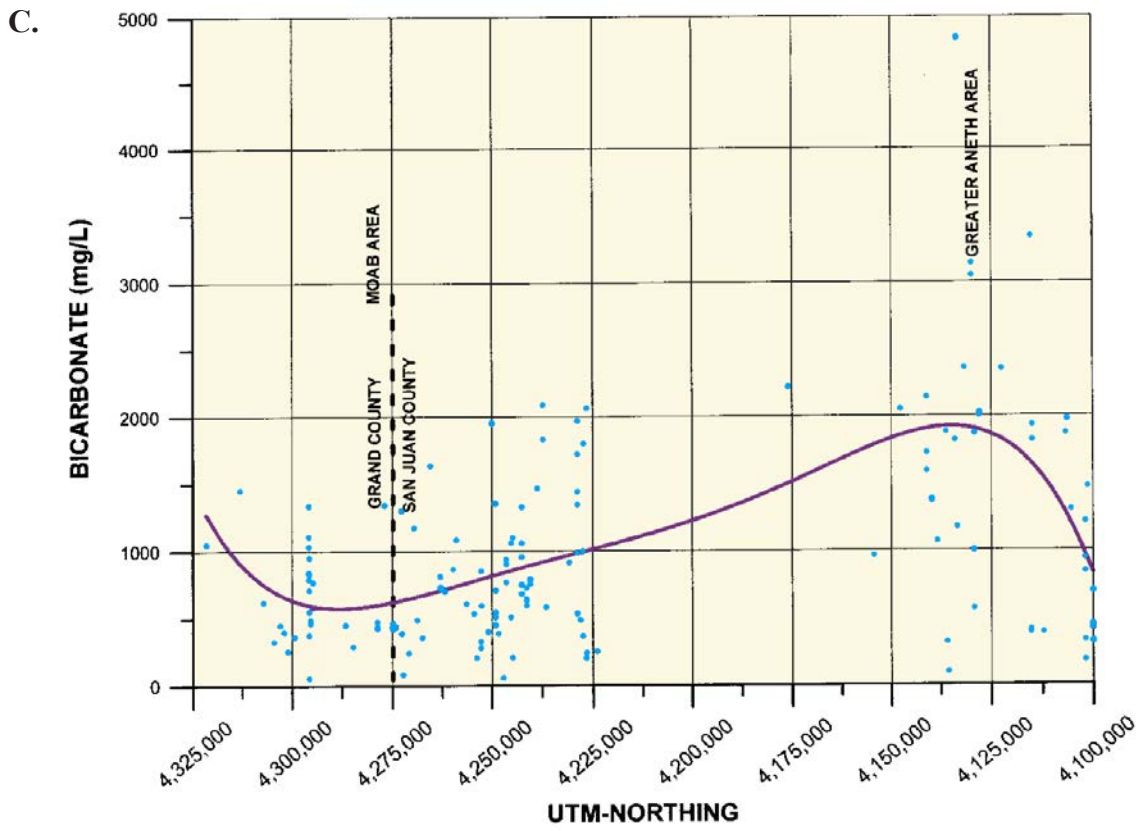


Figure 7.6 continued. Scatter plots of chloride (A), sulfate (B), bicarbonate (C), and total dissolved solids (D) concentrations versus geographic location (UTM-northing) for the Devonian/Mississippian samples. Fifth-degree polynomial best-fit lines indicate data trends from north (left) to south (right) through the length of the Paradox Basin. The general Greater Aneth and Moab areas are shown, as well as the Grand-San Juan County line.

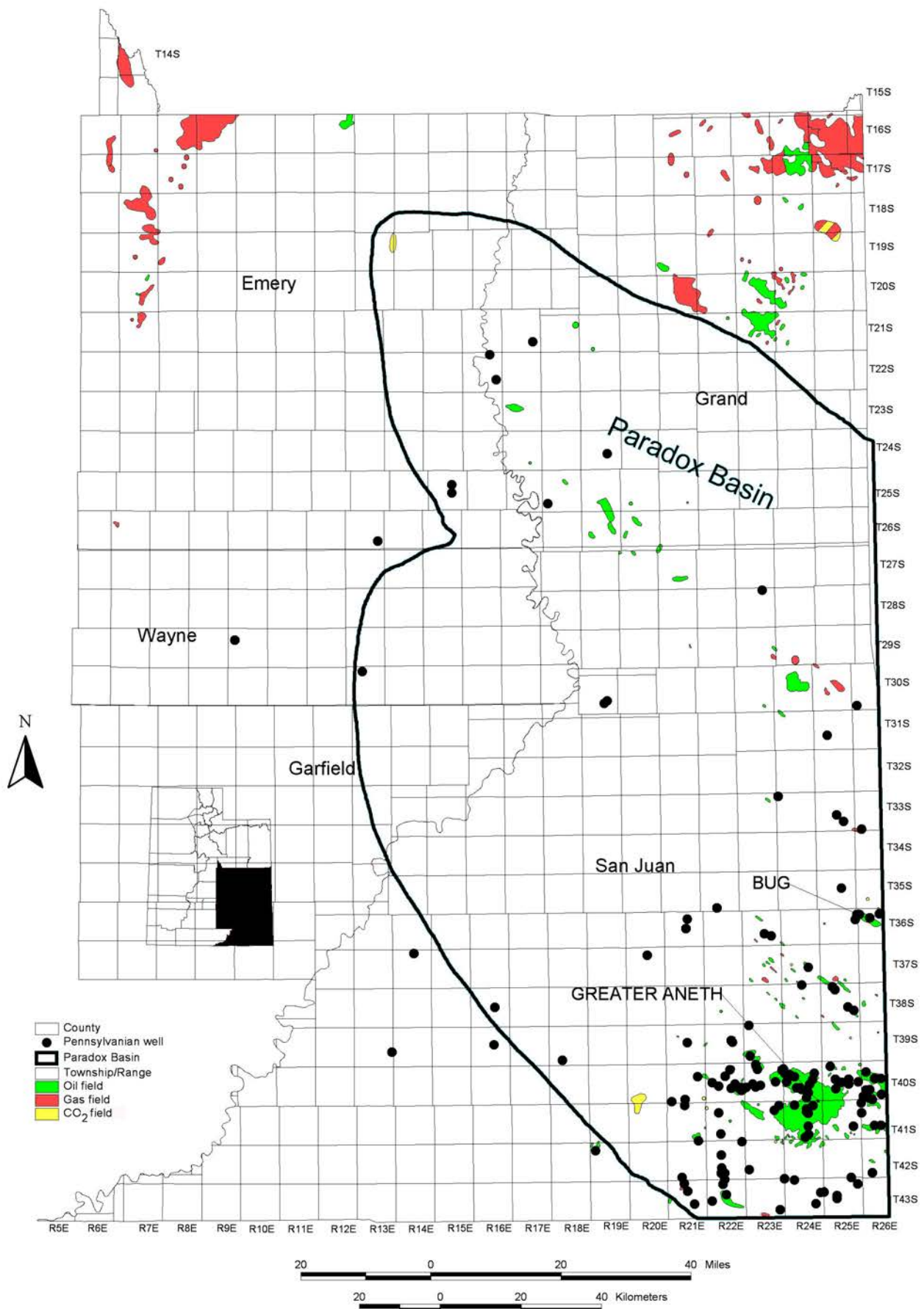


Figure 7.7. Wells used for Pennsylvania brine analyses and oil and gas fields in the Paradox Basin and vicinity, Utah.

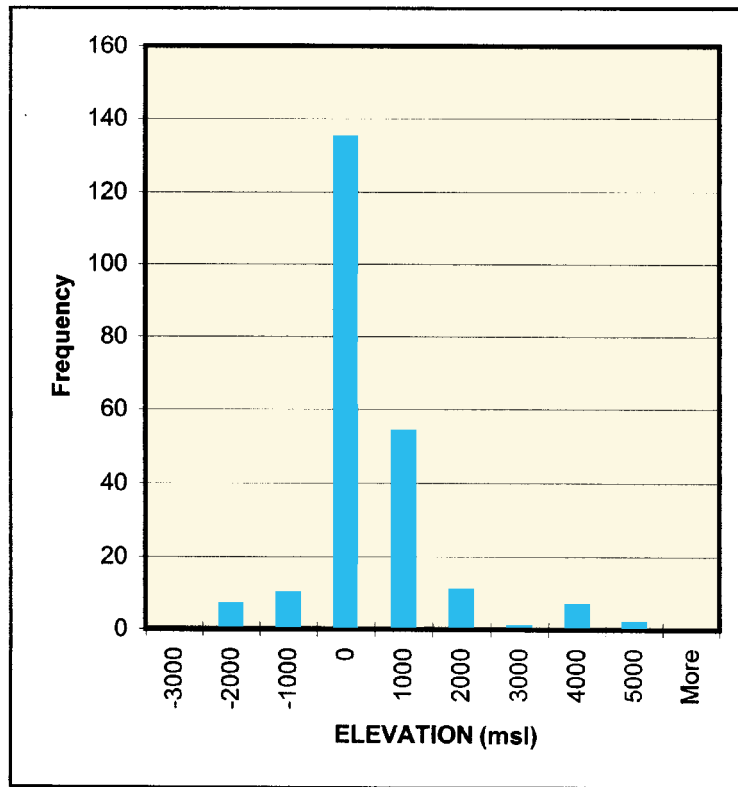


Figure 7.8. Elevation (feet) of the top of sampled interval for Pennsylvanian brine samples. msl = mean sea level.

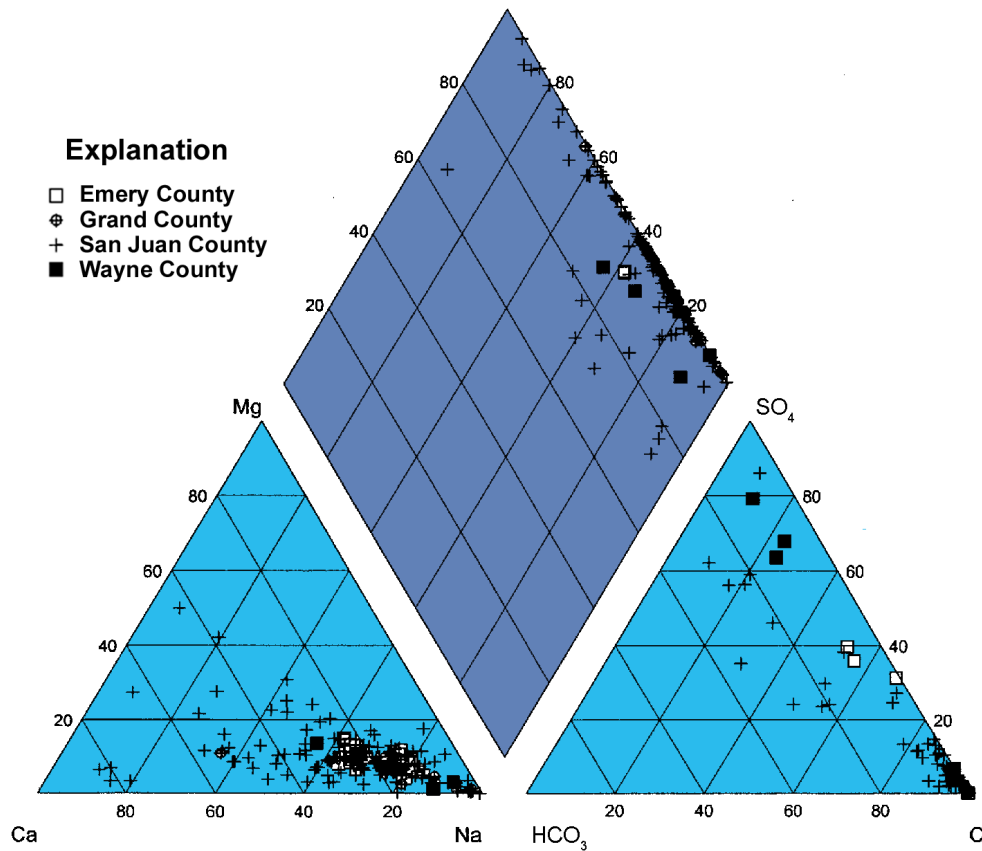


Figure 7.9. Piper diagram showing the chemical composition of the Pennsylvanian brines in the Paradox Basin by county.

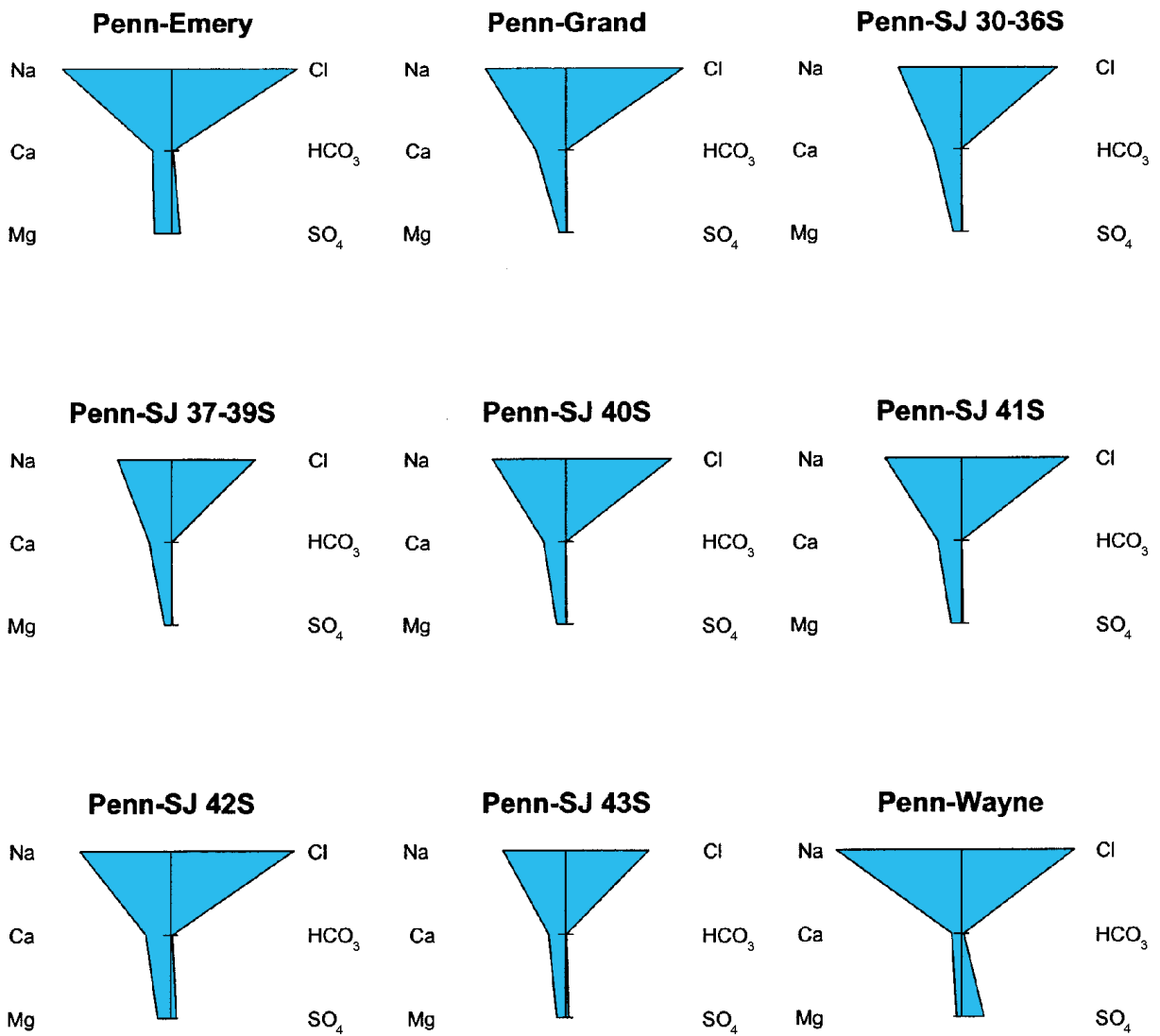


Figure 7.10. Stiff diagrams for Pennsylvanian (Penn) brines by county (SJ = San Juan County) and township interval within the range indicated above the diagram.

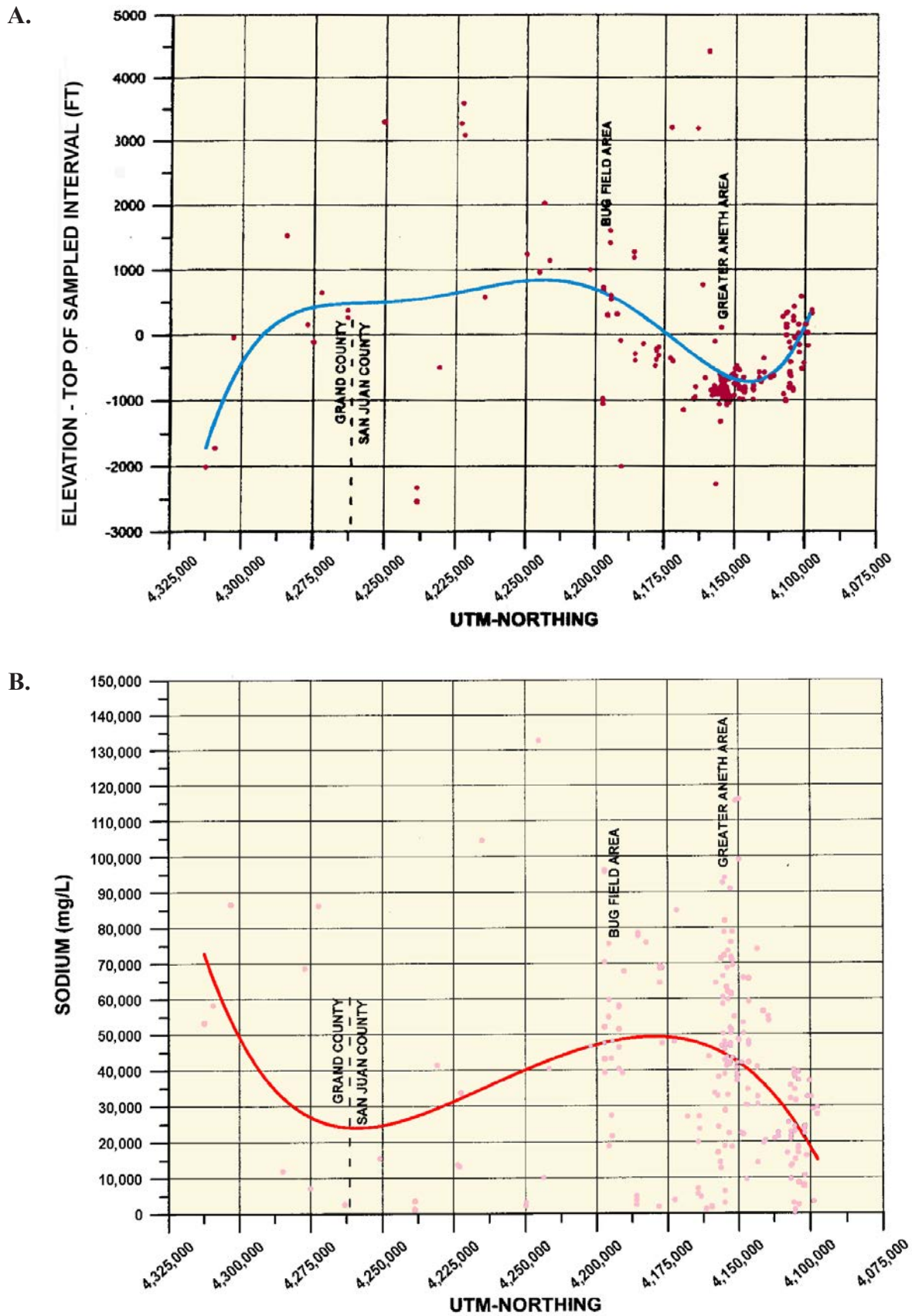


Figure 7.11. Scatter plots showing the elevation of the top of the sample interval (A), and sodium (B), magnesium (C), and calcium (D) concentrations versus geographic location (UTM northing) for the Pennsylvanian samples. Fifth-degree polynomial best-fit lines indicate data trends from north (left) to south (right) through the length of the Paradox Basin. The general areas of the Greater Aneth and Bug fields are shown, as well as the Grand-San Juan County line.

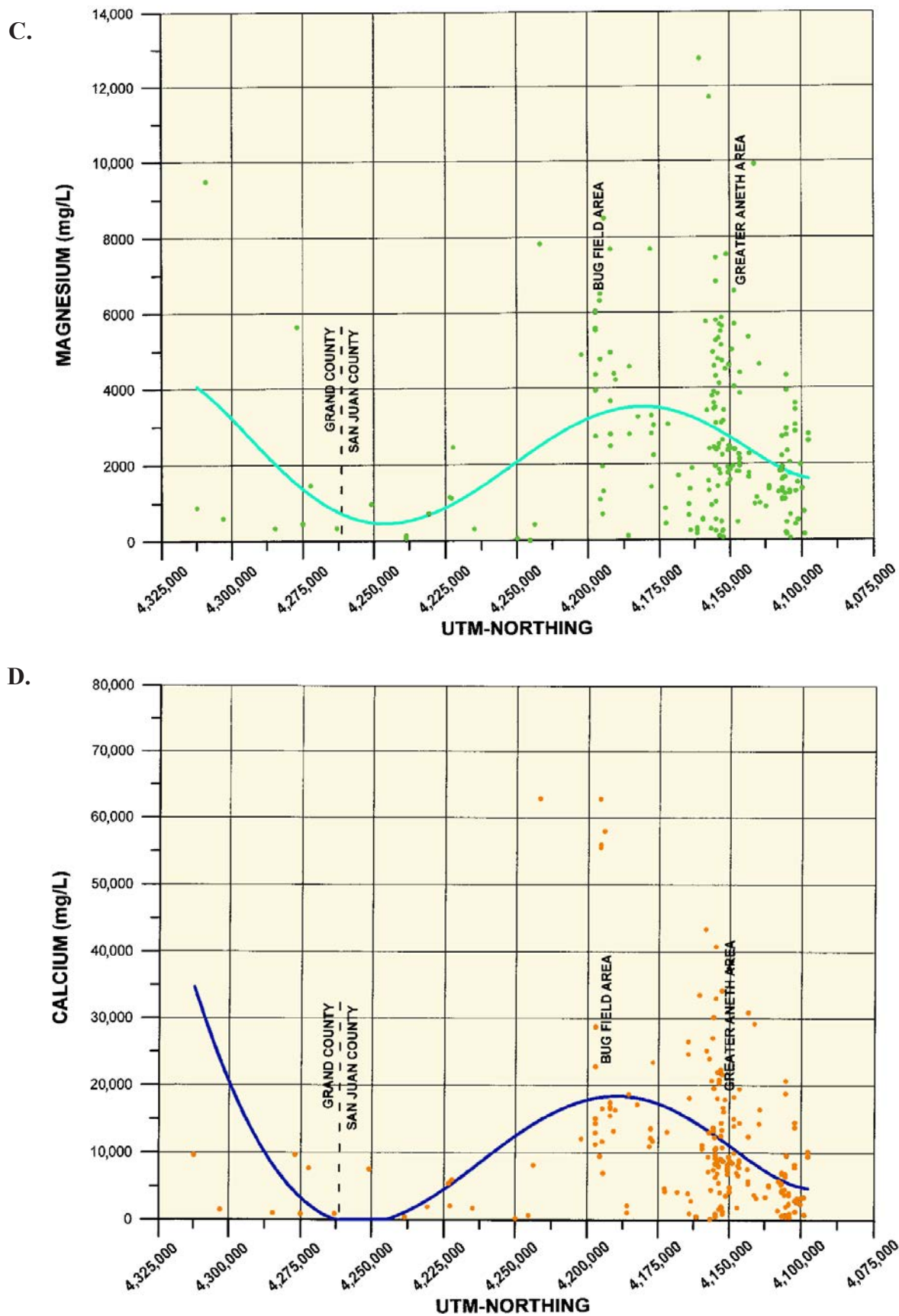


Figure 7.11 continued. Scatter plots showing the elevation of the top of the sample interval (A), and sodium (B), magnesium (C), and calcium (D) concentrations versus geographic location (UTM northing) for the Pennsylvanian samples. Fifth-degree polynomial best-fit lines indicate data trends from north (left) to south (right) through the length of the Paradox Basin. The general areas of the Greater Aneth and Bug fields are shown, as well as the Grand-San Juan County line.

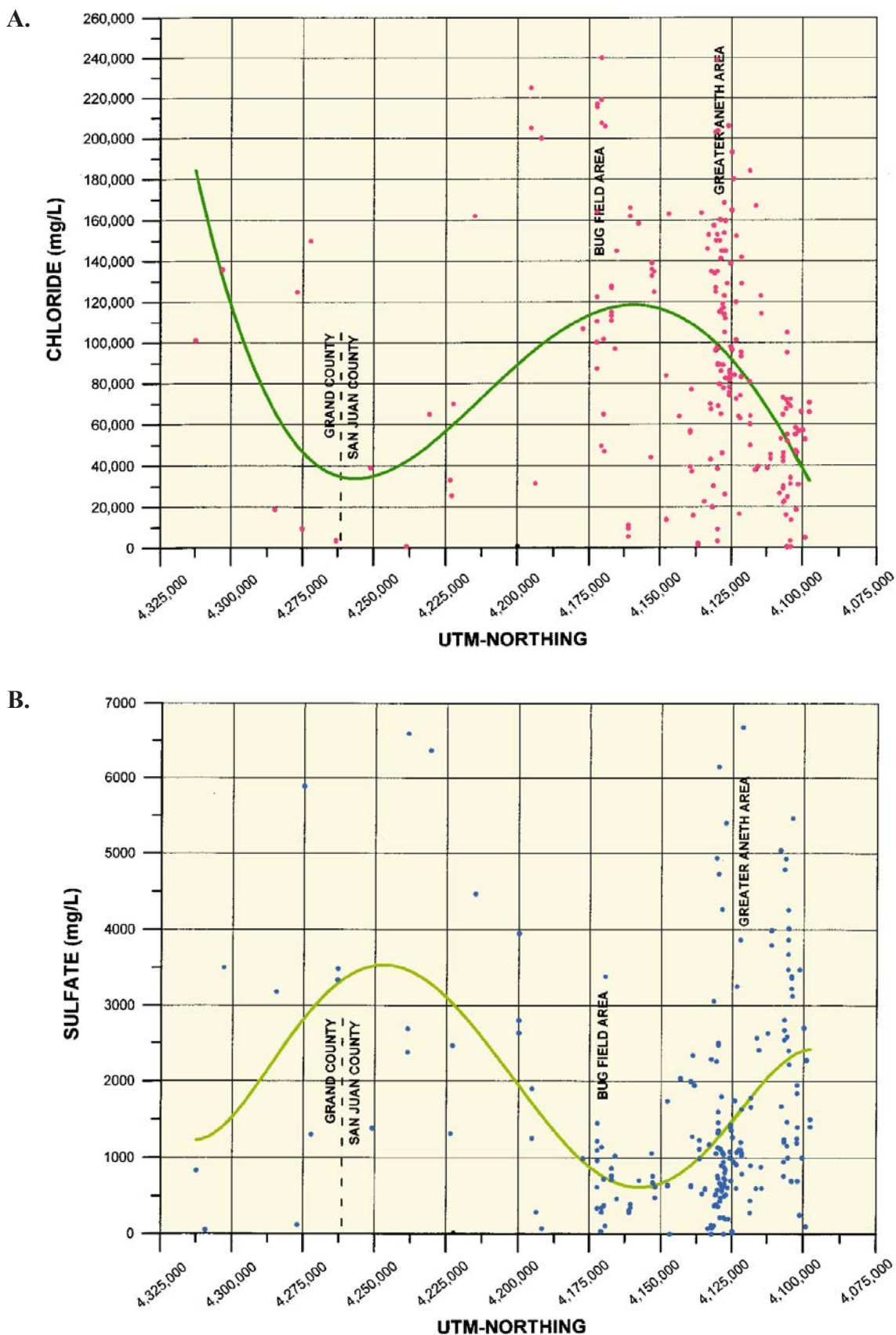


Figure 7.12. Scatter plots of chloride (A), sulfate (B), bicarbonate (C), and total dissolved solids (D) concentrations versus geographic location (UTM northing) for the Pennsylvanian samples. Fifth-degree polynomial best-fit lines indicate data trends from north (left) to south (right) through the length of the Paradox Basin. The general areas of the Greater Aneth and Bug fields are shown, as well as the Grand-San Juan County line.

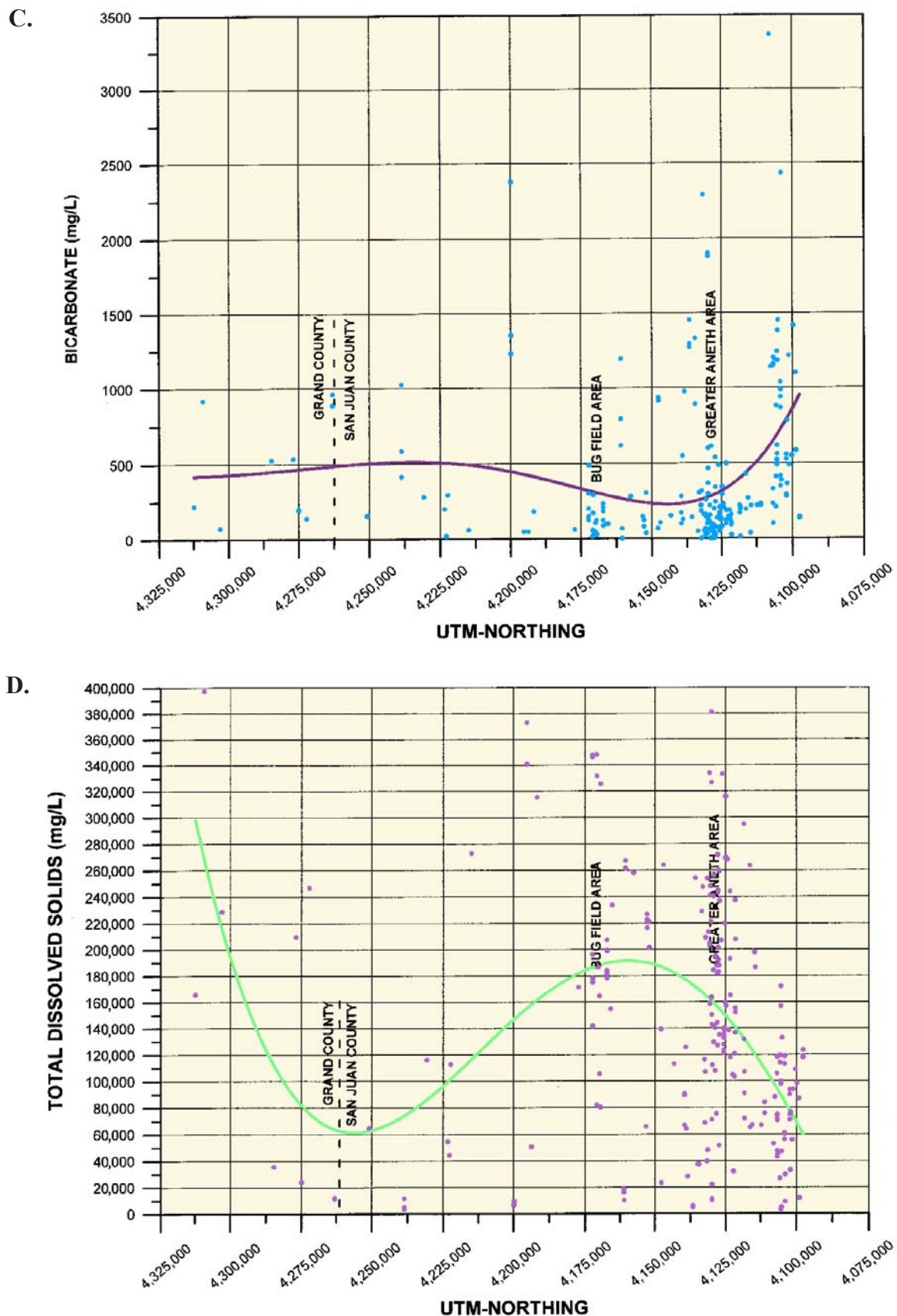


Figure 7.12 continued. Scatter plots of chloride (A), sulfate (B), bicarbonate (C), and total dissolved solids (D) concentrations versus geographic location (UTM northing) for the Pennsylvanian samples. Fifth-degree polynomial best-fit lines indicate data trends from north (left) to south (right) through the length of the Paradox Basin. The general areas of the Greater Aneth and Bug fields are shown, as well as the Grand-San Juan County line.

Table 7.1. Brine sample location, averaged ground elevation, top and bottom elevation of the sampled interval, TDS, and ions for individual counties, and for township intervals within San Juan County.

COUNTY	AGE	TWP-INTERVAL	ELEV (ft)	TOP-ELEV (ft)	BOT-ELEV (ft)	TDS	Na	Mg	Ca	Cl	SO ₄	HCO ₃
Emery	Dev/Miss	Emery	4852	-2116	-2250	81,229	27,407	741	2906	46,963	2432	710
Garfield	Dev/Miss	Garfield	5936	-1268	-1322	7472	1595	164	650	1848	2018	1197
Grand	Dev/Miss	Grand	4561	-4089	-4116	156,376	54,959	876	4481	92,829	2578	651
San Juan	Dev/Miss	SJ 27-29S	5630	-798	-893	141,402	55,153	1643	2191	77,243	4546	719
San Juan	Dev/Miss	SJ 30-35S	6320	-2300	-2422	84,321	24,886	1651	5004	50,137	1637	966
San Juan	Dev/Miss	SJ 37-39S	5617	1090	1001	52,048	18,284	349	997	27,727	3266	1426
San Juan	Dev/Miss	SJ 40S	4608	-2594	-2718	95,537	33,750	474	2234	54,115	2463	2501
San Juan	Dev/Miss	SJ 41S	4848	-1759	-1872	109,684	36,913	996	3742	63,057	3269	1707
San Juan	Dev/Miss	SJ 42-43S	5070	-873	-946	66,618	18,705	1071	5033	38,828	1869	1113
		SJ Average	5349	-1206	-1308	91,602	31,282	1031	3200	51,851	2842	1405
Grand	Penn	Grand	4518	-321	-385	214,249	59,288	2550	19,198	131,066	1772	375
Emery	Penn	Emery	5160	172	92	64,339	20,317	1690	3084	35,399	3206	645
Wayne	Penn	Wayne	4892	-1976	-2056	34,699	11,815	246	788	16,763	4510	577
San Juan	Penn	SJ 30-36S	6319	953	1004	177,196	45,717	3102	17,185	109,702	1228	262
San Juan	Penn	SJ 37-39S	5226	503	434	115,110	30,044	2003	10,679	71,006	878	501
San Juan	Penn	SJ 40S	4781	-825	-888	190,857	53,925	3611	14,187	117,895	1050	189
San Juan	Penn	SJ 41S	4721	-800	-868	148,979	41,502	2997	11,241	91,442	1627	172
San Juan	Penn	SJ 42S	4987	-170	-314	71,723	20,231	1511	4775	41,637	2675	894
San Juan	Penn	SJ 43S	5202	-199	-257	79,159	22,916	1692	5379	46,398	2332	739
		SJ Average	5206	-90	-148	130,504	35,723	2486	10,574	79,680	1632	460

TWP-interval = township interval. A single county name means the average of all samples within that county.

SJ = San Juan County.

ELEV = Average ground elevation of all sampling sites.

TOP-ELEV, BOT-ELEV = Average elevations of the top and bottom of the sampled intervals.

TDS = Total dissolved solids, reported in mg/L.

Individual ion values are reported in mg/L.

Table 7.2. Total dissolved solids (mg/L) and ions on a dry-weight-percent basis for brines from the Paradox Basin, Utah, by county.

Devonian/Mississippian Brine

Area	TDS	Na	Mg	Ca	Cl	SO ₄	HCO ₃
Grand Co.	156,376	35	1	3	59	2	<1
Emery Co.	81,229	34	1	4	58	3	1
Garfield Co.	7472	21	2	9	25	27	16
All of San Juan Co.	91,602	34	1	3	57	3	2

Pennsylvanian Brine

Area	TDS	Na	Mg	Ca	Cl	SO ₄	HCO ₃
Grand Co.	214,249	28	1	9	61	1	<1
Emery Co.	64,339	32	3	5	55	5	1
Wayne Co.	34,699	34	1	2	48	13	2
All of San Juan Co.	130,504	28	2	8	62	1	<1

CHAPTER 8: REGIONAL MIDDLE PALEOZOIC HYDRODYNAMIC PRESSURE REGIME OF THE PARADOX BASIN, UTAH AND COLORADO

by

Richard G. Allis (retired), Craig D. Morgan (retired), Sonja Heuscher (formerly Utah Geological Survey), and Ammon McDonald (now at Utah Division of Oil, Gas and Mining), Utah Geological Survey

CHAPTER 8:

REGIONAL MIDDLE PALEOZOIC HYDRODYNAMIC PRESSURE REGIME OF THE PARADOX BASIN, UTAH AND COLORADO

INTRODUCTION

Although most oil in the Paradox Basin has been found in carbonate buildups (algal mounds and ooid shoals) of the Pennsylvanian (Chidsey and others, 2016, and references therein), the northwest-trending fold and fault belt near the northern margin of the basin contains several Mississippian oil and gas fields, the largest being Lisbon, Utah (figures 1.1 and 1.3), described in detail in Chapters 2 through 4. McElmo Dome field (figures 1.1 and 1.3), southwest Colorado, near the southeastern margin of the basin is a major producer of carbon dioxide (CO₂) from the Mississippian Leadville Limestone (Gerling, 1983; Tremain, 1993). Two minor oil fields (abandoned) occur near the southern margin of the basin, close to the Utah-Arizona state line.

One factor providing insight into recent secondary or tertiary migration of oil within the Mississippian is the present hydrodynamic condition. A horizontal pressure gradient within relatively permeable reservoir rock may indicate significant water movement that displaces trapped oil, whereas abnormally high pressures could indicate hydrocarbon generation and accumulation in relatively low-permeability rocks.

Previous Work

The only prior systematic compilation of pressure trends within the Mississippian system of the Paradox Basin appears to be by Hanshaw and Hill (1969). They studied the potentiometric trends in seven “aquifers” ranging in age between the Cambrian through Devonian and the Permian. Their potentiometric map for the Mississippian (reproduced as figure 8.1) shows a head gradient of about 2400 feet (730 m) between the Utah-Colorado state line and eastern margin of the Paradox Basin adjacent to the San Juan Mountains (i.e., head increasing eastwards), which they interpreted as a major recharge area in the vicinity of the mountains. An area to the southwest of the Abajo Mountains near the northern end of the Monument upwarp (figure 1.1) is shown as having more than 1000 feet (300 m) of head above the surrounding region of southeastern Utah. We noted that hydrology here is complicated, with mixed evidence of oil wells that were dry to at least the Mississippian, and other wells that indicated an elevated water column.

The compilation by Hanshaw and Hill (1969) has several limitations, which were acknowledged by the authors at that time. Firstly, it is dependent on analysis of only about 600 drill-stem tests (DSTs) supplied by oil companies from wells

drilled through 1961. Of these, about 300 were usable, so the number of DSTs for a particular horizon’s potentiometric map is presumably a small fraction of these. Unfortunately, the maps do not show the data points used to constrain the contours. Secondly, Hanshaw and Hill (1969) chose to present the pressure measurements in the form of a potentiometric surface obtained by converting the pressure to a freshwater column. Whereas the overall pressure trends should be reasonable, the local elevation of the column is less useful.

Several thousand more wells have been drilled in the Paradox Basin since 1961, and many had DSTs performed on various formations. The purpose of this study was to review this data and compile a new map of pressure variations across the Mississippian strata of the basin. This study will improve the understanding of geological constraints on fluid flow within the largely carbonate units of the Paleozoic part of the geologic section. As described previously, Mississippian Leadville Limestone underlies much of the basin, and it is underlain by Devonian limestone of the Ouray and Elbert Formations (figures 2.1, 5.1, and 8.2). Some oil exploration reports from wells to the south of the basin refer to the Mississippian Redwall Limestone, and occasionally the name Madison Limestone is used. The Leadville Limestone is overlain by a thin shale (Molas Formation, <150 feet [46 m] thick) at the base of the Pennsylvanian, which is overlain by the Hermosa Group containing the main oil-producing zones of the basin (Paradox Formation) (figures 2.1, 5.1, and 8.2).

Depth to the Mississippian and General Structure

The Leadville Limestone does not crop out in the Paradox Basin, but it occurs at about 1000 feet (300 m) depth in the Cataract Canyon section of the Colorado River, just downstream of the junction with the Green River (the oldest outcrops in Cataract Canyon are evaporites of the Paradox Formation). On the northeastern margin of the basin, the Leadville Limestone is at more than 15,000 feet (4600 m) depth, close to where it is faulted against the Uncompahgre uplift. The carbonate deposition represents a time when there was a stable cratonic platform, prior to the development of a paleoforedeep structure that formed the Paradox Basin. Across much of the eastern half of the basin the Mississippian is overlain by 7000 to 10,000 feet (2100–3000 m) of mostly Pennsylvanian and Permian strata (figure 8.2). These cover rocks include low-permeability units of shale, anhydrite, and salt of the Paradox Formation, so there is the potential for significant overpres-

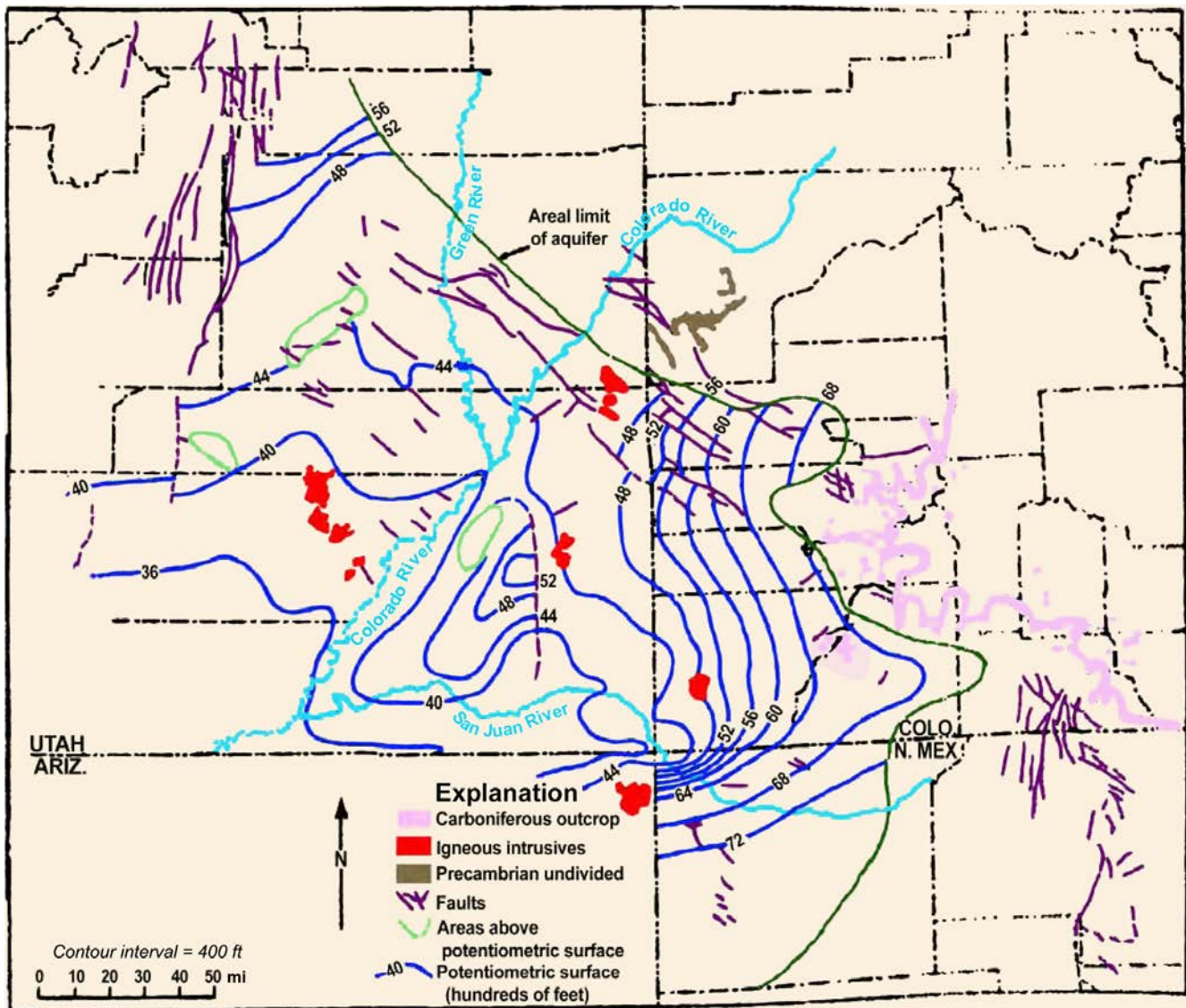


Figure 8.1. Potentiometric map for the Mississippian stratigraphic section derived from oil and gas DST pressure data through 1961. Modified from Hanshaw and Hall (1969).

sure in the underlying Mississippian over the eastern half of the basin, and therefore potential for significant lateral variations in fluid pressure there.

Simplified maps of the depth to Leadville Limestone (figure 8.3) and structural contours on the top of the Leadville Limestone (figure 8.4) show the gross trends of the Laramide uplifts and the regional erosion patterns across the Paradox Basin. The contours on both maps are based only on picks of the top of the Leadville in oil exploration wells, and local incision in canyons or local faulting and folding is not accounted for. East of the Colorado River in the Monument upwarp, and west of the Green River in the San Rafael Swell, the top of the Leadville rises to 5000 feet (1500 m) above sea level (ft asl [m asl]). This elevation is 1000 feet (300 m) above the level of these sections of the Colorado River and the Green River (3800 to 4000 feet asl [1160–1200 m asl]), which are presumably controlling at least the near-surface hydrology in these areas.

DATA SOURCE AND METHODOLOGY

About 5000 DST reports compiled by PI/Dwights Plus-IHS Energy/Well Data (2008) were used for this pressure compilation. The “shut-in” pressure values included with this report have been used without further correction for recovery to equilibrium. This dataset is very noisy, so criteria were applied to screen out obviously inaccurate data. The most common source of error is incomplete pressure recovery because of low permeability, either due to local mud-cake problems or inherently low permeability in the formation (Bredehoeft, 1965; Nelson, 2002). If the shut-in time was less than 30 minutes, or no shut-in time recorded, the shut-in pressure was discarded. The 30-minute threshold sometimes appeared to indicate reliable data for the most permeable formations such as the Leadville Limestone, but was far too short for low-permeability rocks. Even after 240 to 300 minutes, pressures in all reported “salt” formations and some “shale” formations were

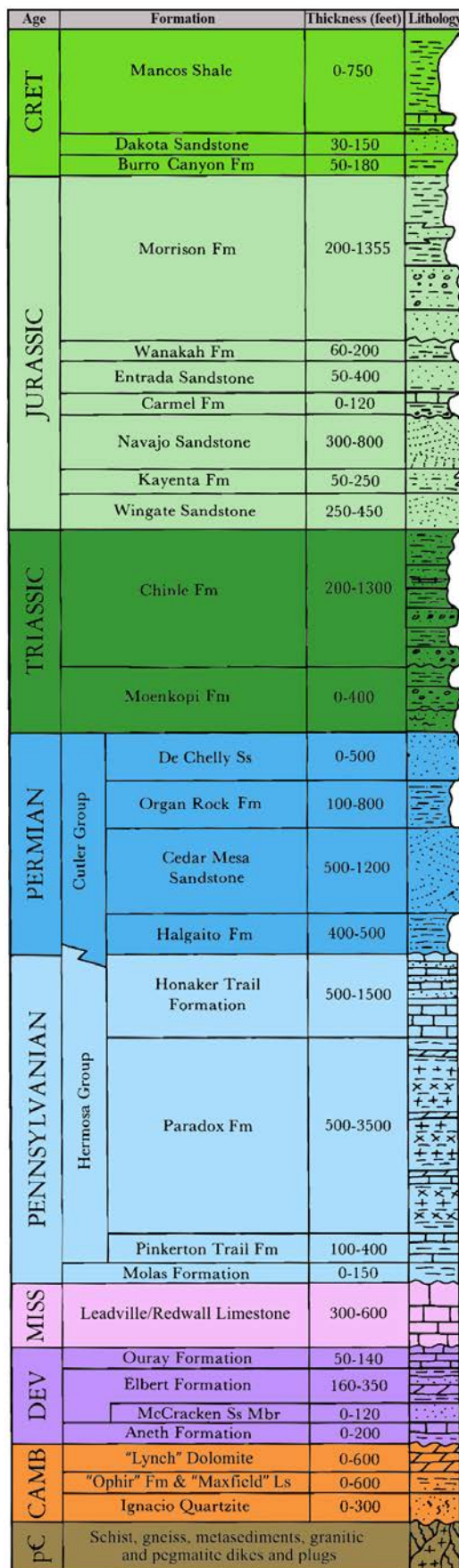


Figure 8.2. Stratigraphic section for the central Paradox Basin near Monticello, Utah. After Hintze and Kowallis (2009).

still clearly far from equilibrium. Most DSTs reported an “initial” and a “final” shut-in pressure, and in such cases the larger of the two values was chosen. The topographically lowest part of the Paradox Basin is the Colorado River, which should control the minimum pressure in the basin. Any pressure values less than about 70% of hydrostatic pressure beneath the Colorado River were therefore eliminated. Any DSTs that did not identify the formation being tested, or had incomplete depth information, were also eliminated.

As a result of this screening process, between 50% and 75% of the pressure data were removed from further study. To allow further averaging of the pressure data, the Paradox Basin was subdivided into six, one-degree quadrangles (figure 8.5), and the pressure data were plotted at the elevation of the DST (midpoint of the open interval). This resulted in as few as 27 data points for the Mississippian in the Glen Canyon quadrangle, which has no producing fields, and 614 data points in the Aneth quadrangle. In all, 1529 pressure points were spread over the six quadrangles. To investigate the vertical pressure trends in each quadrangle, the data were subdivided based on geological time. The Paleozoic was split into the periods Mississippian and older, Pennsylvanian, Permian, and where appropriate, a Mesozoic era was included. The total number of Mississippian and older pressure values is 395, representing less than 10% of the initial DST dataset for the Paradox Basin.

PRESSURE TRENDS BY QUADRANGLE

Figures 8.6 through 8.11 show the vertical pressure trends for each quadrangle, and a map of the well locations where the DSTs were made. Sometimes more than one DST is from the same well, and within oil and gas fields, wells are close together and occasionally obscure other well locations. To facilitate comparison between the quadrangles, each graph has the same reference line superimposed on it based on a composite pressure trend for the Mississippian and older strata discussed in a later section. This composite trend line has a slope of 0.47 pounds per square inch/foot (psi/ft [10.6 kPa/m]), which is almost 10% above the hydrostatic gradient for fresh water. The composite trend line is equivalent to a static pressure gradient in a column of water with a salinity of 100,000 to 150,000 milligrams per kilogram (mg/kg) (J.W. Gwynn, UGS, verbal communication, June 2008), which is reasonable for the Paleozoic section of the Paradox Basin. Shallow groundwater in the Paradox Valley, Colorado, has an average dissolved solids concentration of 250,000 mg/kg (Chafin, 2002). However, the springs and geysers near the town of Green River in the northern part of the basin have concentrations of 11,000 to about 20,000 mg/kg (Baer and Rigby, 1978; Shipton and others, 2004), so there is probably a gradient in salinity across the basin. Note that the main source of error with DST shut-in pressures is failure to completely come to equilibrium during the test, and for the pressure to be less than actual pressure. These

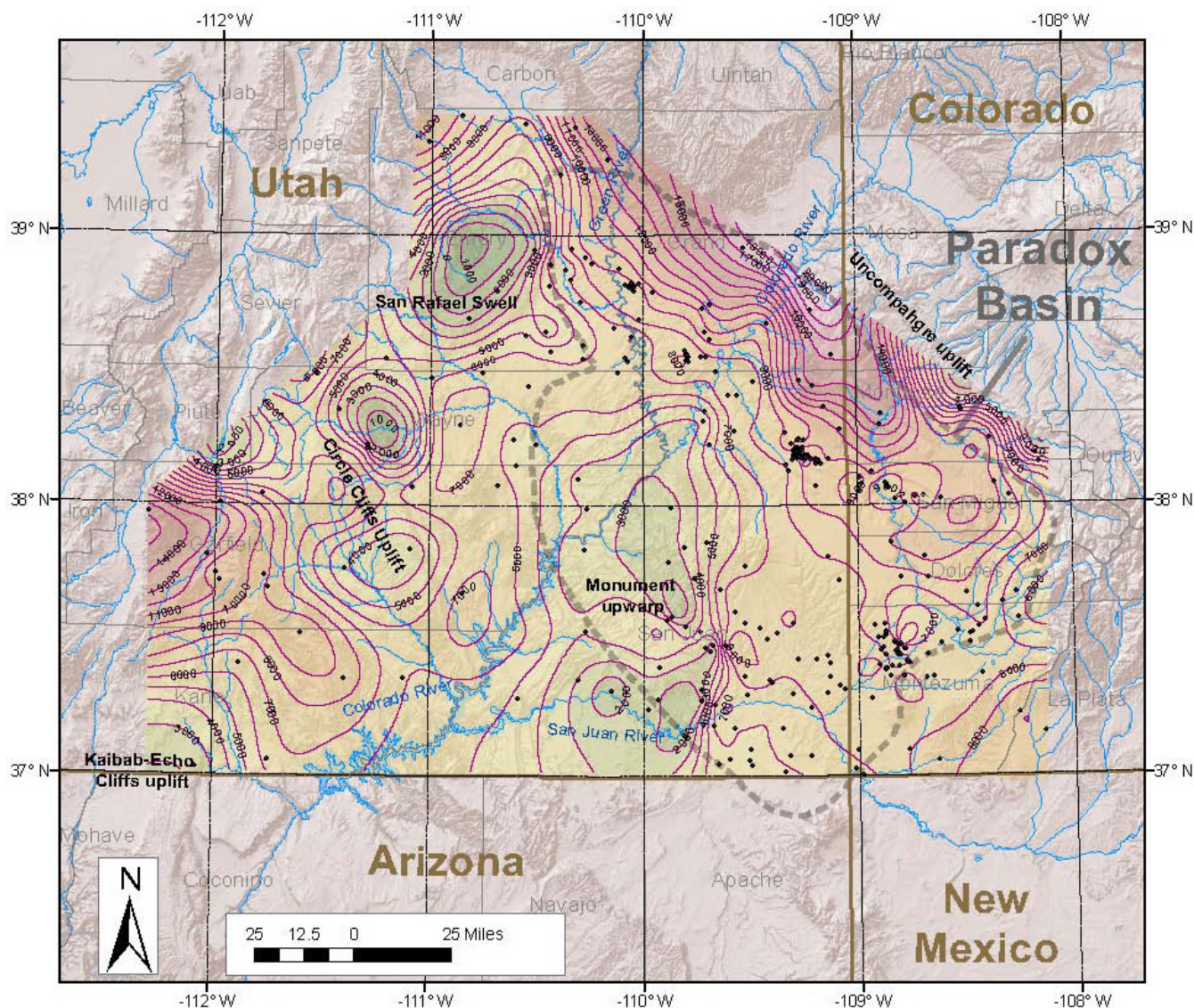


Figure 8.3. Depth to top of the Mississippian Leadville Limestone derived from oil and gas exploration wells. Note that the contours do not consider local topographic relief between the wells, such as the Colorado River canyon and mountains. Black dots indicates wells penetrating the Leadville. Contour interval is 1000 feet (300 m).

uncertainties are such that the inferred pressure gradient of 0.47 psi/ft (10.6 kPa/m) has an estimated 10% uncertainty.

Glen Canyon Quadrangle

The DST pressure data from the Mississippian and older strata are sparse for the Glen Canyon quadrangle (figure 8.6A), but consistent with a hydrostatic trend when compared with data from the surrounding quadrangles. Although it is possible that the deeper pressures (i.e., below sea level) may be less than the composite Mississippian regional trend shown on the graph (figure 8.6B), this is considered unlikely since this area is in the hydrologically lowest part of the Paradox Basin (Colorado River at 3800 ft asl [1160 m]). Pennsylvanian and Permian formations are largely consistent with the one hydrostatic trend extending from nearsurface to at least -4000 ft asl (-1200 m asl). Two Pennsylvanian pressure values at shal-

low depth suggest a locally perched water table near the surface (head at close to 5000 ft asl [1520 m asl]). Both pressure points are from wells on the eastern boundary of the quadrangle and are consistent with a nearsurface pressure trend that is more strongly identified on the adjacent quadrangle (Aneth). Hanshaw and Hall (1969) reported that several exploration wells drilled east of Cataract Canyon on the northern end of the Monument upwarp encountered dry conditions down into the Mississippian, which as figure 8.4 shows, suggests the deep head is at an elevation of less than 4000 to 5000 ft asl (1200–1500 m asl), and consistent with the trend in figure 8.6.

West Green River Quadrangle

The DST pressure data for the West Green River quadrangle (figure 8.7A) indicate one linear trend from a shallow water table elevation of about 4000 ft asl (1200 m asl) in the Trias-

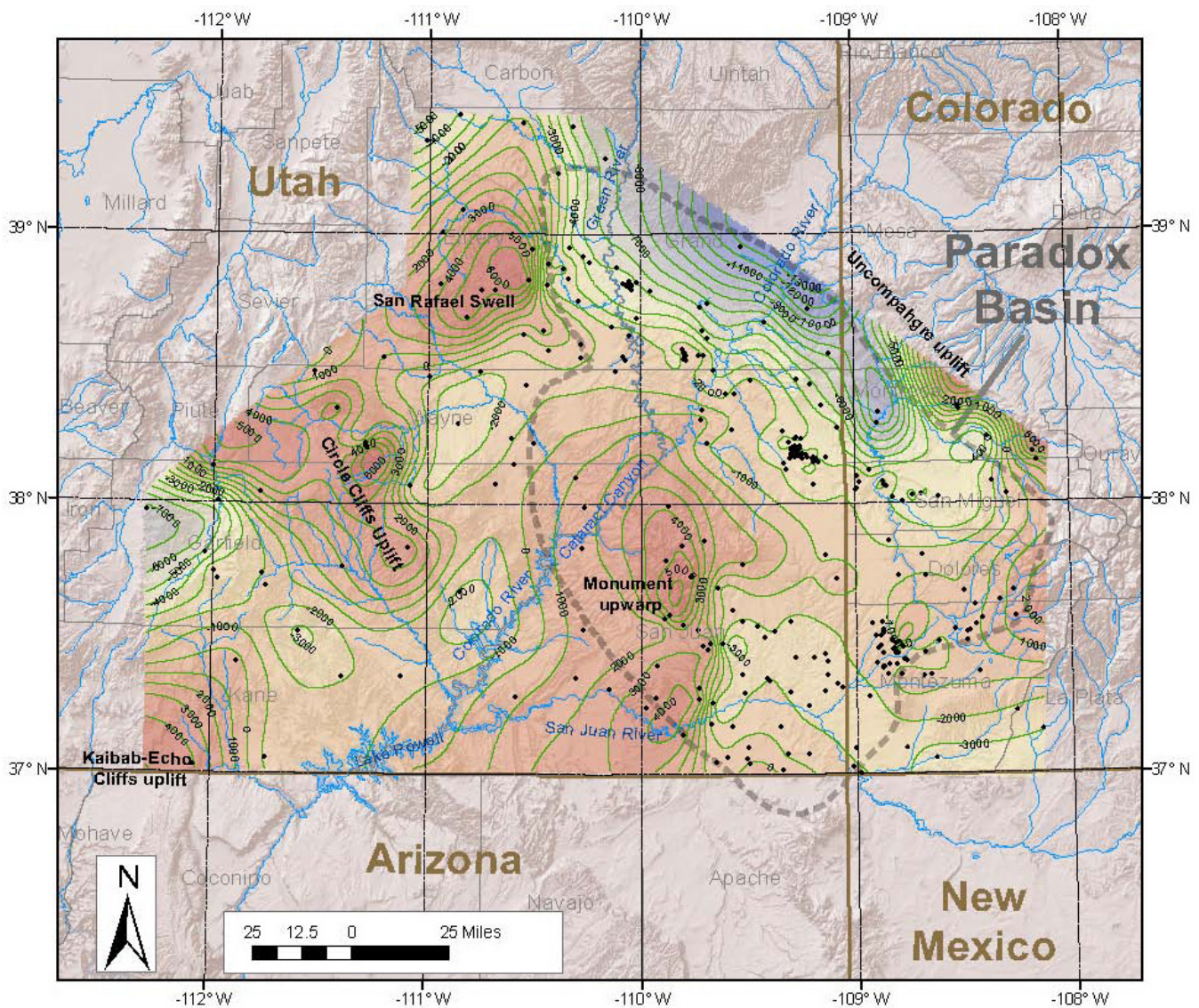


Figure 8.4. Structural contours on the top of the Leadville Limestone derived from oil and gas exploration wells. Note that the contours do not consider fault offsets and folding between the wells. Black dots indicates wells penetrating the Leadville. The contour interval is 1000 feet (300 m) (relative to sea level). The structural highs correspond to Laramide uplifts.

sic to the deepest Mississippian at -6000 ft asl (-1800 m asl) (figure 8.7B). The slope is 0.47 psi/ft (10.6 kPa/m), consistent with saline water. The pressure trend likely is 100 to 200 psi (690–1380 kPa) higher than the composite trend shown on the graph because of the tendency for DST shut-in pressure to be less than the actual pressure. In addition, in the northeastern corner of the quadrangle immediately east of the Green River, saline water and CO₂ flow to the surface in the form of springs and geyser activity in abandoned wells. These fluids are interpreted to originate from deep within the Paradox Basin (Heath, 2004; Shipton and others, 2004; Allis and others, 2005). The elevation of the springs and overflowing wells is 4050 ft asl (1230 m asl), implying a hydrostatic trend at least 250 feet (75 m) (about 100 psi [690 pKa]) higher than the composite trend on the graph. There may be locally higher pressures within the Pennsylvanian section, with a few pressure points 500 psi (3450 kPa) higher than the regional trend.

Aneth Quadrangle

A relatively large amount of data from the Pennsylvanian exists in the Aneth quadrangle (figure 8.8A) because of the intensive drilling that has occurred in Greater Aneth and other oil fields in the Blanding sub-basin (figure 1.1). The Mississippian data are split into two sets: those below sea level (typically > 5000 feet [1500 m] depth) and those above sea level (1000 to 3500 ft asl [300–1100 m asl]). The former are in the eastern half of the quadrangle, the latter are mostly in the western half (Monument upwarp). Both sets of data are consistent with a regionally extensive pressure trend with a head at 3800 ft asl (1160 m asl), the average elevation of the Colorado River in the adjacent Glen Canyon quadrangle. The Pennsylvanian data show more scatter, with most data clustering close to the underlying Mississippian pressure trend (figure 8.8B). However, there is also clear evi-

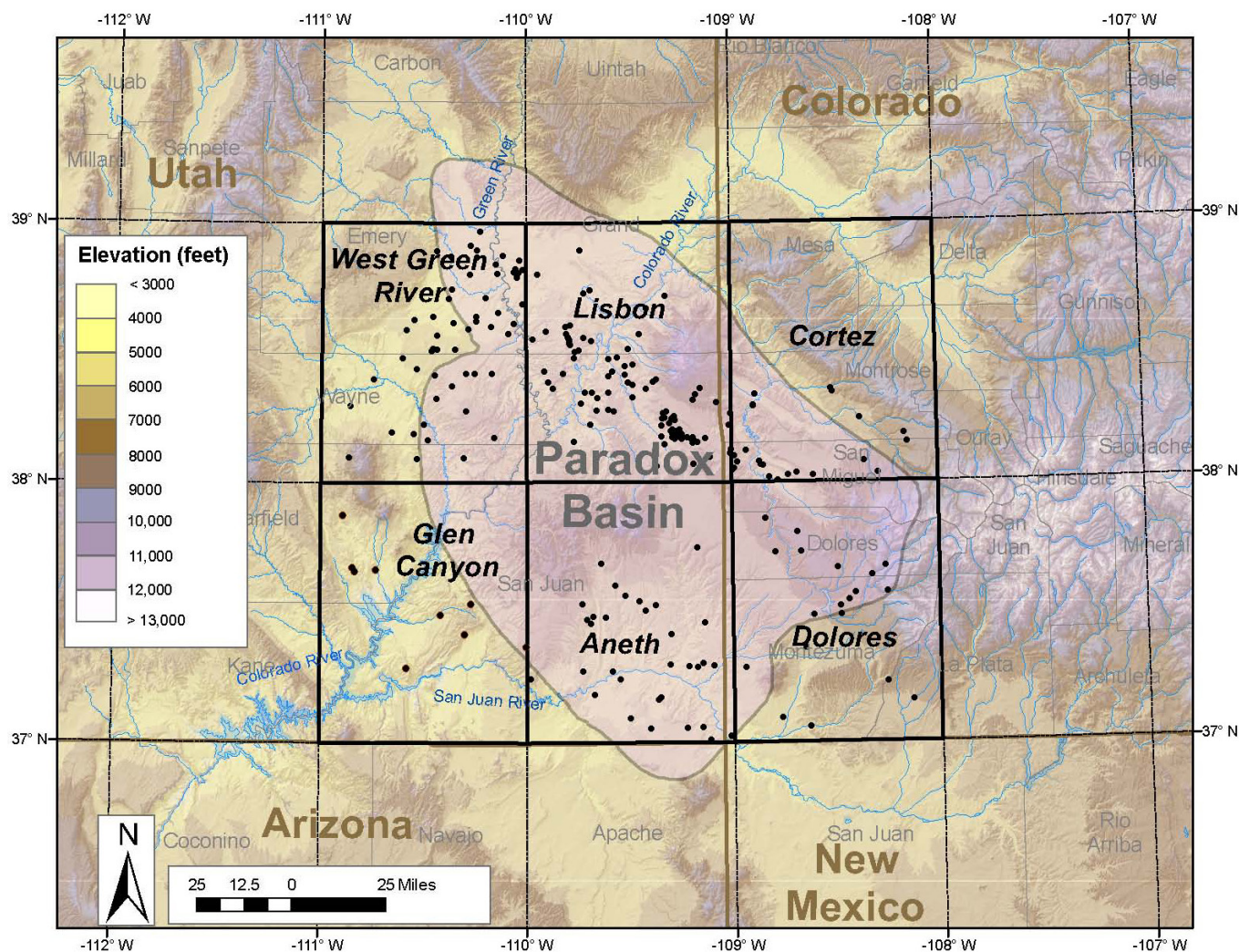


Figure 8.5. Subdivision of the Paradox Basin into six, 1° by 1° quadrangles, for which DST pressure data are consolidated. Black dots indicate the distribution of wells which had DST measurements within the Mississippian or older formations. Names assigned to the quadrangles are for this report only and do not correspond to U.S. Geological Survey quadrangles.

dence of overpressures of up to 2000 psi (13,790 kPa) relative to the Mississippian trend and is likely related to locally lower permeability and hydrocarbon generation within the Pennsylvanian section. The Permian pressure data suggest a hydrostatic gradient with control by surface recharge from a ground elevation of 4500 to 5000 ft asl (1400–1500 m asl). The elevation of the San Juan River near Aneth field is 4400 ft asl (1340 m asl). The Mississippian pressure trend in parts of the quadrangle where it is situated above sea level (mostly western half) is between 500 and 1000 psi (3450–6900 kPa) lower than where the Permian section occurs at a similar elevation (mostly eastern half).

Note that the pressure trends in the higher elevation areas in the north part of the quadrangle (Abajo Mountains) are unknown. However, Kirby (2008) reported that groundwater levels in the vicinity of the city of Blanding (10 to 15 miles [16–24 km] south of the Abajo Mountains) range between 6400 ft asl (1950 m asl) in the north to 5300 ft asl (1600 m asl) near Blanding. The groundwater is “perched” within

the Dakota and Burro Canyon Formations (Cretaceous) on top of the underlying Morrison Formation (Upper Jurassic) (figure 8.2). Groundwater wells drilled into the Navajo Sandstone (Lower Jurassic) near Blanding have water levels close to 5400 ft asl (1800 m asl), and encountered good quality drinking water (Bill Loughlin, Loughlin Water Associates, verbal communication, 2008). Both Mesozoic aquifers appear to be perched relative to water in Permian and underlying formations.

Lisbon Quadrangle

The Lisbon quadrangle contains more Mississippian pressure data (figure 8.9A) than the others because of the Mississippian oil and gas fields in the Paradox fold and fault belt (figure 1.3). The pressure trend (figure 8.9B) is consistent with, and largely controls (because of the amount of data), the composite pressure trend for the basin. Pennsylvanian pressure data are very scattered, but as in the Aneth quadrangle, there is evidence of local overpressuring by up to

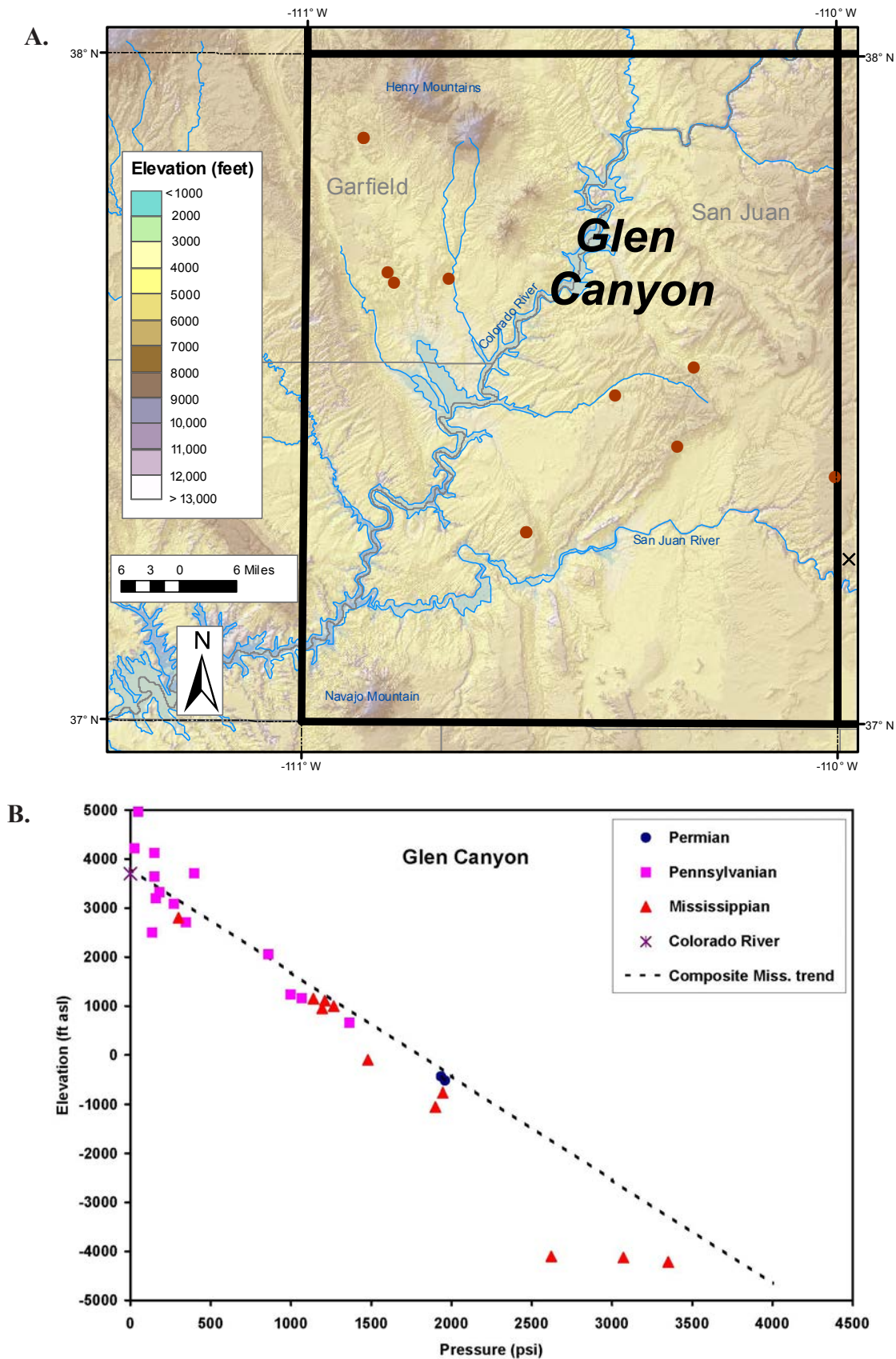


Figure 8.6. Glen Canyon quadrangle. (A) Location of wells (orange dots) within the quadrangle for which DST measurements from the Mississippian (and older) strata have been used in the pressure trend graph in (B). Sometimes more than one DST is available from a well. (B) Trend of DST shut-in pressures in the quadrangle. The dashed line is derived from a composite pressure plot discussed later and shown on figure 8.12. Note that the pressures from DSTs tend to be minimums because of possible lack of full equilibrium at the end of the test.

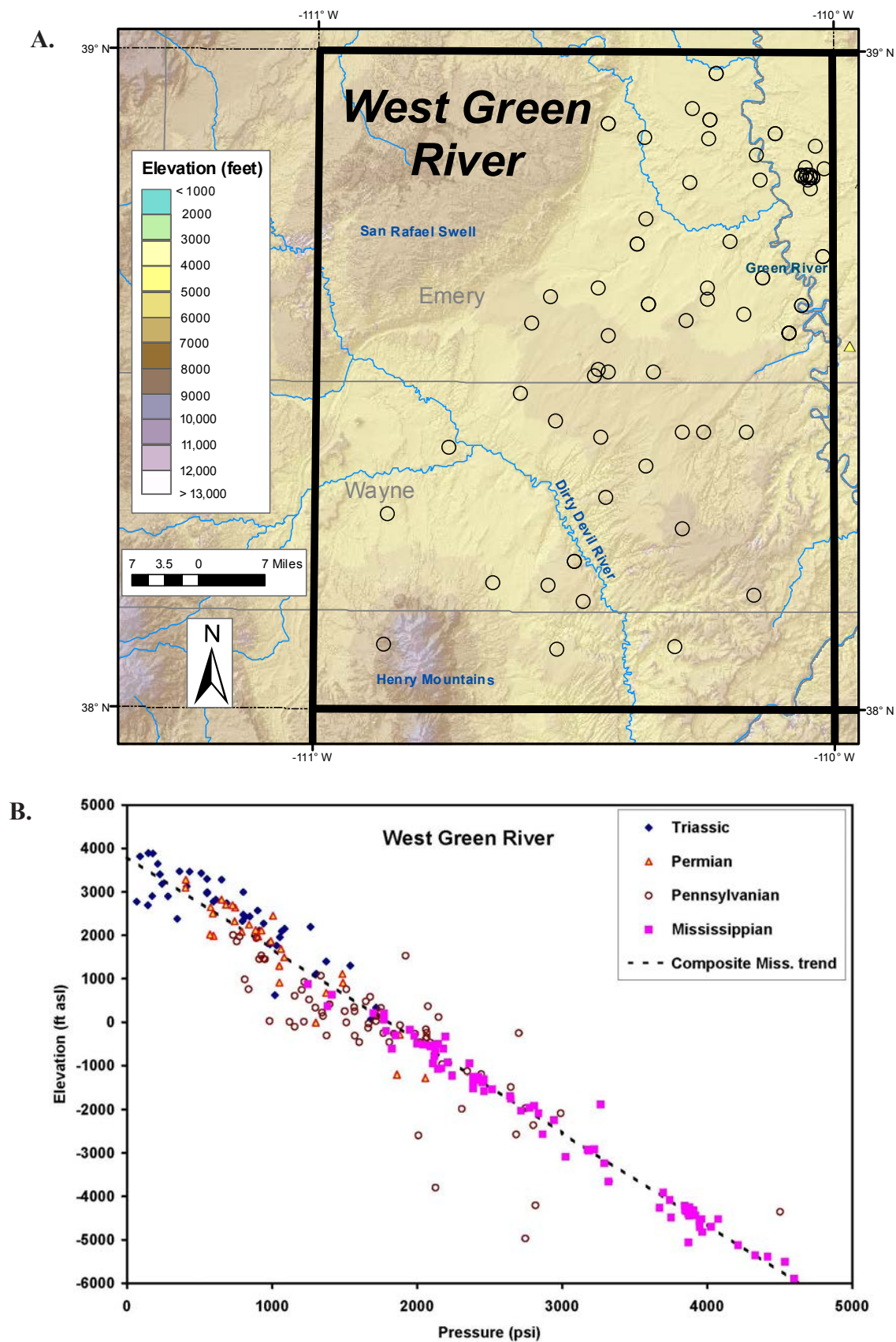


Figure 8.7. West Green River quadrangle. (A) Location of wells (open circles) within the quadrangle for which DST measurements from the Mississippian (and older) strata have been used in the pressure trend graph in (B). Sometimes more than one DST is available from a well. (B) Trend of DST shut-in pressures in the quadrangle. The dashed line is derived from a composite pressure plot discussed later and shown on figure 8.12. Note that the pressures from DSTs tend to be minimums because of possible lack of full equilibrium at the end of the test.

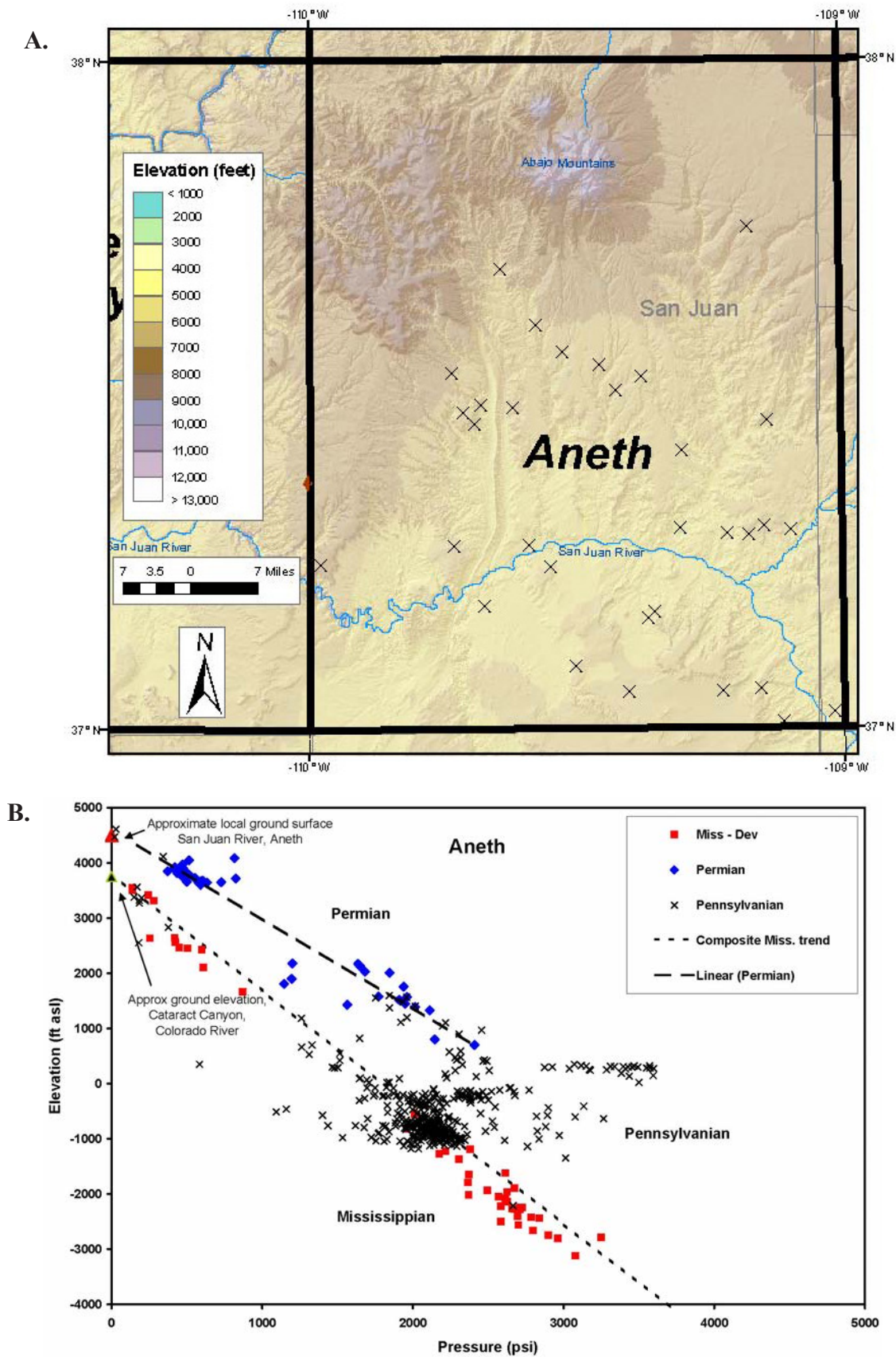


Figure 8.8. Aneth quadrangle. **(A)** Location of wells (Xs) within the quadrangle for which DST measurements from the Mississippian (and older) strata have been used in the pressure trend graph in **(B)**. Sometimes more than one DST is available from a well. **(B)** Trend of DST shut-in pressures in the quadrangle. The dashed line is derived from a composite pressure plot discussed later and shown on figure 8.12. Note that the pressures from DSTs tend to be minimums because of possible lack of full equilibrium at the end of the test.

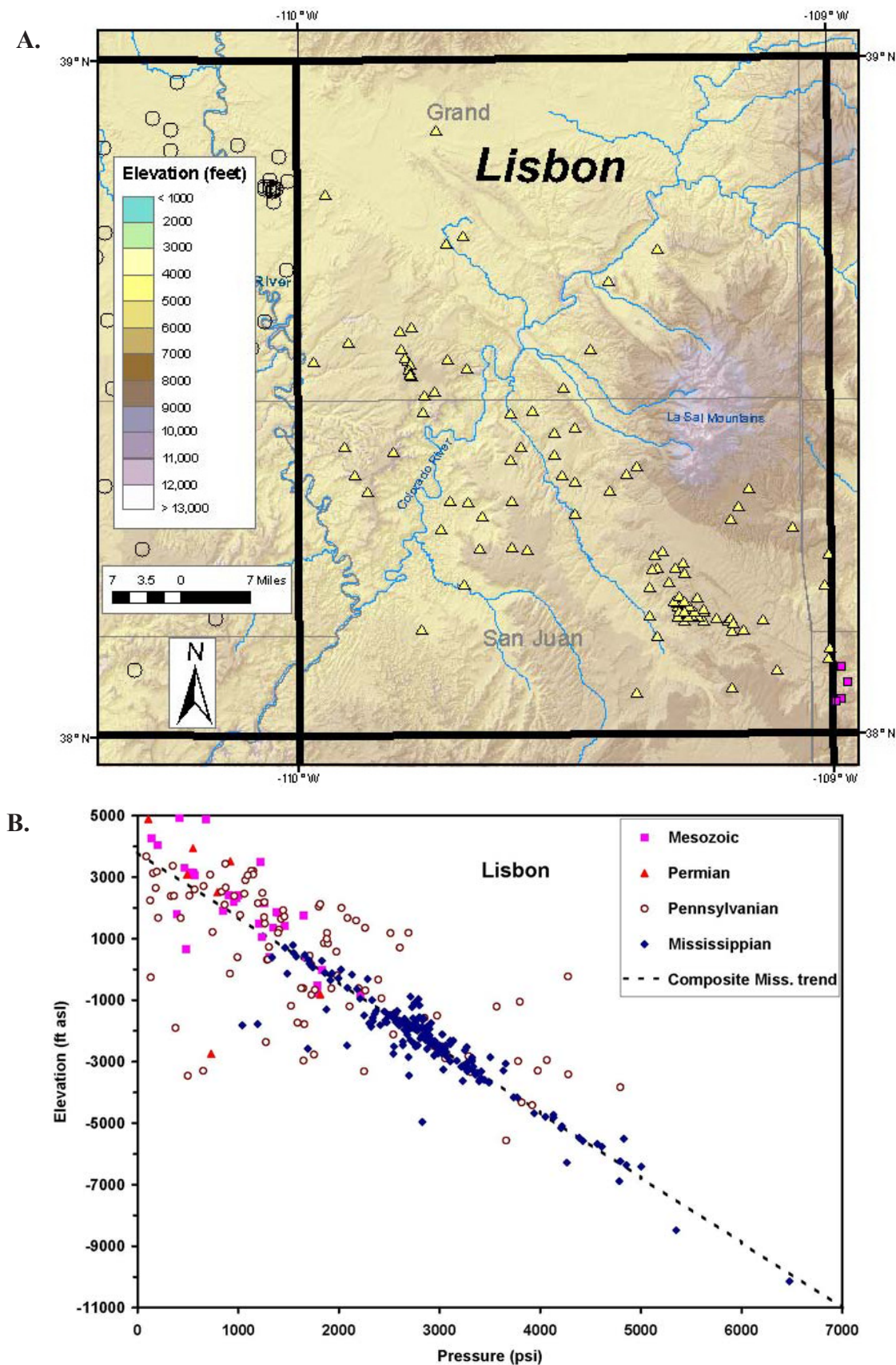


Figure 8.9. Lisbon quadrangle. **(A)** Location of wells (yellow triangles) within the quadrangle for which DST measurements from the Mississippian (and older) strata have been used in the pressure trend graph in **(B)**. Sometimes more than one DST is available from a well. **(B)** Trend of DST shut-in pressures in the quadrangle. The dashed line is derived from a composite pressure plot discussed later and shown on figure 8.12. Note that the pressures from DSTs tend to be minimums because of possible lack of full equilibrium at the end of the test.

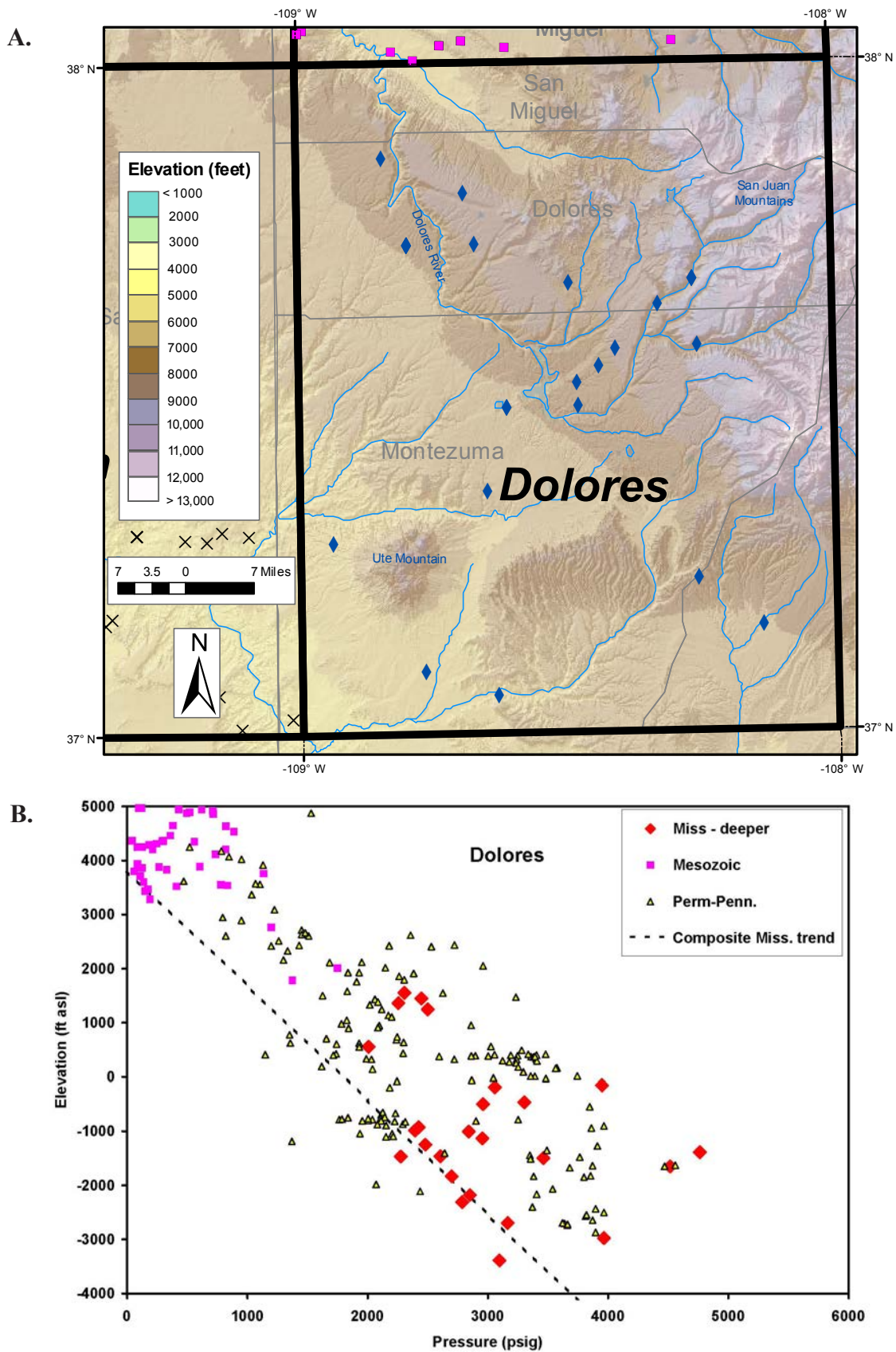


Figure 8.10. Dolores quadrangle. (A) Location of wells (blue diamonds) within the quadrangle for which DST measurements from the Mississippian (and older) strata have been used in the pressure trend graph in (B). Sometimes more than one DST is available from a well. (B) Trend of DST shut-in pressures in the quadrangle. The dashed line is derived from a composite pressure plot discussed later and shown on figure 8.12. Note that the pressures from DSTs tend to be minimums because of possible lack of full equilibrium at the end of the test.

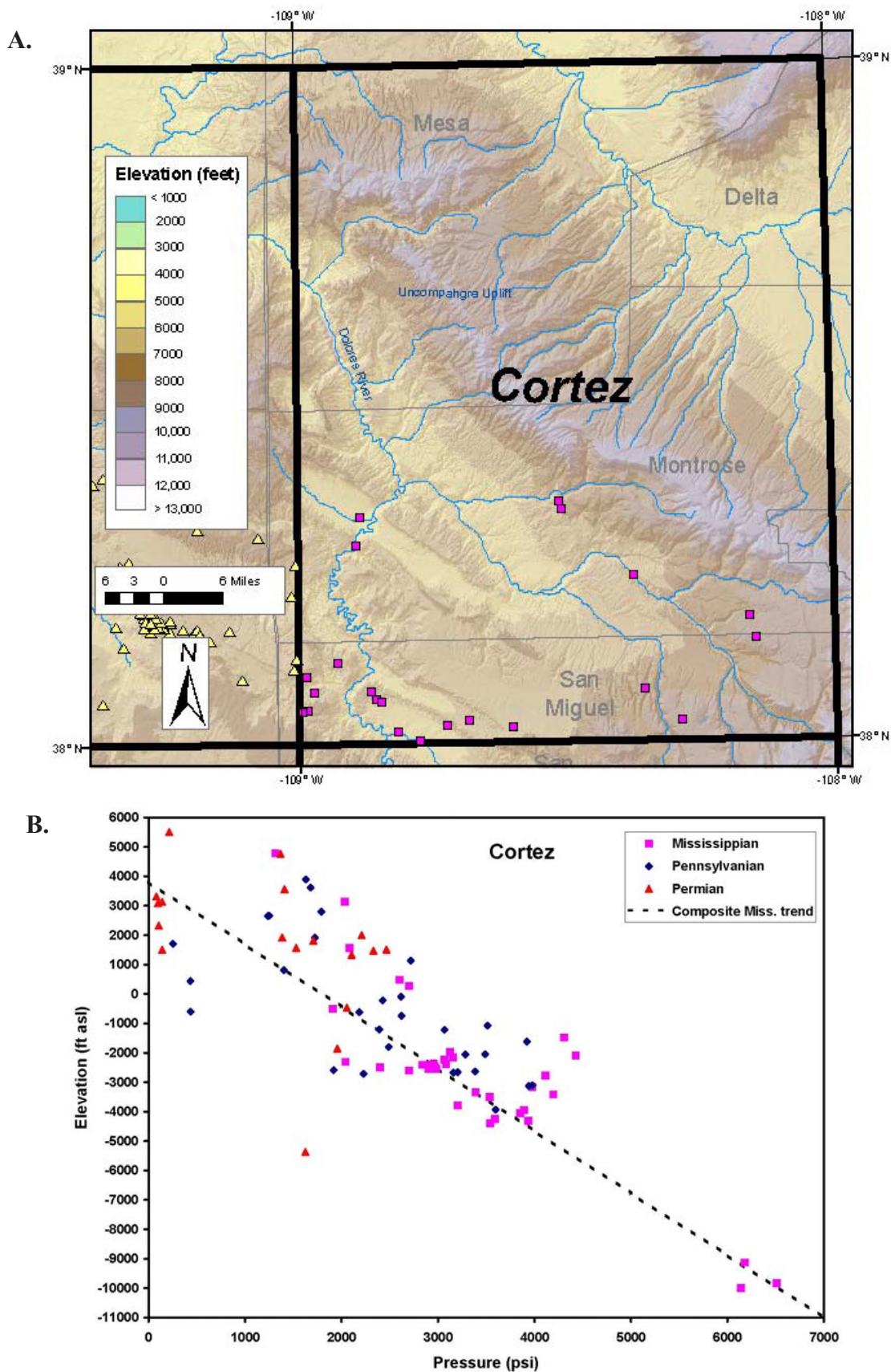


Figure 8.11. Cortez quadrangle. **(A)** Location of wells (purple squares) within the quadrangle for which DST measurements from the Mississippian (and older) strata have been used in the pressure trend graph in **(B)**. Sometimes more than one DST is available from a well. **(B)** Trend of DST shut-in pressures in the quadrangle. The dashed line is derived from a composite pressure plot discussed later and shown on figure 8.12. Note that the pressures from DSTs tend to be minimums because of possible lack of full equilibrium at the end of the test.

about 1000 psi (6900 kPa). The Permian and Mesozoic pressures suggest a trend that is systematically higher than the Mississippian trend, but due to poor data quality, it is unclear whether there is one aquifer trend or locally varying pressure trends with zero-pressure intercepts between 4500 and about 6000 ft asl (1370–1800 m).

Dolores Quadrangle

In the Dolores quadrangle (figure 8.10), most data lie at higher pressures (figure 8.10B), although some Mississippian DST pressure data (figure 8.10A) lie close to the composite pressure trend. The same higher-pressure pattern occurs in the Permian-Pennsylvanian and the Mesozoic sections. The scatter in the Mesozoic section appears to be smaller than that in the underlying sections, and these data suggest zero-pressure head elevations of between 4000 and 7000 ft asl (1220–2130 m asl). The northeastern part of the quadrangle has higher ground elevations associated with the western flank of the San Juan Mountains, which range up to 14,000 ft asl (4260 m asl) to the east of the quadrangle. The deeper trends (Permian and below) are up to about 2000 psi (13,790 kPa) above the composite pressure trend. The well locations for most of these higher-pressure DSTs are situated in the northeastern part of the quadrangle, suggesting the area is affected by recharge from the San Juan Mountains to the east.

Cortez Quadrangle

The DST pressure data are scattered in the Cortez quadrangle, although the deep Mississippian pressures are constrained by data from injection wells drilled by the U.S. Bureau of Reclamation near the Dolores River in the Paradox Valley, western Colorado (figure 8.11A). The three DSTs on figure 8.11B imply a pressure of 6300 psi (43,400 kPa) at an elevation of -9500 ft asl (-2900 m) which is in agreement with the undisturbed pressures quoted by Ake and others (2005) of 6235 psi (43,000 kPa) at 9200 feet (2800 m) below sea level for the deep wells in the Paradox Valley. The pressure confirms that the Mississippian near the western edge of this quadrangle has pressures like the composite trend in the rest of the Paradox Basin farther west. However, there are other Mississippian pressure data up to about 1000 psi (7000 kPa) higher than the composite trend, and two points almost 2000 psi (13,900 kPa) higher. Inspection of the well locations of those DSTs shows them to be in the eastern half of the quadrangle. The same pattern applies to the Pennsylvanian and Permian DSTs. A hydrostatic pressure trend that is an upper boundary to the DSTs would have a zero-pressure intercept of about 8000 ft asl (2400 m asl). The Uncompahgre uplift that diagonally traverses the quadrangle rises to over 9000 ft asl (2700 m asl). Recharge on the uplift may be contributing to the higher pressures occurring in the quadrangle.

COMPOSITE MISSISSIPPIAN PRESSURE TREND

The Mississippian DST pressure data was compiled onto one graph, coded by quadrangle (figure 8.12). A linear trend is apparent over an elevation range of 14,000 feet (4300 m), and has a slope of 0.47 psi/ft (10.6 kPa/m) as discussed above. To clarify the pattern of a small amount of data plotting at significantly higher pressures than this trend, figure 8.13 examines the amplitude of the pressure departure from the composite trend against the ground elevation of the well with the DST measurement. The plot indicates that a systematic pattern of increased pressure departure (i.e., higher pressures) with higher ground elevation occurs in the Cortez and Dolores quadrangles. Elsewhere, there is not a significant correlation.

INTERPRETATION

For most of the Paradox Basin, an area of at least 100 by 100 miles (260 x 260 km) including the Glen Canyon, West Green River, Aneth, and Lisbon quadrangles, the Mississippian pressure regime is remarkably uniform, close to hydrostatic, and independent of laterally varying pressure in overlying formations. This pressure regime implies relatively high permeability, presumably because of interconnected fractures throughout the section and development of karst topography at the top due to subaerial exposure at the end of the Mississippian (figures 3.1A, 3.2, and 5.9). The zero-pressure head on this pressure regime varies between 4000 ft asl (1200 m asl) in the north (West Green River quadrangle) and 3800 ft asl (1200 m asl) in the two southern quadrangles. This variability corresponds to the elevation of the adjacent sections of the Colorado and Green Rivers, which are acting as the pressure control for this entire region.

In the West Green River quadrangle adjacent to the Green River, saline water (11,000 to 20,000 mg/kg TDS) flows to the surface at several localities, indicating a major discharge point for the basin. Presumably the stretch of the Colorado River south of the junction with the Green River (Cataract Canyon, possibly extending into Glen Canyon/Lake Powell) is also a zone of hydrological connection, and potentially major discharge, for the Mississippian. Any discharge is presumably obscured by the confined, high flow of the Colorado River within the canyon here. Large-scale intrusion of Paradox salt has deformed the canyon (Needles District of Canyonlands National Park), and faults link the northern Monument upwarp to Cataract Canyon (Lewis and Campbell, 1965). The top of the Mississippian section is within about 1000 feet (300 m) of the river level here, when elevations from the wells (figure 8.3) are interpolated and compared to the river elevation. In the Monument upwarp, the top of the Mississippian section rises to 5000 ft asl (1500 m asl).

Near the eastern margin of the Paradox Basin, the pressure in the Mississippian section increases compared to the regional trend

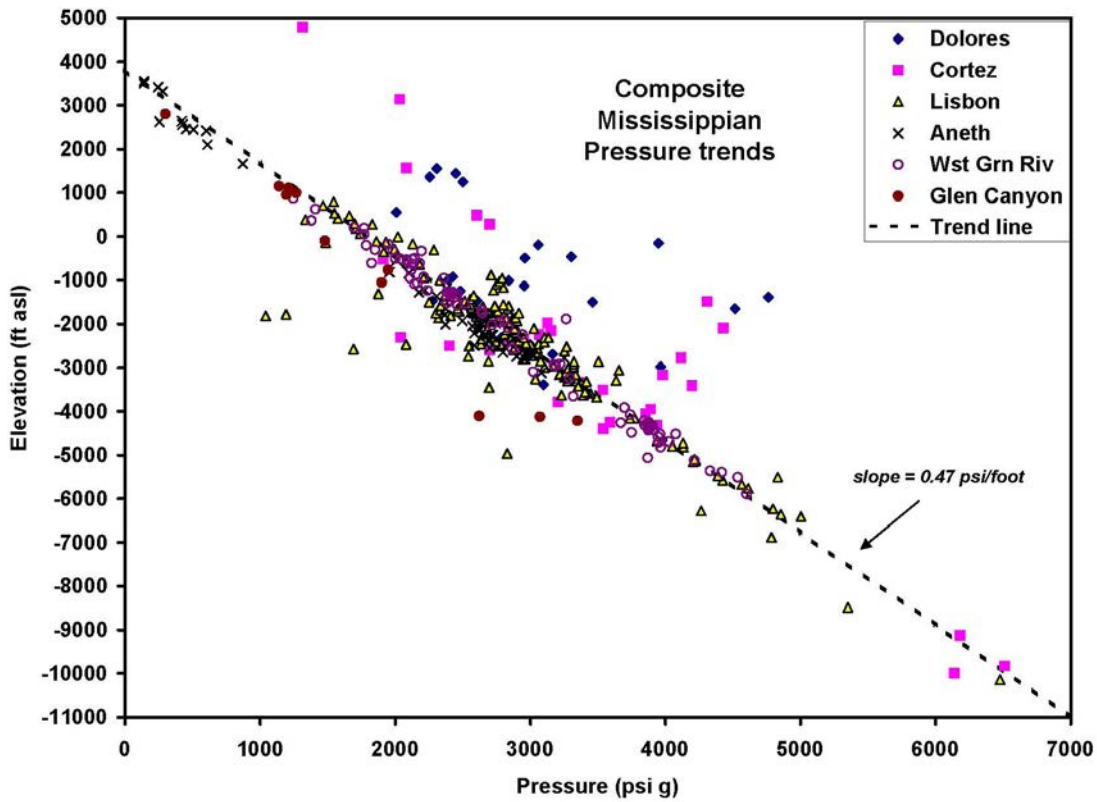


Figure 8.12. Compilation of DST pressure measurements from all six quadrangles for the Mississippian and older formations. Dashed line is referred to in the text as the “composite pressure trend.”

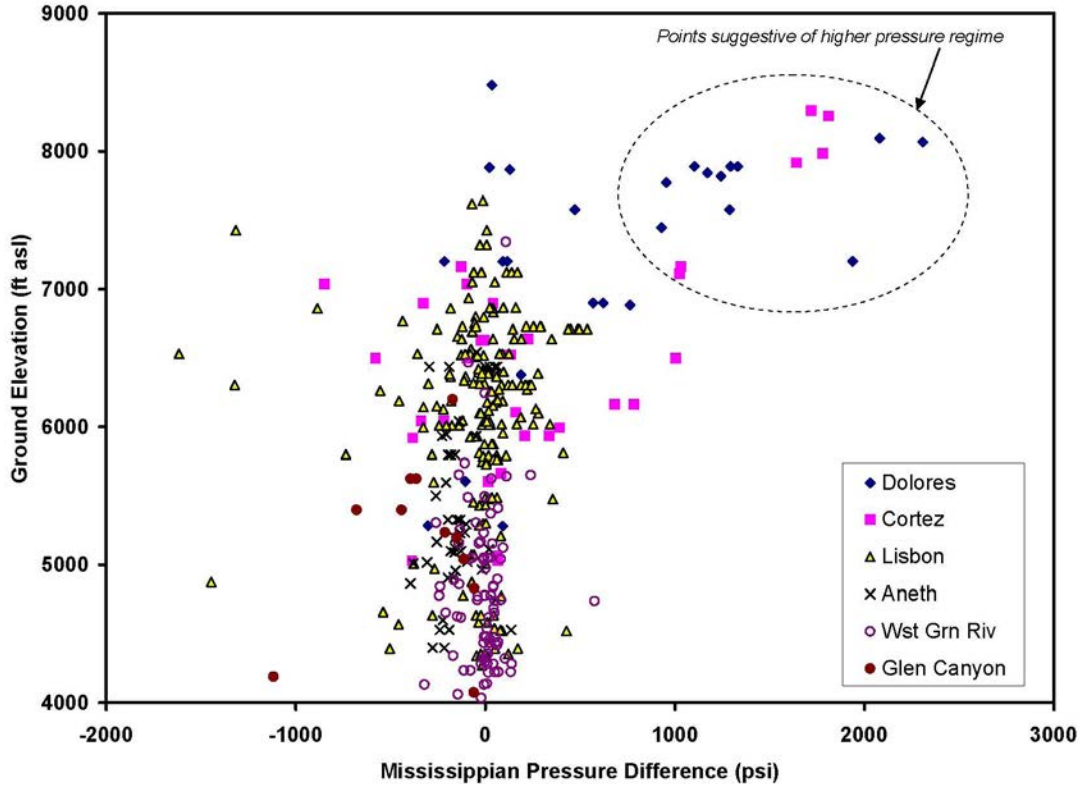


Figure 8.13. Distribution of pressure differences between the actual DST pressure measurement and the pressure inferred from the composite line for that elevation. The pressure differences are plotted against the ground elevation for the well with the DST. This plot shows that most of the DSTs in the Dolores and Cortez quadrangles that plot at systematically higher pressures in figure 8.12 are also at higher ground elevations. They also are in the eastern parts of the two quadrangles, as shown in figure 8.14.

elsewhere by as much as 2000 psi (14,000 kPa) (figure 8.14). This rise in pressure occurs adjacent to the San Juan Mountains farther east, and presumably represents a major recharge area to the Mississippian and older section. There is no evidence of hydrological transition or boundary zones to the Mississippian section in the north or the west of the studied area. However, other recharge areas are likely northwest and west of the six quadrangles studied in this report, perhaps beyond the conventional boundaries of the Paradox Basin as shown in figure 1.1. Around the northern and northeastern boundaries, the Mississippian dips beneath the Uinta Basin and may also be faulted against the Uncompahgre uplift (Frahme and Vaughn, 1983), so significant recharge from this direction seems unlikely.

The broad, uniform pressure regime within the Mississippian raises questions about how long it has existed and its implications for past oil and gas migration. Widespread permeability in the Mississippian strata suggests that it could have been a major fairway for hydrocarbon migration at various times in the past. The top of the Mississippian in the major anticlines in and adjacent to the Paradox Basin (figure 8.4) is situated above the zero-pressure intercept for the regional pressure trend discussed above. This means that if any fluids are still present, they are likely to be at a low pressure and possibly discontinuous. De-

pending on the vertical permeability of the overlying strata, the Mississippian could be air-filled (dry) as reported by Hanshaw and Hill (1969) for some wells on the Monument upwarp. However, this may not have been the case several million years ago. Downcutting by the Colorado River system has hydrologically intercepted the Mississippian section. Using the calculated incision rate near the center of the Colorado Plateau (Lee's Ferry, Arizona) of about 14 inches per thousand years (35 cm/k.y.) (Pederson and others, 2013), several million years ago there would have been several thousand feet more of section overlying and potentially sealing the Mississippian. Today's relative underpressure of the Mississippian relative to the Pennsylvanian and Permian as seen in the Aneth quadrangle would not have been present, and the hydrodynamic gradient could have been in a different direction. That is, the large-scale fluid flow that is inferred to be occurring today towards the Colorado River would not have been occurring, and the Mississippian would have been fully saturated within the Paradox Basin and could have held significant quantities of oil and gas within the structural highs. Some of this volume of oil could be preserved as the tar sand deposits (Tar Sand Triangle, White Canyon, and Ten Mile Wash), found along the western margin of the Paradox Basin, that may have been a larger pool trapped in what is now partially breached Monument upwarp.

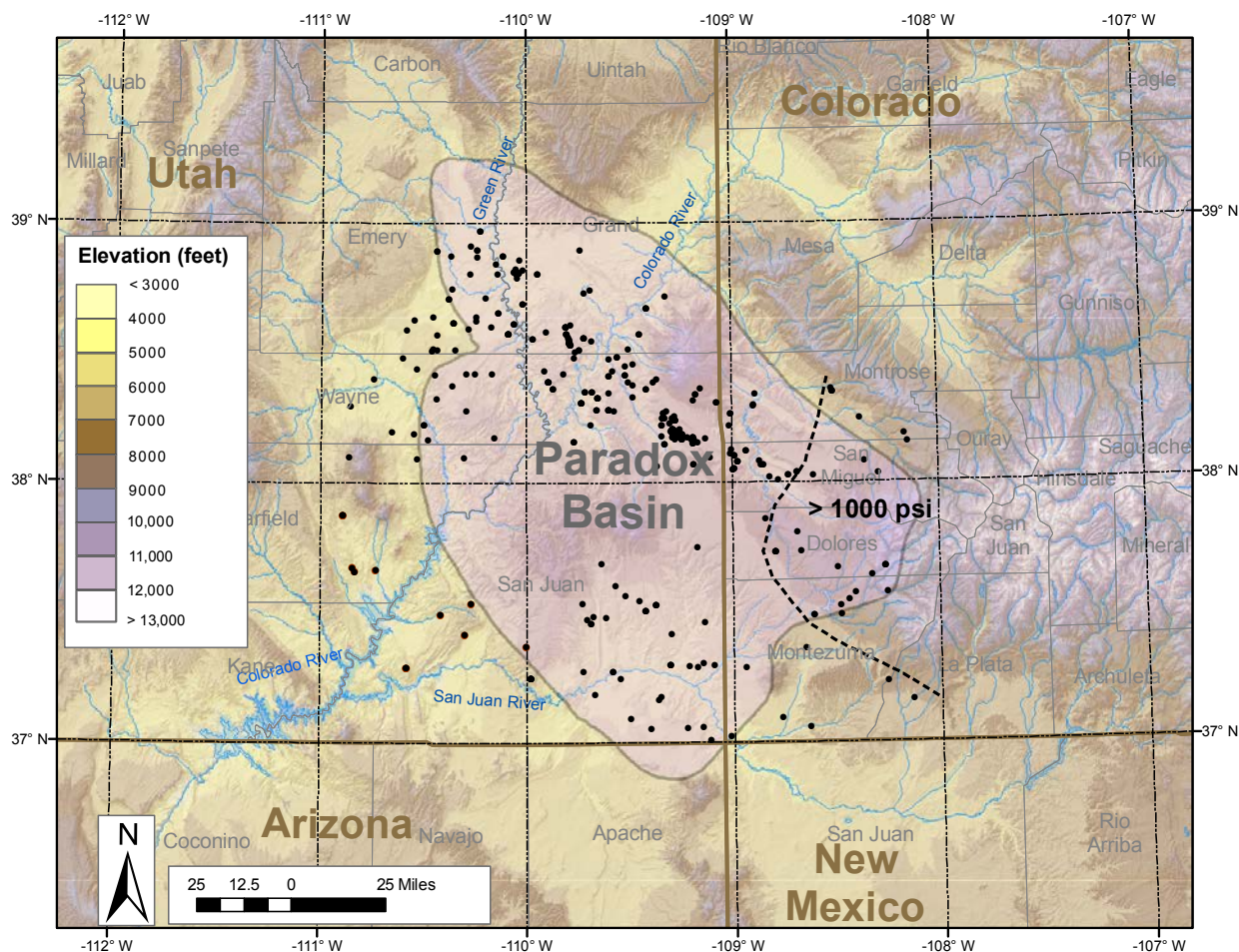


Figure 8.14. Summary of the region of anomalous pressures (> 1000 psi) identified in figures 8.12 and 8.13 for Mississippian and older rocks of the Paradox Basin. Elsewhere, pressures are close to hydrostatic with a zero-pressure intercept of 3800 to 4000 feet asl (1160–1220 m asl). Black dots indicate the distribution of wells which had DST measurements within the Mississippian or older formations.

CHAPTER 9: MODERN RESERVOIR ANALOGS FOR THE LEADVILLE LIMESTONE—SOUTHERN FLORIDA AND THE BAHAMAS

by

Thomas C. Chidsey, Jr., Utah Geological Survey

and

Scott M. Ritter, Department of Geological Sciences, Brigham Young University

CHAPTER 9:

MODERN RESERVOIR ANALOGS FOR THE LEADVILLE LIMESTONE—SOUTHERN FLORIDA AND THE BAHAMAS

INTRODUCTION

The oil and gas reservoirs from the Mississippian Leadville Limestone of the Paradox Basin represent a variety of warm, shallow-shelf, carbonate depositional environments as described in previous chapters. Deposition of the Leadville and other carbonate formations was widespread in Paleozoic and Mesozoic epeiric seas. However, there are relatively few places on Earth where shallow-marine carbonates are actively being deposited on a major scale and over millions of years. Platform-scale carbonate deposition today is restricted to the southern Florida-Bahamas region, the Yucatan, the Arabian Gulf, and Australia.

Leadville environments have modern analogs in the southern Florida-Bahamas region—a world-class natural laboratory to study “tropical” carbonate depositional systems (figure 9.1). This region represents a time horizon from which one can observe carbonate deposition, the conditions (physical, biological, and chemical) that create various carbonate sediments, and the processes by which the deposits change. Understanding the facies types, distribution, geometry, and depositional patterns of these modern analogs helps to better (1) determine sediment source and accumulation, (2) estimate reservoir heterogeneity and capacity, (3) establish initial pore-space characteristics, and (4) identify areas regionally that have the greatest petroleum potential of the Leadville Limestone.

BASIC PRINCIPLES OF CARBONATE DEPOSITION

Carbonate Factories and Platforms

Southern Florida and the Bahamas are carbonate “factories.” Carbonate production is at a maximum in the carbonate-factory areas (Pomar and Hallock, 2008; Michel and others, 2019). Noel P. James (1979), pre-eminent scholar in the processes that produce modern limestone, stated “Carbonates are born, not made.” That is, they result largely from biological and biochemical processes and carbonate mineral precipitation is mediated by microbes (cyanobacteria), plants, and animals. Some carbonate sediment is created by direct precipitation from seawater (Bosence and Wilson, 2005). Skeletal materials become particles and accumulations become limestone.

Three basic rules control the nature (formation, distribution, and deposition) of carbonate depositional systems (Schlager,

1992): (1) carbonate sediments are largely organic in origin, (2) carbonate systems can build wave-resistant structures, and (3) they undergo extensive diagenetic alteration. The rate at which organisms and plants produce carbonate sediment depends on latitude, temperature, salinity, oxygen content, water depth, acidity (pH), sunlight intensity, turbidity, water circulation, partial pressure of carbon dioxide (pCO₂), and nutrient supply (Schlager, 2003, 2005).

Most carbonates are produced close to where they are deposited as opposed to typical siliciclastic sediments. However, storms, tides, and currents transport large quantities of fine sediment into adjacent areas (including both shallow- and deep-water settings). Carbonate factories develop where clean, shallow (less than 300 feet [<100 m]) marine waters cover large platforms; the highest sediment productivity occurs at water depth less than 30 feet (<10 m) (Schlager, 2003, 2005).

Carbonate platforms are recent and ancient, thick, widespread deposits of carbonate rocks (Bosence and Wilson, 2005). Factors that influence differences in the platforms upon which warm-water carbonates are deposited include (1) climate, (2) platform morphology (such as ramp or rimmed attached platforms or isolated unattached platforms), (3) lithology (carbonate only, carbonate/siliciclastic, or carbonate/evaporate), (4) fauna, (5) subsidence, (6) siliciclastic source, and (7) eustasy (greenhouse, icehouse, or transitional) (Schlager, 2003, 2005; Michel and others, 2019).

There are four main types of carbonate factories: (1) warm water, (2) cool water, (3) microbial, and (4) pelagic (Schlager, 2003; Bosence and Wilson, 2005). The southern Florida and Bahamas region is a warm-water carbonate factory. The Mississippian Leadville Limestone was deposited in a warm-water carbonate factory on an epeiric-attached platform (i.e., an extensive cratonic area covered by a shallow sea) (figures 3.1A, 5.5, and 5.6). Warm-water carbonate factories are located generally between low latitudes (30° north and 30° south), both presently and in the geologic past. Shallow-marine tropical waters support rapidly calcifying communities of organisms that use photosynthesis for energy. Examples of these communities include calcified green and red algae, and corals with symbiotic algae. Forams, mollusks, sponges, and echinoderms are also common members of such communities. These communities build shallow-water coral reefs, shoals composed of skeletal grains, and other types of carbonate accumulations.

The warm water is also often supersaturated with respect to calcium carbonate, which can be precipitated to form carbon-



Figure 9.1. Satellite image of southern Florida and the Bahama Islands. Annotated NASA Landsat image.

ate grains such as ooids, peloids, grapestone, and carbonate mud. Shallow warm-water carbonate accumulation rates range from about 0.6 to 24 feet (0.2–8 m) per 1000 years and can keep pace with a rise in sea level when the rate of sediment production is highest (Bosence and Wilson, 2005).

Taphonomic Processes

Another key aspect of studying modern carbonate analogs to better interpret the lithofacies of the Leadville Limestone is using tropical taphonomy to go from biofacies (biotic communities) to lithofacies (carbonate sediments). Early taphonomic processes (biostratinomy) take place after an organism dies but before its final burial. These processes are largely destructive (bioerosion) and include physical, biological, and chemical effects. As a result, much of the information about the biotic community is lost, but the gain is a depositional envi-

ronment with information “encoded.” Thus, the sedimentary lithofacies mimic the former biological communities (Purdy, 1963; Harris and others, 2015).

Physical processes consist of reorientation, transport, breakage, disarticulation, and exhumation. Biological processes consist of decay, scavenging, bioturbation, boring, and encrustation. Chemical processes consist of corrosion, dissolution, and recrystallization. The roles of organisms in these processes may be ecological, sedimentological, or diagenetic. Ecologic roles of organisms are that of a primary producer, grazer, predator, or filter feeder. Sedimentological organism roles include sand makers, mud makers, sediment binders, sediment bafflers, frame builders, sediment eaters, burrowers, borers, and encrusters. Diagenetic roles consist of producing aragonite versus calcite, micritization, and grain boring (Bathurst, 1972; Moore and Wade, 2013).

Warm-Water Biologic Communities

Although the organisms in warm-water carbonate settings today are different from those of the past, due to organic evolution, the roles of sediment producer, modifier, etc., have remained largely unchanged through time. According to Enos (1977), “for modern ecology to have maximum applicability to ancient limestone, consideration should be given to evolutionary replacement. Replacement is the adaptation of an organism or groups to approximately duplicate the way of life of an earlier group. Replacement may result from successful competition with the earlier group or from simply filling an available ecological niche, long since vacated by the earlier group.” Examples include Paleozoic tabulate corals and modern scleractinian corals, or the Pennsylvanian green algae *Ivanovia* and the modern green algae *Halimeda*. Southern Florida and the Bahamas team with a wide variety of life to fill the ecological, sedimentological, and diagenetic roles (described above), which have counterparts in the Leadville Limestone.

Cyanobacteria

Cyanobacteria are a phylum of free-living bacteria (formerly called blue-green algae) that produce and release oxygen as a byproduct of photosynthesis. Cyanobacteria are prokaryotes having cells that are very small and contain only a cell wall, which encases undifferentiated cytoplasm inside a membrane with only vague, poorly organized structures known as nucleoids, ribosomes, and plasmids. Microbialites form as a result of cyanobacteria (microbial) activities and represent deposits that have accreted as a result of a benthic microbial community trapping and binding detrital sediment and/or forming the locus of carbonate mineral precipitation (Burne and Moore, 1987). Cyanobacteria commonly form carbonate mats in supratidal environments in Florida Bay and the Bahamas (figure 9.2).

Protozoans

Protozoans are mainly foraminifera. Most of the shelf foraminifera belong to two families: Miliolidae and Peneroplidae. They are mobile benthonic forms that live on grass (figure 9.3) and in or on sediment (Enos, 1977). The regional distribution of foraminifera is controlled by a range of environmental factors, indicating that foraminifera are sensitive to the environment and diagnostic of past depositional settings (Bock and others, 1971).

Plants

Plants include algae and vascular plants. Calcareous algae are classified based on pigmentation, composition, and habit. They consist of two phyla: (1) Rhodophyta (red algae), and (2) Chlorophyta (green algae). The red algae make up about 10% of the calcareous algae whereas the bulk of the volume of sediment produced from calcareous algae comes from the green algae (figures 9.4 and 9.5). The segmented green algae *Halimeda* (figure 9.5) is a sand maker found in relatively high-

energy environments. Multiple generations grow each year. *Halimeda* is a major producer of carbonate sediment—estimated to be as much as 22,000 grains per year per 11 square feet (1 m²) or 65% of the sediment in some areas (Neumann and Land, 1975). Mud-making green algae include *Penicillus*, *Udotea*, and *Rhipocephalus* (figures 9.4 and 9.6). *Penicillus* and *Udotea* produce needles of aragonite when they die. *Penicillus* (“shaving brush”) is the major contributor of fine aragonite mud; the similarity of Holocene muds and many ancient lime muds (textures, structures, and fossils) implies that these plants have been a significant source of fine-grained sediment in the geologic past (Stockman and others, 1967), including possibly Leadville Limestone. The most common red algae is *Neogoniolithon* typically found on shelf margins. It can be flat, saucer-shaped crusts to erect, branching plants (figure 9.7) (Enos, 1977).

Vascular plants include sea grasses (angiosperms) and mangroves. The most widespread sea grass is *Thalassia testudinum* (turtle grass) (figure 9.8), which requires adequate sunlight and stable, thick sediment for its root system. Turtle grass plays an important role as a baffle and sediment trap (Enos, 1977). Mangroves, which are classified as red (*Rhizophora mangle*) with roots going down (figure 9.9) and black (*Avecinna*) with roots going up (figure 9.10), form around the edges of islands, lagoons, and marshes. These plants can ultimately form peat.

Invertebrates

Invertebrates include the phyla Porifera (sponges), Cnidaria, and Mollusca. Sponges generally require a hard surface for attachment. The larger sponges contain siliceous spicules. The overall contribution of sponge spicules as a sediment constituent is low. Phylum Cnidaria represents the most important invertebrates in warm-water carbonate platforms—the corals. The three main classes are Hydrozoa (fire corals), Scyphozoa (jellyfish), and Anthozoa, which includes the order Scleractinia (Triassic through modern corals). Hydrozoans are common but only the fire coral *Millepora* secretes a calcareous skeleton (figure 9.11) (Enos, 1977). They may be branching or bladed requiring a firm substrate in high-energy environments. Alcyonaria (also known as Octocroallia because they have eight-fold symmetry) is a subclass of Anthozoa. They include sea fans, sea whips (figure 9.12), sea pens, sea feathers, and soft corals. Alcyonarians grow on dead coral or rubble in outer reefs and patch reefs around living coral where the water is shallow and has strong wave action. When they die, many species disintegrate and become sediment consisting of little rods.

The spectacular reefs of the southern Florida-Bahamas region are primarily built by scleractinian corals (hard corals) (Lidz and others, 1991). These corals are zoned and grow in a variety of sub-environments. The chief framework builder of the outer reefs is the massive, branching *Acropora palmata* (moosehorn coral) occurring where there is maximum wave action and water circulation on the reef crest (figure 9.13A).



Figure 9.2. Microbial mats (cyanobacteria) in a supratidal environment on Cotton Key, one of many islands in Florida Bay.

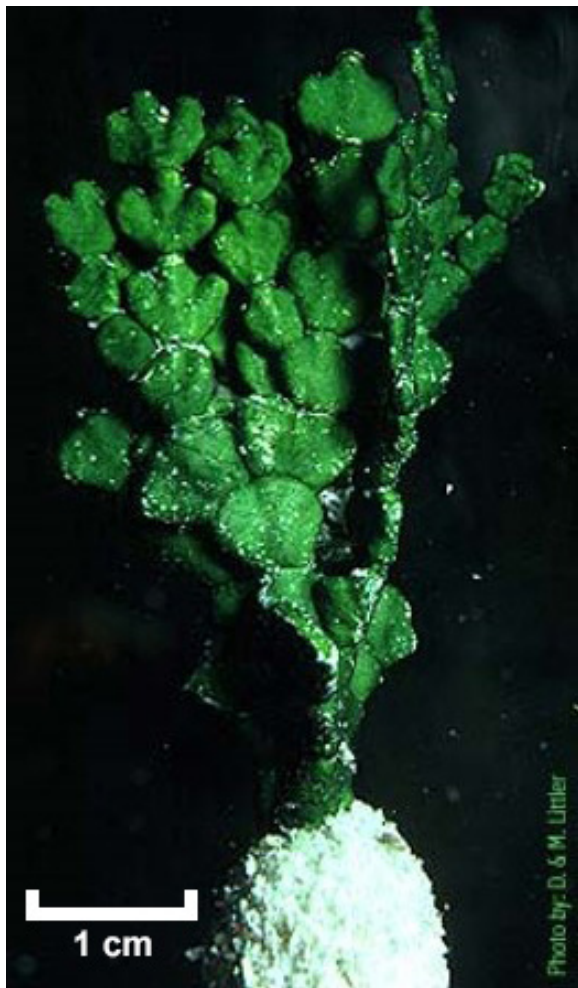


Figure 9.3. Foraminifera attached to sea grass, Florida Bay.



Figure 9.4. Green algae *Halimeda* and *Penicillus* growing on the sandy bottom of Florida Bay.

A.



B.



Figure 9.5. Close-up of *Halimeda* (A) and the sand grains (B) derived from its disintegration.



Figure 9.6. Mud-making green algae (from left to right) *Penicillus*, *Udotea*, and *Rhizocephalus*.



Figure 9.7. Branching red algae *Neogoniolithon* near Rodriguez Bank, Florida.

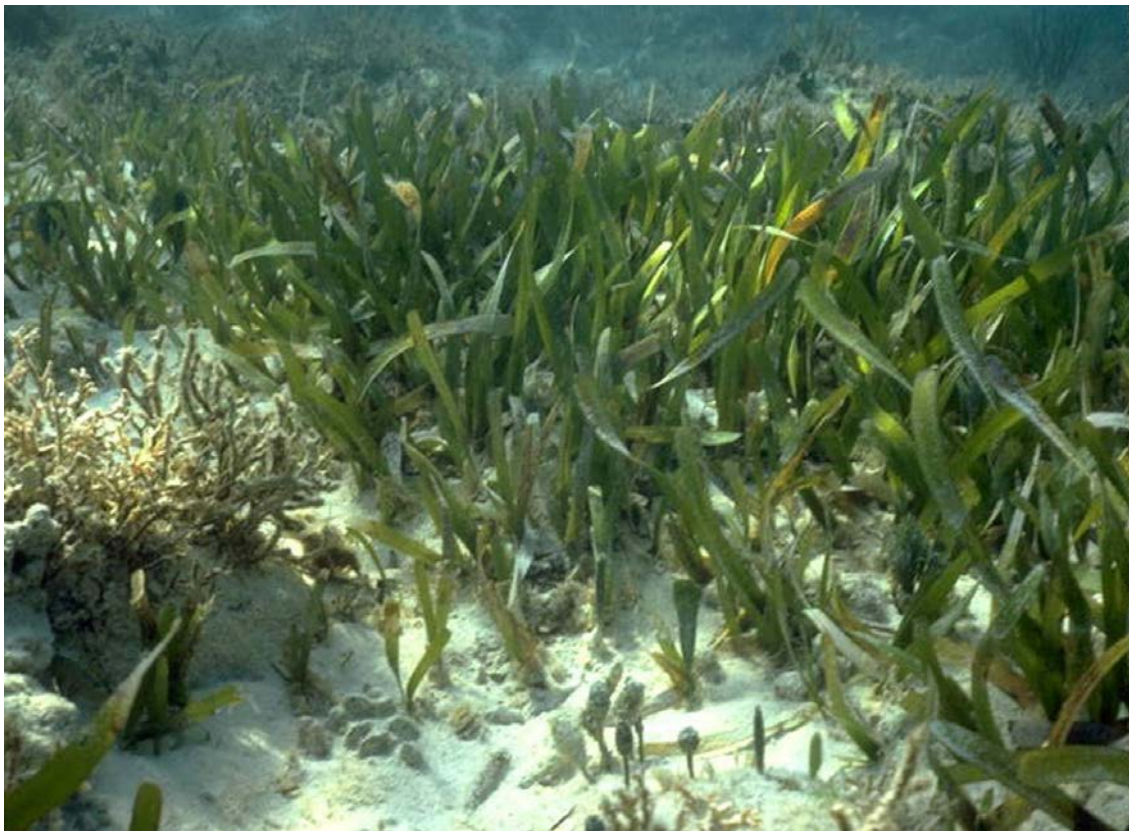


Figure 9.8. Turtle grass (*Thalassia*) illustrating its ability to act as a sediment trap, Florida Bay.



Figure 9.9. Red mangrove (*Rhizophora mangle*), Florida Bay area.

Acropora cervicornis (elkhorn coral) (figure 9.13A) and *Porites porites* (finger coral) (figure 9.13B) are found in quieter waters of the outer reef and back reef areas. The branches of elkhorn and moosehorn corals often break off, especially due to storms or when they die, forming rubble zones in the back reef, reef front, and forereef areas. *Porites* also occurs on patch reefs in the back reef and lagoonal areas where it is well rooted or attached. Massive head corals are the dominant forms in patch reefs but can also grow in sheltered parts of outer reefs. The most abundant head coral in patch reefs is the large, massive *Montastrea annularis* (star coral) (figure 9.13C). Other common patch reef corals are *Diploria* (brain coral) (figure 9.13D) and *Siderastrea* (golfball coral) (figure 9.13E). Some patch reef corals, such as *Siderastrea* and *Porites*, also occur in semi-restricted environments where they may be widely distributed but populations are sparse and their size small. In addition, small *Porites* and *Siderastrea* are very abundant around muddy shoals (main mud mounds) or tidal channels (Enos, 1977). Some corals are mud tolerant such as *Manicina* (rose coral) (figure 9.13F), which are comparable to Paleozoic horn (rugose) corals common in the Leadville Limestone (figure 3.5).

Members of the phylum Mollusca, particularly gastropods (snails) and bivalves (clams and oysters), are significant con-

tributors of sand-size skeletal grains. Whereas skeletal grains from crinoids may have been prevalent to create shoals in the Mississippian, gastropods, for example, are a major contributor now (figure 9.14). Molluscs are varied, abundant, and good ecological guides (Enos, 1977).

Of the arthropods, the crustaceans are the most significant. They live in all marine environments in the carbonate platform. They contribute huge amounts of fecal pellets to the carbonate system and are major burrowers, particularly the shrimp *Callinassa* (figure 9.15). Ostracods are common in restricted inner shelf areas.

Echinoderms are also common in all marine environments and include echinoids (sea urchins and sand dollars), holothurians (sea cucumbers), ophiuroids (brittle stars), and asterozoans (star fishes). Yet, in comparison to Paleozoic environments, their modern contribution is relatively minor. Sand-size calcite plates from sand dollars (figure 9.16) can yield significant quantities of carbonate sand in some areas.

Annelid worms affect carbonate deposits of platforms by burrowing, pelleting, and boring (Enos, 1977). Bryozoans, so common in the Paleozoic fossil record, play a relatively minor role in modern carbonate environments.



Figure 9.10. Black mangrove (Avecinnia), Florida Bay area.



Figure 9.11. Branching fire coral *Millepora*.



Figure 9.12. Alcyonarian sea fans (A) and sea whips (B).

A.



B.



C.



D.



E.



F.



Figure 9.13. Various scleractinian corals: (A) moosehorn (*Acropora palmata*) and elkhorn (*Acropora cervicornis*) corals, (B) finger coral (*Porites*), (C) star coral (*Montastrea annularis*), (D) brain coral (*Diploria*), (E) golfball coral (*Siderastrea*), and (F) rose coral (*Manicina*).



Figure 9.14. Large concentration of small, high spiral gastropods, which feed on the microbial mats of the intertidal zone in the carbonate tidal flats, northwestern side of Andros Island, Bahamas. This deposit would ultimately yield a skeletal packstone to wackestone in the rock record.



Figure 9.15. Numerous mounds made by the burrowing shrimp *Callinassa* (inset), Bahamas.

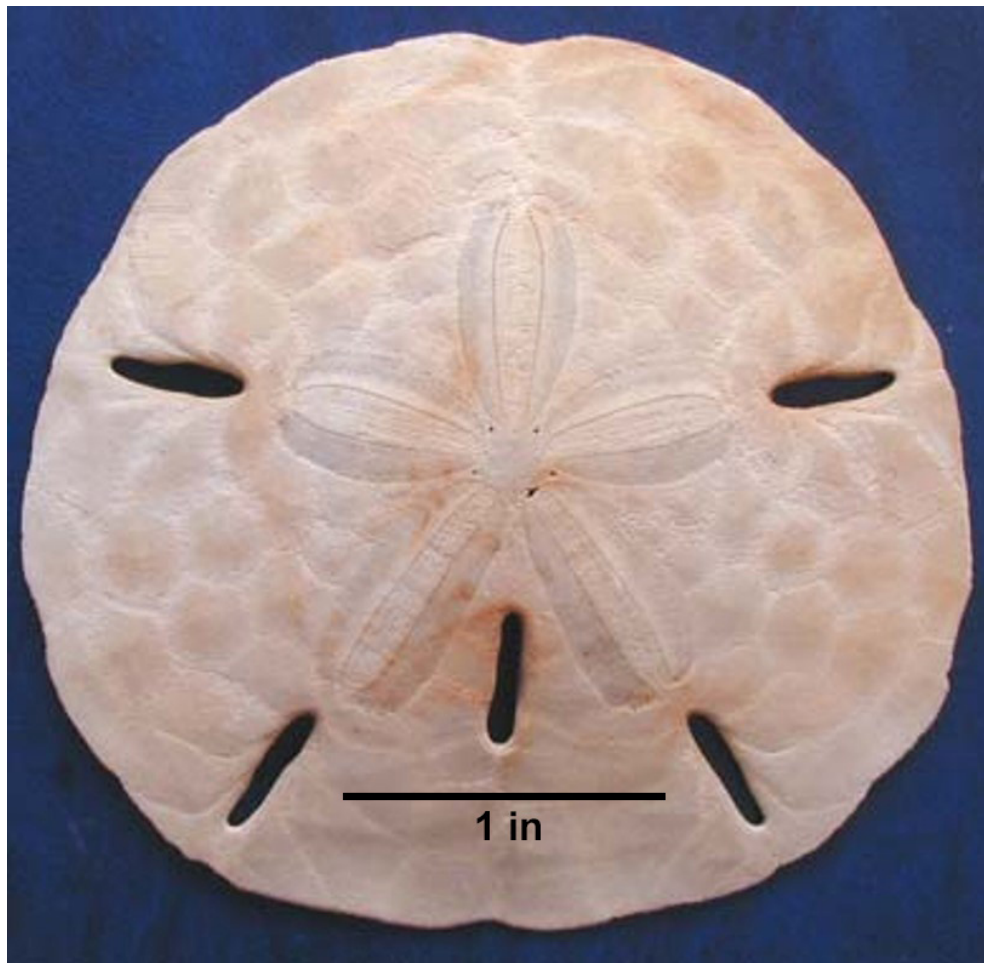


Figure 9.16. Typical grain-making sand dollar echinoid.

SOUTHERN FLORIDA – FLORIDA BAY TO THE OUTER REEF

Southern Florida provides an opportunity to examine transgressive depositional conditions and sediments across several facies belts ranging from the Everglades to shelf-edge barrier reefs, including supratidal microbial flats, restricted marine mudbanks and “lakes,” tidal channels, and outer shelf sand bodies (Ball, 1967; Enos, 1977; Enos and Perkins, 1979). Here one can observe two complementary facets of each environment: (1) the influence of physical and biological processes on the distribution of marine plants and animals, and (2) the relationship between the organisms that inhabit the area and the type of sediment and sedimentary textures produced in each environment.

Southern Florida is an attached, rimmed carbonate platform (figures 9.17 and 9.18). This shallow shelf, warm-water carbonate factory lies on the late Pleistocene Key Largo Limestone. The Key Largo Limestone reef forms the present-day Florida Keys, the islands that separate the modern arcuate reef tract from Florida Bay. From northwest to southeast, the platform consists of mangrove swamps and supratidal flats (Everglades), an inner shelf (Florida Bay), inner and outer shelf

margins, and a shallow slope into the Straits of Florida (figures 9.17 and 9.18) (Enos, 1977).

Southern Florida has a semi-humid to sub-tropical climate (40 to 45 inches [100–114 cm] of rain per year) with a wet season from July to December (Bosence and Wilson, 2005). Southeast trade winds during the summer swing to the northeast during the winter generating bottom currents of 1.5 feet (0.5 m) per second. The region is within the microtidal range (2 feet [0.7 m]) and tidal currents only affect channels and flood-tidal deltas except during storms (Missimer, 1984). The platform hinterland (Everglades) is large with an abundance of fresh water.

Florida Bay

Florida Bay is triangular shaped due to barriers that restrict circulation (figure 9.17) (Enos and Perkins, 1979). Water depths range from 0 to 10 feet (0–3 m) and maximum local relief is 12 feet (4 m). Water circulation is restricted with periodic tides only on the margins. The surface water temperature ranges from 59° to 104°F (15°–40°C) and the salinity varies from 10 to 70 parts per thousand (‰) (Fourquean and Robblee, 1999). Plankton and nutrient availability are low, and the turbidity is generally high.

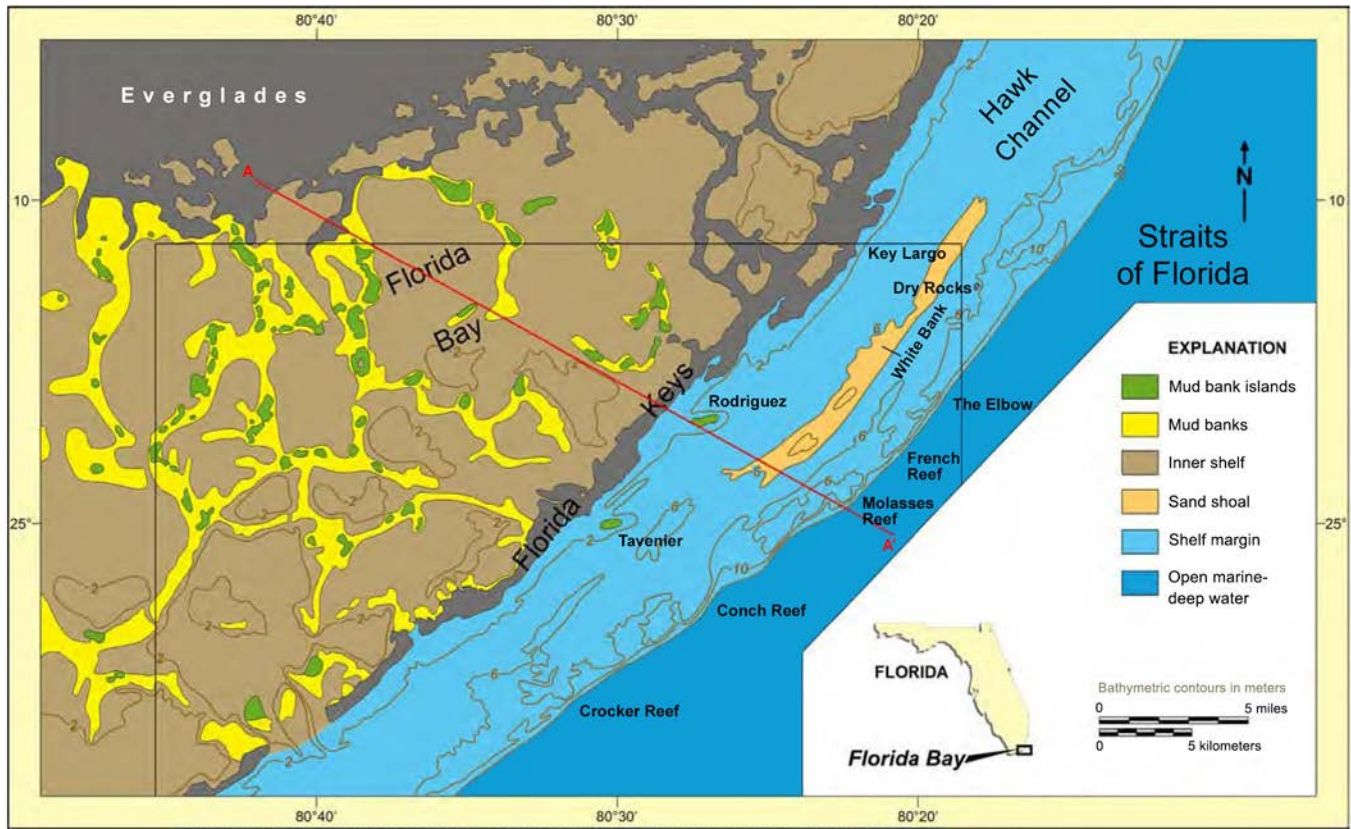


Figure 9.17. Features of the southern Florida attached, rimmed carbonate platform including bathymetry, the Florida Keys (Pleistocene reefs of the Key Largo Limestone), major depositional environments, and modern reefs (modified from Ginsburg, 1956). Cross section A–A' shown on figure 9.18. Map projected from regional Landsat image below.

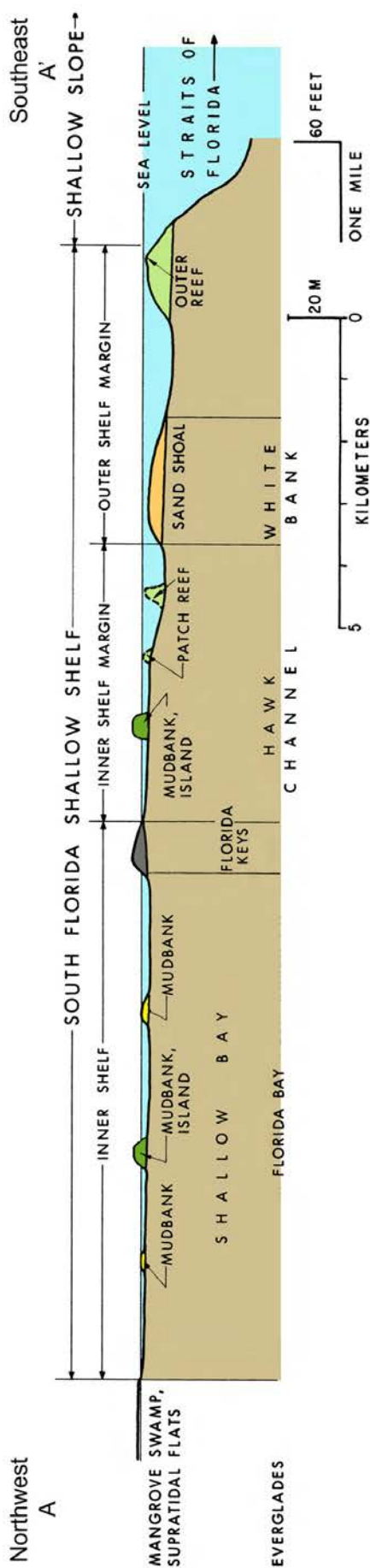


Figure 9.18. Generalized northwest-southeast cross section through the southern Florida attached, rimmed carbonate platform displaying major features and depositional environments. Modified from Enos (1977). Line of section shown on figure 9.17.

There are four hydrological influences on the environmental characteristics of Florida Bay: (1) the Gulf of Mexico, (2) the reef tract, (3) the Everglades, and (4) the bay itself. Waters and biota in the bay are derived from the Gulf of Mexico to the west, the Atlantic Ocean (Straits of Florida) through breaks in the exposed Pleistocene reef tract (the Florida Keys) to the south and east, and the Everglades to the north. The Gulf of Mexico has the greatest effect although broad carbonate mud banks restrict tidal action. Tidal channels through the Keys into the bay represent high-energy environments that support a high diversity of larger organisms (gastropods, clams, and corals) in deposits of *Halimeda*-produced sand that are relatively free of mud (which has been winnowed out by currents) (figures 9.4 and 9.5). In the Everglades, fresh water accumulates during the rainy season then flows southward into the northern part of the bay during the winter, thus significantly lowering the salinity to as little as 10‰ from a summer high of 50‰. Such a wide range limits the biota of the bay (Fourqean and Robblee, 1999). The honeycomb nature of the mud-bank distribution within the bay (figure 9.17) further restricts currents, salinity, tides, etc.

A variety of sedimentary environments are represented in Florida Bay as part of a transgressive record: (1) fresh-water pond, (2) coastal mangrove swamp, (3) broad, shallow bay basins (“lake”), (4) mud bank, and (5) island. From our work on the Leadville Limestone, we recognize the shallow bay basins and mud banks (mounds) as modern analogs, which are described in the following sections.

Shallow Bay Basins (“Lakes”)

Broad shallow bay basins, locally known as “lakes,” occupy about 90% of the total area of Florida Bay (Stockman and others, 1967). In the eastern part of the bay, these shallow basins are polygonal (figures 9.19 and 9.20) due to the honeycomb nature of the surrounding mud mounds and cover an area typically of 2 to 8 square miles (5–21 km²). They are 3 to 7 feet (1–2 m) deep with an average sediment thickness of only 6 inches (15 cm) composed of shelly sediment on Pleistocene bedrock (Stockman and others, 1967; Enos and Perkins, 1979). Limited wave action and currents are strong enough to winnow out fine material, which is deposited on the leeward side of mud mounds. Over 70% of the sand-size sediment consists of molluscan skeletal fragments (figure 9.21) (Ginsburg, 1956). This environment does not support a large and diverse biotic community. Sea grasses are lacking but the sediment is completely burrowed by worms and crustaceans. The mud that is present is pelleted by these organisms (Shinn, 1968; Enos and Perkins, 1979).

The shallow bay basins in the western part of Florida Bay receive a strong influence from the Gulf of Mexico. Sediment is thicker and contains up to 3 feet (1 m) of mud, which supports turtle grass (further trapping mud) and a larger, diverse fauna. The deposits within the shallow bay basins of Florida Bay would produce skeletal-peloidal packstone, wackestone, and mudstone like those found in the Leadville Limestone (see figures 3.2 and 3.9).



Figure 9.19. Oblique aerial view of Florida Bay shallow bay basins (“lakes”), mud mounds, and islands.



Figure 9.20. Typical view of Florida Bay from sea level of a shallow bay basin and islands (Keys).



Figure 9.21. Sieved samples of coarse, shelly sediment from the shallow bay basin near Sign Bank, Florida Bay.

Mud Mounds (Mud Banks)

Mud mounds (or mud banks as they are often referred to in the literature) are prominent features in Florida Bay. They represent localized accumulations of muddy biogenic carbonate sediments built up by winter storm winds from the northeast (figure 9.22). The windward sides are steeper and covered by a thin skeletal lag. The muddy leeward sides slope more gently and are stabilized with turtle grass (Enos and Perkins, 1979). Mounds migrate slowly in the leeward direction (Bosence, 1995; Bosence and Wilson, 2005). Mound tops are flat and awash at low tides. Some mounds build up to sea level to become islands colonized by mangroves. Saline ponds and microbial mats are also common on the mud-mound islands (figure 9.2). Mud mound thicknesses range from 6 to 12 feet (2–4 m) (Enos and Perkins, 1979).

The green algae *Penicillus* (figures 9.4 and 9.6) is responsible for the production of one-third of the aragonite mud in the mounds (Stockman and others, 1967). Other sedimentary particles include poorly sorted shell fragments and pellets. Mound sediments are completely burrowed, and the upper zones penetrated by roots and rhizomes of turtle grass (figure 9.8) (Enos and Perkins, 1979).

Mud mounds contain sedimentological, paleontological, and geochemical records of past conditions in Florida Bay (Robert B. Halley, U.S. Geological Survey, verbal communication, 1998). Therefore, such records likely exist in Mississippian Waulsortian-type (mud mound) buildups. The deposits that make up Florida Bay mud mounds would produce skeletal/pelletal wackestone and locally packstone or mudstone (see figures 3.2 and 3.6) as found in the Leadville Limestone.

Reef Tract

The southern Florida attached platform has a rimmed margin formed by the arcuate reef track band (figures 9.17 and 9.18). Water depths range from 0 to 300 feet (0–100 m) and maximum local relief is 30 feet (10 m). Water circulation is open with semi-diurnal tide exchange with the Florida current. The surface water temperature ranges from 59° to 91°F (15°–33°C) and the salinity varies from 32‰ to 38‰. Plankton and nutrient availability are normal for the tropics and the turbidity is periodically high in the lagoonal part of the shelf margin (Multer, 1977; Shinn, 1988; Lidz and Shinn, 1991; Lidz and others, 1991).

The reef track is 150 miles (240 km) long, averages 4 miles (6 km) in width, and coincides with the inner and outer shelf margins (figure 9.18). Sedimentary environments include the seaward forereef, discontinuous outer barrier reef (subdivided into a reef front, reef crest, and reef flat), and back reef consisting of a sand apron and lagoon (containing patch reefs and sand shoals). The differences among these environments are due to water depth and circulation, which also is reflected in sediment types and biological communities. Areas of mud accumulation (mud mounds) are found in front of the Keys representing a transition from open-marine conditions to those of Florida Bay.

The Leadville Limestone has no known barrier reefs. However, from our work, we recognize the marine mud mounds, patch reefs, and sand shoals in the reef tract as modern analogs, which are described in the following sections.

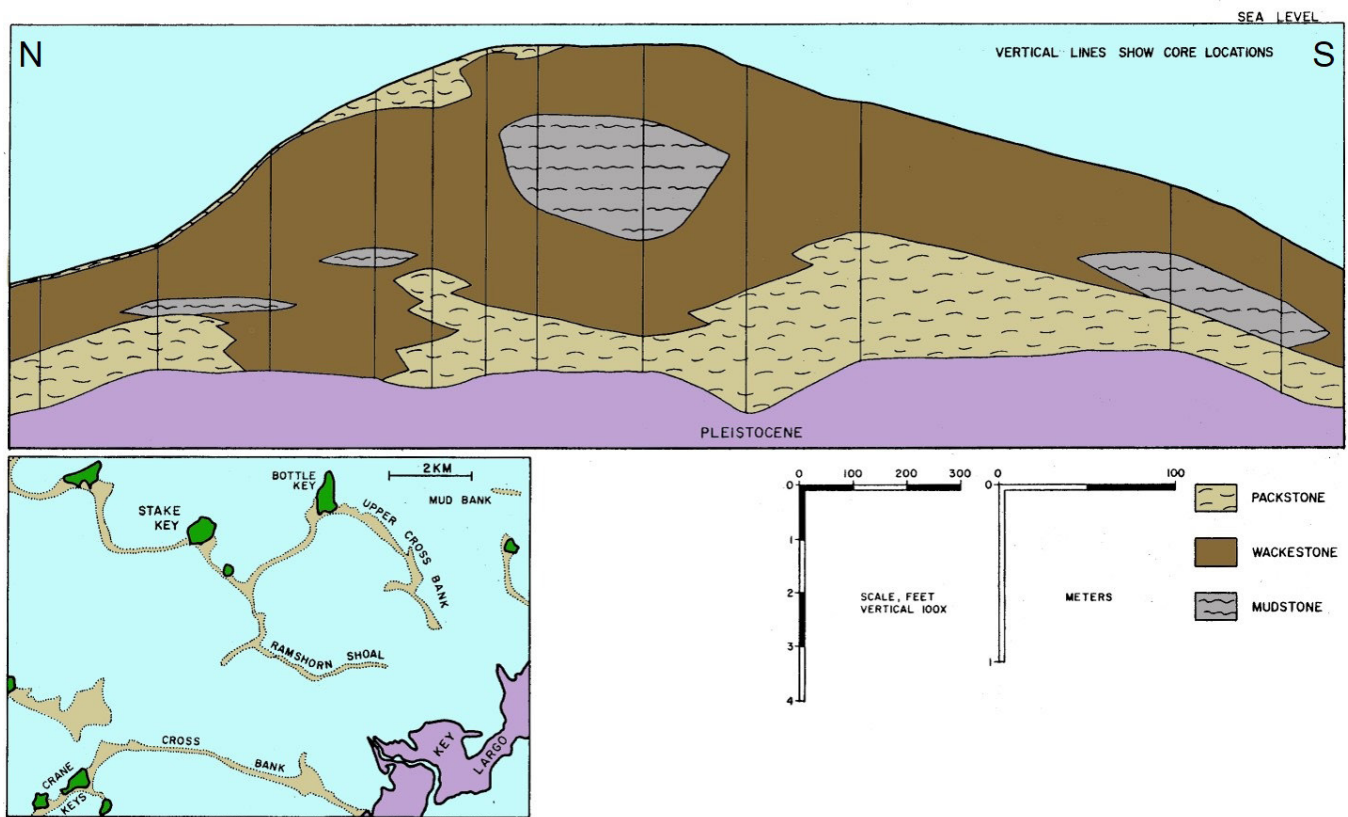


Figure 9.22. Generalized cross section through Cross Bank, a typical Florida Bay mud mound. The steeper northern, windward side is capped by a layer of shelly sediment that would produce a packstone. Modified from Enos and Perkins (1979).

Mud Mounds

Besides being a dominant feature of Florida Bay, mud mounds (or carbonate mud banks) have also formed in the inner shelf margin of the reef tract. They have similar characteristics to the mud mounds in Florida Bay. Examples include Rodriguez Key and Tavernier Key (figure 9.17). Rodriguez Key is a flat-topped island, about 1.5 miles (2.4 km) long and 0.7 miles (1.1 km) wide, with the surface varying around mean sea level. The axis of the island is covered with black mangroves and the margins with red mangroves. Surrounding the windward side of Rodriguez Key are three biologic zones (figure 9.23): (1) an inner zone of turtle grass and green algae (*Halimeda*, *Penicillus*, *Udotea*, and *Rhypocephalus* [figures 9.5 and 9.6]) in the bank environment, (2) a middle zone of finger coral (*Porites* [9.13B]) and thickets of branching red algae (*Neogoniolithon* [9.7]) in the windward bank margin, and (3) and an outer zone of turtle grass and green algae in the off-bank environment (Turmel and Swanson, 1976; Bosence, 1985).

The mound is composed of skeletal calcite mud produced principally by green algae (Turmel and Swanson, 1976). The maximum thickness of the sediments is 15 feet (5 m). The mound developed over a topographic low in the underlying Key Largo Limestone. This low filled with mud, which was probably stabilized by turtle grass resulting in eventual mound development—a possible key for predicting mud mounds in the Mississippian. The resulting sediments outward from the

island are (1) mixtures of lime mud and skeletal sand, (2) skeletal sand and gravel, and (3) lime mud and skeletal sand.

Patch Reefs

Patch reefs are common in the inner shelf margin of the reef tract lagoon and back reef areas (figure 9.18). Though small in area, many are named such as Hens and Chicken reef, for example. They rise 10 or more feet (3 m+) above the sea floor to within 6 to 12 feet (2–4 m) of the surface. Patch reefs are circular to elliptical in plan view and can range up to several hundred feet in length. They develop over slight topographic highs, changes in slope, or on the rims of depressions (Enos, 1977). Ecologically, patch reefs require similar conditions for development as barrier reefs except for lower wave energy.

Patch reefs may include large and small corals of *Montastrea annularis* (star coral), *Porites* (finger coral), *Siderastrea* (golf-ball coral), and *Diploria* (brain coral) (figures 9.13B through 9.13E). Alcyonarians (sea fans and sea whips [figure 9.12]) grow on dead coral, which is often encrusted with coralline algae. Patch reefs are usually surrounded by an apron of rubble and sand grains produced by physical erosion (currents and wave action) and bioerosion (from sponges, worms, parrot fish, echinoids, and molluscs). The bottom of the lagoon where patch reefs grow is usually skeletal containing 10% to 60% lime mud produced by the green, mud-making algae and trapped by carpets of turtle grass.



Figure 9.23. Generalized map of sediments and environments of Rodriguez Key. Inset photograph of Neogoniolithon. Modified from Turmel and Swanson (1976).

Carbonate Sand Shoals

Calcareous sand shoals, such as White Bank (figures 9.17 and 9.18), lie between the outer reef and the inner shelf margin. Sand deposits are thin, clean, and ripple marked (figure 9.24) (and probably cross-bedded), and the grain size is medium to coarse (figure 9.25). The ripples are usually oscillation types formed from normal current and tidal conditions (Enos, 1977). Water depths of the shoals are 12 feet (4 m) or less. Skeletal sand accumulates in depressions or on topographic highs. The sediment is derived from the outer reef and transported landward (Enos, 1977), thus the size of the shoal is proportional to that of the nearby outer reef. However, some sediment is produced within the sand shoals from sand dollar echinoids (figure 9.16). Worms, crustaceans, and molluscs also inhabit carbonate sand shoals.

White Bank is the largest carbonate sand shoal along the reef tract. It is 1 mile (1.6 km) wide and 20 miles (32 km) long. Large carbonate sand shoals, like White Bank, were common in the Leadville Limestone. Instead of skeletal grains of coral and mollusc fragments, the Leadville shoals consisted of crinoid columnals (see figures 3.2 and 3.5).



Figure 9.25. Coarse, clean skeletal (primarily coral) sand grains from the White Bank sand shoal.



Figure 9.24. Clean, rippled, calcareous sands of the White Bank sand shoal.

GREAT BAHAMA BANK – ANDROS ISLAND AREA

The Great Bahama Bank, centered around Andros Island, provides another opportunity to examine classic examples of modern carbonate deposition in an unattached, isolated, rimmed carbonate platform (figure 9.26). These examples include the origin, sedimentary dynamics, and reservoir properties of ooid shoals, carbonate tidal flats, and the Earth's third longest barrier reef.

The Bahama platform is composed of Pleistocene limestone that lies above 19,000 feet (6000 m) of Tertiary and Cretaceous limestone and dolomite. Strata represent continuous carbonate deposition for nearly 135 million years on a basement of oceanic (basaltic) crust. Holocene sediments reach a thickness of no more than 10 feet (3 m) (Bergman and others, 2010). The platform is separated from other isolated platforms by wide, deep channels that are, in actuality, canyons that were maintained during platform deposition (the Dolomites in northern Italy are an ancient example).

Like southern Florida, the Bahamas climate is semi-humid to subtropical. The Bahamas are within the northeasterly trade-wind belt. The platform is in the microtidal range of 2.5 feet (0.8 m) and the water depths are 0 to 30 feet (0–10 m). The surface water temperature ranges from 72° to 88°F (22°–31°C). Open-marine waters have an average salinity of 36‰.

Basic Depositional Setting

From east to west, the Great Bahama Bank consists of the following features: (1) the barrier reef with a steep reef front dropping rapidly into the Tongue of the Ocean, which reaches a depth of 8000 feet (2500 m), (2) a narrow lagoon, (3) Andros Island composed of exposed Pleistocene limestone with modern carbonate tidal flats on the western side, (4) the shelf lagoon over 40 miles (60 km) wide, and (5) ooid shoals (figure 9.27). The maximum storm wave energy and turbulence takes place at the barrier reef on the eastern side of the platform. Current velocity and wave action are low in the shelf lagoon, but still very important in depositional processes. Turbulence due to tidal currents, not waves, increases along the rimming ooid shoals (Multer, 1977; Bosence and Wilson, 2005; Bergman and others, 2010).

The biological communities within the Great Bahama Bank vary according to water depth, temperature, salinity, wave and tidal energy, substrate, and other living organisms. When compared, the distribution of biotic communities (figure 9.28) has an obvious correlation and interdependency with facies (figure 9.27). In the case of the Great Bahama Bank, a direct relationship exists between biologic communities and two physical factors—wave action (turbulence) and substrate—and therefore facies (Newell and others, 1959; Purdy, 1963; Harris and others, 2015).

Platform Facies

The Great Bahama Bank has many of the same facies, with some differences, as the southern Florida platform reef tract. The barrier and patch reefs have similar biological communities and generate similar sediments. However, Bahamian carbonate sand shoals are distributed completely different than sand shoals of the Florida reef tract and their composition is almost entirely of ooids. Sand shoals rim the shelf lagoon, which is also very dissimilar to lagoons along the Florida reef tract (Newell and others, 1959; Purdy, 1963; Harris and others, 2015). From our work on the Leadville Limestone, we recognized ooid shoals and shelf lagoonal sedimentation as modern analogs, which are described in the following sections.

Ooid Shoals

The ooid shoals of the Great Bahama Bank (platform) are almost pure ooids. Ooids grow as concentric rings around a nucleus of a fecal pellet or shell fragment in water of elevated temperature and salinity. Wave action is not required for calcite to precipitate as layers on the ooids as previously thought. Calcite precipitation forms ooids by a chemical reaction dependent on pH and the calcium and bicarbonate concentrations in seawater (Dave Tingey, Brigham Young University, verbal communication, 2008). Ooid shoals tend to initiate on topographic highs, but their facies distribution and geometry is due to syndepositional processes (Grammer and others, 2001). Waves suspend the finer sediments and the tides sweep them off the platform (Milliman and others, 1993). Thus, a tide-dominated system yields a grain-dominated facies, such as the ooid shoals (Eugene Rankey, Iowa State University, verbal communication, 2009). Currents and wave action distribute and build ooids into shoals that follow the leeward margins of the platform (figures 9.26 and 9.27; also see figure 3.2) in shallow water where there are no reefs.

Joulter's Cay off the north end of Andros Island (figures 9.26, 9.27, 9.29, and 9.30A) is a world-class geosite to examine modern ooid shoals and their characteristics. The ooid shoals display flat-topped, bi-directional current ripples due to shallow tidal currents (figures 9.30A and 9.30B). Megaripples are also present in deeper water shoals. Ripple orientation is random as one traverses from area to area across the shoals. Small tidal pools (figure 9.30C) display small-scale tidal deltas and tidal channels. Shoals are cross-bedded and often show a slight variation in ooid size from very fine (figure 9.30A inset) to coarse in different parts of the shoal complex. There are some thin zones of shell hash and coated grains. The shoal complex is active and thickens to the east. Bioturbation is intermittent, perhaps occurring every 30 feet (10 m), mainly by the rapidly burrowing bivalve *Tivela abaconia* (figure 9.30D). Only a few large starfish can be found grazing in the shallow water of the shoals.

Prolonged subaerial exposure leads to the establishment of stable grain flats (figure 9.30E). They generally thicken west

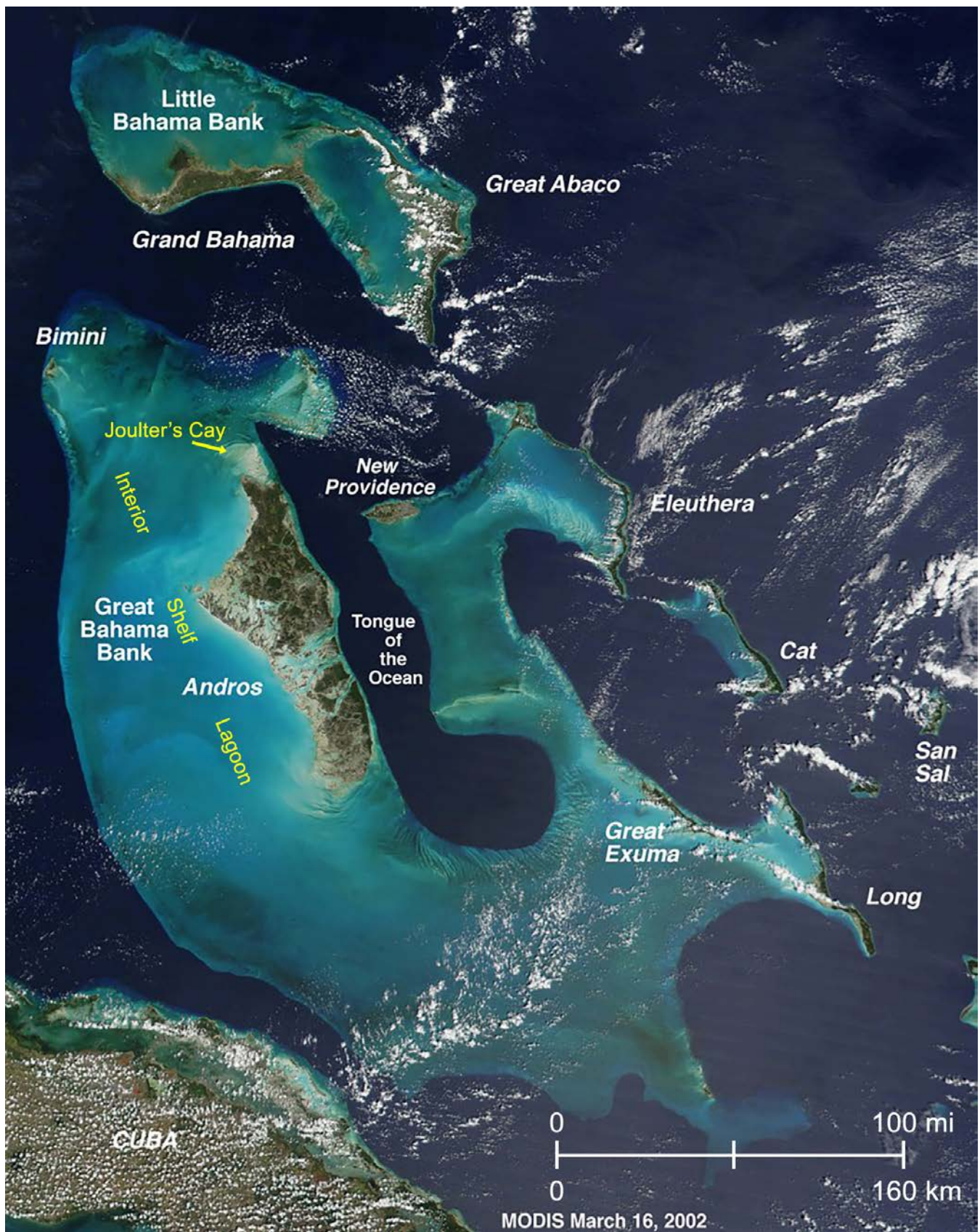


Figure 9.26. Satellite image of the Great Bahama Bank and the Bahama Islands. Annotated NASA Landsat image.

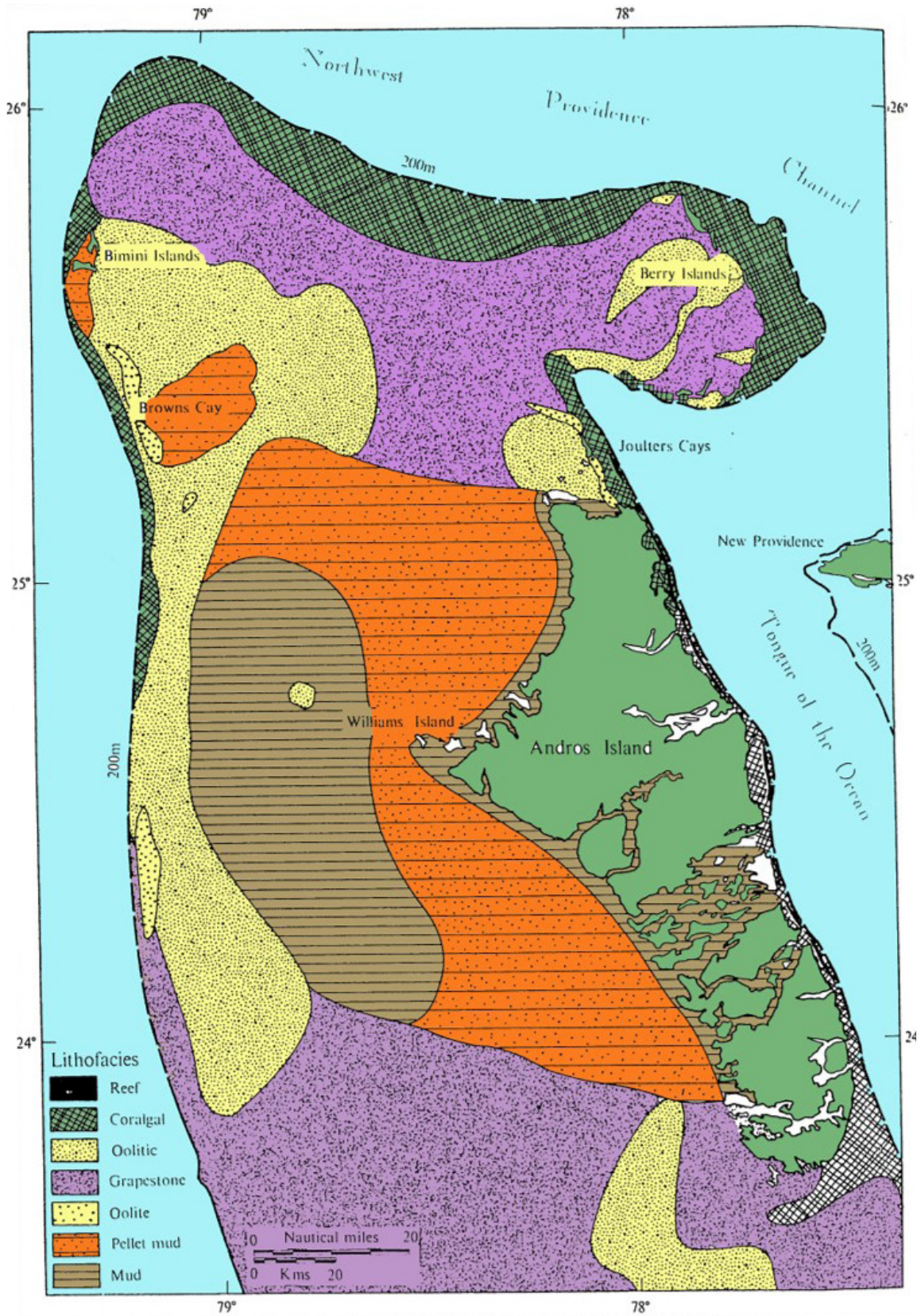


Figure 9.27. Generalized facies map of the Great Bahama Bank. Modified from Newell and others (1959) and Purdy (1963).

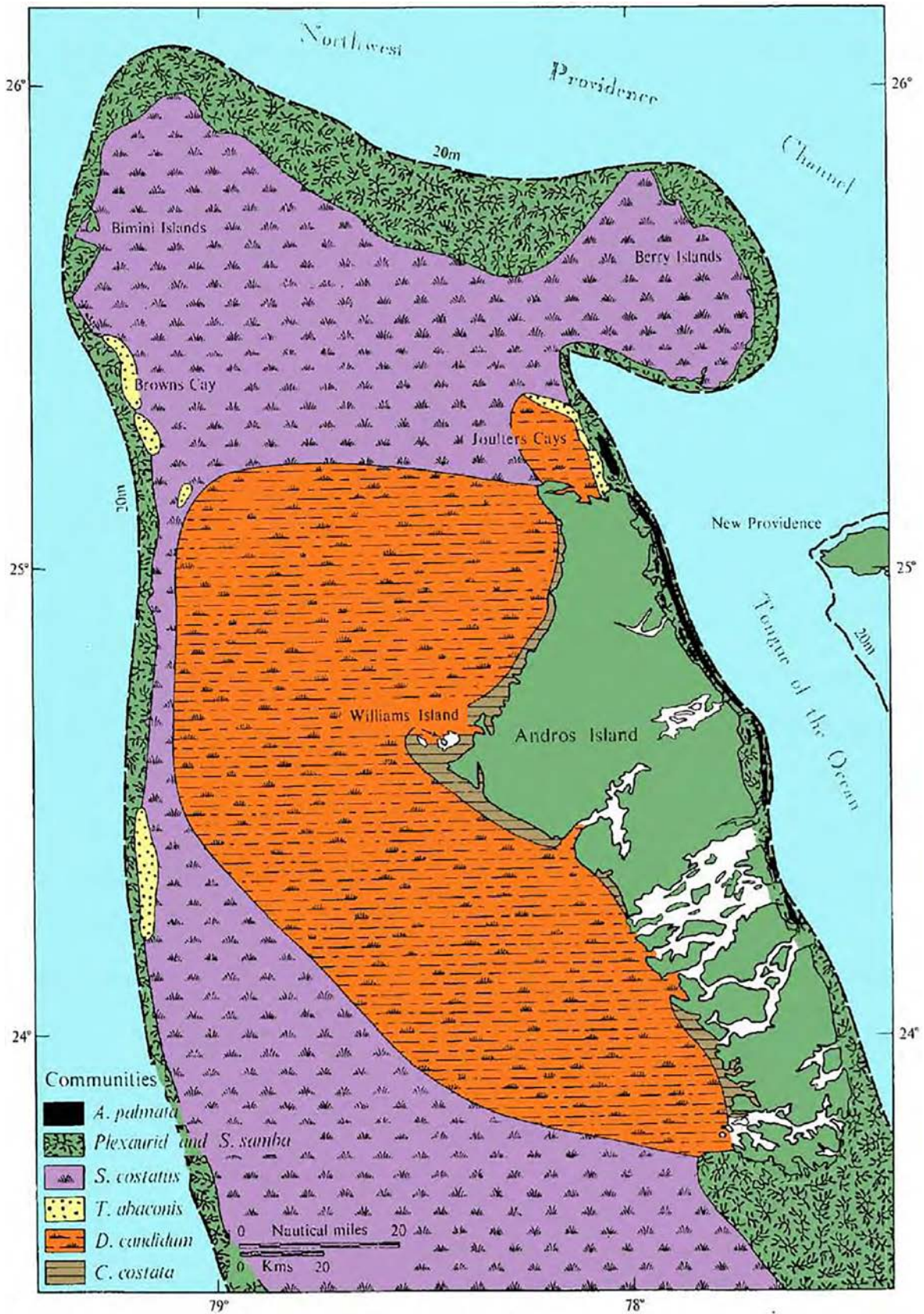


Figure 9.28. Biological communities on the Great Bahama Bank. Modified from Newell and others (1959).



Figure 9.29. Satellite image of the Joulter's Cay ooid shoal complex and the north end of Andros Island. NASA Landsat image.

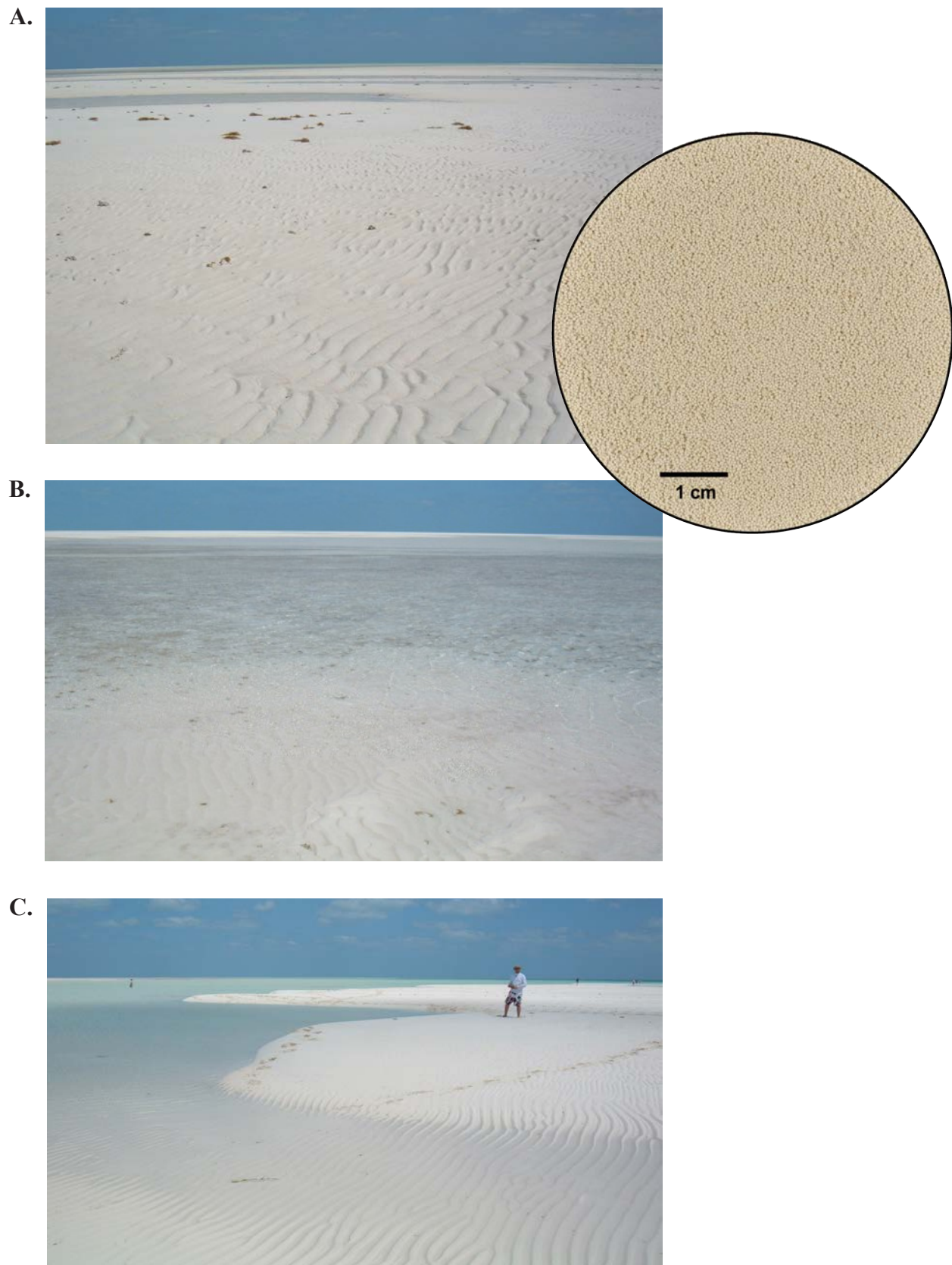


Figure 9.30. Joulter's Cay ooid shoal complex. **(A)** Ooid shoals (view to the north). Flat-topped current ripples due to flood-tidal currents. Inset is close-up of typical Joulter's Cay ooids. **(B)** Slightly flooded ooid shoals forming bi-directional current ripples. **(C)** Shallow tidal pools and rippled, exposed shoals of ooids (cross-bedded). **(D)** Small burrow by the bivalve *Tivela abaconia* in rippled ooid sediments. **(E)** Stabilized grain flats composed of ooids and peloids, colonized by red mangroves. Note numerous active *Callianassa* burrows. **(F)** Tidal channel that leads to northeasterly directed ebb-tidal delta.



Figure 9.30 continued. Joulter's Cay ooid shoal complex. **(A)** Ooid shoals (view to the north). Flat-topped current ripples due to flood-tidal currents. Inset is close-up of typical Joulter's Cay ooids. **(B)** Slightly flooded ooid shoals forming bi-directional current ripples. **(C)** Shallow tidal pools and rippled, exposed shoals of ooids (cross-bedded). **(D)** Small burrow by the bivalve *Tivela abaconia* in rippled ooid sediments. **(E)** Stabilized grain flats composed of ooids and peloids, colonized by red mangroves. Note numerous active *Callianassa* burrows. **(F)** Tidal channel that leads to northeasterly directed ebb-tidal delta.

at Joulter's Cay and consist of very fine grained ooids and peloids. Red mangroves colonize the surface and *Callianassa* burrows are common along tidal channels (figure 9.15). A large tidal channel is located at the south end of the Joulter's Cay shoal complex (figures 9.29 and 9.30F). Oncolites (algal balls) form within the channel. The dominant flow of currents in the channel is northeasterly toward the open sea where an ebb-tidal delta is built (figure 9.29).

Shallow-Shelf Lagoon

West of Andros Island, the semi-restricted, shallow-shelf lagoon of the Bahama platform covers an area of 3900 square miles (10,000 km²) (figures 9.26, 9.27, and 9.31A). The water temperature and salinity are elevated compared to surrounding open-marine waters. Salinity increases up to 46‰ toward Andros Island. Currents decrease toward Andros Island and wave energy becomes negligible. Therefore, ripples and cross-bedding are absent in the sediments. Carbonate (aragonite) muds are produced from direct precipitation in seawater (Bosence and Wilson, 2005). However, the "mud" is mainly composed of peloids (fecal pellets) and grapestone (aggregates of shell fragments and peloids, coated and cemented by aragonite), which would produce grainstone and packstone in the rock record. These sediments are widely distributed across the shallow-shelf lagoon (figure 9.27).

Mud and pellet mud facies dominate the lagoon directly west of Andros Island, whereas grapestone facies are found north to northwest and south to southwest of the island (figure 9.27) (Newell and others, 1959; Purdy, 1963; Harris and others, 2015). Tidal channels from tidal flats in northwestern Andros Island can produce small pellet shoals in the shallowest parts of the lagoon, in Red Bay for example (figure 9.31B). Exposed sediments also may experience early marine dolomitization (figure 9.31C).

In the lagoon, turtle grass is locally dense. *Halimeda* (9.5) and the mud-making *Penicillus*, *Udotea*, and *Rhipocephalus* green algae are significant contributors to the sediment mix (figure 9.6). Fauna are sparse, limited to a few species of sponges, molluscs, echinoids, and rose coral (*Manicina* [figure 9.13F]). Burrowing by worms and *Callianassa* (figure 9.15) is massive and the presence of these organisms is responsible for the peloids that make up the major portion of the sediments in the lagoon.

The sediments and facies observed in the Bahama platform shallow-shelf lagoon are very similar to those found in the Leadville Limestone (figure 3.2). They would produce carbonate fabrics ranging from peloidal grainstone to mudstone (see figures 3.7 through 3.8), all having reservoir potential.

Carbonate Tidal Flats

As with other facies on the Bahama platform, the carbonate tidal flats on the northwestern part of Andros Island are spectacular features. They have been the subjects of numerous studies such as those by Shinn and Lloyd (1969), Hardie and Shinn (1986), Reid and Browne (1991), Rankey (2002), Rankey and Morgan (2002), and Rankey and others (2004), to name just a few.

The Andros Island carbonate tidal flats consist of three tidal zones: (1) subtidal, (2) intertidal, and (3) supratidal (Shinn and Lloyd, 1969). Sediment in the subtidal zone is deposited below low tide in channels (figure 9.32A) and the nearby lagoon. Sediment in tidal channels is mainly thin skeletal (shells) sand, and scours can reach Pleistocene bedrock. Channels contain thickets of turtle grass and *Callianassa* burrows (figure 9.15). Sediment in the intertidal zone is deposited between normal low and normal high tide as soft peloid grains and laminated microbial mats (figure 9.32B). Mudcracks develop on microbial mats during dry periods; they then provide "pastures" for grazing gastropods (figure 9.14). Sediment in the supratidal zone is deposited above normal high tide but within the range of spring and storm tides. The sediment forms channel levees (figure 9.32A), beach ridges, marshes, and ponds (figure 9.32C). Levee sediments are often heavily burrowed (figure 9.32D).

Carbonate tidal flats are laterally extensive along strike and represent part of a shallowing upward cycle (Grammer and others, 2001). Paleotidal flat deposits are productive in Williston Basin fields and other carbonate reservoirs (Roehl, 1967). Recognizing the modern characteristics of carbonate tidal flats in the Leadville Limestone may provide additional target areas for drilling.

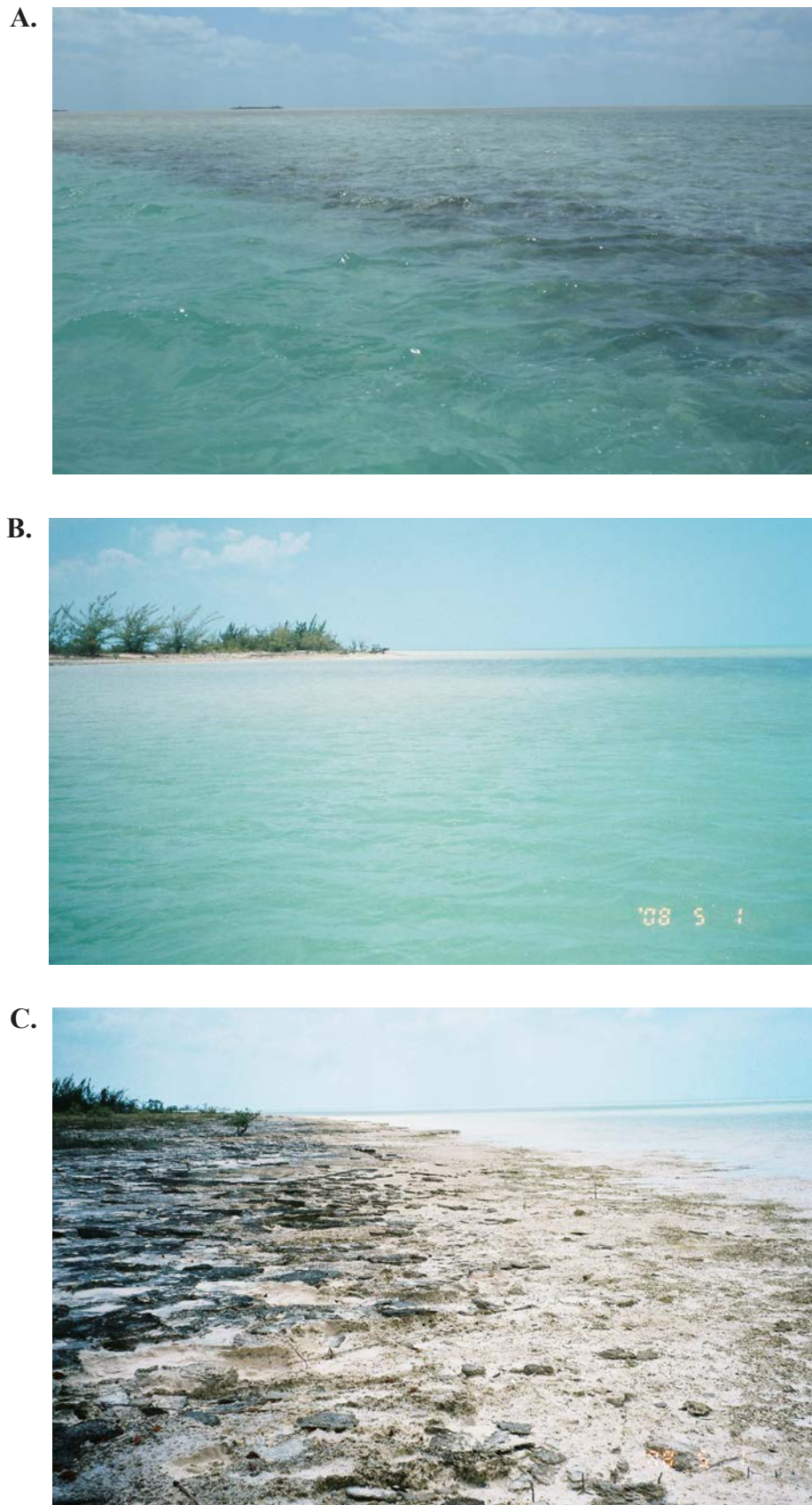


Figure 9.31. Great Bahama Bank shelf lagoon. (A) View to the west of the 40-mile-wide (60 km) lagoon where carbonate pellet-bearing muds are actively being deposited. (B) Red Bay part of the shelf lagoon and pellet shoals near the mouth of a tidal channel from a tidal flat along the northwestern coast of Andros Island (view to the southwest). (C) Exposed pellet-bearing muds from the shelf lagoon undergoing early marine dolomitization.

A.



B.



C.



D.



Figure 9.32. Carbonate tidal flats, Three Creeks area on the northwestern side of Andros Island. **(A)** Tidal channel (subtidal zone) and levee (supratidal zone) composed of carbonate, pellet-bearing mud. **(B)** Microbial mats and laminated, soft peloid grains in the intertidal zone of the tidal flats. **(C)** Shallow ponds within the supratidal zone. **(D)** Burrowing on the tidal channel levee deposits.

CHAPTER 10:
OUTCROP RESERVOIR ANALOGS FOR THE
LEADVILLE LIMESTONE— SOUTHERN FLANK OF
THE UINTA MOUNTAINS, UTAH

by

David E. Eby, Eby Petrography & Consulting, Inc.

and

Thomas C. Chidsey, Jr., and Douglas A. Sprinkel (retired),
Utah Geological Survey

CHAPTER 10:

OUTCROP RESERVOIR ANALOGS FOR THE LEADVILLE LIMESTONE— SOUTHERN FLANK OF THE UINTA MOUNTAINS, UTAH

INTRODUCTION

Utah is fortunate that representative outcrop analogs (depositional or diagenetic) for the Leadville Limestone play are present in the northern part of the state (figure 10.1). Production-scale analogs provide an excellent view, often in 3D, of facies, geometry, distribution, diagenetic characteristics, and the nature of boundaries, all of which contribute to the overall heterogeneity of reservoir rocks in the Leadville. The specific objectives of this chapter are to (1) increase understanding of vertical and lateral facies variations and relationships within Leadville reservoirs, (2) describe the lithologic and diagenetic characteristics, (3) determine the morphology, internal geometries, and possible permeability and porosity distributions, (4) identify potential impediments and barriers to fluid flow, and (5) determine the causes of brecciation features.

An outcrop-analog model, combined with the details of internal lithofacies characteristics, can be used as a “template” for evaluating data from conventional core, geophysical and petrophysical logs, and seismic surveys. When combined with subsurface geological and production data, the analog model will improve development drilling and production strategies, reservoir-simulation models, reserve calculations, and design and implementation of secondary/tertiary oil recovery programs and other best practices used in the Leadville oil and gas fields of the Paradox Basin as well as similar fields in other basins.

SOUTHERN FLANK OF THE UINTA MOUNTAINS, UTAH

The Leadville Limestone is not exposed in southeastern Utah; however, equivalent Mississippian crop out along the flanks of the east-west-trending Uinta Mountains in northern Utah (figure 10.1). Uplift of this range occurred during the Laramide orogeny from latest Cretaceous time (Maastriichtian, about 70 Ma) through the Eocene (about 34 Ma). The Mississippian rock section along the southern flank of the Uinta Mountains is over 1600 feet (490 m) thick (Sprinkel, 2018) (figures 10.2 and 10.3). Mississippian outcrops along the western end of the Uinta Mountains include the Madison, Humbug, and Doughnut Formations (Bryant, 1990; figures 10.2 and 10.3). However, Bryant’s (1990) Madison includes the Fitchville Formation (Upper Devonian-Lower Mississippian [385–340 Ma]). In addition, the Madison includes a phosphatic shale interval identified by Sandberg and Gutschick (1980) and mapped by

Sprinkel (2018) as the Delle Phosphatic Member of the Deseret Limestone. The Delle Phosphatic Member separates lower cliff-forming carbonate (Gardison Limestone) from upper cliff-forming carbonate (Deseret Limestone). Thus, the terms Gardison and Deseret Limestones are recommended for the western Uinta Mountains and are overlain by the Humbug and Doughnut Formations (figures 10.2 and 10.3). The Delle Phosphatic Member either pinches out or grades to mostly thin-bedded carbonate rocks in the eastern Uinta Mountains. Where the Delle is not recognized and the Gardison and Deseret cannot be easily separated, the term Madison Limestone is used (Sprinkel, 2006, 2007). For simplicity, the interval will be collectively referred to as the Mississippian section in this study.

The Madison, Deseret, and Humbug Formations have similar characteristics as the Leadville Limestone. They provide production-scale analogs of the facies and diagenetic characteristics, geometry, distribution, and nature of boundaries contributing to the overall heterogeneity of Leadville reservoirs.

General Characteristics

The Mississippian section along the southern flank of the Uinta Mountains was deposited in a tropical, warm-water, shallow-shelf, variable energy epicontinental sea that extensively covered a large part of the North American craton (figure 3.1A). The Mississippian formations are mostly light- to dark-gray, fine- to coarse-crystalline, cherty limestone (figures 10.4 and 10.5A). Dolomitic units are gray to tan, sucrosic to crystalline, and medium bedded with occasional silty partings; both limestone and dolomite are the main reservoir lithologies for the Leadville Limestone. Chert is typically light gray, forming lenses and nodules. In the Whiterocks Canyon area (figure 10.1), the Deseret Limestone contains some thin-bedded, tan, calcareous, fine- to medium-grained sandstone (Kinney, 1955; Sprinkel, 2018). The most common carbonate fabrics of the Mississippian section include peloidal, skeletal, and oolitic grainstone, packstone, and wackestone; skeletal and intraclast rudstone and floatstone are also present. Cross-bedded grainstone fabrics of crinoid debris are referred to as encrinites. Mudstones appear as microcrystalline and cryptocrystalline limestone and dolomite. The Mississippian section is generally thick to massive and unevenly bedded, forming vertical cliffs and dip slopes.

Marine fauna in the Mississippian section are corals, brachiopods, pelecypods, bryozoans, and crinoids; however, fossils are relatively rare in some areas. Other common biota includes ostracods, benthic foraminifera, and gastropods. Microbial-

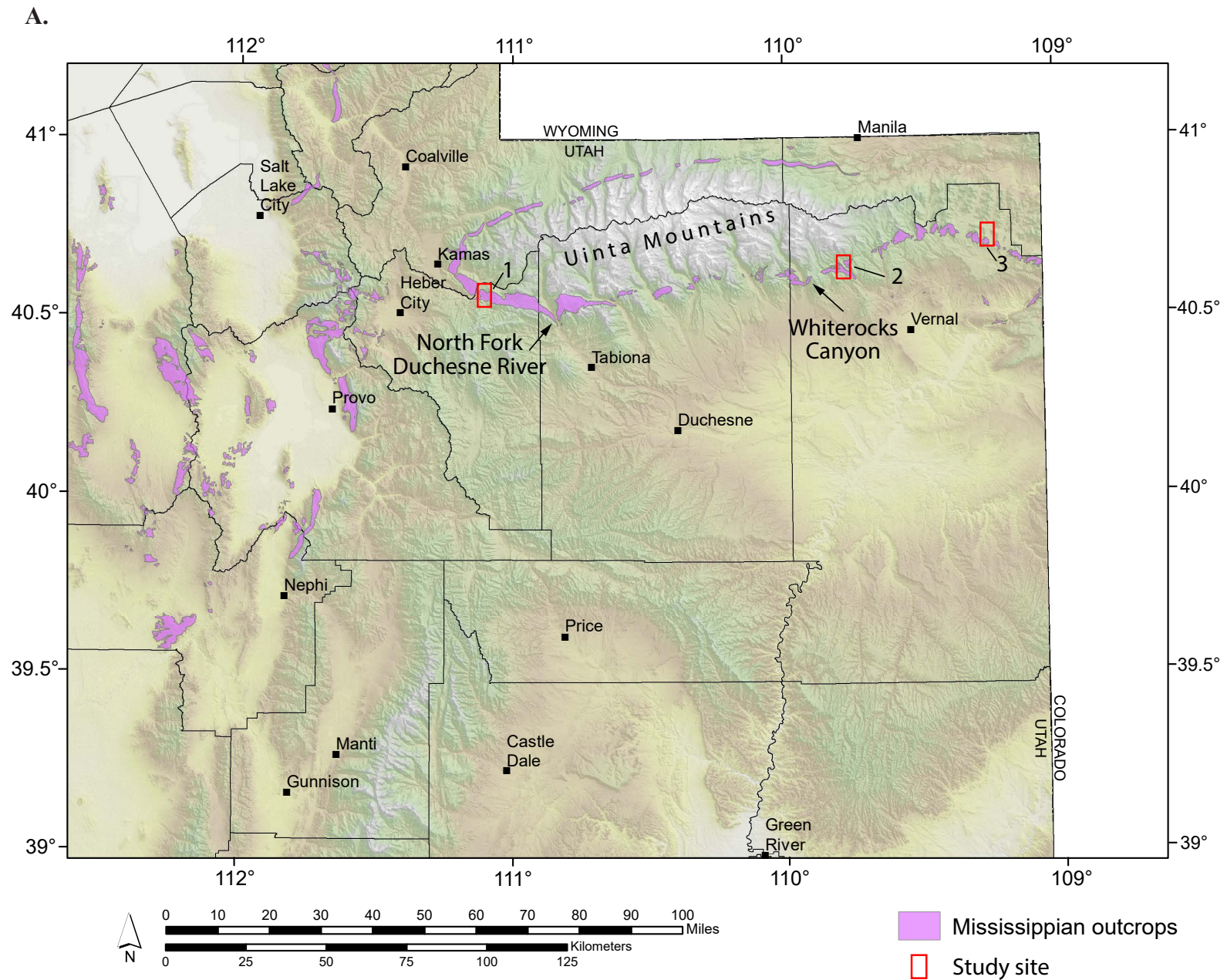


Figure 10.1. Mississippian outcrop reservoir analogs in Utah showing the location of the study sites. (A) Location of Mississippian rock outcrops in Utah equivalent to the Leadville Limestone. (B) Generalized geologic map of the Uinta Mountains, northeastern Utah, showing the location of the sites. Modified from Hintze and others (2000).

B.

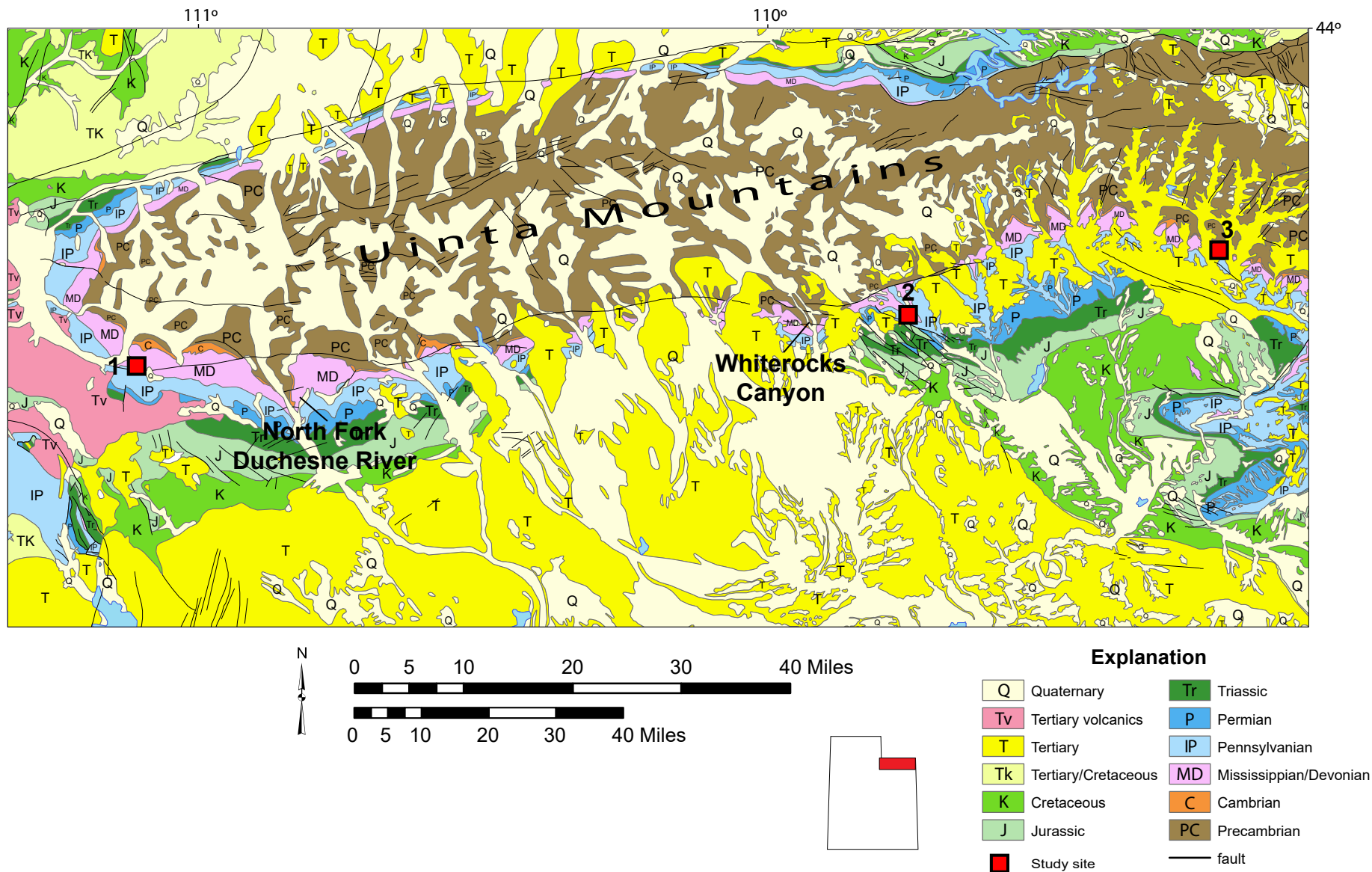


Figure 10.1 continued. Mississippian outcrop reservoir analogs in Utah showing the location of the study sites. (A) Location of Mississippian rock outcrops in Utah equivalent to the Leadville Limestone. (B) Generalized geologic map of the Uinta Mountains, northeastern Utah, showing the location of the sites. Modified from Hintze and others (2000).

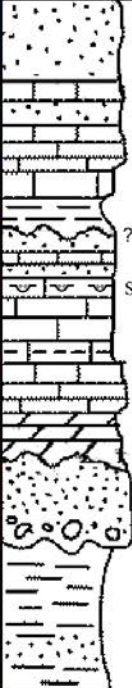
Age	Formation		Thickness (ft)	Lithology
Permian	Oquirrh Group	Weber Sandstone	1700	
Pennsylvanian		Morgan Fm	200–325	
		Round Valley Ls	200–300	
Mississippian	Doughnut Fm		200–300	
	Humberg Fm		360–410	
	Deseret Limestone		590–650	
	Gardison Limestone		250	
Devonian	Fitchville Fm		150	
Cambrian	Tintic Quartzite		0–395	
Precambrian	Uinta Mountain Group (part)	Red Pine Shale	0–1800	

Figure 10.2. Lithologic column of a part of the Paleozoic section along the western end of the southern flank of the Uinta Mountains. Modified from Hintze and Kowallis (2009) and Sprinkel (2018).


Age	Formation		Thickness (ft)	Lithology
Permian	Weber Sandstone		660–1320	
Pennsylvanian	Morgan Fm	Upper member	620–950	
		Lower mbr		
	Round Valley Ls		210–400	
Mississippian	Doughnut Shale		80–300	
	Humberg Fm		100–300	
	“Madison” Limestone		500–1000	
Cambrian	Tintic Quartzite		0–600	
Precambrian	Uinta Mountain Group		as much as 15,000	

Figure 10.3. Lithologic column of a part of the Paleozoic section along the eastern end of the southern flank of the Uinta Mountains. Modified from Hintze and Kowallis (2009).



Figure 10.4. Mississippian Deseret Limestone forming a jagged, vertical cliff, North Fork of the Duchesne River, Duchesne County, Utah. Note the cavernous nature of the outcrop. See figure 10.1 for location of North Fork of the Duchesne River area.

dominated rocks are present, but uncommon. Depositional environments include mud-rich tidal flats; burrowed peloid mud in subtidal settings; high-energy ooid shoals; crinoid banks with mud-rich intershoals; storm-dominated, outer shelf offshore open-marine; and offshore low-energy, open-marine settings below wave base.

The contacts between the Fitchville, Gardison, Deseret, Madison, Humbug, and Doughnut Formations are mostly conformable (Sadlick, 1955, 1957; Carey, 1973; Hintze and Kowallis, 2009), whereas the Mississippian Leadville Limestone and overlying Pennsylvanian Molas Formation are separated by a major unconformity in southeastern Utah. This same unconformity is found at the top of the stratigraphically equivalent Mississippian Redwall Limestone in the Grand Canyon (McKee, 1969), where subaerial exposure resulted in development of karst topography with carbonate breccia-filled collapse features (paleo-sinkholes) and terra rosa (cave fills) near the top of the formation; similar features are recognized in Leadville cores (see Chapter 4) (Chidsey and others, 2020).

The upper Deseret Limestone has numerous “young,” actively forming caverns (figure 10.4), sinkholes, and springs. Controls on these features are vertical joints, fractures, and selected bedding planes rather than the unconformity at the top of the Mississippian (Hamblin and Rigby, 1968). Underground drainage is common and larger caves are related to sinking

streams (White, 1979). In addition, high dolomite content can influence cave development (White, 1979). Many units display dissolution activity in the form of large and small vugs (figures 10.5B and 10.5C).

The Mississippian section contains local zones or pipes of breccia due to either natural hydrofracturing or collapse as identified in several Leadville cores throughout the northern Paradox Basin (Eby and others, 2009; Chidsey and others, 2020). A breccia pipe is a cylindrical- or irregular-shaped mass of brecciated rock (figure 10.6) that forms when hydrothermal solutions have forced their way towards the surface through zones of weakness or fracture zones and naturally break up the rocks in the process (i.e., hydrofracturing); breccia pipes can also form by collapse. Brecciation caused by explosive natural hydrofracturing created the same shattered-looking, pulverized rock also identified in Lisbon cores (see Chapter 4). Possible breccia pipes may be related to past hydrothermal activity. Breccia associated with sediment-filled collapsed cavities is relatively common in several areas. These cavities may be related to paleokarstification during periods of exposure.

Fractures are common in the Mississippian section. They are best expressed as closely spaced, vertical fractures throughout thin- to medium-thick beds or as swarms associated with large and small faults and collapse features. Stylolites and jointing are also present (figures 10.5A, 10.5B, and 10.5D).

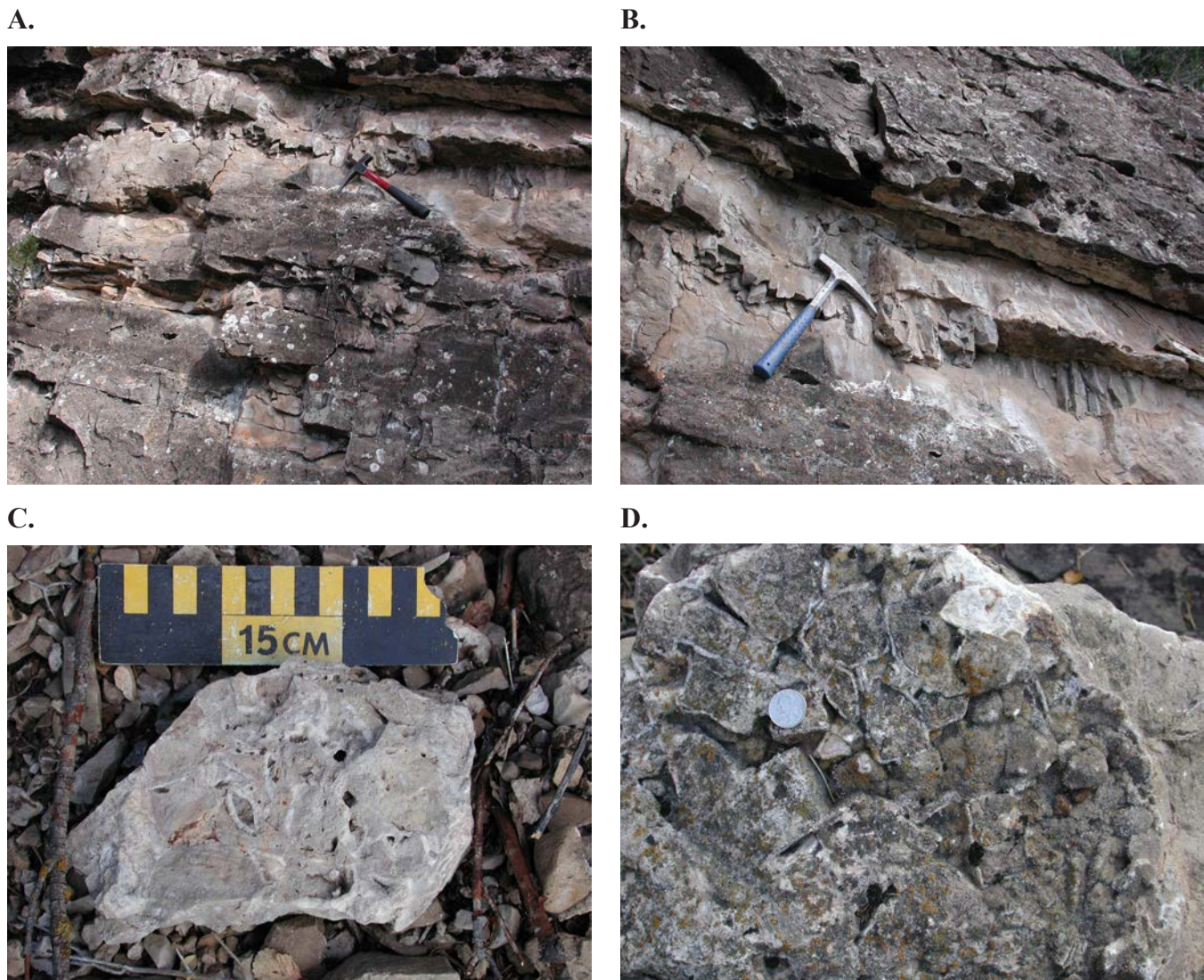


Figure 10.5. Characteristics of the Mississippian Madison Limestone along the southern flank of the Uinta Mountains, Whiterocks Canyon, Uintah County, Utah. (A) Typical exposure of light- to dark-gray, medium-bedded, fine- to coarse-crystalline, limestone and dolomite containing fractures, stylolites, and crinoid hash. (B) Vugs and fractures in limestone and dolomitic units. (C) Close-up of open and calcite-filled vugs in limestone matrix. (D) Close-up of small-scale, calcite-filled rectilinear fractures in limestone matrix. See figure 10.1 for location of Whiterocks Canyon.

Study Sites

Three sites were selected for detailed outcrop studies (figure 10.1): (1) South Fork Provo River, (2) Dry Fork Canyon, and (3) Crouse Reservoir/Diamond Mountain Plateau. Each study site has a unique set of depositional lithofacies and post-depositional characteristics in the Mississippian section that are identical or very similar to those observed in Leadville Limestone cores from Lisbon field in the Paradox Basin (figure 1.3). Samples were collected for slabbing and thin section analysis. Two short stratigraphic sections (less than 120 feet [40 m]) were measured, using a compass, tape, or Jacob staff, at study sites 2 and 3 (see appendix I) specifically targeting lithofacies. Dockal (1980) published 10 nearly complete measured sections of the Mississippian section from the canyons around the core of the Uinta Mountains and they serve as an excellent reference set for further comparison.

Study Site 1 – South Fork Provo River

The South Fork Provo River study site is on the western end of the southern flank of the Uinta Mountains, Wasatch County (figure 10.1). The site is a series of roadcuts along the eastern side of State Highway 35, 11 miles (18 km) east of the town of Francis, and 25 miles (42 km) northwest of the town of Hanna, Utah (figure 10.6). The study site and surrounding area was mapped by Eskelsen (1953), McDougald (1953), and Bryant (1990). Sprinkel (2018) mapped the adjacent area along the southern flank of the Uinta Mountains and western Uinta Basin. A large breccia pipe in the Deseret Limestone is the most striking feature at study site 1 (figure 10.7) (Chidsey and others, 2019, 2020).

The Deseret Limestone at study site 1 is dark- to light-gray limestone consisting of skeletal grainstone to packstone

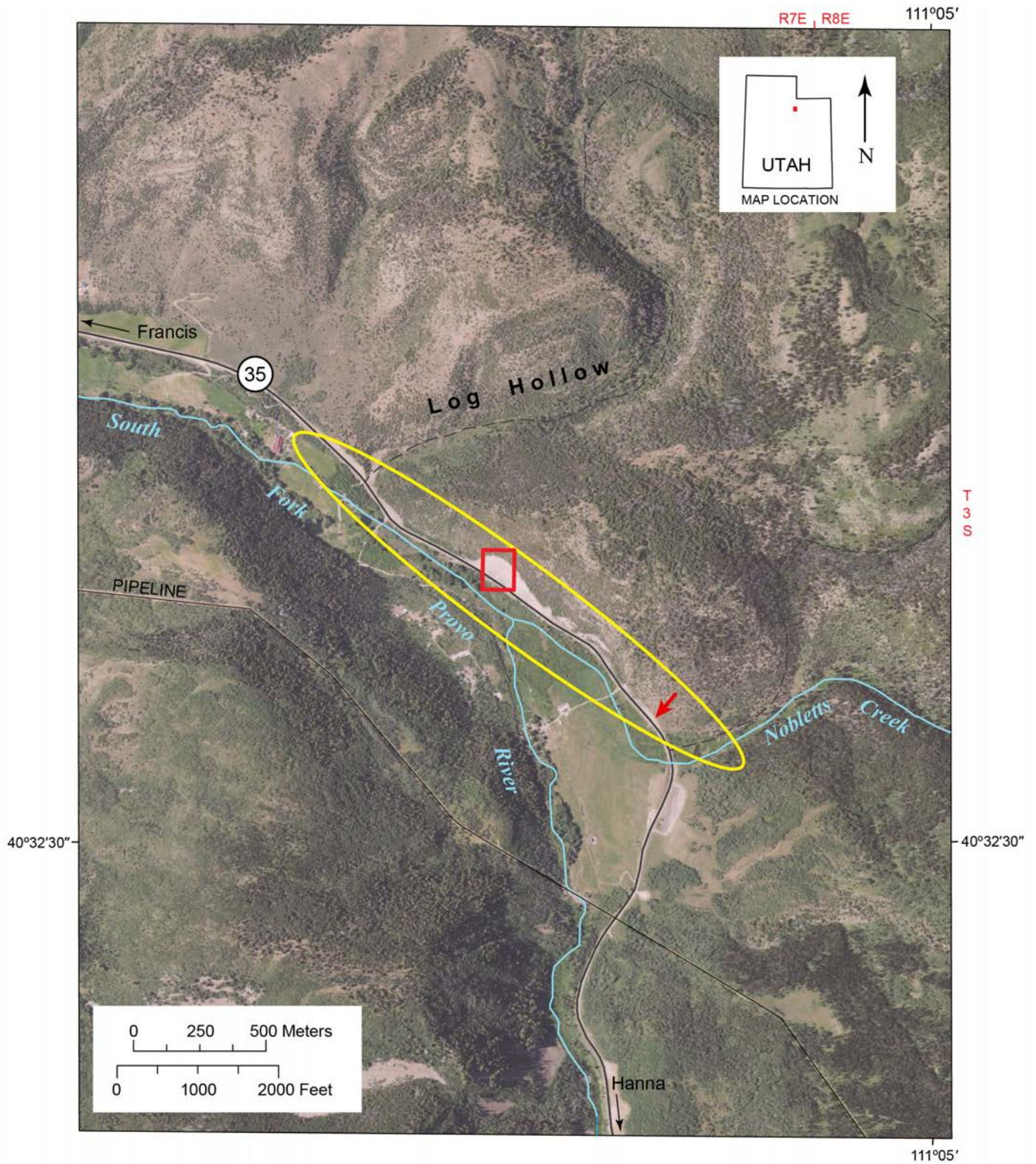


Figure 10.6. Google Earth image (© 2018 Google) showing the location of study site 1, South Fork of the Provo River and the hydrothermal breccia pipe along the western end of the southern flank of the Uinta Mountains in Wasatch County, Utah. The Mississippian Deseret Limestone outcrops are best exposed in roadcuts within the elongated yellow oval; the red square is the location of the breccia pipe and red arrow is the location of possible paleokarst features.



Figure 10.7. Large breccia pipe penetrating the Desert Limestone at study site 1. Note pulverized nature of the material that comprises the pipe, the sharp contact with the country rock and parallel, calcite-filled vertical fractures.

(figure 10.8A). Skeletal grains are composed of disarticulated crinoids and rugose coral fragments representing a high-energy, open-marine environment. Some units contain in-place *Syringopora* corals and common burrows (figure 10.8B), indicating a low-energy environment. Other units are dolomitized and include chert nodules (figure 10.8C). Vertical fractures are also common (figure 10.8D). The contact with the overlying Humbug Formation is difficult to recognize due to the poor nature of the outcrops and extensive slope cover. Eskelsen (1953), McDougald (1953), and Bryant (1990) mapped them together in the area as Desert-Humbug undifferentiated.

The breccia pipe is subvertical, 17 feet (5 m) wide at the base of the outcrop, and cuts vertically through about 30 feet (9 m) of Desert Limestone. The interior of the pipe contains a poorly sorted breccia having small to large clasts surrounded by pulverized rock (figure 10.9A). Calcite veins, dolomitized zones, and vugs are widespread (figure 10.9B). The contacts of the pipe with the unaltered limestone country rock are sharp. Vertical, commonly calcite-filled fractures are prevalent on both sides of the breccia pipe. Thin sections reveal the presence of mini-Herkimer (i.e., doubly terminated) quartz crystals (figure 10.9C), which were also found in Leadville cores from Lisbon field. There, the mini-Herkimer crystals had high-temperature fluid inclusions (see Chapter 4). The presence of mini-Herkimer crystals suggests that a high-temperature event occurred at the study site, presumably emplacing the breccia pipe.

In Desert outcrops immediately southeast of the breccia pipe site, we recognized possible paleokarst features having some of the same characteristics found in Leadville cores (Chidsey and others, 2019, 2020) and the Redwall Limestone outcrops in the Grand Canyon. Stratiform polymictic brecciation (collapse) is extensive (figures 10.10A and 10.10B) but without the calcite veins, dolomitization, and explosive characteristic of a breccia pipe. Red staining at the top of the Desert Limestone, mapped as the Madison Limestone by Bryant (1990), is possible terra rosa (red earth) weathering (i.e., a reddish-colored clay-rich layer containing hematite that ranges in thickness from a few inches to several feet and can be found coating limestone in ancient and modern karst areas), but could be coming from the overlying Humbug Formation (figure 10.10C). Karstification and formation of collapse breccias may have begun shortly after deposition of the Desert, which would argue for an unconformity between the Desert and Humbug; however, this has not been identified elsewhere in the region. Several sinkholes are mapped in undivided Desert and Humbug outcrops, as well as the Gardison Limestone and Weber Sandstone (Pennsylvanian-Permian), in the area by Eskelsen (1953). These karst-related features likely postdate the Mississippian beginning as early as late Eocene to Oligocene (Godfrey, 1985; Spangler, 2005). Mayo and others (2010) also suggested the cave system formed relatively recently (Pleistocene).

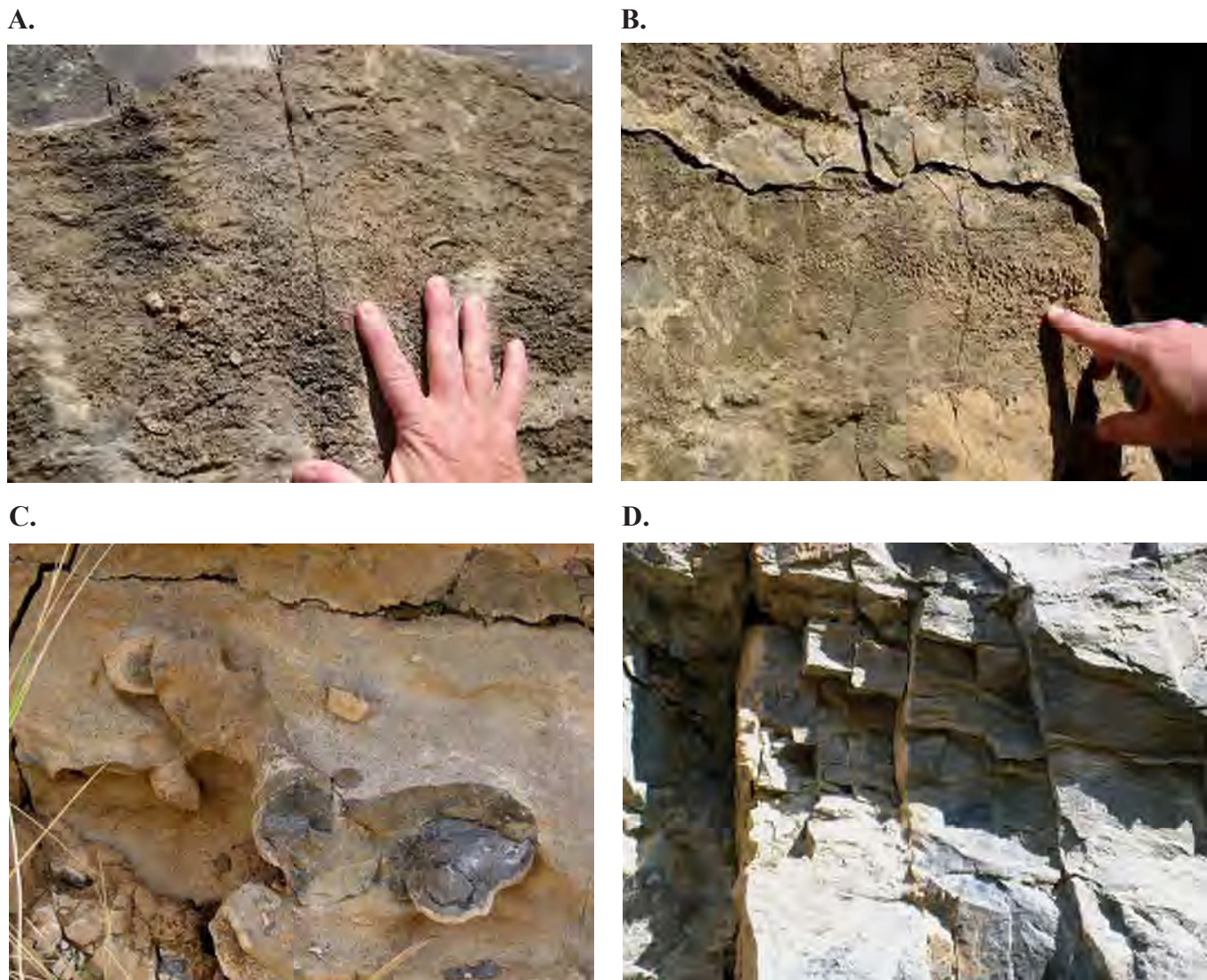


Figure 10.8. Typical characteristics of the Desert Limestone just northwest of the breccia pipe at study site 1 (within the yellow oval on figure 10.6). (A) Skeletal (crinoid and rugose coral) grainstone and packstone. (B) In-place *Syringopora* coral. (C) Chert nodules in dolomitized packstone. (D) Vertical fractures.

Study Site 2 – Dry Fork Canyon

The Dry Fork Canyon study site is in the east-central part of the southern flank of the Uinta Mountains, Uintah County (figure 10.1), 20 miles (32 km) northwest of the town of Vernal, Utah. The site includes a measured stratigraphic section (appendix I) and several noteworthy outcrops along the Red Cloud Loop Road where it forks and turns up Brownie Canyon (figure 10.11).

The Dry Fork Canyon stratigraphic section demonstrates the heterogeneity as well as cyclicity (two shoaling upwards cycles) of the Madison Limestone depositional environments within a 40-foot-thick (12 m) outcrop (figure 10.12). The Madison at this site is predominately dolomite. The base of the section is oolitic/hard pellet grainstone with distinctive pock-marked weathering and has well-defined, planar to low-angle cross-stratification; the upper 6 inches (15 cm) may contain

beach rock and semi-lithified rip-up clasts (figure 10.13A). The depositional environment was a beach/foreshore. The next unit is a calcareous, peloidal/skeletal packstone to grainstone (figure 10.13B) with hard pellets, benthic forams, and other microfossils. Bedding is wavy to bioturbated and the top may be channelized. The depositional environment was a stable, shallow, subtidal bay. The section coarsens up to oolitic/hard pellet grainstone with small- to medium-scale cross-stratification (figure 10.13C) representing an ooid shoal. Tidal-flat mud and deeper, subtidal, burrowed, pellet mud (figure 10.13D) overlies the ooid shoal consisting of soft pellet mudstone with crinkly continuous cryptalgal (microbial) laminates and skeletal microfossils (ostracods and benthic forams). These sediments are overlain by thin-bedded to bioturbated, peloidal/skeletal packstone to grainstone with endothyrid forams (figure 10.13E) and other microfossils indicating return to a stable, shallow, subtidal bay. The cycle continues to coarsen upward with low- to medium-angle cross-stratified oolitic

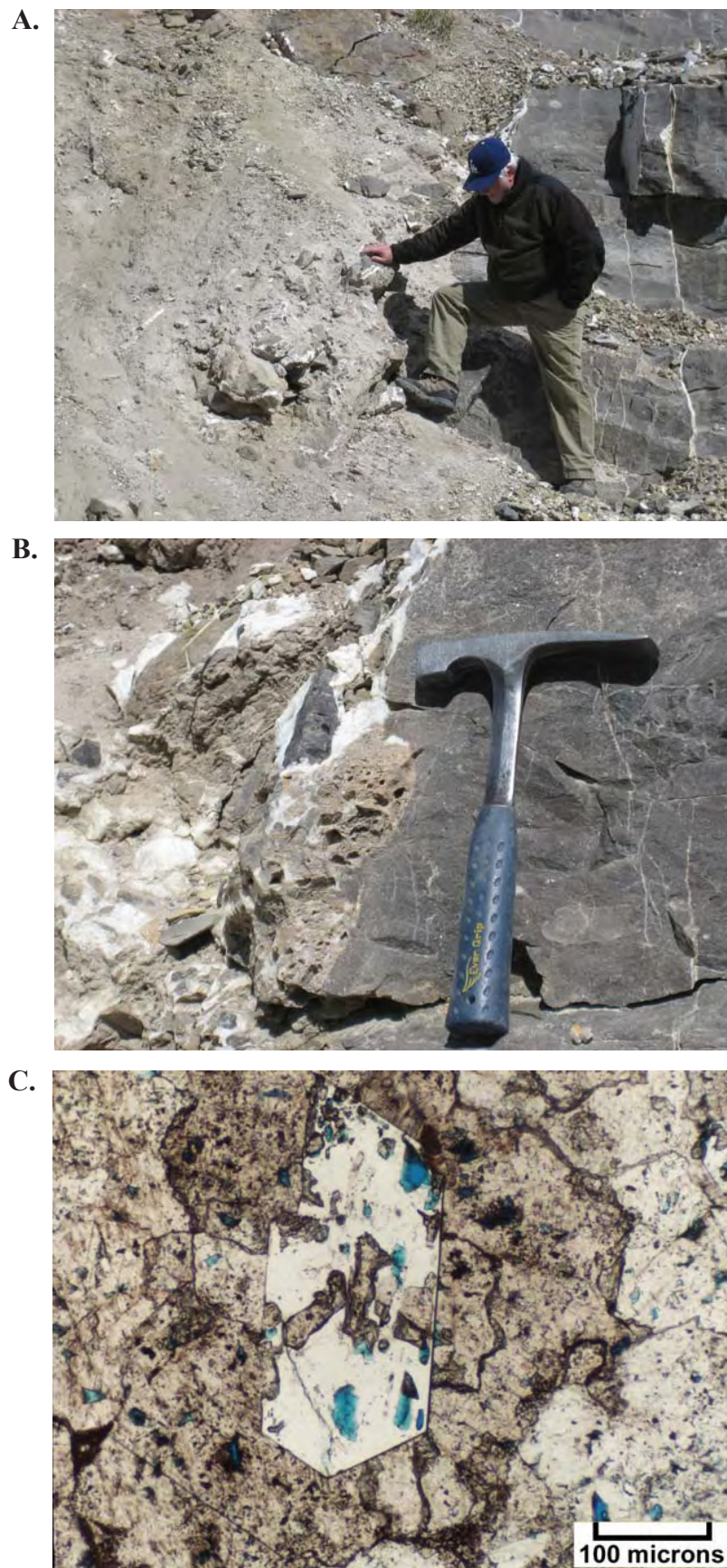


Figure 10.9. Characteristics of the explosive hydrothermal breccia pipe at study site 1. (A) Brecciated rock in shattered-looking, pulverized groundmass. (B) Close-up of sharp contact with unaltered limestone country rock. Note vuggy dolomite and white calcite veins. (C) Photomicrograph (plane light) of dolomite containing a mini-Herkimer quartz crystal (center) suggesting a high-temperature event.

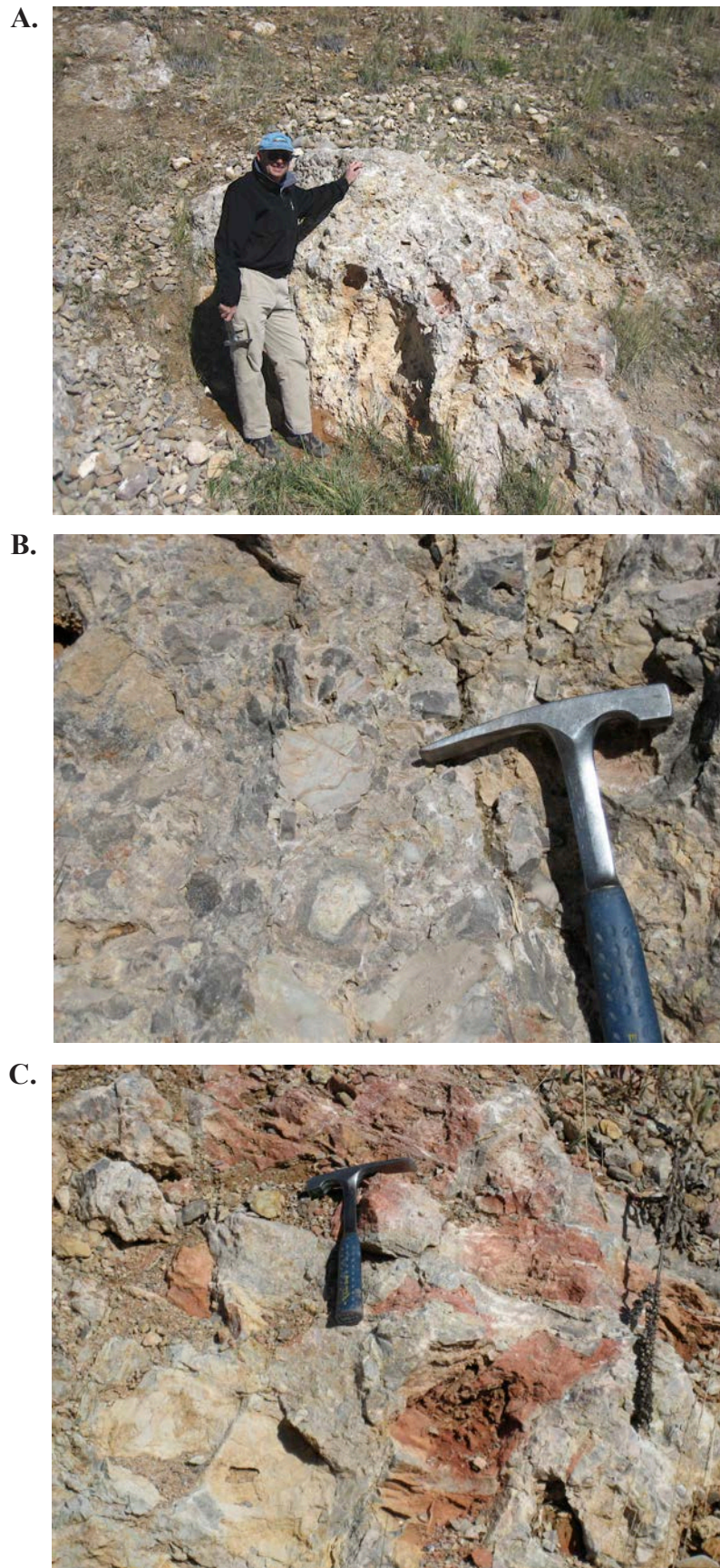
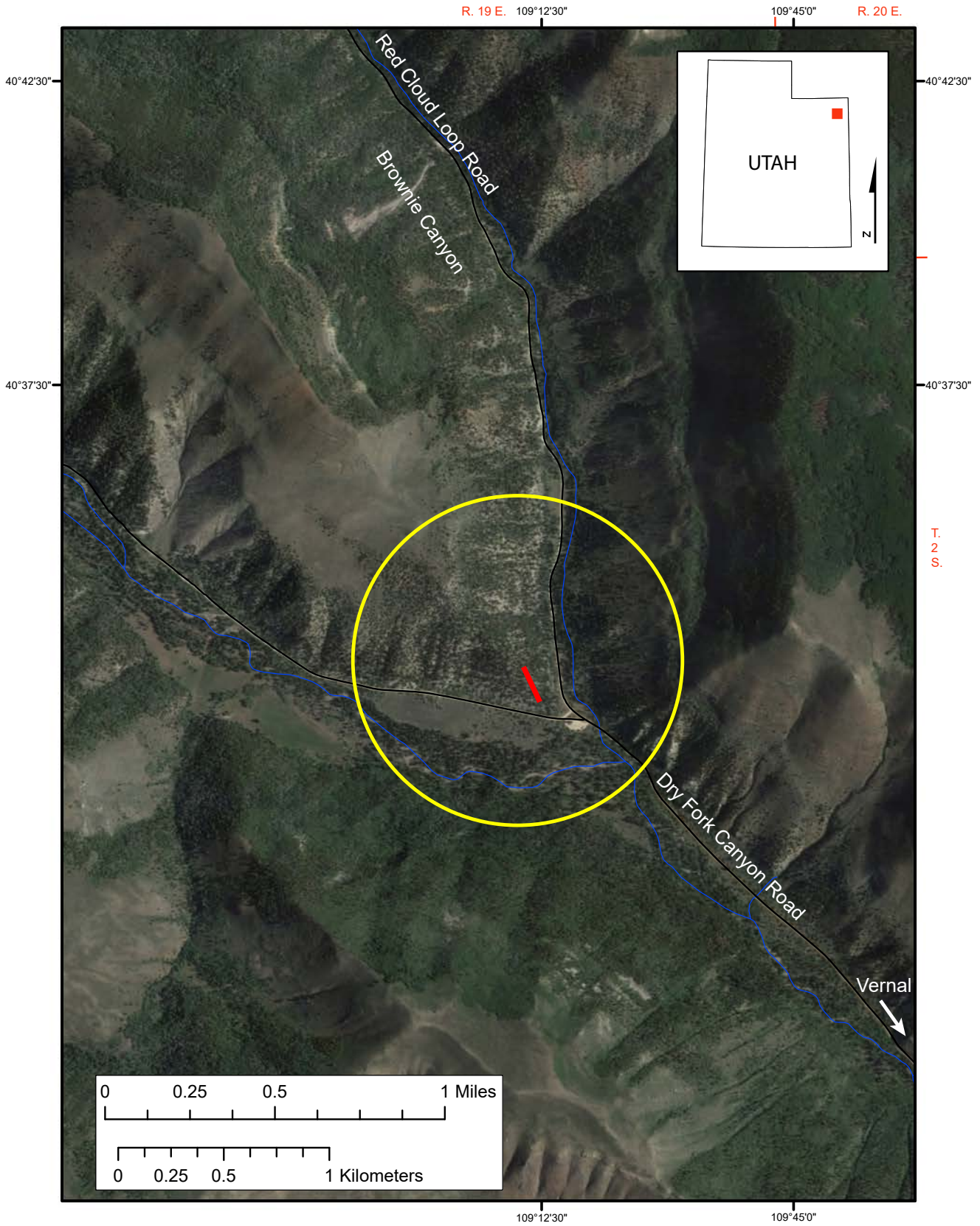


Figure 10.10. Possible paleokarst features just southeast of the breccia pipe at study site 1 (see red arrow within the yellow oval on figure 10.6). (A) Extensive collapse polymictic breccia. (B) Close-up of limestone and chert breccia clasts. Note the lack of calcite veins and dolomite. (C) Red staining, possibly terra rosa weathering, at the top of the Deseret Limestone near the contact with the overlying Humbug Formation(?).



Explanation
— Measured section

Figure 10.11. Google Earth image (© 2018 Google) showing the location of study site 2, Dry Fork Canyon (yellow circle).

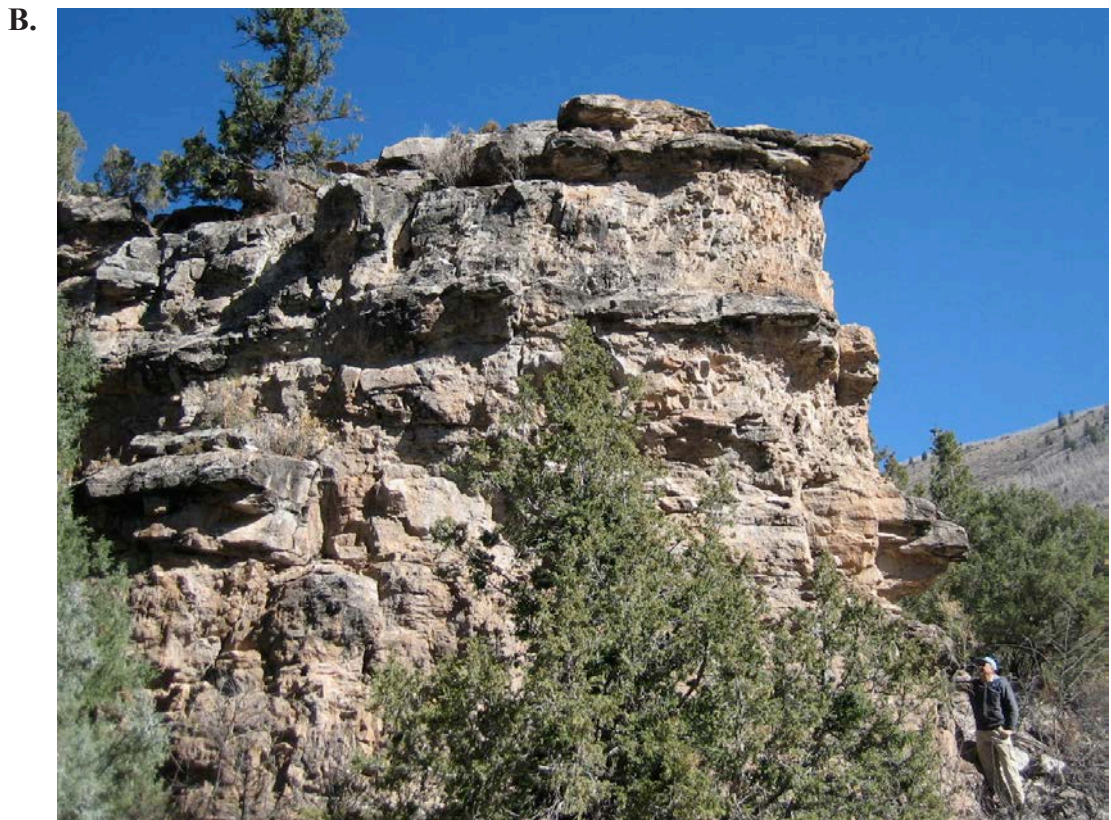
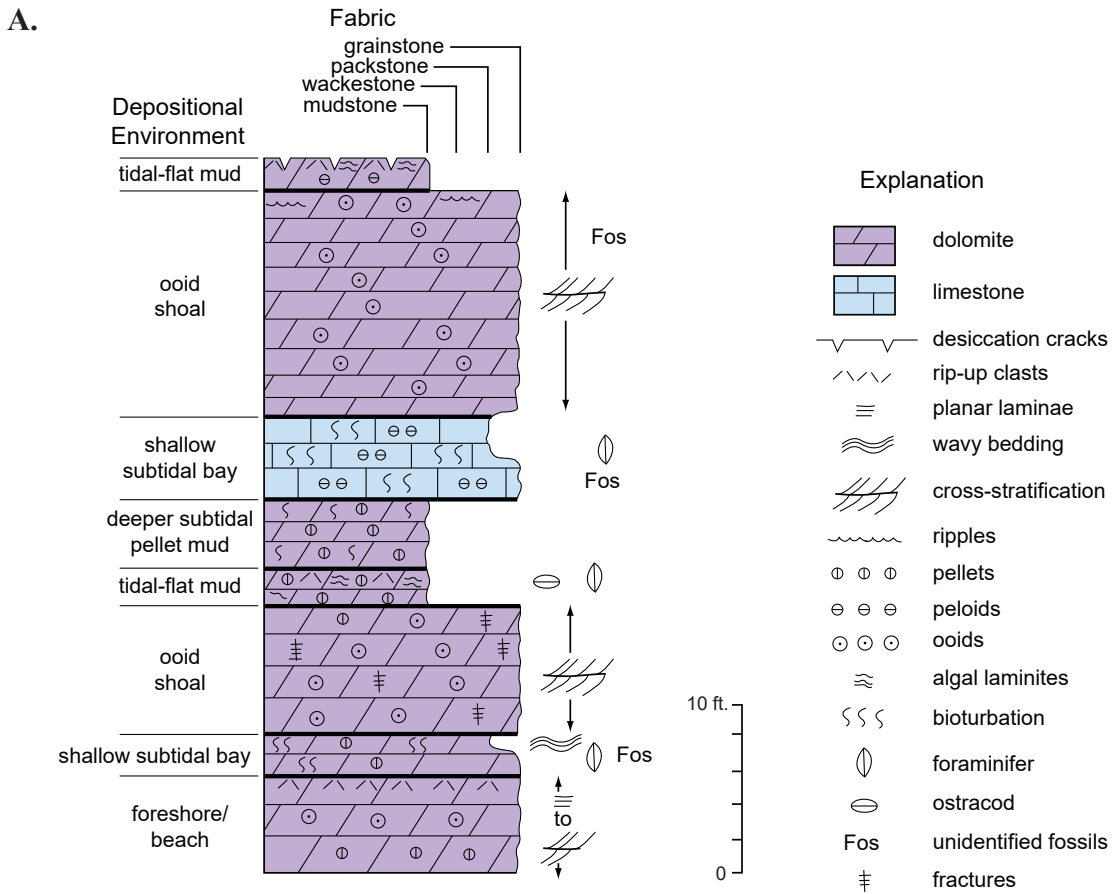


Figure 10.12. Madison Limestone section at study site 2. (A) Stratigraphic column from the Madison Limestone 2 showing carbonate fabrics and textures, fossils, and depositional environments. (B) Outcrop of measured stratigraphic section.

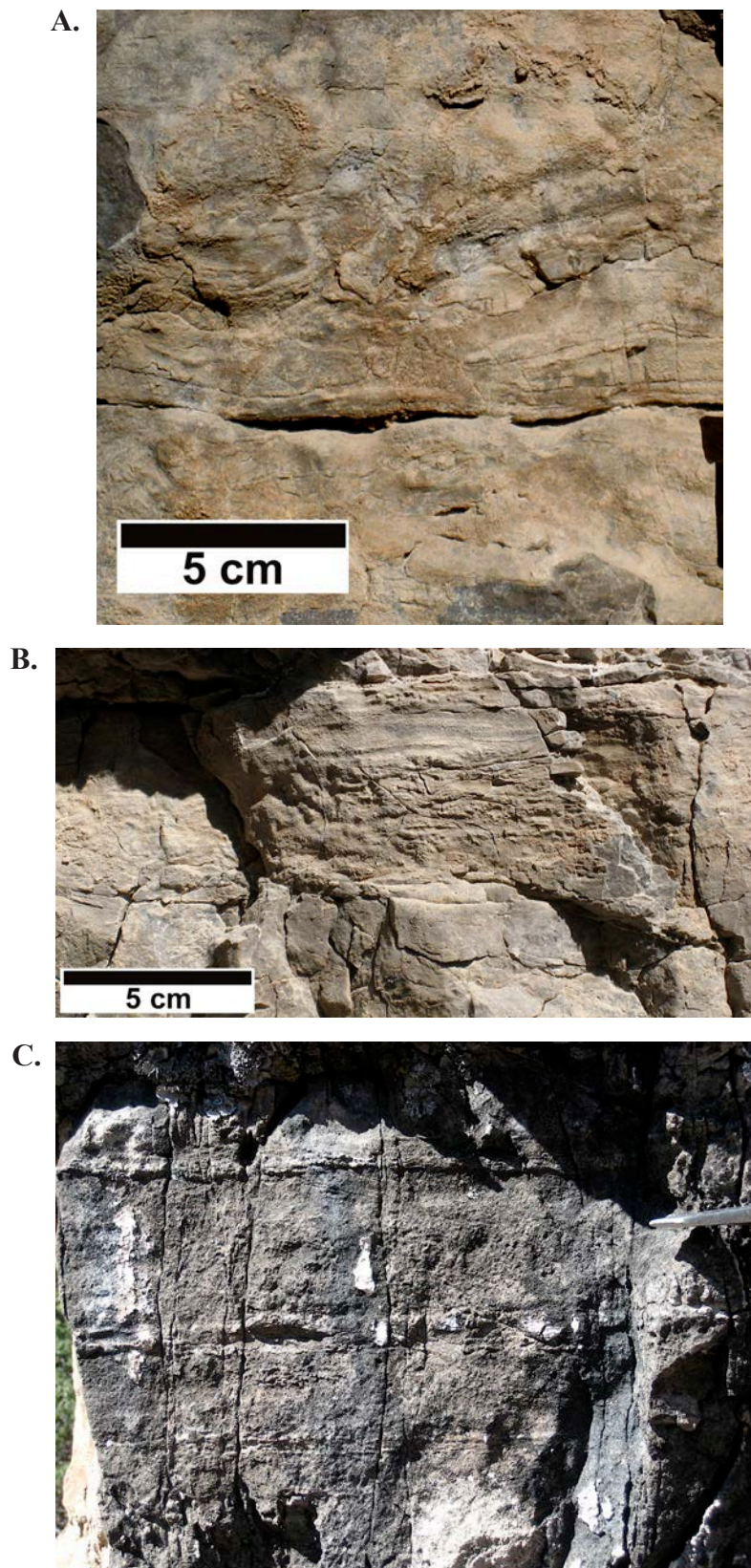
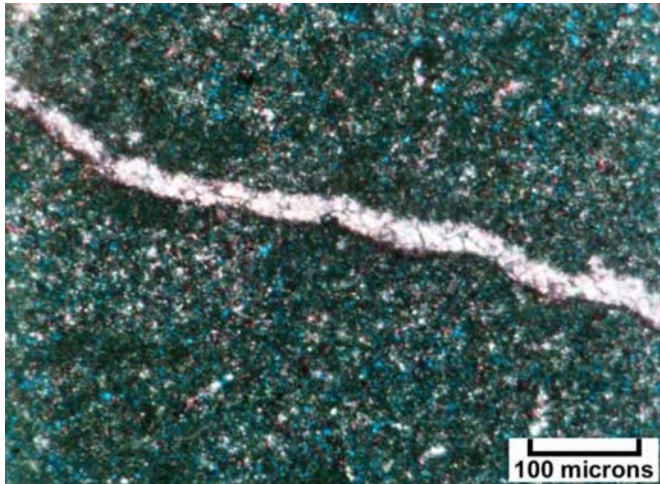
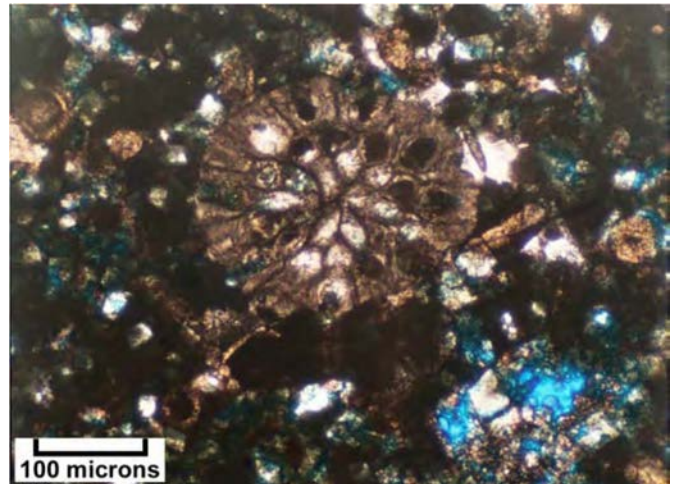


Figure 10.13. Examples of Madison Limestone lithofacies from study site 2. (A) Oolitic/hard pellet grainstone with “beachrock” clasts. (B) Peloidal/skeletal packetone/grainstone of a stable, shallow subtidal bay. (C) Oolitic/hard pellet grainstone with small- to medium-scale cross-beds. Note closely spaced swarms of vertical fractures. (D) Photomicrograph (plane light) of soft pellet mudstone (note dolomite-filled fracture across the image) containing organic material representing deeper-water subtidal mud. (E) Photomicrograph (plane light) of endothyrid forams in a peloidal/skeletal grainstone. (F) Oolitic grainstone with “cookie-chip-like” rip-up clasts. (G) Photomicrograph (plane light) of a highly dolomitized grainstone with relic ooids. (H) Photomicrograph (plane light) of dolomitic mudstone with cryptalgal (microbial) laminates.

D.



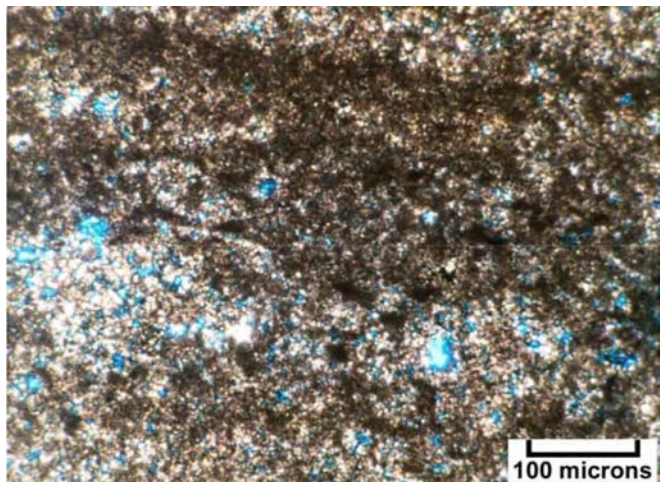
E.



F.



G.



H.

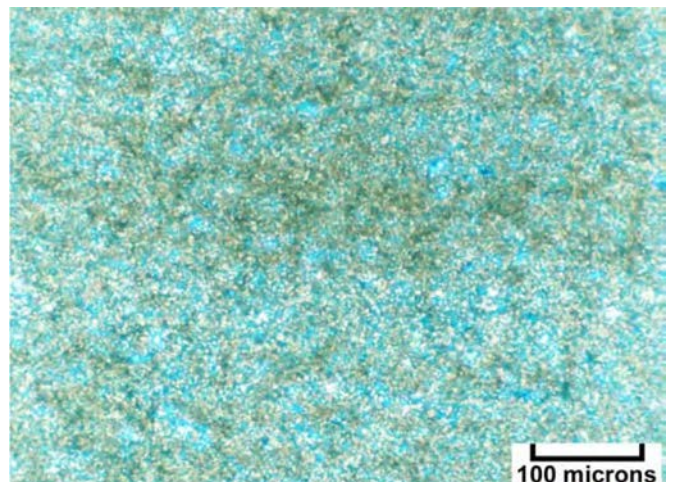


Figure 10.13 continued. Examples of Madison Limestone lithofacies from study site 2. (A) Oolitic/hard pellet grainstone with “beachrock” clasts. (B) Peloidal/skeletal packetone/grainstone of a stable, shallow subtidal bay. (C) Oolitic/hard pellet grainstone with small- to medium-scale cross-beds. Note closely spaced swarms of vertical fractures. (D) Photomicrograph (plane light) of soft pellet mudstone (note dolomite-filled fracture across the image) containing organic material representing deeper-water subtidal mud. (E) Photomicrograph (plane light) of endothyrid forams in a peloidal/skeletal grainstone. (F) Oolitic grainstone with “cookie-chip-like” rip-up clasts. (G) Photomicrograph (plane light) of a highly dolomitized grainstone with relic ooids. (H) Photomicrograph (plane light) of dolomitic mudstone with cryptalgal (microbial) laminates.

grainstone of an ooid shoal (figures 10.13F and 10.13G). The upper surface of the oolitic grainstone appears to be rippled to channelized with “cookie-chip-like” muddy rip-up clasts and fossil fragments in the troughs. Local nodular calcite masses may be relic evaporite structures. The top of the Dry Fork Canyon section is mudstone with continuous cryptalgal laminates (microbial) (figure 10.13H), pellets, possible desiccation cracks and rip-up clasts, and no fossils, all features indicative of a peritidal tidal-flat mud.

Several post-depositional features can also be found at study site 2 (Chidsey and others, 2020). A megabreccia is exposed at the western end of the Madison outcrop where the section was described (figure 10.14A). This breccia is a paleokarst collapse feature where limestone and dolomite clasts are set in a non-porous mud-rich matrix. In thin section (figure 10.14B), this breccia appears similar to collapse breccia seen in core from Lisbon field (compare to figure 4.9). The country rock is cross-bedded, oolitic dolograinstone (ooid shoal) capped by low-angle, stratified dolograinstone (foreshore) (figure 10.14A). An outcrop along the road a short distance up Brownies Canyon from the measured section displays spectacular, high-amplitude, bed-parallel stylolites in bioturbated mudstone (figure 10.15).

Study Site 3 – Crouse Reservoir/Diamond Mountain Plateau

The Crouse Reservoir/Diamond Mountain Plateau study site is in the eastern part of the southern flank of the Uinta Mountains, Uintah County (figure 10.1), 29 miles (47 km) northeast of Vernal. The site also includes a measured stratigraphic section (appendix I) and a key outcrop of brecciation on the western side of the improved gravel road to Crouse Reservoir (figure 10.16).

Unaltered units of entirely limestone, mapped as Madison Limestone, show cycles of three depositional environments within the 116-foot-thick (35 m) outcrop (figure 10.17): (1) storm-dominated, outer-shelf, crinoid shoals, (2) low-energy, open-marine, mud-rich intershoal (inner ramp or inner shelf), and (3) low-energy, open-marine, outer-shelf above storm wave base. Storm-dominated, outer-shelf, crinoid shoals consist of well-sorted, coarse sand to granule size crinoid fragments in wavy-thin to medium- or large-scale cross-bedded grainstone (encrinite) (figures 10.18A and 10.18B). The upper contact is often sharp with undulatory topography, possible small-scale interference ripples, and small rugose corals on top. Syntaxial cements are well developed. Low-energy, open-marine, muddy intershoal depositional environments are represented by burrowed, soft peloid/crinoid wackestone to packstone (figures 10.18C and 10.18D) containing some well-preserved fenestrate bryozoans. Low-energy, open-marine, outer-shelf, above storm wave base depositional environments consists of skeletal wackestone to packstone with grainstone burrow infills of biogenetic skeletal material. Burrow fillings occur at several scales. The larger burrow networks are open burrows filled with coarse, storm-pumped shells (tubular tempestites) (figures 10.18E and 10.18F). Within muds are

well-preserved, articulated crinoid columnals and fenestrate bryozoans. Locally abundant nodular cherts probably follow burrow systems.

A unique feature at study site 3 is a ridge with two topographic depressions (sags) dominated by intense breccia zones (pipes?) (figures 10.19 and 10.20), 75 to 100 feet (25–30 m) wide composed of highly brecciated dolomitic matrix (Chidsey and others, 2020). They are characterized by coarse calcite vein-like mineralization (figures 10.21 and 10.22A). Dolomitization and leaching of the matrix limestone has occurred throughout the zones (figure 10.22B). These distinctive elements imply a hydrothermal event rather than a paleokarst collapse origin for the breccia zones.

Discussion

Similar depositional environments described from outcrops above are also observed in Leadville cores from Lisbon field (see Chapter 3). Carbonate buildups containing good porosity/permeability are the best reservoir analog units, whereas low-porosity/permeability, open-marine packstones and wackestones represent less attractive reservoir analog units, unless they have experienced dolomitization in the subsurface that improved reservoir quality. Breccia pipes, paleokarst features, and fractures also enhance reservoir quality. The post-burial breccias associated with hydrothermal events, fracturing, and dissolution in the Leadville Limestone yield the best reservoirs at Lisbon field (see Chapter 4).

The breccia pipes and zones discovered at study sites 1 and 3 are likely the result of hydrothermal activity in the geologic past. The presence of the basal Cambrian Tintic Quartzite in the southern flank of the western Uinta Mountains (figure 10.2) and the stratigraphically equivalent Lodore Formation in the eastern part of the range (figure 10.3) may serve as hydrothermal recharge aquifers and are important contributors to the hydrothermal story. The Tintic is a very coarse to granular, or pebble, sandstone with moderately sorted, subrounded to spherical, monocrystalline and polycrystalline quartz grains. It is thin to thick cross-bedded, moderately indurated, and contains a few shale partings, which have small amounts of mica and some biogenic feeding trails (Dockal, 1980). The contact of the Tintic with overlying Mississippian strata is fairly sharp. The Lodore is a very fine to medium-grained, well-sorted, very thinly bedded to cross-bedded (with undulatory surfaces) sandstone marked by argillaceous partings (figure 10.23). Quartz grains are subrounded to spherical. The Lodore can be calcareous and slightly ferruginous. The top appears to be eroded (Dockal, 1980). Both the Lodore and Tintic can have porous and permeable units. As aquifers, they likely supplied hot water to the former hydrothermal system (Chidsey and others, 2020).

Three-dimensional numerical models of seafloor hydrothermal convection by Coumou and others (2008) demonstrated that convection cells organize themselves into pipe-like up-flow zones surrounded by narrow zones of warm downflow.

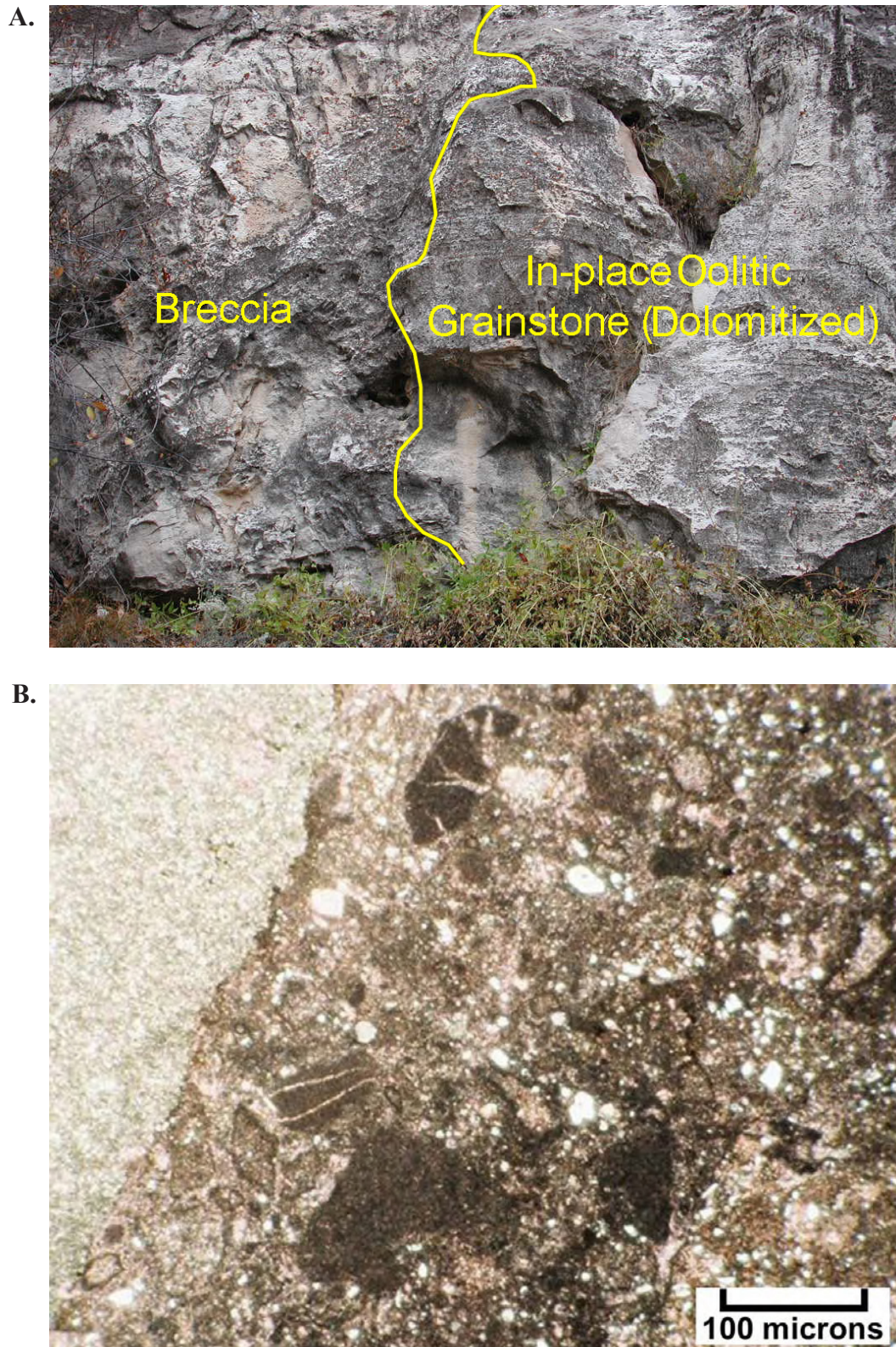


Figure 10.14. Megabreccia at study site 2. (A) Small-scale ooid shoal and collapse breccia (outcrop is approximately 10 feet [3 m] high). (B) Photomicrograph (plane light) showing the contact between dolomitic grainstone (light gray, upper left) and the dolomitized karst cavity filling of small carbonate clasts.



Figure 10.15. High-amplitude, bed parallel stylolites in bioturbated mudstone (close-up of stylolites shown in inset).

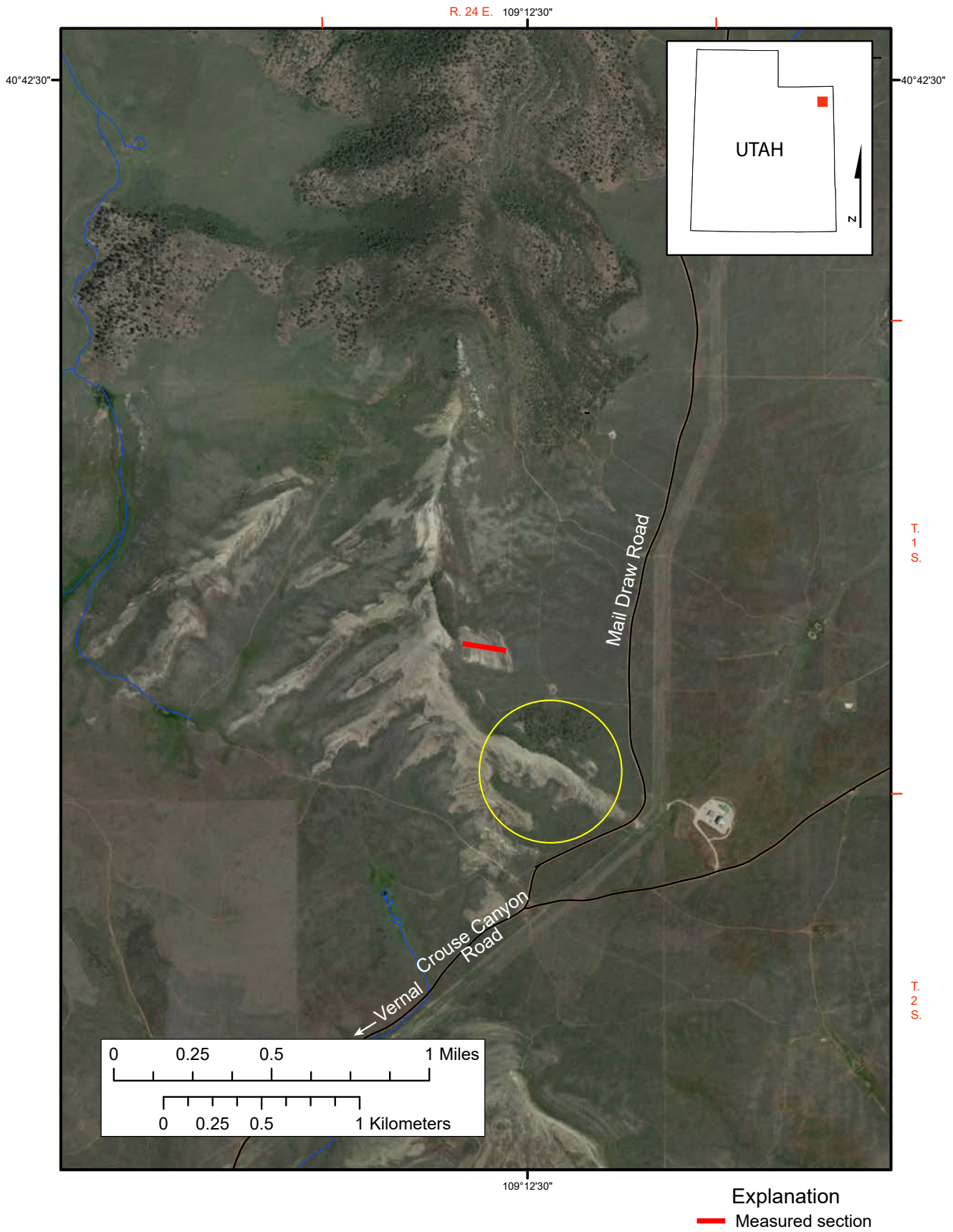


Figure 10.16. Google Earth image (© 2018 Google) showing the location of study site 3, Crouse Reservoir/Diamond Mountain Plateau (key brecciated outcrop indicated with yellow circle).

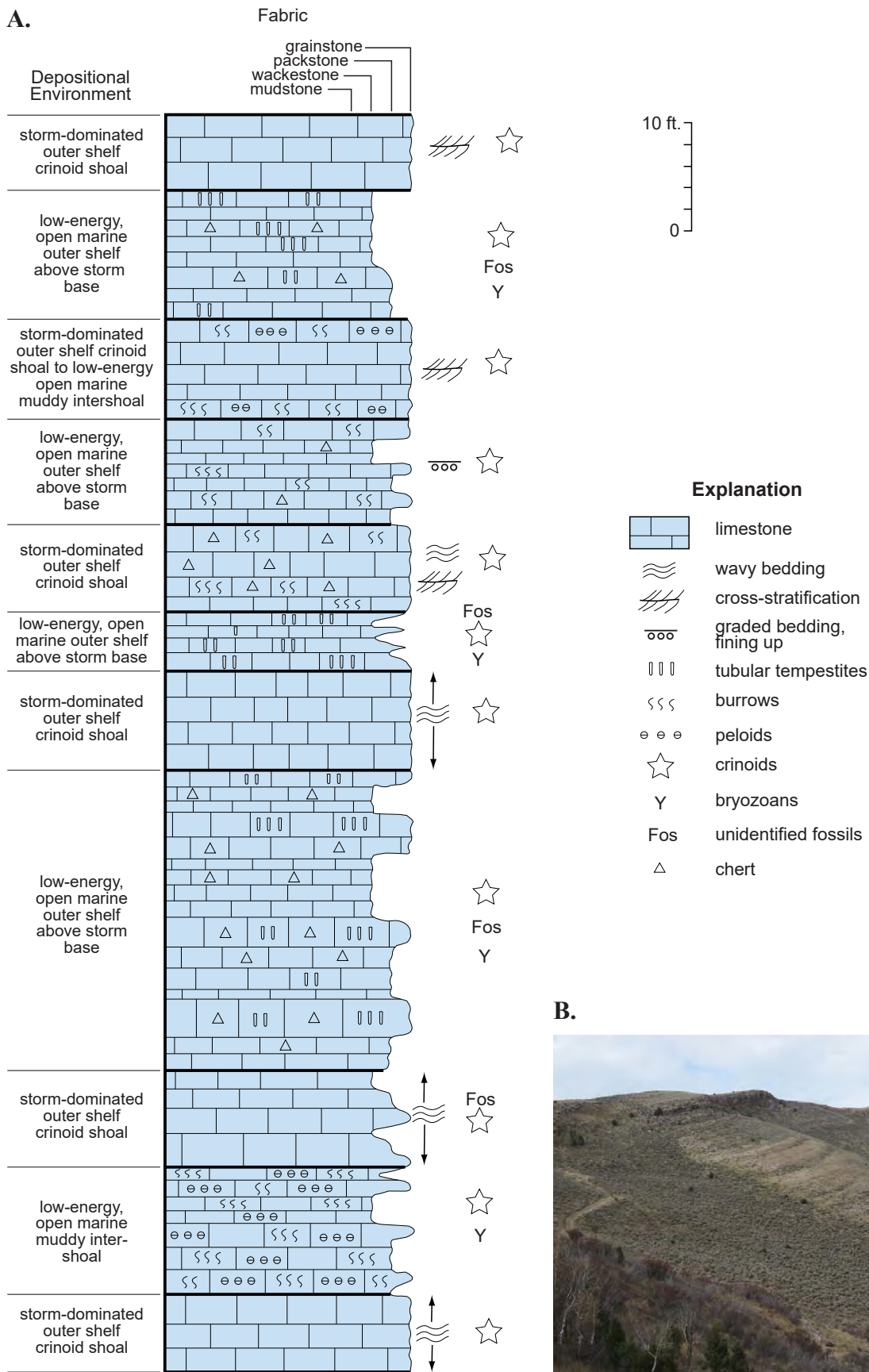


Figure 10.17. Madison Limestone section at study site 3. **(A)** Stratigraphic column from the Madison Limestone at study site 3 showing carbonate fabrics and textures, fossils, and depositional environments. **(B)** Outcrop of measured stratigraphic section.

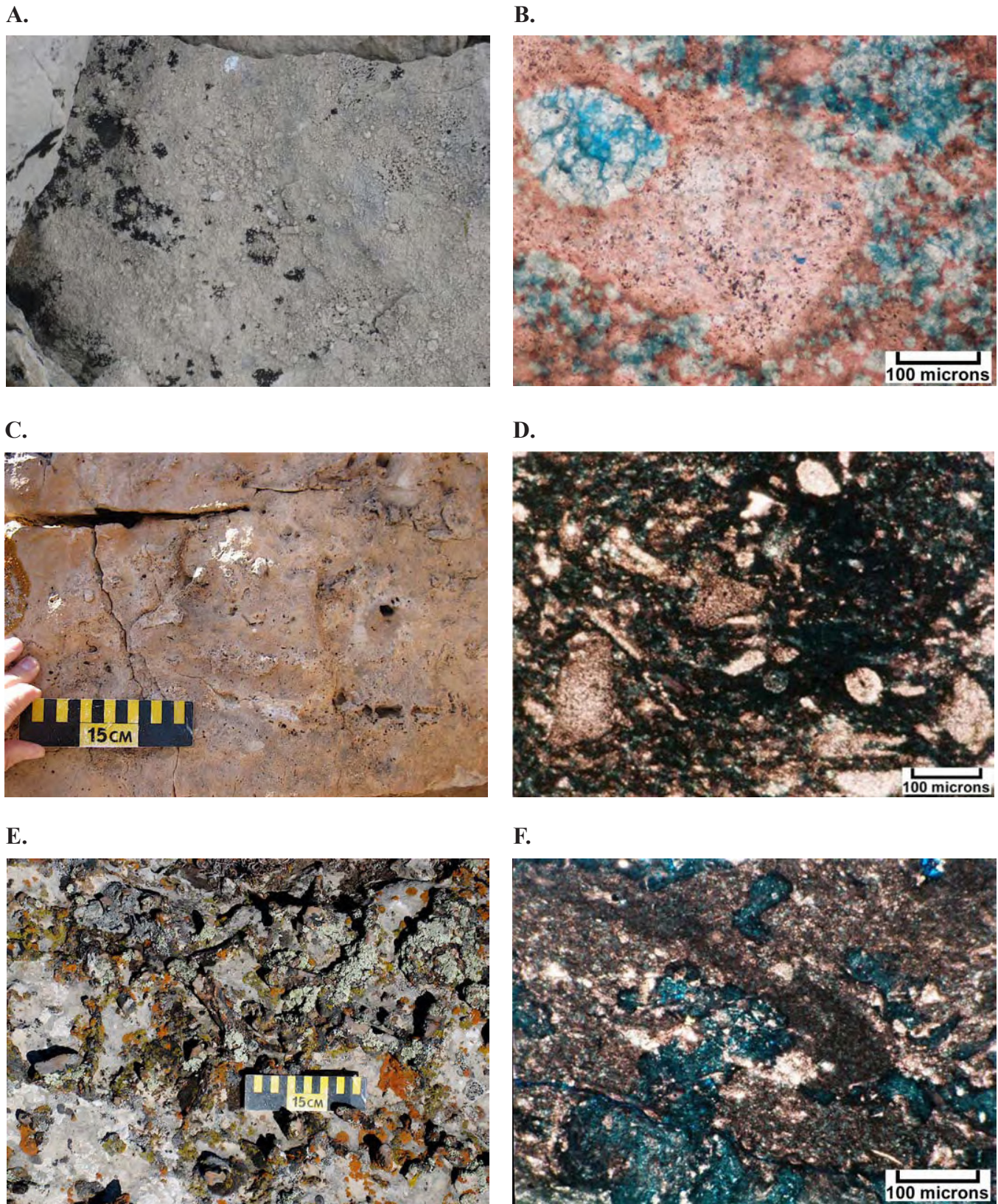


Figure 10.18. Examples of Madison Limestone lithofacies from study site 3. (A) Coarse-grained, skeletal/crinoidal grainstone (encrinite). (B) Photomicrograph (plane light) of a crinoid columnal within a typical limestone encrinite. Note some syntaxial cement overgrowths. (C) Typical burrowed soft peloid/crinoid packstone. (D) Photomicrograph (plane light) of a low-energy, open-marine peloidal wackestone. (E) Weathered out tubular tempestites in a skeletal packstone. (F) Photomicrograph (plane light) of a tubular tempestite containing skeletal debris.



Figure 10.19. Topographic depressions (sags) at the sites of major breccia zones (pipes?) along a ridge of Madison Limestone (view to the southeast).



Figure 10.20. Slabbed specimen of highly brecciated rock typical of that present at study site 3.

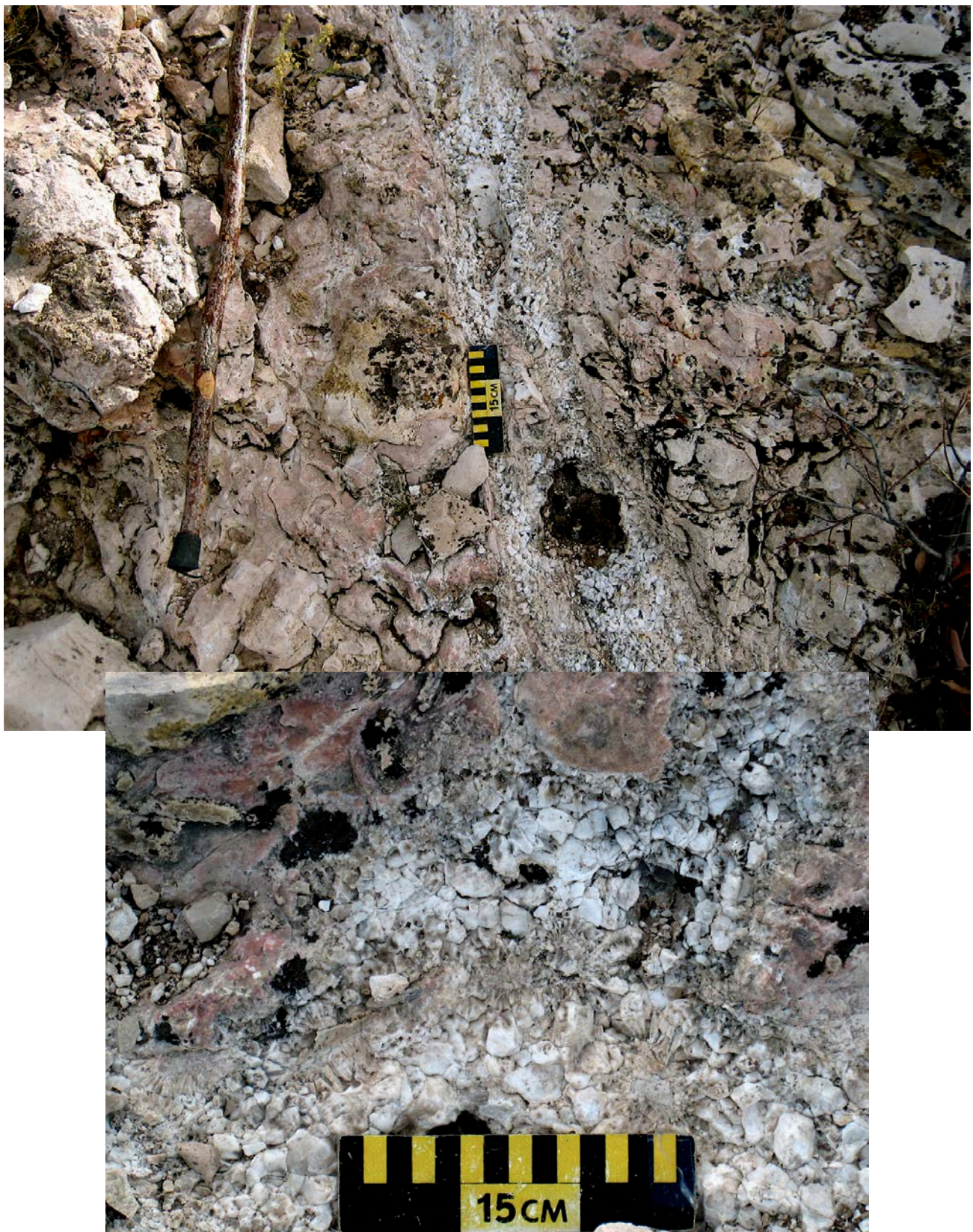
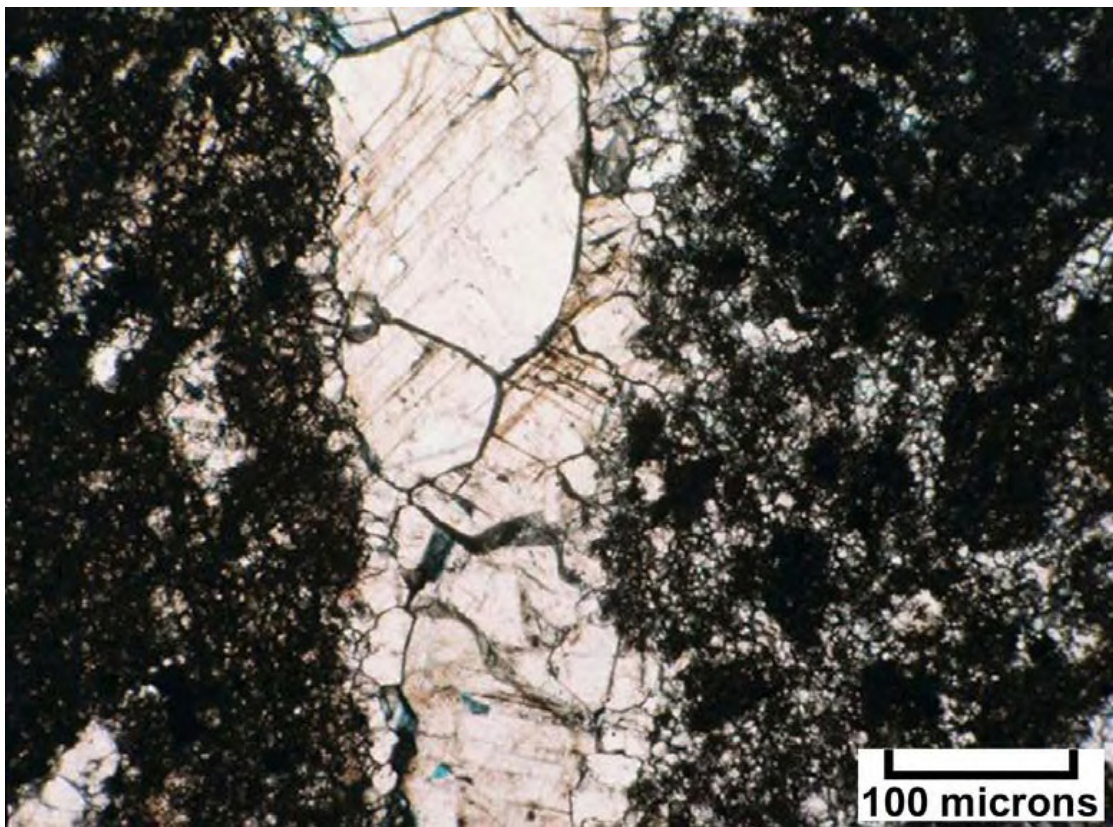


Figure 10.21. Coarse calcite vein in a highly brecciated dolomitic matrix. Inset: close-up of large, representative, calcite crystals.

A.



B.

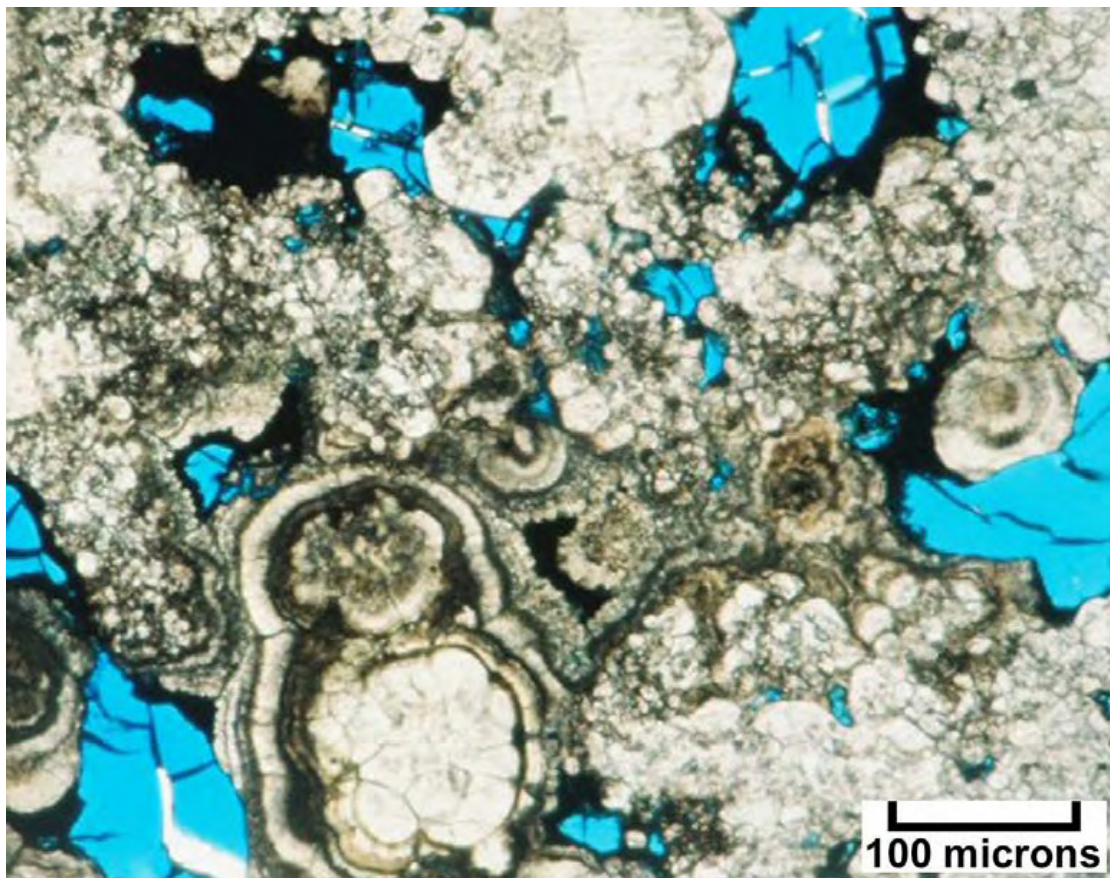


Figure 10.22. Photomicrographs (plane light) from breccia samples at study site 3. (A) Vein of coarse calcite in a low-permeability dolomitic matrix. (B) Unusual concentric dolomite cement (high temperature?) overgrowths in a dolomitic breccia matrix.

A.



B.



Figure 10.23. Basal Cambrian Lodore Formation. (A) Outcrop of thin-bedded Lodore Formation north of study site 3, southwest of Crouse Reservoir. (B) Lodore Formation hand sample of very fine grained, well-sorted, cross-bedded, slightly ferruginous sandstone.

Recharge can occur over an extensive area or along faults as water migration pathways. The Tintic Quartzite is mapped on the western end of the Uinta Mountains whereas the Lodore Formation is present on the eastern end. Through the central part of the southern flank of the Uinta Mountains, porous Cambrian sandstone is absent and Mississippian strata lie unconformably on Precambrian (middle Neoproterozoic) Red Pine Shale and older formations of the Uinta Mountain Group (as observed in Whiterocks Canyon [figure 10.1]). No hydrothermal breccia zones or pipes are found in the central part of the southern flank, lending credence to the concept that aquifers in the Tintic and Lodore were a required condition

for past hydrothermal activity to have occurred. After pressure builds up to a certain point, the hydrothermal fluids within the aquifer can very rapidly and explosively break through zones of weakness at the intersections of fractures or along faults; this can occur as a single event or over several stages. Thus, when targeting the Leadville Limestone in the Paradox Basin for potential hydrothermal dolomite and enhanced reservoir quality due to natural hydrofracturing, the presence of an underlying aquifer, and fracture zones or faults may be necessary ingredients, supported in part from what can be observed from the breccia zones at study sites 1 and 3.

CHAPTER 11:

SUMMARY AND CONCLUSIONS

by

Thomas C. Chidsey, Jr., Utah Geological Survey

CHAPTER 11: SUMMARY AND CONCLUSIONS

The Mississippian (late Kinderhookian to early Meramecian) Leadville Limestone is a shallow, open-marine, carbonate-shelf deposit. The Leadville has produced over 53 million barrels of oil/condensate and 830 BCFG (including cycled gas), from seven fields in the Paradox fold and fault belt of the Paradox Basin, Utah and Colorado. This environmentally sensitive, 7500-square-mile (19,400 km²) area is relatively unexplored with only about 100 exploratory wells that penetrated the Leadville (less than one well per township), and thus the potential for new discoveries remains significant. There have been no significant new oil discoveries since the early 1960s and only independent producers continue to explore for Leadville oil targets in the region, 85% of which is under the stewardship of the federal government.

The overall goals of this study were to (1) develop and demonstrate techniques and exploration methods never tried on the Leadville Limestone, (2) target areas for exploration, (3) increase production from new and old Leadville fields through detailed reservoir characterization, (4) reduce exploration costs and risk especially in environmentally sensitive areas, and (5) add new oil discoveries and reserves.

LISBON FIELD, SAN JUAN COUNTY, UTAH—A CASE STUDY OF LEADVILLE LIMESTONE LITHOFACIES AND DIAGENETIC HISTORY

Prior to this study, reservoir characterization of the Leadville Limestone was poorly defined and little pertinent information (core descriptions, permeability data, and diagenetic analysis) had been published. Lisbon field, San Juan County, Utah, accounts for most of the Leadville oil and gas production in the Paradox Basin. Its reservoir characteristics, particularly diagenetic overprinting and history, and Leadville lithofacies can be applied regionally to other fields and exploration trends in the basin. The Utah Geological Survey had a wealth of undescribed core and other raw data at the Utah Core Research Center. Initial investigations indicated the possible presence of hydrothermal dolomite, a key component in the development of diagenetic hydrocarbon traps, which would imply a new potential for the Leadville in the Paradox Basin. Therefore, Lisbon field was selected as the case study for this Leadville Limestone project. The following sections summarize the lithofacies, diagenesis (including scanning electron microscopy, epifluorescence, cathodoluminescence), fluid inclusion, isotopic, and burial history studies of Lisbon field, and provides conclusions and recommendations for exploring Leadville targets.

Lithofacies

1. Leadville lithofacies include open marine (crinoidal banks or shoals and Waulsortian-type buildups), ooid and peloid shoals, and middle shelf.
2. Rock units with open-marine and restricted-marine lithofacies constitute a significant reservoir potential, having both effective porosity and permeability when dissolution of skeletal grains followed by dolomitization has occurred.

Diagenetic History

1. Leadville reservoir quality at Lisbon field is greatly enhanced by dolomitization and dissolution of shallow-water limestone. There are two basic types of dolomite: (1) very fine, early dolomite, and (2) coarse, late dolomite. Early dolomitization preserves depositional fabrics and has limited porosity development, except for limited dissolution of fossils, and has very low permeabilities. Late dolomitization has two morphologies: rhombic dolomites and saddle dolomites. Most reservoir rocks within Lisbon field appear to be associated with the second, late type of dolomitization and associated leaching events.
2. Pyrobitumen coats most intercrystalline dolomite as well as dissolution pores associated with the second type of dolomite. Fracturing and brecciation caused by hydrofracturing are widespread within Lisbon field. Sediment-filled cavities, related to karstification of the previously exposed Leadville Limestone, are relatively common throughout the upper one-third of the formation in the field. Other diagenetic products include syntaxial cement, sulfide minerals, anhydrite cement and replacement, and late macrocalcite.
3. Late dolomitization, saddle dolomite, and dolomite cement precipitation, as well as sulfides and brecciation, may have developed from hydrothermal events that can greatly improve reservoir quality. The result can be the formation of large, diagenetic-type hydrocarbon traps.

Scanning Electron Microscopy

Scanning electron microscopy (SEM) clearly identifies the various diagenetic events that affected reservoir quality at Lisbon and probably other Leadville fields.

- Reservoir quality is greatly enhanced by late, coarse dolomitization and dissolution. Microporosity occurs

in the form of intercrystalline porosity. Dissolution has created moldic, vuggy, and channel porosity.

- Pyrobitumen coats most intercrystalline dolomite in the Leadville as well as dissolution pores associated with the second type of dolomite resulting in reduced permeability. Fractures enhance the permeability in several intervals.
- Minor euhedral quartz is present in several samples. Anhydrite (which often plugs pore throats) and sulfide mineral(s) are also present in moderate abundance.
- The general diagenetic sequence for these samples, based on SEM analysis, is (1) dolomitization, (2) dissolution, (3) dolomite cementation, (4) fracturing, (5) quartz cementation, (6) calcite cementation, (7) clay precipitation, (8) anhydrite cementation, (9) pyrobitumen emplacement, and (10) sulfide precipitation.

Epifluorescence

Epifluorescence (EF) petrography makes it possible to clearly identify grain types and shapes, within both limestone and dolomite reservoir intervals in Leadville thin sections from cores used in the study. In particular, identification of peloids, skeletal grain types, and coated grains is easy in rocks where these grains have been poorly preserved, partially leached, or completely dolomitized. Depositional textures that are frequently hidden or poorly preserved can often be clearly distinguished using blue-light EF microscopy.

- In many limestones and finely crystalline dolomites of the Leadville reservoir at Lisbon field, the differences between muddy and calcarenitic fabrics can only be clearly appreciated with fluorescence lighting.
- Epifluorescence petrography clearly and rapidly images pore spaces that cannot otherwise be seen in standard viewing under transmitted polarized lighting. In addition, the cross-sectional size and shape of pores are easy to determine.
- Much of the Leadville porosity is very heterogeneous and poorly connected as viewed under EF. In particular, intercrystalline porosity within some of the reservoir in Lisbon field can be resolved much more clearly than with transmitted polarized lighting. The EF examination helps see the origin of most types of porosity. Transmitted polarized lighting does not image intercrystalline porosity in carbonate samples very well, even though blue-dyed epoxy can be impregnated into even very small pores. In addition, opaque bitumen linings prevent light from passing through some of the pores to the observer. Without the aid of the EF view, the amount of visible open pore space would be underestimated in the plane-light image.

- Where dolomitization has occurred, EF petrography often shows the crystal size, shape, and zonation far better than transmitted plane or polarized lighting. This information is often very useful when considering the origin and timing of dolomitization as well as evaluating the quality of the pore system within the dolomite.
- Permeability differences within dolomite and limestone samples are also easy to image because of the differential oil saturations between the low-permeability areas and the more permeable lithologies. Low-permeability carbonates from this study area show bright yellow fluorescence due to trapped live oil that is retained within low-permeability parts of the reservoir system. More permeable rocks show red fluorescence due to the epoxy fluorescence where oil has almost completely drained from the better-quality parts of the reservoir.

Cathodoluminescence

Cathodoluminescence (CL) imaging of samples nicely complements the types of information derived from EF of carbonate thin sections. Cathodoluminescence also displays original depositional textures and the outlines of original carbonate grains, and distinctly images pore spaces. This information is often very useful when considering the origin and timing of dolomitization as well as evaluating the quality of the pore system within the dolomite.

- Cathodoluminescence shows a wide range of Leadville crystal size and growth habits within the dull red luminescing, matrix-replacing dolomite. Most of the dolomite within areas of fabric-selective dolomitization is a deep or intense red color. Between many of the grains, a lighter red luminescence occurs where early cements have been dolomitized. Some of the coarser dolomite crystals appear to have an overgrowth of brighter red luminescent material.
- The amount of open porosity under CL is considerably greater than that visible under plane-light microscopy. Between other grains are interparticle pores that are still open. In a few areas, these early pores have been solution-enlarged and lined with a later generation of coarse, rhombic dolomite.
- Examination of saddle dolomites in the Leadville Limestone can provide more information about these late, elevated-temperature (often hydrothermal) mineral phases. For instance, saddle dolomites show nice growth banding. These saddle dolomites display dull, red luminescence in their core areas and slightly bright, orange-red luminescence toward their rim areas. In addition, CL makes it possible to see the growth bands in these coarse dolomite crystals due to slight luminescence differences between each growth zone.

- Cathodoluminescence imaging shows that the contact between the transported material related to karstification and the limestone country rock can be sharp, irregular, and corroded.

Fluid Inclusions

During crystal growth, imperfections may trap fluids present in the environment at that time. Later mineral precipitation and deformation, such as development of fractures, can create additional crystal imperfections that may also trap fluids. Fluid inclusions provide pressure, volume, and temperature information about the conditions when the crystal precipitated. The fluids in the inclusion may be connate water, oil, or a sample of the mineralizing fluid.

- The fluid inclusion and mineral relationships suggest the following diagenetic sequence of events for the Lisbon Leadville reservoir: (1) dolomite precipitation, (2) anhydrite deposition, (3) anhydrite dissolution and quartz precipitation, (4) dolomite dissolution and late calcite precipitation, (5) trapping of a mobile oil phase, and (6) formation of bitumen.
- Aqueous fluid inclusions in early calcite, which typically forms coarse-grained crystals, display a range of liquid to vapor ratios suggesting they have necked. Primary oil inclusions studied in one calcite crystal from the Lisbon No. D-616 well, however, display consistent liquid to vapor ratios. These oil inclusions yielded homogenization temperatures ranging from 48° to 70°C (118°–158°F). These temperatures represent the minimum temperature of oil formation, not of calcite deposition. The oil was generated in place by maturation of organic material. Both the oil inclusions and the common presence of two-phase, necked aqueous inclusions imply trapping at elevated temperatures. Trapping likely occurred when the original calcite recrystallized during burial.
- Fluid inclusions in dolomite have reequilibrated (stretched, necked, refilled) since trapping. The common presence of single-phase aqueous inclusions suggests that the fine-grained dolomite and cores of saddle dolomite were deposited at temperatures less than about 50°C (122°F).
- Coarse-grained quartz crystals containing solid inclusions of anhydrite are found at a depth of 8356 feet (2550 m) in the Lisbon No. D-616 well. Homogenization temperatures of primary inclusions range from 120° to 130°C (248°–266°F). The presence of gas-rich inclusions in the quartz suggests these temperatures are close to the true trapping temperatures and possibly maximum burial temperatures.
- The low ice-melting temperatures of quartz and calcite-hosted inclusions from the Lisbon No. D-616 well suggest chemically complex Ca-Mg-bearing brines associated with evaporite deposits were responsible for mineral deposition. Calcite from the Lisbon NW USA No. B-63 well trapped fluids with lower salinities.
- Oil trapped in early calcite as primary inclusions, as secondary inclusions in calcite of undetermined age, and as “primary” inclusions in recrystallized parts of saddle dolomite fluoresces with a bluish green color, suggesting an API gravity of 35° to 40°. Homogenization temperatures of primary inclusions in early calcite and saddle dolomite are similar and range from 48° to 70°C (118°–158°F). The oil inclusions trapped in the white, recrystallized and inclusion-poor saddle dolomite indicate the temperature was at least 70°C (158°F) during oil deposition and recrystallization. Oil trapped in the saddle dolomite must represent oil that was mobile at this time.
- Oil deposited in healed fractures within late, pore-filling calcite has similar fluorescence as the primary inclusions but lower homogenization temperatures of about 40°C (104°F). The lower temperatures of the secondary oil inclusions allow the possibility that the temperatures were decreasing, perhaps due to unroofing, prior to bitumen formation.
- Live oil was possibly preserved in the calcite and dolomite, but not in the main fractures, which now contain bitumen because the oil was not degassed.

Isotopic Analysis

Stable isotope geochemistry provides insights into the chemical differences between preserved remnants of depositional components and the various diagenetic events in carbonate rocks, as recognized from core examination and thin section petrography. There are broad fields of carbon and oxygen isotope compositions for various carbonate rock settings. Strontium isotope analysis is used most frequently as an age-dating tool in marine carbonates.

- Stable carbon and oxygen isotope data indicate that all Lisbon Leadville dolomites were likely associated with brines whose composition was enriched in ¹⁸O compared with late Mississippian seawater (several per mil heavier than normal seawater).
- Stable oxygen isotope analyses of the Leadville replacement dolomites indicate that temperatures of precipitation ranged from about 60° to 90°C (140°–194°F). Saddle dolomite cements were precipitated at temperatures greater than 90°C (194°F).
- High Sr isotopic ratios for late burial diagenetic mineral phases at Lisbon field indicate contributions by waters enriched in ⁸⁷Sr that were derived from either

granitic Precambrian basement rocks or the Devonian McCracken Sandstone.

Burial History and Possible Heat Sources

We propose a model with thermal convection cells bounded by basement-rooted faults to transfer heat and fluids possibly from the crystalline basement, Pennsylvanian evaporites, and Oligocene igneous complexes.

- Early Tertiary reactivation of basement-involved, high-angle normal faults associated with Precambrian tectonics may have allowed hot, deep-seated fluids from the granitic basement or the McCracken Sandstone to communicate upwards with the Leadville carbonate section. Brines from evaporites in the Pennsylvanian Paradox Formation may have also entered the Leadville Limestone along the large fault bounding the northeastern flank of the field.
- Burial history and temperature profiles for the Leadville Limestone at Lisbon field provide some guidance as to when important diagenetic and porosity-forming events occurred. Porous replacement dolomites probably formed during the early and middle portions of the burial history at Lisbon field.
- Inferred elevated temperature spikes during maximum burial, late Laramide faulting/uplift, and Oligocene igneous activity may account for the high temperatures responsible for quartz precipitation, sulfide mineralization, pyrobitumen formation, late dissolution of carbonates, and late saddle dolomite cements.
- We recommend that any future evaluation of a Leadville Limestone prospect include stable carbon and oxygen isotope analysis of diagenetic components, strontium isotope analysis for tracing the origin of fluids responsible for different diagenetic events, and creation of burial history and temperature profiles to help determine when the diagenetic events occurred.

REGIONAL STUDIES OF THE MISSISSIPPIAN LEADVILLE LIMESTONE HYDROCARBON PLAY

Exploring the Leadville Limestone play has been high risk, with less than a 10% chance of success based on the drilling history of the region. New prospect definition often requires expensive, 3D seismic acquisition in environmentally sensitive areas. These facts make exploring difficult for companies, usually small independents that have limited funds available, to try new, unproven techniques that might increase the chance of successfully discovering oil and gas. Using regional

oil-show data to identify potential oil-prone areas and surface geochemical surveys (Seneshen and others, 2009, 2010) first will reduce the risk taken in looking for Leadville hydrocarbons. These techniques will help to recognize or eliminate areas and exploration targets prior to spending significant financial resources on seismic data acquisition and potential environmental litigation, and therefore increase the chance of successfully finding new economic accumulations of Leadville oil and gas. The regional brine chemistries and hydrodynamic pressure regimes for the Paleozoic formations of the Paradox Basin provide clues to potential Leadville oil and gas migration directions.

General Regional Leadville Play Characteristics

1. Regional facies of the Leadville Limestone were determined by evaluating cores and correlating geophysical well logs throughout the Paradox Basin to target areas for exploration. Leadville facies include open marine (crinoidal banks or ooid shoals and Waulsortian-type buildups), middle shelf, and restricted marine (peloidal muds).
2. The Leadville Limestone is more than 700 feet (200 m) to less than 200 feet (60 m) thick, and thins to the southeast across the Paradox Basin due to both depositional onlap and erosional wedging. The unit is bounded above and below by unconformities within the basin.
3. The Leadville is mostly pure limestone with some reflux dolomitization implying arid conditions on a shallow shelf.
4. Subaerial erosion resulted in lateritic regolith formed over most of the Leadville Limestone in the Paradox Basin. Brecciation and sediment-filled cavities, related to karstification of the exposed Leadville, are relatively common throughout the upper one-third of the formation.
5. Regionally, an intraformational disconformity divides the Leadville Limestone into informal upper and lower members.
6. Early movement on northwest-trending faults may have affected deposition of the Leadville Limestone.
7. Hydrocarbon production and shows are primarily along the northwest-trending faults in the Paradox fold and fault belt. Stratigraphic traps developed by the erosional regolith and Waulsortian mounds, or other carbonate buildups, may exist in the Leadville southwest of the fold and fault belt. Diagenetic traps resulting primarily from late (hydrothermal) dolomitization represent untapped but difficult to identify drilling targets in the fold and fault belt.
8. Hydrocarbons in Leadville Limestone reservoirs were likely generated from source rocks in the Pennsylvanian Paradox Formation.

Potential Oil-Prone Areas in the Paradox Fold and Fault Belt Based on Shows in Drill Cuttings Using Epifluorescence Microscopy Techniques

1. Epifluorescence petrography makes it possible to clearly identify hydrocarbon shows in Leadville cuttings selected for study. It is a non-destructive procedure that can be done using a petrographic microscope equipped with reflected light capabilities, mercury-vapor light, and appropriate filtering. Sample preparation is inexpensive and rapid.
2. Cuttings from 32 productive or dry exploratory wells penetrating the Leadville Limestone in the Utah part of the Paradox fold and fault belt were examined under a binocular microscope. Over 900 samples of porous dolomite and some limestone were selected from various zones over the Leadville section for EF evaluation.
3. Epifluorescence allows one to observe the presence or absence of any soluble hydrocarbons, especially in high-porosity dolomite. Samples displaying fluorescence represent areas where hydrocarbons may have migrated or accumulated. If no fluorescence is observed in porous dolomites, the samples are also good representatives of areas where hydrocarbons have not migrated or accumulated.
4. A qualitative visual "rating" scale (a range and average) based on EF evaluation was applied to the group of cuttings from each depth in each well. The highest maximum and highest average EF reading from each well were plotted and mapped.
5. The maps show a regional southeast-northwest trend of relatively high EF for Leadville cuttings parallels the southwestern part of the Paradox fold and fault belt from Lisbon field northwest to west of the town of Green River. The northeastern part of the fold and fault belt shows a regional trend of low EF including a large area of essentially no EF centered around the town of Moab. As expected, productive Leadville wells have cuttings distinguished by generally higher EF ratings. An exception to these examples are several dry holes in the southeast-northwest trend that also have high EF ratings.
6. Hydrocarbon migration and alteration dolomitization was associated with regional northwest-trending faults and fracture zones, which created potential oil-prone areas along the southwestern part of the fold and fault belt. Hydrocarbons may have migrated from organic-rich shales in the Pennsylvanian Paradox Formation where they are in contact with the Leadville Limestone along faults. Fluid inclusions indicate some hydrocarbons were generated in-place. Hydrothermal alteration associated with these faults and related fracture zones may have generated late, porous dolomite and thus produced diagenetic traps. Hydrocarbons flushed to the southwest by hydrodynamic processes may also account for the lack of significant EF in the

northeastern parts of the fold and fault belt. In addition, these EF trends could be related to facies or karst development in the Leadville.

7. Exploration efforts should be concentrated in suggested oil-prone areas along the southwestern part of the Paradox fold and fault belt.

Devonian/Mississippian and Pennsylvanian Brine Chemistry and Trends within the Paradox Basin, Utah

1. The chemistry of both the Devonian/Mississippian and Pennsylvanian brine systems systematically changes from north to south through the Paradox Basin.
2. The Pennsylvanian-system brines are more saline than the Devonian/Mississippian-system brines. Piper and Stiff diagrams show that the brines from both systems are predominantly sodium-rich in nature, with some samples containing greater percentages of calcium and to a lesser extent magnesium. The Piper and Stiff diagrams also show that both brine systems are high in chloride with some samples being high in sulfate content. Bicarbonate is very low in both brine systems.
3. Based on brine chemistry, the direction of groundwater movement in the Devonian/Mississippian and Pennsylvanian systems is generally southwestward toward the topographically low outcrop areas along the Colorado River in Arizona.

Regional Middle Paleozoic Hydrodynamic Pressure Regime of the Paradox Basin, Utah and Colorado

1. Shut in drill-stem test (DST) pressure data from petroleum exploration and development wells in the Paradox Basin were used to establish the major hydrodynamic trends, especially within the Mississippian (395 DSTs).
2. With the exception of the eastern edge of the basin (western flanks of the San Juan Mountains), there is a single pressure regime for the Mississippian, having a composite pressure gradient of 0.47 pounds per square inch/foot (10.6 kPa/m) over an elevation range of +4000 to -10,000 ft asl (+1200 to -3000 m asl). This remarkably uniform pressure regime over an area of at least 100 by 100 miles (260 X 260 km) indicates relatively high permeability within the Mississippian.
3. The pressure gradient is about 10% above hydrostatic for fresh water but is consistent with the density of relatively saline water having a TDS concentration of 100,000 to 150,000 mg/kg. The head is between 3800 and 4000 ft asl (1160 and 1200 m asl) and coincides with the elevation of

the lower Green River and Cataract Canyon section of the Colorado River where they traverse the basin.

4. The Mississippian and older reservoirs across most of the Paradox Basin are in good hydrological communication with the Colorado River system, perhaps because they are within about 1000 feet (~300 m) of the surface beneath Cataract Canyon. This large-scale hydrological connection between the surface and the Mississippian may be a geologically recent occurrence.
5. Consideration of the rate of incision by the Colorado River system suggests that the Mississippian could have been hydrologically isolated and fully saturated several million years ago and could have held significantly greater quantities of oil and gas. Some of this greater volume of oil could be preserved as the tar sand deposits (Tar Sand Triangle, White Canyon, and Ten Mile Wash) found along the western margin of the Paradox Basin, which may have been a larger pool trapped in what is now the partially breached Monument upwarp.

MODERN AND OUTCROP ANALOGS FOR LEADVILLE LIMESTONE RESERVOIRS

Facies and other characteristics of the Leadville Limestone identified in Lisbon field and regional Paradox Basin cores were compared to both modern and outcrop analogs. Environments of the Leadville have modern analogs in the southern Florida-Bahamas region—a worldclass natural laboratory to study “tropical” carbonate depositional systems. This region represents a time horizon where one can observe carbonate deposition, the conditions (physical, biological, and chemical) that create various carbonate sediments, and the processes by which the deposits change.

Utah is fortunate that representative outcrop analogs (depositional or diagenetic) for the Leadville Limestone play are present along the southern flank of the Uinta Mountains. Production-scale analogs provide an excellent view, often in 3D, of reservoir-facies characteristics, geometry, distribution, diagenetic characteristics, and nature of boundaries, all of which contribute to the overall heterogeneity of reservoir rocks.

Modern Reservoir Analogs—Southern Florida and the Bahamas

1. The southern Florida-Bahamas region is a warm-water carbonate factory. The Leadville Limestone was most likely deposited in a similar warm-water carbonate factory during Mississippian time on an epeiric-attached platform (i.e., an extensive cratonic area covered by a shallow sea).
2. Although the organisms in warm-water carbonate settings today are different from those of the past due to organic

evolution, the roles of sediment producer and modifier have remained largely unchanged through time. Warm marine water is also often supersaturated with respect to calcium carbonate, which can be precipitated to form carbonate grains such as ooids, peloids, grapestone, and carbonate mud.

3. Southern Florida is an attached, rimmed carbonate platform. From northwest to southeast, the platform consists of mangrove swamps and supratidal flats (Everglades), an inner shelf (Florida Bay), inner and outer shelf margins, and a shallow slope into the Straits of Florida.
4. Florida Bay is triangular shaped due to barriers that restrict circulation. A variety of sedimentary environments are represented in Florida Bay as part of a transgressive record: (1) fresh-water pond, (2) coastal mangrove swamp, (3) broad, shallow bay basins (“lake”), (4) mud mounds, and (5) island. From our work on the Leadville Limestone, we recognize the shallow bay basins and mud mounds.
5. The southern Florida attached platform has a rimmed margin formed by the arcuate reef track band. Sedimentary environments include the seaward foreereef, discontinuous outer barrier reef, and back reef consisting of a sand apron and lagoon (containing patch reefs and sand shoals). There are no barrier reefs known in the Leadville Limestone. However, from our work, we recognize the marine mud mounds, patch reefs, and sand shoals in the reef tract.
6. The Great Bahama Bank is an unattached, isolated, rimmed carbonate platform. From east to west, the Great Bahama Bank consists of Earth’s third longest barrier reef, a narrow lagoon, Andros Island (exposed Pleistocene limestone) with modern carbonate tidal flats on the western side, the shelf lagoon, and ooid shoals. The carbonate tidal flats are laterally extensive along strike and represent part of a shallowing upward cycle. From our work on the Leadville Limestone, we recognize ooid shoals and shelf lagoonal sedimentation. Paleocarbonate tidal flats are productive in other carbonate reservoirs. Recognizing the modern characteristics of carbonate tidal flats in the Leadville Limestone may provide additional target areas for drilling.

Outcrop Reservoir Analogs—Southern Flank of the Uinta Mountains, Utah

1. Although not exposed in southeastern Utah, Mississippian rocks equivalent to the Leadville Limestone outcrop along the southern flank of the Uinta Mountains. These formations include the Madison, Gardison, Deseret, and Humbug Formations, and have similar characteristics as the Leadville.
2. The Madison and equivalent formations were deposited in a shallow, warm-water, relatively high-energy, epeiric sea

that extensively covered a large part of the North American craton. Depositional environments include tidal-flat mud; deeper subtidal burrowed pellet muds; shallow subtidal bay; beach/foreshore; ooid shoal; storm-dominated, outer-shelf, crinoid shoals; low-energy, open-marine, mud-rich intershoal; and low-energy, open-marine, outer shelf above storm wave base. All depositional environments in the Madison and Deseret Limestones of the Uinta Mountains are also observed in Leadville cores from Lisbon field.

3. The Deseret and Madison Limestones contain local zones of breccia due to either collapse or natural hydrofracturing. Breccia associated with sediment-filled collapsed cavities is common. These cavities are related to paleokarstification of the Deseret/Madison when subaerially exposed during Late Mississippian time. Brecciation caused by explosive natural hydrofracturing created the similar shattered-looking, pulverized rock identified in Lisbon cores. Breccia pipes may be related to past hydrothermal activity.
4. The basal Cambrian Tintic Quartzite and Lodore Formation were important contributors to the hydrothermal story. They served as aquifers supplying hot water to the hydrothermal system. Through the central part of the southern flank of the Uinta Mountains, porous Cambrian sandstone units are absent, with Mississippian strata lying unconformably on middle Neoproterozoic Red Pine Shale. No Mississippian hydrothermal breccia zones or pipes are found in the central part of the southern flank lending credence to the concept that aquifers below in the Tintic and Lodore may be a required condition for past hydrothermal activity to have occurred. Thus, targeting Leadville Limestone areas for potential hydrothermal dolomite and enhanced reservoir quality due to hydrofracturing may require an aquifer below (i.e., the Devonian McCracken Sandstone) as a necessary ingredient.

ACKNOWLEDGMENTS

Funding for this research was provided as part of the Advanced and Key Oilfield Technologies for Independents (Area 2 – Exploration) Program of the U.S. Department of Energy, National Energy Technology Laboratory, Tulsa, Oklahoma, contract number DE-FC26-03NT15424. Support was also provided by the Utah Geological Survey (UGS), Salt Lake City, Utah; Eby Petrography & Consulting, Inc., Denver, Colorado; ST Oil Company, Denver, Colorado; and the Utah School and Institutional Trust Lands Administration, Salt Lake City, Utah.

Cores and petrophysical data from Lisbon field were provided by Tom Brown, Inc., Denver, Colorado. Additional Leadville cores from the Paradox Basin were donated by the Oklahoma Geological Survey (Gene Kuhlman, Curator, Oklahoma Petroleum Information Center), Norman, Oklahoma.

The compiler/editor was graciously invited to attend the Brigham Young University (BYU) Department of Geological Sciences field course, “Carbonate Geology of Southern Florida and the Bahamas,” April 25–May 4, 2008, instructed by Drs. Scott M. Ritter and Thomas H. Morris. Most of the chapter on modern carbonate analogs was generated from observations made during the field course, lecture notes, and materials provided generously by Drs. Ritter and Morris. Their assistance was invaluable.

Figures were prepared by the following staff of the UGS at the time of the study: Cheryl Gustin, Vicky Clarke, Stevie Emerson, Sharon Hamre, Kevin McClure, James Parker, and Liz Paton. Thomas Dempster, Carolyn Olsen, Michael D. Laine, Brad Wolverton, and Ammon McDonald of the UGS at the time of the study, photographed core, compiled and prepared maps, and collected well cuttings from the Utah Core Research Center. Geographic Information Systems support was provided by Sharon Wakefield and Sonja Heuscher of the UGS at the time of the study.

This study, or parts of it, was reviewed by David E. Tabet, Robert Ressetar, Bryce T. Tripp, Kimm Harty, Richard G. Allis, Michael D. Vanden Berg, Stephanie Carney, Michael Hylland, and Bill Keach of the UGS; and Virginia Weyland, National Energy Technology Laboratory, U.S. Department of Energy, Tulsa, Oklahoma. Their careful reviews and constructive criticism greatly improved the manuscript. Finally, Jen Miller, John Good, and the UGS editorial production team are thanked for producing a very high-quality publication.

REFERENCES

- Ahr, W.M., 1989, Mississippian reef facies in the Southwest—a spectrum of variations in depositional style and reservoir characteristics: Ft. Worth Geological Society and Texas Christian University, Symposium on the Petroleum Geology of Mississippian Carbonates in North Central Texas, p. 1–19.
- Ake, J., Mahrer, K., O’Connell, D., and Block, L., 2005, Deep-injection and closely monitored induced seismicity at Paradox Valley, Colorado: Bulletin of the Seismological Society of America, v. 95, no. 2, p. 664–683.
- Al-Aasm, I.S., and White, T., 1995, Mississippian hydrothermal dolomitization of the upper Debolt Formation, Sikanni gas field, northeastern British Columbia [abs.]: Geological Association of Canada, Mineralogical Association of Canada, and Canadian Geophysical Union Joint Meeting, Program with Abstracts, v. 20, p. 1.
- Allan, J.R., and Wiggins, W.D., 1993, Dolomite reservoirs—geochemical techniques for evaluating origin and distribution: American Association of Petroleum Geologists, Continuing Education Course Note Series 36, 129 p.

- Allis, R.G., Bergfield, D., Moore, J.N., McClure, K., Morgan, C., Chidsey, T.C., Jr., Heath, J., and McPherson, B., 2005, Implications of results from CO₂ systems for long-term monitoring: Proceedings Volume, Fourth Annual Conference on Carbon Capture and Sequestration, May 2–5, 2005, Alexandria, VA, p. 1367–1388.
- Anderson, J.H., 1985, Depositional facies and carbonate diagenesis of the downslope reefs in the Nisku Formation (Upper Devonian) central Alberta, Canada: Austin, University of Texas, Ph.D. dissertation, 393 p.
- Anderson, J.H., and Machel, H.G., 1988, The Upper Devonian Niski reef trend in central Alberta, in Geldsetzer, H.H.J., James, N.P., and Tebbutt, G.E., editors, Reefs, Canada and adjacent areas: Canadian Society of Petroleum Geologists Memoir 13, p. 391–398.
- Baars, D.L., 1966, Pre-Pennsylvanian paleotectonics—key to basin evolution and petroleum occurrences in the Paradox Basin, Utah and Colorado: American Association of Petroleum Geologists Bulletin, v. 50, no. 10, p. 2082–2111.
- Baars, D.L., and Stevenson, G.M., 1981, Tectonic evolution of the Paradox Basin, Utah and Colorado, in Wiegand, D.L., editor, Geology of the Paradox Basin: Rocky Mountain Association of Geologists Guidebook, p. 23–31.
- Baer, J.L., and Rigby, J.K., 1978, Geology of the Crystal Geyser and environmental implications of its effluent, Grand County, Utah: Utah Geological and Mineral Survey, Utah Geology, v. 5, no. 2, p. 125–130.
- Ball, M.M., 1967, Carbonate sand bodies of Florida and the Bahamas: Journal of Sedimentary Petrology, v. 37, p. 556–591.
- Bathurst, R.C.G., 1972, Chapter 9—Diagenesis on the sea floor, in Carbonate sediments and their diagenesis: Elsevier, Developments in Sedimentology, v. 12, p. 361–413.
- Barker, C.E., and Kopp, O.C., editors, 1991, Luminescence microscopy—quantitative and qualitative aspects: Society for Sedimentary Geology (SEPM) Short Course 25 Notes, p. 1–7.
- Bebout, D.G., and Loucks, R.G., 1984, Handbook for logging carbonate rocks: Bureau of Economic Geology, University of Texas at Austin, Handbook 5, 43 p.
- Bergman, K.L., Westphal, H., Janson, X., Pioriez, A., and Eberli, G. P., 2010, Controlling parameters on facies geometries of the Bahamas, an isolated carbonate platform environment, in Westphal, H., Riegl, B., and Eberli, G.P., editors, Carbonate depositional systems—assessing dimensions and controlling parameters: Springer Science, p. 5–80.
- Blakey, R., and Ranney, W., 2008, Ancient landscapes of the Colorado Plateau: Grand Canyon, Grand Canyon Association, p. 21–27.
- Bock, W.D., Lynts, G.W., Smith, S., Wright, R., Hay, W.W., and Jones, J.L., 1971, A symposium of Recent South Florida Foraminifera: Miami Geological Society, Memoir 1, 245 p.
- Bodnar, R.J., 1993, Revised equation and table for determining the freezing-point depression of H₂O-NaCl solutions: Geochimica Cosmochimica Acta, v. 57, p. 683–684.
- Bodnar, R.J., 2017, Fluid inclusions, in White, W.M., editor, Encyclopedia of geochemistry—a comprehensive reference source on the geochemistry of the Earth: Springer, Chem Switzerland, Encyclopedia of Earth Science Series, p. 383–391.
- Bosence, D.W.J., 1985, The morphology and ecology of a mound-building coralline alga (*Neogoniolithon strictum*) from the Florida Keys: Paleontology, v. 28, p. 189–206.
- Bosence, D.W.J., 1995, Anatomy of a Recent biodetrital mud-mound, Florida Bay, USA, in Monty, C.L.V., Bosence, D.W.J., Bridges, P.H., and Pratt, B.R., editors, Carbonate mud-mounds—their origin and evolution: International Association of Sedimentologists Special Publication 23, p. 475–493.
- Bosence, D.W.J., and Wilson, R.C.L., 2005, Carbonate depositional systems, in Coe, A.L., editor, The sedimentary record of sea-level change: New York, Cambridge University Press, p. 209–227.
- Brass, G.W., 1976, The variation of the marine ⁸⁷Sr/⁸⁶Sr ratio during Phanerozoic time—interpretation using a flux model: Geochimica et Cosmochimica Acta, v. 40, p. 721–730.
- Bredehoeft, J.D., 1965, The drill-stem test—the petroleum industry's deep-well pumping test: Ground Water, v. 3, p. 31–36.
- Breit, G.N. (compiler), no date, Produced waters database: U.S. Geological Survey: Online, <<http://energy.cr.usgs.gov/prov/prodwat/>>, accessed May 2003.
- Bruckschen, P., Onesmann, S., and Viezer, J., 1999, Isotope stratigraphy of the European Carboniferous—proxy signals for ocean chemistry, climate and tectonics: Chemical Geology, v. 161, p. 127–163.
- Bryant, B., 1990, Geologic map of the Salt City 30' x 60' quadrangle, north-central Utah and Uinta County, Wyoming: U.S. Geological Survey Miscellaneous Investigations Map I-1944, 2 plates, scale 1:100,000.
- Budd, D.A., Hammes, U., and Ward, W.B., 2000, Cathodoluminescence in calcite cements—new insights on Pb and Zn sensitizing, Mn activation, and Fe quenching at low trace-element concentrations: Journal of Sedimentary Petrology, v. 70, p. 217–226.
- Burke, W.H., Denison, R.E., Heatherington, E.A., Koepnick, R.B., Nelson, H.F., and Otto, J.B., 1982, Variation of seawater ⁸⁷Sr/⁸⁶Sr throughout Phanerozoic time: Geology, v. 10, p. 516–519.
- Burne, R.V., and Moore, L.S., 1987, Microbialites; organosedimentary deposits of benthic microbial communities: Palaios, v. 2, p. 241–254.
- Burruss, R.C., 1981, Hydrocarbon fluid inclusions in studies of sedimentary diagenesis, in Hollister, L.S., and Craw-

- ford, M.L., editors, Fluid inclusions—applications in petrology: Mineralogical Association of Canada Short Course Notes, v. 6, p. 138–156.
- Burruss, R.C., 1991, Practical aspects of fluorescent microscopy of petroleum fluid inclusions, *in* Barker, C.E., and Kopp, O.C., editors, Luminescence microscopy—quantitative and qualitative aspects: Society for Sedimentary Geology (SEPM) Short Course 25 Notes, p. 1–7.
- Burruss, R.C., Cercone, K.R., and Harris, P.M., 1986, Timing of hydrocarbon migration—evidenced from fluid inclusions in calcite cements, tectonics and burial history, *in* Schneidermann, Nahum, and Harris, P.M., editors, Carbonate cements: Society for Sedimentary Geology (SEPM) Special Publication 36, p. 277–289.
- Burtner, R.L., 1987, Origin and evolution of Weber and Tensleep Formation waters in the greater Green and Uinta-Piceance Basins, northern Rocky Mountains area, USA: *Chemical Geology*, v. 65, p. 255–282.
- Cander, H.S., Kauffman, J., Daniels, L.D., and Meyers, W.J., 1988, Regional dolomitization in the Burlington-Keokuk Formation (Mississippian), Illinois and Missouri—constraints from cathodoluminescent zonal stratigraphy, *in* Shukla, V., and Baker, P.A., editors, Sedimentology and geochemistry of dolostones: Society for Sedimentary Geology (SEPM) Special Publication No. 43, p. 129–144.
- Carey, M.A., 1973, Chesterian-Morrowan conodont biostratigraphy from northeastern Utah: Salt Lake City, University of Utah, M.S. thesis, 83 p.
- Cather, M.E., Morrow, N.R., Brower, K.R., and Buckley, J.S., 1989a, Uses of epi-fluorescent microscopy in evaluation of Mesaverde tight gas sands [abs.]: *American Association of Petroleum Geologists Bulletin*, v. 73, p. 1150–1151.
- Cather, M.E., Morrow, N.R., and Klich, I., 1989b, Applications of fluorescent dye staining techniques to reservoir studies of tight gas sands, Mesaverde Group, southwestern Colorado [abs.]: *American Association of Petroleum Geologists Bulletin*, v. 73, p. 342.
- Cercone, K.R., and Pedone, V.A., 1987, Fluorescence (photoluminescence) of carbonate rocks—instrumental and analytical sources of observational error: *Journal of Sedimentary Petrology*, v. 57, p. 780–782.
- Chafin, D.T., 2002, Effect of the Paradox Valley Unit on the dissolved-solids load of the Dolores River near Bedrock, Colorado, 1988–2001: U.S. Geological Survey Water-Resources Investigations Report 02-4275, 6 p.
- Chidsey, T.C., Jr., 2018, Characteristics and source rocks of Utah crude oils, *in* Emerman, S.H., Bowen, B., Schamel, S., and Simmons, S., editors, Geofluids of Utah: Utah Geological Association Publication 47, p. 149–177, 1 plate, 26 appendices.
- Chidsey, T.C., Jr., and Eby, D.E., 2016, Chapter 9—Mississippian Leadville Limestone Paradox Basin play, *in* Chidsey, T.C., Jr., editor, Major oil plays in Utah and vicinity: Utah Geological Survey Bulletin 137, p. 145–157, <https://doi.org/10.34191/B-137>.
- Chidsey, T.C., Jr., and Eby, D.E., 2017, Potential oil-prone areas in the Cane Creek shale play, Paradox Basin, Utah, identified by epifluorescence microscope techniques: Utah Geological Survey Special Study 160, 170 p., <https://doi.org/10.34191/SS-160>.
- Chidsey, T.J., Eby, D.E., and Sprinkel, D.A., 2019, A breccia pipe in the Deseret Limestone, south flank of the Uinta Mountains, northern Utah, *in* Milligan, M., Biek, R.F., Inkenbrandt, P., and Nielsen, P., editors, Utah geosites: Utah Geological Association Publication 48, 10 p., <https://doi.org/10.31711/geosites.v1i1.55>.
- Chidsey, T.C., Jr., Eby, D.E., and Sprinkel, D.A., 2020, A tale of two breccia types in the Mississippian Leadville Limestone of Lisbon and other fields, Paradox Basin, southeastern Utah: *Geology of the Intermountain West*, v. 7, p. 243–280, <https://doi.org/10.31711/giw.v7>.
- Chidsey, T.C., Jr., Morgan, C.D., and Eby, D.E., 2016, Chapter 10—Pennsylvanian Paradox Formation Paradox Basin play, *in* Chidsey, T.C., Jr., editor, Major oil plays in Utah and vicinity: Utah Geological Survey Bulletin 137, p. 159–206, <https://doi.org/10.34191/B-137>.
- Choquette, P.W., and Pray, L.C., 1970, Geologic nomenclature and classification of porosity in sedimentary carbonates: *American Association of Petroleum Geologists Bulletin*, v. 54, no. 2, p. 207–250.
- Clark, C.R., 1978, Lisbon, San Juan County, Utah, *in* Fassett, J.E., editor, Oil and gas fields of the Four Corners area: Four Corners Geological Society, v. II, p. 662–665.
- Colorado Oil and Gas Conservation Commission, 2020, Colorado oil and gas information system (COGIS)—production data inquiry: Online, <oil-gas.state.co.us/cogis/ProductionSearch2.asp>, accessed September 2020.
- Coniglio, M., Zheng, Q., and Carter, T.R., 2003, Dolomitization and recrystallization of Middle Silurian reefs and platform carbonates of the Guelph Formation, Michigan Basin, southwestern Ontario: *Bulletin of Canadian Petroleum Geology*, v. 51, p. 177–199.
- Coumou, D., Driesner, T., Heinrich, A., 2008, The structure and dynamics of mid-ocean ridge hydrothermal system: *Science Magazine*, v. 321, p. 1825–1828.
- Dansereau, P., and Bourque, P.A., 2001, The Neigette breccia—remnant of the West Point reef tract in the Matapeia Valley area, and witness to Late Silurian synsedimentary faulting, Gaspé Belt, Northern Appalachians, Quebec: *Bulletin of Canadian Petroleum Geology*, v. 49, p. 327–345.
- Davies, G.R., 2004, Hydrothermal (thermobaric) dolomite and leached limestone reservoirs—general principles, genetic connections, and economic significance in Canada [abs.]: *American Association of Petroleum Geologists Annual Convention, Official Program with Abstracts*, v. 13, p. A32.

- Davies, G.R., and Smith, L.B., Jr., 2006, Structurally controlled hydrothermal alteration of carbonate reservoirs—an overview: *American Association of Petroleum Geologists Bulletin* (Special Issue: Hydrothermally altered carbonate reservoirs), v. 90, no. 11, p. 1641–1690.
- Denison, R.E., Koepnick, R.B., Burke, W.H., Heatherington, E.A., and Fletcher, A., 1994, Construction of the Mississippian, Pennsylvanian and Permian seawater $^{87}\text{Sr}/^{86}\text{Sr}$ curve: *Chemical Geology*, v. 112, p. 145–167.
- DePaolo, D.J., 1986, Detailed record of the Neogene strontium isotopic evolution of seawater from DSDP site 5908: *Geology*, v. 14, p. 103–106.
- DePaolo, D.J., and Finger, K.L., 1991, High-resolution strontium-isotope stratigraphy and biostratigraphy of the Miocene Monterey Formation, central California: *Geological Society of America Bulletin*, v. 103, p. 112–124.
- DePaolo, D.J., and Ingram, B., 1985, High-resolution stratigraphy with strontium isotopes: *Science*, v. 227, p. 938–941.
- Dockal, J.A., 1980, Petrology and sedimentary facies of Redwall Limestone (Mississippian) of Uinta Mountains, Utah and Colorado: Iowa City, Iowa State University, Ph.D. dissertation, 423 p.
- Doelling, H.H., 2010, Geology of Arches National Park, *in* Sprinkel, D.A., Chidsey, T.C., Jr., and Anderson P.B., editors, *Geology of Utah's parks and monuments* (third edition): Utah Geological Association Publication 28, p. 11–36.
- Dorobek, S.L., Read, J.F., Niemann, J.M., Pong, T.C., and Haralick, R.M., 1987, Image analysis of cathodoluminescence-zoned calcite cements: *Journal of Sedimentary Petrology*, v. 57, p. 766–770.
- Dravis, J.J., 1988, Deep-burial microporosity in Upper Jurassic Haynesville oolitic grainstones, East Texas: *Sedimentary Geology*, v. 63, p. 325–341.
- Dravis, J.J., 1991, Carbonate petrography—update on new techniques and applications: *Journal of Sedimentary Petrology*, v. 61, p. 626–628.
- Dravis, J.J., 1992, Burial dissolution in limestones and dolomites—criteria for recognition and discussion of controls—a case study approach (Part 1—Upper Jurassic Haynesville limestones, East Texas; Part 2—Devonian Upper Elk Point dolomites, western Canada): *American Association of Petroleum Geologists Bulletin/Canadian Society of Petroleum Geologists Short Course on Sub-surface Dissolution Porosity in Carbonates*, Calgary, Canada, 171 p.
- Dravis, J.J., and Yurewicz, D.A., 1985, Enhanced carbonate petrography using fluorescence microscopy: *Journal of Sedimentary Petrology*, v. 55, p. 795–804.
- Dunham, R.J., 1962, Classification of carbonate rocks according to depositional texture, *in* Ham, W.E., editor, *Classification of carbonate rocks*: *American Association of Petroleum Geologists Memoir* 1, p. 108–121.
- Eby, D.E., and Hager, R.C., 1986, Fluorescence petrology of San Andres dolomites—H.O. Mahoney lease, Wasson field, Yoakum County, Texas: *Permian Basin Section, Society for Sedimentary Geology (SEPM) Publication* 86–26, p. 37–38.
- Eby, D.E., Chidsey, T.C., Jr., and Sprinkel, D.A., 2014, Marine microbial carbonate facies, fabrics, and petroleum reservoirs in Utah [abs.]: *Geological Society of America Rocky Mountain/Cordilleran Section Abstracts with Program*, v. 46, no. 5, p. 12.
- Eby, D.E., Chidsey, T.C., Jr., Sprinkel, D.A., and Laine, M.D., 2009, A tale of two breccia types in the Mississippian Leadville Limestone, Lisbon field, Paradox Basin, southeastern Utah [abs.]: *American Association of Petroleum Geologists Annual Convention Abstracts*, v. 18, p. 61.
- Elderfield, H., 1986, Strontium isotope stratigraphy, *in* Shackleton, N.J., editor, *Boundaries and events in the Paleogene: Paleogeography, Paleoclimatology, Paleocology*, v. 57, p. 71–90.
- Embry, A.R., and Klován, J.E., 1971, A Late Devonian reef tract on northeastern Banks Island, Northwest Territories: *Canadian Petroleum Geologists Bulletin*, v. 19, p. 730–781.
- Enos, P., 1977, Holocene sediment accumulations of the south Florida shelf margin, *in* Enos, P., and Perkins, R.D., editors, *Quaternary sedimentation of South Florida*: *Geological Society of America Memoir* 147, p. 1–130.
- Enos, P., and Perkins, R.D., 1979, Evolution of Florida Bay from island stratigraphy: *Geological Society of America Bulletin, Part I*, v. 90, p. 59–83.
- Eskelsen, Q.M., 1953, Geology of the Soapstone Basin and vicinity, Wasatch, Summit, and Duchesne Counties, Utah: Salt Lake City, University of Utah, M.S. thesis, 56 p., 2 plates, scale 1:31,680.
- Evans, J.E., and Reed, J.M., 2006, Pennsylvanian fluvial cave sediments in the Mississippian Leadville Limestone, southwestern Colorado, U.S.A.: *The Mountain Geologist*, v. 43, p. 283–297.
- Evans, J.E., and Reed, J.M., 2007, Integrated loessite-paleokarst depositional system, early Pennsylvanian Molas Formation, Paradox Basin, southwestern Colorado, U.S.A.: *Sedimentary Geology*, v. 195, p. 161–181.
- Fairchild, I.J., 1983, Chemical studies of cathodoluminescence of natural dolomites and calcites: *Sedimentology*, v. 30, p. 572–583.
- Faure, G., 1977, *Principles of isotope geology*: New York, John Wiley and Sons, 464 p.
- Faure, G., and Powell, J.L., 1972, *Strontium isotope geology*: Berlin, Springer Verlag, 188 p.
- Filippelli, G.M., and DeLaney, M.L., 1992, Quantifying cathodoluminescent intensity with an on-line camera and exposure meter: *Journal of Sedimentary Petrology*, v. 62, p. 724–725.

- Folk, R.L., 1987, Detection of organic matter in thin sections of carbonate rocks using a white card: *Sedimentary Geology*, v. 54, p. 193–200.
- Fouret, K.L., 1982, Depositional and diagenetic environment of the Mississippian Leadville Formation at Lisbon field, Utah: College Station, Texas A&M University, M.S. thesis, 119 p.
- Fouret, K.L., 1996, Depositional and diagenetic environment of the Mississippian Leadville Limestone at Lisbon field, Utah, in Huffman, A.C., Jr., Lund, W.R., and Godwin, L.H., editors, *Geology and resources of the Paradox Basin*: Utah Geological Association Publication 25, p. 129–138.
- Fourqurean, J.W., and Robblee, M.B., 1999, Florida Bay—a history of recent ecological changes: *Estuaries*, v. 22, p. 345–357.
- Frahme, C.W., and Vaughn, E.B., 1983, Paleozoic geology and seismic stratigraphy of the northern Uncompahgre front, Grand County, Utah, in Lowell, J.D., editor, *Rocky Mountain foreland basins and uplifts*: Rocky Mountain Association of Geologists Guidebook, p. 201–211.
- Frank, J.R., Carpenter, A.B., and Oglesby, T.W., 1982, Cathodoluminescence and composition of calcite cement in Taum Sauk Limestone (Upper Cambrian), southeast Missouri: *Journal of Sedimentary Petrology*, v. 52, p. 631–638.
- Frank, T.D., Lohmann, K.C., and Meyers, W.J., 1996, Chemostratigraphic significance of cathodoluminescence zoning in syntaxial cement—Mississippian Lake Valley Formation, New Mexico: *Sedimentary Geology*, v. 105, p. 29–50.
- Gardner, K.L., 1980, Impregnation technique using colored epoxy to define porosity in petrographic thin sections: *Canadian Journal of Earth Sciences*, v. 17, p. 1104–1107.
- Gerling, C.R., 1983, McElmo Dome Leadville carbon dioxide field, Colorado, in Fassett, J.E., editor, *Oil and gas fields of the Four Corners area*: Four Corners Geological Society, v. III, p. 735–739.
- Gies, R.M., 1987, An improved method for viewing micro-pore systems in rocks with the polarizing microscope: *Society of Petroleum Engineers Formation Evaluation*, v. 2, p. 209–214.
- Ginsburg, R.N., 1956, Environmental relationships of grain size and constituent particles in some south Florida carbonate sediments: *American Association of Petroleum Geologists Bulletin*, v. 40, p. 2384–2427.
- Godfrey, A.E., 1985, Karst hydrology of the south slope of the Uinta Mountains, Utah, in Picard, M.D., editor, *Geology and energy resources, Uinta Basin of Utah*: Utah Geological Association Publication 12, p. 277–293.
- Goldstein, R.H., and Reynolds, T.J., 1994, Systematics of fluid inclusions in diagenetic minerals: *Society for Sedimentary Geology (SEPM) Short Course 31*, 199 p.
- Grammer, M.G., Harris, P.M., and Eberli, G.P., 2001, Carbonate platforms—exploration- and production-scale insight from modern analogs in the Bahamas: *The Leading Edge*, March 2001, p. 252–261.
- Gregg, J.M., and Karakus, M., 1991, A technique for successive cathodoluminescence and reflected light microscopy: *Journal of Sedimentary Petrology*, v. 61, p. 613–635.
- Grummon, M.L., 1993, Exploiting the self-sourced Cane Creek zone of the Paradox Formation with horizontal well bores [abs.]: *American Association of Petroleum Geologists Bulletin*, v. 77, no. 8, p. 1449–1450.
- Guihaumou, N., Szydłowski, N., and Padier, B., 1990, Characterization of hydrocarbon fluid inclusions by infrared and fluorescence microspectrometry: *Mineralogical Magazine*, v. 54, p. 311–324.
- Gwynn, J.W., 1995, Resistivities and chemical analyses of selected oil and gas field, water well, and spring waters, Utah: *Utah Geological Survey Circular 87*, 142 p., <https://doi.org/10.34191/C-87>.
- Hahn, G.A., and Thorson, J.P., 2006, Geology of the Lisbon Valley sandstone-hosted disseminated copper deposits, San Juan County, Utah, in Bon, R.L., Gloyd, R.W., and Park, G.M., editors, *Mining districts of Utah*: Utah Geological Association Publication 32, p. 511–533.
- Hamblin, W.K., and Rigby, J.K., 1968, Guidebook to the Colorado River, part 1—Lee's Ferry to Phantom Ranch in Grand Canyon National Park (Studies for Students No. 4): Provo, Utah, Brigham Young University Geology Studies, v. 15, pt. 5, 84 p.
- Hanshaw, B.B., and Hill, G.A., 1969, Geochemistry and hydrodynamics of the Paradox Basin region, Utah, Colorado, and New Mexico, in Angino, E.E., and Billings, G.K., editors, *Geochemistry of subsurface brines*: *Chemical Geology*, v. 4, no. 1/2, p. 263–294.
- Hardie, L.A. and Shinn, E.A., 1986, Carbonate Depositional Environments, part 3—tidal flats: *Colorado School of Mines Quarterly*, v. 81, p. 1–74.
- Harr, C.L., 1996, Paradox oil and gas potential of the Ute Mountain Ute Indian Reservation, in Huffman, A.C., Jr., Lund, W.R., and Godwin, L.H., editors, *Geology and resources of the Paradox Basin*: Utah Geological Association Publication 25, p. 13–28.
- Harris, P.M., Purkis, S.J., Ellis, J., and Swart, P.K., 2015, Mapping bathymetry and depositional facies on Great Bahama Bank: *Sedimentology*, v. 62, p. 566–589.
- Harry, D.L., and Mickus, K.L., 1998, Gravity constraints on lithospheric flexure and the structure of the late Paleozoic Ouachita orogen in Arkansas and Oklahoma, south-central North America: *Tectonics*, v. 17, no. 2, p. 187–202.
- Heath, J.E., 2004, Hydrogeochemical characterization of leaking carbon dioxide-charged fault zones in east-central Utah: Logan, Utah State University, M.S. thesis, 175 p.

- Hemming, N.G., Meyers, W.J., and Grams, J.C., 1989, Cathodoluminescence in diagenetic calcites—the roles of Fe and Mn as deduced from electron probe and spectrophotometric measurements: *Journal of Sedimentary Petrology*, v. 59, p. 404–411.
- Hintze, L.F., and Kowallis, B.J., 2009, Geologic history of Utah: Provo, Utah, Brigham Young University Geology Studies Special Publication 9, 225 p.
- Hintze, L.F., Willis, G.C., Laes, D.Y.M., Sprinkel, D.A., and Brown, K.D., 2000, Digital geologic map of Utah: Utah Geological Survey Map 179DM, scale 1:500,000, <https://doi.org/10.34191/M-179dm>.
- Hite, R.J., Anders, D.E., and Ging, T.G., 1984, Organic-rich source rocks of Pennsylvanian age in the Paradox Basin of Utah and Colorado, in Woodward, J., Meissner, F.F., and Clayton, J.L., editors, Hydrocarbon source rocks of the greater Rocky Mountain region: Rocky Mountain Association of Geologists Guidebook, p. 255–274.
- Howells, L., 1990, Base of moderately saline ground water in San Juan County, Utah: Utah Department of Natural Resources Technical Publication 94, 35 p.
- Huntoon, P.W., 1979, The occurrence of ground water in the Canyonlands area of Utah, with emphasis on water in the Permian section, in Baars, D.L., editor, Permianland: Four Corners Geological Society Guidebook, 9th Annual Field Conference, p. 39–46.
- James, N.P., 1979, Chapter 11—Reefs, in Walker, R.G., editor, Facies models: Geoscience, Canada Reprint Series 1, p. 121–132.
- James, N.P., and Ginsburg, R.N., 1979, The seaward margin of Belize barrier and atoll reefs: International Association of Sedimentologists Special Publication 3, 191 p.
- Johnson, C.F., 1970, Top of structure of the Leadville Limestone, Lisbon field: unpublished map, Union Oil Company of California files.
- Kinney, D.M., 1955, Geology of the Uinta River-Brush Creek area, Duchesne and Uintah Counties, Utah: U.S. Geological Survey Bulletin 1007, 185 p.
- Kirkby, K.C., and Tinker, S.W., 1992, The Keg River/Winnipegosis petroleum system in northeast Alberta [abs.]: American Association of Petroleum Geologists Annual Convention, Official Program with Abstracts, v. 1, p. A66.
- Kirby, S., 2008, Geologic and hydrologic characterization of the Dakota-Burro Canyon aquifer near Blanding, San Juan County, Utah: Utah Geological Survey Special Study 123, 53 p., <https://doi.org/10.34191/SS-123>.
- Kitcho, C.H., 1981, Characteristics of surface faults in the Paradox Basin, in Wiegand, D.L., editor, Geology of the Paradox Basin: Rocky Mountain Association of Geologists Guidebook, p. 1–21.
- Kluth, C.F., 1986, Plate tectonics of the Ancestral Rocky Mountains, in Peterson, J.A., editor, Paleotectonics and sedimentation in the Rocky Mountain region, United States: American Association of Petroleum Geologists Memoir 41, p. 353–369.
- Kluth, C.F., and Coney, P.J., 1981, Plate tectonics of the Ancestral Rocky Mountains: *Geology*, v. 9, p. 10–15.
- LaFlamme, A.K., 1992, Replacement dolomitization in the Upper Devonian Leduc and Swan Hills Formations, Caroline area, Alberta, Canada [abs.]: American Association of Petroleum Geologists Annual Convention, Official Program with Abstracts, v. 1, p. A70.
- Land, L.S., 1980, The isotopic and trace element geochemistry of dolomite—the state of the art, in Zenger, D.H., Dunham, J.B., and Ethington, R.L., editors, Concepts and models of dolomitization: Society for Sedimentary Geology (SEPM) Special Publication 28, p. 87–110.
- LaVoie, D., Chi G., and Fowler, M.G., 2001, The Lower Devonian Upper Gaspe Limestones in eastern Gaspe—carbonate diagenesis and reservoir potential: *Bulletin of Canadian Petroleum Geology*, v. 49, p. 346–365.
- LaVoie, D., and Morin, C., 2004, Hydrothermal dolomitization in the Lower Silurian Sayabee Formation in northern Gaspe–Matapedia (Quebec)—constraint on timing of porosity and regional significance for hydrothermal reservoirs: *Bulletin of Canadian Petroleum Geology*, v. 52, p. 256–269.
- Lees, A., and Miller, J., 1995, Waulsortian banks, in Monty, C.L.V., Bosence, D.W.J., Bridges, P.H., and Pratt, B.R., editors, Carbonate mud-mounds—their origin and evolution: International Association of Sedimentologists Special Publication No. 23, p. 191–271.
- Lewis, R.Q., Sr., and Campbell, R.H., 1965, Geology and uranium deposits of Elk Ridge and vicinity, San Juan County, Utah: U.S. Geological Survey Professional Paper 474-B, 69 p., 2 plates, scale 1:62,500.
- Lidz, B.H., Hine, A.C., Shinn, E.A., and Kindinger, J.L., 1991, Multiple outer-reef tracts along the south Florida bank margin—outlier reefs, a new windward-margin model: *Geology*, v. 19, p. 115–118.
- Lidz, B.H., and Shinn, E.A., 1991, Paleoshorelines, reefs, and a rising sea, South Florida, USA: *Journal of Coastal Research*, v. 7, p. 203–229.
- MacDonald, R.W., and Davies, G.R., 1997, Revised Livingstone/Turner Valley to Mount Head stratigraphy; Mississippian of southwestern Alberta Foothills: Canadian Society of Petroleum Geologists/Society for Sedimentary Geology (SEPM) Convention Publication, p. 169–199.
- Machel, H.G., 2000, Application of cathodoluminescence to carbonate diagenesis, in Pagel, M., Barbin, V., Blanc, P., and Ohnenstetter, D., editors, Cathodoluminescence in geosciences: New York, Springer, p. 271–301.
- Machel, H.G., and Burton, E.A., 1991, Factors governing cathodoluminescence in calcite and dolomites and their implications for studies of carbonate diagenesis, in Barker, C.E.,

- and Kopp, O.C., editors, Luminescence microscopy—quantitative and qualitative aspects: Society for Sedimentary Geology (SEPM) Short Course 25 Notes, p. 37–57.
- Marshall, D.J., 1988, Cathodoluminescence of geological materials: Winchester, Massachusetts, Allen and Unwin, 128 p.
- Marshall, D.J., 1991, Combined cathodoluminescence and energy dispersive spectroscopy, *in* Barker, C.E., and Kopp, O.C., editors, Luminescence microscopy—quantitative and qualitative aspects: Society for Sedimentary Geology (SEPM) Short Course 25 Notes, p. 27–36.
- Mayo, A.L., Herron, D., Nelson, S.T., Tingey, D.G., and Tranel, M.J., 2010, Geology and hydrology of Timpanogos Cave National Monument, Utah, *in* Sprinkel, D.A., Chidsey, T.C., Jr., and Anderson, P.B., editors, Geology of Utah's parks and monuments: Utah Geological Association Publication 28 (third edition), p. 269–283.
- McArthur, J.M., and Howard, R.J., 2004, Strontium isotope stratigraphy, *in* Gradstein, F.M., Ogg, J.G., and Smith, A.G., editors, A geologic time scale 2004: Cambridge, Massachusetts, Cambridge University Press, p. 96–105.
- McDougald, W.D., 1953, Geology of Beaver Creek and adjacent areas, Utah: Salt Lake City, University of Utah, M.S. thesis, 54 p., 2 separate plates, scale 1:31,680.
- McKee, E.D., 1969, Paleozoic rocks of the Grand Canyon, *in* Baars, D.L., editor, Geology and natural history of the Grand Canyon region: Four Corners Geological Society, 5th Field Conference, Powell Centennial River Expedition, p. 78–90.
- Meyers, W.J., 1974, Carbonate cement stratigraphy of the Lake Valley Formation (Mississippian), Sacramento Mountains, New Mexico: Journal of Sedimentary Petrology, v. 44, p. 837–861.
- Meyers, W.J., 1978, Carbonate cements—their regional distribution and interpretation in Mississippian limestones of southwestern New Mexico: Sedimentology, v. 25, p. 371–400.
- Meyers, W.J., 1991, Cement stratigraphy—an overview, *in* Barker, C.E., and Kopp, O.C., editors, Luminescence microscopy—quantitative and qualitative aspects: Society for Sedimentary Geology (SEPM) Short Course 25 Notes, p. 133–148.
- Michel, J., Laugie, M., Pohl, A., Lanteaume, C., Masse, J-P., Donnadieu, Y., and Borgomano, J., 2019, Marine carbonate factories—a global model of carbonate platform distribution: International Journal of Earth Sciences, v. 108, p. 1773–1779.
- Miller, J., 1988, Cathodoluminescence microscopy, *in* Tucker, M., editor, Techniques in sedimentology: Oxford, Blackwell Publications, p. 174–190.
- Milliman, J.D., Freile, D., Steinen R.P., and Wilber, R.J., 1993, Great Bahama Bank aragonitic muds—mostly inorganically precipitated, mostly exported: Journal of Sedimentary Petrology, v. 63, p. 589–595.
- Missimer, T.M., 1984, The geology of south Florida—a summary, *in* Gleason, P.J., editor, Environments of South Florida, Present and Past; II: Miami Geological Society, p. 385–404.
- Mitchell, J.G., 1961, A detailed lithologic zonation of the Mississippian at Northwest Lisbon field, San Juan County, Utah, *in* Symposium on lower and middle Paleozoic rocks of Colorado: Rocky Mountain association of Geologists, 12th Field Conference, p. 175–184.
- Moore, C.H., and Wade, W.J., 2013, Chapter 6—Marine diagenetic environment, *in* Carbonate reservoirs—porosity and diagenesis in a sequence stratigraphic framework: Developments in Sedimentology, v. 67, p. 93–131.
- Morgan, C.D., 1993, Mississippian Leadville Limestone, *in* Hjellming, C.A., editor, Atlas of major Rocky Mountain gas reservoirs: New Mexico Bureau of Mines and Mineral Resources, p. 94.
- Morgan, C.D., Carney, S.M., Nielsen, P.J., Vanden Berg, M.D., and Wood, R.E., 2014, Play analysis of the Cane Creek shale, Pennsylvanian Paradox Formation, Paradox Basin, southeast Utah [abs.]: American Association of Petroleum Geologists, Rocky Mountain Section Meeting Official Program with Abstracts, p. 36.
- Morrow, D.W., Cumming, G.L., and Aulstead, K.L., 1990, The gas-bearing Devonian Manetoe facies, Yukon and Northwest Territories: Geological Survey of Canada Bulletin, v. 400, 40 p.
- Multer, H.G., 1977, Field guide to some carbonate rock environments, Florida Keys and western Bahamas: Dubuque, Iowa, Kendell Hunt Publication Co., 415 p.
- Nelson, P.H., 2002, Subsurface fluid pressures from drill-stem test, Uinta Basin, Utah: The Mountain Geologist, v. 39, no. 1, p. 17–26.
- Neumann, A.C., and Land, L.S., 1975, Lime mud deposition and calcareous algae in the Bight of Abaco, Bahamas—a budget: Journal of Sedimentary Petrology, v. 45, p. 763–786.
- Newell, N.D., Imbrie, J., Purdy, E.G., and Thurber, D.L., 1959, Organism communities and bottom facies, Great Bahama Bank: American Museum of Natural History Bulletin, v. 117, p. 183–228.
- Nuccio, V.F., and Condon, S.M., 1996, Burial and thermal history of the Paradox Basin, Utah and Colorado, and petroleum potential of the Middle Pennsylvanian Paradox Formation, *in* Huffman, A.C., Jr., Lund, W.R., and Godwin, L.H., editors, Geology and resources of the Paradox Basin: Utah Geological Association Publication 25, p. 57–76.
- Packard, J.J., Pellegrin, G.J., Al-Aasm, I.S., Samsson, I.M., and Gagnon, J., 1990, Diagenesis and dolomitization associated with hydrothermal karst in Famennian upper Wabamun ramp sediments, northwestern Alberta, *in* Bloy, G.R., and Hadley, M.G., editors, The

- development of porosity in carbonate reservoirs: Canadian Society of Petroleum Geologists Short Course Notes, p. 9.1–9.27.
- Parker, J.W., and Roberts, J.W., 1963, Devonian and Mississippian stratigraphy of the central part of the Colorado Plateau, *in* Bass, R.O., editor, Shelf carbonates of the Paradox Basin: Four Corners Geological Society, 4th Field Conference Guidebook, p. 31–60.
- Pederson, J.L., Cragun, W.S., Hidy, A.J., Rittenour, T.M., and Grosse, J.C., 2013, Colorado River chronostratigraphy at Lee's Ferry, Arizona, and the Colorado Plateau bull's-eye of incision: *Geology*, v. 41, no. 4, p. 427–430.
- Peterson, J.A., 1992, Aneth field—U.S.A., Paradox Basin, Utah, *in* Foster, N.H., and Beaumont, E.A., editors, Stratigraphic traps III: American Association of Petroleum Geologists Treatise of Petroleum Geology and Atlas of Oil and Gas Fields, p. 41–82.
- Petroleum Information, 1984, Paradox Basin—unravelling the mystery: *Petroleum Frontiers*, v. 1, no. 4, p. 22.
- PI/Dwights Plus, 2008, IHS Energy/Welldata, v. 18, issue 5.
- Pomar, L., and Hallock, P., 2008, Carbonate factories—a conundrum in sedimentary geology: *Earth-Science Reviews*, v. 87, p. 134–169.
- Purdy, E.G., 1963, Recent calcium carbonate facies of the Great Bahama Bank: *Journal of Geology*, v. 72, p. 334–355; 479–497.
- Qing, H., and Mountjoy, E.W., 1994, Origin of dissolution vugs, caverns, and breccias in the Middle Devonian Presqu'ile barrier, host of Pine Point Mississippi Valley-type deposits: *Economic Geology*, v. 89, no. 4, p. 858–876.
- Radke, B.M., and Mathis, R.L., 1980, On the formation and occurrence of saddle dolomite: *Journal of Sedimentary Petrology*, v. 50, p. 1149–1168.
- Rankey, E.C., 2002, Spatial patterns of sediment accumulation on a Holocene carbonate tidal flat, northwest Andros Island, Bahamas: *Journal of Sedimentary Research*, v. 72, p. 591–601.
- Rankey, E.C., Enos, S., Steffen, K., and Druke, D., 2004, Lack of impact of Hurricane Michelle on tidal flats, Andros Island, Bahamas—integrated remote sensing and field observations: *Journal of Sedimentary Research*, v. 74, p. 654–661.
- Rankey, E.C., and Morgan, J., 2002, Quantified rates of geomorphic change on a modern carbonate tidal flat, Bahamas: *Geology*, v. 30, no. 7, p. 583–586.
- Reid, R.P., and Browne, K.M., 1991, Intertidal stromatolites in a fringing Holocene reef complex, Bahamas: *Geology*, v. 19, p. 15–18.
- Roehl, P.O., 1967, Stony Mountain (Ordovician) and Interlake (Silurian) facies analogs of recent low-energy marine and subaerial carbonates, Bahamas: *American Association of Petroleum Geologists Bulletin*, v. 51, no. 10, p. 1979–2032.
- Rost, F.W.D., 1992, *Fluorescence microscopy*, v. 1: New York, Cambridge University Press, 253 p.
- Roylance, M.H., 1990, Depositional and diagenetic history of a Pennsylvanian algal-mound complex—Bug and Papoose Canyon fields, Utah and Colorado: *American Association of Petroleum Geologists Bulletin*, v. 74, p. 1087–1099.
- Sadlick, W., 1955, The Mississippian-Pennsylvanian boundary in northeastern Utah: Salt Lake City, University of Utah, M.S. thesis, 77 p.
- Sadlick, W., 1957, Regional relations of Carboniferous rocks of northeastern Utah, *in* Seal, O.G., editor, Guidebook to the geology of the Uinta Basin: Intermountain Association of Petroleum Geologists 8th Annual Field Conference, p. 57–77.
- Sandberg, C.A., and Gutschick, R.C., 1980, Sedimentation and biostratigraphy of Osagean and Meramecian starved basin and foreslope of the western United States, *in* Fouch, T.D., and Magathan, E.R., editors, Paleozoic paleogeography of the west-central United States-Rocky Mountain symposium I: Rocky Mountain Section, Society of Economic Paleontologist and Mineralogists (Society for Sedimentary Geology), p. 129–147.
- Schlager, W., 1992, Sedimentology and sequence stratigraphy of reefs and carbonate platforms: American Association of Petroleum Geologists Continuing Education Course Note Series no. 34, 71 p.
- Schlager, W., 2003, Benthic carbonate factories of the Phanerozoic: *International Journal of Earth Sciences*, v. 92, p. 445–464.
- Schlager, W., 2005, Carbonate sedimentology and sequence stratigraphy: SEPM (Society for Sedimentary Geology), *Concepts in Sedimentology and Paleontology*, v. 8, 200 p.
- Scholle, P.A., and Ulmer-Scholle, D.S., 2003, A color guide to the petrography of carbonate rocks: American Association of Petroleum Geologists Bulletin Memoir 77, p. 427–440.
- Schultz, J.L., Boles, J.R., and Tilton, G.R., 1989, Tracking calcium in the San Joaquin Basin, California—a strontium isotope study of carbonate cements at North Coles Levee: *Geochimica et Cosmochimica Acta*, v. 53, p. 1991–1999.
- Seneshen, D.M., Chidsey, T.C., Jr., Morgan, C.D., and Vanden Berg, M.D., 2009, New techniques for new discoveries—results from the Lisbon field area, Paradox Basin, Utah, *in* Houston, W.S., Wray, L.L., and Moreland, P.G., editors, The Paradox Basin revisited—new developments in petroleum systems and basin analysis: Rocky Mountain Association of Geologists Special Publication, p. 604–633.
- Seneshen, D.M., Chidsey, T.C., Jr., Morgan, C.D., and Vanden Berg, M.D., 2010, New techniques for new hydrocarbon discoveries—surface geochemical surveys in the Lisbon and Lightning Draw Southeast field areas, San

- Juan County, Utah: Utah Geological Survey Miscellaneous Publication 10-2, 62 p., <https://doi.org/10.34191/MP-10-2>.
- Shinn, E.A., 1968, Burrowing in recent lime sediments of Florida and the Bahamas: *Journal of Paleontology*, v. 42, p. 879–894.
- Shinn, E.A., 1988, The geology of the Florida Keys: *Oceanus*, v. 31, no. 1, p. 46–53.
- Shinn, E.A., and Lloyd, R.M., 1969, Anatomy of a modern carbonate tidal-flat, Andros Island, Bahamas: *Journal of Sedimentary Petrology*, v. 39, no. 3, p. 1202–1228.
- Shipton, Z.K., Evans, J.P., Kirschner, D., Kolesar, P.T., Williams, A.P., and Heath, J., 2004, Analysis of CO₂ leakage through ‘low permeability’ faults from natural reservoirs in the Colorado Plateau, east-central Utah, *in* Baines, S.J., and Worden, R.H., editors, *Geological storage of carbon dioxide*: London, Geological Society Special Publication 233, p. 43–58.
- Sipple, R.F., and Glover, E.D., 1965, Structures in carbonate rocks made visible by luminescence petrography: *Science*, v. 150, p. 1283–1287.
- Smith, K.T., 1978, Big Flat, Grand County, Utah, *in* Fassett, J.E., Thomaidis, N.D., Matheny, M.L., and Ullrich, R.A., editors, *Oil and gas fields of the Four Corners area: Four Corners Geological Society*, v. II, p. 596–598.
- Smith, K.T., and Prather, O.E., 1981, Lisbon field—lessons in exploration, *in* Wiegand, D.L., editor, *Geology of the Paradox Basin: Rocky Mountain Association of Geologists Guidebook*, p. 55–59.
- Smith, L.B., Jr., 2004, Hydrothermal alteration of carbonate reservoirs—how common is it? [abs.]: American Association of Petroleum Geologists Annual Convention, Official Program with Abstracts, v. 13, p. A130.
- Smith, L.B., Jr., 2006, Origin and reservoir characteristics of Upper Ordovician Trenton—Black River hydrothermal dolomite reservoirs in New York: *American Association of Petroleum Geologists Bulletin (Special Issue: Hydrothermally altered carbonate reservoirs)*, v. 90, no. 11, p. 1691–1718.
- Smith, L.B., Jr., and Davies, G.R., 2006, Structurally controlled hydrothermal alteration of carbonate reservoirs—introduction: *American Association of Petroleum Geologists Bulletin (Special Issue: Hydrothermally Altered Carbonate Reservoirs)*, v. 90, no. 11, p. 1635–1640.
- Smouse, DeForrest, 1993, Lisbon, *in* Hill, B.G., and Bereskin, S.R., editors, *Oil and gas fields of Utah: Utah Geological Association Publication 22*, non-paginated.
- Soeder, D.J., 1990, Applications of fluorescent microscopy to study of pores in tight rocks: *American Association of Petroleum Geologists Bulletin*, v. 74, p. 30–40.
- Spangler, L.E., 2005, Geology and karst hydrology of the eastern Uinta Mountains—an overview, *in* Dehler, C.M., Pederson, J.L., Sprinkel, D.A., and Kowallis, B.J., editors, *Uinta Mountain Geology: Utah Geological Association Publication 33*, p. 201–214.
- Spangler, L.E., Naftz, D.L., and Peterman, Z.E., 1996, Hydrology, chemical quality, and characterization of salinity in the Navajo aquifer and near the Greater Aneth oil field, San Juan County, Utah: U.S. Geological Survey Water-Resources Investigations Report 96-4155, 90 p.
- Sprinkel, D.A., 2006, Interim geologic map of the Dutch John 30' x 60' quadrangle, Daggett and Uintah Counties, Utah, Moffat County, Colorado, and Sweetwater County, Wyoming: Utah Geological Survey Open-File Report 491DM, compact disc, GIS data, 3 plates, scale 1:100,000, <https://doi.org/10.34191/OFR-491dm>.
- Sprinkel, D.A., 2007, Interim geologic map of the Vernal 30' x 60' quadrangle, Uintah and Duchesne Counties, Utah, Moffat and Rio Blanco Counties, Colorado: Utah Geological Survey Open-File Report 506DM, compact disc, GIS data, 3 plates, scale 1:100,000, <https://doi.org/10.34191/OFR-506dm>.
- Sprinkel, D.A., 2018, Interim geologic map of the Duchesne 30' x 60' quadrangle, Duchesne and Wasatch Counties, Utah: Utah Geological Survey Open-File Report 689, 37 p., 2 plates, scale 1:62,500, <https://doi.org/10.34191/OFR-689>.
- Stevenson, G.M., and Baars, D.L., 1986, The Paradox—a pull-apart basin of Pennsylvanian age, *in* Peterson, J.A., editor, *Paleotectonics and sedimentation in the Rocky Mountain region, United States: American Association of Petroleum Geologists Memoir 41*, p. 513–539.
- Stevenson, G.M., and Baars, D.L., 1987, The Paradox—a pull-apart basin of Pennsylvanian age, *in* Campbell, J.A., editor, *Geology of Cataract Canyon and vicinity: Four Corners Geological Society, 10th Field Conference*, p. 31–55.
- Stockman, K.W., Ginsburg, R.N., and Shinn, E.A., 1967, The production of lime mud by algae in south Florida: *Journal of Sedimentary Petrology*, v. 37, no. 2, p. 633–648.
- Stowe, Carlton, 1972, Oil and gas production in Utah to 1970: *Utah Geological and Mineral Survey Bulletin 94*, p. 41, <https://doi.org/10.34191/B-94>.
- Teichmuller, M., and Wolf, M., 1977, Application of fluorescence microscopy in coal petrology and oil exploration: *Journal of Microscopy*, v. 109, p. 49–73.
- Tremain, C.M., 1993, Low-BTU gas in Colorado, *in* Hjellming, C.A., editor, *Atlas of major Rocky Mountain gas reservoirs: New Mexico Bureau of Mines and Mineral Resources*, p. 172.
- Trudgill, B.D., and Paz, M., 2009, Restoration of mountain front and salt structures in the northern Paradox Basin, SE Utah, *in* Houston, W.S., Wray, L.L., and Moreland, P.G., editors, *The Paradox Basin revisited—new developments in petroleum systems and basin analysis: Rocky Mountain Association of Geologists Special Publication*, p. 132–177.

- Turmel, R.J., and Swanson, R.G., 1976, The development of Rodriguez Bank, a Holocene mudbank in the Florida reef tract: *Journal of Sedimentary Petrology*, v. 46, no. 3, p. 497–518.
- Utah Division of Oil, Gas and Mining, 2020, Oil and gas production report by field, June 2020: Online, <https://oilgas.ogm.utah.gov/oilgasweb/publications/monthly-rpts-by-fld.xhtml?rptType=FLD>, accessed September 2020.
- van Gijzel, P., 1967, Palynology and fluorescence microscopy: *Reviews of Paleobotany and Palynology*, v. 1, p. 49–79.
- Veizer, J., 1989, Strontium isotopes in seawater through time: *Earth and Planetary Scientific Letters*, v. 17, p. 141–167.
- Veizer, J., Ala, D., Azmy, K., Bruckschen, P., Buhl, D., Bruhn, F., Carden, G.A.F., Diener, A., Ebner, S., Godderis, Y., Jasper, T., Korte, C., Pawellek, F., Podlaha, O.G., and Strauss, H., 1999, $^{87}\text{Sr}/^{86}\text{Sr}$, $\delta^{13}\text{C}$ and $\delta^{18}\text{O}$ evolution of Phanerozoic seawater: *Chemical Geology*, v. 161, no. 1-3, p. 59–88.
- Walker, G., and Burley, S., 1991, Luminescence petrography and spectroscopic studies of diagenetic minerals, *in* Barker, C.E., and Kopp, O.C., editors, Luminescence microscopy—quantitative and qualitative aspects: Society for Sedimentary Geology (SEPM) Short Course 25 Notes, p. 83–96.
- Welsh, J.E., and Bissell, H.J., 1979, The Mississippian and Pennsylvanian (Carboniferous) Systems in the United States—Utah: U.S. Geological Survey Professional Paper 1110-Y, 35 p.
- White, W.B., 1979, Karst landforms in the Wasatch and Uinta Mountains, Utah: *National Speleological Society Bulletin* 41, p. 80–88.
- Wilson, J.L., 1975, Carbonate facies in geologic history: New York, Springer-Verlag, 471 p.
- Wood, W.W., Sanford, W.E., and Al Habshi, A.R.S., 2002, Source of solutes to the coastal sabkha of Abu Dhabi: *Geological Society of America Bulletin*, v. 114, no. 3, p. 259–268.
- Yanatieva, O.K., 1946, Polythermal solubilities in the systems $\text{CaCl}_2\text{-MgCl}_2\text{-H}_2\text{O}$ and $\text{CaCl}_2\text{-NaCl-H}_2\text{O}$: *Zhurnal Prikladnoy Khimii*, v. 19, p. 709–722.
- Yanguas, J.E., and Dravis, J.J., 1985, Blue fluorescent dye technique for recognition of microporosity in sedimentary rocks: *Journal of Sedimentary Petrology*, v. 55, p. 600–602.

APPENDIX A:

FIELD MAPS AND CROSS SECTIONS, LISBON FIELD, SAN JUAN COUNTY, UTAH

Link to supplemental data download:

<https://ugspub.nr.utah.gov/publications/bulletins/b-139/b-139-a.zip>

APPENDIX B:

**CORE DESCRIPTIONS, CORE PHOTOGRAPHS, AND CORE ANALYSIS,
LISBON FIELD, SAN JUAN COUNTY, UTAH**

Link to supplemental data download:
<https://ugspub.nr.utah.gov/publications/bulletins/b-139/b-139-b.zip>

APPENDIX C:

**GEOPHYSICAL WELL LOGS TIED TO CORE DESCRIPTIONS, LISBON FIELD,
SAN JUAN COUNTY, UTAH**

Link to supplemental data download:

<https://ugspub.nr.utah.gov/publications/bulletins/b-139/b-139-c.pdf>

APPENDIX D:**CATALOG OF LEADVILLE POROSITY TYPES AND DIAGENESIS, LISBON FIELD,
SAN JUAN COUNTY, UTAH**

Link to supplemental data download:

<https://ugspub.nr.utah.gov/publications/bulletins/b-139/b-139-d.pdf>

APPENDIX E:

**SCANNING ELECTRON MICROSCOPY, EPIFLUORESCENCE,
CATHODOLUMINESCENCE, AND FLUID INCLUSIONS, LISBON FIELD,
SAN JUAN COUNTY, UTAH**

Link to supplemental data download:

<https://ugspub.nr.utah.gov/publications/bulletins/b-139/b-139-e.pdf>

APPENDIX F:**EPIFLUORESCENCE ANALYSES AND DESCRIPTIONS OF WELLCUTTINGS FROM
THE PARADOX FOLD AND FAULT BELT AREA, UTAH**

Link to supplemental data download:

<https://ugspub.nr.utah.gov/publications/bulletins/b-139/b-139-f.pdf>

APPENDIX G:

REGIONAL STRATIGRAPHIC CROSS SECTIONS, PARADOX BASIN, UTAH

Link to supplemental data download:

<https://ugspub.nr.utah.gov/publications/bulletins/b-139/b-139-g.pdf>

APPENDIX H:**REGIONAL LEADVILLE FACIES AND CORE DESCRIPTIONS FROM WELLS IN
THE PARADOX AND FAULT BELT AREA, UTAH**

Link to supplemental data download:

<https://ugspub.nr.utah.gov/publications/bulletins/b-139/b-139-h.pdf>

APPENDIX I:

**MEASURED STRATIGRAPHIC SECTIONS, MISSISSIPPIAN MADISON LIMESTONE,
SOUTHERN FLANK OF THE UINTA MOUNTAINS**

Link to supplemental data download:

<https://ugspub.nr.utah.gov/publications/bulletins/b-139/b-139-i.pdf>